rapy Solutions

by MicroVention®

HydroFrame®

HydroCoil® Embolic System

HydroFill®

HydroCoil® Embolic System

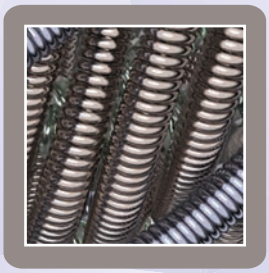

HydroSoft®

HydroCoil® Embolic System

HYDROGEL ADVANCED COILS

The clinical benefits of **Hydrogel** NOW engineered with the softness of bare platinum on the **V-Trak® Advanced Coil System**.

- CLINICALLY STUDIED HYDROGEL
- EFFECTIVE[1,2,3]
- ESTABLISHED SAFETY PROFILE[4]
- SOFTER DESIGN[5]

For more information or a product demonstration, contact your local MicroVention representative:

MicroVention® TERUMO

MicroVention, Inc.
Worldwide Headquarters PH +1.714.247.8000
1311 Valencia Avenue
Tustin, CA 92780 USA
MicroVention UK Limited PH +44 (0) 191 258 6777
MicroVention Europe, S.A.R.L. PH +33 (1) 39 21 77 46
MicroVention Deutschland GmbH PH +49 211 210 798-0
microvention.com

stryker

NEW

Indication for Trevo® Retrievers

A New Standard of Care in Stroke

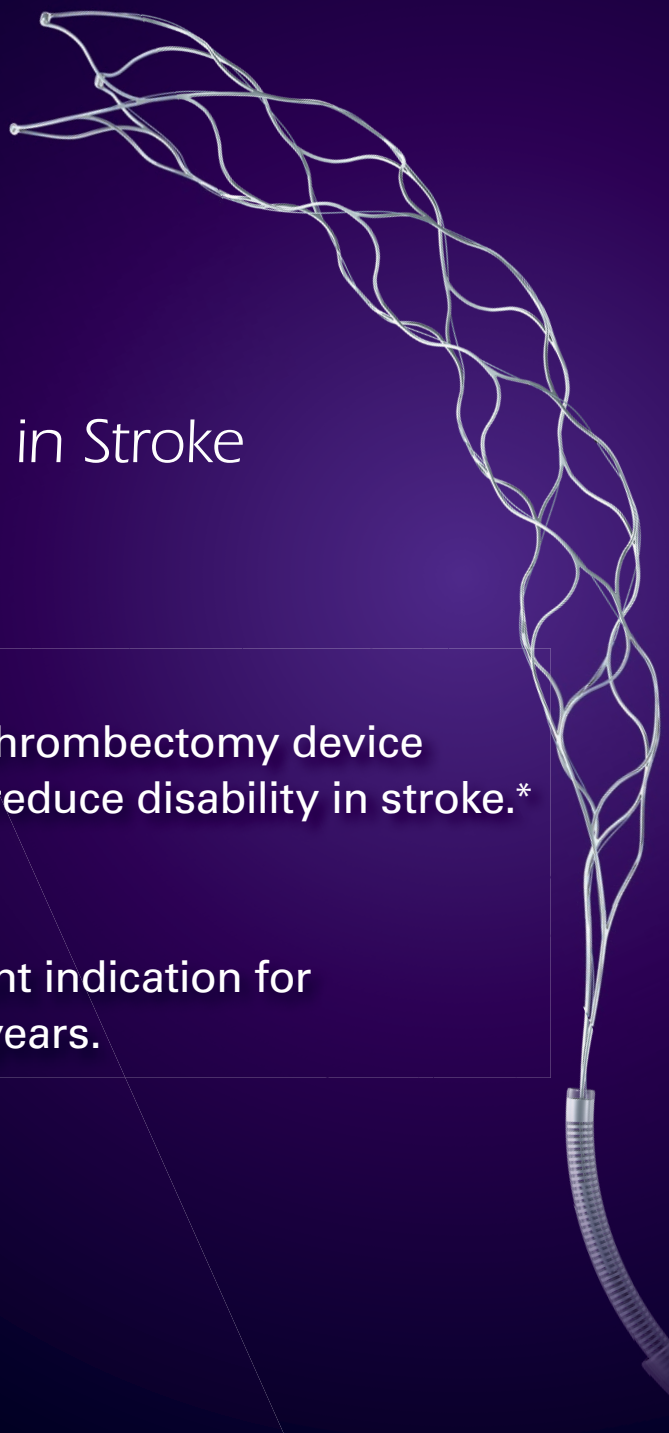

1st

FIRST
mechanical thrombectomy device indicated to reduce disability in stroke.*

FIRST
new treatment indication for stroke in 20 years.

Trevo XP
PROVUE RETRIEVER

Success accelerated.

*The Trevo Retriever is indicated for use to restore blood flow in the neurovasculature by removing thrombus for the treatment of acute ischemic stroke to reduce disability in patients with a persistent, proximal anterior circulation, large vessel occlusion, and smaller core infarcts who have first received intravenous tissue plasminogen activator (IV t-PA). Endovascular therapy with the device should start within 6 hours of symptom onset.

Magic

BALT

FLOW-DEPENDENT MICROCATHETER

NOW AVAILABLE THROUGH BLOCKADE™ MEDICAL

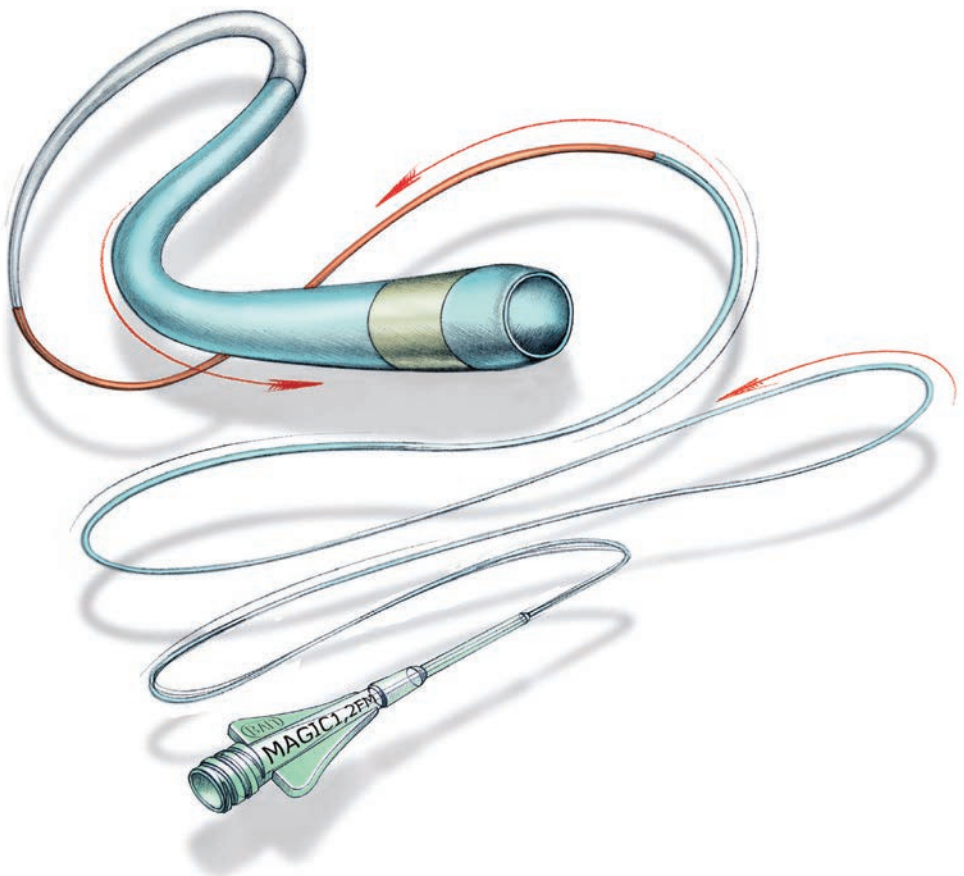

ORDERMAGICS@BLOCKADEMEDICAL.COM

MAGIC catheters are designed for general intravascular use. They may be used for the controlled, selective regional infusion of therapeutic agents or embolic materials into vessels.[1]

1. Magic Catheters IFU – Ind 19

MKTG-068 Rev. A

18 Technology Drive #169, Irvine Ca 92618
P 949.788.1443 | **F** 949.788.1444

BLOCKADE MEDICAL
A BALT Company

The brain at your fingertips

Rapid Medical

www.rapid-medical.com > tigertriever

ASNR 56th Annual Meeting & The Foundation of the ASNR Symposium 2018

The Vancouver Convention Centre East

Welcome and Greetings

Please join us in Vancouver, CANADA for the **56th Annual Meeting of the American Society of Neuroradiology** on June 2–7, 2018 at the Vancouver Convention Centre East. Surrounded by the coastal mountains and located on the waterfront, you can enjoy these spectacular views in the heart of downtown Vancouver. With its undeniable charm and friendly atmosphere, Vancouver is known around the world as both a popular tourist attraction and one of the best places to live.

ASNR enthusiastically presents **Neuroradiology: Adding Value and Improving Healthcare** at the Symposium of the Foundation of the ASNR, as well as the common thread throughout the Annual Meeting. Implementing a value-based strategy in imaging has grasped the attention of nearly every healthcare provider; in particular with Radiologists understanding that the future will demand their imaging practices deliver better value. Value in healthcare is typically defined as those imaging strategies that yield improved outcomes, lower costs, or both. As payment transitions from a fee-for-service to a value-based system, thus creating a fundamentally different marketplace dynamic, measuring good outcomes are at the center of this changeover. At this time of uncertainty what little remains clear is that without a well-defined knowledge of their outcomes, no medical specialty will be able to succeed in the future value-based system. The Symposium will feature how Neuroradiology, in its many subspecialty areas, adds value to clinical care pathways by directing healthcare practice towards better outcomes. The annual meeting programming will continue on this theme emphasizing imaging that improves health outcomes, while considering costs, thus adding value. Our discussions will incorporate many innovative approaches to how neuroimaging currently does and will continue to improve overall healthcare performance.

As the Program Chair for ASNR 2018, it is my pleasure and honor to welcome you to Vancouver, CANADA for our annual meeting! Vancouver is known for being a very walkable city with a compact downtown core hosting many places to enjoy. So pack your comfortable walking shoes and let's tour together with our colleagues and friends!

Pina Sanelli

Pina C. Sanelli, MD, MPH, FACR
ASNR 2018 Program Chair/President-Elect

NEURORADIOLOGY
Adding Value & Improving Healthcare

ASNR 2018 ▪ VANCOUVER

ASFNR ASHNR ASPNR ASSR SNIS

THE FOUNDATION OF THE ASNR

Pina C. Sanelli, MD, MPH, FACR
ASNR 2018 Program Chair/President-Elect

Programming developed in cooperation with the…

American Society of Functional Neuroradiology (ASFNR)
Max Wintermark, MD

American Society of Head and Neck Radiology (ASHNR)
Deborah R. Shatzkes, MD

American Society of Pediatric Neuroradiology (ASPNR)
Ashok Panigrahy, MD

American Society of Spine Radiology (ASSR)
John D. Barr, MD, FACR, FSIR, FAHA

Society of NeuroInterventional Surgery (SNIS)
Mahesh V. Jayaraman, MD

ASNR Health Policy (HPC) Committee
Robert M. Barr, MD, FACR

ASNR Computer Sciences & Informatics (CSI) Committee
John L. Go, MD, FACR

ASNR Research Scientist Programming Committee
Dikoma C. Shungu, PhD, Timothy P.L. Roberts, PhD

The International Hydrocephalus Imaging Working Group (IHIWG) / CSF Flow Group
William G. Bradley, Jr., MD, PhD, FACR, Harold L. Rekate, MD and Bryn A. Martin, PhD

Fairmont Waterfront Hotel

Pan Pacific Hotel

ASNR 56th Annual Meeting
c/o American Society of Neuroradiology
800 Enterprise Drive, Suite 205
Oak Brook, Illinois 60523-4216
Phone: 630-574-0220 + Fax: 630 574-0661
2018.asnr.org

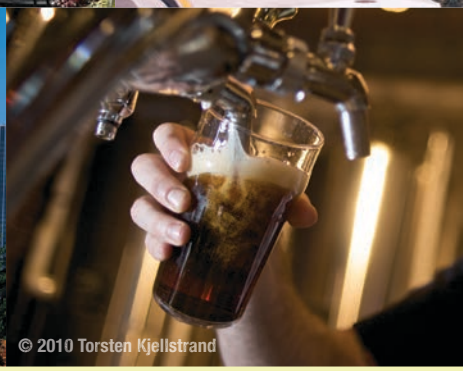

WE'VE MOVED TO FALL 2017!

11th Annual Meeting of the

American Society of

FUNCTIONAL NEURORADIOLOGY

October 9-11, 2017 • the Nines • Portland, Oregon

Optional Hands-on BOLD fMRI Workshop • October 8, 2017

PLEASE CONTACT EDUCATIONAL SYMPOSIA AT
813-806-1000 or ASFNR@edusymp.com or visit www.ASFNR.org for additional information.

The Korean Society of Radiology

K-RAD Open · Balanced Sustainable

KCR 2017

The 73rd Korean Congress of Radiology
And Annual Delegate Meeting of
The Korean Society of Radiology

2017.10.25 Wed – 2017.10.28 Sat
Coex, Seoul, Korea

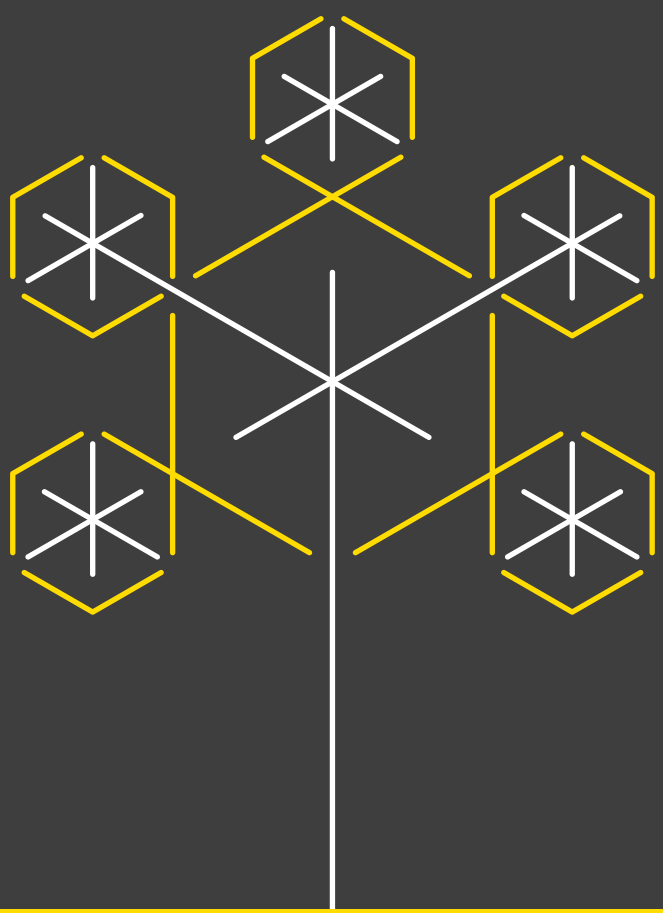

Important Dates

- Abstract Submission — by May 31 (Wed)
- Abstract Acceptance Notice — on July 5 (Wed)
- Presenter Registration — by July 31 (Mon)
- Early Registration — by July 31 (Mon)
- Pre-registration — by August 31 (Thu)
- Hotel Reservation — by August 31 (Thu)

Hosted by **The Korean Society of Radiology**

www.kcr4u.org

We're Inside Every Great Neuroradiologist!

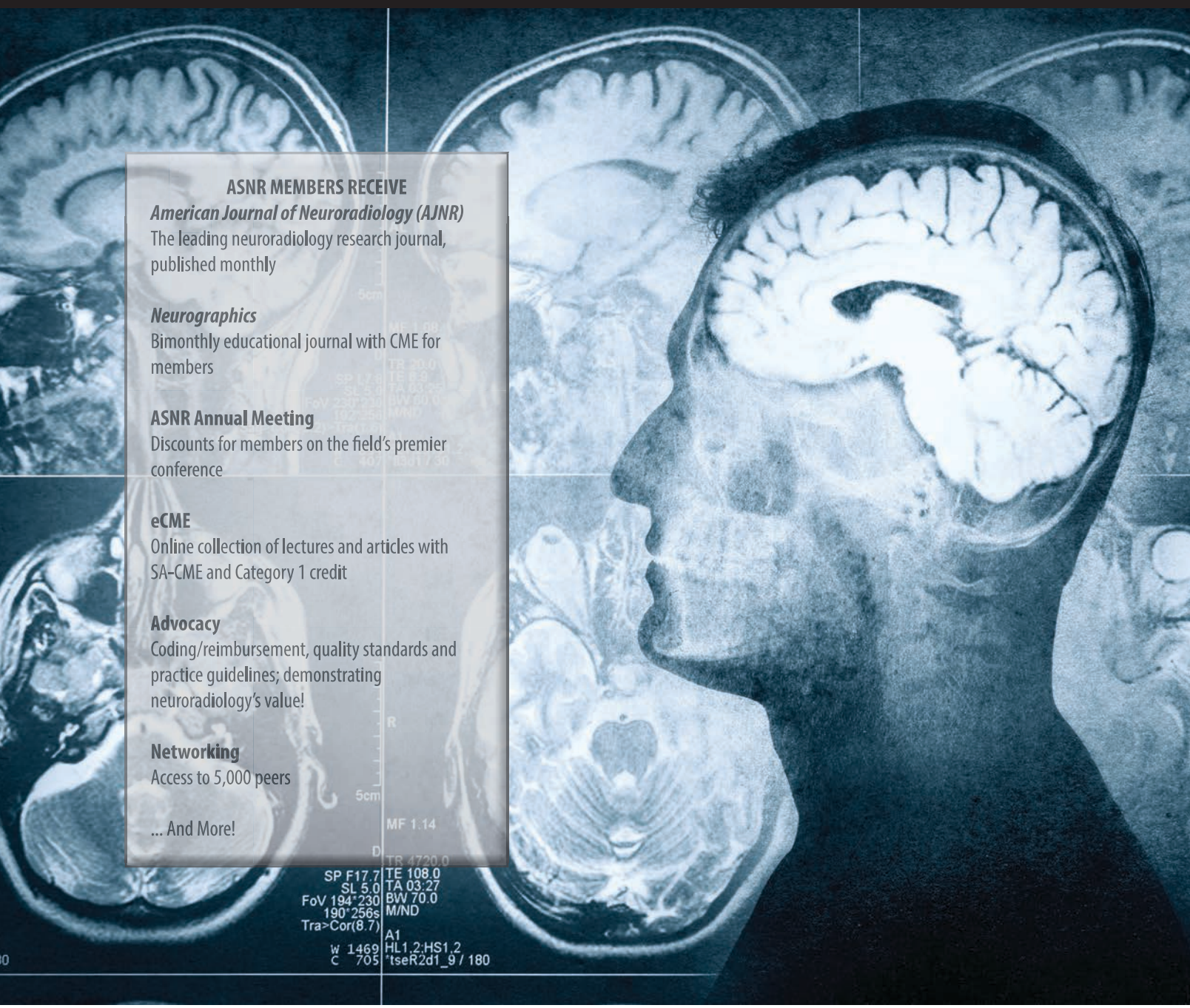

Join the leaders in neuroradiology today!
Learn more at www.asnr.org/join

ASNR
American Society of Neuroradiology

800 Enterprise Dr., Suite 205, Oak Brook, IL 60523 • (630)574-0220 • membership@asnr.org • www.asnr.org

ASHNR
American Society of
Head & Neck Radiology

51st Annual Meeting

American Society of

Head & Neck Radiology

Head and Neck Imaging in the City of Lights

Caesars Palace • Las Vegas, NV

September 16 – 20, 2017
(Saturday - Wednesday)

Please contact Educational Symposia at 813-806-1000 or ASHNR@edusymp.com or visit www.ASHNR.org for additional information.

Trevo® XP ProVue Retrievers

See package insert for complete indications, complications, warnings, and instructions for use.

INDICATIONS FOR USE

1. The Trevo Retriever is indicated for use to restore blood flow in the neurovasculature by removing thrombus for the treatment of acute ischemic stroke to reduce disability in patients with a persistent, proximal anterior circulation, large vessel occlusion, and smaller core infarcts who have first received intravenous tissue plasminogen activator (IV t-PA). Endovascular therapy with the device should start within 6 hours of symptom onset.
2. The Trevo Retriever is intended to restore blood flow in the neurovasculature by removing thrombus in patients experiencing ischemic stroke within 8 hours of symptom onset. Patients who are ineligible for intravenous tissue plasminogen activator (IV t-PA) or who fail IV t-PA therapy are candidates for treatment.

COMPLICATIONS

Procedures requiring percutaneous catheter introduction should not be attempted by physicians unfamiliar with possible complications which may occur during or after the procedure. Possible complications include, but are not limited to, the following: air embolism; hematoma or hemorrhage at puncture site; infection; distal embolization; pain/headache; vessel spasm, thrombosis, dissection, or perforation; emboli; acute occlusion; ischemia; intracranial hemorrhage; false aneurysm formation; neurological deficits including stroke; and death.

COMPATIBILITY

3x20mm retrievers are compatible with Trevo® Pro 14 Microcatheters (REF 90231) and Trevo® Pro 18 Microcatheters (REF 90238). 4x20mm retrievers are compatible with Trevo® Pro 18 Microcatheters (REF 90238). 4x30mm retrievers are compatible with Excelsior® XT-27® Microcatheters (150cm x 6cm straight REF 275081) and Trevo® Pro 18 Microcatheters (REF 90238). 6x25mm Retrievers are compatible with Excelsior® XT-27® Microcatheters (150cm x 6cm straight REF 275081). Compatibility of the Retriever with other microcatheters has not been established. Performance of the Retriever device may be impacted if a different microcatheter is used.

Balloon Guide Catheters (such as Merci® Balloon Guide Catheter and FlowGate® Balloon Guide Catheter) are recommended for use during thrombus removal procedures.

Retrievers are compatible with the Abbott Vascular DOC® Guide Wire Extension (REF 22260).

Retrievers are compatible with Boston Scientific RHV (Ref 421242).

SPECIFIC WARNINGS FOR INDICATION 1

- The safety and effectiveness of the Trevo Retrievers in reducing disability has not been established in patients with large core infarcts (i.e., ASPECTS ≤ 7). There may be increased risks, such as intracerebral hemorrhage, in these patients.
- The safety and effectiveness of the Trevo Retrievers in reducing disability has not been established or evaluated in patients with occlusions in the posterior circulation (e.g., basilar or vertebral arteries) or for more distal occlusions in the anterior circulation.

WARNINGS APPLIED TO BOTH INDICATIONS

- Administration of IV t-PA should be within the FDA-approved window (within 3 hours of stroke symptom onset).
- Contents supplied STERILE, using an ethylene oxide (EO) process. Nonpyrogenic.
- To reduce risk of vessel damage, adhere to the following recommendations:
  - Take care to appropriately size Retriever to vessel diameter at intended site of deployment.
  - Do not perform more than six (6) retrieval attempts in same vessel using Retriever devices.
  - Maintain Retriever position in vessel when removing or exchanging Microcatheter.
- To reduce risk of kinking/fracture, adhere to the following recommendations:
  - Immediately after unsheathing Retriever, position Microcatheter tip marker just proximal to shaped section. Maintain Microcatheter tip marker just proximal to shaped section of Retriever during manipulation and withdrawal.
  - Do not rotate or torque Retriever.
  - Use caution when passing Retriever through stented arteries.
- Do not resterilize and reuse. Structural integrity and/or function may be impaired by reuse or cleaning.
- The Retriever is a delicate instrument and should be handled carefully. Before use and when possible during procedure, inspect device carefully for damage. Do not use a device that shows signs of damage. Damage may prevent device from functioning and may cause complications.
- Do not advance or withdraw Retriever against resistance or significant vasospasm. Moving or torquing device against resistance or significant vasospasm may result in damage to vessel or device. Assess cause of resistance using fluoroscopy and if needed resheath the device to withdraw.
- If Retriever is difficult to withdraw from the vessel, do not torque Retriever. Advance Microcatheter distally, gently pull Retriever back into Microcatheter, and remove Retriever and Microcatheter as a unit. If undue resistance is met when withdrawing the Retriever into the Microcatheter, consider extending the Retriever using the Abbott Vascular DOC guidewire extension (REF 22260) so that the Microcatheter can be exchanged for a larger diameter catheter such as a DAC® catheter. Gently withdraw the Retriever into the larger diameter catheter.
- Administer anti-coagulation and anti-platelet medications per standard institutional guidelines.

PRECAUTIONS

- Prescription only – device restricted to use by or on order of a physician.
- Store in cool, dry, dark place.
- Do not use open or damaged packages.
- Use by "Use By" date.
- Exposure to temperatures above 54°C (130°F) may damage device and accessories. Do not autoclave.
- Do not expose Retriever to solvents.
- Use Retriever in conjunction with fluoroscopic visualization and proper anti-coagulation agents.
- To prevent thrombus formation and contrast media crystal formation, maintain a constant infusion of appropriate flush solution between guide catheter and Microcatheter and between Microcatheter and Retriever or guidewire.
- Do not attach a torque device to the shaped proximal end of DOC® Compatible Retriever. Damage may occur, preventing ability to attach DOC® Guide Wire Extension.

Concentric Medical
301 East Evelyn Avenue
Mountain View, CA 94041

Stryker Neurovascular
47900 Bayside Parkway
Fremont, CA 94538

strykerneurovascular.com

Date of Release: SEP/2016

EX_EN_US

NV00018973.AB

Target® Detachable Coil

See package insert for complete indications, contraindications, warnings and instructions for use.

INTENDED USE / INDICATIONS FOR USE

Target Detachable Coils are intended to endovascularly obstruct or occlude blood flow in vascular abnormalities of the neurovascular and peripheral vessels.

Target Detachable Coils are indicated for endovascular embolization of:

- Intracranial aneurysms
- Other neurovascular abnormalities such as arteriovenous malformations and arteriovenous fistulae
- Arterial and venous embolizations in the peripheral vasculature

CONTRAINDICATIONS

None known.

POTENTIAL ADVERSE EVENTS

Potential complications include, but are not limited to: allergic reaction, aneurysm perforation and rupture, arrhythmia, death, edema, embolus, headache, hemorrhage, infection, ischemia, neurological/intracranial sequelae, post-embolization syndrome (fever, increased white blood cell count, discomfort), TIA/stroke, vasospasm, vessel occlusion or closure, vessel perforation, dissection, trauma or damage, vessel rupture, vessel thrombosis. Other procedural complications including but not limited to: anesthetic and contrast media risks, hypotension, hypertension, access site complications.

WARNINGS

- Contents supplied STERILE using an ethylene oxide (EO) process. Do not use if sterile barrier is damaged. If damage is found, call your Stryker Neurovascular representative.
- For single use only. Do not reuse, reprocess or resterilize. Reuse, reprocessing or resterilization may compromise the structural integrity of the device and/or lead to device failure which, in turn, may result in patient injury, illness or death. Reuse, reprocessing or resterilization may also create a risk of contamination of the device and/or cause patient infection or cross-infection, including, but not limited to, the transmission of infectious disease(s) from one patient to another. Contamination of the device may lead to injury, illness or death of the patient.
- After use, dispose of product and packaging in accordance with hospital, administrative and/or local government policy.
- **This device should only be used by physicians who have received appropriate training in interventional neuroradiology or interventional radiology and preclinical training on the use of this device as established by Stryker Neurovascular.**
- Patients with hypersensitivity to 316LVM stainless steel may suffer an allergic reaction to this implant.
- MR temperature testing was not conducted in peripheral vasculature, arteriovenous malformations or fistulae models.
- The safety and performance characteristics of the Target Detachable Coil System (Target Detachable Coils, InZone Detachment Systems, delivery systems and accessories) have not been demonstrated with other manufacturer's devices (whether coils, coil delivery devices, coil detachment systems, catheters, guidewires, and/or other accessories). Due to the potential incompatibility of non Stryker Neurovascular devices with the Target Detachable Coil System, the use of other manufacturer's device(s) with the Target Detachable Coil System is not recommended.
- To reduce risk of coil migration, the diameter of the first and second coil should never be less than the width of the ostium.
- In order to achieve optimal performance of the Target Detachable Coil System and to reduce the risk of thromboembolic complications, it is critical that a continuous infusion of appropriate flush solution be maintained between a) the femoral sheath and guiding catheter, b) the 2-tip microcatheter and guiding catheters, and c) the 2-tip microcatheter and Stryker Neurovascular guidewire and delivery wire. Continuous flush also reduces the potential for thrombus formation on, and crystallization of infusate around, the detachment zone of the Target Detachable Coil.
- Do not use the product after the "Use By" date specified on the package.
- Reuse of the flush port/dispenser coil or use with any coil other than the original coil may result in contamination of, or damage to, the coil.
- Utilization of damaged coils may affect coil delivery to, and stability inside, the vessel or aneurysm, possibly resulting in coil migration and/or stretching.
- The fluoro-saver marker is designed for use with a Rotating Hemostatic Valve (RHV). If used without an RHV, the distal end of the coil may be beyond the alignment marker when the fluoro-saver marker reaches the microcatheter hub.
- If the fluoro-saver marker is not visible, do not advance the coil without fluoroscopy.
- Do not rotate delivery wire during or after delivery of the coil. Rotating the Target Detachable Coil delivery wire may result in a stretched coil or premature detachment of the coil from the delivery wire, which could result in coil migration.
- Verify there is no coil loop protrusion into the parent vessel after coil placement and prior to coil detachment. Coil loop protrusion after coil placement may result in thromboembolic events if the coil is detached.
- Verify there is no movement of the coil after coil placement and prior to coil detachment. Movement of the coil after coil placement may indicate that the coil could migrate once it is detached.
- Failure to properly close the RHV compression fitting over the delivery wire before attaching the InZone® Detachment System could result in coil movement, aneurysm rupture or vessel perforation.
- Verify repeatedly that the distal shaft of the catheter is not under stress before detaching the Target Detachable Coil. Axial compression or tension forces could be stored in the 2-tip microcatheter causing the tip to move during coil delivery. Microcatheter tip movement could cause the aneurysm or vessel to rupture.
- Advancing the delivery wire beyond the microcatheter tip once the coil has been detached involves risk of aneurysm or vessel perforation.
- The long term effect of this product on extravascular tissues has not been established so care should be taken to retain this device in the intravascular space.

Damaged delivery wires may cause detachment failures, vessel injury or unpredictable distal tip response during coil deployment. If a delivery wire is damaged at any point during the procedure, do not attempt to straighten or otherwise repair it. Do not proceed with deployment or detachment. Remove the entire coil and replace with undamaged product.

- After use, dispose of product and packaging in accordance with hospital, administrative and/or local government policy.

CAUTIONS / PRECAUTIONS

- Federal Law (USA) restricts this device to sale by or on the order of a physician.
- Besides the number of InZone Detachment System units needed to complete the case, there must be an extra InZone Detachment System unit as back up.
- Removing the delivery wire without grasping the introducer sheath and delivery wire together may result in the detachable coil sliding out of the introducer sheath.
- Failure to remove the introducer sheath after inserting the delivery wire into the RHV of the microcatheter will interrupt normal infusion of flush solution and allow back flow of blood into the microcatheter.
- Some low level overhead light near or adjacent to the patient is required to visualize the fluoro-saver marker; monitor light alone will not allow sufficient visualization of the fluoro-saver marker.
- Advance and retract the Target Detachable Coil carefully and smoothly without excessive force. If unusual friction is noticed, slowly withdraw the Target Detachable Coil and examine for damage. If damage is present, remove and use a new Target Detachable Coil. If friction or resistance is still noted, carefully remove the Target Detachable Coil and microcatheter and examine the microcatheter for damage.
- If it is necessary to reposition the Target Detachable Coil, verify under fluoroscopy that the coil moves with a one-to-one motion. If the coil does not move with a one-to-one motion or movement is difficult, the coil may have stretched and could possibly migrate or break. Gently remove both the coil and microcatheter and replace with new devices.
- Increased detachment times may occur when:
  - Other embolic agents are present.
  - Delivery wire and microcatheter markers are not properly aligned.
  - Thrombus is present on the coil detachment zone.
- Do not use detachment systems other than the InZone Detachment System.
- Increased detachment times may occur when delivery wire and microcatheter markers are not properly aligned.
- Do not use detachment systems other than the InZone Detachment System.

Stryker Neurovascular
47900 Bayside Parkway
Fremont, CA 94538

strykerneurovascular.com

Date of Release: MAR/2016

EX_EN_US

NV00018669.AB

Aneurysm The

V-Trak® Advanced Coil System

ENHANCED CONTROL TO MAXIMIZE COIL PERFORMANCE

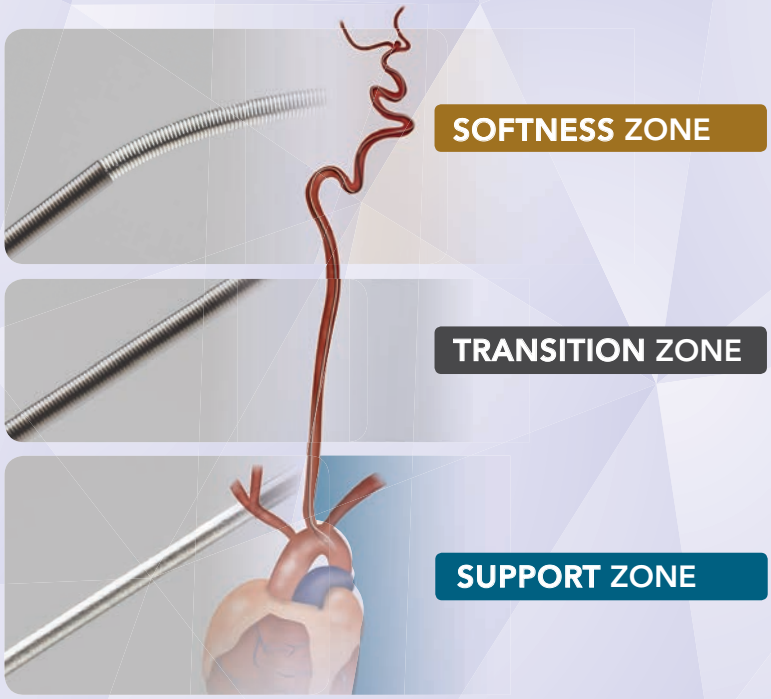

The **V-Trak® Advanced Coil System,** the next generation to power the performance of our most technically advanced line of coils. Offering the optimal combination of support and flexibility.

References
1. Speirs, Burke, Lee, and Ala. The next generation HydroCoil: initial clinical experience with the HydroFill embolic coil. J NeuroIntervent Surg, 2013.
2. Brinjikiji et al. Abstract 112. Presented at: International Stroke Conference 2015, Nashville, Tennessee, February 11-13, 2015.
3. Lee, Seo, Less, Cho, Kang and Han. Mid-term outcome of intracranial aneurysms treated with HydroSoft coils compared to historical controls treated with bare platinum coils: a single-center experience. Acta Neurochir, 156:1687-1694, 2014.
4. Laymond et al. Patients prone to recurrence after endovascular treatment: periprocedural results of the PRET randomized trial on large and recurrent aneurysms, AJNR AM J Neuroradiol, 2014.
5. Data on file at MicroVention, Inc.

INDICATIONS FOR USE:
The HydroCoil® Embolic System (HES) is intended for the endovascular embolization of intracranial aneurysms and other neurovascular abnormalities such as arteriovenous malformations and arteriovenous fistulae. The HES is also intended for vascular occlusion of blood vessels within the neurovascular system to permanently obstruct blood flow to an aneurysm or other vascular malformation and for arterial and venous embolizations in the peripheral vasculature. The device should only be used by physicians who have undergone pre-clinical training in all aspects of HES procedures as prescribed by MicroVention.

CE 0297

stryker®
Neurovascular

Purposeful innovation in mind.

Smooth and stable.

Target Detachable Coils deliver consistently smooth deployment and exceptional microcatheter stability. Designed to work seamlessly together for framing, filling and finishing. Target Coils deliver the high performance you demand.

For more information, please visit www.strykerneurovascular.com/Target or contact your local Stryker Neurovascular sales representative.

Target®
DETACHABLE COILS

NV00018669.AA

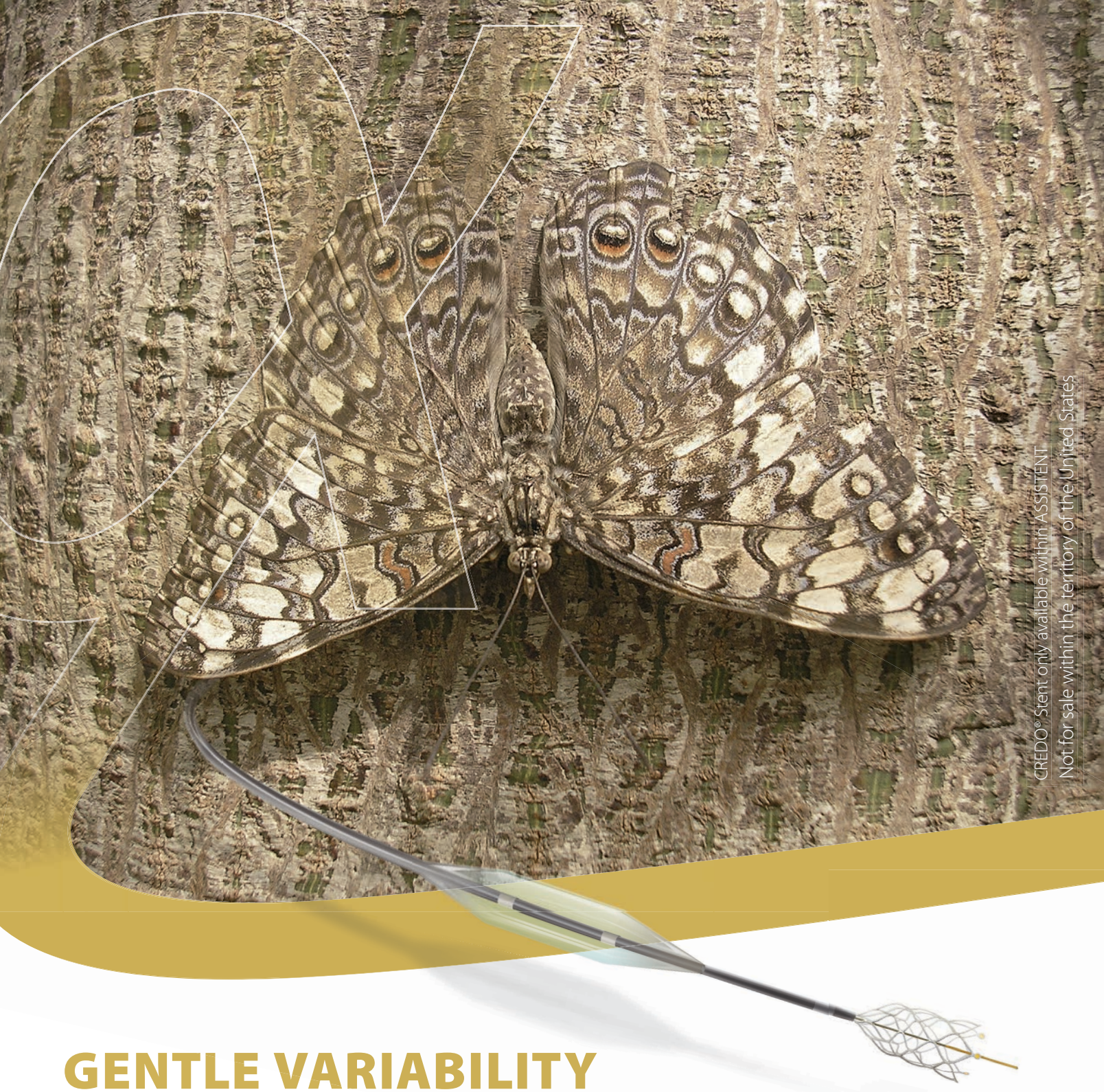

CREDO® Stent only available within ASSISTENT.
Not for sale within the territory of the United States.

GENTLE VARIABILITY

CREDO® Stent with NeuroSpeed® PTA Balloon Catheter

Unique treatment concept comprising a flexible self-expanding stent deliverable through a compliant PTA balloon catheter for gentle, efficient and timesaving treatment of intracranial stenosis.

VARIABLE. EFFICIENT. GENTLE.

www.acandis.com

acandis®

ENGINEERING STROKE SOLUTIONS

AJNR

AMERICAN JOURNAL OF NEURORADIOLOGY

MAY 2017
VOLUME 38
NUMBER 5
WWW.AJNR.ORG

THE JOURNAL OF DIAGNOSTIC AND INTERVENTIONAL NEURORADIOLOGY

Abnormalities in congenital Zika syndrome with and without arthrogryposis

Thrombus fragmentation during endovascular stroke treatment

Imaging characteristics of diffuse intracranial dolichoectasia

Official Journal ASNR • ASFNR • ASHNR • ASPNR • ASSR

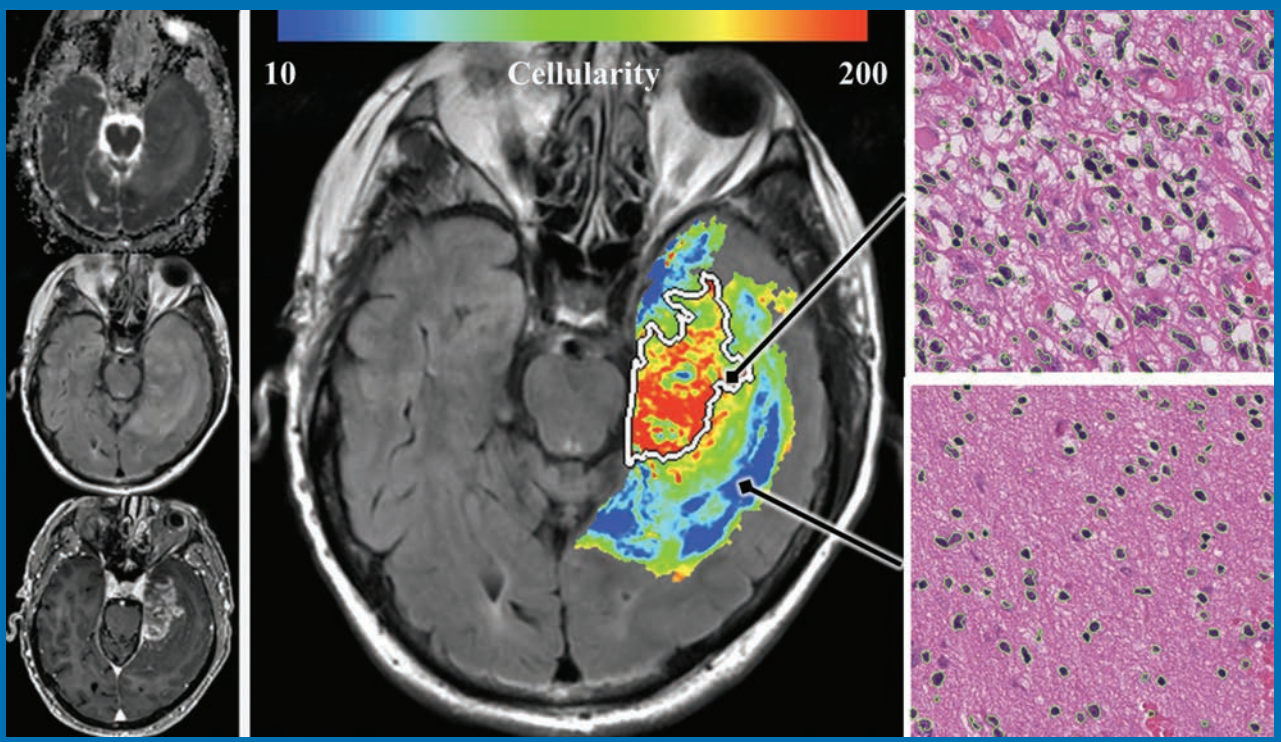

AJNR

AMERICAN JOURNAL OF NEURORADIOLOGY

MAY 2017
VOLUME 38
NUMBER 5
WWW.AJNR.ORG

Publication Preview at www.ajnr.org features articles released in advance of print. Visit www.ajnrblog.org to comment on AJNR content and chat with colleagues and AJNR's News Digest at http://ajnrdigest.org to read the stories behind the latest research in neuroimaging.

AJNR (Am J Neuroradiol ISSN 0195–6108) is a journal published monthly, owned and published by the American Society of Neuroradiology (ASNR), 800 Enterprise Drive, Suite 205, Oak Brook, IL 60523. Annual dues for the ASNR include $170.00 for journal subscription. The journal is printed by Cadmus Journal Services, 5457 Twin Knolls Road, Suite 200, Columbia, MD 21045; Periodicals postage paid at Oak Brook, IL and additional mailing offices. Printed in the U.S.A. POSTMASTER: Please send address changes to American Journal of Neuroradiology, P.O. Box 3000, Denville, NJ 07834, U.S.A. Subscription rates: nonmember $390 ($460 foreign) print and online, $310 online only; institutions $450 ($520 foreign) print and basic online, $895 ($960 foreign) print and extended online, $370 online only (basic), extended online $805; single copies are $35 each ($40 foreign). Indexed by PubMed/Medline, BIOSIS Previews, Current Contents (Clinical Medicine and Life Sciences), EMBASE, Google Scholar, HighWire Press, Q-Sensei, RefSeek, Science Citation Index, and SCI Expanded.

ONLINE FEATURES

LETTERS

BOOK REVIEWS *R.M. Quencer, Section Editor*

Please visit www.ajnrblog.org to read and comment on Book Reviews.

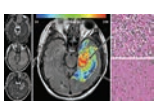

ADC, FLAIR, T1 C+ images (left) are utilized to estimate tumor cellularity (middle). Histopathology (right) shows variation in cellularity around the area of tumor enhancement.

Indicates Editor's Choices selection

Indicates Fellows' Journal Club selection

Indicates open access to non-subscribers at www.ajnr.org

Indicates article with supplemental on-line table

Indicates article with supplemental on-line photo

Indicates article with supplemental on-line video

Evidence-Based Medicine Level 1

Evidence-Based Medicine Level 2

AJNR

AMERICAN JOURNAL OF NEURORADIOLOGY

Publication Preview at www.ajnr.org features articles released in advance of print. Visit www.ajnrblog.org to comment on AJNR content and chat with colleagues and AJNR's News Digest at http://ajnrdigest.org to read the stories behind the latest research in neuroimaging.

MAY 2017 • VOLUME 38 • NUMBER 5 • WWW.AJNR.ORG

Official Journal:
American Society of Neuroradiology
American Society of Functional Neuroradiology
American Society of Head and Neck Radiology
American Society of Pediatric Neuroradiology
American Society of Spine Radiology

Title: Big Hole. Big Hole is a sidewater loop of the Myakka River southeast of Sarasota, Florida in the Myakka River State Park. For unknown reasons, it is an extremely popular area for "alligator lounging" with as many as 70–80 gators often visible at any one time. This, coupled with its natural beauty, makes the 2.5-mile hike popular among those seeking to refresh themselves "far from the things of man!"

John H. Rees, Chief, Neuroradiology, Partners Imaging Center, Bradenton, Florida

Benign Spine Lesions: Advances in Techniques for Minimally Invasive Percutaneous Treatment

A. Tomasian, A.N. Wallace, and J.W. Jennings

ABSTRACT

SUMMARY: Minimally invasive percutaneous imaging-guided techniques have been shown to be safe and effective for the treatment of benign tumors of the spine. Techniques available include a variety of tumor ablation technologies, including radiofrequency ablation, cryoablation, microwave ablation, alcohol ablation, and laser photocoagulation. Vertebral augmentation may be performed after ablation as part of the same procedure for fracture stabilization or prevention. Typically, the treatment goal in benign spine lesions is definitive cure. Painful benign spine lesions commonly encountered in daily practice include osteoid osteoma, osteoblastoma, vertebral hemangioma, aneurysmal bone cyst, Paget disease, and subacute/chronic Schmorl node. This review discusses the most recent advancement and use of minimally invasive percutaneous therapeutic options for the management of benign spine lesions.

ABBREVIATIONS: PVA = percutaneous vertebral augmentation; RF = radiofrequency; RFA = radiofrequency ablation

The role of minimally invasive percutaneous imaging-guided techniques for the treatment of benign tumors of the spine has increased during the past decade. Although previously limited by the complex anatomy of the vertebral column and the proximity of neural elements, new technologies, including radiofrequency ablation (RFA), cryoablation, microwave ablation, alcohol ablation, and laser photocoagulation, now provide an attractive alternative or adjunct therapeutic options for the treatment of benign spinal tumors beyond medical pain management, surgery, radiation therapy, and standard vertebral augmentation.

Benign tumors compose only 4%–13% of spinal lesions[1] and are treated with curative intent. Most commonly, the pain secondary to benign spine lesions is managed with nonsteroidal antiinflammatory drugs and opioids titrated to achieve pain relief while attempting to minimize side effects.[2] In the absence of neurologic deficits and spinal instability, radiation therapy may be the standard of care when medical management is insufficient.[3–6] Although described in malignant spine lesions, pain relief following radiation therapy may be delayed and transient.[7] Surgical interventions are invasive and result in increased morbidity, which, in the absence of pending neurologic compromise and instability, is undesirable for these patients.

Minimally invasive, percutaneous, image-guided interventions for the management of benign spine lesions are indicated when pharmacologic therapy (analgesics and nonsteroidal antiinflammatory drugs) is inadequate or contraindicated (such as side effects and pregnancy), radiation therapy is contraindicated or not desired by the patient, and surgical intervention is not recommended (absence of spinal instability and neurologic compromise). The contraindications include spinal instability with or without concomitant pathologic fracture, focal neurologic deficit, advanced coagulopathy, and systemic infection. Although no published literature exists directly comparing an operation with percutaneous ablation, these minimally invasive percutaneous procedures may be more cost-effective compared with traditional surgical interventions. This review details the armamentarium available and the most recent advances in minimally invasive, image-guided percutaneous techniques for the treatment of benign spinal lesions.

General Considerations, Procedural Setup, and Patient Care

Preprocedural consultation with the patient is mandatory and should include an explanation of the benefits, risks, potential complications, and alternative treatment options. In addition, the patient's clinical status and procedural indications should be discussed with the referring clinicians. Initial preprocedural work-up includes a history and physical examination to confirm focal pain/tenderness at the lesion site and neurologic examina-

From the Department of Radiology (A.T.), University of Southern California, Los Angeles, California; and Mallinckrodt Institute of Radiology (A.N.W., J.W.J.), St Louis, Missouri.

Please address correspondence to Anderanik Tomasian, MD, Department of Radiology, University of Southern California, 1500 San Pablo St, Los Angeles, CA 90033; e-mail: tomasian.andy@gmail.com

http://dx.doi.org/10.3174/ajnr.A5084

tion to assess potential focal neurologic deficits. Laboratory tests are used to evaluate the coagulation status (platelet count of >50,000 per microliter and international normalized ratio of <1.5 are generally acceptable) and, at times, the possibility of systemic infection (complete blood count, erythrocyte sedimentation rate, C-reactive protein level, and cultures, if clinically indicated). Thermal ablation of bone and soft-tissue tumors is painful and requires moderate sedation or general anesthesia, in particular with technically challenging spinal ablations, to minimize the risk of voluntary patient movement and potential subsequent complications.

Preprocedural imaging includes dedicated weight-bearing spine radiographs, CT, and/or MR imaging. Radiographs are used to determine the presence and extent of vertebral compression fractures, kyphosis, scoliosis, the integrity of the osseous central canal, and the suitability of fluoroscopy for imaging guidance. CT is used to determine the bone lesion density (osteolytic, osteoblastic, or mixed), which has implications for the choice of thermal ablation technique, and to identify cortical discontinuities due to tumor erosion and pathologic fracture clefts, which are sources of pain and sites where cement is most likely to leak during postablation cementoplasty. MR imaging is important for delineating the extent of the tumor, including the presence of marrow replacement and extraosseous tumor extension that may be occult on CT. Pretreatment imaging also provides information regarding procedural planning in terms of the choice of thermal ablation technology, approach, probe placement, and the need for thermal protection and cementation. Vertebral augmentation is often performed under fluoroscopic guidance, which is readily available and allows near-real-time monitoring of cement distribution. Thermal ablation of benign lesions of the spine is most commonly performed under CT guidance. Postprocedural care should include a follow-up physical examination and questionnaire to determine the efficacy of treatment and identify potentially recurrent symptoms. For benign spine lesions, contrast-enhanced MR imaging is the technique of choice for posttreatment imaging and is performed at the discretion of the referring physician to evaluate treatment adequacy or when symptoms recur. Postprocedural imaging should be performed 6–8 weeks after treatment to allow ablation-related inflammation to subside.

Minimally Invasive Percutaneous Techniques

Vertebral Augmentation. Percutaneous vertebral augmentation (PVA) encompasses several techniques aimed at internal vertebral body stabilization with bone cement. Traditional vertebroplasty involves instillation of methyl methacrylate cement directly into the vertebral body, while kyphoplasty involves first creating a cavity or several cavities with inflatable balloons, bone tamps, or osteotomes to attempt more controlled cement delivery and improved cement interdigitation.[8-11] Although both vertebroplasty and kyphoplasty offer durable pain relief, improved quality of life, and improved spine alignment, no randomized clinical trials exist for direct comparison of these techniques.[12] Indirect comparison of these techniques based on systematic reviews shows no substantial difference in patient outcome.[12] However, the rate of asymptomatic cement leakage is higher in vertebroplasty.[12] Bone cement is delivered under real-time conventional fluoroscopy or CT-fluoroscopic guidance to minimize cement leakage by using a transpedicular approach. Several randomized controlled trials have demonstrated the safety, efficacy, and durability of PVA for the management of benign and malignant spine compression fractures.[8-11] It is the position of multiple radiologic and neurosurgical societies that PVA remains an appropriate therapy for the treatment of painful vertebral compression fractures refractory to nonoperative medical therapy and for vertebrae weakened by neoplasia when performed for the medical indications outlined in the published standards.[9]

Recently, radiofrequency (RF)-induced high-viscosity cement has been used for PVA to potentially reduce intervertebral disc and venous cement leakage.[13,14] Anselmetti et al[13] performed PVA in 60 patients (190 vertebrae) and reported asymptomatic venous leak in 8.2% versus 41.3% of patients and intervertebral disc cement leakage in 6.1% versus 13% of patients (high-viscosity cement versus standard viscosity cement). Several mechanisms have been postulated to contribute to pain relief following PVA, including stabilization of vertebral body macro- and microfractures, exothermic reaction associated with the setting of cement to thermally ablate nerve endings, and a possible embolization effect with reduction of vascular congestion due to cement filling of enlarged bone marrow spaces.

Radiofrequency Ablation. In RFA, a RF generator is used to deliver high-frequency, alternating current (375–600 kHz) to the patient through an RF probe. The current passes through the exposed active tip of the probe and results in oscillation of charged tissue molecules (ions) within the ablation zone, producing frictional heat. The thermal effect depends on the electrical conducting properties of the treated tissue and the characteristics of the RF probe.[15] When local tissue temperature between 60°C and 100°C is reached, there is protein denaturation and immediate coagulative necrosis.[15] Several RFA probe-design technologies exist, attempting to achieve an improved ablation zone.[15] Unipolar systems use dispersing grounding pads placed on patient skin near the ablation site to serve as the receiving limb of the electrical circuit to prevent potential skin burns while bipolar systems use built-in transmitting and receiving electrical elements within the probe; this feature eliminates the need for grounding pads and the possibility of skin burns.[15] Internally cooled probes decrease tissue char (carbonization) by maintaining a lower temperature surrounding the active probe tip.[15]

More recently navigational bipolar RFA probes with built-in thermocouples have become available, which allow real-time monitoring of the ablation zone size by measuring the temperatures along the periphery of the ablation zone during the procedure.[16] The navigating tip of the probe can be articulated in different orientations through the same entry site; this procedure is beneficial for accessing lesions in challenging locations and achieving larger ablation zones.[16] The choice of the RF probe depends in large part on the volume of tissue to be ablated and the proximity to vital structures.[15,16] RFA is typically used for the treatment of vertebral lesions with no or small extraosseous components. The main advantage of RFA is precise determination of the geometry of the ablation zone beyond which tissues are safe from thermal injury.[15,16] Intact cortical bone also serves as a boundary for undesired RF energy propagation.[15,16] RFA is pri-

marily used for the treatment of lesions that are mainly osteolytic because the higher intrinsic impedance of sclerotic bone lesions prevents the radiofrequency circuit from generating sufficiently high temperatures to ensure cell death and renders RFA ineffective.[17] Limitations of RFA include nonvisualization of the ablation margin with CT, pain associated with the procedure, and, frequently, increased pain during the immediate posttreatment period.

Cryoablation. In closed cryoablation systems used in percutaneous tumor ablation, a liquid gas, commonly argon, is used to rapidly cool the tip of the cryoprobe (taking advantage of the Joule-Thomson effect—that is, pressurized gas, when allowed to expand, results in a drop in temperature), forming an enlarging ice ball with time followed by a "thawing" phase, commonly achieved with helium gas, resulting in an osmotic gradient.[15,18] Formation of extracellular ice results in a relative imbalance of solutes between the intra- and extracellular environment, subsequent intracellular water extraction by osmosis, and cellular dehydration. The increase in intracellular concentration of solutes results in damage to both the enzymatic machinery of the cell and the cell membrane.[15,18] The formation of intracellular ice crystals damages the cellular organelles. Thawing results in an osmotic gradient and consequent cell membrane injury.[15,18] A temperature of −40°C or lower is necessary to ensure complete cell death.[15] At present, the cryoprobes of 2 major manufacturers are used in spines with diameters of 1.2 mm (17-ga) and 1.7 mm (13-ga), generating predictable ablation zones using at least 1 freeze/active thaw/freeze cycle (typically 1/5/10 minutes).[19]

Cryoablation is typically used for benign lesions with large soft-tissue components or large lesions involving the posterior vertebral elements and is preferred to RFA for the management of osteoblastic lesions. Advantages of cryoablation include formation of a hypoattenuating ice ball, which is readily identified by CT,[20] beyond which tissues are safe from thermal injury; decreased intraprocedural and postprocedural pain compared with RFA or microwave ablation; and the ability to use multiple probes in various orientations to achieve additive overlapping ablation zones. An interprobe distance of 1.5–2 cm is typically recommended with probe tips at bone-tumor or tumor–soft-tissue interfaces.[19] In addition, the outer margin of the ice ball corresponds to 0°C, which is usually not sufficient for permanent tumor destruction. Reliable cell death is achieved at 3 mm from the outer edge; therefore, the ice ball should extend beyond the tumor margins.[18] MR imaging–compatible cryoprobes offer an alternative imaging technique, which may permit safe ablation of spinal lesions, given the proximity of the neural elements.[21]

Laser Ablation. Laser ablation uses optical fibers to transmit infrared light energy into a tumor to produce rapid temperature elevation, protein denaturation, and coagulative necrosis. A continuous wave semiconductor diode laser with an 805-nm wavelength delivers energy to the tumor by using a flexible single-use bare-tipped 400-μm optical fiber with polymer cladding placed coaxially.[22-25] The amount of energy to be delivered is calculated according to the formula [Nidus Size (mm) × 100 Joules + 200 Joules], and the duration of the ablation is typically 200–600 seconds, depending on the nidus size.[22-25] The size of the induced ablation zone depends on the laser wavelength, thermal and optical properties of the tissue, total duration of energy delivery, laser power, diameter of the laser fiber, and the number of fibers used.[26] The maximum coagulation effect is reached at 1000–1200 J, and more energy at the same location does not increase the volume of coagulation.[26] Spine laser ablation has been mainly used in the treatment of osteoid osteomas and osteoblastomas,[22-25] and an energy amount of 1200 J is usually adequate. However, for larger lesions, a greater amount of energy may be necessary.[22] The advantages of laser ablation include a predictable size of the ablation in proportion to the energy delivered, lack of the need to use a neutral electrode, lack of interaction with stimulators and pacemakers, and the relatively low cost of disposable laser fiber.[22-25] A disadvantage is the lack of visualization of the ablation zone with CT.

Microwave Ablation. Microwave ablation uses antennae to deliver electromagnetic microwaves (approximately 900 MHz) to target tissue, which result in agitation of ionic molecules and frictional heat and, subsequently, tissue coagulative necrosis. It is theorized that microwave ablation is less influenced by variable tissue impedance and perfusion-mediated tissue cooling; this feature potentially results in higher intratumoral temperatures and creates a larger, more uniform ablation zone and faster ablation times by using a single probe.[27] Additional advantages of microwave ablation include efficacy in the management of osteoblastic lesions due to less susceptibility to increased impedance of attenuated bone, diminished heat sink phenomena, and lack of the need for grounding pads and thus diminished risk of skin burns.[27-29] The antenna shaft cooling system implemented in the latest generations of microwave ablation equipment eliminates the risk of back-heating phenomena.[28,29] The ability to rapidly deliver high amounts of power (up to 100 Watts) to large ablation zones might be a disadvantage when applied to spinal lesions because surrounding overheating could potentially lead to injuries to adjacent neural elements.[28,29] Although hypoattenuating ablated tissue is often identified on CT, the margins of the ablation zone are not well-defined; this feature is considered a disadvantage of spinal microwave ablation. The literature regarding the efficacy and safety of spine microwave ablation is sparse, and this technology should be used with caution for spinal applications. While 2 retrospective studies have shown its safety and efficacy for the management of spine metastases,[28,29] this technology has not been used for the management of benign spine lesions.

Alcohol Ablation. Alcohol ablation is a relatively inexpensive percutaneous tumor ablation technique that causes tumor necrosis directly through cellular dehydration and indirectly through vascular thrombosis and tissue ischemia.[30] Instillation of iodinated contrast or venography, before alcohol ablation, to delineate the extent of ethanol diffusion has been described as a strategy for reducing the risk of the vascular intravasation and potential injury to adjacent structures.[30-32] In alcohol ablation, volumes of 3–30 mL are directly injected into the target tissue.[30-32] The most important limitation of alcohol ablation is the poorly predictable size and configuration of the ablation zone due to poorly reproducible diffusion of alcohol through tumoral (particularly cortical bone) and peritumoral tissues.[30]

Benign Spinal Lesions

Osteoid Osteoma. Osteoid osteoma is a benign painful bone-forming lesion that typically occurs in patients younger than 30 years of age with a male predilection (2–4:1). In the spine, these lesions classically involve the posterior elements and in 60% of cases are located in the lumbar spine. A central nidus with or without central mineralization (typically <15 mm) and surrounding osseous sclerosis are the typical imaging manifestations. Osteoid osteomas have been traditionally treated with surgical excision, which has substantial morbidity, including spinal instability, nerve injury, infection, and blood loss as well as cost burden.[33] Spinal osteoid osteomas account for 10%–20% of cases, and although spontaneous regression of these tumors has been reported, 70% of untreated patients develop painful scoliosis.[22,34] The entire nidus of osteoid osteoma must be ablated to ensure complete treatment. Due to the proximity of neural elements, percutaneous ablation of spinal osteoid osteoma may require logistic considerations. However, thermal protective effects of intact cortical bone, flow of CSF, and small vessels in the epidural space have been hypothesized.[35,36]

Given the small size of spinal osteoid osteomas (typically <15 mm), RFA and laser ablation are recommended as treatment options with no need for cementation. Both RFA and laser ablation have similar efficacy and safety profiles,[26] and the choice is at the discretion of the operator. Imaging guidance is typically achieved with CT with thin sections (1–2 mm) and 3D reconstructions to allow precise positioning of the probe at the center of the nidus. Since the initial reports of RFA for the treatment of osteoid osteoma,[33] this technique has almost completely supplanted surgical resection. If RFA is to be used, monopolar noncooled straight electrodes are recommended with application of RF energy to achieve temperature of 90°C for 5–6 minutes (Fig 1). Recently, navigational bipolar RFA probes have been successfully used to treat spinal osteoid osteomas (Fig 2).[16] These probes allow real-time monitoring of the ablation zone size by using built-in thermocouples and are beneficial for larger lesions and challenging locations due to the articulating tip, which may be placed in various orientations by using a single skin-entry site, obviating grounding pads. Adequate ablation is achieved in 2–3 minutes.[16] Investigators have successfully used RFA for management of spinal osteoid osteomas by using thermoprotective techniques for lesions as close as 1 mm to neural elements without complications (Figs 1 and 2).[15,16,22,35-40] During RFA, patients under general anesthesia have a fairly predictable response with elevated heart (average increase, 40%) and respiratory rates (average increase, 50%) during both the biopsy and ablation portions of the treatment.[41]

Morassi et al[40] treated 13 patients with spinal osteoid osteomas (11 in the posterior elements and 2 in the vertebral bodies) by using a non-cool-tip unipolar system with a 5-mm active tip (90°C for 6 minutes) using thermoprotection, achieving pain relief in 11 patients with no complications. In case of laser ablation, typically a single flexible bare-tip laser fiber is adequate; it is placed in the center of the nidus coaxially through an 18-ga spinal needle, with a delivered energy of approximately 1200 J for 200–600 sec-

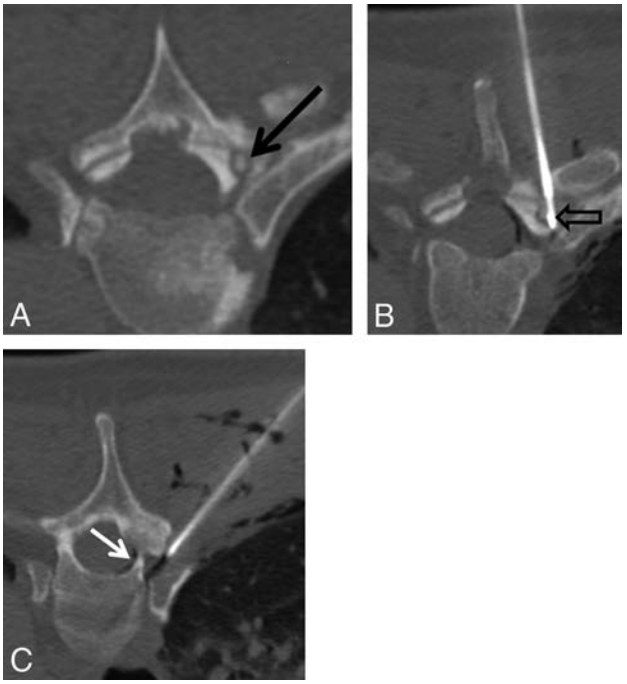

FIG 1. A 45-year-old man with several months of night-time predominant, right-sided midthoracic pain relieved by ibuprofen. *A*, Prone axial noncontrast CT image shows a small osteolytic lesion with a central mineralization in the right T5 superior articular facet (*black arrow*). *B*, Prone axial noncontrast CT image shows the radiofrequency ablation probe in the nidus of the osteoid osteoma (*black open arrow*). *C*, Prone axial noncontrast CT image shows an 18-ga spinal needle placed in the right T4–T5 neural foramen for temperature monitoring, carbon dioxide injection, and cooled dextrose 5% in water infusion. Note the gas tracking into the soft tissue and within the epidural space (*white arrow*).

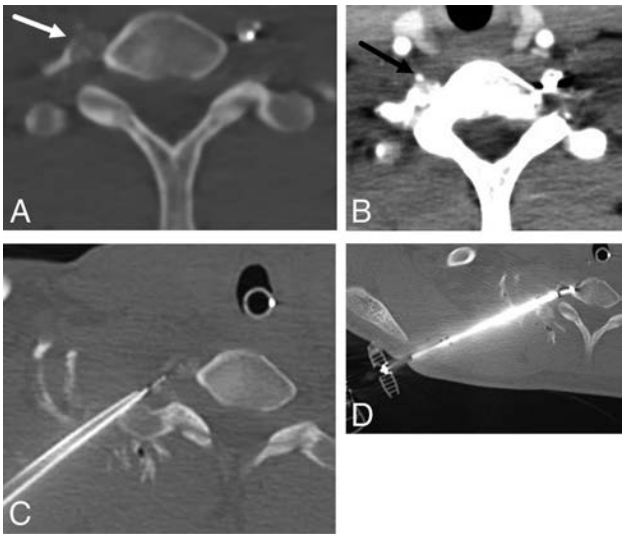

FIG 2. A 14-year-old boy with painful right transverse process C7 osteoid osteoma (*A*, *arrow*). Preprocedural neck CT angiography demonstrates the course and location of the right vertebral artery (*B*, *arrow*). *C*, Thermal monitoring and protection are achieved by placement of a thermocouple and spinal needle in the right C7–T1 neuroforamen. *D*, RF ablation is performed by using a bipolar navigational probe with slight posterior articulation of the probe tip for optimal positioning.

onds.[23] However, for larger lesions, 2 fibers and larger energy amounts may be necessary to ensure the adequacy of the ablation. Tsoumakidou et al[23] reported successful laser ablation of spine osteoid osteomas in 57 patients (vertebral body, $n = 18$, and posterior elements/facet joints, $n = 36$) by using thermoprotection with most lesions located closer than 5 mm to the neural structures. Sixty-one ablations (mean delivered energy, 1271 J) were performed with a technical success rate of 100% and a primary clinical success rate of 98.2% (at 1 month) with no major complications.[23] Cryoablation has been successfully used for management of a spine osteoid osteoma.[42]

Osteoblastoma. Osteoblastomas are rare benign tumors with striking histologic similarity to osteoid osteomas. There is a male predilection (2.5–1). They are typically larger (>2 cm) and expansile with less sclerotic components compared with osteoid osteomas with thin peripheral sclerosis and may be associated with aneurysmal bone cyst.[43,44] On MR imaging, they demonstrate avid osseous and extraosseous enhancement. Spinal osteoblastomas compose approximately 40% of cases and often involve the posterior elements and are located in the cervical spine in 10%–40% of cases. Most untreated lesions lead to painful scoliosis, and surgical excision has traditionally been the treatment of choice for spinal osteoblastomas, which is associated with morbidity, especially given the size of the osseous defect.[43,44] The entire osteolytic component and the soft-tissue component (if present) must be ablated for definitive cure. The imaging guidance (CT) and thermoprotective measures are similar to those in osteoid osteoma ablation. Typically, there is no need for postablation vertebral augmentation. Given the larger size of osteoblastomas and particularly with involvement of posterior elements and potential soft-tissue components, cryoablation could be safely and efficiently performed with simultaneous placement of multiple probes with visualization of the hypoattenuating ice ball.[26]

Both RFA and laser ablation are also recommended for management of these lesions.[15,26,43,44] In case of RFA, considering lesion size, ≥2 ablations with straight unipolar probes should be performed to cover the entire lesion (90°C for 6 minutes each). Alternatively, a navigational bipolar RFA probe could be used to articulate the probe tip in different orientations through a single entry site, with precise determination of the size of the ablation zone by using built-in thermocouples. Although the RF ablation zone could not be visualized on CT, the intact surrounding cortical bone serves as a barrier for undesired RF energy propagation.[26] Similarly, with laser ablation, at least 2 probes and more energy deposition are required to achieve a cure (Fig 3). A substantial inflammatory reaction may occur following thermal ablation of osteoblastomas, and nonsteroidal anti-inflammatory drugs may be administered for management. Weber et al[44] successfully managed 2 spinal osteoblastomas with a unipolar cool-tip RFA system (90°C for approximately 400 seconds) by using >1 ablation to cover the entire nidus with no complications.

Aneurysmal Bone Cyst. Aneurysmal bone cyst is a benign expansile lesion of uncertain etiology comprising numerous blood-filled channels. It occurs in patients younger than 20 years of age in 80% of cases. Aneurysmal bone cyst involves the vertebral column in 20%–30% of cases (typically the posterior elements), of

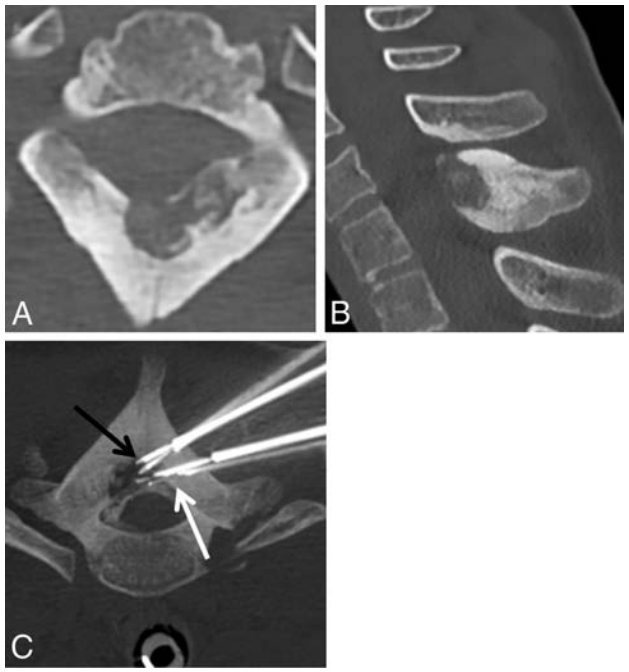

FIG 3. A 13-year-old girl who had cervicothoracic junction pain due to a T1 osteoblastoma. Axial (*A*) and sagittal (*B*) CT demonstrates an osteolytic lesion within the anterior aspect of the T1 spinous process with cortical thickening and sclerosis surrounding the lesion. *C*, Prone axial maximum-intensity-projection image of a T1 osteoblastoma during laser ablation demonstrates 2 posterior laser photoelectrodes (*black arrow*) within the lesion and 2 anterior spinal needles (*white arrow*) placed for temperature monitoring.

which about 40% involve the vertebral body. Aneurysmal bone cysts are expansile osteolytic lesions with fluid-fluid levels on MR imaging and thin peripheral/septal enhancement. These lesions may result in pain and neurologic compromise, prompting treatment. Standard surgical management depends on the lesion size and includes curettage, bone grafting, and internal fixation as well as en bloc or wide excision.[45,46] Although no large studies exist to evaluate the efficacy of thermal ablation for the treatment of spinal aneurysmal bone cysts, given their larger size, typical involvement of posterior elements, and possible soft-tissue components, cryoablation is suggested as the thermal ablation technique of choice, and thermoprotection is recommended in all cases (Fig 4).[26,45,46] Preablation embolization is also suggested to reduce the risk of hemorrhage and heat sink effect in large lesions.[46] In case of pathologic fracture or extensive involvement of the vertebral body or pedicles, postablation cementation is recommended for stabilization.[26,45] Griauzde et al[46] reported the case of a spinal aneurysmal bone cyst involving the posterior elements of C6–T1 and the right C8 nerve root managed by cryoablation 4 days following embolization with *N*-butyl cyanoacrylate and lipiodol. The patient developed sensory neuropathy, which improved at 16-month follow-up, and imaging demonstrated no evidence of recurrence.[46]

Hemangioma. Vertebral hemangiomas are the most common benign vertebral neoplasms, with a slight female predilection, with most located in the thoracic spine. Most of these lesions are asymptomatic and incidentally identified on imaging. Classic imaging features include a polka-dotted appearance on CT and T1

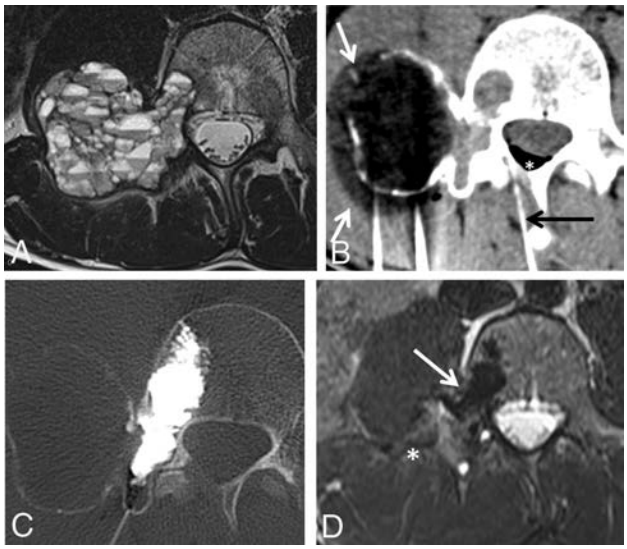

FIG 4. A 17-year-old boy with low back pack due to a right L4 aneurysmal bone cyst. *A*, Axial T2-weighted image demonstrates an expansile lesion in the right L4 transverse process, pedicle, and posterior vertebral body with multiple fluid-fluid levels, most compatible with aneurysmal bone cyst. *B*, Axial CT image during cryoablation of the transverse process portion of the lesion. Note the hypoattenuating ice ball (*white arrows*) extending beyond portions of the lesion into the soft tissues. A spinal needle (*black arrow*) was placed into the epidural space for temperature monitoring and carbon dioxide injection (*white asterisk*) into the epidural space. *C*, Axial CT image during cementoplasty of the right L4 pedicle and posterior vertebral body components of the lesion. *D*, Axial T2-weighted image 3 months post-treatment demonstrates near-complete resolution of the expansile component of the tumor (*white asterisk*) and hypointense cement (*white arrow*) in the right pedicle and posterior vertebral body.

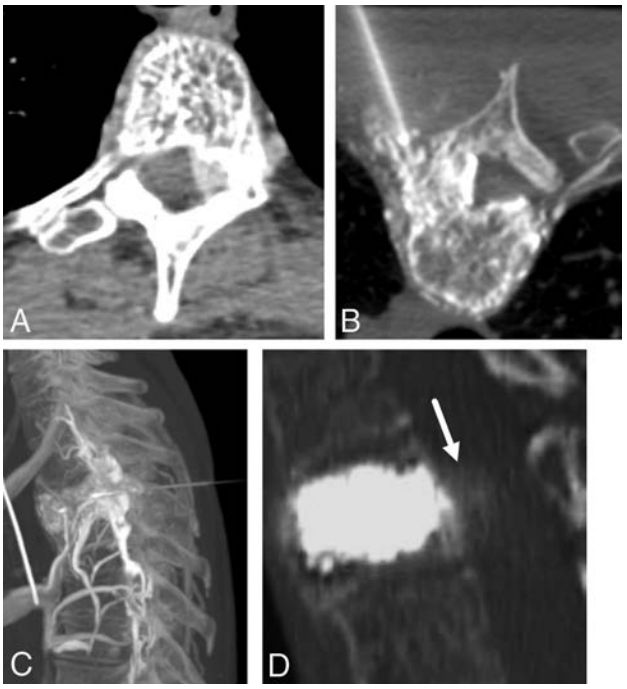

FIG 5. A 46-year-old man with upper back pain due to an aggressive T3 hemangioma. *A*, Axial contrast-enhanced CT scan demonstrates an aggressive T3 hemangioma with intraosseous and extraosseous components. *B*, Axial prone intraprocedural CT scan during a venogram performed via an 18-gauge needle in the left pedicle/vertebral body. Note extensive vascularity in the vertebral body and in the soft tissues surrounding the vertebral body, including the epidural space. *C*, Sagittal maximum-intensity-projection CT of a T3 venogram before alcohol ablation demonstrates a vascular lesion with epidural flow. Ethanol ablation was followed by vertebral augmentation for stabilization of the vertebral body. *D*, Post-alcohol ablation and vertebral augmentation CT demonstrates cement filling the vertebral body and the hyperattenuating ablated extraosseous component posterior to the vertebral body (*white arrow*).

hyperintensity and enhancement on MR imaging. Painful vertebral hemangiomas are typically due to impingement of the central canal or neuroforamina or concomitant pathologic fractures. Surgical intervention for vertebral hemangiomas is reserved for patients with neurologic compromise and spinal instability, and radiation therapy is used when immobilization fails to resolve neurologic symptoms or in cases of lesion progression following immobilization.[47,48] PVA has been successfully used for minimally invasive management of symptomatic vertebral hemangiomas in the absence of neurologic compromise and spinal instability.[47,48] PVA is associated with substantially less morbidity compared with an operation and radiation therapy and is more cost-effective. Liu et al,[48] treated 33 symptomatic vertebral hemangiomas in 31 patients with PVA (mean follow-up, 15.8 months) and evaluated the clinical effects by using the Visual Analog Scale and Roland-Morris Disability Questionnaire at 1 week,1 month, and final follow-up. The authors reported substantial improvement in the Visual Analog Scale and Roland-Morris Disability Questionnaire scores and no major complications. Aggressive spinal hemangiomas, which are associated with extraosseous epidural and paravertebral components, compose approximately 1% of spinal hemangiomas and can be successfully treated with PVA.[49,50] In a case series of 16 patients, Cloran et al[49] treated 4 patients with symptomatic aggressive vertebral hemangiomas without neurologic compromise by using PVA, achieving complete pain resolution in all patients with no major complications.

Alcohol ablation followed by PVA has also been successfully used for management of symptomatic vertebral hemangiomas, including aggressive hemangiomas (Fig 5).[30-32] As indicated previously, preablation venography with iodinated contrast should be performed by placement of a needle within the vertebral body to delineate the extent of ethanol diffusion to reduce the risk of the vascular intravasation and potential injury to adjacent structures. Doppman et al[32] treated 11 patients with vertebral hemangiomas and neurologic symptoms using alcohol ablation with no immediate complications. Radiculopathy improved in 4 of 5 patients. Two patients who received the largest volumes of ethanol, 42 and 50 mL, developed pathologic compression fractures 4 and 16 weeks following treatment, respectively.[32]

Paget Disease. Approximately 35%–50% of patients with Paget disease have spinal involvement, half of whom experience back pain.[51] It can be seen in up to 10% of patients older than 80 years of age. The classic features of vertebral Paget disease include a "picture frame" appearance and squaring of vertebral bodies. Findings on MR imaging can be variable on the basis of the disease phase. Conservative management of painful vertebral Paget disease includes a combination of bisphosphonate therapy and analgesics.[51-54] Patients with spinal instability and concomitant neurologic compromise are managed by surgical intervention. Patients refractory to conservative management, in the absence of

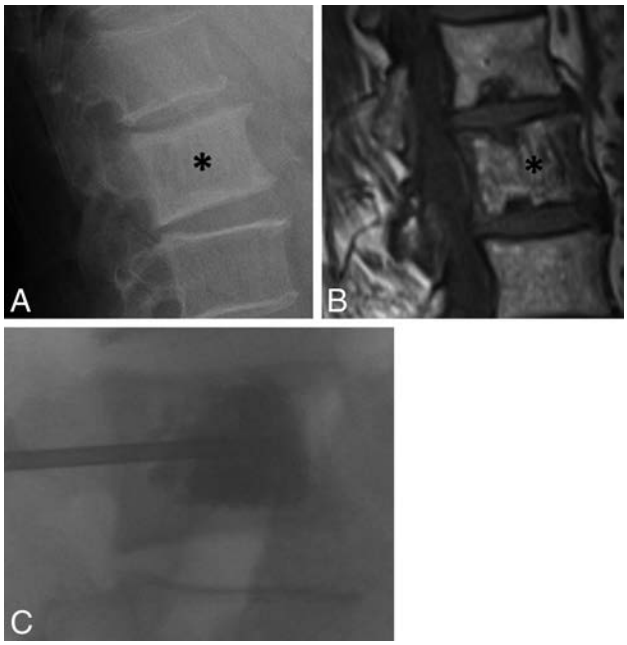

FIG 6. A 71-year-old man with chronic low back pain. *A*, Lateral radiograph of the lumbar spine shows an enlarged L2 vertebral body with cortical and trabecular thickening (*asterisk*), with a presumed diagnosis of Paget disease. *B*, Sagittal T1-weighted MR image of the lumbar spine shows vertically oriented trabecular thickening and enlargement of the L2 vertebral body (*asterisk*). *C*, Fluoroscopic image during vertebral augmentation shows cement filling the L2 vertebral body. At the conclusion of the procedure, the patient reported complete resolution of back pain.

spinal instability and neurologic deficit, have been successfully managed by PVA with no major complications (Fig 6).[51-54] Pedicelli et al[51] treated a patient with painful L4 Paget disease refractory to opioid analgesics and bisphosphonates with PVA and achieved substantially improved Visual Analog Scale pain and Roland-Morris Disability Questionnaire scores at day 1 and 6-month follow-up, with no complications.

Schmorl Nodes. Schmorl nodes are common in all ages and may be associated with trauma. Symptomatic Schmorl nodes reflect acute or subacute vertebral endplate fracture, typically along the posterior margin, allowing vertical disc herniation and nuclear migration.[55] Schmorl nodes as pain generators and their management remain a controversial topic. In cases of symptomatic Schmorl nodes, fluid-sensitive MR imaging sequences typically demonstrate hyperintensity along the node and vertebral endplate, which has been hypothesized as the source of pain.[55] PVA may be an alternative option for the management of painful Schmorl nodes and degenerative Modic changes of the spine refractory to analgesics and conservative management (Fig 7).[55,56] Masala et al[55] managed 23 patients with painful Schmorl nodes refractory to medial and conservative management by using PVA. Pain improvement was achieved in 18 patients as evaluated 4 hours after the procedure (mean Visual Analog Scale score, 8.4 versus 2.3). The authors reported no cement leakage into the Schmorl nodes or intervertebral disc space (Fig 8).[55] In addition, a Rami communicans nerve block has been successfully used for the management of symptomatic Schmorl nodes.[57]

Other Benign Spine Lesions. Several other benign spinal lesions

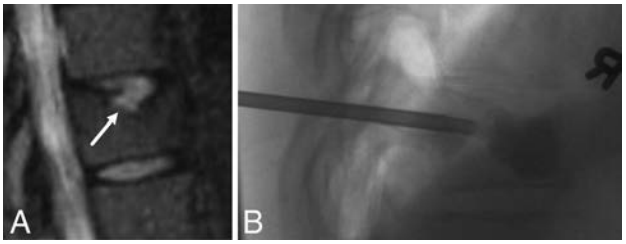

FIG 7. A 49-year-old woman with chronic midback pain. *A*, Sagittal STIR MR image of the thoracic spine demonstrates a large Schmorl node (*arrow*) along the superior endplate of the T10 vertebral body with associated hyperintensity. *B*, Lateral fluoroscopic image of the lower thoracic spine during kyphoplasty demonstrates filling of the anterior half of T10 vertebral body extending to surround the Schmorl node. Before the procedure, the patient had 6/10 pain. After the procedure, there was near-complete resolution of pain.

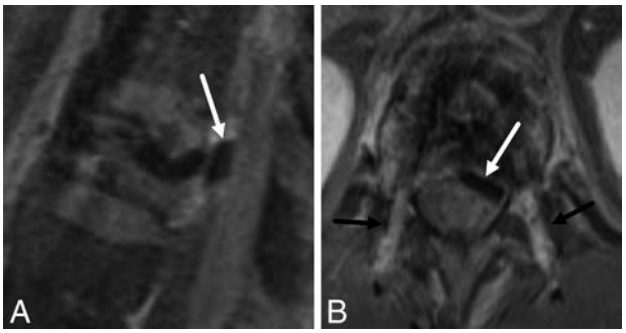

FIG 8. A 55-year-old man with cement leakage following radiofrequency ablation and vertebral augmentation. Sagittal (*A*) and axial (*B*) fat-suppressed T1-weighted contrast-enhanced MR images show hypointense cement within the epidural space, compatible with a leak (*A* and *B*, *white arrow*). Note enhancing granulation tissue along the transpedicular needle tracts (*B*, *black arrows*).

have been successfully treated by using minimally invasive percutaneous thermal ablation and PVA with no major complications (Fig 9).[58-62] However, the available literature is scant and limited to case reports, including PVA for the management of eosinophilic granuloma,[58,59] RFA for the management of intraosseous glomus tumor and hibernoma,[60,61] and cryoablation for the management of epithelioid hemangioendothelioma.[62]

Complications

The most important potential complication of percutaneous thermal ablation of the spine is injury to the spinal cord and nerve roots due to the proximity of the ablation zone to neural elements. In addition, there remains a risk of thermal skin injury. Furthermore, in ablation of vertebral body or pedicle lesions or large tumors, there is a potential risk of ablation-related fracture, which may be minimized with cementation.

Posttreatment Imaging

As stated earlier, contrast-enhanced MR imaging is the technique of choice for posttreatment imaging of benign spine lesions, which is performed at the discretion of the referring physician, if symptoms recur. The necrotic ablated volume shows no enhancement on postcontrast imaging, with variable signal intensity on T1- and T2-weighted sequences, depending on the relative amounts of sclerotic bone, residual vascular and yellow marrow, and hemorrhagic products.[63] The ablated volume is surrounded

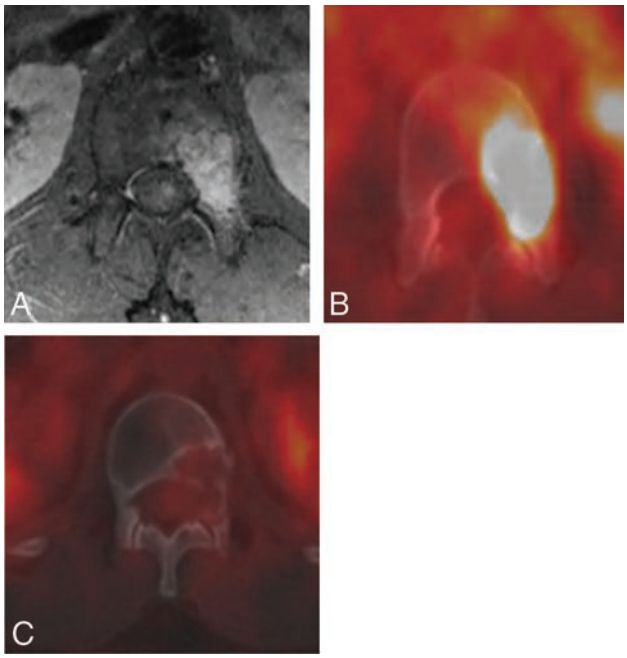

FIG 9. A 21-year-old man with L1 pseudomyogenic hemangioendothelioma. *A* and *B*, MR imaging and PET-CT demonstrate an enhancing hypermetabolic bone marrow–replacing lesion within the L1 vertebra involving the left pedicle and posterior vertebral body. *C*, PET-CT performed 1 year following RFA demonstrates no evidence of residual or recurrent tumor.

by a T1-hypointense, T2-hyperintense rim that enhances after contrast administration and corresponds histologically to granulation tissue or vascular fibrosis.[63] Cement appears as a signal void in the ablation cavity on all pulse sequences. Residual or recurrent tumor typically appears as T2-hyperintense, enhancing tissue at the margin of the ablation cavity; however, granulation tissue and vascular fibrosis can have identical MR imaging signal and enhancement characteristics,[63] and the decision to proceed with further treatment should be based on clinical evaluation.

Thermoprotection and Thermal Monitoring

Percutaneous thermal tumor ablation in the spine poses an inherent risk of injury to the spinal cord and nerve roots due to the proximity of the ablation zone to the susceptible neural elements, which is the most important potential complication of these procedures. Numerous parameters affect the extent and severity of neurologic thermal injury, including absolute temperature, duration of thermal effect, distance from margins of ablation zone, presence or absence of intact osseous cortex, and type of nerve fiber.[26] A slight motor function loss becomes evident at 10°C, and mild sensory loss, at 7°C, while both functions disappear between 5°C and 0°C.[26]

Current practice to prevent thermal injury during thermal spine ablation procedures involves the use of thermal insulation, and temperature and neurophysiologic monitoring.[22,26,64,65] Thermal insulation can be achieved by hydrodissection or instillation of warm or cool liquid, which actively modifies the temperature surrounding the structure at risk. Hydrodissection in RFA procedures should be performed by using nonionic solutions such as dextrose 5% in water. Saline solutions should be avoided with RFA because the electrical conductivity may result in expansion of the ablation zone and creation of a plasma field.[22,26] Carbon dioxide insufflation of the epidural space or neuroforamina can also be used to dissect and actively insulate the neural structures.[22,26,64,65] In addition to insulation, continuous real-time and precise temperature monitoring may be undertaken during spine ablations by placing thermocouples close to the threatened structures, typically within the neuroforamina.[22,26,64,65] In clinical practice, active thermoprotection (Figs 1–4) is initiated once the temperature reaches 45°C (heat) and 10°C (cold).[22,26,64,65]

Investigators have implemented neurophysiologic monitoring and nerve electrostimulation during spine thermal ablation procedures by using estimations of motor- and somatosensory-evoked potential amplitudes.[65,66] Substantial reduction in the amplitude of evoked potential amplitudes affords early detection of impending neurologic injury, which should prompt active thermoprotection or modification in the ablation procedure. Skin injury is another potential complication of percutaneous thermal ablation. Careful assessment of the boundaries of the ablation zone minimizes the risk of skin injury. Active skin thermoprotection such as surface application of warm saline during cryoablation should be implemented to minimize skin injury. In the case of RFA, using a bipolar system inherently obviates the risk of skin burn, and use of grounding pads with unipolar systems decreases the risk of skin injury.

Summary of benign spine lesions and preferred treatment modalities

Benign Spine Lesion	Recommended Treatment Modality
Osteoid osteoma	Radiofrequency ablation, laser ablation
Osteoblastoma	Cryoablation (if large or coexisting soft-tissue component) Radiofrequency ablation, laser ablation
Aneurysmal bone cyst	Cryoablation (due to involvement of posterior elements, soft-tissue component, and large size) Cementation if extensive vertebral body involvement or pathologic fracture Preablation embolization suggested
Hemangioma	Vertebral augmentation, alcohol ablation
Paget disease	Vertebral augmentation
Schmorl node	Vertebral augmentation

Summary

Continuously evolving image-guided percutaneous vertebral augmentation and spine thermal ablation procedures have been proved safe and effective tools in minimally invasive management of selected patients with benign spine lesions (Table). With the progressively increasing role of these procedures in clinical practice, radiologists should be familiar with the indications, techniques, potential complications, and most recent advances of these procedures for optimal patient care. Special attention to the details of procedural techniques, including the choice of treatment technology; thermoprotection; and the adequacy of treatment will translate into improved patient outcomes.

Disclosures: Adam N. Wallace—*UNRELATED*: *Support for Travel to Meetings for the Study or other Purposes*: DFINE,* *Comments*: DFINE paid my travel to a meeting to discuss a prospective clinical trial funded by the company; *Other*: DFINE,* Galil Medical,* Medtronic,* *Comments*: These companies donated ablation probes for an animal research study I am conducting. Jack W. Jennings—*UNRELATED*: *Grant*: DFINE, *Comments*: Principal Investigator for the STARRT trial*; *Consulting Fee or*

Honorarium: Medtronic, Galil Medical, *Comments*: I have done consulting work with Galil Medical for almost a year. *Money paid to the institution.

REFERENCES

1. Kelley SP, Ashford RU, Rao AS, et al. **Primary bone tumours of the spine: a 42-year survey from the Leeds Regional Bone Tumour Registry.** *Eur Spine J* 2007;16:405–09 CrossRef Medline
2. Hara S. **Opioids for metastatic bone pain.** *Oncology* 2008;74(suppl 1):52–54 Medline
3. Jiang L, Liu XG, Yuan HS, et al. **Diagnosis and treatment of vertebral hemangiomas with neurologic deficit: a report of 29 cases and literature review.** *Spine J* 2014;14:944–54 CrossRef Medline
4. Boyaci B, Hornicek FJ, Nielson GP, et al. **Epithelioid hemangioma of the spine: a case series of six patients and review of the literature.** *Spine J* 2013;13:e7–13 CrossRef Medline
5. Wang C, Liu X, Jiang L, et al. **Treatments for primary aneurysmal bone cysts of the cervical spine: experience of 14 cases.** *Chin Med J (Engl)* 2014;127:4082–86 Medline
6. Pennekamp W, Peters S, Schinkel C, et al. **Aneurysmal bone cyst of the cervical spine (2008:7b).** *Eur Radiol* 2008;18:2356–60 CrossRef Medline
7. Lutz S, Berk L, Chang E, et al; American Society for Radiation Oncology (ASTRO). **Palliative radiotherapy for bone metastases: an ASTRO evidence-based guideline.** *Int J Radiat Oncol Biol Phys* 2011; 79:965–76 CrossRef Medline
8. McConnell CT Jr, Wippold FJ 2nd, Ray CE Jr, et al. **ACR appropriateness criteria management of vertebral compression fractures.** *J Am Coll Radiol* 2014;11:757–63 CrossRef Medline
9. Barr JD, Jensen ME, Hirsch JA, et al; Society of Interventional Radiology, American Association of Neurological Surgeons, Congress of Neurological Surgeons, American College of Radiology, American Society of Neuroradiology, American Society of Spine Radiology, Canadian Interventional Radiology Association, Society of Neurointerventional Surgery. **Position statement on percutaneous vertebral augmentation: a consensus statement developed by the Society of Interventional Radiology (SIR), American Association of Neurological Surgeons (AANS) and the Congress of Neurological Surgeons (CNS), American College of Radiology (ACR), American Society of Neuroradiology (ASNR), American Society of Spine Radiology (ASSR), Canadian Interventional Radiology Association (CIRA), and the Society of NeuroInterventional Surgery (SNIS).** *J Vasc Interv Radiol* 2014;25:171–81 CrossRef Medline
10. Schupfner R, Stoevelaar HJ, Blattert T, et al. **Treatment of osteoporotic vertebral compression fractures: applicability of appropriateness criteria in clinical practice.** *Pain Physician* 2016;19:E113–20 Medline
11. Wardlaw D, Cummings SR, Van Meirhaeghe J, et al. **Efficacy and safety of balloon kyphoplasty compared with non-surgical care for vertebral compression fracture (FREE): a randomised controlled trial.** *Lancet* 2009;373:1016–24 CrossRef Medline
12. Yimin Y, Zhiwei R, Wei M, et al. **Current status of percutaneous vertebroplasty and percutaneous kyphoplasty: a review.** *Med Sci Monit* 2013;19:826–36 CrossRef Medline
13. Anselmetti GC, Zoarski G, Manca A, et al. **Percutaneous vertebroplasty and bone cement leakage: clinical experience with a new high-viscosity bone cement and delivery system for vertebral augmentation in benign and malignant compression fractures.** *Cardiovasc Intervent Radiol* 2008;31:937–47 CrossRef Medline
14. Trumm CG, Jakobs TF, Stahl R, et al. **CT fluoroscopy-guided vertebral augmentation with a radiofrequency-induced, high-viscosity bone cement (StabiliT®): technical results and polymethylmethacrylate leakage in 25 patients.** *Skeletal Radiol* 2013;42:113–20 CrossRef Medline
15. Rybak L. **Fire and ice: thermal ablation of musculoskeletal tumors.** *Radiol Clin North Am* 2009;47:455–69 CrossRef Medline
16. Wallace AN, Tomasian A, Chang RO, et al. **Treatment of osteoid osteomas using a navigational bipolar radiofrequency ablation system.** *Cardiovasc Intervent Radiol* 2016;39:768–72 CrossRef Medline
17. Singh S, Saha S. **Electrical properties of bone: a review.** *Clin Orthop Relat Res* 1984:249–71 Medline
18. Gage AA, Baust JG. **Cryosurgery for tumors.** *J Am Coll Surg* 2007; 205:342–56 CrossRef Medline
19. Tomasian A, Wallace A, Northrup B, et al. **Spine cryoablation: pain palliation and local tumor control for vertebral metastases.** *AJNR Am J Neuroradiol* 2016;37:189–95 CrossRef Medline
20. Saliken JC, McKinnon JG, Gray R. **CT for monitoring cryotherapy.** *AJR Am J Roenrgenol* 1996;166:853–55 CrossRef Medline
21. Callstrom MR, Kurup N. **Percutaneous ablation for bone and soft tissue metastases: why cryoablation?** *Skeletal Radiol* 2009;28:835–89 Medline
22. Rybak LD, Gangi A, Buy X, et al. **Thermal ablation of spinal osteoid osteomas close to neural elements: technical considerations.** 2010; 195:W293–98 CrossRef Medline
23. Tsoumakidou G, Thénint MA, Garnon J, et al. **Percutaneous image-guided laser photocoagulation of spinal osteoid osteoma: a single-institution series.** *Radiology* 2016;278:936–43 CrossRef Medline
24. Gangi A, Basile A, Buy X, et al. **Radiofrequency and laser ablation of spinal lesions.** *Semin Ultrasound CT MR* 2005;26:89–97 CrossRef Medline
25. Gangi A, Alizadeh H, Wong L, et al. **Osteoid osteomas: percutaneous laser ablation and follow-up in 114 patients.** *Radiology* 2007;242: 293–301 CrossRef Medline
26. Tsoumakidou G, Koch G, Caudrelier J, et al. **Image-guided spinal ablation: a review.** *Cardiovasc Intervent Radiol* 2016;39:1229–38 CrossRef Medline
27. Kurup AN, Callstrom MR. **Ablation of skeletal metastases: current status.** *J Vasc Interv Radiol* 2010;21:S242–50 CrossRef Medline
28. Kastler A, Alnassan H, Aubry S, et al. **Microwave thermal ablation of spinal metastatic bone tumors.** *J Vasc Interv Radiol* 2014;25:1470–75 CrossRef Medline
29. Pusceddu C, Sotgia B, Fele RM, et al. **Treatment of bone metastases with microwave thermal ablation.** *J Vasc Interv Radiol* 2013;24: 229–33 CrossRef Medline
30. Gangi A, Buy X. **Percutaneous bone tumor management.** *Semin Intervent Radiol* 2010;27:124–36 CrossRef Medline
31. Gabal AM. **Percutaneous technique for sclerotherapy of vertebral hemangioma compressing spinal cord.** *Cardiovasc Intervent Radiol* 2002;25:494–500 CrossRef Medline
32. Doppman JL, Oldfield EH, Heiss JD. **Symptomatic vertebral hemangiomas: treatment by means of direct intralesional injection of ethanol.** *Radiology* 2000;214:341–48 CrossRef Medline
33. Rosenthal DI, Alexander A, Rosenberg AE, et al. **Ablation of osteoid osteomas with a percutaneously placed electrode: a new procedure.** *Radiology* 1992;183:29–33 CrossRef Medline
34. Haibach H, Farrell C, Gaines RW. **Osteoid osteoma of the spine: surgically correctable cause of painful scoliosis.** *CMAJ* 1986;135: 895–99 Medline
35. Dupuy DE, Hong R, Oliver B, et al. **Radiofrequency ablation of spinal tumors: temperature distribution in the spinal canal.** *AJR Am J Roentgenol* 2000;175:1263–66 CrossRef Medline
36. Cové JA, Taminiau AH, Obermann WR, et al. **Osteoid osteoma of the spine treated with percutaneous computed tomography-guided thermocoagulation.** *Spine* 2000;25:1283–86 CrossRef Medline
37. Klass D, Marshall T, Toms A. **CT-guided radiofrequency ablation of spinal osteoid osteomas with concomitant perineural and epidural irrigation for neuroprotection.** *Eur Radiol* 2009;19:2238–43 CrossRef Medline
38. Vanderschueren GM, Obermann WR, Dijkstra SP, et al. **Radiofrequency ablation of spinal osteoid osteoma: clinical outcome.** *Spine (Phila Pa 1976)* 2009;34:901–04 CrossRef Medline
39. Martel J, Bueno A, Nieto-Morales ML, et al. **Osteoid osteoma of the spine: CT-guided monopolar radiofrequency ablation.** *Eur J Radiol* 2009;71:564–69 CrossRef Medline
40. Morassi LG, Kokkinis K, Evangelopoulos DS, et al. **Percutaneous radiofrequency ablation of spinal osteoid osteoma under CT guidance.** *Br J Radiol* 2014;87:20140003 CrossRef Medline

41. Rosenthal DI, Marota JJ, Hornicek FJ. **Osteoid osteoma: elevation of cardiac and respiratory rates at biopsy needle entry into tumor in 10 patients.** *Radiology* 2003;226:125–28 CrossRef Medline
42. Whitmore MJ, Hawkins CM, Prologo JD, et al. **Cryoablation of osteoid osteoma in the pediatric and adolescent population.** *J Vasc Interv Radiol* 2016;27:232–37; quiz 238 CrossRef Medline
43. Rehnitz C, Sprengel SD, Lehner B, et al. **CT-guided radiofrequency ablation of osteoid osteoma and osteoblastoma: clinical success and long-term follow up in 77 patients.** *Eur J Radiol* 2012;81:3426–34 CrossRef Medline
44. Weber MA, Sprengel SD, Omlor GW, et al. **Clinical long-term outcome, technical success, and cost analysis of radiofrequency ablation for the treatment of osteoblastomas and spinal osteoid osteomas in comparison to open surgical resection.** *Skeletal Radiol* 2015;44:981–93 CrossRef Medline
45. Tsoumakidou G, Too CW, Garnon J, et al. **Treatment of a spinal aneurysmal bone cyst using combined image-guided cryoablation and cementoplasty.** *Skeletal Radiol* 2015;44:285–89 CrossRef Medline
46. Griauzde J, Gemmete JJ, Farley F. **Successful treatment of a Musculoskeletal Tumor Society grade 3 aneurysmal bone cyst with N-butyl cyanoacrylate embolization and percutaneous cryoablation.** *J Vasc Interv Radiol* 2015;26:9050–59 CrossRef Medline
47. Hao J, Hu Z. **Percutaneous cement vertebroplasty in the treatment of symptomatic vertebral hemangiomas.** *Pain Physician* 2012;15:43–49 Medline
48. Liu XW, Jin P, Wang LJ, et al. **Vertebroplasty in the treatment of symptomatic vertebral haemangiomas without neurological deficit.** *Eur Radiol* 2013;23:2575–81 CrossRef Medline
49. Cloran FJ, Pukenas BA, Loevner LA, et al. **Aggressive spinal haemangiomas: imaging correlates to clinical presentation with analysis of treatment algorithm and clinical outcomes.** *Br J Radiol* 2015;88:20140771 CrossRef Medline
50. Guarnieri G, Ambrosanio G, Vassallo P, et al. **Vertebroplasty as treatment of aggressive and symptomatic vertebral hemangiomas: up to 4 years of follow-up.** *Neuroradiology* 2009;51:471–76 CrossRef Medline
51. Pedicelli A, Papacci F, Leone A, et al. **Vertebroplasty for symptomatic monostotic Paget disease.** *J Vasc Interv Radiol* 2011;22:400–03 CrossRef Medline
52. Kremer MA, Fruin A, Larson TC 3rd, et al. **Vertebroplasty in focal Paget disease of the spine: case report.** *J Neurosurg (Spine)* 2003;99:110–13 CrossRef Medline
53. Tancioni F, Di Leva A, Levi D, et al. **Spinal decompression and vertebroplasty in Paget's disease of the spine.** *Sury Neurol* 2006;66:189–91 CrossRef Medline
54. Wallace AN, Chang RO, Hsi AC, et al. **Painful Pagetic vertebra palliated with percutaneous vertebral augmentation.** *Diagn Interv Imaging* 2016;97:269–72 CrossRef Medline
55. Masala S, Pipitone V, Tomassini M, et al. **Percutaneous vertebroplasty in painful Schmorl nodes.** *Cardiovasc Intervent Radiol* 2006;29:97–101 CrossRef Medline
56. Masala S, Anselmetti GC, Marcia S, et al. **Treatment of painful Modic type I changes by vertebral augmentation with bioactive resorbable bone cement.** *Neuroradiology* 2014;56:637–45 CrossRef Medline
57. Jang JS, Kwon HK, Lee JJ, et al. **Rami communicans nerve block for the treatment of symptomatic Schmorl's nodes: a case report.** *Korean J Pain* 2010;23:262–65 CrossRef Medline
58. Tan HQ, Li MH, Wu CG, et al. **Percutaneous vertebroplasty for eosinophilic granuloma of the cervical spine in a child.** *Pediatr Radiol* 2007;37:1053–57 CrossRef Medline
59. Cardon T, Hachulla E, Flipo RM, et al. **Percutaneous vertebroplasty with acrylic cement in the treatment of a Langerhans cell vertebral histiocytosis.** *Clin Rheumatol* 1994;13:518–21 CrossRef Medline
60. Ringe KI, Imeen Ringe K, Rosenthal H, et al. **Radiofrequency ablation of a rare case of an intraosseous hibernoma causing therapy-refractory pain.** *J Vasc Interv Radiol* 2013;24:1754–56 CrossRef Medline
61. Becce F, Richarme D, Letovanec I, et al. **Percutaneous radiofrequency ablation of primary intraosseous spinal glomus tumor.** *Skeletal Radiol* 2012;41:467–72 CrossRef Medline
62. Sebastian AS, Adair MJ, Morris JM, et al. **Minimally invasive treatment of a painful osteolytic lumbar lesion secondary to epithelioid hemangioendothelioma.** *Global Spine J* 2015;5:135–39 CrossRef Medline
63. Wallace AN, Greenwood TJ, Jennings JW. **Use of imaging in the management of metastatic spine disease with percutaneous ablation and vertebral augmentation.** *AJR Am J Roentgenol* 2015;205:434–41 CrossRef Medline
64. Buy X, Tok CH, Szwarc D, et al. **Thermal protection during percutaneous thermal ablation procedures: interest of carbon dioxide dissection and temperature monitoring.** *Cardiovasc Intervent Radiol* 2009;32:529–34 CrossRef Medline
65. Tsoumakidou G, Garnon J, Ramamurthy N, et al. **Interest of electrostimulation of peripheral motor nerves during percutaneous thermal ablation.** *Cardiovasc Intervent Radiol* 2013;36:1624–28 CrossRef Medline
66. Kurup AN, Morris JM, Boon AJ, et al. **Motor evoked potential monitoring during cryoablation of musculoskeletal tumors.** *J Vasc Interv Radiol* 2014;25:1657–64 CrossRef Medline

Brain Perivascular Spaces as Biomarkers of Vascular Risk: Results from the Northern Manhattan Study

J. Gutierrez, M.S.V. Elkind, C. Dong, M. Di Tullio, T. Rundek, R.L. Sacco, and C.B. Wright

ABSTRACT

BACKGROUND AND PURPOSE: Dilated perivascular spaces in the brain are associated with greater arterial pulsatility. We hypothesized that perivascular spaces identify individuals at higher risk for systemic and cerebral vascular events.

MATERIALS AND METHODS: Stroke-free participants in the population-based Northern Manhattan Study had brain MR imaging performed and were followed for myocardial infarction, any stroke, and death. Imaging analyses distinguished perivascular spaces from lesions presumably ischemic. Perivascular spaces were further subdivided into lesions with diameters of ≤3 mm (small perivascular spaces) and >3 mm (large perivascular spaces). We calculated relative rates of events with Poisson models and hazard ratios with Cox proportional models.

RESULTS: The Northern Manhattan Study participants who had MR imaging data available for review ($n = 1228$; 59% women, 65% Hispanic; mean age, 71 ± 9 years) were followed for an average of 9 ± 2 years. Participants in the highest tertile of the small perivascular space score had a higher relative rate of all deaths (relative rate, 1.38; 95% CI, 1.01–1.91), vascular death (relative rate, 1.87; 95% CI, 1.12–3.14), myocardial infarction (relative rate, 2.08; 95% CI, 1.01–4.31), any stroke (relative rate, 1.79; 95% CI, 1.03–3.11), and any vascular event (relative rate, 1.74; 95% CI, 1.18–2.56). After we adjusted for confounders, there was a higher risk of vascular death (hazard ratio, 1.06; 95% CI, 1.01–1.11), myocardial infarction (hazard ratio, 2.22; 95% CI, 1.12–4.42), and any vascular event (hazard ratio, 1.04; 95% CI, 1.01–1.08) with higher small perivascular space scores.

CONCLUSIONS: In this multiethnic, population-based study, participants with a high burden of small perivascular spaces had increased risk of vascular events. By gaining pathophysiologic insight into the mechanism of perivascular space dilation, we may be able to propose novel therapies to better prevent vascular disorders in the population.

ABBREVIATIONS: HR = hazard ratio; LPI = lesions presumably ischemic; MI = myocardial infarction; NOMAS = Northern Manhattan Study; PP = pulse pressure; PVS = perivascular space; RR = relative rate; WMHV = white matter hyperintensity volume

On entering the skull, large arteries of the circle of Willis become encircled by a layer of leptomeninges and pial cells that accompany them through their course in the subarachnoid space and into the brain parenchyma, creating a potential perivascular space (PVS).[1-3] The physiologic role of these PVSs relates to the drainage of brain interstitial fluid into perivascular pathways, subarachnoid space, and the glymphatic drainage system.[1,4] Perivascular spaces are heterogeneous in their anatomic and physiologic characteristics. For example, basal ganglia PVSs are anatomically distinct from cortical PVSs, and arterial PVSs differ from venous PVSs.[1-3] These anatomic differences may have implications for interstitial fluid drainage rates in different brain regions.[5,6]

An increased prevalence of PVSs has been associated with multiple sclerosis,[7] which may suggest altered clearance of inflammatory cells and exudates from the PVSs.[7,8] PVSs have also been associated with pulsatile blood hemodynamics and hypertension.[6] It may be that through these associations, PVSs relate to carotid atherosclerosis,[9] imaging biomarkers of brain small-artery disease such as white matter hyperintensities, and lacunar stroke,[10,11] as well as brain atrophy.[12,13] The coexistence with other imaging biomarkers of small-artery disease, such as lacunar infarcts and white matter disease, which themselves are associated with hypertension,[12,14] may suggest a shared physiopathology.

Received October 11, 2016; accepted after revision January 6, 2017.

From the Departments of Neurology (J.G., M.S.V.E.) and Medicine (M.D.), Columbia University Medical Center, New York, New York; Department of Epidemiology (M.S.V.E.), Mailman School of Public Health, Columbia University, New York, New York; and Department of Neurology (C.D., T.R., R.L.S., C.B.W.), Miller School of Medicine, University of Miami, Miami, Florida.

This work was supported by National Institutes of Health 2R01NS029993–23A1.

Please address correspondence to Jose Gutierrez, MD, MPH, 710 W 168th St, 6th floor, Suite 639, New York, NY 10032; e-mail: jg3233@cumc.columbia.edu; @drjosegc

Indicates open access to non-subscribers at www.ajnr.org

Indicates article with supplemental on-line tables.

http://dx.doi.org/10.3174/ajnr.A5129

Nonetheless, dilated PVSs have been associated with higher systolic blood pressure and pulse pressure (PP) to a greater extent than other imaging biomarkers of small-artery disease[6,15]; this association suggests a differential role for greater pulsatility as a predisposing factor for these lesions. The validity of dilated PVSs as imaging biomarkers of risk has not been validated prospectively, however, to our knowledge.

Because of the links between PVSs and vascular disease, we tested the hypothesis that brain PVSs are independent imaging biomarkers of vascular risk and that this risk is greater in individuals with high PP and among those with evidence of established non-PVS-related small-artery disease in the Northern Manhattan Study (NOMAS) MR imaging substudy.

MATERIALS AND METHODS

The NOMAS MR imaging substudy represents a population-based sample of adults 50 years of age or older at the time of MR imaging who have prospective follow-up. A detailed report of the criteria for enrollment in the NOMAS cohort and the MR imaging substudy has been provided elsewhere.[6] In brief, participants needed to be free of stroke symptoms at the time of enrollment and had to provide informed consent to undergo brain MR imaging. The study was approved by the local institutional review board (Columbia University and University of Miami). Demographic data were self-reported. Hypertension, diabetes, and hypercholesterolemia were defined at the time of MR imaging and during follow-up by either self-reported diagnoses, medication use to treat these vascular risks, or blood pressure and/or laboratory evidence of these vascular risks, as previously reported.[6,9] Blood pressure measurements were taken twice (>1 hour apart) at the time of the brain MR imaging. Smoking was defined as self-reported current smoking at the time of MR imaging and during follow-up.

Brain MR Imaging Protocol and Postprocessing

Imaging was performed on a dedicated 1.5T research MR imaging system (Philips Healthcare, Best, the Netherlands). The FLAIR image was acquired in the multisection turbo spin-echo mode with an FOV of 250 mm, rectangular FOV of 80%, acquisition matrix of 192 × 133 scaled to 256 × 256 in reconstruction, 3-mm section thickness with no gap, a TE of 144 ms, a TR of 5500 ms, an inversion recovery delay of 1900 ms, and a flip angle of 90°. Dilated PVSs have been subdivided into 4 types: type III lacunes, a to d. Dilated PVSs of small diameter (ie, <3 mm) have been called "type III lacunes a" or "criblures,"[5] and here we call them small PVSs. They are often numerous, and it is not practical to count them. Consequently, semiquantitative scores have been proposed.[14] Small PVSs are defined here as brain parenchymal voids observed on axial T1 images of no more than 5 mm in any axial diameter (Fig 1).[16,17] A semiquantitative score ranging from 0 to 2 was used to rate 13 separate anatomic areas in the brain, with a possible overall score thus ranging from 0 to 26. The intra- and interreader reliabilities were excellent (intraclass correlation coefficient = 0.90) and good (intraclass correlation coefficient = 0.73).[6,9] For T1 voids of >5 mm, we noted their anatomic location and the associated FLAIR characteristics (ie, hyperintense rim) and obtained the longest axial diameter, a diameter perpendicular to that, and a vertical diameter (multiplying the number of sections by section thickness [1.3 mm in this case]) to account for the rostral path of perivascular spaces. The volume of each large T1 void was calculated by using the ABC/2 formula for ovoid bodies,[18] which yielded a minimum volume-derived diameter of 3 mm. Motion artifacts on T1 were noted as none, mild-to-moderate, or severe. The measurement and visual ratings were performed with 3D Slicer open source software, Version 4.3.1 (http://www.slicer.org), which permits measurements below the pixel resolution of our scans.

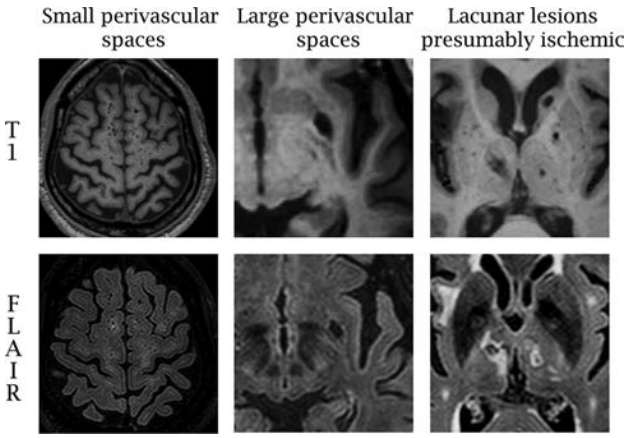

FIG 1. Examples of parenchymal voids rated in the Northern Manhattan Study MR imaging substudy.

We developed a previously published probabilistic method informed by anatomic-radiologic correlation studies that differentiates subclinical lesions presumably ischemic (LPI) and large PVSs (Fig 1).[6] Large PVSs correspond to lacunes type IIIb (subcortical or cerebellar) and type IIIc (infraputaminal).[5] With the shape, anatomic location, and features of the T1 voids, we classified lesions as more likely LPI, large PVS, or uncertain. With these criteria, the FLAIR rim was the dominant feature in determining LPI versus large PVSs, except in the brain stem and the upper two-thirds of the basal ganglia, where pathologic evidence showed that voids in these areas are more likely to represent infarcts.[17,19,20] Uncertain voids were found in 56 participants and were isolated from LPI or large PVSs in only 9 participants. Due to the lack of confirmatory testing about the nature of these voids, we left them out of this analysis. This method has proved to have moderate-to-good reliability.[6,9] The total volume of large perivascular spaces was calculated as the sum of the individual volume of each large perivascular space noted per participant, and the large perivascular spaces score consisted of the number of large perivascular spaces per participant.

White matter hyperintensity volume (WMHV), total intracranial volume (ie, head size), and total cerebral volume were obtained automatically with a Quantum 6.2 package on an Ultra 5 workstation (Sun Microsysytems, Santa Clara, California) as described before. Briefly, tracing the dura allowed the removal of brain elements from the scan, keeping anterior and middle cranial fossae but excluding the posterior fossa, resulting in total intracranial volume. Total cerebral volume was computed as the sum of whole-brain volume voxels from the T1 segmentation process, and white matter hyperintensity volume was calculated as the sum

of voxels of ≥3.5 SDs above the mean image intensity multiplied by pixel dimensions and section thickness using axial FLAIR images.[21] For this study, the percentage of atrophy was obtained by using the formula [(Total Intracranial Volume − Total Cerebral Volume) / Total Intracranial Volume × 100].[22]

Longitudinal Follow-Up

Participants in the NOMAS MR imaging substudy are screened annually with standardized telephone interviews and/or in-person visits if the participant was screened positive for a predefined outcome and/or censoring (ie, no outcome reported). The outcomes include any stroke, MI, or death (including cause of death). Any vascular event was defined as a composite of vascular death, any stroke, or myocardial infarction (MI), as described previously.[23] Briefly, death and vascular death were adjudicated by NOMAS investigators with a negligible loss to follow-up. Most NOMAS participants are admitted for inpatient evaluation in case of major vascular outcomes such as stroke or MI. For participants not admitted to Columbia University Medical Center, we collect their medical records from the reported hospital of admission. Subsequently, stroke subtypes are adjudicated independently by 2 study vascular neurologists (blinded to the baseline MR imaging), and MI is adjudicated by a study cardiologist with the criteria from the Cardiac Arrhythmia Suppression Trial and the Lipid Research Clinics Coronary Primary Prevention Trial.[24,25]

Statistical Analysis

Differences in continuous variables were tested with Student *t* tests, and differences in categoric variables were assessed with χ^2 tests. The 2 main independent variables were the small and large PVSs. Outcomes were all deaths, vascular death, MI, any stroke, and any vascular events. The small and large PVS scores were used continuously with a Poisson distribution or categorically with arbitrary cutoffs of tertiles for the small PVS score, and ≥2 large PVSs for the large PVS score. To build risk models, we adjusted for total intracranial volume as a covariate. We calculated incidence rates, relative rates, and their 95% confidence intervals with Poisson regression and hazard ratios (HRs) and their 95% CIs with Cox proportional hazard regressions, with robust sandwich error variance, adjusting for demographics, prevalent and incident vascular risk factors, and competing risks between death and the other outcomes.[26] To verify that the effect of small or large PVSs was not confounded by pulsatility, we repeated fully adjusted models, substituting hypertension with PP, mean arterial pressure, and a variable for the use of antihypertensives. We tested whether an interaction existed between small and large PVSs with PP and separately with WMHV or LPI at the time of MR imaging and performed stratified models if indicated. The statistical analysis was performed with SAS software, Version 9.4 (SAS Institute, Cary, North Carolina).

RESULTS

Description of the Cohort

After excluding those without available T1 sequences, 1228 NOMAS participants were included in this analysis (On-line Table 1). Participants were followed for an average of 9 ± 2 years (median, 9 years; range, 0.5–12.0 years), contributing a total of 10,905 person-years of follow-up with negligible loss to follow-up.

Small PVSs were found in 91% of the sample (per-participant mean, 5.5 ± 3.8; median, 5; range, 0–22), while large PVSs were present in 42% (20% had only 1 large PVS; 22% had ≥2 large PVSs). Small PVSs were more often found in the basal ganglia (83%), followed by subcortical white matter (79%) and the posterior fossa (17%). Large PVSs were more often infraputaminal (29%) than subinsular (13%) or subcortical (7%). With linear regression with total intracranial volume as the outcome and adjusted for age, sex, and ethnicity, a small PVS score ($\beta = 0.0001$, $P = .02$) and large perivascular spaces total volume ($\beta = 0.05$, $P = .04$) were associated with total intracranial volume, but a large PVS score was not ($\beta = 0.60$, $P = .80$).

In adjusted models, hypertension was associated with small ($\beta = 0.14 \pm 0.05$, $P = .001$) and large PVS scores ($\beta = 0.52 \pm 0.11$, $P < .001$). Men ($\beta = -0.13 \pm 0.05$, $P = .01$) and older age ($\beta = 0.05 \pm 0.01$ per year, $P = .001$) were associated with a small PVS score, and a lower body mass index was associated with a large PVS score ($\beta = -0.03 \pm 0.01$, $P = .001$, On-line Table 2). There was no association between brain atrophy and small PVS ($\beta = -0.01$, $P = .34$) or large PVS scores (by number $\beta = 0.01$, $P = .64$; or by volume $\beta = 0.001$, $P = .21$).

Incidence and Risk of Outcome Events

Compared with participants in the lowest tertile of small PVSs, those in the highest tertile had a higher relative rate (RR) of all deaths (RR, 1.38; 95% CI, 1.01–1.91), vascular death (RR, 1.87; 95% CI, 1.12–3.14), MI (RR, 2.08; 95% CI, 1.01–4.31), any stroke (RR, 1.79; 95% CI, 1.03–3.11), and any vascular event (RR, 1.74; 95% CI, 1.18–2.56). There were no significant differences in the rate of events by the number of large PVSs (On-line Table 3).

In adjusted Cox proportional models, participants with higher small PVS scores had a higher risk of vascular death, MI, or any vascular events but not of any stroke (Table 1). Adjusting for WMHV and LPI attenuated the association of small PVSs with the risk of vascular death (HR, 1.04; 95% CI, 0.98–1.09) and any vascular events (HR,1.02; 95% CI, 0.99–1.06) but not with the risk of MI (HR, 2.15; 95% CI, 1.07–4.33). Substituting PP, mean arterial pressure, and antihypertensive use at the time of MR imaging instead of hypertension did not change the significance of these associations.

Large PVSs were not predictors of outcome events in this sample, either by number, volume, or categorized as ≥2 large PVSs. Stratifying the small and large PVS scores by anatomic location demonstrated that participants with higher small PVS scores in the basal ganglia were at a higher risk of vascular death (HR, 1.12; 95% CI, 1.02–1.22) and any vascular event (HR, 1.06; 95% CI, 1.00–1.13), while a higher small PVS score in the subcortical regions conferred a higher risk of any stroke (HR, 1.08; 95% CI, 1.00–1.16) but not of MI or vascular death (Table 2).

Interactions with Pulsatile Hemodynamics and Other Biomarkers of Small-Artery Disease

Pulse pressure measured at MR imaging was an effect modifier of the association between small PVSs and vascular death ($P = .011$),

Table 1: Hazard ratios between perivascular spaces and outcome events[a]

	All Deaths	Vascular Death	Myocardial Infarction	Any Stroke	Any Vascular Event
Small PVS score					
Continuously	1.01, 0.98–1.04	1.06, 1.01–1.11	1.03, 0.98–1.08	1.04, 0.98–1.10	1.04, 1.01–1.07
Categorically					
First tertile	Reference	Reference	Reference	Reference	Reference
Second tertile	0.72, 0.53–0.96	1.13, 0.68–1.87	2.21, 1.10–4.45	0.96, 0.54–1.72	1.23, 0.86–1.75
Third tertile	0.95, 0.71–1.27	1.34, 0.80–2.23	1.81, 0.89–3.71	1.51, 0.88–2.57	1.38, 0.97–1.98
Large PVS score					
Continuously	0.99, 0.90–1.10	0.99, 0.89–1.10	1.10, 0.93–1.04	1.07, 0.88–1.28	1.08, 0.97–1.21
Categorically					
≤1	Reference	Reference	Reference	Reference	Reference
≥2	1.02, 0.77–1.36	1.03, 0.77–1.67	1.40, 0.83–2.36	0.99, 0.60–1.61	1.07, 0.78–1.48

[a] Models are adjusted for head size, motion artifacts, age, sex, ethnicity, vascular risk factors at MRI and during follow-up (hypertension, hypercholesterolemia, diabetes, and smoking), prior cardiac disease, and body mass index. Data are hazard ratios and 95% CIs.

Table 2: Risk of vascular events by anatomic location[a]

	All Deaths	Vascular Death	Myocardial Infarction	Any Stroke	Any Vascular Event
Small PVS score					
Basal ganglia	1.01, 0.95–1.08	1.12, 1.02–1.22	1.06, 0.94–1.19	1.00, 0.90–1.12	1.06, 1.00–1.13
Subcortical	1.01, 0.95–1.07	1.06, 0.99–1.14	1.01, 0.94–1.12	1.08, 1.00–1.16	1.05, 0.99–1.14
Posterior fossa	1.02, 0.80–1.36	1.19, 0.79–1.76	1.26, 0.83–1.91	1.09, 0.70–1.67	1.09, 0.83–1.44
Large PVS score					
Subcortical white matter	0.68, 0.43–1.07	0.81, 0.42–1.47	1.26, 0.85–1.85	1.32, 0.95–1.85	1.08, 0.79–1.47
Subinsular	0.94, 0.80–1.10	1.21, 0.92–1.39	1.10, 0.84–1.43	1.08, 0.80–1.45	1.11, 0.93–1.30
Basal ganglia supraputaminal	1.73, 1.07–2.77	0.54, 0.22–2.25	1.17, 0.31–4.37	1.45, 0.61–3.43	0.90, 0.40–1.91
Basal ganglia infraputaminal	1.05, 0.88–1.25	1.24, 0.93–1.66	0.98, 0.63–1.46	0.92, 0.70–1.22	1.09, 0.89–1.33

[a] Models are adjusted for head size, motion artifacts, age, sex, ethnicity, vascular risk factors at MRI and during follow-up (hypertension, hypercholesterolemia, diabetes, smoking), prior cardiac disease, and body mass index. Data are hazard ratios and 95% CIs.

Table 3: Stratified risk model by tertiles of pulse pressure and systolic blood pressure[a]

Stratified by	Low Tertile	Middle Tertile	High Tertile
Pulse pressure at MRI			
Small PVS score			
Vascular death	1.07 (0.96–1.18)	1.05 (0.96–1.14)	1.08 (1.01–1.17)
Any stroke	1.01 (0.90–1.13)	1.03 (0.90–1.18)	1.07 (0.98–1.16)
Any vascular event	1.05 (0.98–1.13)	1.02 (0.96–1.09)	1.05 (0.99–1.10)
Systolic blood pressure at MRI			
Small PVS score			
Vascular death	1.08 (0.99–1.18)	0.96 (0.86–1.08)	1.11 (1.04–1.20)
Any stroke	1.05 (0.94–1.17)	0.95 (0.83–1.09)	1.08 (1.01–1.16)
Any vascular event	1.05 (0.98–1.12)	1.02 (0.95–1.09)	1.05 (1.00–1.11)

[a] Models are adjusted for head size, motion artifacts, age, sex, ethnicity, vascular risk factors at MRI and during follow-up (hypertension, hypercholesterolemia, diabetes, and smoking), prior cardiac disease, and body mass index. Data are hazard ratios and 95% CIs.

Table 4: Stratified risk models by white matter hyperintensities volume tertiles[a]

Stratified by	WMH Low Tertile	WMH Middle Tertile	WMH High Tertile
Small PVS score			
All deaths	Referent group	1.01 (1.97–1.05)	1.04 (1.01–1.07)
Vascular death		1.06 (1.00–1.11)	1.08 (1.04–1.12)
Any stroke		1.01 (0.94–1.08)	1.07 (1.02–1.12)
Any vascular event		1.03 (0.99–1.07)	1.05 (1.02–1.08)

[a] Models are adjusted for head size, motion artifacts, age, sex, ethnicity, vascular risk factors at MRI and during follow-up (hypertension, hypercholesterolemia, diabetes, and smoking), prior cardiac disease, and body mass index. Data are hazard ratios and 95% CIs.

any stroke ($P = .095$), and any vascular event ($P = .019$, On-line Table 4). In a stratified analysis, a small PVS score was predictive of vascular death, any stroke, and any vascular event only among participants in the highest tertile of PP and/or systolic blood pressure at the time of their MR imaging (Table 3).

There were statistical interactions between small and large PVSs with either WMHV or LPI (On-line Table 5). In stratified models, the risk of all deaths, vascular death, any stroke, and any vascular events related to the small PVS score increased in a dose-effect manner with increasing tertiles of white matter hyperintensity volume (Tables 4 and 5). The risk of MI related to small and large PVSs was higher among participants with coexisting LPI than in those without LPI. Similarly, the risk of vascular death and any vascular events related to a high PVS score was higher among participants with coexisting LPI than in those without LPI.

DISCUSSION

In this population-based study of stroke-free participants, higher incidence rates of death, vascular death, MI, stroke, and any vascular event were noted among those with the highest burden of brain small PVSs but not large PVSs. The risk of events was enhanced when PVSs coexisted with other imaging biomarkers of cerebrovascular disease, similar to what has been reported in other cohorts.[27,28] Also, small PVSs predicted risk among those in the highest tertile of PP and systolic blood pressure, which we interpret as epidemiologic evidence that small PVSs may be considered imaging biomarkers of high systemic pulsatility and may represent end-organ (brain) damage of arterial stiffness.

The discrepancy noted by anatomic location and by coexistence with other biomarkers of cerebrovascular disease suggests a different pathophysiology of proximal-versus-distal small PVSs.

Table 5: Stratified risk models by models by LPI-SBI status[a]

Stratified by	No LPI Present	Any LPI Present
Small PVS score		
Myocardial infarction	Referent group	1.06 (1.01–1.11)
Large PVS score		
Vascular death	Referent group	1.34 (1.12–1.60)
Myocardial infarction		1.27 (1.01–1.58)
Any vascular event		1.18 (1.04–1.35)

[a] Models are adjusted for head size, motion artifacts, age, sex, ethnicity, vascular risk factors at MRI and during follow-up (hypertension, hypercholesterolemia, diabetes, and smoking), prior cardiac disease, and body mass index. Data are hazard ratios and 95% CIs.

For example, as the pulse-wave pressure dissipates centrifugally from the aorta, progressive arterial stiffness limits attenuation of the pulse-wave as it travels into branching arteries leading to end organs.[29] Low-resistance organs like the brain are especially susceptible to damage related to high pulsatility.[30] As the pulse-wave enters the brain, it encounters first the lenticulostriate penetrating branches of the middle cerebral arteries supplying the subtantia innominata and the basal ganglia and, posteriorly, the vertebrobasilar system that supplies the brain stem and the cerebellum. The abrupt change in caliber from large to penetrating arteries renders these smaller vessels susceptible to systemic hemodynamic stresses, and it may explain why small PVSs in these proximal locations better predict vascular outcomes other than stroke.[31,32] For example, NOMAS participants with PVSs in the posterior fossa had a nominal 26% higher risk of MI per PVS noted, while the risk of MI with evidence of subcortical small perivascular spaces was only 1% higher. Some studies have shown that subcortical (distal) PVSs are more common in nonvascular dementias and multiple sclerosis, while basal ganglia (proximal) PVSs are common with vascular dementias and hypertension.[10,33,34] Another possible explanation for the disparities in the rates of PVS by location may be related to the double meningeal wrapping of penetrating arteries in the basal ganglia compared with single-layered coating in other locations,[3] which may affect the drainage efficacy of interstitial fluids. Growing interest has been paid to the interplay among the glymphatic drainage system, PVSs, and arachnoid granulations in the drainage of interstitial brain fluid,[4] but it remains unclear in humans whether glymphatic drainage differs by anatomic location.

Another relevant finding from our work is the lack of correlation between large PVSs and vascular risk, despite their association with hypertension. Initially, we theorized that large PVSs could represent an extreme on a continuum starting with small PVSs; consequently, we hypothesized that large PVSs might confer greater vascular risk. However, the data presented here only suggest an increased risk of vascular events related to large PVSs among those with coexisting LPI. Consequently, large PVSs might be anatomic variants that occasionally may come to clinical attention if they enlarge enough to cause compressive symptoms, but they may not be good biomarkers of vascular risk in the general population (unlike small PVSs or LPI).[35,36] These data also serve as validation of the effort to classify PVSs into distinct pathologic subtypes[5] and should motivate researchers to systematically separate large PVSs from infarcts.[37]

The results presented here prospectively validate small VPSs as imaging biomarkers of vascular risk in an unselected population. We have attempted to systematically differentiate PVSs from infarcts as other groups have,[10,14] but we have incorporated pathologic information that we believe may improve the accuracy of our methods. We lack pathology of these brains, which limits the claim that our method is valid and accurate. The reliability of ratings of brain parenchymal lesions, particularly <3 mm, is less than ideal, even in large epidemiologic studies such as NOMAS, Atherosclerosis Risk in Communities, and others.[6,10,38] The error in measurement may explain the lack of statistical significance in some of our models as it pertains to small PVSs. Because large PVSs are larger and easier to quantify, error is unlikely to be the explanation for the lack of association between large PVSs and outcomes. Automatization of the rating of small and large PVSs and LPI should be a priority in this field, but it appears daunting, given the complexities of the brain anatomy and the conflicting data among studies. The use of PP and systolic blood pressure as biomarkers of arterial stiffness is not unprecedented.[39-41] The lack of more accurate measurements of arterial stiffness, however, is a limitation of our methods.

CONCLUSIONS

We present evidence that individuals with a higher burden of small PVSs on brain MR imaging are at a higher risk of vascular events, especially if their PP or systolic blood pressure is elevated. Among individuals with subcortical but not deep small perivascular spaces who also have coexpression of white matter hyperintensity and LPI, the risk of stroke is higher. These results emphasize the need for an integrated approach to the study of brain arterial disease that takes into account systemic and intracranial anatomic variations among individuals. By gaining this pathophysiologic insight, we may be able to propose novel therapies for palliating the effects of cerebrovascular disorders in the general population.

Disclosures: Jose Gutierrez—*RELATED*: *Grant*: National Institute of Neurological Disorders and Stroke*; *UNRELATED*: *Consultancy*: Prophase, Pfizer; *Expert Testimony*: medico-legal testimony; *Grants/Grants Pending*: National Institute of Neurological Disorders and Stroke*; *Payment for Development of Educational Presentations*: Prophase. Mitchell S.V. Elkind—*RELATED*: *Grant*: National Institutes of Health/National Institute of Neurological Disorders and Stroke, *Comments*: R01 29993 for the Northern Manhattan Study*; *UNRELATED*: *Board Membership*: American Heart Association/American Stroke Association, *Comments*: national, regional, and local boards; *Consultancy*: Boehringer-Ingelheim, Bristol-Myers Squibb–Pfizer Partnership, Sanofi-Regeneron, BioTelemetry/CardioNet, *Comments*: Boehringer-Ingelheim, dabigatran; Bristol-Myers Squibb–Pfizer Partnership, apixaban; Sanofi-Regeneron, PCSK9 inhibitors; Biotelemetry/Cardionet, cardiac monitoring for paroxysmal atrial fibrillation; *Expert Testimony*: Merck/Organon, *Comments*: NuvaRing; *Royalties*: UpToDate, *Comments*: chapters on cryptogenic stroke and hemicraniectomy. Marco Di Tullio—*RELATED*: *Grant*: National Institutes of Health/National Institute of Neurological Disorders and Stroke, *Comments*: research grants to support NOMAS*; *UNRELATED*: *Grants/Grants Pending*: National Institutes of Health/National Institute of Neurological Disorders and Stroke, *Comments*: R01 research grant to study the frequency of asymptomatic atrial fibrillation in the community.* Tatjana Rundek—*RELATED*: *Grant*: National Institutes of Health*. Ralph L. Sacco—*RELATED*: *Grant*: Northern Manhattan Study, National Institute of Neurological Disorders and Stroke*; *UNRELATED*: *Board Membership*: American Academy of Neurology officer; *Consultancy*: Boehringer-Ingelheim. Clinton B. Wright—*RELATED*: *Grant*: National Institutes of Health/National Institute of Neurological Disorders and Stroke, *Comments*: R01 NS 29993*; *UNRELATED*: *Royalties*: UpToDate.com for 2 chapters on vascular dementia. *Money paid to the institution.

REFERENCES

1. Zhang ET, Inman CB, Weller RO. **Interrelationships of the pia mater and the perivascular (Virchow-Robin) spaces in the human cerebrum.** *J Anat* 1990;170:111–23 Medline
2. Fleury J, Gherardi R, Poirier J. **The perivascular spaces of the central nervous system: histophysiological data.** *Ann Pathol* 1984;4:245–47 Medline
3. Pollock H, Hutchings M, Weller RO, et al. **Perivascular spaces in the basal ganglia of the human brain: their relationship to lacunes.** *J Anat* 1997;191(pt 3):337–46 CrossRef Medline
4. Louveau A, Smirnov I, Keyes TJ, et al. **Structural and functional features of central nervous system lymphatic vessels.** *Nature* 2015; 523:337–41 CrossRef Medline
5. Poirier J, Derouesne C. **Cerebral lacunae: a proposed new classification.** *Clin Neuropathol* 1984;3:266 Medline
6. Gutierrez J, Elkind MS, Cheung K, et al. **Pulsatile and steady components of blood pressure and subclinical cerebrovascular disease: the Northern Manhattan Study.** *J Hypertens* 2015;33:2115–22 CrossRef Medline
7. Wuerfel J, Haertle M, Waiczies H, et al. **Perivascular spaces: MRI marker of inflammatory activity in the brain?** *Brain* 2008;131: 2332–40 CrossRef Medline
8. Millen JW, Woollam DH. **The reticular perivascular tissue of the centra nervous system.** *J Neurol Neurosurg Psychiatry* 1954;17: 286–94 CrossRef Medline
9. Gutierrez J, Rundek T, Ekind MS, et al. **Perivascular spaces are associated with atherosclerosis: an insight from the Northern Manhattan Study.** *AJNR Am J Neuroradiol* 2013;34:1711–16 CrossRef Medline
10. Zhu YC, Tzourio C, Soumaré A, et al. **Severity of dilated Virchow-Robin spaces is associated with age, blood pressure, and MRI markers of small vessel disease: a population-based study.** *Stroke* 2010;41: 2483–90 CrossRef Medline
11. Doubal FN, MacLullich AM, Ferguson KJ, et al. **Enlarged perivascular spaces on MRI are a feature of cerebral small vessel disease.** *Stroke* 2010;41:450–54 CrossRef Medline
12. Awad IA, Johnson PC, Spetzler RF, et al. **Incidental subcortical lesions identified on magnetic resonance imaging in the elderly, II: postmortem pathological correlations.** *Stroke* 1986;17:1090–97 CrossRef Medline
13. Pullicino PM, Miller LL, Alexandrov AV, et al. **Infraputaminal 'lacunes': clinical and pathological correlations.** *Stroke* 1995;26: 1598–602 CrossRef Medline
14. Heier LA, Bauer CJ, Schwartz L, et al. **Large Virchow-Robin spaces: MR-clinical correlation.** *AJNR Am J Neuroradiol* 1989;10:929–36 Medline
15. Bradbury MW, Cserr HF, Westrop RJ. **Drainage of cerebral interstitial fluid into deep cervical lymph of the rabbit.** *Am J Physiol* 1981; 240:F329–36 Medline
16. Rollins NK, Deline C, Morriss MC. **Prevalence and clinical significance of dilated Virchow-Robin spaces in childhood.** *Radiology* 1993;189:53–57 CrossRef Medline
17. Jungreis CA, Kanal E, Hirsch WL, et al. **Normal perivascular spaces mimicking lacunar infarction: MR imaging.** *Radiology* 1988;169: 101–04 CrossRef Medline
18. Kothari RU, Brott T, Broderick JP, et al. **The ABCs of measuring intracerebral hemorrhage volumes.** *Stroke* 1996;27:1304–05 CrossRef Medline
19. Bokura H, Kobayashi S, Yamaguchi S. **Distinguishing silent lacunar infarction from enlarged Virchow-Robin spaces: a magnetic resonance imaging and pathological study.** *J Neurol* 1998;245:116–22 CrossRef Medline
20. Adachi M, Hosoya T, Haku T, et al. **Dilated Virchow-Robin spaces: MRI pathological study.** *Neuroradiology* 1998;40:27–31 CrossRef Medline
21. Dong C, Nabizadeh N, Caunca M, et al. **Cognitive correlates of white matter lesion load and brain atrophy: the Northern Manhattan Study.** *Neurology* 2015;85:441–49 CrossRef Medline
22. Kloppenborg RP, Nederkoorn PJ, Grool AM, et al; SMART Study Group. **Cerebral small-vessel disease and progression of brain atrophy: the SMART-MR study.** *Neurology* 2012;79:2029–36 CrossRef Medline
23. Boden-Albala B, Roberts ET, Bazil C, et al. **Daytime sleepiness and risk of stroke and vascular disease: findings from the Northern Manhattan Study (NOMAS).** *Circ Cardiovasc Qual Outcomes* 2012;5: 500–07 CrossRef Medline
24. Echt DS, Liebson PR, Mitchell LB, et al. **Mortality and morbidity in patients receiving encainide, flecainide, or placebo: the Cardiac Arrhythmia Suppression Trial.** *N Engl J Med* 1991;324:781–88 CrossRef Medline
25. Schaefer EJ, Lamon-Fava S, Jenner JL, et al. **Lipoprotein(a) levels and risk of coronary heart disease in men: the Lipid Research Clinics Coronary Primary Prevention Trial.** *JAMA* 1994;271:999–1003 Medline
26. So Y, Lin G, Johnston G. **Using the PHREG procedure to analyze competing-risks data.** In: *Proceedings of the SAS Global Forum 2015 Conference*. Cary, NC: SAS Institute Inc; 2015. http://support.sas.com/resources/papers/proceedings15/SAS1855-2015.pdf. Accessed September 5, 2016
27. Huijts M, Duits A, van Oostenbrugge RJ, et al. **Accumulation of MRI markers of cerebral small vessel disease is associated with decreased cognitive function: a study in first-ever lacunar stroke and hypertensive patients.** *Front Aging Neurosci* 2013;5:72 CrossRef Medline
28. Staals J, Makin SD, Doubal FN, et al. **Stroke subtype, vascular risk factors, and total MRI brain small-vessel disease burden.** *Neurology* 2014;83:1228–34 CrossRef Medline
29. Mitchell GF. **Arterial stiffness and wave reflection: biomarkers of cardiovascular risk.** *Artery Res* 2009;3:56–64 CrossRef Medline
30. Kalvach P, Gregová D, Skoda O, et al. **Cerebral blood supply with aging: normal, stenotic and recanalized.** *J Neurol Sci* 2007;257: 143–48 CrossRef Medline
31. Cole FM, Yates PO. **Comparative incidence of cerebrovascular lesions in normotensive and hypertensive patients.** *Neurology* 1968; 18:255–59 CrossRef Medline
32. Hughes W. **Hypothesis.** *Lancet* 1965;286:19–21 CrossRef
33. Varma AR, Laitt R, Lloyd JJ, et al. **Diagnostic value of high signal abnormalities on T2 weighted MRI in the differentiation of Alzheimer's, frontotemporal and vascular dementias.** *Acta Neurol Scand* 2002;105:355–64 CrossRef Medline
34. Etemadifar M, Hekmatnia A, Tayari N, et al. **Features of Virchow-Robin spaces in newly diagnosed multiple sclerosis patients.** *Eur J Radiol* 2011;80:e104–08 CrossRef Medline
35. Salzman KL, Osborn AG, House P, et al. **Giant tumefactive perivascular spaces.** *AJNR Am J Neuroradiol* 2005;26:298–305 Medline
36. Papayannis CE, Saidon P, Rugilo CA, et al. **Expanding Virchow Robin spaces in the midbrain causing hydrocephalus.** *AJNR Am J Neuroradiol* 2003;24:1399–403 Medline
37. Gupta A, Giambrone AE, Gialdini G, et al. **Silent brain infarction and risk of future stroke: a systematic review and meta-analysis.** *Stroke* 2016;47:719–25 CrossRef Medline
38. Bezerra DC, Sharrett AR, Matsushita K, et al. **Risk factors for lacune subtypes in the Atherosclerosis Risk in Communities (ARIC) Study.** *Neurology* 2012;78:102–08 CrossRef Medline
39. Mitchell GF, van Buchem MA, Sigurdsson S, et al. **Arterial stiffness, pressure and flow pulsatility and brain structure and function: the Age, Gene/Environment Susceptibility–Reykjavik study.** *Brain* 2011;134:3398–407 CrossRef Medline
40. Franklin SS, Khan SA, Wong ND, et al. **Is pulse pressure useful in predicting risk for coronary heart disease? The Framingham Heart Study.** *Circulation* 1999;100:354–60 CrossRef Medline
41. McEniery CM, Yasmin, Hall IR, et al; ACCT Investigators. **Normal vascular aging: differential effects on wave reflection and aortic pulse wave velocity: the Anglo-Cardiff Collaborative Trial (ACCT).** *J Am Coll Cardiol* 2005;46:1753–60 CrossRef Medline

Site and Rate of Occlusive Disease in Cervicocerebral Arteries: A CT Angiography Study of 2209 Patients with Acute Ischemic Stroke

D.C. Rotzinger, P.J. Mosimann, R.A. Meuli, P. Maeder, and P. Michel

ABSTRACT

BACKGROUND AND PURPOSE: CTA can rapidly and accurately detect and localize occlusive disease in patients with ischemic stroke. We have used CTA to assess arterial stenosis and occlusion in an ischemic stroke population arriving at a tertiary stroke center within 24 hours of symptom onset in order to obtain a comprehensive picture of occlusive disease pattern, and to determine the proportion of eligible candidates for endovascular treatment.

MATERIALS AND METHODS: Data from consecutive patients with acute ischemic stroke admitted to a single center between 2003 and 2012, collected in the Acute Stroke Registry and Analysis of Lausanne data base, were retrospectively analyzed. Patients with a diagnostic CTA within 24 hours of symptom onset were selected. Relevant extra- and intracranial pathology, defined as stenosis of ≥50% and occlusions, were registered and classified into 21 prespecified segments.

RESULTS: Of the 2209 included patients (42.1% women; median age, 72 years), 1075 (48.7%) had pathology in and 308 (13.9%) had pathology outside the ischemic territory. In the 50,807 arterial segments available for revision, 1851 (3.6%) abnormal segments were in the ischemic (symptomatic) territory and another 408 (0.8%) were outside it (asymptomatic). In the 1211 patients with ischemic stroke imaged within 6 hours of symptom onset, 40.7% had symptomatic large, proximal occlusions potentially amenable to endovascular therapy.

CONCLUSIONS: CTA in patients with acute ischemic stroke shows large individual variations of occlusion sites and degrees. Approximately half of such patients have no visible occlusive disease, and 40% imaged within 6 hours show large, proximal segment occlusions amenable to endovascular therapy. These findings show the importance of early noninvasive imaging of extra- and intracranial arteries for identifying occlusive disease, planning recanalization strategies, and designing interventional trials.

ABBREVIATIONS: AIS = acute ischemic stroke; ASTRAL = Acute Stroke Registry and Analysis of Lausanne

More than 80% of strokes are ischemic, usually caused by large-artery atherosclerosis, cardiac embolism, or cerebral microangiopathy.[1] CTA or MR arterial neuroimaging is frequently used at admission[2,3] to determine occlusion sites and clot extent and to plan acute recanalization strategies.[4-7] CTA is widely available and allows rapid assessment of the entire arterial vasculature from the aortic arch to the vertex. In addition, it accurately depicts arterial occlusive disease with good interrater agreement.[8] Most clinically relevant arterial occlusive disease is found in the extra- and intracranial arteries, supporting aortic arch-to-vertex CTA for patients with acute ischemic stroke (AIS).[9] Potential drawbacks of CTA are iodinated contrast allergy and radiation exposure.

The purpose of this study was to obtain a comprehensive picture of cerebrovascular occlusive disease in a representative AIS population, using admission CTA, to determine the proportion of eligible candidates for endovascular treatment. Such patients were identified by looking for symptomatic proximal arterial occlusions readily accessible with endovascular devices. Moreover, we aimed at determining the proportion

Received August 23, 2016; accepted after revision December 13.

From the Department of Diagnostic and Interventional Radiology (D.C.R., P.J.M., R.A.M., P. Maeder) and Neurology Service (P. Michel), Department of Clinical Neurosciences, Centre Hospitalier Universitaire Vaudois, Lausanne, Switzerland.

David C. Rotzinger and Pascal J. Mosimann contributed equally to this work.

The Swiss Heart Foundation supported this project.

Paper previously presented at: The Joint annual meeting 2014 (Swiss Society of Intensive Care Medicine, 190th Annual Meeting of the Swiss Neurological Society, Swiss Society of Neuroradiology SSNR Educational Course 2014, Swiss Stroke Society, Swiss Society of Emergency Medicine), October 29–31, 2014; Congress Centre Kursaal Interlaken, Switzerland; and Annual Meeting of the Swiss Congress of Radiology, June 8–10, 2014; Davos, Switzerland.

Please address correspondence to David C. Rotzinger, MD, Department of Diagnostic and Interventional Radiology, Centre Hospitalier Universitaire Vaudois, Rue du Bugnon 46, 1011 Lausanne, Switzerland; e-mail: david.rotzinger@chuv.ch

Indicates open access to non-subscribers at www.ajnr.org

Indicates article with supplemental on-line tables.

Indicates article with supplemental on-line photos.

http://dx.doi.org/10.3174/ajnr.A5123

of patients with abnormal segments in ischemic and nonischemic territories and describing the distribution of arterial occlusive disease in extra- versus intracranial vessels, anterior-versus-posterior circulation, and serial (tandem) pathologies.

MATERIALS AND METHODS

Patients

We used the patients admitted with AIS between January 2003 and December 2012 from the prospectively constructed Acute Stroke Registry and Analysis of Lausanne (ASTRAL), which collects information on all patients with AIS referred to the stroke center and/or intensive care unit of Lausanne University hospital (Centre Hospitalier Universitaire Vaudois) within 24 hours of the last-known-well time.[1] We included all consecutive patients who had a diagnostic CTA available for analysis. CTA studies were rated as diagnostic or nondiagnostic by at least 2 authors, and the latter studies were excluded when at least 1 author considered them nondiagnostic (On-line Fig 1). A diagnostic CTA provides a sharp delineation of head and neck vessels, allowing evaluation of partial or complete filling defects. Patients arriving later than 24 hours from symptom onset and presenting with transient ischemic attack, cerebral or subarachnoid hemorrhage, persistent retinal ischemia, amaurosis fugax, and spinal cord ischemia were excluded. Reasons for exclusion were collected.

CTA-based imaging information, demographic data, cardiovascular risk factors, and ischemic side and territory were extracted and analyzed retrospectively. Stroke was categorized according to the TOAST (Trial of ORG 10172 in Acute Stroke Treatment) classification,[10] and we added dissection, likely patent foramen ovale–related stroke, and combinations of mechanisms.

Neuroimaging Protocol

All included patients underwent standard AIS imaging, including noncontrast head CT, cerebral perfusion CT, and cervicocerebral CT angiography. In patients undergoing thrombolysis, CTA was acquired immediately before or immediately after the rtPA bolus; therefore, this process made it unlikely that thrombolysis influenced the arterial occlusive pathology. Imaging was performed on a 16–detector row CT scanner (LightSpeed 16 Advantage; GE Healthcare, Milwaukee, Wisconsin) until November 2005 and afterwards on a 64–detector row CT scanner (LightSpeed VCT 64; GE Healthcare). Technical parameters for cerebral and extracranial CTA were the following: multidetector-array in a helical mode, 120 kV(peak), 150–300 mAs, section thickness = 1.25 mm before 2006 and 0.63 mm thereafter, pitch = 0.9:1. Image-acquisition delay depended on the arrival time of a 20-mL contrast bolus test (range, 15–20 seconds). Acquisition was then performed after intravenous administration of 50 mL of iohexol (300 mg/mL of iodine, Accupaque; GE Healthcare) at a rate of 5 mL per second with a power injector (Stellant D CT Injection System; Medrad, Indianola, Pennsylvania) in the arterial phase. Coverage extended from the origin of the aortic arch to the top of the corpus callosum. Delayed phase images were obtained on the brain only.

Image Interpretation

Only CTA images were used for this study. Raw CTA source images in the axial plane were analyzed for focal arterial occlusive disease. Maximum intensity projections were then reconstructed in axial, sagittal, and coronal planes. Curvilinear reconstructions were obtained routinely.

A senior board-certified vascular neurologist (P. Michel) or neuroradiologists (R.A.M. or P. Maeder) with >10 years' experience analyzed the acute CTAs within 7 days after admission. In cases of discordance, images were reviewed by the vascular neurologist and at least 1 neuroradiologist to reach agreement. Interrater agreement was assessed on 100 consecutive patients in the data base by using κ statistics and comparing the CTA interpretations by 1 vascular neurologist (P. Michel) and 1 neuroradiologist (P.J.M.). Both independently assessed the presence or absence of extracranial and intracranial segmental occlusive disease in the proximal (carotid siphon, M1, basilar artery) and distal circulation in the ischemic territory.

Twenty-one arterial segments (counting left and right sides, listed below) were analyzed separately for each patient and graded as normal, stenotic, or occluded. Segments were the following: extracranial vertebral artery (V1–3 segments); intracranial vertebral artery (V4 segment); basilar artery; posterior cerebral artery, P1, P2, and P3 segments; extracranial internal carotid artery; intracranial carotid artery, noting whether T-occlusion was present or not; middle cerebral artery, M1, M2, M3 segments; and anterior cerebral artery, A1, A2, and A3 segments. Imaging data are continuously recorded in the ASTRAL data base.

The term "abnormal" was used for stenotic or occluded segments.

"Occlusion" was defined as the absence of contrast medium filling the examined arterial segment on initial acquisition.[11] For extracranial arteries, stenosis was defined by using the NASCET criteria: caliber reduction of ≥50% for vertebral arteries and ≥70% for carotid arteries.[12] For intracranial arteries, stenosis was defined by using the Warfarin-Aspirin Symptomatic Intracranial Disease method (ie, ≥50% caliber reduction).[13] "Tandem patterns" are defined as arterial occlusive disease affecting both the extra- and intracranial circulation in the same vascular axis. Abnormal segments on CTA were further categorized as symptomatic if the stenosis or occlusion was ipsilateral and proximal to the acute ischemic territory, or asymptomatic, if they were in the nonacute ischemic territory.

To evaluate the number of possible acute mechanical revascularization procedures in readily accessible large arteries, we subjected all occlusions in the extracranial and intracranial carotid arteries, V1–3, V4, basilar artery, P1, A1, M1, and M2 segments to a specific group analysis.

Data Processing and Statistical Analysis

Univariate analysis was performed to compare the characteristics of included and excluded patients by using the Wilcoxon 2-sample test for continuous variables and the χ^2 test for categoric variables. P values < .05 were considered significant. All data were processed by using STATA statistical software (Version 13.1, October 30 2013; StataCorp, College Station, Texas). Odds ratios were obtained by using an on-line calculator.[14]

ASTRAL was approved for scientific use by the institutional ethical commission, which did not require that individual informed consent be obtained.

RESULTS

Of 5022 patients with AIS symptoms who arrived at our institution during the observation period, 2209 patients were enrolled. Reasons for exclusion from ASTRAL were vascular diagnoses other than AIS ($n = 2370$). These and radiologic reasons for exclusion from the study ($n = 443$) are detailed in On-line Fig 1.

Baseline characteristics of the included ($n = 2209$) and excluded ($n = 443$) patients with AIS are described in Table 1. In univariate comparison, patients with AIS excluded for radiologic reasons were older and more often women and tended to have more hypertension and atrial fibrillation and lower admission NIHSS scores. Stroke onset-to-CT and door-to-CT delays were longer, as expected in this group, because a main reason for study exclusion was a CTA performed after 24 hours of onset.

Cervicocerebral CTA analysis of the 2209 enrolled patients yielded 50,807 analyzable arterial segments.

Interrater agreement in the ischemic territory was almost perfect for intracranial proximal occlusive disease ($\kappa = 0.87$) and substantial for intracranial distal and extracranial occlusive disease ($\kappa = 0.61$ and 0.64, respectively), similar to previously published data.[8]

One thousand two hundred twenty-six patients (55.5%) had any arterial occlusion or stenosis (ischemic and nonischemic territories combined), while 983 patients (44.5%) did not show relevant occlusive disease (for details see Tables 2 and 3). One thousand seventy-five patients (48.7% of all patients) had such major abnormalities in the ischemic (ie, symptomatic) territory. Three hundred eight patients (13.9% of all patients) had stenosis or occlusion in territories not related to ischemia (ie, asymptomatic abnormalities) (see On-line Tables 1 and 2 for full details).

If one considered arterial segments, arterial occlusion or stenosis occurred in 2259 segments (4.5% of all segments) (for details, see Tables 2 and 3); 1851 segmental abnormalities (81.9% of all abnormal segments or 3.6% of all examined segments) were in the ischemic ter-

Table 1: Patient characteristics and univariate comparison with the patients excluded for radiologic reasons[a]

	Study Population ($N = 2209$)		Excluded Patients ($n = 443$)		
	No.	% or IQR	No.	% or IQR	*P* Value
Female sex (%)	929	42.1	216	48.8	<.01
Age (yr) (IQR)	72	21	77	24	<.01
Risk factors					
Hypertension (%)	1268	66.9	318	71.8	.02
Heart valves (%)	61	3.2	11	2.5	.51
Coronary artery disease (%)	295	15.5	80	18.1	.20
Dyslipidemia (%)	1325	69.5	270	60.9	<.01
Diabetes (%)	331	17.4	82	18.5	.34
Atrial fibrillation (%)	480	25.2	141	31.8	<.01
Low ejection fraction (%)	91	4.7	24	5.4	.60
Smoking (%)	807	42.3	160	36.1	.06
Stroke mechanism					
Atherosclerosis (%)	304	13.8	99	22.3	.05
Undetermined (%)	553	25	92	20.8	.06
Cardiac (%)	641	29	145	32.7	.12
Lacunar/microangiopathic (%)	269	12.2	62	14.0	.19
Dissections (%)	107	4.8	14	3.2	.07
PFO/other determined/rare (%)	159	7.2	40	9.0	.07
Multiple/coexisting (%)	118	5.3	21	4.7	.48
NIHSS admission (IQR)	7	12	5	9	<.01
Onset-to-CT delay (IQR) (min)	275	565	420	667	<.01
Door-to-CT delay (IQR) (min)	183	469	380	771	<.01

Note:—IQR indicates interquartile range; PFO, patent foramen ovale.

[a] Values are expressed as medians and IQR for continuous variables or absolute counts and percentage for categoric variables unless otherwise stated.

Table 2: Distribution of arterial occlusive disease in numbers and rates, given per patient ($N = 2209$)[a]

	Ischemic Territory				Subtotal for Ischemic Territory		All Abnormalities (Related to Ischemia or Not)			
Circulation	Occlusion		Stenosis		Occlusion and/or Stenosis		Occlusion and/or Stenosis		No Relevant Abnormalities	
Extracranial abnormalities per segment										
Extracranial ICA or CCA	206	9.3%	165	7.5%	369	16.7%	437	19.8%	1772	80.2%
Extracranial vertebral	51	2.3%	26	1.2%	75	3.4%	139	6.3%	2070	93.7%
Subtotal extracranial abnormalities	257	11.6%	190	8.6%	442	20.0%	543	24.6%	1666	75.4%
Isolated extracranial abnormalities	35	1.6%	103	4.7%	136	6.2%	231	10.5%	1978	89.5%
Intracranial abnormalities per patient										
Anterior intracranial	429	19.4%	88	4.0%	508	23.0%	534	24.2%	1675	75.8%
Posterior intracranial	96	4.4%	51	2.3%	135	6.1%	174	7.9%	2035	92.1%
Subtotal intracranial abnormalities	523	23.7%	135	6.1%	633	28.7%	683	30.9%	1526	69.1%
Isolated intracranial abnormalities	519	23.5%	133	6.0%	627	28.4%	669	30.3%	1526	69.1%
Total extra- and intracranial circulation per patient	780	35.3%	325	14.7%	1075	48.7%	1226	55.5%	983	44.5%

Note:—CCA indicates common carotid artery.

[a] The totals and subtotals may be smaller than the sum of the columns because patients may have arterial occlusive disease simultaneously in different segments or on different levels.

Table 3: Distribution of occlusive disease for each arterial segment[a]

Circulation	Ischemic territory				Subtotal Ischemic		All Abnormalities (Related to Ischemia or Not)			
Segments	Occlusion		Stenosis		Occlusion or Stenosis		Occlusion or Stenosis		No Relevant Abnormalities	
Extracranial abnormalities per segment in 2209 patients (n = 50,807 segments)										
Extracranial ICA or CCA	207	4.7%	167	3.8%	374	8.5%	520	11.8%	3898	88.2%
V1–3	59	1.3%	29	0.7%	88	2.0%	160	3.6%	4258	96.4%
Subtotal extracranial	266	3.0%	196	2.2%	462	5.2%	680	7.7%	8156	92.3%
Intracranial abnormalities per segment										
Carotid siphon without T	85	1.9%	47	1.1%	132	3.0%	172	3.9%	4246	96.1%
Carotid siphon with T	124	2.8%	—	0.0%	124	2.8%	125	2.8%	4293	97.2%
MCA: M1	405	9.2%	54	1.2%	457	10.3%	480	10.9%	3938	89.1%
MCA: M2–3 only	226	5.1%	42	1.0%	268	6.1%	279	6.3%	4139	93.7%
ACA: A1	104	2.4%	11	0.3%	115	2.6%	130	2.9%	4288	97.1%
ACA: A2–3 only	9	0.2%	3	0.1%	12	0.3%	14	0.3%	4404	99.7%
Subtotal anterior intracranial	953	3.6%	157	0.6%	1108	4.2%	1200	4.5%	25,308	95.5%
PCA: P1	41	0.9%	10	0.2%	51	1.2%	71	1.6%	4347	98.4%
PCA: P2–3 only	33	0.8%	13	0.3%	46	1.0%	64	1.5%	4354	98.6%
V4	73	1.7%	30	0.7%	103	2.3%	148	3.4%	4270	96.7%
BA	55	2.5%	26	1.2%	81	3.7%	96	4.4%	2113	95.7%
Subtotal posterior intracranial	202	1.3%	79	0.5%	281	1.8%	379	2.5%	15,084	97.6%
Subtotal intracranial	1155	2.8%	236	0.7%	1389	3.3%	1579	3.8%	40,392	96.2%
Subtotal anterior circulation	1160	3.8%	324	1.0%	1482	4.8%	1720	5.6%	29,206	94.4%
Subtotal posterior circulation	261	1.3%	108	0.5%	369	1.9%	539	2.7%	19,342	97.3%
Total extra- and intracranial abnormalities per segment	1421	2.8%	432	0.9%	1851	3.6%	2259	4.5%	48,548	95.5%

Note:—ACA indicates anterior cerebral artery; PCA, posterior cerebral artery; BA, basilar artery; CCA, common carotid artery.

[a] For each arterial segment, numbers and rates are given. Subtotal and total rates are calculated by dividing by all segments in the subtotal/total. A single patient may have several pathologic arterial segments.

ritory (ie, symptomatic). Four hundred eight segmental abnormalities (18.1% of all abnormalities or 0.8% of all examined segments) were in the nonischemic territory (ie, asymptomatic) (see On-line Tables 1 and 2 for full details).

Occlusive disease was most commonly seen in the anterior circulation (76.1% of all abnormal segments). This was more often intracranial than extracranial (30.9% versus 24.6% of all patients).

The proximal MCA (24.7% of all symptomatic abnormalities) was most frequently affected by symptomatic occlusive disease, followed by the extracranial ICA (20.2%) and then the distal MCA (14.5%).

As seen in the tables, occlusion was more frequent than stenosis. Symptomatic tandem patterns (On-line Table 3) were predominantly observed in the anterior circulation (82.1%) in 302 patients (28.1% of all patients with symptomatic abnormalities, 13.7% of all patients in the study). A graphic representation of observed occlusive disease per segment (symptomatic and asymptomatic stenosis or occlusions) is available in Fig 1. A column plot representation of arterial occlusive disease according to localization and type (stenosis versus occlusion) as defined in the "Materials and Methods" section is available in On-line Fig 2. Of patients having a symptomatic intracranial abnormality, 40% had a coexisting extracranial abnormality (tandem pattern). Only 34 of the tandem lesions (10.1% of all tandem lesions) were asymptomatic.

In 743 (33%) of the patients with AIS imaged within 24 hours of symptom onset, we found at least 1 symptomatic occlusion in a large, proximal artery and therefore readily accessible to endovascular treatment. These numbers increased to 640 (38.1%) of the 1679 patients imaged within 12 hours, 531 (40.7%) of 1304 imaged within 6 hours, and 480 (42.0%) of 1143 patients imaged within 4.5 hours. Of the patients arriving within 6 hours, the following segments were found occluded on CTA: extracranial ICA (n = 150, 11.5% of patients); V1–V3 (n = 31, 2.4% of patients); intracranial ICA (n = 34, 2.6% of patients); M1 (n = 193, 14.8% of patients); M2 (n = 114, 8.7% of patients); A1 (n = 32, 2.5% of patients); P1 (n = 23, 1.8% of patients); V4 (n = 11, 0.8% of patients); basilar artery (n = 22, 1.7% of patients). This is a total of 610 segments, found in 531 patients.

DISCUSSION

In the largest series to date of patients with AIS undergoing CTA within 24 hours from symptom onset, we found relevant arterial abnormalities in 55.5% of patients, most of which were observed in the ischemic territory. Regarding individual cervical and cerebral arterial segments, only 4.5% were abnormal, again affecting predominantly the ischemic territory. Arterial segments with the highest blood supply (anterior > posterior circulation, larger > smaller arteries) had the most occlusive disease.

Approximately half of the patients with AIS did not have any visible arterial abnormalities on CTA, increasing the chances of a better outcome[15] and making endovascular treatment unnecessary. The fact that an overwhelming proportion of arterial seg-

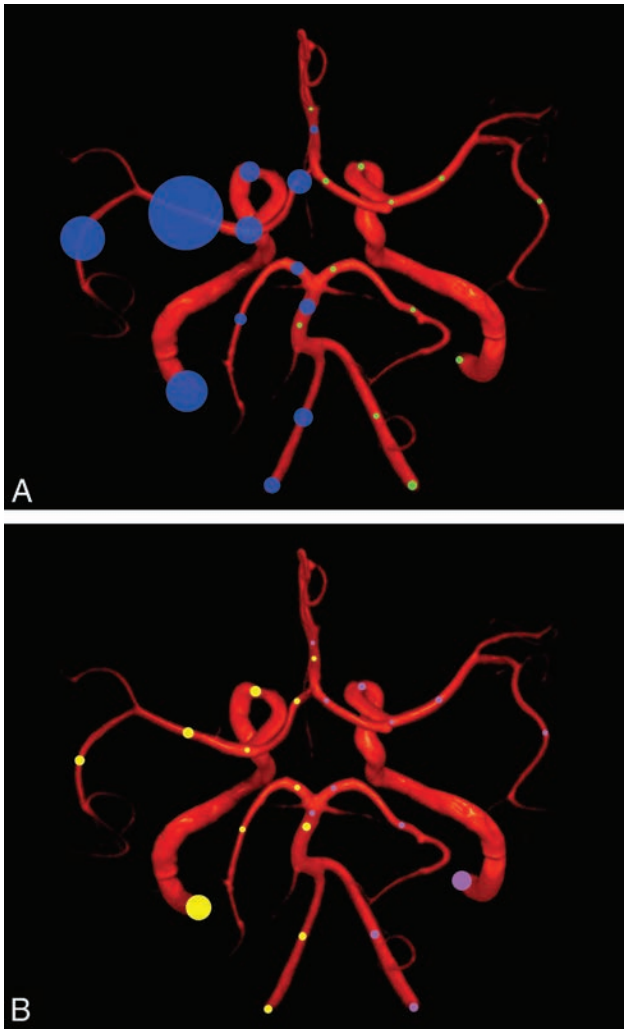

FIG 1. Graphic representation of observed occlusive disease per segment. The area of the circle is proportional to the observed rate. *A*, Rate of symptomatic (right patient side, *blue circles*) and asymptomatic arterial occlusions (left patient side, *green circles*). *B*, Rate of symptomatic (right patient side, *yellow circles*) and asymptomatic arterial stenoses (left patient side, *pink circles*).

ments are patent in AIS (95.5%) is a reminder that there is a great potential for collateral blood supply into the ischemic territory, potentially allowing access of thrombolytic or neuroprotective drugs to the acutely ischemic brain.

Symptomatic arterial abnormalities were more often found in the anterior circulation (76.1% of all abnormal segments, occurring in 81.6% of patients with symptomatic abnormalities), which is consistent with the proportion of blood flow being directed to this part of the cerebral circulation. In addition, there is significantly more arterial occlusive disease in patients with anterior-versus-posterior circulation stroke (see odds ratios in Table 4). This may be related to posterior circulation strokes being more often of microangiopathic origin,[16] with less detectable arterial pathology on noninvasive imaging.

Patients more often had symptomatic arterial abnormalities in the intra- rather than the extracranial circulation (28.6% versus 20.0% of all patients). This may be because most emboli from the heart and proximal extracranial arteries are too small to occlude the cervical arteries and get blocked only in smaller, intracranial

Table 4: Localization of arterial occlusive disease in the ischemic territory[a]

	Per Patient (Table 2)		Per Segment (Table 3)	
	OR	95% CI	OR	95% CI
Anterior vs posterior circulation strokes	6.7	5.6–7.9	2.8	2.5–3.1
Intracranial segments	4.6	3.7–5.6	2.5	2.2–2.8
Extracranial segments	5.8	4.5–7.4	4.6	3.7–5.9
Intracranial vs extracranial localization	1.6	1.4–1.8	0.6	0.6–0.8
Anterior circulation	1.5	1.3–1.7	0.5	0.4–0.5
Posterior circulation	1.8	1.4–2.4	0.9	0.7–1.2
Tandem pattern: anterior vs posterior circulation	5.0	3.7–6.7	–	–

[a] Results are expressed as odds ratios plus 95% confidence intervals.

vessels. The finding that the proportion of abnormal arterial segments is lower intracranially (3.8% versus 7.7%, Table 3) is because the intracranial circulation is divided into subsegments. Our results, therefore, show that it is crucial to examine both the extracranial arteries and the circle of Willis in patients with AIS.

Not surprising, symptomatic abnormalities are usually occlusive, whereas asymptomatic abnormalities are typically stenotic, likely explained by a reduced-but-sufficient blood flow through the stenosis. We found a low overall rate (0.7%) of symptomatic intracranial stenosis in our cohort, likely consisting of a combination of atherosclerotic plaques and partially resorbed emboli. A higher rate of intracranial stenosis has been described in Asian patients with ischemic stroke.[17]

The 40% concurrent extracranial (tandem) pathology observed in patients with a symptomatic intracranial abnormality has practical implications because it may complicate endovascular access. This situation seems to be particularly frequent in the anterior circulation (odds ratio of 5.0 for anterior-versus-posterior tandem lesions in our population).

Rapid endovascular treatment by using predominantly stent retrievers has recently been shown to be more effective than IV thrombolysis alone in well-selected patients with proximal intracranial occlusions of the anterior circulation[18] and is now considered the standard of care.[19,20] This is because recanalization is one of the most important predictors of prognosis in AIS,[21,22] and proximal occlusions insufficiently respond to IV thrombolysis in many cases.[23] Endovascular stroke trials have mostly excluded patients with posterior circulation strokes. Although large posterior circulation occlusions are also likely to benefit from endovascular treatment, this benefit has to first be proved by a randomized controlled trial such as the Basilar Artery International Cooperation Study trial.[24]

The proportion of 40.7% of such patients in this tertiary care setting imaged within 6 hours provides an estimate of the number of patients who could benefit from such interventions. When adding clinical and other radiologic criteria as well as contraindications, this number may be reduced by half in the real world, however.[25] Still, improved prehospital identification and transport of patients with probable proximal intracranial occlusions[26] are likely to increase the number of endovascularly treatable patients in comprehensive stroke centers.[27]

The spontaneous recanalization rate of proximal occlusions

between 4.5 and 24 hours from symptom onset is approximately 9% based on the aforementioned proportions of patients with such occlusions. In contrast, early digital subtraction studies reported an estimated 17% spontaneous recanalization at 6–8 hours from stroke onset.[28]

Limitations are the retrospective, uncontrolled nature of the study with data from a single-center registry, which may not have a population representative of other settings for acute stroke care. We excluded a certain number of patients because acute CTA was not performed, mainly due to contrast contraindications. Images of head and neck vessels were analyzed in the arterial phase only, possibly overestimating the degree and extent of proximal occlusive disease. Also, the results are based on CTA, which is a reliable method for assessment of arterial pathology in AIS[4,29,30] but may not be generalizable to other angiographic methods. We did not analyze associations among arterial imaging, clinical variables, and functional outcome because this was the purpose of recent publications.[26,31]

On the other hand, the available data may represent the best possible approximation of a real-world AIS population, given that some patients will always be unable to undergo acute angiographic evaluations.

CONCLUSIONS

This study gives a comprehensive picture of the frequency and distribution of relevant arterial pathology on CTA obtained within 24 hours of symptom onset. Approximately half of patients had relevant arterial pathology in the ischemic territory, mostly in the intracranial anterior circulation; a significant number also had tandem pathology. The 40% of patients with AIS having proximal intracranial arterial occlusions in the first 6 hours give an estimate of the eligibility for acute endovascular therapy.

Disclosures: David Rotzinger—*UNRELATED*: *Employment*: Lausanne University Hospital (Centre Hospitalier Universitaire Vaudois), *Comments*: my employer since 2011. Patrik Michel—*RELATED*: *Grant*: Swiss Heart Foundation*; *UNRELATED*: *Board Membership*: Boehringer-Ingelheim, Bayer Healthcare, Pfizer*; *Consultancy*: Pierre-Fabre, AstraZeneca, Amgen*; *Payment for Lectures Including Service on Speakers Bureaus*: Boehringer-Ingelheim, Bayer Healthcare, Medtronic-Covidien, Stryker*; *Travel/Accommodations/Meeting Expenses Unrelated to Activities Listed*: Boehringer-Ingelheim, Bayer Healthcare.* *Money paid to the institution.

REFERENCES

1. Michel P, Odier C, Rutgers M, et al. **The Acute STroke Registry and Analysis of Lausanne (ASTRAL): design and baseline analysis of an ischemic stroke registry including acute multimodal imaging.** *Stroke* 2010;41:2491–98 CrossRef Medline
2. González RG. **Current state of acute stroke imaging.** *Stroke* 2013;44:3260–64 CrossRef Medline
3. Schramm P, Schellinger PD, Klotz E, et al. **Comparison of perfusion computed tomography and computed tomography angiography source images with perfusion-weighted imaging and diffusion-weighted imaging in patients with acute stroke of less than 6 hours' duration.** *Stroke* 2004;35:1652–58 CrossRef Medline
4. Bash S, Villablanca JP, Jahan R, et al. **Intracranial vascular stenosis and occlusive disease: evaluation with CT angiography, MR angiography, and digital subtraction angiography.** *AJNR Am J Neuroradiol* 2005;26:1012–21 Medline
5. Josephson SA, Bryant SO, Mak HK, et al. **Evaluation of carotid stenosis using CT angiography in the initial evaluation of stroke and TIA.** *Neurology* 2004;63:457–60 CrossRef Medline
6. Obach V, Oleaga L, Urra X, et al. **Multimodal CT-assisted thrombolysis in patients with acute stroke: a cohort study.** *Stroke* 2011;42:1129–31 CrossRef Medline
7. Lansberg MG, Thijs VN, Bammer R, et al. **The MRA-DWI mismatch identifies patients with stroke who are likely to benefit from reperfusion.** *Stroke* 2008;39:2491–96 CrossRef Medline
8. Knauth M, von Kummer R, Jansen O, et al. **Potential of CT angiography in acute ischemic stroke.** *AJNR Am J Neuroradiol* 1997;18:1001–10 Medline
9. Deipolyi AR, Hamberg LM, Gonzaléz RG, et al. **Diagnostic yield of emergency department arch-to-vertex CT angiography in patients with suspected acute stroke.** *AJNR Am J Neuroradiol* 2015;36:265–68 CrossRef Medline
10. Adams HP Jr, Bendixen BH, Kappelle LJ, et al. **Classification of subtype of acute ischemic stroke.** *Stroke* 1993;23:35–41 Medline
11. Vanacker P, Lambrou D, Eskandari A, et al. **Improving prediction of recanalization in acute large-vessel occlusive stroke.** *J Thromb Haemost* 2014;12:814–21 CrossRef Medline
12. North American Symptomatic Carotid Endarterectomy Trial Collaborators. **Beneficial effect of carotid endarterectomy in symptomatic patients with high-grade carotid stenosis.** *N Engl J Med* 1991;325:445–53 CrossRef Medline
13. Chimowitz MI, Lynn MJ, Howlett-Smith H, et al; Warfarin-Aspirin Symptomatic Intracranial Disease Trial Investigators. **Comparison of warfarin and aspirin for symptomatic intracranial arterial stenosis.** *N Engl J Med* 2005;352:1305–16 CrossRef Medline
14. Calculator for confidence intervals of odds ratio in an unmatched case control study. http://www.hutchon.net/confidor.htm. Accessed June 18, 2013
15. Medlin F, Amiguet M, Vanacker P, et al. **Influence of arterial occlusion on outcome after intravenous thrombolysis for acute ischemic stroke.** *Stroke* 2015;46:126–31 CrossRef Medline
16. Libman R, Kwiatkowski T, Hansen MD, et al. **Differences between anterior and posterior circulation stroke in TOAST.** *Cerebrovasc Dis* 2001;11:311–16 CrossRef Medline
17. Wang Y, Zhao X, Liu L, et al; CICAS Study Group. **Prevalence and outcomes of symptomatic intracranial large artery stenoses and occlusions in China: the Chinese Intracranial Atherosclerosis (CICAS) study.** *Stroke* 2014;45:663–69 CrossRef Medline
18. Goyal M, Menon BK, Van Zwam WH, et al; HERMES collaborators. **Endovascular thrombectomy after large-vessel ischaemic stroke: a meta-analysis of individual patient data from five randomised trials.** *Lancet* 2016;387:1723–31 CrossRef Medline
19. Fiehler J, Cognard C, Gallitelli M, et al. **European recommendations on organisation of interventional care in acute stroke (EROICAS).** *Eur Stroke J* 2016;11:155–70 CrossRef Medline
20. Powers WJ, Derdeyn CP, Biller J, et al; American Heart Association Stroke Council. **2015 American Heart Association/American Stroke Association Focused Update of the 2013 Guidelines for the Early Management of Patients with Acute Ischemic Stroke Regarding Endovascular Treatment: A Guideline for Healthcare Professionals from the American Heart Association/American Stroke Association.** *Stroke* 2015;46:3020–35 CrossRef Medline
21. Vanacker P, Lambrou D, Eskandari A, et al. **Improving the prediction of spontaneous and post-thrombolytic recanalization in ischemic stroke patients.** *J Stroke Cerebrovasc Dis* 2015;24:1781–86 CrossRef Medline
22. Bill O, Zufferey P, Faouzi M, et al. **Severe stroke: patient profile and predictors of favorable outcome.** *J Thromb Haemost* 2013;11:92–99 CrossRef Medline
23. Vanacker P, Heldner MR, Seiffge D, et al. **ASTRAL-R score predicts non-recanalisation after intravenous thrombolysis in acute ischaemic stroke.** *Thromb Haemost* 2015;113:1121–26 CrossRef Medline
24. van der Hoeven EJ, Schonewille WJ, Vos JA, et al; BASICS Study Group. **The Basilar Artery International Cooperation Study (BASICS): study protocol for a randomised controlled trial.** *Trials* 2013;14:200 CrossRef Medline
25. Vanacker P, Lambrou D, Eskandari A, et al. **Eligibility and predictors**

for acute revascularization procedures in a stroke center. *Stroke* 2016;47:1844–49 CrossRef Medline
26. Vanacker P, Heldner M, Amiguet M, et al. **Prediction of large vessel occlusions in acute stroke: National Institute of Health Stroke Scale is hard to beat.** *Crit Care Med* 2016;44:336–43 CrossRef Medline
27. Michel P. **Prehospital scales for large vessel occlusion: closing in on a moving target.** *Stroke* 2017 Jan 13. [Epub ahead of print] Medline
28. Kassem-Moussa H, Graffagnino C. **Nonocclusion and spontaneous recanalization rates in acute ischemic stroke: a review of cerebral angiography studies.** *Arch Neurol* 2002;59:1870–73 CrossRef Medline
29. Schramm P, Schellinger PD, Fiebach JB, et al. **Comparison of CT and CT angiography source images with diffusion-weighted imaging in patients with acute stroke within 6 hours after onset.** *Stroke* 2002; 33:2426–32 CrossRef Medline
30. Nguyen-Huynh MN, Wintermark M, English J, et al. **How accurate is CT angiography in evaluating intracranial atherosclerotic disease?** *Stroke* 2008;39:1184–88 CrossRef Medline
31. Ntaios G, Papavasileiou V, Faouzi M, et al. **Acute imaging does not improve ASTRAL score's accuracy despite having a prognostic value.** *Int J Stroke* 2014;9:926–31 CrossRef Medline

Ipsilateral Prominent Thalamostriate Vein on Susceptibility-Weighted Imaging Predicts Poor Outcome after Intravenous Thrombolysis in Acute Ischemic Stroke

X. Zhang, S. Zhang, Q. Chen, W. Ding, B.C.V. Campbell, and M. Lou

ABSTRACT

BACKGROUND AND PURPOSE: The impact of deep cerebral veins on neurologic outcome after intravenous thrombolysis in patients with acute ischemic stroke is unclear. We investigated the relationship between the appearance of deep cerebral veins on susceptibility-weighted imaging and neurologic outcome in patients who underwent thrombolysis.

MATERIALS AND METHODS: We retrospectively analyzed 109 consecutive patients with acute ischemic stroke who had pretreatment SWI and received intravenous thrombolysis within 6 hours. We calculated the signal difference ratio (defined as the relative difference in signal intensity between the ipsilateral and contralateral veins) of the thalamostriate vein, septal vein, and internal cerebral vein on pretreatment SWI.

RESULTS: Only the signal difference ratio of the thalamostriate vein was significantly associated with poor outcome (3-month modified Rankin Scale score >2, $P = .008$). The optimal threshold was relative hypointensity of the ipsilateral vein of $>4.8\%$ (sensitivity of 53.7% and specificity of 80.9%). We defined a signal difference ratio of the thalamostriate vein of $\geq 5\%$ as an ipsilateral prominent thalamostriate vein. Patients with an ipsilateral prominent thalamostriate vein were more likely to have poor outcome (OR = 3.66; 95% CI, 1.25–10.68; $P = .02$) and a lower rate of successful reperfusion (reperfusion rate of $\geq 70\%$; OR = 0.35; 95% CI, 0.13–0.92; $P = .03$), compared with those without an ipsilateral prominent thalamostriate vein. However, patients with an ipsilateral prominent thalamostriate vein were still less likely to experience poor outcome when reperfusion was achieved compared with when reperfusion did not occur (80.0% versus 44.4%, $P = .04$).

CONCLUSIONS: A pretreatment ipsilateral prominent thalamostriate vein was associated with reduced reperfusion after thrombolysis and poor outcome. More intensive reperfusion approaches may be required for patients with an ipsilateral prominent thalamostriate vein.

ABBREVIATIONS: AIS = acute ischemic stroke; ICV = internal cerebral vein; IPTSV = ipsilateral prominent TSV; IVT = intravenous thrombolysis; SDR = signal difference ratio; SV = septal vein; TSV= thalamostriate vein

Venous changes in the affected hemisphere after acute ischemic stroke (AIS) may play a crucial role in determining clinical outcome.[1-3] Susceptibility-weighted imaging is useful for evaluating cerebral veins in AIS because it is extremely sensitive to paramagnetic substances such as deoxyhemoglobin, thus reflecting the oxygen extraction fraction and the cerebral metabolic rate of oxygen of the hypoxic tissue.[1-4] Shortly after vascular occlusion, the uncoupling between oxygen supply and demand in the hypoperfused region leads to an elevated oxygen extraction fraction and subsequent increased level of deoxyhemoglobin in the vessel, which contributes to prominent hypointensity of the draining veins on SWI.[5-7]

Asymmetric cortical veins, which can be visualized on SWI after AIS and are considered an indicator of salvageable ischemic penumbra, were found to be associated with 3-month outcome.[4,8] However, it was difficult to differentiate cortical veins from leptomeningeal collaterals because there were no obvious morphologic differences between them.[9] Additionally, the anatomic variability of cortical veins also contributes to reduced interrater agreement when assessing the cortical veins. In contrast to

Received September 2, 2016; accepted after revision December 30.

From the Departments of Neurology (X.Z., S.Z., Q.C., M.L.) and Radiology (W.D.), the Second Affiliated Hospital of Zhejiang University, School of Medicine, Hangzhou, China; and Department of Neurology (B.C.V.C.), Royal Melbourne Hospital, Grattan St, Parkville, Victoria, Australia.

This work was supported by the Science Technology Department of Zhejiang Province (2013C13G2010032) and the National Natural Science Foundation of China (81471170&81622017). The perfusion analysis software (MIStar) used in this study was provided to the site as part of their involvement in the International Stroke Perfusion Imaging Registry (INSPIRE; inspire.webmistar.com) study funded by the National Health and Medical Research Council of Australia.

Please address correspondence to Min Lou, MD, PhD, Department of Neurology, the Second Affiliated Hospital of Zhejiang University, School of Medicine, No. 88 Jiefang Rd, Hangzhou, China; e-mail: loumingxc@vip.sina.com

http://dx.doi.org/10.3174/ajnr.A5135

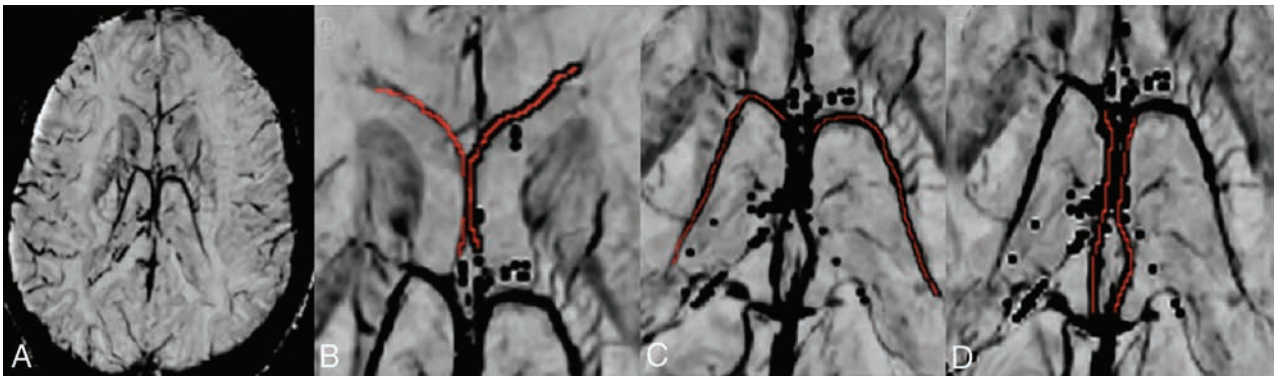

FIG 1. Veins selected for analysis on reconstructed susceptibility-weighted imaging. *A*, Reconstructed imaging in a minimum intensity projection of 20-mm thickness. Septal vein (*B*), thalamostriate vein (*C*), and internal cerebral vein (*D*). Red indicates the ROI.

cortical veins, leptomeningeal collaterals do not interfere with the assessment of deep cerebral veins, and anatomic variation in deep veins is less prevalent.

On the basis of SWI, it was demonstrated that prominent hypointense cortical veins and medullary veins predicted infarct growth and poor outcome after AIS.[2] However, most of the included patients did not undergo revascularization therapy, and salvage of potentially penumbral regions was therefore unlikely. The imaging was also acquired up to 72 hours after AIS, which limits its applicability to hyperacute treatment decision-making. Furthermore, hypointense veins were only associated with prognosis in patients with large-vessel occlusion after AIS. Actually, slight perfusion abnormalities could even cause signal changes in the internal cerebral vein (ICV) and thalamostriate vein (TSV) on SWI.[10]

Therefore, we developed a quantitative method to assess signal asymmetry in the major deep cerebral veins, including the ICA, TSV, and septal vein (SV), and hypothesized that this could sensitively reflect cerebral metabolic changes in hypoxic brain tissue after AIS and may be associated with clinical outcome after intravenous thrombolysis (IVT).

MATERIALS AND METHODS

Ethics Statement

The protocol of MR imaging–guided intravenous thrombolysis has been approved by our local human ethics committee. All clinical investigations were conducted according to the principles expressed in the Declaration of Helsinki. Informed consent was obtained for all patients.

Patient Selection

We retrospectively reviewed our consecutive patients with AIS who received intravenous alteplase (0.9 mg/kg, up to a maximum of 90 mg; 10% of the total dosage as a bolus and the rest infused for 1 hour) between June 2009 and July 2015. We then included patients under the following circumstances: 1) They received IVT within 6 hours of symptom onset; 2) underwent pretreatment multimodal MR imaging, including SWI, diffusion-weighted imaging, and perfusion-weighted imaging; 3) had hypoperfusion (time-to-maximum of >6 seconds) in the supratentorial brain; and 4) underwent follow-up DWI or NCCT at 24 hours after IVT. Patients were excluded for the following reasons: 1) Their prestroke modified Rankin Scale score was ≥2; 2) their MR imaging was degraded due to motion artifacts; or 3) there were bilateral perfusion lesions.

Imaging Acquisition

Multimodal MR imaging was performed on a 3T system (Signa Excite HD; GE Healthcare, Milwaukee, Wisconsin) equipped with an 8-channel phased array head coil. Foam pads were inserted into the space between the subject's head and the MR imaging head coil to minimize head motion. The MR imaging protocol included axial isotropic diffusion-weighted imaging (TR = 4000 ms; TE = 69.3 ms; b-value = 1000 s/mm^2; FOV = 240 mm; section thickness = 5 mm; section gap = 1 mm; acquisition matrix = 160 × 160; acquisition duration = 32 seconds); TOF-MRA (TR = 20 ms; TE = 3.2 ms; flip angle = 15°; acquisition matrix = 320 × 224; section thickness = 1.4 mm; 3 slabs, acquisition duration = 3 minutes 46 seconds); SWI (TE = 4.5 ms [first echo]; interecho spacing = 4.5 ms; TR = 58 ms; FOV = 24 × 24 cm^2; matrix size = 256 × 256; flip angle = 20°; section thickness = 2.0 mm with no gap between sections; acquisition duration = 3 minutes 27 seconds); and perfusion-weighted imaging (FOV = 240 mm; 50 repetitions with TR = 1500 ms; TE = 30 ms; acquisition matrix = 128 × 128; section thickness = 5 mm; section gap = 1 mm, gadolinium dose = 15 mL; flow rate = 4–5 mL/s; acquisition duration = 1 minute 15 seconds). The entire duration of the MR imaging protocol was 15 minutes.

Imaging Analysis

Assessment of Deep Veins on Pretreatment SWI. To assess venous structures, we reconstructed SWI in a minimum intensity projection of 20-mm thickness with OsiriX Imaging Software (http://www.osirix-viewer.com) (Fig 1*A*). As indicated in Fig 1*B–D*, the mean signal-intensity value of ICV, TSV, and SV was measured by drawing a line (1 pixel in width) along the center of each vein. After obtaining the contralateral mean signal-intensity value ($S_{co\text{-}v}$) and ipsilateral mean signal-intensity value ($S_{ip\text{-}v}$) of each vein, we calculated the signal difference ratio (SDR) by using the following equation:

$$SDR = (S_{co\text{-}v} - S_{ip\text{-}v})/S_{co\text{-}v} \times 100\%.$$

Two stroke fellows (S.Z. and X.Z.) who were blinded to other imaging and clinical data independently assessed the SDR of SV,

Table 1: Univariate comparison between patients with good and poor outcomes[a]

	Good Outcome (mRS ≤2) (*n* = 68)	Poor Outcome (mRS > 2) (*n* = 41)	Test Value	*P* Value
Age (yr)	66.1 ± 12.7	72.0 ± 12.4	$t = -2.36$	.02[c]
Female (No.) (%)	21 (30.9)	19 (46.3)	$\chi^2 = 2.63$	.15
Risk factors				
Hypertension (No.) (%)	46 (67.6)	29 (70.1)	$\chi^2 = 0.11$	.83
Diabetes mellitus (No.) (%)	12 (17.6)	13 (31.7)	$\chi^2 = 2.86$	.10
Atrial fibrillation (No.) (%)	21 (30.9)	21 (51.2)	$\chi^2 = 4.47$	.04[c]
Smoking (No.) (%)	30 (44.1)	13 (31.7)	$\chi^2 = 1.65$	.23
Previous stroke/TIA (No.) (%)	11 (16.2)	6 (14.6)	$\chi^2 = 0.05$	1.00
Large-artery occlusion (No.) (%)	28 (41.2)	32 (78.0)	$\chi^2 = 14.05$	<.001[c]
Baseline SBP (mm Hg)	155.4 ± 20.5	151.0 ± 24.9	$t = 0.64$	.53
Baseline DBP (mm Hg)	87.1 ± 17.1	83.2 ± 14.8	$t = 1.21$	.23
ONT (min)	251.2 ± 74.8	235.1 ± 73.4	$t = -1.11$	.27
Baseline glucose level (mmol/L)	7.7 ± 2.6	8.1 ± 2.7	$t = -0.77$	.44
Baseline NIHSS score	6.0 (3.0–10.0)	14.0 (8.5–18.0)	$Z = -5.11$	<.001[c]
Baseline diffusion lesion volume (mL)	1.0 (0–14.2)	8.4 (2.9–51.2)	$Z = -3.12$	.002[c]
Baseline hypoperfusion volume (mL)	22.7 (3.0–74.6)	81.8 (31.9–166.6)	$Z = -4.16$	<.001[c]
SDR of TSV (%)	1.2 (−2.6–3.6)	5.8 (−1.1–8.9)	$Z = -2.61$	.009[c]
SDR of SV (%)	−0.3 (−2.4–2.6)	0.1 (−3.0–3.7)	$Z = -0.45$	.65
SDR of ICV (%)	−0.1 (−4.1–3.5)	0.9 (−5.1–5.7)	$Z = -.71$	.48
Proportion of penumbral tissue loss (%)[b]	1.3 (0–19.9)	38.4 (4.9–95.3)	$Z = -4.23$	<.001[c]
Infarct volume at 24 hr (mL)	4.2 (1.0–9.9)	38.8 (11.5–107.0)	$Z = -5.54$	<.001[c]

Note:—SBP indicates systolic blood pressure; DBP, diastolic blood pressure; ONT, onset-to-needle time.

[a] Table cells express results in mean ± SD for normally distributed continuous variables, No. (%) for dichotomous variables, and median (interquartile range) for ordinal variables and non-normally distributed continuous variables, respectively.

[b] Proportion of Penumbral Tissue Loss = 100 × (Posttreatment Infarct Volume − Pretreatment Infarct Volume)/(Pretreatment Hypoperfusion Volume − Pretreatment Infarct Volume).

[c] $P < .05$.

TSV, and ICV. Cases with differences of >3% for SDR were reassessed by a neuroimaging physician (W.D.). The average value of the 2 SDRs was used.

Radiologic and Clinical Assessment

Diffusion lesion volume was calculated by applying a signal-intensity threshold of the apparent diffusion coefficient of <600 to pretreatment and 24-hour follow-up DWI.[11] For patients with CT follow-up, the area of hypoattenuation was manually outlined. Volumetric analysis was performed by using the commercial software MIStar (Apollo Medical Imaging Technology, Melbourne, Australia). Hypoperfusion was defined as time-to-maximum of >6 seconds. Reperfusion was assessed in patients with a baseline hypoperfusion volume of >10 mL. Successful reperfusion was defined as ≥70% reduction in hypoperfusion volume between pretreatment and 24-hour perfusion imaging.[12] The proportion of penumbral tissue loss was defined as described previously: 100 × (Posttreatment Infarct Volume − Pretreatment Infarct Volume)/(Pretreatment Hypoperfusion Volume − Pretreatment Infarct Volume).[13]

Large-artery occlusion was defined as occlusion of the internal carotid, proximal middle cerebral (M1), or proximal posterior cerebral (P1) artery. The modified Rankin Scale score was assessed at 3 months and dichotomized into good (0–2) and poor (3–6) outcomes.

Statistical Analysis

All metric and normally distributed variables were reported as mean ± SD; non-normally distributed variables, as median (25th–75th percentile). Categoric variables were presented as frequency (percentage). The Fisher exact test was used to compare dichotomous variables between groups; the *t* test, for normally distributed continuous variables; the Mann-Whitney *U* test, for non-normally distributed continuous variables; and the Pearson $\chi 2$ test, for categoric data. The Benjamini-Hochberg correction was used to control the false discovery rate of multiple comparisons. The interrater reliability was assessed by use of the intraclass correlation coefficient. The Spearman correlation coefficient was used to analyze the association of SDR in each vein with outcomes. The receiver operating characteristic curve analysis was performed, and the optimal threshold for deep vein asymmetry was determined by using the Youden index. The Mann-Whitney *U* test was used to analyze the relationship between the asymmetry of deep veins and the proportion of penumbral loss. Univariate and multivariate logistic regression analyses were conducted to investigate whether asymmetry of the deep veins was independently associated with clinical outcome. Results are reported as odds ratios with 95% confidence intervals. A P value $< .05$ was considered statistically significant. All statistical analyses were conducted by using SPSS, Version 19.0 (IBM, Armonk, New York).

RESULTS

Patient Characteristics

A total of 109 patients was included in the final analysis. The mean age was 68 ± 13 years with 40 (36.7%) women. The mean pretreatment NIHSS score was 7 (interquartile range, 4–14), the median time from onset to MR imaging was 193 minutes (interquartile range, 144–245 minutes), and the median time from onset to treatment was 230 minutes (interquartile range, 180–283 minutes). At 3-month follow-up, 41 (37.6%) had poor outcomes.

Table 2: Characteristics of patients with and without the IPTSV sign[a]

	IPTSV (n = 35)	Non-IPTSV (n = 74)	Test Value	P Value
Age (yr)	68.9 ± 12.8	68.0 ± 13.0	$t = -0.34$	.74
Female (No.) (%)	10 (28.6)	30 (40.5)	$\chi^2 = 1.47$	.29
Risk factors				
Hypertension (No.) (%)	28 (80.0)	47 (63.5)	$\chi^2 = 3.01$	.12
Diabetes mellitus (No.) (%)	9 (25.7)	16 (21.6)	$\chi^2 = 0.23$	.63
Atrial fibrillation (No.) (%)	13 (37.1)	29 (39.2)	$\chi^2 = 0.04$	1.00
Smoking (No.) (%)	18 (51.4)	25 (33.8)	$\chi^2 = 3.10$	.10
Previous stroke/TIA (No.) (%)	6 (17.1)	11 (14.9)	$\chi^2 = 0.10$	.78
Large-artery occlusion (No.) (%)	26 (74.3)	34 (45.9)	$\chi^2 = 7.02$	.007[e]
Baseline SBP (mm Hg)	153.7 ± 20.0	153.7 ± 23.4	$t = 0.01$	.99
Baseline DBP (mm Hg)	83.1 ± 10.7	86.8 ± 18.3	$t = 1.32$	.19
ONT (min)	266.9 ± 68.6	229.0 ± 73.8	$t = -2.56$	.01[e]
Baseline glucose level (mmol/L)	7.7 ± 2.1	7.9 ± 2.9	$t = 0.42$	.67
Baseline NIHSS score	13.0 (7.0–18.0)	7.0 (3.8–11.5)	$Z = -2.87$	.004[e]
Baseline diffusion lesion volume (mL)	5.9 (0.9–65.9)	2.0 (0–15.1)	$Z = -2.74$	.006[e]
Baseline hypoperfusion volume (mL)	111.2 (44.0–173.3)	29.3 (5.0–71.4)	$Z = -4.04$	<.001[e]
24-Hr CT scan (No.) (%)[b]	1 (2.9)	3 (4.3)	$\chi^2 = 0.096$	1.00
Proportion of penumbral tissue loss (%)[c]	32.6 (0.6–100.0)	4.5 (0–27.4)	$Z = -2.89$	.004[e]
Infarct volume at 24 hours (mL)	40.8 (7.5–113.6)	5.0 (1.0–19.6)	$Z = -4.27$	<.001[e]
Poor outcome (No.) (%)[d]	22 (62.9)	19 (25.7)	$\chi^2 = 14.00$	<.001[e]

Note:—SBP indicates systolic blood pressure; DBP, diastolic blood pressure; ONT, onset-to-needle time.

[a] Table cells express results in mean ± SD for normally distributed continuous variables, No. (%) for dichotomous variables, and median (interquartile range) for ordinal variables and non-normally distributed continuous variables, respectively.

[b] Twenty-four-hour CT scan: the proportion of patients imaged with CT rather than MRI for 24-hour follow-up imaging.

[c] Proportion of Penumbral Tissue Loss = 100 × (Posttreatment Infarct Volume − Pretreatment Infarct Volume)/(Pretreatment Hypoperfusion Volume − Pretreatment Infarct Volume).

[d] Poor outcome = 3-month modified Rankin Scale score ≥ 2.

[e] $P < .05$.

Table 3: Multivariate regression analysis for poor outcome

	OR	95% CI	P Value
Age	1.04	1.00–1.09	.04
Baseline NIHSS score	1.11	1.03–1.20	.009
Atrial fibrillation	1.66	0.60–4.60	.33
Diabetes mellitus	1.99	0.64–6.18	.24
Large-artery occlusion	1.99	0.56–7.03	.29
Baseline hypoperfusion volume	1.00	0.99–1.01	.68
IPTSV	3.66	1.25–10.68	.02

Deep Cerebral Veins and Outcome

Interrater agreement was excellent for the SDR of the SV (intraclass correlation coefficient = 0.82), TSV (intraclass correlation coefficient = 0.88), and ICV (intraclass correlation coefficient = 0.90). The SDR of the TSV was correlated with poor outcome (ρ = 0.25, P = .008), but there was no correlation for the SV (ρ = 0.04, P = .73) or ICV (ρ = 0.07, P = .47). Patients with poor outcome had a higher SDR of the TSV (median, 4.5%, versus 0.7%; Z = −2.61, P = .009) (Table 1). Receiver operating characteristic analysis revealed that the SDR of the TSV was associated with poor outcome (area under the curve = 0.65; 95% CI, 0.54–0.76; P = .009), with the optimal threshold of 4.8% for identifying poor outcome (sensitivity of 53.7% and specificity of 80.9%, Youden index = 0.35).

Ipsilateral Prominent Thalamostriate Vein and Outcome

On the basis of the cutoff of 4.8%, we then defined ipsilateral prominent TSV (IPTSV) as an SDR of the TSV of ≥5% and dichotomized patients into IPTSV and non-IPTSV groups. As seen in Table 2, univariate analysis showed that patients with IPTSV had a higher rate of large-artery occlusion (74.3% versus 45.9%, P = .007), higher baseline NIHSS scores (median, 13 versus 7; P = .004), and longer onset-to-needle time (266.9 ± 68.6 minutes versus 229.0 ± 73.8 minutes, P = .01), compared with those with non-IPTSV. Baseline hypoperfusion volume was independently associated with the presence of IPTSV (OR = 1.01; 95% CI, 1.00–1.02; P = .02) after adjusting for large-artery occlusion, NIHSS score, and onset-to-needle time.

Patients with IPTSV had significantly higher rates of poor outcome than those with non-IPTSV (62.9% versus 25.7%), which remained significant in multivariate regression, which included age, NIHSS score, atrial fibrillation, diabetes, large-artery occlusion status, and baseline hypoperfusion volume (OR = 3.66; 95% CI, 1.25–10.68; P = .02) (Table 3 and Fig 2). The presence of IPTSV was associated with a high proportion of penumbral tissue loss (32.6% versus 4.5%, P = .004).

Relationship between Ipsilateral Prominent Thalamostriate Vein and Reperfusion

Reperfusion status was evaluated in 77 patients. The presence of the IPTSV was associated with a lower successful reperfusion rate (37.5% versus 60.0%; OR = 0.35; 95% CI, 0.13–0.92; P = .03) after adjusting for baseline diastolic blood pressure and onset-to-needle time.

In the subgroup of patients without reperfusion, patients with IPTSV had a significantly higher rate of poor outcome (80.0% versus 44.4%, P = .04) compared with those without IPTSV. IPTSV was not associated with poor functional outcome in patients with successful reperfusion (41.7% versus 25.9%, P = .46) (Fig 3).

DISCUSSION

Our study quantitatively described the relationship between deep cerebral veins and neurologic outcomes after IVT based on SWI

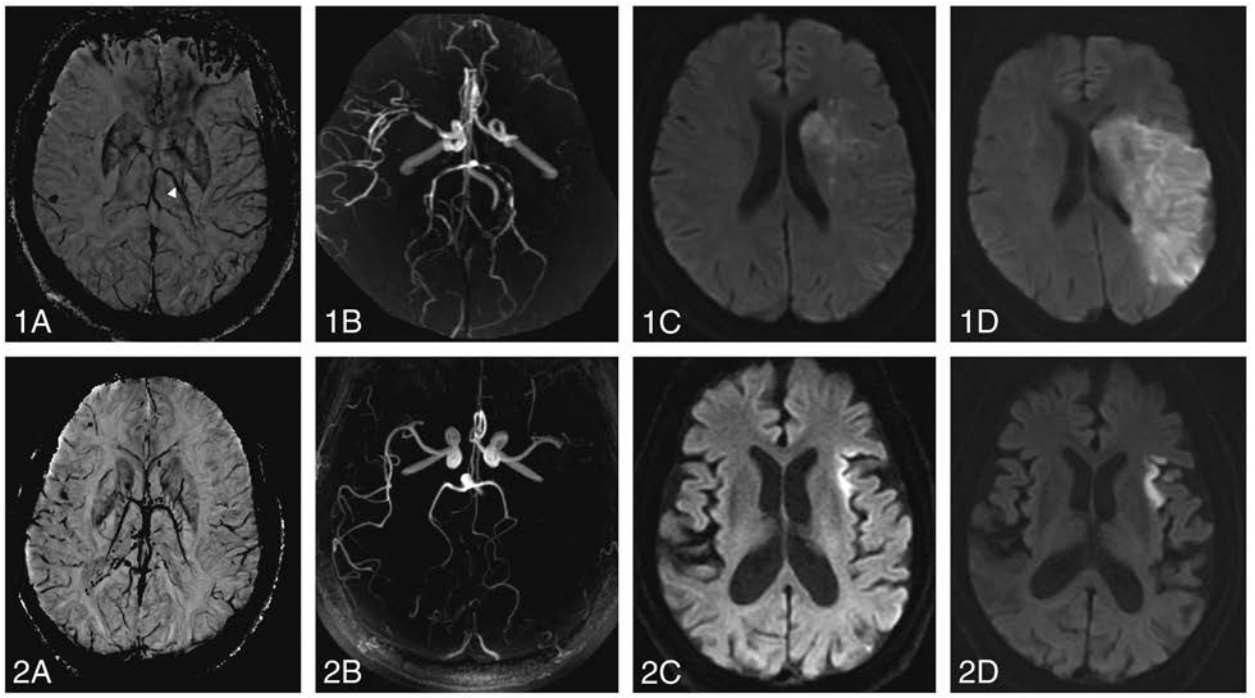

FIG 2. Outcome in patients with and without an ipsilaterally prominent thalamostriate vein. Two illustrative cases: a 55-year old female patient with left-sided thromboembolic occlusion of the M1 segment (1*B*) and IPTSV (1*A*, *arrow*) who developed major infarct growth between pretreatment (1*C*) and 24-hour postthrombolysis imaging (1*D*). The 3-month modified Rankin Scale score was 5. A 54-year old male patient with left-sided thromboembolic occlusion of the M1-segment (2*B*) without IPTSV (2*A*) who had similar pretreatment diffusion lesion volume (2*C*) but less infarct growth at 24 hours (2*D*). The 3-month mRS was 1.

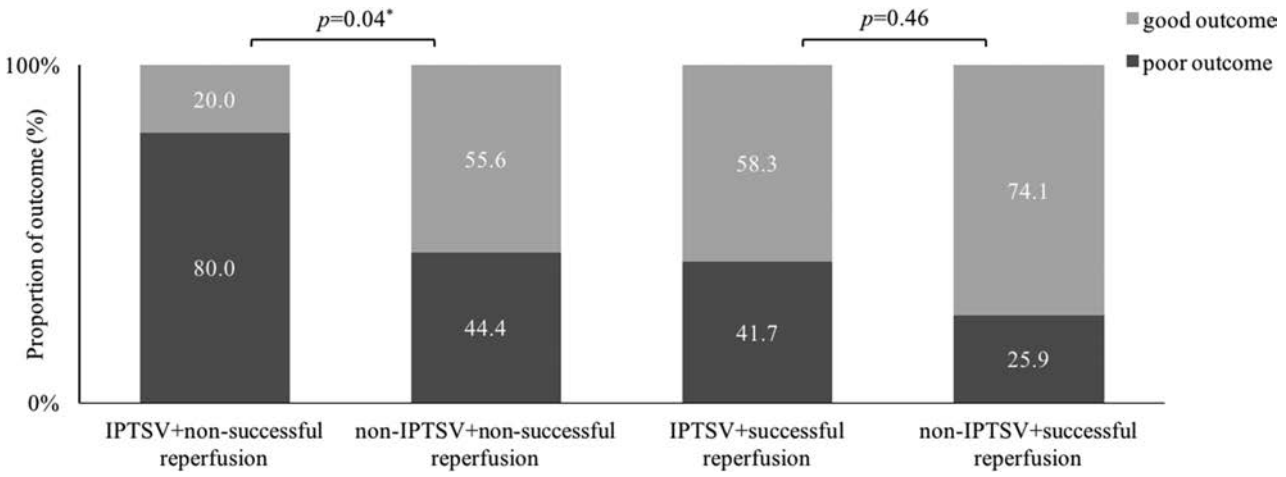

FIG 3. Relationship between categories of outcome with reperfusion and the presence of the ipsilaterally prominent thalamostriate vein. Note successful reperfusion is ≥70% reduction in hypoperfusion volume between pretreatment and 24 hours. Poor outcome is a 3-month modified Rankin Scale score ≥ 2. *Asterisk* indicates $P < .05$.

and revealed that the presence of IPTSV (defined as an SDR of the TSV of ≥5%) was strongly associated with poor outcome after IVT. Without reperfusion, >80% of patients with IPTSV had poor outcomes, while this rate decreased to 42% if reperfused, which reinforced the importance of reperfusion treatment in patients with IPTSV.

In the current study, we found an association only between poor outcome and SDR of the TSV and not the SV or ICV. This may reflect the functional impact of the brain regions that drain to each vein. The TSV mainly drains the basal ganglia and thalamus, which play important roles in motor control and motor learning,[14-16] and these functions have a strong influence on the mRS score.[17] Lesions within the territory draining to the SV, such as the septum pellucidum, rostral corpus callosum, and white matter of the frontal lobe, may have less impact on the mRS score. The ICV receives tributaries from subcortical, periventricular structures and the choroid plexus within the lateral ventricle, and this extensive venous drainage territory may dilute the relationship between critical functions and changes in venous signal.

The presence of IPTSV was associated with a larger hypoperfusion volume at baseline. This finding is consistent with a previous study that demonstrated that prominent deep cerebral veins

on gradient-echo T2*-weighted imaging correlated with a large perfusion lesion.[18] When the oxygen extraction fraction is elevated in hypoperfused tissue, the increased level of deoxyhemoglobin is reflected in abnormal hypointensity of the veins draining that region of the brain. Furthermore, we found that patients with IPTSV were likely to have a high proportion of penumbral tissue loss at 24-hour follow-up. The ischemic penumbra represents the potentially salvageable hypoperfused region,[19-21] which retains structural integrity but has lost function after AIS. Without timely reperfusion, the penumbra becomes irreversibly damaged. Recent studies interpreted the presence of extensive prominent cortical vessels and asymmetry of deep medullary veins after AIS as evidence of poor leptomeningeal collateralization, because good collateralization should lead to less deoxygenated blood in the veins.[22-24] Collateral status is one of the most important factors determining penumbral tissue loss, and good collaterals have been associated with reduced penumbral loss.[13,25] Therefore, we speculated that the presence of IPTSV might indicate poor collaterals after acute ischemia, which would result in increased penumbral tissue loss. However, it is challenging to directly investigate the relationship between IPTSV and leptomeningeal collaterals in our data because we included patients with both large-artery occlusion and more distal occlusions. Further studies are required to explore this.

Our data also showed that patients with IPTSV were less likely to achieve reperfusion. Experimental studies have demonstrated venous endothelial injury and subsequent clot formation in cerebral veins due to oxidative stress and inflammation in the upstream ischemic area.[26] Occlusion of microthrombi in venules was found within 30 minutes after acute reduction of CBF in mice, leading to decreased venous flow velocity.[27] It is possible that the decreased venous outflow could result in an increase in intracranial pressure as blood accumulates in the capillary system. Subsequently, increased intracranial pressure may lead to decreased arterial perfusion, particularly in collateral pathways, and may contribute to the evolution of penumbral tissue into infarct.[28]

Successful reperfusion appeared beneficial to patients with IPTSV, reducing the rate of poor outcome from 80% to 42%. This finding indicates the presence of salvageable penumbra in patients with IPTSV. Intra-arterial thrombectomy has been established as a more effective reperfusion therapy in patients with documented occlusion of the distal internal carotid or proximal middle cerebral artery.[29,30] Our results may not directly affect clinical decision-making; however, further studies are required to evaluate whether patients with IPTSV are particularly likely to benefit from thrombectomy in addition to thrombolysis.

Our study has several limitations. First, it is a retrospective analysis and has a potential risk of selection bias. However, consecutive patients were included in a prospective stroke registry from our stroke center with highly homogeneous and standardized medical care. Second, both CT and MR imaging were used for follow-up imaging, which may increase the heterogeneity of volume measurement. However, the proportion of follow-up CT was <5% and was similar in patients with and without IPTSV. Third, we did not evaluate the follow-up status of veins due to the variable follow-up imaging, and this will be the subject of future study. Fourth, chronic arterial stenosis in cervicocranial arteries can result in preexisting abnormal signal in deep veins before an acute ischemic event. This may influence the assessment of asymmetry of the deep venous system after AIS. Our results should be validated in patients with stenosis of the internal carotid artery and intracranial arteries in further investigations. Finally, our conclusions were based on patients receiving IVT. Future studies are needed to validate the use of IPTSV in the context of endovascular thrombectomy.

CONCLUSIONS

Patients with IPTSV had a lower incidence of reperfusion and a higher rate of poor outcome after IVT. The risk of poor outcome was, however, markedly reduced in those patients in whom successful reperfusion was achieved. Our results emphasize the importance of reperfusion, especially for the patients with IPTSV. However, further studies are warranted to validate whether patients with IPTSV can benefit from more successful reperfusion strategies.

Disclosures: Min Lou—*RELATED*: *Grant*: Science Technology Department of Zhejiang Province (2013C13G2010032) and the National Natural Science Foundation of China (81471170 & 81622017).* *Money paid to the institution.

REFERENCES

1. Chen CY, Chen CI, Tsai FY, et al. **Prominent vessel sign on susceptibility-weighted imaging in acute stroke: prediction of infarct growth and clinical outcome.** *PLoS One* 2015;10:e0131118 CrossRef Medline
2. Baik SK, Choi W, Oh SJ, et al. **Change in cortical vessel signs on susceptibility-weighted images after full recanalization in hyperacute ischemic stroke.** *Cerebrovasc Dis* 2012;34:206–12 CrossRef Medline
3. Sun W, Liu W, Zhang Z, et al. **Asymmetrical cortical vessel sign on susceptibility-weighted imaging: a novel imaging marker for early neurological deterioration and unfavorable prognosis.** *Eur J Neurol* 2014;21:1411–18 CrossRef Medline
4. Zaitsu Y, Kudo K, Terae S, et al. **Mapping of cerebral oxygen extraction fraction changes with susceptibility-weighted phase imaging.** *Radiology* 2011;261:930–36 CrossRef Medline
5. Santhosh K, Kesavadas C, Thomas B, et al. **Susceptibility weighted imaging: a new tool in magnetic resonance imaging of stroke.** *Clin Radiol* 2009;64:74–83 CrossRef Medline
6. Robertson CA, McCabe C, Gallagher L, et al. **Stroke penumbra defined by an MRI-based oxygen challenge technique, 1: validation using [14C]2-deoxyglucose autoradiography.** *J Cereb Blood Flow Metab* 2011;31:1778–87 CrossRef Medline
7. De Crespigny AJ, Wendland MF, Derugin N, et al. **Real-time observation of transient focal ischemia and hyperemia in cat brain.** *Magn Reson Med* 1992;27:391–97 CrossRef Medline
8. Fujioka M, Okuchi K, Iwamura A, et al. **A mismatch between the abnormalities in diffusion- and susceptibility-weighted magnetic resonance imaging may represent an acute ischemic penumbra with misery perfusion.** *J Stroke Cerebrovasc Dis* 2013;22:1428–31 CrossRef Medline
9. Huang P, Chen CH, Lin WC, et al. **Clinical applications of susceptibility weighted imaging in patients with major stroke.** *J Neurol* 2012;259:1426–32 CrossRef Medline
10. Doshi H, Wiseman N, Liu J, et al. **Cerebral hemodynamic changes of mild traumatic brain injury at the acute stage.** *PLoS One* 2015;10:e0118061 CrossRef Medline
11. Purushotham A, Campbell BC, Straka M, et al. **Apparent diffusion coefficient threshold for delineation of ischemic core.** *Int J Stroke* 2015;10:348–53 CrossRef Medline

12. Zhang S, Tang H, Yu YN, et al. **Optimal magnetic resonance perfusion thresholds identifying ischemic penumbra and infarct core: a Chinese population-based study.** *CNS Neurosci Ther* 2015;21: 289–95 CrossRef Medline
13. Jung S, Gilgen M, Slotboom J, et al. **Factors that determine penumbral tissue loss in acute ischaemic stroke.** *Brain* 2013;136(pt 12): 3554–60 CrossRef Medline
14. DeLong MR, Alexander GE, Mitchell SJ, et al. **The contribution of basal ganglia to limb control.** *Prog Brain Res* 1986;64:161–74 CrossRef Medline
15. Mink JW, Thach WT. **Basal ganglia motor control. III. Pallidal ablation: normal reaction time, muscle cocontraction, and slow movement.** *J Neurophysiol* 1991;65:330–51 Medline
16. Wichmann T, DeLong MR. **Functional and pathophysiological models of the basal ganglia.** *Curr Opin Neurobiol* 1996;6:751–58 CrossRef Medline
17. Cheng B, Forkert ND, Zavaglia M, et al. **Influence of stroke infarct location on functional outcome measured by the modified Rankin scale.** *Stroke* 2014;45:1695–702 CrossRef Medline
18. Hermier M, Nighoghossian N, Derex L, et al. **Hypointense transcerebral veins at T2*-weighted MRI: a marker of hemorrhagic transformation risk in patients treated with intravenous tissue plasminogen activator.** *J Cereb Blood Flow Metab* 2003;23:1362–70 CrossRef Medline
19. Meoded A, Poretti A, Benson JE, et al. **Evaluation of the ischemic penumbra focusing on the venous drainage: the role of susceptibility weighted imaging (SWI) in pediatric ischemic cerebral stroke.** *J Neuroradiol* 2014;41:108–16 CrossRef Medline
20. Mucke J, Möhlenbruch M, Kickingereder P, et al. **Asymmetry of deep medullary veins on susceptibility weighted MRI in patients with acute MCA stroke is associated with poor outcome.** *PLoS One* 2015; 10: e0120801 CrossRef Medline
21. Phan TG, Wright PM, Markus R, et al. **Salvaging the ischaemic penumbra: more than just reperfusion?** *Clin Exp Pharmacol Physiol* 2002;29:1–10 CrossRef Medline
22. Oh MY, Ko SB, Kim CK, et al. **Abstract 13: Asymmetry of deep medullary veins in susceptibility weighted imaging is associated with poor collaterals in patients with acute ischemic stroke.** *Stroke* 2013; 44(suppl 1):A13
23. Verma RK, Hsieh K, Gratz PP, et al. **Leptomeningeal collateralization in acute ischemic stroke: impact on prominent cortical veins in susceptibility-weighted imaging.** *Eur J Radiol* 2014;83: 1448–54 CrossRef Medline
24. Parthasarathy R, Sohn SI, Jeerakathil T, et al. **A combined arterial and venous grading scale to predict outcome in anterior circulation ischemic stroke.** *J Neuroimaging* 2015;25:969–77 CrossRef Medline
25. Bang OY, Saver JL, Buck BH, et al; UCLA Collateral Investigators. **Impact of collateral flow on tissue fate in acute ischaemic stroke.** *J Neurol Neurosurg Psychiatry* 2008;79:625–29 Medline
26. Zhou Y, Wang Y, Wang J, et al. **Inflammation in intracerebral hemorrhage: from mechanisms to clinical translation.** *Prog Neurobiol* 2014;115:25–44 CrossRef Medline
27. Schwarzmaier SM, Kim SW, Trabold R, et al. **Temporal profile of thrombogenesis in the cerebral microcirculation after traumatic brain injury in mice.** *J Neurotrauma* 2010;27:121–30 CrossRef Medline
28. Li Q, Khatibi N, Zhang JH. **Vascular neural network: the importance of vein drainage in stroke.** *Transl Stroke Res* 2014;5:163–66 CrossRef Medline
29. Berkhemer OA, Fransen PS, Beumer D, et al. **A randomized trial of intraarterial treatment for acute ischemic stroke.** *N Engl J Med* 2015; 372:11–20 CrossRef Medline
30. Goyal M, Demchuk AM, Menon BK, et al; ESCAPE Trial Investigators. **Randomized assessment of rapid endovascular treatment of ischemic stroke.** *N Engl J Med* 2015;372:1019–30 CrossRef Medline

Restriction Spectrum Imaging Improves Risk Stratification in Patients with Glioblastoma

A.P. Krishnan, R. Karunamuni, K.M. Leyden, T.M. Seibert, R.L. Delfanti, J.M. Kuperman, H. Bartsch, P. Elbe, A. Srikant, A.M. Dale, S. Kesari, D.E. Piccioni, J.A. Hattangadi-Gluth, N. Farid, C.R. McDonald, and N.S. White

ABSTRACT

BACKGROUND AND PURPOSE: ADC as a marker of tumor cellularity has been promising for evaluating the response to therapy in patients with glioblastoma but does not successfully stratify patients according to outcomes, especially in the upfront setting. Here we investigate whether restriction spectrum imaging, an advanced diffusion imaging model, performed after an operation but before radiation therapy, could improve risk stratification in patients with newly diagnosed glioblastoma relative to ADC.

MATERIALS AND METHODS: Pre-radiation therapy diffusion-weighted and structural imaging of 40 patients with glioblastoma were examined retrospectively. Restriction spectrum imaging and ADC-based hypercellularity volume fraction (restriction spectrum imaging–FLAIR volume fraction, restriction spectrum imaging–contrast-enhanced volume fraction, ADC-FLAIR volume fraction, ADC–contrast-enhanced volume fraction) and intensities (restriction spectrum imaging—FLAIR 90th percentile, restriction spectrum imaging–contrast-enhanced 90th percentile, ADC-FLAIR 10th percentile, ADC–contrast-enhanced 10th percentile) within the contrast-enhanced and FLAIR hyperintensity VOIs were calculated. The association of diffusion imaging metrics, contrast-enhanced volume, and FLAIR hyperintensity volume with progression-free survival and overall survival was evaluated by using Cox proportional hazards models.

RESULTS: Among the diffusion metrics, restriction spectrum imaging–FLAIR volume fraction was the strongest prognostic metric of progression-free survival ($P = .036$) and overall survival ($P = .007$) in a multivariate Cox proportional hazards analysis, with higher values indicating earlier progression and shorter survival. Restriction spectrum imaging—FLAIR 90th percentile was also associated with overall survival ($P = .043$), with higher intensities, indicating shorter survival. None of the ADC metrics were associated with progression-free survival/overall survival. Contrast-enhanced volume exhibited a trend toward significance for overall survival ($P = .063$).

CONCLUSIONS: Restriction spectrum imaging–derived cellularity in FLAIR hyperintensity regions may be a more robust prognostic marker than ADC and conventional imaging for early progression and poorer survival in patients with glioblastoma. However, future studies with larger samples are needed to explore its predictive ability.

ABBREVIATIONS: CE = contrast-enhanced; CPH = Cox proportional hazards; FLAIR-HI = FLAIR hyperintensity; GBM = glioblastoma; HC = hypercellularity; HR = hazard ratio; MRSI = MR spectroscopic imaging; PFS = progression-free survival; OS = overall survival; RSI = restriction spectrum imaging; RT = radiation therapy; vf = volume fraction; vol = volume

Glioblastoma (GBM) is the most common and aggressive malignant primary brain tumor. Unfortunately, there has been only incremental improvement in the 5-year survival rate in the past decade.[1] The standard of care for newly diagnosed GBM remains fairly uniform, with maximal permissible surgical resection followed by radiation therapy (RT) with concurrent and adjuvant temozolomide.[2] Currently, novel molecular and cellular targeted therapies for treating GBMs are being investigated with many of

Received June 21, 2016; accepted after revision December 9.

From the Multimodal Imaging Laboratory (A.P.K., K.M.L., T.M.S., J.M.K., H.B., P.E., A.S., A.M.D., N.F., C.R.M., N.S.W.) and Departments of Radiation Medicine (R.K., T.M.S., J.A.H.-G., C.R.M.), Radiology (R.L.D., J.M.K., H.B., A.M.D., N.F., N.S.W.), Neurosciences (A.M.D., D.E.P.), and Psychiatry (C.R.M.), University of California, San Diego, La Jolla, California; and Department of Translational Neuro-Oncology and Neurotherapeutics (S.K.), John Wayne Cancer Institute and Pacific Neuroscience Institute at Providence Saint John's Health Center, Santa Monica, California.

C.R. McDonald and N.S. White contributed equally to this work as co-senior authors.

This work was supported by the National Science Foundation grant 1430082 (N.S.W.); GE Healthcare, Investigator Initiated Research Award BOK92325 (N.S.W.); National Institutes of Health grants R01NS065838 (C.R.M.), RC2 DA29475 (A.M.D.), and EB00790-06 (A.M.D.); National Cancer Institute, Cancer Center Specialized Grant P30CA023100 (C.R.M.); National Institutes of Health UL1TR000100 (J.A.H.-G.) and KL2TR00144 (J.A.H.-G.); American Cancer Society Award ACS-IRG 70-002 (J.A.H.-G.); and American Cancer Society Research Scholar Grant RSG-15-229-01-CCE (C.R.M.).

Please address correspondence to N.S. White, PhD, Multimodal Imaging Laboratory, Center for Multimodal Imaging and Genetics (CMIG), Floor 4W, 9452 Medical Center Dr, La Jolla, CA 92037; e-mail: nswhite@ucsd.edu

Indicates open access to non-subscribers at www.ajnr.org
Indicates article with supplemental on-line photo.
http://dx.doi.org/10.3174/ajnr.A5099

them now in phase II clinical trials.[3] With the advent of these new therapies and a recent study showing that radiation dose escalation to 75 Gy (above the standard dose of 60 Gy) is safe and possibly more effective in newly diagnosed GBM,[4] stratification of patients at the highest risk for early progression is imperative because more aggressive or experimental treatments may be pursued in these individuals. These treatment decisions are usually considered within the first several weeks postsurgery once any residual tumor has been identified, making the pre-RT imaging pivotal for guiding the course of treatment.

Conventional MR imaging, including T1-postcontrast and FLAIR, is nonspecific because the former represents the breakdown of the blood-brain barrier due to tumor- and non-tumor-related causes, and the latter may represent tumor-related edema, postradiation change, or any cause of gliosis. Advanced MR imaging techniques, such as DWI, may offer more specific information related to the underlying physiology of the tissue and may complement existing measures. ADC estimates the magnitude of water diffusion in relation to the physical barriers in its environment. It is frequently used as an imaging biomarker for tumor cellularity[5,6] and is inversely correlated with tumor cell density.[7] However, at the typical b-values used clinically (b=0, 1000 s/mm^2), the diffusion signal primarily arises from the extracellular space.[8] Therefore, in addition to estimating cell density, the ADC calculated at these b-values is also influenced by factors such as edema and necrosis, subsequently making ADC a rather nonspecific measure of tumor cellularity.

To account for the influence of edema and necrosis on ADC intensities in the tumor and peritumoral regions, histogram analysis of normalized ADC intensities[9,10] (normalized with respect to mean ADC in normal-appearing white matter) and 2 Gaussian mixture modeling of the ADC intensities within the tumor[5,6] have been proposed. However, these statistical methods seek only to reclassify voxels within an ROI so that voxels with presumably solid tumor are included in the analysis, while potentially problematic voxels that are confounded by partial voluming with edema and necrosis are removed. These methods have shown some promise for evaluating treatment response and predicting progression-free survival (PFS) in both the upfront[5,11] and recurrent[6,12] setting following treatment with antiangiogenic therapy. However, the utility of these ADC metrics for predicting response to standard chemoradiation has been less frequently explored. Some data suggest that though ADC intensities are not predictive of PFS or overall survival (OS) in the upfront setting,[5,10] the volume of ADC with a large tumor burden (normalized ADC $<$ 1.5; hypercellularity [HC] volume) within the T2 volume stratifies OS both pre-[13] and postsurgery.[9] However, it is unclear whether the hypercellularity volume was correlated with the underlying T2 volume and whether its predictive value merely reflects the association of the T2 volume with survival. Multiple studies have used the increase or decrease of HC volume fraction (ie, the HC volume defined with respect to the variation in a mixture of normal-appearing white and gray matter) as a predictive marker for evaluating treatment response[14] because this metric may capture the percentage of the tumor that is highly cellular and correlated with the structural volumes. However, the utility of the HC volume fraction at individual time points for early risk stratification has not been explored, to our knowledge.

Table 1: Patient characteristics

	Resection Type: STR (n = 22); GTR (n = 18)[a]
Sex	24 Male; 16 female
Age (median) (range) (yr)	58 (31–84)
PFS (median) (range) (mo)	8.42 (3.5–50.53); 7 censored
OS (median) (range) (mo)	19.48 (6.37–50.93); 8 censored
Bevacizumab at recurrence	17 Patients
MGMT status	12 Unmethylated, 8 methylated, 20 unknown
IDH status	15 WT, 25 unknown
EGFR amplification	7 Unamplified, 12 amplified, 21 unknown
EGFRVIII status	12 Positive, 9 negative, 19 unknown

Note:—STR indicates subtotal resection; GTR, gross total resection; WT, wild type.
[a] Resection type was determined from the immediate postsurgical scan acquired within 48 hours of the operation for all patients, which included both T1-postcontrast and FLAIR sequences.

Multicompartment models of diffusion based on advanced multishell acquisitions can provide a more straightforward approach for mitigating the confounding effects of edema and necrosis at the voxel level. In particular, restriction spectrum imaging (RSI) is an advanced diffusion imaging model that separates the relative contributions of hindered and restricted signals originating from extracellular and intracellular water compartments, respectively, by using a multi-b-shell acquisition in conjunction with a linear mixture model.[15-17] Furthermore, RSI incorporates geometric information to disambiguate isotropic-restricted diffusion in tumor cells from anisotropic-restricted diffusion in elongated neuronal processes (axons/dendrites collectively called "neurites"). Previous studies have demonstrated the increased sensitivity and specificity of RSI over ADC and DWI in both brain tumors[18] and prostate cancer,[19] and McDonald et al[20] have recently demonstrated that RSI cellularity is a stronger predictor of both PFS and OS in patients following treatment with bevacizumab relative to ADC. However, its utility for predicting survival in patients newly diagnosed with GBM has not been explored, to our knowledge.

Here we investigate the application of RSI for risk stratification in newly diagnosed, resected GBMs. Our hypothesis was that RSI, due to its multi-b-shell acquisition and its inherent ability to decouple diffusion signal within tumor cells from that of extracellular pathology (eg, edema), would be a more robust marker of patient outcomes.

MATERIALS AND METHODS

This institutional review board–approved retrospective study included 45 patients with pathologically confirmed primary GBM who had pre-RT MRIs (median, 23 days; range, 9–113 days from the operation; median, 10 days; range, 1–29 days before start of RT) that included standardized RSI and conventional imaging sequences acquired between January 2011 and November 2015. All patients were followed for at least 6 months (May 2016). Patient characteristics are shown in Table 1. PFS and OS were defined relative to the pre-RT scan. All scans were reviewed by a neuroradiologist to ensure image quality and determine the basis for exclusion. Of the 45 eligible candidates, 17 patients underwent a second resection, with histopathology confirming tumor in 14 and showing predom-

inantly radiation necrosis in 3. Given the expected bias that would be introduced in the calculation of PFS and OS by including patients with pathologically proved radiation necrosis, these 3 patients were excluded. An additional 2 patients who were excluded had a gross total resection with marked FLAIR hyperintensity within the surgical cavity (presumed to be blood products or proteinaceous material) with associated high RSI and low ADC signal, which essentially masked any usable diffusion signal at the margins of the surgical cavity. Tumor progression was determined on the basis of consensus between the treating neuro-oncologist and neuroradiologist by using the Response Assessment in Neuro-Oncology criteria.[21] In case of no progression or death, PFS was censored at the date of last stable imaging and OS was censored at the date of last contact.

MR Imaging Acquisition and Image Preprocessing

MR imaging was performed on a 3T Signa Excite HDx scanner (GE Healthcare, Milwaukee, Wisconsin) equipped with an 8-channel head coil. The imaging protocol included pre- and postgadolinium 3D volumetric T1-weighted inversion recovery spoiled gradient-recalled sequences (TE/TR = 2.8/6.5 ms, TI = 450 ms, flip angle = 8°, FOV = 24 cm, matrix = 0.93 × 0.93 × 1.2 mm) and a 3D T2-weighted FLAIR sequence (TE/TR = 126/6000 ms, TI = 1863 ms, FOV = 24 cm, matrix = 0.93 × 0.93 × 1.2 mm). For RSI, a single-shot pulsed-field gradient spin-echo EPI sequence was used (TE/TR = 96 ms/17 seconds, FOV = 24 cm, matrix = 96 × 96 × 48, voxel size = 2.5 mm) with 4 b-values (b=0, 500, 1500, and 4000 s/mm^2), with 6, 6, and 15 unique diffusion directions for each nonzero b-value, respectively (~8 minutes scan time).

Before analysis, raw data were corrected for geometric distortions due to susceptibility, gradient nonlinearities, and eddy currents.[22] This correction was followed by correction of patient motion and rigid registration of the pre- and postcontrast 3D inversion recovery spoiled gradient-recalled images and the FLAIR images to each other by using in-house software. The diffusion maps were registered to the postcontrast images through the B0 images (b=0 mm^2/s volume), which were registered to the FLAIR images.

ADC values were calculated from a tensor fit to the b=0, 500, and 1500 s/mm^2 data. Technical details of the RSI mathematic framework are described in their entirety elsewhere,[15-17] and the model used has been applied in other recent publications.[20] Briefly, the measured signal in each voxel was modeled as the sum of signals from 4 distinct tissue compartments: (1) the signal from water trapped within small spheric cells that is restricted in all directions, (2) the signal from water trapped in elongated neuronal processes (ie, neurites) that is restricted in the transverse direction, (3) the signal from extracellular water that is hindered by cells and neuronal processes, and (4) the signal from free water residing in CSF-filled compartments. RSI "cellularity" estimates were computed by combining the signal fraction from the intracellular compartment (1) with the isotropic restricted component of the neurite compartment (2). The RSI cellularity maps were finally transformed to a standard z score by scaling each patient's data by the population mean and SD in normal-appearing white matter of all patients in this study.

VOIs

Contrast-enhanced volumes (CE_{vol}) and FLAIR hyperintensity (FLAIR-HI) volumes ($FLAIR_{vol}$), excluding the resection cavity and intrinsically T1 hyperintense regions (ie, postsurgical blood products), were segmented semiautomatically (Amira software package; Visage Imaging, San Diego, California.) on the coregistered postcontrast 3D inversion recovery spoiled gradient-recalled images and FLAIR images by a single expert image analyst with 8 years of experience. For patients whose pre-RT scan was acquired within 2 weeks after the operation, the immediate postsurgery scan was used to exclude areas of restricted diffusion caused by resection-induced cytotoxic edema.

Imaging Metrics

In this study, we chose to evaluate the utility of both the HC intensities and HC volume fractions as prognostic factors of PFS and OS. On the basis of a recent study,[19] the 90th percentile of RSI cellularity values was selected for our analysis and the HC volume fraction was defined as the volume having an RSI cellularity z score of ≥1.5 within the CE and FLAIR-HI VOIs because the HC volume estimated with this pre-RT normalized ADC threshold was successful in stratifying survival.[9] Imaging metrics included in the analysis were the following: FLAIR volume ($FLAIR_{vol}$), CE volume (CE_{vol}), the 90th percentile of RSI cellularity values in the CE (RSI-$CE_{90\%}$) and in the FLAIR-HI (RSI-$FLAIR_{90\%}$) VOIs and the RSI-based HC volume fraction in the CE (RSI-CE_{vf}) and the FLAIR-HI (RSI-$FLAIR_{vf}$) VOIs. The following ADC metrics were estimated for comparing against the respective RSI metrics: the 10th percentile of ADC[11] in the CE (ADC-$CE_{10\%}$) and in the FLAIR-HI (ADC-$FLAIR_{10\%}$) VOIs and the ADC-based HC volume fraction (ADC z score of ≤1.5) in the CE (ADC-CE_{vf}) and FLAIR-HI (ADC-$FLAIR_{vf}$) VOIs.

Statistical Analysis

Univariate Cox proportional hazards (CPH) models were used to determine the contribution of resection type (subtotal resection, gross total resection), age, and sex to PFS and OS. Multivariate CPH models that included a single imaging metric combined with any significant clinical covariates (namely age, gender and resection type) were used to determine the relationship between each continuous pre-RT imaging metric and PFS/OS. Kaplan-Meier curves for the imaging metrics that were significant in the multivariate CPH models were obtained by dichotomizing the population on the basis of their median value and were compared by using a log-rank test. Due to the exploratory nature of the study, we did not control for type I error. P values < .05 were considered statistically significant. Statistical analysis was performed by using R Version 3.2.2 statistical and computing software (http://www.r-project.org/).[23]

RESULTS

Clinical

Median PFS in the final cohort (n = 40) was 8.4 months, and median OS was 19.5 months. Nine patients progressed within 6 months, 24 patients progressed within 12 months, 30 patients

progressed within 18 months, and 33 patients progressed within 24 months. The results of univariate CPH analyses for the clinical and imaging metrics are summarized in Table 2. CPH models revealed that the resection type (subtotal resection-1 versus gross total resection-2) had a trend toward significance for PFS and was significant for OS (Table 2); hence, it was included as a covariate in multivariate CPH analyses. Age and sex (male-1, female-2) were not predictive of PFS or OS in this cohort. Boxplots of the imaging metrics are shown in Fig 1, and the boxplots split by the median PFS and OS excluding the values from the censored patients for the relevant metrics that achieved significance in Table 3 are shown in On-line Fig 1.

Table 2: Results of univariate CPH analyses of the continuous clinical imaging metrics

	PFS		OS	
Metrics	***P* Value**	**HR (95% CI)**	***P* Value**	**HR (95% CI)**
Age	.562	0.992 (0.965–1.019)	.857	0.997 (0.965–1.03)
Sex	.063	0.512 (0.253–1.037)	.376	0.699 (0.316–1.546)
Resection type	.066	0.511 (0.249–1.046)	.002[a]	0.235 (0.095–0.58)
$FLAIR_{vol}$	.381	1.004 (0.994–1.014)	.404	1.005 (0.994–1.016)
CE_{vol}	.047[a]	1.04 (1.001–1.08)	.010[a]	1.06 (1.014–1.108)
$ADC\text{-}FLAIR_{vf}$	.397	0.939 (0.811–1.087)	.52	0.936 (0.766–1.145)
$ADC\text{-}CE_{vf}$	.804	1.011 (0.925–1.105)	.932	0.995 (0.891–1.112)
$ADC\text{-}FLAIR_{10\%}$	.384	1.001 (0.999–1.004)	.624	1.001 (0.998–1.004)
$ADC\text{-}CE_{10\%}$	.735	0.999 (0.997–1.002)	.704	1.001 (0.998–1.003)
$RSI\text{-}FLAIR_{vf}$	.038[a]	1.031 (1.002–1.061)	.006[a]	1.051 (1.015–1.089)
$RSI\text{-}CE_{vf}$	.12	1.03 (0.992–1.069)	.021[a]	1.048 (1.007–1.091)
$RSI\text{-}FLAIR_{90\%}$	.092	1.522 (0.934–2.482)	.028[a]	2.041 (1.081–3.855)
$RSI\text{-}CE_{90\%}$	.154	1.507 (0.858–2.649)	.099	1.822 (0.893–3.716)

[a] Significant.

CE and FLAIR-HI Volumes

In a univariate CPH analysis, CE_{vol} was significantly associated with PFS and OS (Table 2). When adjusted for resection type, CE_{vol} was no longer significant for PFS and had a trend toward significance for OS ($P = .063$, Table 3). The Kaplan-Meier curves of the 2 groups obtained by a median split and compared by using the log-rank test were significantly different for PFS (χ^2 [1] = 4.7, $P = .029$) but not for OS (χ^2 [1] = 3.1, $P = .078$; Fig 2). Based on this stratification, the median PFS for the 2 groups was 218 and 338.5 days. $FLAIR_{vol}$ was not associated with PFS or OS.

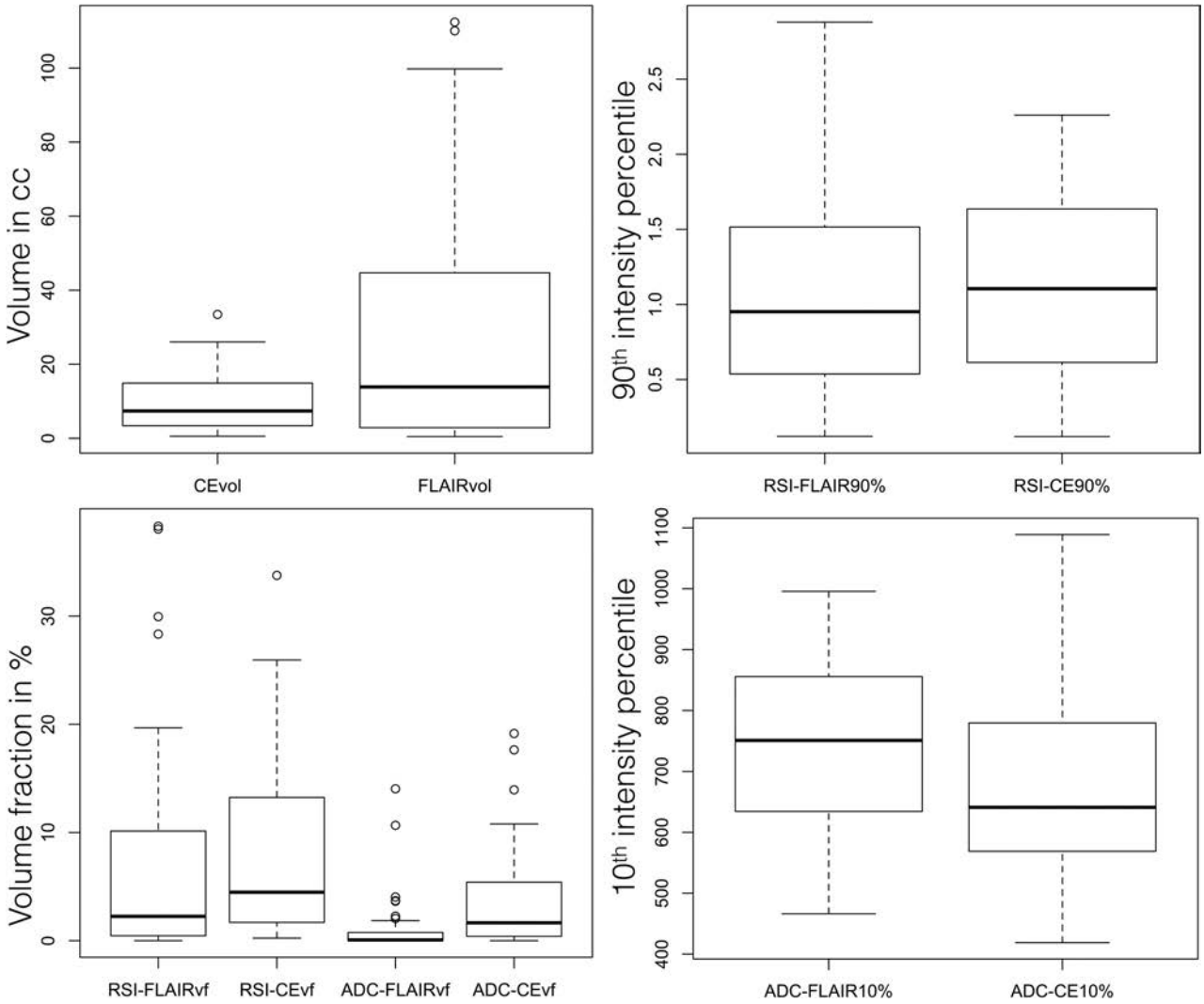

FIG 1. Boxplots of the imaging metrics.

RSI and ADC Metrics

In a multivariate CPH analysis, RSI-FLAIR$_{90\%}$ was significantly associated with OS ($P = .043$) so that higher RSI intensities were associated with shorter survival (Table 3) and RSI-FLAIR$_{vf}$ was significantly associated with both PFS ($P = .036$) and OS ($P = .007$, Table 3) so that higher HC volume fractions were associated with earlier progression and shorter survival. None of the RSI metrics in the CE VOI were significant for PFS/OS.

The Kaplan-Meier curves of the 2 groups obtained by a median split of RSI-FLAIR$_{vf}$ were significantly different for both PFS (χ^2 [1] = 6.1, $P = .013$) and OS (χ^2 [1] = 7.7, $P = .005$; Fig 2). The median PFS of the 2 groups was 201.5 and 367.5 days, and the median OS of the 2 groups was 451 and 750.5 days. Despite a strong trend, stratification by the median RSI-FLAIR$_{90\%}$ did not yield significant group differences in PFS (χ^2 [1] = 2.8, $P = .095$) and OS (χ^2 [1] = 3.4, $P = .065$).

To understand the influence of the threshold for defining HC volume fraction on the prognostic value, we repeated the analysis with HC volume fraction defined with a threshold of RSI

Table 3: Results of multivariate CPH analyses of the continuous imaging metrics covaried with resection type

	PFS		OS	
Metrics	*P* Value	HR (95% CI)	*P* Value	HR (95% CI)
RSI-FLAIR$_{vf}$	.036[a]	1.033 (1.002–1.064)	.007[a]	1.057 (1.015–1.100)
RSI-CE$_{vf}$	.258	1.022 (0.984–1.062)	.183	1.028 (0.987–1.070)
RSI-FLAIR$_{90\%}$	.097	1.535 (0.925–2.545)	.043[a]	2.111 (1.024–4.350)
RSI-CE$_{90\%}$	.210	1.439 (0.814–1.543)	.217	1.568 (0.767–3.203)
FLAIR$_{vol}$	.845	1.001 (0.990–1.012)	.979	1.000 (0.989–1.011)
CE$_{vol}$	.165	1.029 (0.988–1.073)	.063[a]	1.044 (0.998–1.092)

[a] Significant.

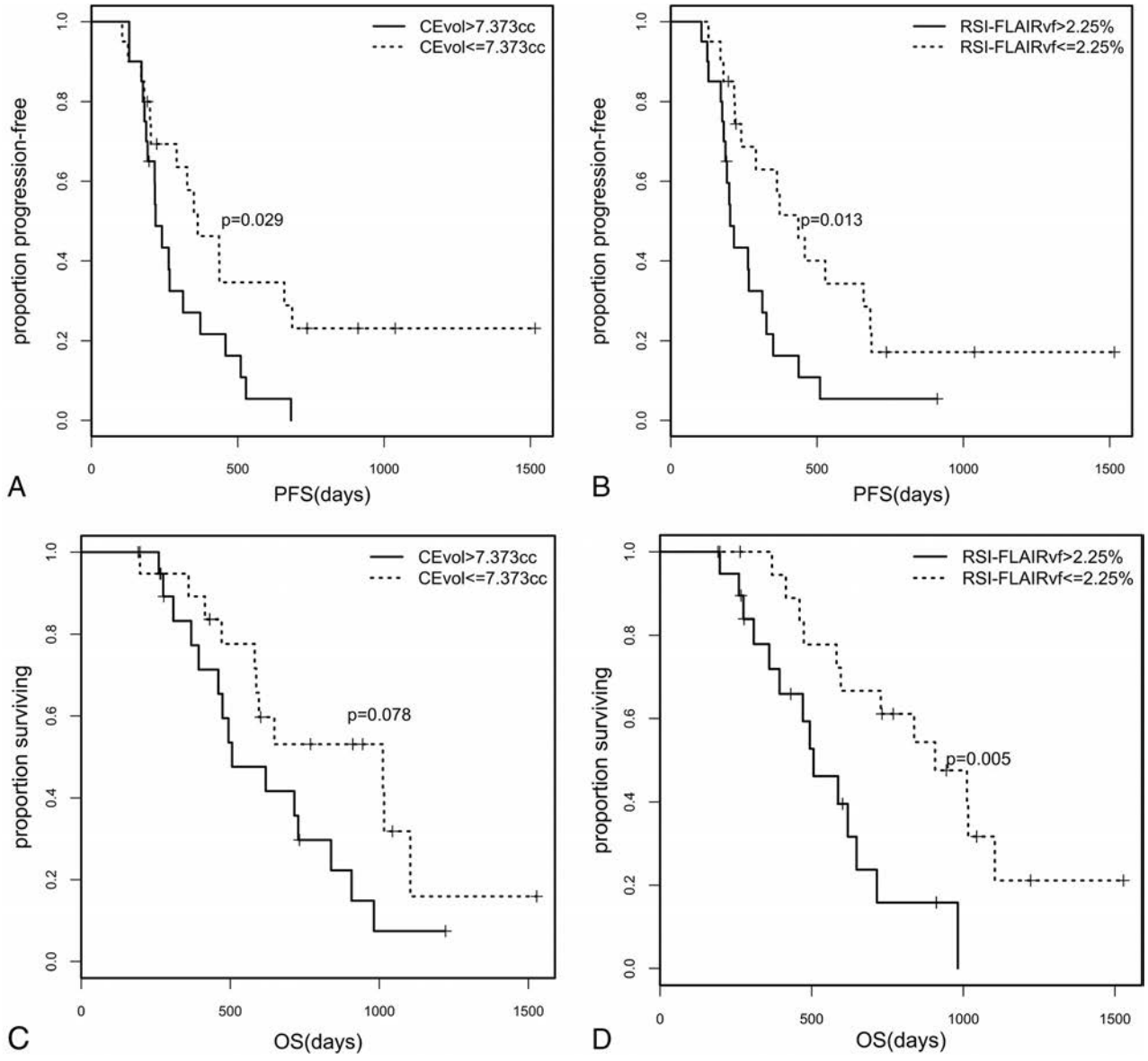

FIG 2. Kaplan-Meier curves for the cohort stratified on the basis of the median values for CE$_{vol}$ for PFS (*A*) and OS (*C*), and RSI-FLAIR$_{vf}$ for PFS (*B*) and OS (*D*).

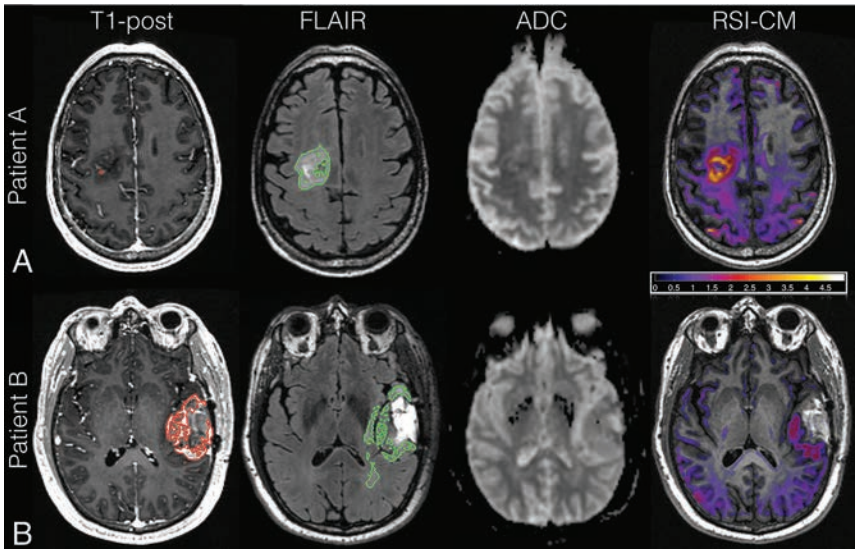

FIG 3. Shown here are the axial T1-postcontrast, FLAIR, ADC, and RSI-cellularity *z* score maps acquired postsurgery but pre-RT for 2 patients, A and B. The VOI contours are shown in red and green for the CE and FLAIR-HI, respectively. Patient A is a 63-year-old man with a right posterior frontal GBM who underwent subtotal resection. This patient had high RSI cellularity in the FLAIR-HI region. Although there is corresponding ADC hypointensity in this region, it is subtle and inconspicuous. He had a shorter PFS and OS (PFS, 4.2 months; OS, 6.6 months) than patient B. Patient B is a 31-year-old woman with a right frontal GBM. There are no areas of high RSI cellularity or low ADC signal in the FLAIR-HI or CE region. She had a correspondingly longer PFS (PFS, 14.5 months; OS, 19.9 months).

cellularity *z* score ≥1 and ≥2. RSI-FLAIR$_{vf}$ at $z \geq 1$ was significantly associated with PFS ($P = .03$, hazard ratio [HR] = 1.023) and OS ($P = .042$, HR = 1.027). While RSI-FLAIR$_{vf}$ at $z \geq 2$ was significant for OS ($P = .009$, HR = 1.096), it was not significant for PFS ($P = .09$, HR = 1.043). Similarly, we also explored the prognostic value of the absolute HC volume with $z \geq 1.5$, which were prognostic for OS (HC$_{vol}$ in CE: $P = .018$, HR = 1.543; FLAIR-HI: $P = .042$, HR = 1.262) in a multivariate CPH analysis. HC$_{vol}$ within CE was significant for PFS in a univariate analysis ($P = .025$, HR = 1.141) but was not significant in a multivariate analysis with resection type as a covariate.

In a univariate CPH analysis, none of the ADC metrics were associated with PFS (Table 2). The absolute ADC HC volumes with $z \leq 1.5$ within the FLAIR-HI VOI were significantly prognostic of OS in a univariate CPH analysis ($P = .015$, HR = 58.89) but only had a trend toward significance ($P = .079$, HR = 20.06) after accounting for resection type in a multivariate CPH analysis and were not associated with PFS (univariate: $P = .138$, HR = 4.835). The ADC HC volumes within the CE VOI were not associated with outcomes.

Representative images of 2 patients in this cohort with short (patient A) and long (patient B) PFS are shown in Fig 3. Patient A had lower CE$_{vol}$, FLAIR$_{vol}$, and ADC-FLAIR$_{10\%}$ but higher RSI-FLAIR$_{90\%}$, RSI-FLAIR$_{vf}$, and ADC-FLAIR$_{vf}$ than patient B, likely reflecting higher tumor cellularity in the patient's FLAIR-HI region. RSI-cellularity maps exhibited greater conspicuity in this region compared with ADC maps. Accordingly, patient A had shorter PFS and OS compared with patient B.

DISCUSSION

In the management of a highly aggressive tumor like GBM, the ability to stratify patient survival postoperatively is important because this information can directly impact therapeutic decision-making. In this study, we found RSI metrics to better stratify patients according to both PFS and OS compared with conventional imaging and ADC metrics. Unfortunately, CE$_{vol}$ and FLAIR$_{vol}$ may have limited prognostic value in this setting once the extent of the resection is considered. Patients with glioblastoma often have a more infiltrative tumor pattern and possibly a more hypoxic tumor biology,[24] with some of them responding poorly to radiation therapy or conventional chemotherapy.[25] The nonspecificity of these conventional metrics could potentially be due to the hypoxic tumors not having contrast enhancement and the presence of infiltrative tumors not having a noticeable signal in both T1 and T2 images. Hence, there is a need for better imaging metrics that perform reliably and may aid in identification of patients with GBM at high risk for early recurrence and worse survival.

Among the imaging metrics, we found that the pre-RT RSI-derived measures of cellularity within the FLAIR-HI region were associated with PFS and OS. The prognostic value of RSI appeared robust to the threshold used to determine the HC volume. Conversely, ADC metrics within the FLAIR-HI region were not associated with outcomes. Tumor progression results in areas of increased tumor cellularity (ie, decrease in diffusivity) and also areas of increased edema (ie, increase in diffusivity), both of which can occur simultaneously within an imaging voxel. Furthermore, postsurgery but pre-RT, a significant portion of the enhancing HC volume of the tumor has probably been resected and the residual HC tumor is interspersed with edema. Because ADC is a composite measure, the effects of these 2 opposing factors may cancel each other out, therefore limiting the prognostic value of ADC. RSI overcomes this limitation by separating the diffusivities associated with intracellular, restricted diffusion from the extracellular effects of edema. In contrast to a previous study,[9] the absolute ADC HC volume was not significantly associated with OS, and this finding might be due to the inclusion of resection type as a covariate in the analysis. Even though the absolute RSI HC volume was prognostic of OS, the volume fraction was a stronger prognostic metric of PFS/OS. We did not find an association between any of our diffusion metrics in the CE region, similar to findings of previous studies.[9,10] Although the reason for this outcome is not clear, it is likely that the CE region was quite limited in size in most patients, given the short interval between surgery and RT.

Other advanced imaging techniques, including perfusion,[10] MR spectroscopic imaging (MRSI),[26] and PET[27] have also been shown to stratify outcomes in patients with GBM. While perfusion imaging provides information on vascular density and flow, MRSI and PET provide metabolic information. Pre-RT perfusion

imaging metrics have been shown to predict PFS,[10] but perfusion is limited in the central core of a solid tumor with hypoxic cancer cells[28] and with antiangiogenic therapy in which the vasculature is normalized, removing the leaky vessels in the tumor.[29] Pre-RT MRSI metrics are associated with both PFS and OS[26] but have lower spatial resolution compared with conventional, perfusion, and diffusion MR imaging. Although diffusion metrics should perform better than perfusion and MRSI with hypoxic tumor and antiangiogenic therapy, none of the previous studies have shown an association of pre-RT diffusion with outcomes. Here, we show that RSI-based cellularity is a prognostic metric of PFS and OS and may offer advantages over perfusion and MRSI in the pre-RT setting.

One of the main limitations of the current study is the small sample size obtained at a single institution (University of California, San Diego). The current study represents our effort to explore the clinical utility of RSI in a highly controlled study in which all the patients were scanned in the same scanner and all images were processed in a highly uniform manner, which included robust corrections for motion and geometric distortions. Given our modest size, we might be underpowered to detect smaller associations between some of our imaging metrics and survival. The generalizability and reproducibility of our results will need to be tested in prospective, multisite clinical trials across multiple vendor platforms. A second limitation is that the heterogeneity of the therapeutic approaches that each patient received following standard RT and temozolomide made it difficult to stratify patients according to treatment regimen. However, our major finding is that RSI performed better than ADC and conventional imaging in the same patient cohort, which is not confounded by between-patient treatment variance. Future studies with cohorts large enough to stratify patients according to the additional therapies received would be of great benefit for better delineating predictors of response to various therapies. Another possible limitation is that the tumors were segmented by a single imaging expert. Thus, intra- and interobserver variability of the tumor segmentations was not evaluated. In addition, although all patients had pathology-confirmed GBMs at the outset, histologic validation of tumor progression was not available for all patients. Furthermore, correlation with genomic information and molecular markers (such as *MGMT* and *IDH* status), which are known to provide prognostic information, could not be performed because these data were only available for a subset of the cohort (Table 1). Molecular information is now systematically collected for patients with GBM at our institution, facilitating future studies investigating the prognostic value of these markers. Although the results from our recent preclinical study[30] show that the RSI cellularity metric correlates with histopathologic markers of cellularity, additional validation in patients with GBM is warranted.

CONCLUSIONS

Following the operation but before initiating RT, RSI-derived cellularity in the FLAIR-HI region performed better than ADC and conventional imaging for risk stratification in patients with GBM. Therefore, RSI could be potentially useful for identifying patients at highest risk for early progression and shorter survival. However, future studies with larger sample sizes are needed to explore its predictive ability.

ACKNOWLEDGMENTS

We would like to thank patients at the University of California, San Diego, Moores Cancer Center Neuro-Oncology Program, for their generous participation.

Disclosures: Anitha Priya Krishnan—*RELATED*: *Grant*: National Science Foundation and National Institutes of Health, *Comments*: I was funded for my postdoctoral work from a National Science Foundation grant (Principal Investigator: Nathan S. White) and a National Institutes of Health grant (Principal Investigator: Anders M. Dale). Tyler M. Seibert—*UNRELATED*: *Grants/Grants Pending*: Varian Medical Systems, *Comments*: research grant*; *Payment for Development of Educational Presentations*: WebMD, *Comments*: honoraria for providing continuing education materials for physicians. Anders M. Dale—*RELATED*: *Grant*: GE Healthcare, *Comments*: I am the principal investigator of a comprehensive research agreement between GE Healthcare and the University of California, San Diego*; *Other*: *Comments*: I am a coinventor on a patent covering the restriction spectrum imaging technology used in the article. The patent is assigned to the University of California*; *UNRELATED*: *Board Membership*: Human Longevity and CorTechs Labs, *Comments*: I serve on the scientific advisory boards of Human Longevity and CorTechs Labs; *Grants/Grants Pending*: National Institutes of Health, *Comments*: numerous research grants*; *Patents (Planned, Pending, or Issued)*: *Comments*: numerous patents*; *Stock/Stock Options:* CorTechs Labs, *Comments*: I am a founder of and hold equity in CorTechs Labs. Jona A. Hattangadi-Gluth—*UNRELATED*: *Grants/Grants Pending*: Varian Medical Systems, *Comments*: A research grant from Varian Medical Systems was made to my institution to fund pilot imaging projects. One of these is my project as Principal Investigator*. Carrie McDonald—*RELATED*: *Grant*: American Cancer Society*. *Money paid to the institution.

REFERENCES

1. Dolecek TA, Propp JM, Stroup NE, et al. **CBTRUS statistical report: primary brain and central nervous system tumors diagnosed in the United States in 2005–2009.** *Neuro Oncol* 2012;14(suppl 5):v1–49.21 CrossRef Medline
2. Stupp R, Mason WP, van den Bent MJ, et al; European Organisation for Research and Treatment of Cancer Brain Tumor and Radiotherapy Groups, National Cancer Institute of Canada Clinical Trials. **Radiotherapy plus concomitant and adjuvant temozolomide for glioblastoma.** *N Engl J Med* 2005;352:987–96 CrossRef Medline
3. Carlsson SK, Brothers SP, Wahlestedt C. **Emerging treatment strategies for glioblastoma multiforme.** *EMBO Mol Med* 2014;6:1359–70 CrossRef Medline
4. Tsien CI, Brown D, Normolle D, et al. **Concurrent temozolomide and dose-escalated intensity-modulated radiation therapy in newly diagnosed glioblastoma.** *Clin Cancer Res* 2012;18:273–79 CrossRef Medline
5. Pope WB, Lai A, Mehta R, et al. **Apparent diffusion coefficient histogram analysis stratifies progression-free survival in newly diagnosed bevacizumab-treated glioblastoma.** *AJNR Am J Neuroradiol* 2011;32:828–31 CrossRef Medline
6. Ellingson BM, Sahebjam S, Kim HJ, et al. **Pretreatment ADC histogram analysis is a predictive imaging biomarker for bevacizumab treatment but not chemotherapy in recurrent glioblastoma.** *AJNR Am J Neuroradiol* 2014;35:673–79 CrossRef Medline
7. Higano S, Yun X, Kumabe T, et al. **Malignant astrocytic tumors: clinical importance of apparent diffusion coefficient in prediction of grade and prognosis.** *Radiology* 2006;241:839–46 CrossRef Medline
8. Mulkern RV, Gudbjartsson H, Westin C-F, et al. **Multi-component apparent diffusion coefficients in human brain.** *NMR Biomed* 1999; 12:51–62 Medline
9. Saraswathy S, Crawford F, Lamborn K, et al. **Evaluation of MR markers that predict survival in patients with newly diagnosed GBM prior to adjuvant therapy.** *J Neurooncol* 2009;91:69–81 CrossRef Medline
10. Li Y, Lupo JM, Polley MY, et al. **Serial analysis of imaging parame-**

ters in patients with newly diagnosed glioblastoma multiforme. *Neuro Oncol* 2011;13:546–57 CrossRef Medline
11. Wen Q, Jalilian L, Lupo JM, et al. **Comparison of ADC metrics and their association with outcome for patients with newly diagnosed glioblastoma being treated with radiation therapy, temozolomide, erlotinib and bevacizumab.** *J Neurooncol* 2015;121:331–39 CrossRef Medline
12. Pope WB, Kim HJ, Huo J, et al. **Recurrent glioblastoma multiforme: ADC histogram analysis predicts response to bevacizumab treatment.** *Radiology* 2009;252:182–89 CrossRef Medline
13. Crawford FW, Khayal IS, McGue C, et al. **Relationship of pre-surgery metabolic and physiological MR imaging parameters to survival for patients with untreated GBM.** *J Neurooncol* 2009;91:337–51 CrossRef Medline
14. Ellingson BM, Cloughesy TF, Zaw T, et al. **Functional diffusion maps (fDMs) evaluated before and after radiochemotherapy predict progression-free and overall survival in newly diagnosed glioblastoma.** *Neuro Oncol* 2012;14:333–43 CrossRef Medline
15. White NS, Leergaard TB, D'Arceuil H, et al. **Probing tissue microstructure with restriction spectrum imaging: histological and theoretical validation.** *Hum Brain Mapp* 2013;34:327–46 CrossRef Medline
16. White NS, Dale AM. **Optimal diffusion MRI acquisition for fiber orientation density estimation: an analytic approach.** *Hum Brain Mapp* 2009;30:3696–703 CrossRef Medline
17. White NS, Dale AM. **Distinct effects of nuclear volume fraction and cell diameter on high b-value diffusion MRI contrast in tumors.** *Magn Reson Med* 2014;72:1435–43 CrossRef Medline
18. White NS, McDonald CR, Farid N, et al. **Improved conspicuity and delineation of high-grade primary and metastatic brain tumors using "restriction spectrum imaging": quantitative comparison with high B-value DWI and ADC.** *AJNR Am J Neuroradiol* 2013;34:958–64, S1 CrossRef Medline
19. McCammack KC, Kane CJ, Parsons JK, et al. **In vivo prostate cancer detection and grading using restriction spectrum imaging-MRI.** *Prostate Cancer Prostatic Dis* 2016;19:168–73 CrossRef Medline
20. McDonald CR, Delfanti RL, Krishnan AP, et al. **Restriction spectrum imaging predicts response to bevacizumab in patients with high-grade glioma.** *Neuro Oncol* 2016;18:1579–90 Medline
21. Wen PY, Macdonald DR, Reardon DA, et al. **Updated response assessment criteria for high-grade gliomas: response assessment in neuro-oncology working group.** *J Clin Oncol* 2010;28:1963–72 CrossRef Medline
22. Holland D, Kuperman JM, Dale AM. **Efficient correction of inhomogeneous static magnetic field-induced distortion in echo planar imaging.** *Neuroimage* 2010;50:175–83 CrossRef Medline
23. R Core Team. *R: A Language and Environment for Statistical Computing. R Foundation for Statistical Computing.* Vienna; the R Foundation for Statistical Computing; 2015
24. Vanan MI, Eisenstat DD. **Management of high-grade gliomas in the pediatric patient: past, present, and future.** *Neurooncol Pract* 2014;1:145–57 CrossRef Medline
25. Haar CP, Hebbar P, Wallace GC 4th, et al. **Drug resistance in glioblastoma: a mini review.** *Neurochem Res* 2012;37:1192–200 CrossRef Medline
26. Li Y, Lupo JM, Parvataneni R, et al. **Survival analysis in patients with newly diagnosed glioblastoma using pre- and postradiotherapy MR spectroscopic imaging.** *Neuro Oncol* 2013;15:607–17 CrossRef Medline
27. Tralins KS, Douglas JG, Stelzer KJ, et al. **Volumetric analysis of 18F-FDG PET in glioblastoma multiforme: prognostic information and possible role in definition of target volumes in radiation dose escalation.** *J Nucl Med* 2002;43:1667–73 Medline
28. Eales KL, Hollinshead KER, Tennant DA. **Hypoxia and metabolic adaptation of cancer cells.** *Oncogenesis* 2016;5:e190 CrossRef Medline
29. Plate KH, Scholz A, Dumont DJ. **Tumor angiogenesis and anti-angiogenic therapy in malignant gliomas revisited.** *Acta Neuropathol* 2012;124:763–75 CrossRef Medline
30. Hope TR, White NS, Kuperman J, et al. **Demonstration of non-gaussian restricted diffusion in tumor cells using diffusion time-dependent diffusion-weighted magnetic resonance imaging contrast.** *Front Oncol* 2016;6:179 CrossRef Medline

A Multiparametric Model for Mapping Cellularity in Glioblastoma Using Radiographically Localized Biopsies

P.D. Chang, H.R. Malone, S.G. Bowden, D.S. Chow, B.J.A. Gill, T.H. Ung, J. Samanamud, Z.K. Englander, A.M. Sonabend, S.A. Sheth, G.M. McKhann II, M.B. Sisti, L.H. Schwartz, A. Lignelli, J. Grinband, J.N. Bruce, and P. Canoll

ABSTRACT

BACKGROUND AND PURPOSE: The complex MR imaging appearance of glioblastoma is a function of underlying histopathologic heterogeneity. A better understanding of these correlations, particularly the influence of infiltrating glioma cells and vasogenic edema on T2 and diffusivity signal in nonenhancing areas, has important implications in the management of these patients. With localized biopsies, the objective of this study was to generate a model capable of predicting cellularity at each voxel within an entire tumor volume as a function of signal intensity, thus providing a means of quantifying tumor infiltration into surrounding brain tissue.

MATERIALS AND METHODS: Ninety-one localized biopsies were obtained from 36 patients with glioblastoma. Signal intensities corresponding to these samples were derived from T1-postcontrast subtraction, T2-FLAIR, and ADC sequences by using an automated coregistration algorithm. Cell density was calculated for each specimen by using an automated cell-counting algorithm. Signal intensity was plotted against cell density for each MR image.

RESULTS: T2-FLAIR ($r = -0.61$) and ADC ($r = -0.63$) sequences were inversely correlated with cell density. T1-postcontrast ($r = 0.69$) subtraction was directly correlated with cell density. Combining these relationships yielded a multiparametric model with improved correlation ($r = 0.74$), suggesting that each sequence offers different and complementary information.

CONCLUSIONS: Using localized biopsies, we have generated a model that illustrates a quantitative and significant relationship between MR signal and cell density. Projecting this relationship over the entire tumor volume allows mapping of the intratumoral heterogeneity in both the contrast-enhancing tumor core and nonenhancing margins of glioblastoma and may be used to guide extended surgical resection, localized biopsies, and radiation field mapping.

ABBREVIATIONS: CE = contrast-enhancing; HPF = high-power field; NE = nonenhancing

Glioblastoma is a complex malignancy characterized by heterogeneous radiographic and histopathologic features. This intratumoral heterogeneity, combined with the diffuse infiltration of glioblastoma, renders correlations between imaging and underlying tissue critical for better understanding of tumor behavior.[1] Stereotactically localized biopsies allow this comparison of local radiologic characteristics across multiple sequences with histopathologic or molecular analysis and provide a means for understanding underlying tissue characteristics that lead to macroscopic appearances on MR imaging.[1-4] However to date, histopathologic-radiographic correlations have been limited by the following: 1) the surgical challenge of obtaining stereotactically localized biopsies with reliable accuracy, 2) the maintenance of spatial fidelity across multiple MR images, and 3) the application of quantitative histopathologic analysis.

Radiographically, glioblastoma typically appears as a contrast-enhancing (CE) mass with surrounding nonenhancing (NE) tissue marked by abnormal T2-FLAIR and DWI-derived ADC signals.[5-7] These heterogeneous MR signal characteristics in the NE area are known to represent a combination of vasogenic edema

Received June 13, 2016; accepted after revision December 9.

From the Departments of Radiology (P.D.C., L.H.S., A.L., J.G.), Neurological Surgery (H.R.M., S.G.B., B.J.A.G., T.H.U., Z.K.E., A.M.S., S.A.S., G.M.M., M.B.S., J.N.B.), and Pathology and Cell Biology (P.C.), College of Physicians and Surgeons at Columbia University, New York, New York; Gabriele Bartoli Brain Tumor Laboratory and the Irving Cancer Research Center (H.R.M., S.G.B., B.J.A.G., T.H.U., J.S., Z.K.E., A.M.S., J.N.B., P.C.), New York, New York; and Department of Radiology (D.S.C.), University of San Francisco School of Medicine, San Francisco, California.

Peter D. Chang and Hani R. Malone contributed equally to this work.

This work was supported by the James S. McDonnell Foundation and a Collaborative and Multidisciplinary Pilot Research Award from the Irving Institute for Clinical and Translational Research, Columbia University Medical Center.

Please address correspondence to Peter Canoll, MD, PhD, Department of Pathology and Cell Biology, Columbia University Medical Center, ICRC 1130 St. Nicholas Ave, NY, NY 10032; e-mail: pc561@cumc.columbia.edu; Jeffrey N. Bruce, MD, Department of Neurological Surgery, Columbia University Medical Center, Neurological Institute of New York, 710 West 168th St, NY, NY 10032; e-mail: jnb2@cumc.columbia.edu

Indicates article with supplemental on-line figures.

http://dx.doi.org/10.3174/ajnr.A5112

and infiltrating glioma cells[8-10]; however, correlating these MR imaging abnormalities with underlying histopathology remains challenging. Nonetheless, there has been much effort with a variety of MR images to draw such radiologic-histologic correlations to better understand the tumor environment,[1-4] which is critical for refining radiation treatment fields, assessing response to therapy, and evaluating progression.

Early studies have suggested that tumor cellularity as a surrogate for infiltration correlates with decreased apparent diffusivity,[3,10-13] reduced T2-FLAIR hyperintensity,[14,15] and increased gadolinium-related T1 signal.[16,17] More recent effort has combined these changes on multiple MR images to help distinguish glioma cell infiltration and edema. Akbari et al[14] used a machine-learning algorithm to identify several multiparametric features that spatially colocalized with areas of future radiographic recurrence, with the implication that these regions likely harbor underlying infiltrative tumor. However, this study did not confirm the proposed radiographic features with histologic data. Hu et al[18] incorporated multiple MR imaging textural features with histologic data to identify areas of high tumor content for targeting diagnostic biopsies. The resulting model was able to sort tissue into 2 categories of high and low tumor content. Together, these initial studies suggested that important imaging patterns exist amid the complex signal changes within the peritumoral region and that careful analysis may yield correlates to tumor infiltration.

We hypothesized that quantitative measures of tissue cellularity from localized biopsies will correlate with voxel-level signal on multiple MR images and will provide more informative maps of tumor infiltration at the margins of glioblastomas. To this end, a fully automated cell counting and image coregistration pipeline was developed to eliminate subjective bias and improve reliability. With this approach, the objective of this study was to generate a model capable of predicting cellularity at each voxel within an entire tumor volume as a function of signal intensity, thus providing a means of quantifying tumor infiltration into surrounding brain tissue.

MATERIALS AND METHODS

Patient Selection

A retrospective review was performed on our data base of adult patients with MR imaging–localized biopsies obtained during open surgical resection for glioma at Columbia University Medical Center between January 2012 and January 2015. Patient selection was limited to those with newly diagnosed glioblastoma (World Health Organization grade IV) resected by 1 of 2 attending neurosurgeons (M.B.S., J.N.B.), who had complete preoperative MR imaging available for analysis (ADC, T2-FLAIR, and T1-weighted precontrast and postcontrast sequences). Patients were excluded if their localized samples were determined to be inadequate for any for any of the following reasons: poor neuronavigational registration, excessive MR imaging motion artifacts, errors in the automated screen capture, or problems with histologic processing pipeline.

Image Acquisition

All imaging was performed on a 3T MR imaging system (Signa; GE Healthcare, Milwaukee, Wisconsin) by using an 8-channel head-array coil (Signa HDxt; GE Healthcare). The following sequences were assessed for each patient: pre- and postcontrast T1-weighted, T2-FLAIR, and DWI. Pre- and postcontrast volumetric acquisition was performed with a T1-weighted 3D inversion recovery fast-spoiled gradient-recalled sequence with the following parameters: TI = 450 ms, TR = 10.2 ms, TE = 4.2 ms, flip angle α = 13°, FOV = 250 mm; matrix = 256 × 256, section thickness = 1.2 mm. The total scan time was approximately 4 minutes 15 seconds. Postcontrast images were acquired by using intravenous gadobenate dimeglumine (MultiHance; Bracco Diagnostics, Princeton, New Jersey) at a dose of 0.2 mL/kg. The time between injection and postcontrast imaging was approximately 5 minutes. Axial T2-FLAIR was performed with the following parameters: TR/TE = 9500/127 ms, TI = 2250 ms, section thickness = 5 mm with no gap, FOV = 225 mm. DWI was performed with a single-shot, spin-echo, echo-planar sequence with the following parameters: TR/TE =7000/73 ms, FOV = 220 mm, matrix = 128 × 192, section thickness = 5 mm with no gap, bandwidth = 1953 Hz/pixel with b-values of 0 and 1000 s/mm^2. ADC maps were generated in FuncTool software (GE Healthcare) for the quantitative determination of mean diffusivity measurements.

Image Preprocessing

Raw image data from T1-precontrast, T2-FLAIR, and ADC maps were aligned to the volumetric T1-postcontrast sequence by using the FMRIB Linear Image Registration Tool (FLIRT; http://www.fmrib.ox.ac.uk/).[19,20] The linear affine transformation algorithm was implemented by using 12 *df*, trilinear interpolation, and a mutual information cost function. Each sequence was further processed with a histogram normalization algorithm to standardize intensity values among patients. The algorithm is based on a method previously described that maximizes the cross-correlation between cumulative histogram distribution functions of each input volume with a reference standard.[21] A mean reference template was created for each sequence by pooling data from the study subjects, each set to a mean intensity of 0 and an SD of 1. T1-postcontrast subtraction images were obtained by subtracting coregistration-normalized T1-precontrast volumes from T1-postcontrast volumes.

Biopsy Acquisition

All tissue sampling was performed within the normal surgical plan when it posed no additional risk to the patient. Samples were taken from the CE tumor core in all cases and the NE region around the tumor in some cases. Sampling of the NE, T2-FLAIR hyperintense region was permissible in 2 scenarios: 1) when the surgical trajectory required dissection through brain parenchyma en route to the tumor, and 2) when resection of tissue lateral or superficial to the CE region was part of the surgical goal. Biopsies were obtained before tumor debulking to maximize the spatial fidelity of localization. Stereotactic guidance was provided by a volumetric T1-weighted postcontrast sequence on a neuronavigation system (Brainlab Curve; Brainlab, Feldkirchen, Germany). The location of the biopsy was recorded by screen capture of the surgical navigation system at the time of tissue sampling.

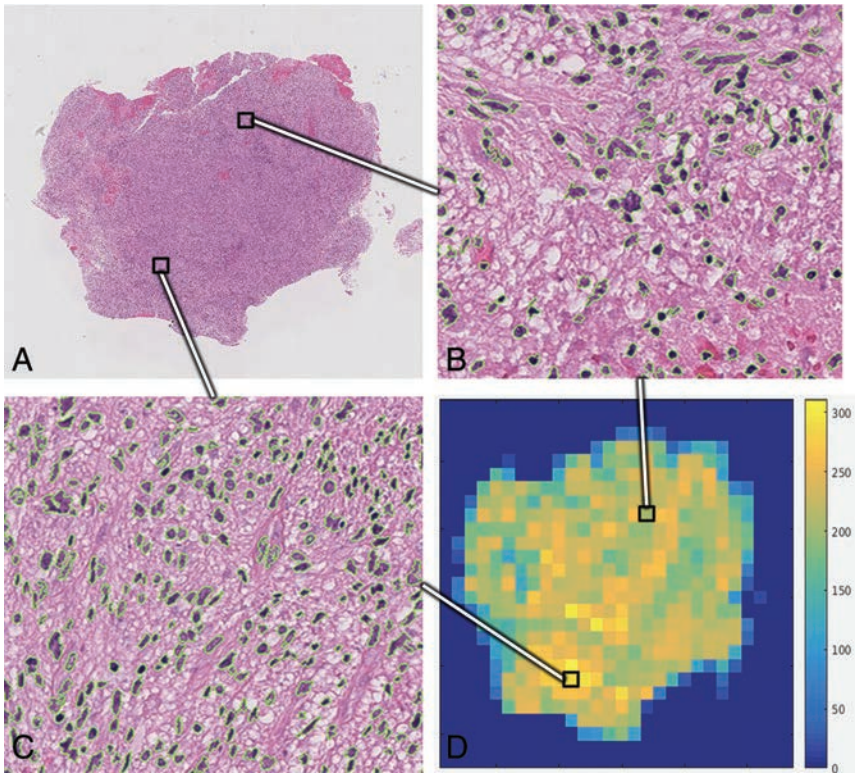

FIG 1. Whole-cell counting. *A*, Digitized, low-power magnification view of a single H&E-stained slide. Two representative 400× fields from this single tissue specimen of relatively lower (*B*) and higher (*C*) cell density illustrate the tissue heterogeneity present at a microscopic level. Stained cellular nuclei identified by the automated counting algorithm are outlined in green. *D,* The "heat map" demonstrates distribution of cell density at the level of a HPF throughout the tissue sample.

Biopsy Coregistration

A custom fully automated 2D-to-3D coregistration algorithm was developed to convert the crosshairs from the neuronavigation system screenshot image into an MR imaging coordinate (On-line Fig 1). The algorithm is implemented in the following steps: First, a cropped subimage of the biopsy crosshair in the axial orientation is obtained. Subsequently, a 2D convolution is applied to a single axial section from the original MR imaging by using the cropped axial subimage as a convolution kernel. The process is iterated over a number of subimage scales (30%–200% zoom) and MR imaging sections by using a grid search technique. The maximum from each resulting cross-correlation response matrix is recorded, and the parameters are updated until convergence is achieved. A final 2D convolution is applied to the image by using a kernel reflecting a mask of the expected crosshair, thus localizing the point of interest. With this coordinate as the center point, all voxels within a spheric ROI radius of 1 mm are recorded for each coregistered sequence. The final intensity value used for analysis from each biopsy point is a Gaussian-weighted mean of the voxels within the spheric ROI.

Histopathologic Processing and Analysis

The samples were divided into 2 pieces in the operating suite. One piece was immediately flash frozen in liquid nitrogen for future genetic studies. The second piece was fixed in 10% (volume/volume) formalin and infiltrated with low-temperature paraffin for histologic analysis. Five-micrometer sections were stained with hematoxylin-eosin. The slides were then scanned and digitalized to BigTIFF files (http://bigtiff.org/) at ×40 magnification by using a Leica SCN400 system (Leica Biosystems, Wetzlar, Germany). The high-resolution image was acquired at 40,000 pixels per centimeter (2.5×10^{-5} cm per pixel).

Whole-Slide Cell Counting

A fully automated cell-counting algorithm was developed by using a convolutional neural network (Fig 1 and On-line Fig 2). The algorithm was trained to count the number of nuclei present in a single high-power field (HPF), defined by a 2.25 × 2.25 mm square (900 × 900 pixels). Subsequently, the neural network was iteratively processed through tiles of HPFs until the entire H&E slide was counted (Fig 1*B–D*). HPFs at the border of the tissue specimen (eg, only a fraction of the field contained cells) were excluded from analysis.

The neural network was trained to classify the center pixel of a 21 × 21 × 3 RGB color input into 1 of 3 categories: cellular nuclei, densely staining artifacts mimicking cellular nuclei, and background staining. After a hyperparameter grid search, the final neural network architecture consisted of 5 convolutional layers of 5 × 5 filters (with increasing channel filter depths of 20, 40, 60, 80, and 120) followed by a final fully connected layer. Rectified linear activation functions were used after each convolutional layer, and a final softmax loss function was used to classify each input image. The network was trained on 5000 annotated examples of each class and validated on separate 1000 ground truth examples. A final validation classification error of 3.8% was achieved after training for 100 epochs.

As a final test set validation, 25 high-power fields were chosen at random. Each field was manually inspected to determine the number of nuclei present. The same field was then evaluated by the automated cell-counting algorithm. The human reviewer was blinded to the final total cell count obtained by the automated method. A high correlation was observed between the automated algorithm and the manual cell counts as determined by a Pearson coefficient ($r = 0.984$, Fig 2*A*).

Statistical Analysis

For each biopsy, MR signal intensity (ADC, T2-FLAIR, and T1-weighted postcontrast) was correlated against cell density per HPF. Single variable linear regression analysis and Pearson correlation coefficients were determined. In addition, a multiple linear regression model was created as defined by:

$$F(x) = ax_1 + bx_2 + cx_3 + d, \quad (1)$$

where the predicted cellularity, $F(x)$, was a linear function of signal intensity on ADC, T2-FLAIR, and T1-weighted postcontrast sequences (x_1, x_2, and x_3, respectively).

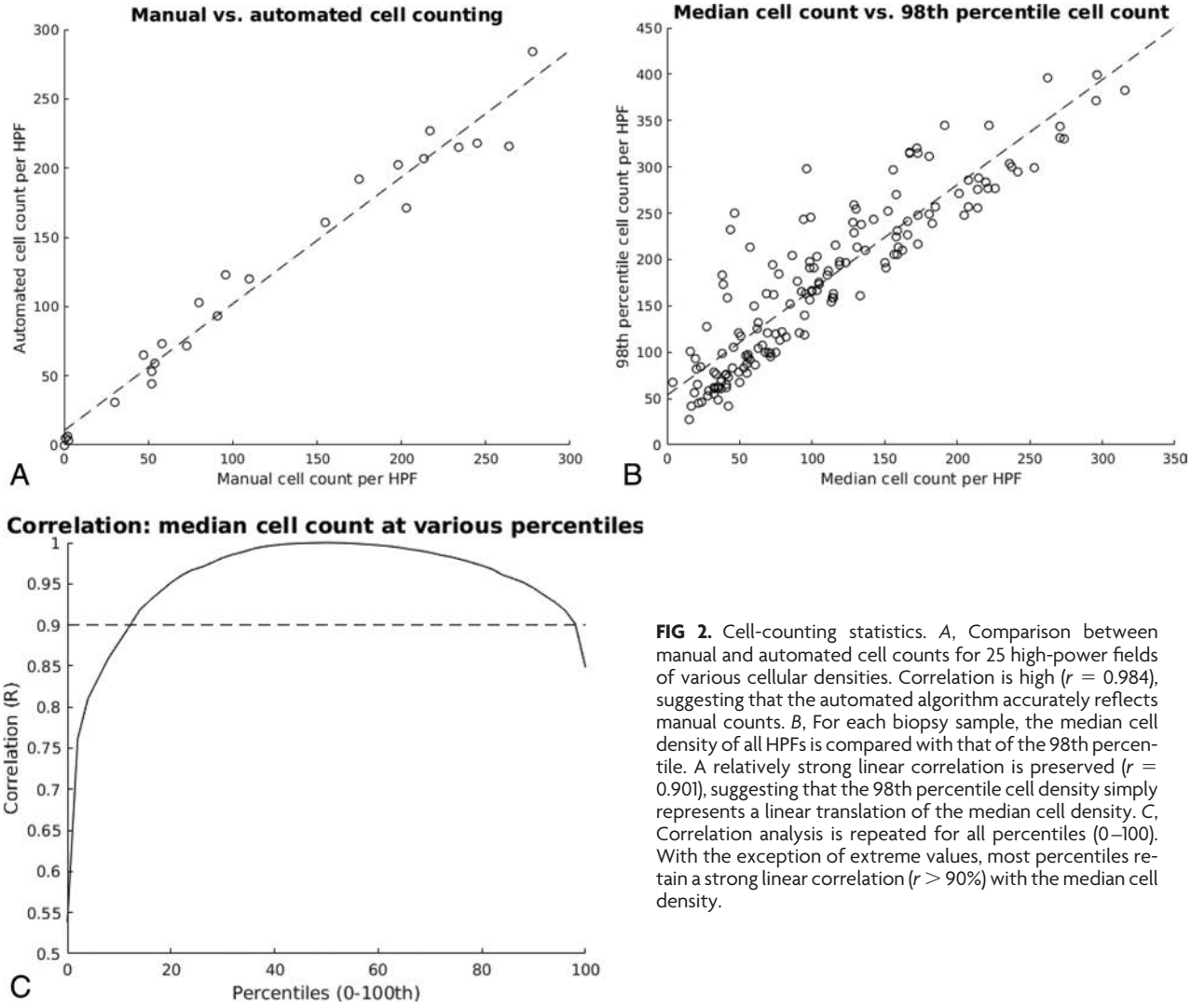

FIG 2. Cell-counting statistics. *A*, Comparison between manual and automated cell counts for 25 high-power fields of various cellular densities. Correlation is high ($r = 0.984$), suggesting that the automated algorithm accurately reflects manual counts. *B*, For each biopsy sample, the median cell density of all HPFs is compared with that of the 98th percentile. A relatively strong linear correlation is preserved ($r = 0.901$), suggesting that the 98th percentile cell density simply represents a linear translation of the median cell density. *C*, Correlation analysis is repeated for all percentiles (0–100). With the exception of extreme values, most percentiles retain a strong linear correlation ($r > 90\%$) with the median cell density.

To quantify the effects of potential biopsy misregistration, we repeated the above linear correlations iteratively by replacing the original spheric ROI with concentric shells of voxels at an increasing distance from the biopsy center. The resulting changes to the correlation of the model with increasing distance were plotted and fit with a sigmoidal regression curve. All statistical and image analyses were performed by using Matlab 2015b (MathWorks, Natick, Massachusetts).

RESULTS

Patient Population

Thirty-six patients were included in this study, of whom 15 were male and 21 were female. The mean patient age at the operation was 65.2 years (range, 24–88 years). Eight patients were excluded due to poor neuronavigational registration, excessive motion artifacts, or errors in radiographic or tissue processing. A total of 91 localized biopsies were analyzed (median, 2 samples per patient; range, 1–6 samples). Each biopsy point was coregistered individually on ADC, T2-FLAIR, and T1-weighted postcontrast subtraction sequences, yielding 273 sets of data points for analysis.

Cell Density

Ninety-one H&E slides, 30,578 HPFs (mean, 336 HPFs per sample), were analyzed.

The median cell density was 98 nuclei per HPF (range, 4–296 nuclei) among all biopsies. The median was used as a representative measure for cell density in an H&E slide, given the presence of both outlying high- and low-density HPFs in almost all tissue samples (Fig 1*B*, -*C*). Other percentile cell densities were also considered, but it was shown that these represented an approximately linear translation of the median within any given H&E slide (Fig 2*B*, -*C*). For example, the 98th percentile cell density of any given H&E slide was directly linearly correlated to the median cell count ($r = 0.901$), displaced by approximately 50 additional nuclei/HPFs. Thus, although the following analysis was evaluated with the median cell density, the linear nature of the relationship between signal intensity and cellularity would remain valid across most cell density percentiles.

Correlation between Signal Intensity and Cell Density

Scatterplots were used to assess the relationship between MR signal intensity and cellularity on multiple sequences (Fig 3). The correlation between ADC and cellularity was $r = 0.63$; the corre-

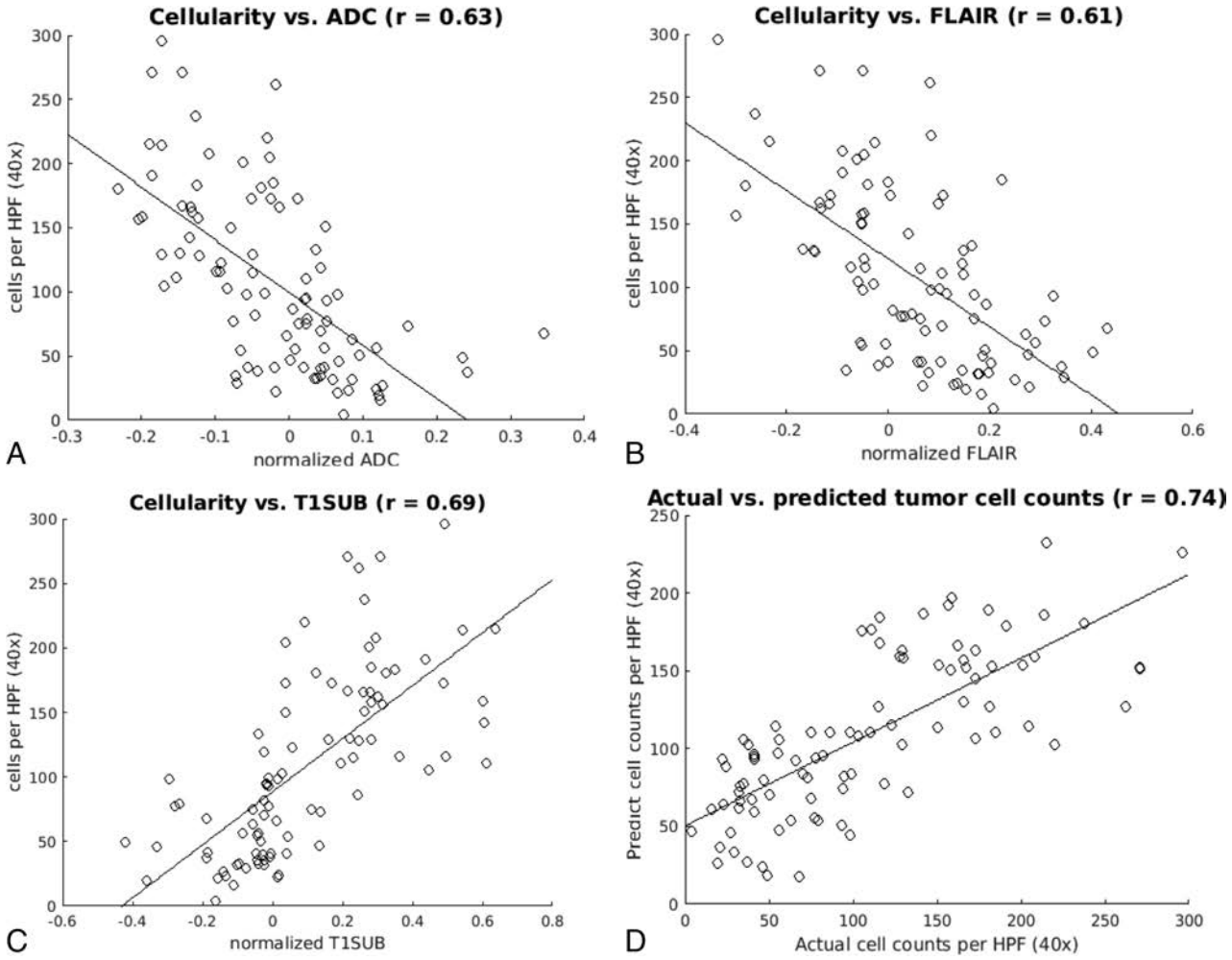

FIG 3. Cell count versus MR signal intensity. Scatterplots demonstrate median cell density as a function of signal intensity on ADC (*A*), T2-FLAIR (*B*), and T1-postcontrast subtraction sequences (*C*) correlated by using single-variable regression analysis. The linear regression and Pearson correlation (*r*) were significant ($P < .05$) for all 3 sequences. *D*, The scatterplot shows the actual and predicted cell counts as estimated by combining all 3 imaging modalities in a multiple-variable regression model.

Multivariate linear regression model coefficients

	β	SE	*T*-Score	*P* Value
Constant	102	5.98	17.1	<.001
ADC	−106	32.0	−3.30	<.001
FLAIR	−56.0	23.5	−2.38	<.001
T1-subtracted	129	24.6	5.27	<.001

Note:—SE indicates standard error.

lation between T2-FLAIR and cellularity was $r = 0.61$; and the correlation between T1-weighted postcontrast subtraction and cellularity was $r = 0.69$. A multivariable linear regression was performed to assess the predictive power of the combined MR images. The Table shows the results of this analysis. The combined model correlation improves to $r = 0.74$ with a model variance of $R^2 = 0.55$.

Effects of Possible Misregistration

The ability to correlate voxel-level signal intensities and histopathology is contingent on accurate biopsy colocalization. To estimate the detrimental effect of possible misregistrations by our automated coregistration algorithm, we compared the relationship between MR signal intensity at varying degrees of registration error. The spheric ROI used for the model correlation was systematically replaced with voxels displaced at 0.5-mm increments from the center up to 5 mm of displacement. For example, the first ROI included all voxels located 0.5 mm from the center, the second ROI included all voxels 1.0 mm from the center, and so on, resulting in a series of concentric spheric shells. The correlations between signal intensity and these projected biopsy locations are shown in Fig 4. As expected, the correlation decreased as a function of distance from the original biopsy site. After 5 mm of displacement, near-zero correlation was observed for ADC and T2-FLAIR sequences, suggesting that our registration algorithm was accurate to >5-mm spatial resolution. Of note, increasing sampling distance beyond this threshold for T1-weighted postcontrast subtraction sequences inverts the correlation from positive to negative. This outcome is likely because beyond a certain distance, voxels originally within the CE tumor are now predominantly in the NE region, while voxels within the NE portion of the tumor likely begin to incorporate portions of CE tumor, thus inverting the expected relationship between enhancement and cellularity.

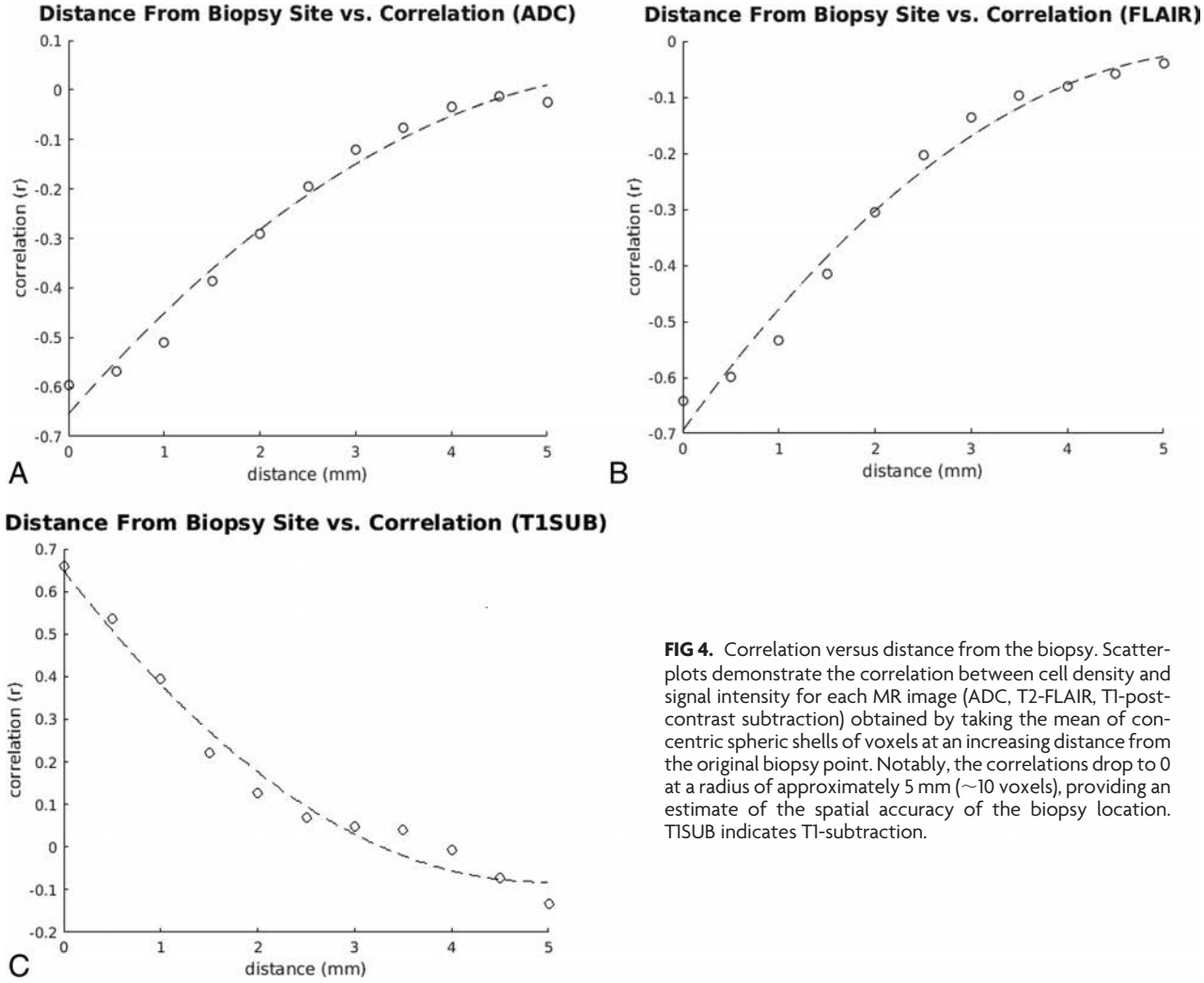

FIG 4. Correlation versus distance from the biopsy. Scatterplots demonstrate the correlation between cell density and signal intensity for each MR image (ADC, T2-FLAIR, T1-postcontrast subtraction) obtained by taking the mean of concentric spheric shells of voxels at an increasing distance from the original biopsy point. Notably, the correlations drop to 0 at a radius of approximately 5 mm (~10 voxels), providing an estimate of the spatial accuracy of the biopsy location. T1SUB indicates T1-subtraction.

Cell Density Map

Estimates for cellularity were projected at each voxel within the tumor volume by using the multivariable linear regression model and coregistered MR imaging sequences (Fig 5). Given that all biopsies were obtained within the boundaries of T2-FLAIR signal abnormality, the projected model estimates are limited to these regions.

DISCUSSION

In this study, we describe a voxel-level multiparametric MR imaging model of glioblastoma cellularity derived from the radiologic and histologic features of radiographically localized biopsies. We found that tumor cellularity is inversely correlated with ADC and T2-FLAIR signal and directly correlated with T1-weighted postcontrast signal. A multiparametric linear regression model based on these correlations captured approximately 54% of the variance in cellularity within the tumor. Projection of these estimates throughout the tumor volume provided a noninvasive map of glioblastoma cellularity, suggesting a means of visualizing infiltrative margins that may be derived from routine standard imaging. Clinically, this model may be used to guide extended surgical resection, localized biopsies, and/or radiation field mapping. Furthermore, it can be used as an outcome measure for tracking progression and response to treatment.

Cellularity was inversely correlated to ADC signal; this correlation is consistent with the notion that water diffusion is restricted in hypercellular neoplastic environments.[11,12,22-24] This concept would suggest reduced ADC signal from frank tumor tissue in the area of CE region, but also from infiltrating tumor in the surrounding NE area. Our results are concordant with prior studies using localized biopsies in the CE area, which found an inverse relationship between ADC and cellularity in the CE core.[3,25] However, studies that used this technique in the peritumoral region yielded contradictory results. Sadeghi et al[3] failed to identify any significant relationship of ADC and cellularity in the peritumoral region; however, this study consisted largely of lower grade gliomas and the peritumoral region was defined histologically rather than radiologically. Conversely, the postmortem analysis of ex vivo tissue samples of LaViolette et al[10] found a significant inverse relationship between ADC and cellularity in areas of tissue coregistered to peritumoral T2-FLAIR hyperintensity. In summary, the mixed results and differences in techniques yielded no strong conclusions but, together with our results, suggested that ADC offers some information in characterizing the peritumoral region. However, additional study is necessary to understand precisely how tumor histology is represented by ADC.

Cellularity was also inversely correlated with T2-FLAIR signal

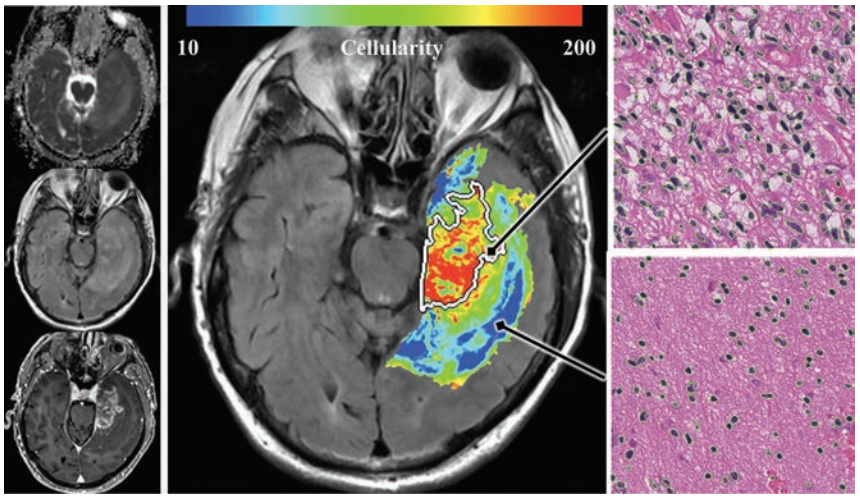

FIG 5. Whole-tumor model overlay. Estimated cellularity by applying the multiple regression model on a voxelwise basis across the tumor. The model is derived from linear regression by using ADC, T2-FLAIR, and TI-postcontrast sequences shown in the inset on the *left*. In the *right panels*, corresponding biopsy specimens (400× magnification, H&E stained sections) are shown from 2 regions obtained on the same section, highlighting the considerable variation in cellularity in and around the region of contrast enhancement (demarcated by a *white outline*).

intensity. This correlation confirms earlier hypotheses of variations in T2-FLAIR hyperintensity. Specifically, areas of high cell density result in an intermediate intensity signal, while tissue with greater proportions of vasogenic edema is more uniformly hyperintense.[15] This distinction was previously suggested by Akbari et al,[14] in which a mild loss in T2-FLAIR signal was found to be a significant predictor of cellular infiltration, leading to recurrent glioblastoma. Our results are the first to confirm this observation with histologic sampling, to our knowledge.

Conversely, cellularity was directly correlated with T1-shortening on gadolinium-enhanced sequences. This finding is in line with evidence of the perivascular migration of malignant cells, disruption of endothelial tight junctions, and subsequent leakage of gadolinium.[16,17,26,27] Notably, instead of a bimodal distribution of T1 signal intensity corresponding to CE-versus-NE tumor, a broad range of MR imaging intensity values was observed. These observations corresponded to a similarly continuous broad distribution of cellularity. These findings suggest that even within apparently similar tumor compartments, marked histologic heterogeneity is present.

To account for the possible effects of intrinsic T1 shortening as may be seen with intratumoral blood products or dystrophic mineralization, we performed an analysis by using images obtained by subtracting T1-weighted precontrast and postcontrast data. Compared with results with native T1-weighted postcontrast images, the overall correlation in both single and multivariable models is slightly superior (On-line Fig 3). One potential explanation is the reduced confounding influence of intrinsic T1 shortening when using subtraction images, though no significant hemorrhage or dystrophic mineralization was identified on histopathologic evaluation of localized biopsy samples. A second possible source of improved correlation is that subtraction images facilitate an internal reference for intensity normalization so that local magnetic field inhomogeneities or other artifacts present on both pre- and postcontrast imaging would be reduced.

A multiple linear regression model combining these individual relationships improved overall correlation from 61%–69% to 74%. This improvement confirms that these MR images contribute different and complementary information about the magnetic properties of the tumor environment. Specifically, our model is informed by tumor effects on Brownian motion of water, tissue heterogeneity in vasogenic edema, and the degree of tumor-induced blood-brain barrier breakdown.

Multiparametric modeling has been previously leveraged to investigate the imaging surrogates of peritumoral infiltration. Akbari et al[14] used imaging evidence of tumor recurrence in lieu of histologic markers for cellularity to identify MR imaging features suggestive of glioblastoma infiltration, yielding a predictive model for recurrence. Hu et al[18] expanded on this technique with histologic correlation, by using textural features extracted from multiple MR images to identify regions of tumor-rich biopsy targets (defined as ≥80% tumor content) in both the CE and NE regions. Our investigation builds on the described previous work for multiparametric analysis by implementing quantitative analysis of cellularity in the localized biopsies from both CE and NE regions. The use of this continuous variable provides a predictive model of underlying tissue heterogeneity.

Furthermore, this study relates radiologic and histologic characteristics at a more granular level, estimating cellularity on a voxel-by-voxel basis. This feature necessitates accurate and precise biopsy acquisition, coregistration of multiple imaging sequences, and quantitative histologic analysis of tissue samples. This effort remains nontrivial, with several potential sources of error, including the following: neuronavigational registration to the patient's cranial features, intraoperative brain shift, initial conversion of the biopsy image capture to 3D MR imaging space, differences in acquisition matrices and patient motion, and analysis of whole-tissue specimens for full representation of their heterogeneity.[2,28]

Measures were taken intraoperatively, and downstream processing was fully automated to minimize these potential sources of errors. By using changes in the model correlation as a reference for deleterious effects secondary to possible misregistration, we demonstrate that gradually displacing our original biopsy coordinate by >0.5 mm causes an overall loss of signal correlation with tumor cellularity. This outcome suggests that the coordinates derived from the neuronavigation system screen capture correspond well to the true location of tissue sampling. Furthermore, the cell-counting algorithm provided unbiased measures of cell density over the entirety of these heterogeneous tissue samples.

This proposed multivariable model reflects simple and intuitive signal-intensity responses to varying tissue cellularity; however, ultimately only 55% of the variance in observed tumor cel-

lularity is captured. The variance not accounted for by our model may stem from several sources: The first is localization error, which includes shifts in tissue position during an operation, errors in registration between the MR imaging and neuronavigational system, and errors in registration in each patient's multimodal MRIs. An additional source of unexplained variance comes from the MR imaging intensity of each voxel being affected by many physical and physiologic factors (eg, cell size and shape, water volume, diffusion anisotropy, and so forth). Although these factors are affected by tumor cellularity, a one-to-one relationship between cellularity and MR imaging intensity of any given sequence does not exist. While a multivariable approach, in part, reduces this phenomenon by minimizing the effects of uncorrelated noise, the proposed model is ultimately limited to linear relationships between signal intensity and cellularity, unable to account for the more spatially complex radiologic features of glioblastoma. The ability to model nonlinear behavior in signal intensity may be improved in future iterations by using machine-learning algorithms to implement both supervised and unsupervised feature detection.

While cellularity provided a simple metric for radiographic-histologic correlation, future studies would benefit from using localized biopsies to analyze additional histologic characteristics and molecular markers to capture other, more sophisticated features of biologic heterogeneity in glioblastoma. In fact, the use of machine-learning algorithms to implement both supervised and unsupervised feature detection may allow the model to account for potential complex and nonlinear radiographic-histologic relationships. The incorporation of additional physiologic imaging parameters such as dynamic susceptibility contrast perfusion, diffusion tensor imaging, and resting-state blood oxygen level–dependent imaging would likely further improve model prediction. Finally, the model may generalize to other types of gliomas (eg, low-grade gliomas); however, any model predictions beyond glioblastoma would require a validation similar to that performed in the current study.

CONCLUSIONS

This study demonstrates a significant correlation between voxel-level signal intensity and cell density in glioblastoma by single-variable regression as well as a more powerful multiparametric predictive model. Thus, with a precise and rigorous analysis pipeline, we have affirmed the feasibility of meaningful quantitative analysis at the voxel-level between signal intensity and localized biopsies. In addition, the multiparametric model proposed in this study provides a means to noninvasively map cell density at the infiltrative margins of glioblastoma. This characterization, supplemented by other histopathologic features, may be used to guide extended surgical resection, localized biopsy, and/or radiation field mapping, with significant implications for patient management.

Disclosures: Adam M. Sonabend—*UNRELATED*: *Employment*: Columbia University; *Grants/Grants Pending*: National Institutes of Health, *Comments*: I have a DP5 National Institutes of Health grant from the Office of the Director, National Institutes of Health. Lawrence H. Schwartz—*OTHER RELATIONSHIPS*: consulting or advisory role company: Novartis, GlaxoSmithKline; research funding company: Eli Lilly, Astellas Pharma, Merck Sharp & Dohme, Pfizer, Boehringer Ingelheim; patent licensing for Varian Medical Systems. Peter Canoll—*RELATED*: *Grant*: James S. McDonnell Foundation, Irving Institute for Clinical and Translational Research: Pilot Research Award, *Comments*: These grants supported the analysis of the localized biopsies.

REFERENCES

1. Gill BJ, Pisapia DJ, Malone HR, et al. **MRI-localized biopsies reveal subtype-specific differences in molecular and cellular composition at the margins of glioblastoma.** *Proc Natl Acad Sci U S A* 2014;111:12550–55 CrossRef Medline
2. Barajas RF, Phillips JJ, Parvataneni R, et al. **Regional variation in histopathologic features of tumor specimens from treatment-naive glioblastoma correlates with anatomic and physiologic MR imaging.** *Neuro Oncol* 2012;14:942–54 CrossRef Medline
3. Sadeghi N, D'Haene N, Decaestecker C, et al. **Apparent diffusion coefficient and cerebral blood volume in brain gliomas: relation to tumor cell density and tumor microvessel density based on stereotactic biopsies.** *AJNR Am J Neuroradiol* 2008;29:476–82 CrossRef Medline
4. Stadnik TW, Chaskis C, Michotte A, et al. **Diffusion-weighted MR imaging of intracerebral masses: comparison with conventional MR imaging and histologic findings.** *AJNR Am J Neuroradiol* 2001;22:969–76 Medline
5. Wallner KE, Galicich JH, Krol G, et al. **Patterns of failure following treatment for glioblastoma multiforme and anaplastic astrocytoma.** *Int J Radiat Oncol Biol Phys* 1989;16:1405–09 CrossRef Medline
6. Liang BC, Thornton AF, Sandler HM, et al. **Malignant astrocytomas: focal tumor recurrence after focal external beam radiation therapy.** *J Neurosurg* 1991;75:559–63 CrossRef Medline
7. Stupp R, Mason WP, van den Bent MJ, et al; European Organisation for Research and Treatment of Cancer Brain Tumor and Radiotherapy Groups, National Cancer Institute of Canada Clinical Trials Group. **Radiotherapy plus concomitant and adjuvant temozolomide for glioblastoma.** *N Engl J Med* 2005;352:987–96 CrossRef Medline
8. Burger PC, Heinz ER, Shibata T, et al. **Topographic anatomy and CT correlations in the untreated glioblastoma multiforme.** *J Neurosurg* 1988;68:698–704 Medline
9. Price SJ, Gillard JH. **Imaging biomarkers of brain tumour margin and tumour invasion.** *Br J Radiol* 2011;84(Spec No 2):S159–67 CrossRef Medline
10. LaViolette PS, Mickevicius NJ, Cochran EJ, et al. **Precise ex vivo histological validation of heightened cellularity and diffusion-restricted necrosis in regions of dark apparent diffusion coefficient in 7 cases of high-grade glioma.** *Neuro Oncol* 2014;16:1599–606 CrossRef Medline
11. Sugahara T, Korogi Y, Kochi M, et al. **Usefulness of diffusion-weighted MRI with echo-planar technique in the evaluation of cellularity in gliomas.** *J Magn Reson Imaging* 1999;9:53–60 Medline
12. Kono K, Inoue Y, Nakayama K, et al. **The role of diffusion-weighted imaging in patients with brain tumors.** *AJNR Am J Neuroradiol* 2001;22:1081–88 Medline
13. Guo AC, Cummings TJ, Dash RC, et al. **Lymphomas and high-grade astrocytomas: comparison of water diffusibility and histologic characteristics**. *Radiology* 2002;224:177–83 CrossRef Medline
14. Akbari H, Macyszyn L, Da X, et al. **Imaging surrogates of infiltration obtained via multiparametric imaging pattern analysis predict subsequent location of recurrence of glioblastoma.** *Neurosurgery* 2016;78:572–80 CrossRef Medline
15. Pope WB, Chen JH, Dong J, et al. **Relationship between gene expression and enhancement in glioblastoma multiforme: exploratory DNA microarray analysis.** *Radiology* 2008;249:268–77 CrossRef Medline
16. Tynninen O, Aronen HJ, Ruhala M, et al. **MRI enhancement and microvascular density in gliomas: correlation with tumor cell proliferation.** *Invest Radiol* 1999;34:427–34 CrossRef Medline
17. Watkins S, Robel S, Kimbrough IF, et al. **Disruption of astrocyte-vascular coupling and the blood-brain barrier by invading glioma cells.** *Nat Commun* 2014:5:4196 CrossRef Medline
18. Hu LS, Ning S, Eschbacher JM, et al. **Multi-parametric MRI and**

texture analysis to visualize spatial histologic heterogeneity and tumor extent in glioblastoma. *PLoS One* 2015;10:e0141506 CrossRef Medline
19. Jenkinson M, Smith S. **A global optimisation method for robust affine registration of brain images.** *Med Image Anal* 2001;5:143–56 CrossRef Medline
20. Jenkinson M, Bannister P. **Improved methods for the registration and motion correction of brain images.** *Neuroimage* 2002;17:825–41 CrossRef Medline
21. Shapira D, Avidan S, Hel-Or Y. **Multiple histogram matching.** In: *2013 IEEE International Conference on Image Processing*, Melbourne, Australia. September 15–18, 2013:2269–73 CrossRef
22. Lyng H, Haraldseth O, Rofstad EK. **Measurement of cell density and necrotic fraction in human melanoma xenografts by diffusion weighted magnetic resonance imaging.** *Magn Reson Med* 2000;43:828–36 Medline
23. Chenevert TL, Stegman LD, Taylor JM, et al. **Diffusion magnetic resonance imaging: an early surrogate marker of therapeutic efficacy in brain tumors.** *J Natl Cancer Inst* 2000;92:2029–36 CrossRef Medline
24. Hayashida Y, Hirai T, Morishita S, et al. **Diffusion-weighted imaging of metastatic brain tumors: comparison with histologic type and tumor cellularity.** *AJNR Am J Neuroradiol* 2006;27:1419–25 Medline
25. Ellingson BM, Malkin MG, Rand SD, et al. **Validation of functional diffusion maps (fDMs) as a biomarker for human glioma cellularity.** *J Magn Reson Imaging* 2010;31:538–48 CrossRef Medline
26. Cuddapah VA, Robel S, Watkins S, et al. **A neurocentric perspective on glioma invasion.** *Nat Rev Neurosci* 2014;15:455–65 CrossRef Medline
27. Scherer HJ. **Cerebral astrocytomas and their derivatives.** *Cancer Res* 1940;40:159–98 CrossRef
28. Trantakis C, Tittgemeyer M, Schneider JP, et al. **Investigation of time-dependency of intracranial brain shift and its relation to the extent of tumor removal using intra-operative MRI.** *Neurol Res* 2003;25:9–12 CrossRef Medline

Multiparametric Evaluation in Differentiating Glioma Recurrence from Treatment-Induced Necrosis Using Simultaneous ^{18}F-FDG-PET/MRI: A Single-Institution Retrospective Study

A. Jena, S. Taneja, A. Jha, N.K. Damesha, P. Negi, G.K. Jadhav, S.M. Verma, and S.K. Sogani

ABSTRACT

BACKGROUND AND PURPOSE: Differentiating glioma recurrence from treatment-induced necrosis can be a challenge on conventional imaging. This study aimed to assess the diagnostic performance of each functional MR imaging and PET parameter derived by using simultaneous FDG-PET/MR imaging individually and in combination in the evaluation of suspected glioma recurrence.

MATERIALS AND METHODS: Thirty-five treated glioma patients with 41 enhancing lesions (World Health Organization grade II = 9, III = 13, IV = 19) on MR imaging after an operation followed by radiation therapy and/or chemotherapy formed part of this study. Using PET/MR imaging, we calculated the normalized mean relative CBV, mean ADC, Cho/Cr, and maximum and mean target-to-background ratios. Statistical analysis was performed to determine the diagnostic performance of each parameter by receiver operating characteristic analysis individually and in combination with multivariate receiver operating characteristic analysis for the detection of glioma recurrence. Histopathology or clinicoradiologic follow-up was considered the criterion standard.

RESULTS: Of 35 patients, 25 (30 lesions) were classified as having a recurrence and 10 (11 lesions) patients as having treatment-induced necrosis. Parameters like $rCBV_{mean}$ (mean relative CBV), ADC_{mean}, Cho/Cr, and maximum and mean target-to-background ratios were statistically significant in the detection of recurrent lesions with an accuracy of 77.5%, 78.0%, 90.9%, 87.8%, and 87.8%, respectively. On multivariate receiver operating characteristic analysis, the combination of all 3 MR imaging parameters resulted in an area under the curve of 0.913 ± 0.053. Furthermore, an area under the curve of 0.935 ± 0.046 was obtained when MR imaging parameters (ADC_{mean} and Cho/Cr) were combined with the PET parameter (mean target-to-background ratio), demonstrating an increase in diagnostic accuracy.

CONCLUSIONS: Simultaneous PET/MR imaging with FDG offers correlative and synergistic multiparametric assessment of glioma recurrence with increased accuracy and clinical utility.

ABBREVIATIONS: AUC = area under the curve; CE = contrast-enhanced; max = maximum; rCBV = relative cerebral blood volume; ROC = receiver operating characteristic; SUV = standardized uptake value; TBR = target-to-background ratio

Glioma is currently managed by surgical resection followed by radiation therapy and/or chemotherapy, depending on the aggressiveness of the tumor. Most of these tumors, despite treatment, recur or progress during the course of the disease. Furthermore, treatment with chemoradiation therapy is associated with necrosis.[1] Up to 30% of patients with glioblastoma on chemoradiation therapy develop treatment-related effects, which mimic tumor recurrence, and both present as a new enhancing lesion on contrast-enhanced (CE) MR imaging.[2] This effect gets further complicated because recurrences most often occur within or adjacent to the primary tumor site.[3] Moreover, recurrent glioma and radiation necrosis may coexist, further obscuring this differentiation.[4] Hence, differentiation of tumor recurrence from treatment-induced necrosis, which remains a challenge on conventional CE-MR imaging,[2,5] is important because their management and prognosis are completely different.[6]

Advanced neuroimaging with MR imaging and PET has been proposed in the past for assessment of glioma recurrence.[7,8] MR imaging, besides providing superior tissue contrast, also provides functional information through perfusion, diffusion, and spectroscopy. PET imaging, on the other hand, provides additional

Received August 27, 2016; accepted after revision December 21.

From the PET SUITE (A. Jena, S.T., A. Jha, P.N.), Departments of Molecular Imaging and Nuclear Medicine, Radiation Oncology (G.K.J., S.M.V.), and Neurosurgery (N.K.D., S.K.S.), Indraprastha Apollo Hospitals, Sarita Vihar, New Delhi, India.

All procedures performed in studies involving human participants were in accordance with the ethics standards of the institutional and/or national research committee and with the 1964 Declaration of Helsinki and its later amendments or comparable ethics standards.

Please address correspondence to Amarnath Jena, DNB, PET SUITE, Department of Molecular Imaging and Nuclear Medicine, Indraprastha Apollo Hospitals, Sarita Vihar, Delhi-Mathura Rd, New Delhi, India-110076; e-mail: drjena2002@yahoo.com

http://dx.doi.org/10.3174/ajnr.A5124

information about tumor metabolism. FDG has been extensively used in the differentiation of glioma recurrence from radiation necrosis with variable results.[9] High physiologic uptake of FDG in the normal brain and its uptake in inflammatory cells often result in poor tumor-to-background differentiation and make it a moderate test for characterization of tumor recurrence.[10] This outcome has resulted in research into several more accurate PET tracers. Amino acid–based radio tracers such as ^{11}C-methionine, ^{18}F-fluoro-ethyl-tyrosine, and ^{18}F-fluoro-l-thymidine are known to offer better imaging characteristics, however, are not easily available. ^{11}C with a very short half-life needs an in-house cyclotron for production. ^{18}FDG, being a commonly available tracer with low cost suitable for wider application, formed the basis of our work. The role of CT in the diagnosis of glioma recurrence is limited, with CE-MR imaging remaining the mainstay in neuroimaging.[11] In an attempt to improve diagnostic accuracy, PET/CT has been used along with CE-MR imaging with limited success.[12] With an aim to complement information for this purpose, multiparametric assessment with various functional MR imaging parameters such as choline/creatine, choline/*N*-acetylaspartate, relative cerebral blood volume (rCBV), and apparent diffusion coefficient have been used in the past,[13,14] whereas a few studies have tried coregistration of MR imaging with PET parameters such as standardized uptake value (SUV) and target-to-background ratio (TBR) performed separately on different occasions to improve diagnostic accuracy.[12,15,16]

The advent of simultaneous PET/MR imaging has made it possible to assess all the parameters together in the same physical space in a single examination. We believe that simultaneous acquisition may help in overcoming some of the limitations of individual techniques and bring a synergistic effect in improved differentiation of recurrence from treatment-induced necrosis.

The present study aimed to assess the diagnostic performance of each of these parameters derived by using simultaneous FDG-PET/MR imaging individually and in combination by receiver operating characteristic (ROC) analysis for the evaluation of suspected glioma recurrence.

MATERIALS AND METHODS

Patients

In this retrospective study between March 2013 and September 2015, 41 consecutive patients who underwent simultaneous FDG-PET/MR imaging for glioma recurrence evaluation were chosen after obtaining prior approval of the institutional review board and signed informed consent. Inclusion criteria were histopathologic-proved glioma, previous treatment with an operation and radiation therapy with or without chemotherapy, and a high index of clinical suspicion for recurrence along with contrast enhancement on MR imaging. Exclusion criteria were nonglial primary brain tumors, proved malignancy of other sites, pregnancy, being younger than 18 years of age, standard contraindications to MR imaging, and loss of the patient to follow-up. Finally, 35 patients (6 women, 29 men; mean age, 50 ± 12 years) with 41 lesions (World Health Organization grade II = 9, III = 13, IV = 19) formed part of this study. Twenty-nine patients received chemoradiation therapy, whereas 6 patients received only radiation therapy. The interval between radiation therapy and FDG-PET/MR imaging ranged from 7 to 96 months, with a solitary case with a maximum of 233 months. The patient characteristics are available in Table 1.

Table 1: Patient characteristics

Characteristic	Value
Age (mean) (yr)	50 ± 12
Sex (No. of patients) (%)	
Male	29 (82.8)
Female	6 (17.2)
Primary histopathology (No. of lesions) (%)	
Glioblastoma	17 (41.5)
Anaplastic astrocytoma	9 (21.9)
Anaplastic oligodendroglioma	4 (9.8)
Oligodendroglioma	7 (17.1)
Others	4 (9.7)
WHO classification (No. of lesions) (%)	
Grade II	9 (22.0)
Grade III	13 (31.7)
Grade IV	19 (46.3)
Primary site of glioma (No. of lesions) (%)	
Frontal	15 (36.6)
Parietal	2 (4.9)
Temporal	10 (24.4)
Multilobar	14 (34.1)
Primary treatment (No. of patients) (%)	
Operation+radiation therapy	6 (17.2)
Operation+radiation therapy+chemotherapy	29 (82.8)
Final diagnosis (No. of lesions) (%)	
Recurrence	30 (73.2)
Histopathology	21 (51.2)
Clinicoradiologic follow-up	9 (22.0)
Treatment-induced necrosis	11 (26.8)
Histopathology	2 (4.9)
Clinicoradiologic follow-up	9 (21.9)

Note:—WHO indicates World Health Organization.

Lesion Diagnosis

A combination of clinical and imaging follow-up and histopathology was considered the criterion standard. Patients with a disease-related adverse event, progressive disease on imaging, and/or a biopsy positive for viable tumor tissue were positive for recurrence. Patients who were stable or did not show any adverse events clinically and did not progress on imaging were considered positive for treatment-induced necrosis.

Instrumentation: Simultaneous PET/MR Imaging

Simultaneous FDG-PET/MR imaging was performed on a Biograph mMR scanner (Siemens, Erlangen, Germany). This system consists of a modified 3T system (Magnetom Verio; Siemens) with a fully functional PET system, equipped with avalanche photodiode technology. The MR imaging scanner features a high-performance gradient system (45 mT/m) with a slew rate of 200 T/m/s and is equipped with total imaging matrix coil technology. The PET scanner has a spatial resolution of 4.3 mm at 1 and 5.0 mm at 10 cm from the transverse FOV; its sensitivity is 1.47% at the center of the FOV and 1.38% at 10 cm.

Imaging Protocol

The patients fasted for 6 hours before intravenous FDG injection of 352.12 ± 64.26 MBq. PET/MR imaging started 45–60 minutes after injection for 25–30 minutes of PET acquisition, during which various MR imaging sequences were performed.

A simultaneous brain PET/MR imaging protocol was composed of a transversal T1WI ultrashort TE sequence (TR/TE1/TE2, 11.94/0.07/22.46 ms) for attenuation correction and other MR imaging sequences for complete diagnostic evaluation of the brain, which included an axial FLAIR sequence (TR/TE, 7000/94 ms; TI, 2215.2 seconds; section thickness, 5 mm); a T2-weighted turbo spin-echo sequence (TR/TE, 4300/100 ms; section thickness, 5 mm); DWI (TR/TE, 4600/101 ms; $b = 0$, 400, 1000 s/mm^2); PWI/perfusion EPI (TR/TE, 2550/31 ms); and 3D-encoded MPRAGE (TR/TE/TI, 1500/2.33 ms/900 seconds; spatial resolution, $1.2 \times 1 \times 1$ mm) in the sagittal plane. In each case, 3D multivoxel ^{1}H-MR spectroscopy (TR/TE, 1510/135 ms; FOV, 120 mm; matrix, $8 \times 8 \times 8$ cm; acquisition, 1 average; scanning time, 5 minutes 41 seconds) was performed.

After the scan, all coincident data were sorted into a 2D-PET sinogram, which was subsequently reconstructed into transaxial sections, with an iterative 3D-ordered-subset expectation maximization algorithm with 3 iterations and 21 subsets, Gaussian smoothing of 4 mm in full width at half maximum, and a zoom of 1. The voxel size of brain PET images was $1.39 \times 1.39 \times 2.03$ mm. MR imaging, PET, and PET/MR imaging scans were reviewed at a syngo.via platform (Siemens) by using the mMR general workflow.

PET and MR Image Quality Control

All PET/MR imaging studies were performed by using standard imaging protocol for both PET and MR imaging, adhering to the principle of the Quantitative Imaging Biomarkers Alliance protocol and standards (https://www.rsna.org/qiba/): in case of PET, tracer dose, time delay after injection, acquisition time; and, in case of MR imaging, consistency of imaging sequences. Distortion-correction-enabled diffusion-weighed images were acquired to minimize error in the ADC calculation. For PET images, emission data were corrected for randoms, dead time, and scatter, and attenuation correction was performed by using an MR imaging–based ultrashort TE sequence.

Image Analysis

Quantitative analysis of FDG-PET/MR imaging scans was performed by a radiologist and a nuclear medicine physician in consensus, with >10 years' experience in diagnostic radiology or nuclear medicine, who were blinded to the clinical information, histopathologic data, clinicoradiologic follow-up information, and final diagnosis for each lesion.

ROI Selection

First, by subtraction of precontrast from postgadolinium T1WIs, we achieved a software-based postcontrast subtraction series wherever possible to accurately isolate areas of enhancing tumor.[17] We calculated ADC on-line by using system software, applying a monoexponential model. The most representative spectra observed within/around the lesion showing maximum PET uptake was taken for calculation of Cho/Cr.[18]

A freehand 2D ROI was drawn manually over the most representative section with maximum enhancement and was stored. This freehand ROI was duplicated by using the copy-paste function over the FDG-PET image, software generated ADC and CBV maps to find the respective maximum standardized uptake value (SUV_{max}), mean standardized uptake value (SUV_{mean}), mean ADC (ADC_{mean}), and mean CBV (CBV_{mean}) (Figs 1 and 2). Maximum target-to-background ratio (TBR_{max}), mean target-to-background ratio (TBR_{mean}), and $rCBV_{mean}$ were calculated by dividing SUV_{max}, SUV_{mean}, and CBV_{mean} obtained from the lesion ROI by the SUV_{mean}, SUV_{mean}, and CBV_{mean}, respectively, from a separate ROI drawn for normalization on normal contralateral white matter.

Statistical Analysis

Data were checked for normality by using the Shapiro-Wilk test before statistical analysis. Individual PET/MR imaging parameters were evaluated for the difference between glioma recurrence and treatment-induced necrosis by using a 2-tailed independent Student *t* test or Mann-Whitney *U* test. Optimal-threshold value, area under the curve (AUC), sensitivity, specificity, positive predictive value, negative predictive value, and accuracy were calculated by using receiver operating characteristic analysis for each of the PET/MR imaging parameters for their ability to detect recurrence. Multivariate analysis of variance was performed to check whether a combination of parameters was better than individual parameters. A multivariate ROC analysis was performed to analyze the increment offered by a combination of various parameters by conducting a logistical regression analysis to generate a combined ROC curve of different combinations of parameters. All statistical analyses were performed with the SPSS software package (Version 17.0; IBM, Armonk, New York). For all statistical tests, a P value $< .05$ was considered a significant difference.

RESULTS

Patient Information

Thirty-five patients enrolled in this retrospective study had 41 lesions for evaluation. Five patients had multicentric lesions. Histopathology after repeat operation showed viable tumor in 16 patients (21 lesions) and evidence of treatment-induced necrosis in 2 patients (2 lesions).

Eight patients (9 lesions) without histopathologic evaluation were classified as having treatment-induced necrosis based on a stable clinical state on extended follow-up periods, absence of any new neurologic symptoms, and no remarkable increase of the lesion size and/or metabolic activity observed on follow-up PET/MR imaging up to a mean period of 11.8 ± 4.5 months (range, 7–24 months). Nine patients (9 lesions) were finally classified as having recurrent brain tumors due to the development of neurologic symptoms and a progressive increase in size on CE-MR imaging (1 patient) or PET/MR imaging (8 patients) during follow-up.

Scan Information

All 35 patients underwent simultaneous FDG-PET/MR imaging. One patient did not have perfusion MR imaging; in 4 patients (5 lesions), the MR spectroscopy study was not contributory because of noisy spectra, and it was not acquired in 2 patients (3 multicentric lesions) and hence was not included in the analysis.

Among considered parameters, $rCBV_{mean}$, ADC_{mean}, Cho/Cr, TBR_{max}, and TBR_{mean} were found significant ($P < .05$) and used

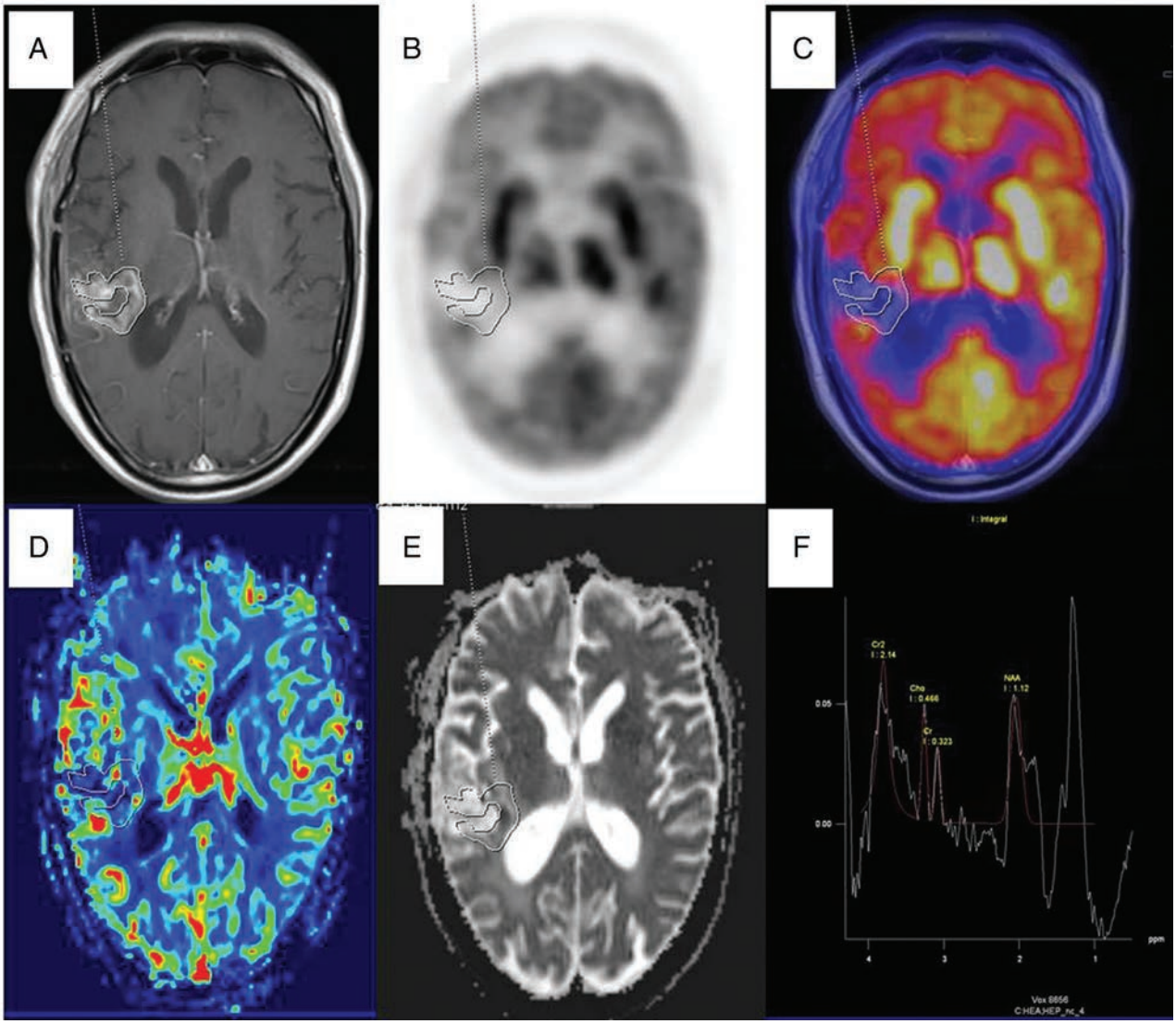

FIG 1. PET/MR imaging of a 73-year-old man with posttreatment (operation, radiation therapy, and chemotherapy) right temporoparietal glioblastoma multiforme with suspected recurrence proved to be treatment-induced necrosis on 11-month PET/MR imaging follow-up. Axial T1-weighted postcontrast image (*A*) shows an enhancing lesion along the margins of the operated bed with a freehand ROI drawn defining the enhancing component, which was copied and pasted on the FDG image (*B*), PET/MR fused image (*C*), CBV map (*D*), and ADC map (*E*) to derive SUV_{max} and SUV_{mean}, CBV_{mean}, and ADC_{mean} show no focal increased FDG uptake, CBV, and diffusion restriction on the ADC map. Multivoxel ^{1}H-MR spectroscopy (*F*) along the enhancing margin shows no increased Cho/Cr ratio.

for further combined analysis (Table 2 and Fig 3). The tumor size ranged from 0.92 to 9.5 cm^2.

Comparison of Advanced MR Imaging Parameters

PWI: $rCBV_{mean}$. In this study, $rCBV_{mean}$ was not significantly higher in patients with recurrence than in patients with treatment-induced necrosis (2.41 ± 1.02 versus 1.82 ± 1.12, $P = .082$; Fig 3*A*). However, the diagnostic accuracy of $rCBV_{mean}$ for correct identification of glioma recurrence reached 77.5% with $rCBV_{mean} \geq 1.71$ (AUC = 0.680 ± 0.111, $P = .008$), which was found to be significant (Table 2 and Fig 4*A*).

DWI: ADC_{mean}. The ADC_{mean} was significantly lower in patients with recurrence than in those with treatment-induced necrosis (1283.13 ± 210.96 versus 1558.55 ± 313.32 × $10^{-6}mm^2/s$, $P = .015$; Fig 3*B*). The diagnostic accuracy of ADC_{mean} for correct identification of glioma recurrence reached 78% with $ADC_{mean} \leq 1507 \times 10^{-6}mm^2/s$ (AUC = 0.752 ± 0.015, $P = .013$; Table 2 and Fig 4*A*).

MR Spectroscopy: Cho/Cr. Cho/Cr was significantly higher in patients with glioma recurrence than in those with treatment-induced necrosis (3.47 ± 2.20 versus 1.63 ± 0.64, $P = .002$; Fig 3*C*). The diagnostic accuracy of Cho/Cr for correct identification of glioma recurrence reached 90.9% by using Cho/Cr ≥ 1.405 (AUC = 0.861 ± 0.08, $P < .001$; Table 2 and Fig 4*A*).

Comparison of FDG Uptake Indices (TBR_{max} and TBR_{mean})

The TBR_{max} and TBR_{mean} were significantly higher in patients with glioma recurrence than in those with treatment-induced necrosis (TBR_{max}, 2.50 ± 0.97 versus 1.53 ± 0.59, $P = .001$ and TBR_{mean}, 1.70 ± 0.61 versus 0.98 ± 0.36, $P < .001$; Fig 3*D*). The diagnostic accuracy of TBR values for the correct identification of

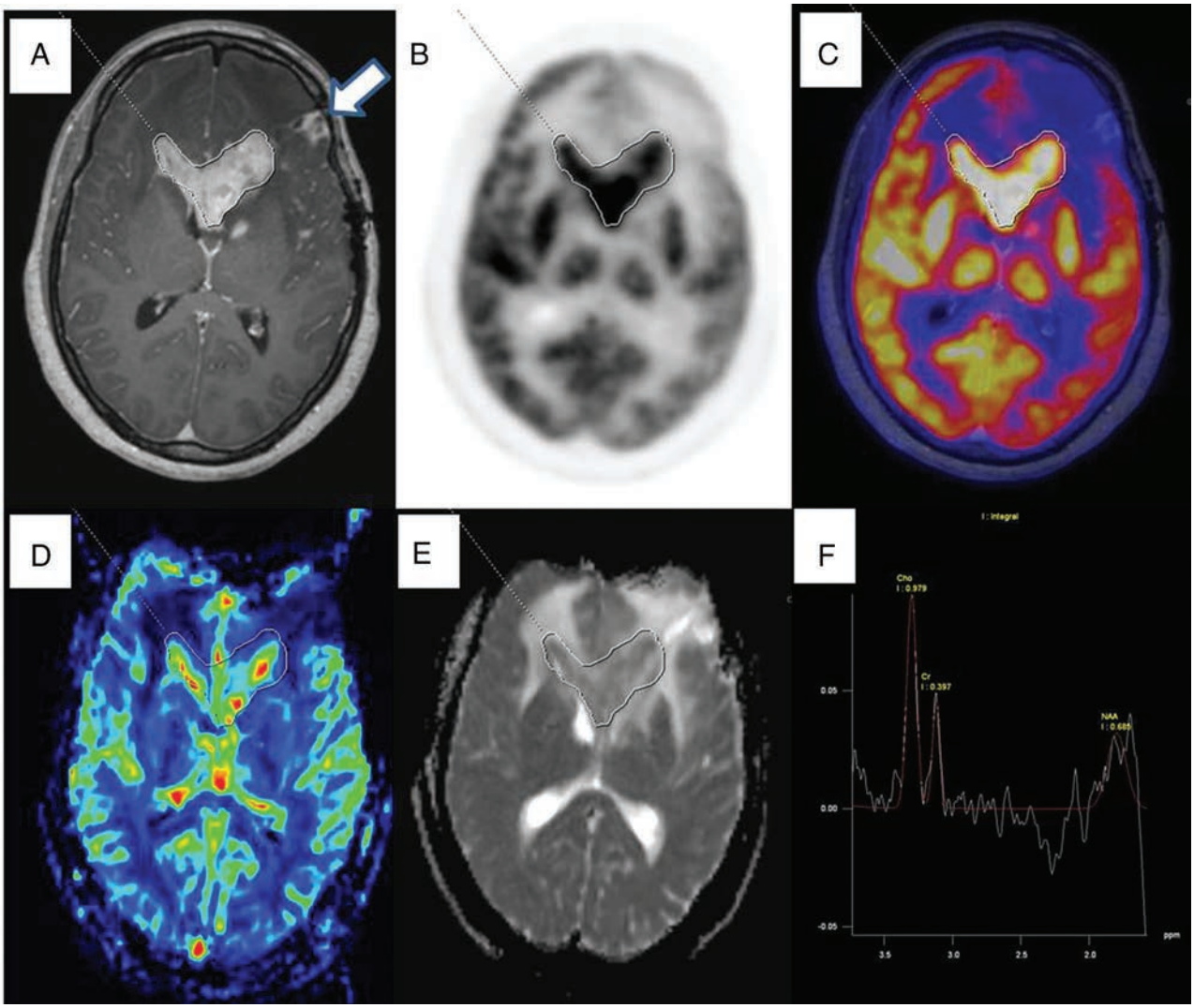

FIG 2. PET/MR images of a 49-year-old woman with posttreatment (operation and radiaton therapy) left frontotemporal anaplastic oligodendroglioma that proved to be a recurrence on histopathologic examination (glioblastoma multiforme with an oligodendroglial component; World Health Organization grade IV with a large area of necrosis). Axial T1-weighted postcontrast image (*A*) shows an enhancing lesion in the tumor bed and involving the corpus callosum. Freehand ROI drawn defining the enhancing component of the lesion and copied and pasted on the FDG image (*B*), the PET/MR fused image (*C*), the CBV map (*D*), and the ADC map (*E*) to derive SUV_{max} and SUV_{mean}, CBV_{mean}, and ADC_{mean} shows increased FDG uptake, CBV, and diffusion restriction in the ADC map. Multivoxel ^{1}H-MR spectroscopy (*F*) obtained on the FDG avid enhancing area shows an increased Cho/Cr ratio. The enhancing region anterior to the target lesion has no FDG uptake and no increased CBV, and diffusion restriction represents necrosis (*white arrow*).

Table 2: Diagnostic performance of individual parameters in the detection of glioma recurrence[a]

	$rCBV_{mean} \geq 1.709$	$ADC_{mean} \leq 1507$	$Cho/Cr \geq 1.405$	$TBR_{max} \geq 1.579$	$TBR_{mean} \geq 1.179$
Sensitivity	82.8%	86.7%	100.0%	93.3%	90.0%
Specificity	63.6%	54.5%	66.7%	72.7%	81.8%
PPV	85.7%	83.9%	88.9%	90.3%	93.1%
NPV	58.3%	60.0%	100.0%	80.0%	75.0%
Accuracy	77.5%	78.0%	90.9%	87.8%	87.8%
AUC±SE	0.68 ± 0.111	0.752 ± 0.015	0.861 ± 0.08	0.827 ± 0.078	0.888 ± 0.059
P value	.008[b]	.013[b]	<.001[b]	<.001[b]	<.001[b]

Note:—PPV indicates positive predictive value; NPV, negative predictive value; SE, standard error.

[a] The ADC_{mean} value is expressed as $\times 10^{-6} mm^2/s$ and $rCBV_{mean}$. Cho/Cr, TBR_{max}, and TBR_{mean} are ratios and hence unitless. *P* values mentioned are generated while calculating the AUC from the ROC analysis.

[b] *P* values of $rCBV_{mean}$, ADC_{mean}, Cho/Cr, TBR_{max}, and TBR_{mean} are <.05 and hence are statistically significant. *P* value reflects the significance of the ROC analysis of individual parameters represented in the table.

recurrence of brain gliomas reached 87.8% with $TBR_{max} \geq 1.58$ (AUC = 0.827 ± 0.078, $P < .001$; Table 2 and Fig. 4*C*) and also with $TBR_{mean} \geq 1.18$ (AUC = 0.888 ± 0.059, $P < .001$; Table 2 and Fig 4*C*), though with a superior AUC.

Comparison of Combined Parameters

On multivariate analysis of variance, a statistically significant difference between glioma recurrence and treatment-induced necrosis ($F_{5,26} = 5.871$, $P = .001$; Wilks $\lambda = 0.470$, partial $\eta^2 = 0.530$) was observed.

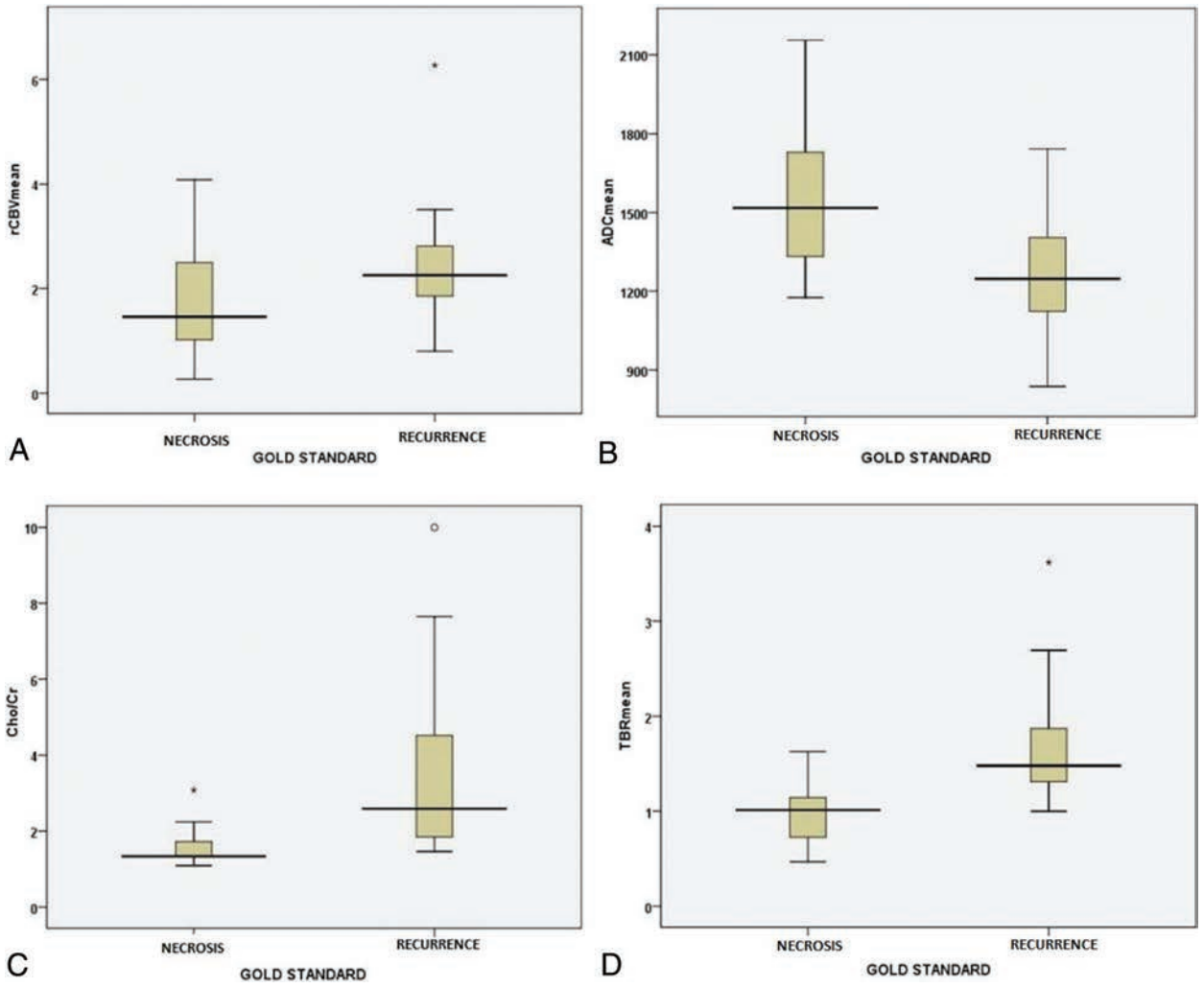

FIG 3. Box-and-whisker plots comparing $rCBV_{mean}$ (*A*), ADC_{mean} (*B*), Cho/Cr (*C*), and TBR_{mean} (*D*) between the glioma recurrence and treatment-induced necrosis. Whiskers represent the range of data; boxes represent the distance between the first and third quartiles.

Combinational Analysis

Various combinations of several parameters were performed, and multivariate ROC analysis was performed as depicted in Table 3 (Fig 4*B*, -*D*).

Combined Analysis of MR Imaging Parameters: Cho/Cr, $rCBV_{mean}$, and ADC_{mean}

Individually, Cho/Cr achieved a maximum AUC of 0.861 ± 0.080 in the detection of glioma recurrence. On multivariate ROC analysis, the addition of ADC_{mean} to either $rCBV_{mean}$ or Cho/Cr resulted in an improved diagnostic capability of both $rCBV_{mean}$ and Cho/Cr as noted by an increment in the AUC of the combinations. The combination of all 3 MR imaging parameters resulted in a combined AUC of 0.913 ± 0.053 (Table 3 and Fig 4*B*).

Combined Analysis of MR Imaging and FDG Parameters: TBR_{max}, TBR_{mean}, Cho/Cr, $rCBV_{mean}$, and ADC_{mean}

Individually, TBR_{mean} has the maximum AUC (0.888 ± 0.059) of all the MR imaging and PET parameters. Among intervariable evaluation with multivariate analysis of variance for the predictability of diagnosis, ADC_{mean} ($P = .001$) and TBR_{mean} ($P = .001$) were found to be the most significant variables in predicting glioma recurrence. On multivariate ROC analysis, the maximum AUC of 0.935 ± 0.046 was achieved with a combination of ADC_{mean}, Cho/Cr, and TBR_{mean} (Fig 4*D*). Moreover, a combination of either TBR_{max} or TBR_{mean} with ADC_{mean} and/or Cho/Cr improved the AUC value significantly beyond that of individual combining parameters (Table 3).

Summary of Results

Among all individual parameters, Cho/Cr in MR imaging and TBR_{mean} in PET are the most significant discriminators for the prediction of recurrence. Among MR imaging parameters alone, $rCBV_{mean}$ should be used in conjunction with Cho/Cr and ADC_{mean} for differentiating recurrence from treatment-induced necrosis. The maximum AUC is achieved by combining TBR_{mean}, ADC_{mean}, and Cho/Cr.

DISCUSSION

Treatment-induced necrosis is a common treatment-related morbidity in the management of gliomas, and the rate of radiation necrosis increases with incorporation of temozolomide into high-grade glioma management.[19] The differentiation of glioma

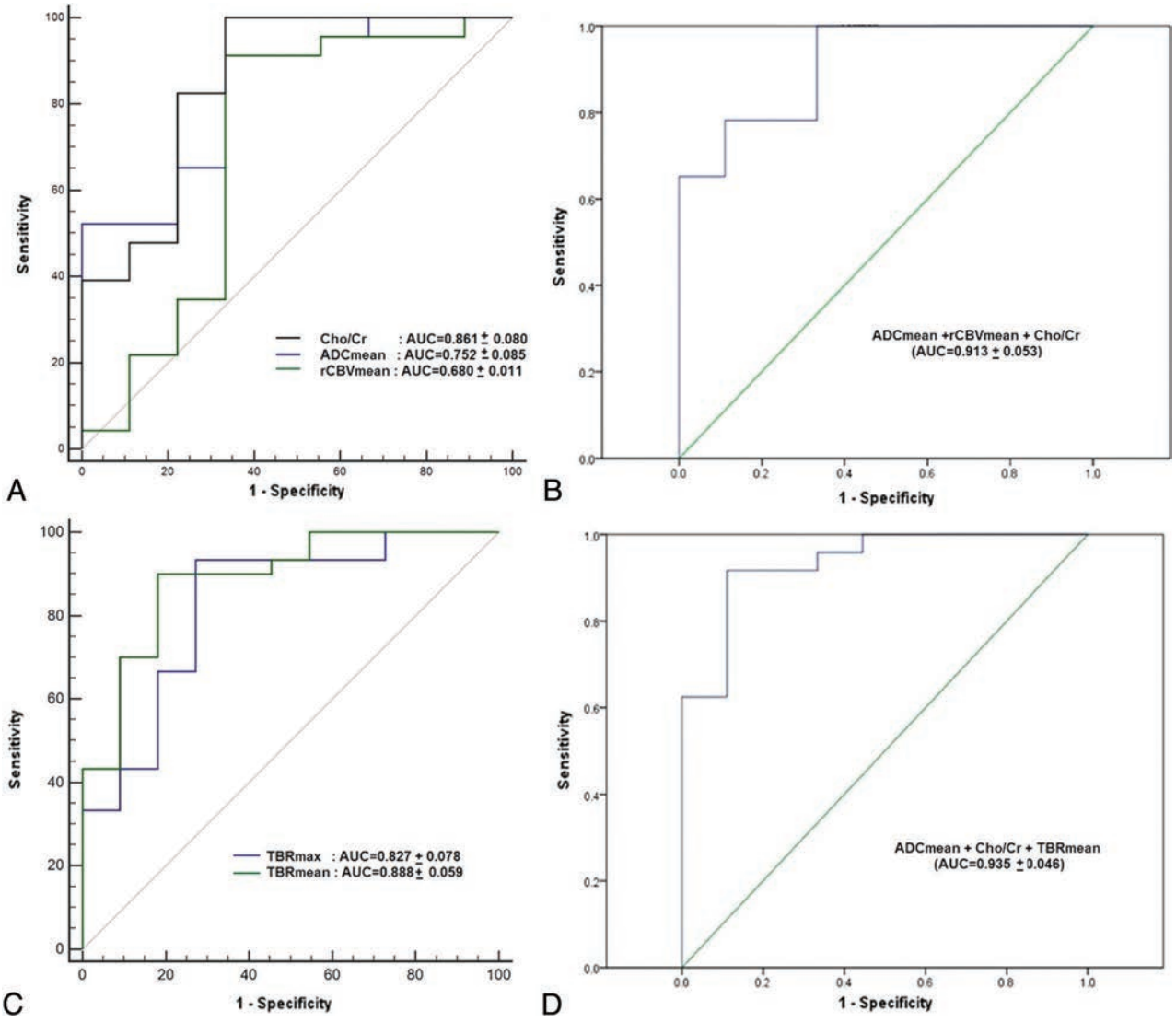

FIG 4. Receiver operating characteristic curves with their respective AUC values of MR imaging parameters (*A*) showing the high diagnostic performance of Cho/Cr in the detection of glioma recurrence. With multivariate ROC analysis, the ROC curve and AUC of all 3 MR imaging parameters combined show a significant increment in AUC over the individual MR imaging parameters (*B*). ROC curves with their respective AUC values of FDG parameters (*C*) show the high diagnostic performance of TBR_{mean} in the detection of glioma recurrence. Multivariate ROC analysis, ROC curve, and AUC of the best performing FDG-PET/MR imaging combination of ADC_{mean}, Cho/Cr, and TBR_{mean} show a significant increment over individual MR imaging or PET parameters (*D*).

Table 3: Multivariate ROC analysis showing AUC ± SE values for various combinations of FDG-PET and MRI parameters in the detection of glioma recurrence[a]

	$rCBV_{mean}$ (0.680 ± 0.011)	ADC_{mean} (0.752 ± 0.085)	Cho/Cr (0.861 ± 0.080)	ADC_{mean} + $rCBV_{mean}$ (0.781 ± 0.079)	ADC_{mean} + Cho/Cr (0.912 ± 0.051)	$rCBV_{mean}$ + Cho/Cr (0.860 ± 0.083)	ADC_{mean} + $rCBV_{mean}$ + Cho/Cr (0.913 ± 0.053)
ADC_{mean} (0.752 ± 0.085)	0.781 ± 0.079						
Cho/Cr (0.861 ± 0.080)	0.860 ± 0.083	0.912 ± 0.051		0.913 ± 0.053[b]			
TBR_{max} (0.827 ± 0.078)	0.831 ± 0.081	0.848 ± 0.072	0.894 ± 0.059	0.850 ± 0.073	0.935 ± 0.044	0.889 ± 0.061	0.932 ± 0.046
TBR_{mean} (0.888 ± 0.059)	0.884 ± 0.063	0.888 ± 0.058	0.935 ± 0.044	0.897 ± 0.057	0.935 ± 0.046[b,c]	0.928 ± 0.047	0.932 ± 0.048[b]

[a] Each entry represents the AUC ± SE of a combination of parameters mentioned in the respective rows and columns. Values in parentheses represent AUC ± SE of that particular parameter or combination. Blank cells are left to avoid repetition of values.

[b] A combination of FDG-PET and MR imaging parameters has a better AUC ± SE than a combination of MR imaging parameters.

[c] Note that the maximum AUC was achieved with a combination of ADC_{mean}, Cho/Cr, and TBR_{mean}.

recurrence or progression from radiation injury can be a radiologic dilemma, irrespective of the imaging technique used.[20]

It is known that functional imaging methods complement anatomic information and yield different aspects of pathophysiology. The combination of PET and CE-MR imaging information with retrospective fusion has been reported to increase diagnostic accuracy over any single technique.[12,15,16] In an integrated PET/MR system, PET and MR imaging information are not only combined but an additional value is expected owing to co-interpretation of both the signals.[21]

In our study, the results derived from individual PET and functional MR imaging parameters from simultaneously ac-

quired FDG-PET/MR imaging are in agreement with the published literature.

With an optimized threshold of 1507 × 10^{-6}mm^2/s for ADC_{mean}, an AUC of 0.752 ± 0.015 was obtained, which is close to the reported threshold of 1490 × 10^{-6}mm^2/s and AUC of 0.779.[22] We achieved an accuracy of 77.5% and an AUC of 0.68 ± 0.111 with an optimized threshold of 1.709 for $rCBV_{mean}$. Our calculated sensitivity and specificity of 82.8% and 63.6% are similar to 86% and 70%, respectively, reported with a comparatively lower threshold of 1.3.[23] However, wide variation has been reported in rCBV thresholds to detect recurrence,[24] and reasons ascribed include rapid extravasation of gadolinium-based contrast agent and vascular leak in the irradiated bed, especially with chemoradiation therapy.[25] With an optimized threshold of 1.405 for Cho/Cr, we achieved an accuracy and AUC of 90.9% and 0.861 ± 0.080, respectively, which are in concordance with the reported values of 93.1% and 0.913, respectively, with 1.54 as a threshold.[26] FDG-PET has been used to detect glioma recurrence with a varied range of reported sensitivities from 43% to 95% and specificities from 50% to 100%.[9] Despite known limitations of FDG in the detection of glioma recurrence of any histology, a recent meta-analysis of FDG found a respectable pooled AUC of 0.866 ± 0.034 for FDG-PET.[9] We achieved an AUC of 0.888 ± 0.059 by using an optimized threshold of 1.18 for TBR_{mean} in the detection of glioma recurrence that is in agreement with the reported AUC of 0.898 by Nozawa et al[16] in the differentiation of recurrent/residual high-grade glioma from posttreatment changes or low-grade glioma, however, by using TBR_{max} with a threshold of 1.8.

Because there is no single technique that can solve this clinical dilemma, researchers have attempted to combine functional MR imaging parameters to achieve an improved diagnostic accuracy beyond any single parameter.[13,27]

Moreover, in the past, retrospective fusion of FDG-PET with CE-MR imaging has aided in improved differentiation of glioma recurrence qualitatively, compared with FDG-PET or MR imaging alone.[12,15,16] In a group of 30 patients with high-grade gliomas, Estrada et al[12] reported an accuracy of 73% for FDG-PET, which improved to 93% with visual qualitative analysis of fused FDG-PET with CE-MR imaging.

Matsusue et al,[27] with a semi-quantitative multiparametric scoring system for ADC ratio, rCBV, Cho/Cr, and Cho/NAA in 15 patients, reported an accuracy of 93.3% in the detection of glioma recurrence. We achieved an AUC of 0.913 ± 0.053 by combining ADC_{mean}, $rCBV_{mean}$, and Cho/Cr by multivariate ROC analysis.

Our quantitative analysis of combined parameters also supports this body of evidence. We observed that combinations of individual parameters demonstrate superior results in comparison with individual parameters. We achieved an AUC of 0.913 ± 0.053 when all MR imaging parameters were combined, which further improved to 0.932 ± 0.046 when TBR_{max} or TBR_{mean} was added, clearly highlighting the utility of combinational analysis. However, the highest AUC of 0.935 ± 0.046 was achieved by combining ADC_{mean}, Cho/Cr, and TBR_{mean}.

We found that a simultaneous PET/MR imaging study offers advantages such as being logistically simple, implying, thereby, that it is performed as a single examination to obtain PET and MR imaging datasets; reduced examination time, thereby improving patient compliance; and correlative image reading and interpretation, which could help in localizing the most suspicious area on the PET image in voxel selection for MR spectroscopy. Furthermore, as observed by Mong et al,[28] we also found that PET uptake could help in accurate classification of suspicious ADC lesions. In the present study, we used an ultrashort TE sequence for MR imaging–based attenuation correction for brain PET, which is reported to result in accurate quantification of PET parameters,[29] more importantly offering comparable accuracy of CT-based attenuation correction.

Our study has several limitations. It is a retrospective study with a small group and a relatively heterogeneous class of patients to perform robust statistical analysis. The present study only provides within-sample prediction characteristics and is not adequately sized to provide a decent out-of-sample prediction. Although desirable, histologic diagnosis in all the lesions could not be obtained due to ethical concerns associated with high morbidity and sampling error.[30]

Hence, further large-scale prospective multicentric trials are required with simultaneous PET/MR imaging and FDG, a commonly available radiotracer, to validate our results.

CONCLUSIONS

Simultaneous PET/MR imaging with FDG offers correlative and synergistic multiparametric assessment of glioma recurrence with increased accuracy and clinical utility.

ACKNOWLEDGMENTS

We thank Dr Aru Singh for technical help in the statistical analysis.

REFERENCES

1. Chamberlain MC, Glantz MJ, Chalmers L, et al. **Early necrosis following concurrent Temodar and radiotherapy in patients with glioblastoma.** *J Neurooncol* 2007;82:81–83 CrossRef Medline
2. Brandes AA, Franceschi E, Tosoni A, et al. **MGMT promoter methylation status can predict the incidence and outcome of pseudoprogression after concomitant radiochemotherapy in newly diagnosed glioblastoma patients.** *J Clin Oncol* 2008;26:2192–97 CrossRef Medline
3. Chan JL, Lee SW, Fraass BA, et al. **Survival and failure patterns of high-grade gliomas after three-dimensional conformal radiotherapy.** *J Clin Oncol* 2002;20:1635–42 CrossRef Medline
4. Sugahara T, Korogi Y, Tomiguchi S, et al. **Posttherapeutic intraaxial brain tumor: the value of perfusion-sensitive contrast-enhanced MR imaging for differentiating tumor recurrence from nonneoplastic contrast-enhancing tissue.** *AJNR Am J Neuroradiol* 2000;21:901–09 Medline
5. Brandsma D, Stalpers L, Taal W, et al. **Clinical features, mechanisms, and management of pseudoprogression in malignant gliomas.** *Lancet Oncol* 2008;9:453–61 CrossRef Medline
6. Alexiou GA, Tsiouris S, Kyritsis AP, et al. **Glioma recurrence versus radiation necrosis: accuracy of current imaging modalities.** *J Neurooncol* 2009;95:1–11 CrossRef Medline
7. Heiss W, Raab P, Lanfermann H. **Multimodality assessment of brain tumors and tumor recurrence.** *J Nucl Med* 2011;52:1585–600 CrossRef Medline
8. Keunen O, Taxt T, Grüner R, et al. **Multimodal imaging of gliomas in the context of evolving cellular and molecular therapies.** *Adv Drug Deliv Rev* 2014;76:98–115 CrossRef Medline
9. Wang X, Hu X, Xie P, et al. **Comparison of magnetic resonance**

spectroscopy and positron emission tomography in detection of tumor recurrence in posttreatment of glioma: a diagnostic meta-analysis. *Asia Pac J Clin Oncol* 2015;11:97–105 CrossRef Medline
10. Nihashi T, Dahabreh IJ, Terasawa T. **Diagnostic accuracy of PET for recurrent glioma diagnosis: a meta-analysis.** *AJNR Am J Neuroradiol* 2013;34:944–50, S1–11 CrossRef Medline
11. Huang RY, Neagu MR, Reardon DA, et al. **Pitfalls in the neuroimaging of glioblastoma in the era of antiangiogenic and immuno/targeted therapy: detecting illusive disease, defining response.** *Front Neurol* 2015;6:33 CrossRef Medline
12. Estrada G, González-Maya L, Celis-López MA, et al. **Diagnostic approach in suspected recurrent primary brain tumors using (18)FDG-PET/MRI, perfusion MRI, visual and quantitative analysis, and three dimensional stereotactic surface projections: first experience in Mexico.** *Rev Esp Med Nucl* 2008;27:329–39 CrossRef Medline
13. Seeger A, Braun C, Skardelly M, et al. **Comparison of three different MR perfusion techniques and MR spectroscopy for multiparametric assessment in distinguishing recurrent high-grade gliomas from stable disease.** *Acad Radiol* 2013;20:1557–65 CrossRef Medline
14. Di Costanzo A, Scarabino T, Trojsi F, et al. **Recurrent glioblastoma multiforme versus radiation injury: a multiparametric 3-T MR approach.** *Radiol Med* 2014;119:616–24 CrossRef Medline
15. Enslow MS, Zollinger LV, Morton KA, et al. **Comparison of 18F-fluorodeoxyglucose and 18F-fluorothymidine PET in differentiating radiation necrosis from recurrent glioma.** *Clin Nucl Med* 2012; 37:854–61 CrossRef Medline
16. Nozawa A, Rivandi AH, Kanematsu M, et al. **Glucose-corrected standardized uptake value in the differentiation of high-grade glioma versus post-treatment changes.** *Nucl Med Commun* 2015;36:573–81 CrossRef Medline
17. Ellingson BM, Kim HJ, Woodworth DC, et al. **Recurrent glioblastoma treated with bevacizumab: contrast-enhanced T1-weighted subtraction maps improve tumor delineation and aid prediction of survival in a multicenter clinical trial.** *Radiology* 2014;271:200–10 CrossRef Medline
18. Kim ES, Satter M, Reed M, et al. **A novel, integrated PET-guided MRS technique resulting in more accurate initial diagnosis of high-grade glioma.** *Neuroradiol J* 2016;29:193–97 CrossRef Medline
19. Peca C, Pacelli R, Elefante A, et al. **Early clinical and neuroradiological worsening after radiotherapy and concomitant temozolomide in patients with glioblastoma: tumour progression or radionecrosis?** *Clin Neurol Neurosurg* 2009;111:331–34 CrossRef Medline
20. Hygino Da Cruz LC, Rodriguez I, Domingues RC, et al. **Pseudoprogression and pseudoresponse: imaging challenges in the assessment of posttreatment glioma.** *AJNR Am J Neuroradiol* 2011;32: 1978–85 CrossRef Medline
21. Garibotto V, Heinzer S, Vulliemoz S, et al. **Clinical applications of hybrid PET/MRI in neuroimaging.** *Clin Nucl Med* 2013;38:e13–18 CrossRef Medline
22. Prager AJ, Martinez N, Beal K, et al. **Diffusion and perfusion MRI to differentiate treatment-related changes including pseudoprogression from recurrent tumors in high-grade gliomas with histopathologic evidence.** *AJNR Am J Neuroradiol* 2015;36:877–85 CrossRef Medline
23. Ozsunar Y, Mullins ME, Kwong K, et al. **Glioma recurrence versus radiation necrosis? A pilot comparison of arterial spin-labeled, dynamic susceptibility contrast enhanced MRI, and FDG-PET imaging.** *Acad Radiol* 2010;17:282–90 CrossRef Medline
24. Deng SM, Zhang B, Wu YW, et al. **Detection of glioma recurrence by ^{11}C-methionine positron emission tomography and dynamic susceptibility contrast-enhanced magnetic resonance imaging: a meta-analysis.** *Nucl Med Commun* 2013;34:758–66 CrossRef Medline
25. Gahramanov S, Raslan AM, Muldoon LL, et al. **Potential for differentiation of pseudoprogression from true tumor progression with dynamic susceptibility-weighted contrast-enhanced magnetic resonance imaging using ferumoxytol vs. gadoteridol: a pilot study.** *Int J Radiat Oncol Biol Phys* 2011;79:514–23 CrossRef Medline
26. Fink JR, Carr RB, Matsusue E, et al. **Comparison of 3 Tesla proton MR spectroscopy, MR perfusion and MR diffusion for distinguishing glioma recurrence from posttreatment effects.** *J Magn Reson Imaging* 2012;35:56–63 CrossRef Medline
27. Matsusue E, Fink JR, Rockhill JK, et al. **Distinction between glioma progression and post-radiation change by combined physiologic MR imaging.** *Neuroradiology* 2010;52:297–306 CrossRef Medline
28. Mong S, Ellingson BM, Nghiemphu PL, et al. **Persistent diffusion-restricted lesions in bevacizumab-treated malignant gliomas are associated with improved survival compared with matched controls.** *AJNR Am J Neuroradiol* 2012;33:1763–70 CrossRef Medline
29. Werner P, Rullmann M, Bresch A, et al. **Impact of attenuation correction on clinical [(18)F]FDG brain PET in combined PET/MRI.** *EJNMMI Res* 2016;6:47 CrossRef Medline
30. McGirt MJ, Woodworth GF, Coon AL, et al. **Independent predictors of morbidity after image-guided stereotactic brain biopsy: a risk assessment of 270 cases.** *J Neurosurg* 2005;102:897–901 CrossRef Medline

Classification of High-Grade Glioma into Tumor and Nontumor Components Using Support Vector Machine

D.T. Blumenthal, M. Artzi, G. Liberman, F. Bokstein, O. Aizenstein, and D. Ben Bashat

ABSTRACT

BACKGROUND AND PURPOSE: Current imaging assessment of high-grade brain tumors relies on the Response Assessment in Neuro-Oncology criteria, which measure gross volume of enhancing and nonenhancing lesions from conventional MRI sequences. These assessments may fail to reliably distinguish tumor and nontumor. This study aimed to classify enhancing and nonenhancing lesion areas into tumor-versus-nontumor components.

MATERIALS AND METHODS: A total of 140 MRI scans obtained from 32 patients with high-grade gliomas and 6 patients with brain metastases were included. Classification of lesion areas was performed using a support vector machine classifier trained on 4 components: enhancing and nonenhancing, tumor and nontumor, based on T1-weighted, FLAIR, and dynamic-contrast-enhancing MRI parameters. Classification results were evaluated by 2-fold cross-validation analysis of the training set and MR spectroscopy. Longitudinal changes of the component volumes were compared with Response Assessment in Neuro-Oncology criteria.

RESULTS: Normalized T1-weighted values, FLAIR, plasma volume, volume transfer constant, and bolus-arrival-time parameters differentiated components. High sensitivity and specificity (100%) were obtained within the enhancing and nonenhancing areas. Longitudinal changes in component volumes correlated with the Response Assessment in Neuro-Oncology criteria in 27 patients; 5 patients (16%) demonstrated an increase in tumor component volumes indicating tumor progression. These changes preceded Response Assessment in Neuro-Oncology assessments by several months. Seven patients treated with bevacizumab showed a shift to an infiltrative pattern of progression.

CONCLUSIONS: This study proposes an automatic classification method: segmented Response Assessment in Neuro-Oncology criteria based on advanced imaging that reliably differentiates tumor and nontumor components in high-grade gliomas. The segmented Response Assessment in Neuro-Oncology criteria may improve therapy-response assessment and provide earlier indication of progression.

ABBREVIATIONS: BAT = bolus arrival time; DCE = dynamic contrast-enhanced; GB = glioblastoma; HGG = high-grade gliomas; k_{ep} = interstitium-to-plasma rate constant; K^{trans} = volume transfer constant; NAWM = normal-appearing white matter; nFLAIR = normalized FLAIR images; nT1WI+Gd = normalized T1-weighted images post-contrast agent; v_e = interstitial volume; v_p = plasma volume; RANO = Response Assessment in Neuro-Oncology; SPGR = spoiled gradient-recalled; sRANO = segmented RANO; SVM = support vector machine

High-grade gliomas (HGG), specifically glioblastoma (GB), remain the most common and aggressive brain tumors in adults. Despite recent advances in treatment, long-term survival remains low.[1,2] Treatment of newly diagnosed and recurrent HGG consists of a combination of surgery, radiation therapy, and chemotherapy and, more recently, biologic and immunotherapies, some of which are under clinical investigation. Unique imaging phenomena characterize therapeutic responses to these therapies, challenging conventional radiologic interpretation.

MRI is the method of choice for the initial diagnosis, follow-up, and therapy response assessment of brain tumors. HGG are typically characterized by contrast-enhanced areas on T1-weighted imaging and hyperintensity on FLAIR and T2WI. The current standard for the radiologist's assessment in

Received October 6, 2016; accepted after revision January 3, 2017.

From the Neuro-Oncology Service (D.T.B., F.B.) and Functional Brain Center (M.A., O.A., D.B.B.), Tel Aviv Sourasky Medical Center, Tel Aviv, Israel; Sackler Faculty of Medicine (D.T.B., M.A., F.B., D.B.B.) and Sagol School of Neuroscience (D.B.B.), Tel Aviv University, Tel Aviv, Israel; and Department of Chemical Physics (G.L.), Weizmann Institute, Tel Aviv, Israel.

D.T. Blumenthal and M. Artzi contributed equally to this work.

Paper previously presented in part at: Annual Meeting and Exhibition of the International Society for Magnetic Resonance in Medicine, May 7–13, 2016; Singapore.

Please address correspondence to Dafna Ben Bashat, PhD, Functional Brain Center, Tel Aviv Sourasky Medical Center, 6 Weizman St, Tel-Aviv 64239 Israel; e-mail: dafnab@tlvmc.gov.il

http://dx.doi.org/10.3174/ajnr.A5127

patients with HGG relies on the Response Assessment in Neuro-Oncology (RANO) criteria,[3] which expand upon the earlier Macdonald[4] criteria, to incorporate the nonenhancing component of the tumor, as this component may indicate infiltrative or diffuse tumor growth. However, the current RANO criteria, which rely on conventional imaging, may fail to distinguish different tissue components that have similar imaging patterns (ie, contrast-enhanced T1WI) yet different prognostic implications (tumor-versus-treatment effects), the identification of which is crucial for appropriate clinical management.[3,5]

Glioblastoma shows high heterogeneity within the lesion area, including areas of active tumor, necrosis, infiltrative tumor cells, and vasogenic edema. Enhancing lesion area can be measured on conventional T1WI; however, it may represent a variety of both tumor and nontumor processes, including tumor progression, pseudoprogression, postsurgical changes, and radiation effects.[3] Differentiation of the nonenhancing area between infiltrative tumor and nontumor area (edema and/or gliosis) is challenging, as both are characterized by hyperintense FLAIR/T2WI signal. Hyperintense FLAIR/T2WI signal can be expected to represent pure vasogenic edema in metastatic tumors (characteristically with well-defined borders between malignant cells and normal brain),[6] while in HGG, the hyperintensity may reflect areas of infiltrating tumor cells and/or vasogenic edema.

Glioblastoma is characterized by a highly complex neovascularization process. The increased vascularity of GB allows analysis and characterization of the tumor using advanced vascular MRI methods, including perfusion and permeability. Dynamic contrast-enhanced (DCE) imaging has been widely used for characterization of tumor biology and therapy-response assessment. DCE relies on dynamic T1WI sequences during bolus injection of contrast agent. Hemodynamic parameters, including plasma volume (v_p) and tissue transfer constants (specifically, volume transfer constant [K^{trans}] and interstitium-to-plasma rate constant [k_{ep}]), can be extracted from DCE data.

Several studies have suggested the utility of DCE parameters as important imaging markers for brain tumor diagnosis, grading, and therapy-response monitoring[7-9]; to differentiate between active and nonactive tumor components[10-14] or infiltrative and noninfiltrative tumor[10,15]; and for early-stage assessment of antiangiogenic therapy response in HGG.[16,17] However, none of these studies have aimed to classify the entire lesion area, both enhancing and nonenhancing, into tumor and nontumor areas at the voxel level.

Various techniques have been proposed for segmentation and classification of brain lesions.[18] Support vector machine (SVM) is a supervised binary classifier, originally aimed at classifying data into 2 classes. Based on a training dataset, the algorithm finds the hyperplane that maximally separates between points. New data are then mapped onto the same space and assigned to a particular class. SVM has been widely used as a classifier of medical images and has proved advantageous over other algorithms of its kind.[18,19]

The aim of this study was to classify lesion areas in patients with HGG using SVM into 4 distinct components: 1) enhancing tumor, 2) enhancing nontumor, 3) nonenhancing tumor, and 4) nonenhancing nontumor. Segmentation of lesion areas into tumor and nontumor components refines the RANO criteria and may improve therapy response MRI assessment.

Table 1: Patient characteristics

Diagnosis	No. of Patients	No. of Scans	Age (yr)	Sex, F/M
Glioblastoma	26	95	52 ± 14	14:12
Anaplastic astrocytoma	5	31	45 ± 12	5:0
Anaplastic oligodendroglioma	1	3	53	0:1
Brain metastasis	6	11	64 ± 13	1:5
Total	38	140		

MATERIALS AND METHODS

Patients

A total of 140 MRI scans were obtained from 38 patients, who were scanned every 2–3 months. Ninety-five scans were from 26 patients with GB; 31 scans (5 patients) were of anaplastic astrocytomas; 3 scans (1 patient) were of anaplastic oligodendroglias; and 11 scans (6 patients) were of brain metastases (4 breast and 2 lung cancers) (Table 1). Inclusion criteria required a normal glomerular filtration rate and no contraindication to MRI. All patients with HGG who were scanned longitudinally ($n = 26$) had recurrent HGG and had been treated initially with standard chemoradiation.[1] Additional therapies are detailed in the On-line Appendix. Nine patients received bevacizumab at recurrence and had pre- and post bevacizumab MRIs.

The study was approved by the Tel Aviv Sourasky Medical Center review board, and written informed consent was obtained from all patients.

MR Imaging Protocol

Scans were performed on 3T MRI scanners: 91 scans were performed on a Signa Excite scanner (GE Healthcare) using an 8-channel head coil, and 49 scans were performed on a Magnetom Prisma scanner (Siemens) using a 20-channel head coil. The protocol included conventional imaging: spoiled gradient-recalled (SPGR)/FLASH T1WI performed before and after contrast agent injection and FLAIR. DCE data were acquired using multiphase 3D T1WI SPGR/FLASH before, during, and after contrast agent injection (FOV 250 mm; matrix 256X256/256X184, section thickness of 5 mm, TR/TE = 5/2.2 ms, and flip angle = 20°. For the T1 maps, variable flip angle SPGR/FLASH data were acquired with nominal flip angles of 5°, 10°, 15°, 20°, and 30°. Dynamic data were acquired with a temporal resolution of 6 seconds and scan duration of 6 minutes. A power injector was used to infuse a single dose (0.2 mL/kg) of contrast agent (gadoterate meglumine, 0.5 mol/L, Dotarem; Guerbet, Aulnay-sous-Bois, France) followed by 20 mL saline flush, both at a constant rate of 5 mL/s second. Fourteen-to-twenty sections were centered on the tumor area as identified in the conventional images, providing brain coverage of 70–100 mm. MR spectroscopy data were acquired with a single-voxel point-resolved sequence by using a cubic volume of ~8 mL located at the lesion area and normal-appearing white matter (NAWM) in the contralateral hemisphere (TR/TE = 1500/35 ms).

Table 2: Mean and SD of the extracted MR imaging parameters between lesion components

		Enhancing		Nonenhancing	
	NAWM	Tumor	Nontumor	Tumor	Nontumor
nT1WI+Gd	0.010 ± 0.000	0.019 ± 0.005[a]	0.013 ± 0.001[a]	0.009 ± 0.001[b]	0.007 ± 0.001[b]
nFLAIR	0.010 ± 0.000	0.017 ± 0.005	0.015 ± 0.004	0.014 ± 0.002[b]	0.018 ± 0.003[b]
v_p	0.010 ± 0.001	0.054 ± 0.030[a]	0.007 ± 0.003[a]	0.021 ± 0.005[b]	0.004 ± 0.001[b]
K^{trans}	0.001 ± 0.001	0.064 ± 0.037[a]	0.006 ± 0.004[a]	0.009 ± 0.005[b]	0.000 ± 0.000[b]
k_{ep}	–	0.016 ± 0.011[a]	0.002 ± 0.003[a]	–	–
v_e	–	0.012 ± 0.009[a]	0.001 ± 0.001[a]	–	–
BAT	1.00 ± 0.20	1.30 ± 0.20	1.20 ± 0.30	1.20 ± 0.20[b]	0.90 ± 0.40[b]
NAA+NAAG/Cr+PCh	1.52 ± 0.25	1.32 ± 0.70	–	1.35	1.04 ± 0.22
GPC+PCh/Cr+PCh	0.30 ± 0.06	0.70 ± 0.25	–	0.46	0.30 ± 0.05

Note:—NAAG indicates *N*-acetyl aspartylglutamate; GPC, glycerolphosphocholine; PCho, phosphocholine.
[a] Significant difference ($P < .05$) between the 2 enhancing components.
[b] Significant difference ($P < .05$) between the 2 nonenhancing components.

Lesion Classification

Lesion classification involved several steps as detailed in the On-line Appendix and shown in On-line Fig 1. Following preprocessing, the enhancing and nonenhancing lesion areas, designated as targets for classification, were automatically segmented from the T1WI and FLAIR (respectively) images by using an adaptive threshold as previously described.[20] Manual correction was performed when necessary. Normalized images of FLAIR (nFLAIR) and postcontrast T1WI (nT1WI+Gd) were calculated relative to NAWM. The DCE pharmacokinetic parameters, v_p, K^{trans}, interstitial volume (v_e), k_{ep}, and bolus arrival time (BAT), were estimated by using DCE-Up-Sampled-Temporal-Resolution (DUSTER).[21]

Classification of the lesion area into 4 components was performed automatically by using the SVM. For the training data, volumes of interest of 5–10 voxels each (30–60 cc) were manually defined with the FMRIB Software Library (FSL; http://www.fmrib.ox.ac.uk/fsl) in areas with known pathology for the 4 tissue types: 1) enhancing tumor, defined retrospectively in patients with progressive HGG based on the RANO assessment on follow-up scans; 2) enhancing nontumor, defined retrospectively in patients with nonprogressive HGG, with treatment-related changes based on stable longitudinal (>6-month) RANO assessments; 3) nonenhancing tumor (infiltrative), defined as a peritumoral area (<2 cm from the enhanced tumor margins) in a nonenhancing FLAIR hyperintense region in patients with HGG with progressive disease; and 4) nonenhancing, nontumor (edema), defined in patients with brain metastasis, in whom the hyperintense FLAIR signal represented pure vasogenic edema, without tumor cell infiltration.[6]

Seven MRI parameters were measured within and compared between tissue types: nT1WI+Gd, nFLAIR, v_p, K^{trans}, v_e, k_{ep}, and BAT. SVM classifier with a linear kernel was trained only on the MRI parameters that were found to be significantly different ($P < .05$) among the tissue types. Voxelwise classification using SVM was performed separately for the enhancing and nonenhancing lesion areas in all patients.

Evaluation

Two-Fold Cross-Validation Analysis. To test the sensitivity and specificity of the method with validating confidence intervals, we performed 300 iterations of the training and testing data based on different random selections of the even and odd partitions. The group was divided into 2 subgroups (randomized, even-versus-odd) with 1 subgroup as training data, the other as the test data, and vice versa.

MR Spectroscopy. Classification results were validated based on MR spectroscopy results, performed off-line using LCModel (http://www.lcmodel.com/).[22] Metabolite ratios of glycerophosphocholine + phosphocholine (GPC+PCho) and of *N*-acetyl aspartate + *N*-acetyl aspartylglutamate (NAA+NAAG) relative to creatine + phosphocreatine (Cr+PCr) were calculated. While many MR spectra were acquired for clinical purposes, MR spectroscopy data were used in this study when voxel location included only 1 tissue component or were defined within the NAWM.

Longitudinal Assessment. Longitudinal assessment of the classification results was performed in patients with primary brain tumors (32 patients). Longitudinal changes in the volume of each component were evaluated relative to RANO criteria assessed by a senior neuroradiologist defining 4 categories: complete response, partial response, stable disease, or progression.[3]

Statistical Analysis

To identify differences between tumor and nontumor components for the various MRI parameters (separately for the enhancing and nonenhancing area), we used the Wilcoxon test (because parameters were not normally distributed).

RESULTS

Classification Results

Training Data. We defined VOIs for the 4 tissue types: the enhancing tumor component in 28 scans from 5 patients with progressive HGG (4 GB and 1 anaplastic astrocytoma); the enhancing nontumor component in 10 scans from 3 patients with high-grade tumors (2 GB and 1 oligodendroglioma); the nonenhancing tumor component in 24 scans from 5 patients with GB; and the nonenhancing, nontumor component in 11 scans from 6 patients with brain metastasis.

Mean values of the 7 MRI parameters, nT1WI+Gd, nFLAIR, v_p, K^{trans}, v_e, k_{ep}, and BAT, measured in the 4 components (tissue types) defined for the training data and NAWM, are provided in Table 2. For the enhancing components, significant differences were detected for the nT1WI+Gd, v_p, k^{trans}, k_{ep}, and v_e parameters, demonstrating higher vascularity (v_p) and impaired permeability (nT1WI+Gd, K^{trans}) in the tumor component relative to

the nontumor component. For the nonenhancing components, significant differences between components were detected for all parameters, demonstrating higher vascularity (v_p) and slightly impaired permeability (nT1WI+Gd, K^{trans}) in the tumor component relative to the nontumor component. The v_e and k_{ep} parameters showed significant group differences yet a substantially high SD (>150%) and were therefore not used in the training set.

Classification of Lesion Area

The SVM classifier was trained on the nT1WI+Gd, v_p, and K^{trans} parameters for enhancing components and on the nT1WI+Gd, nFLAIR, v_p, K^{trans}, and BAT parameters for nonenhancing components. Voxelwise classification was performed on all scans of all patients ($n = 140$), separately for enhancing and nonenhancing lesion areas. Figure 1 shows classification results obtained in 3 patients. In the first patient (Fig 1, case 1) with breast cancer metastasis, the nonenhancing lesion area was classified as nonenhancing, nontumor (ie, edema) and the enhancing lesion area was classified as enhancing tumor. The second patient (Fig 1, case 2) with GB was an example in whom most of the nonenhancing lesion was classified as tumor component. This patient was diagnosed with progressive disease on a subsequent follow-up scan (2 months later). In the third patient (Fig 1, case 3), also with GB, the enhancing lesion and most of the nonenhancing area were classified as tumor component, consistent with a diagnosis of progressive disease as diagnosed on subsequent follow-up.

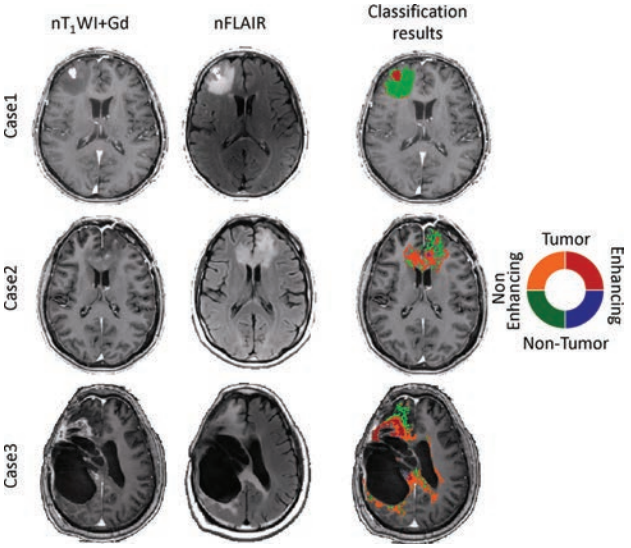

FIG 1. Classification results obtained in a patient with active breast cancer metastasis (case 1) and in 2 patients with glioblastoma (cases 2 and 3).

Longitudinal Assessment

Longitudinal assessment of the volume of each component and the correlating radiologic assessment based on RANO, for 26 patients with high-grade lesions scanned longitudinally >3 times (a total of 118 scans) are shown in On-line Fig 2. Consistent results were obtained between changes in the volume of the lesion components and the radiologist's assessment in 27 patients (of 32, 84%). However, in 5 (16%; patients 1, 17, 18, 20, and 26), increased volume of the nonenhancing tumor component indicating tumor progression preceded the radiologic diagnosis based on RANO criteria by several months.

Figure 2 shows longitudinal data obtained from a 54-year-old patient with anaplastic astrocytoma (patient 18). While the conventional imaging showed a pattern of stability at scans 3 and 5, with reduction/no substantial changes in the enhancing and nonenhancing lesion areas, classification results revealed a different clinical scenario–progressive tumor growth. A continual increase in the nonenhancing tumor component indicated a pattern of infiltrative disease progression through scans 2–5 (particularly from scan 2 to 3). This patient was diagnosed with progressive disease at scan 4 and died 71 days following scan 5.

In 7 of 9 patients who received bevacizumab, substantial reductions (mean, 56%) were detected mainly in the volume of the nonenhancing, nontumor component (interpreted as edema). Three patients of 7 (patients 12,13, and 23), though showing a major reduction in the volume of the nonenhancing, nontumor component, had an increase in the nonenhancing tumor component, suggesting a shift to an infiltrative pattern of tumor progression during bevacizumab treatment.

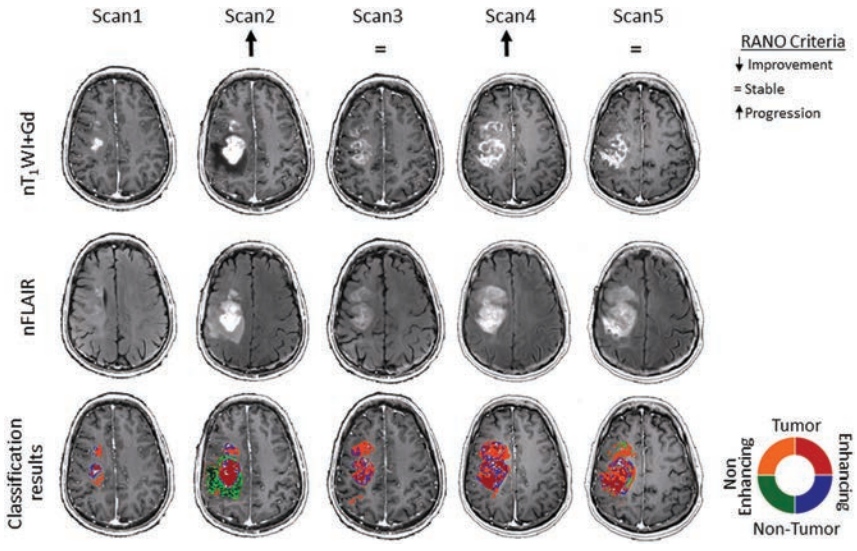

FIG 2. Longitudinal classification and radiologic results obtained in a 54-year-old patient with anaplastic astrocytoma (patient 18) scanned longitudinally every 2 months.

Evaluation

Sensitivity and Specificity of the Training Data. Analysis demonstrated 100% sensitivity (85%/100% for the 5th/90th percentiles) and 100% specificity (100%/100%) for the identification of enhancing tumor and enhancing nontumor components, and 100% sensitivity (100%/100%) and 100% specificity (100%/100%) for identification of the nonenhancing (infiltrative) tumor and nonenhancing nontumor components.

MR Spectroscopy Results. Forty-one spectra were obtained with good quality,

with voxel location consisting of 1 of the 4 components or within NAWM: 14 from NAWM; 6 from nonenhancing, nontumor component; 1 from nonenhancing tumor; and 19 from enhancing tumor components. MR spectroscopy results are provided in Table 2. Spectra from the enhancing, nontumor components showed primarily lipid peaks, without a detectable metabolite ratio. MR spectroscopy supported the classification results, demonstrating a >1.5-fold increase in glycerolphosphocholine + phosphocholine/creatine + phosphocholine (GPC+PCh/Cr+PCr) ratio in the tumor components relative to the nontumor component and NAWM.

DISCUSSION

In this study, longitudinal classification of lesion area into tumor and nontumor components was performed in patients with HGG based on multi-MRI parameters extracted from conventional imaging and DCE MRI. RANO criteria improved the earlier Macdonald[4] criteria by incorporating the nonenhancing component of the lesion. Our proposed method, referred to as segmented RANO (sRANO), provides a logical next step in the evolution of MR clinical imaging, to better assess tumor growth and therapy response. Both enhancing and nonenhancing lesion areas may include tumor and nontumor components. The proposed sRANO classifies the lesion areas and defines each component separately. In 16% of our cases followed longitudinally, we were able to identify tumor progression several months in advance of RANO criteria.

Conventional MRI lacks the precision to reliably differentiate tumor and nontumor areas with similar imaging patterns. However, the implications of such differentiation regarding treatment are substantial. Within the enhancing lesion area, recognition of dynamic, active tumor typically requires a change in therapy. Likewise, the identification of radiation necrosis or treatment-related changes can prevent unnecessary interventions. While salvage re-irradiation of brain tumors can typically be performed with a minimum of resultant treatment necrosis,[23] re-irradiation to an area of preexisting treatment-related necrosis could exacerbate existing tissue damage and lead to potentially life-threatening neurologic toxicity.

Classification between tumor and nontumor areas within the nonenhancing lesion may provide new guidelines for radiation. Standards of treatment-planning techniques differ geographically.[24] Accurate delineation of tumor area may either limit the size of the radiation field and decrease radiation exposure to nontumor brain tissue or define more accurately the optimal radiation field to include the entire tumor area and enable more efficient treatment.

In addition, as the use of immune-mediating therapies in glioma increases, the complexity of interpreting inflammatory responses to treatment ("pseudoprogression") in enhancing and nonenhancing lesion areas will also increase. Misinterpretation of the response to a potentially helpful therapy could lead to premature cessation of a useful therapy and compromise patient outcome.[25]

Within the enhancing lesion area, all measured vascular parameters (except the BAT) clearly differentiated tumor and nontumor components. While both components demonstrated increased tissue permeability, the tumor component was characterized by much higher permeability and v_p compared with the nontumor component and relative to NAWM. GB is characterized by a complex neovascularization process that results in formation of new, abnormal blood vessels and an impaired blood-brain barrier, and thus manifests as a hyperperfused area with increased blood flow, volume, and permeability, as was seen in our cohort study.[26,27] The nontumor component demonstrated reduced v_p compared with NAWM, consistent with data that have shown areas of treatment-related changes characterized by impaired blood brain barrier yet with reduced blood flow and volume, due to treatment-induced vascular endothelial damage and coagulative necrosis.[5,28]

Within the nonenhancing lesion area, despite a similar appearance between tumor and nontumor components on conventional imaging (FLAIR and T2WI), significant differences were found in all measured MRI parameters. The nonenhancing, nontumor component was characterized by reduced v_p, in comparison with the NAWM and the nonenhancing tumor component. This pattern is consistent with previous reports of tissues proximal to brain tumors in patients[10,29,30] and animal models[31] and can be explained by compression of regional capillaries caused by vasogenic edema.[32] The tumor component in our cohort was characterized by increased tissue permeability and increased perfusion as demonstrated by K^{trans} and v_p parameters, consistent with findings in previous studies.[10,29,33]

In this work, classification of lesion area was performed with a linear SVM classifier, a simple form of SVM, highly suitable for a limited training set size, for which the separating hyperplane is simply a plane in the feature space and the relative contribution of the features can be easily obtained. Various machine learning– and computational intelligence–based methods have been proposed for segmentation of brain tumors.[34] In this study, SVM was found to be a robust, rapid method, tailored to the clinical data, easily implemented, and most important, it differentiated lesion components with high sensitivity and specificity.

The success of a supervised algorithm is directly determined by the selected training set. Thus, only clear-cut cases were used for this study while training the classifier, based on retrospective radiologic assessment for several months. Classification into tumor and nontumor components was performed based on conventional parameters (nT1WI+Gd, and nFLAIR) and parameters extracted from DCE (v_p, K^{trans}, and BAT). While perfusion parameters can be obtained using dynamic susceptibility contrast imaging and have been shown to differentiate between tumor and nontumor components,[11-13,35,36] DCE imaging is preferable due to its higher spatial resolution, less sensitivity to susceptibility artifacts, and provision of quantitative parameters, including permeability (K^{trans}).

Several issues are important when interpreting the clinical relevance of classification results. The relatively small sample size and absence of histology-proved diagnosis in our cohort call for additional studies. Tumor components were found to be highly vascular while the nontumor components were found to have reduced vascularity. However, the enhancing, nontumor component may represent a more complex situation. It may reflect treatment-related changes (such as radiation necrosis) but may also represent tumor-associated hy-

poxic necrosis, which is one of the histologic hallmarks of GB.[37] Thus, in such cases, it is important to consider the nontumor component in the context of active tumor surrounding the necrotic area.

CONCLUSIONS

The current study proposes a model of segmented RANO criteria, sRANO, that classifies tumor and nontumor components within a lesion area, with high sensitivity and specificity. Longitudinal assessment in patients demonstrated consistency between the classification results and radiologist's assessment in most cases; in 16% of patients, the segmentation results identified growth of highly vascular components and preceded the conventional radiologic diagnosis of tumor progression by several months. The proposed sRANO method and results presented in this study demonstrate the importance and contribution of segmentation of the enhancing and nonenhancing lesion areas into tumor and nontumor components, to improve therapy-response assessment of patients with malignant brain tumors.

ACKNOWLEDGMENTS

We are grateful to Vicki Myers for editorial assistance, to Faina Vitenstein and Tuvia Ganot for their assistance in patient recruitment and performing MRI scans, and to Dr Ricardo Tarrasch for statistical consulting.

Disclosures: Deborah T. Blumenthal—*UNRELATED*: *Board Membership*: Medical Advisory Board for Vascular Biogenics; *Travel/Accommodations/Meeting Expenses Unrelated to Activities Listed*: Roche, Bristol-Myers Squibb, *Comments*: travel grants to international meetings.* Money paid to the institution.

REFERENCES

1. Stupp R, Mason WP, van den Bent MJ, et al; European Organisation for Research and Treatment of Cancer Brain Tumor and Radiotherapy Groups, National Cancer Institute of Canada Clinical Trials Group. **Radiotherapy plus concomitant and adjuvant temozolomide for glioblastoma.** *N Engl J Med* 2005;352:987–96 CrossRef Medline
2. Friedman HS, Prados MD, Wen PY, et al. **Bevacizumab alone and in combination with irinotecan in recurrent glioblastoma.** *J Neurooncol* 2009;27:4733–40 CrossRef Medline
3. Wen PY, Macdonald DR, Reardon DA, et al. **Updated response assessment criteria for high-grade gliomas: Response Assessment in Neuro-Oncology working group.** *J Clin Oncol* 2010;28:1963–72 CrossRef Medline
4. Macdonald DR, Cascino TL, Schold SC Jr, et al. **Response criteria for phase II studies of supratentorial malignant glioma.** *J Clin Oncol* 1990;8:1277–80 Medline
5. Verma N, Cowperthwaite MC, Burnett MG, et al. **Differentiating tumor recurrence from treatment necrosis: a review of neuro-oncologic imaging strategies.** *Neuro Oncol* 2013;15:515–34 CrossRef Medline
6. Fink KR, Fink JR. **Imaging of brain metastases.** *Surg Neurol Int* 2013; 4(suppl 4):S209–19 CrossRef Medline
7. Fatterpekar GM, Galheigo D, Narayana A, et al. **Treatment-related change versus tumor recurrence in high-grade gliomas: a diagnostic conundrum–use of dynamic susceptibility contrast-enhanced (DSC) perfusion MRI.** *AJR Am J Roentgenol* 2012;198:19–26 CrossRef Medline
8. Sorensen AG, Batchelor TT, Zhang WT, et al. **A "vascular normalization index" as potential mechanistic biomarker to predict survival after a single dose of cediranib in recurrent glioblastoma patients.** *Cancer Res* 2009;69:5296–300 CrossRef Medline
9. Zhang W, Kreisl TN, Solomon J, et al. **Acute effects of bevacizumab on glioblastoma vascularity assessed with DCE-MRI and relation to patient survival.** In: *Proceedings of the Scientific Meeting and Exhibition* of *The International Society for Magnetic Resonance in Medicine,* Honolulu, Hawaii. April 18–24, 2009
10. Artzi M, Bokstein F, Blumenthal DT, et al. **Differentiation between vasogenic-edema versus tumor-infiltrative area in patients with glioblastoma during bevacizumab therapy: a longitudinal MRI study.** *Eur J Radiol* 2014;83:1250–56 CrossRef Medline
11. Barajas RF Jr, Chang JS, Segal MR, et al. **Differentiation of recurrent glioblastoma multiforme from radiation necrosis after external beam radiation therapy with dynamic susceptibility-weighted contrast-enhanced perfusion MR imaging.** *Radiology* 2009;253:486–96 CrossRef Medline
12. Barajas RF, Chang JS, Sneed PK, et al. **Distinguishing recurrent intra-axial metastatic tumor from radiation necrosis following gamma knife radiosurgery using dynamic susceptibility-weighted contrast-enhanced perfusion MR imaging.** *AJNR Am J Neuroradiol* 2009;30:367–72 Medline
13. Bobek-Billewicz B, Stasik-Pres G, Majchrzak H, et al. **Differentiation between brain tumor recurrence and radiation injury using perfusion, diffusion-weighted imaging and MR spectroscopy.** *Folia Neuropathol* 2010;48:81–92 Medline
14. Larsen VA, Simonsen HJ, Law I, et al. **Evaluation of dynamic contrast-enhanced T1-weighted perfusion MRI in the differentiation of tumor recurrence from radiation necrosis.** *Neuroradiology* 2013; 55:361–69 CrossRef Medline
15. Jensen TR, Schmainda KM. **Computer-aided detection of brain tumor invasion using multiparametric MRI.** *J Magn Reson Imaging* 2009;30:481–89 CrossRef Medline
16. Pope WB, Young JR, Ellingson BM. **Advances in MRI assessment of gliomas and response to anti-VEGF therapy.** *Curr Neurol Neurosci Rep* 2011;11:336–44 CrossRef Medline
17. Sourbron S, Ingrisch M, Siefert A, et al. **Quantification of cerebral blood flow, cerebral blood volume, and blood-brain-barrier leakage with DCE-MRI.** *Magn Reson Med* 2009;62:205–17 CrossRef Medline
18. Shah SA, Chauhan N. **Techniques for detection and analysis of tumours from brain MRI images: a review.** *Journal of Biomedical Engineering and Medical Imaging* 2016;3:9–20
19. Vanitha L, Venmathi A. **Classification of medical images using support vector machine.** In: *Proceedings of the 2011 International Conference on Information and Network Technology*, Nanjing, Jiangsu, China. September 24–25, 2011
20. Artzi M, Aizenstein O, Jonas-Kimchi T, et al. **FLAIR lesion segmentation: application in patients with brain tumors and acute ischemic stroke.** *Eur J Radiol* 2013;82:1512–18 CrossRef Medline
21. Artzi M, Liberman G, Blumenthal DT, et al. **Automatic Segmentation and Classification of Glioblastoma using DCE-MRI.** In: *Proceedings of the Annual Meeting and Exhibition of the International Society for Magnetic Resonance in Medicine,* May 7–13, 2016. Singapore
22. Provencher SW. **Estimation of metabolite concentrations from localized in vivo proton NMR spectra.** *Magn Reson Med* 1993;30: 672–79 CrossRef Medline
23. Fogh SE, Andrews DW, Glass J, et al. **Hypofractionated stereotactic radiation therapy: an effective therapy for recurrent high-grade gliomas.** *J Clin Oncol* 2010;28:3048–53 CrossRef Medline
24. Dhermain F. **Radiotherapy of high-grade gliomas: current standards and new concepts, innovations in imaging and radiotherapy, and new therapeutic approaches.** *Chin J Cancer* 2014;33:16–24 CrossRef Medline
25. Pollack IF, Jakacki RI, Butterfield LH, et al. **Immune responses and outcome after vaccination with glioma-associated antigen peptides and poly-ICLC in a pilot study for pediatric recurrent low-grade gliomas.** *Neuro Oncol* 2016;18:1157–68 CrossRef Medline
26. Hardee ME, Zagzag D. **Mechanisms of glioma-associated neovascularization.** *Am J Pathol* 2012;181:1126–41 CrossRef Medline
27. Cloughesy TF, Cavenee WK, Mischel PS. **Glioblastoma: from molec-**

ular pathology to targeted treatment. *Annu Rev Pathol* 2014;9:1–25 CrossRef
28. Artzi M, Liberman G, Nadav G, et al. **Differentiation between treatment-related changes and progressive disease in patients with high grade brain tumors using support vector machine classification based on DCE MRI.** *J Neurooncol* 2016;127:515–24 CrossRef Medline
29. Law M, Cha S, Knopp EA, et al. **High-grade gliomas and solitary metastases: differentiation by using perfusion and proton spectroscopic MR imaging.** *Radiology* 2002;222:715–21 CrossRef Medline
30. Uematsu H, Maeda M, Itoh H. **Peritumoral brain edema in intracranial meningiomas evaluated by dynamic perfusion-weighted MR imaging: a preliminary study.** *Eur Radiol* 2003;13:758–62 Medline
31. Hossman KA, Blöink M. **Blood flow and regulation of blood flow in experimental peritumoral edema.** *Stroke* 1981;12:211–17 CrossRef Medline
32. Kaal EC, Vecht CJ. **The management of brain edema in brain tumors.** *Curr Opin Oncol* 2004;16:593–600 CrossRef Medline
33. Sentürk S, Oğuz KK, Cila A. **Dynamic contrast-enhanced susceptibility-weighted perfusion imaging of intracranial tumors: a study using a 3T MR scanner.** *Diagn Interv Radiol* 2009;15:3–12 Medline
34. Al-Tamimi MSH, Sulong G. **Tumor brain detection through MR images: a review of literature.** *Journal of Theoretical and Applied Information Technology* 2014;62:387–403
35. Hu LS, Baxter LC, Smith KA, et al. **Relative cerebral blood volume values to differentiate high-grade glioma recurrence from posttreatment radiation effect: direct correlation between image-guided tissue histopathology and localized dynamic susceptibility-weighted contrast-enhanced perfusion MR imaging measurements.** *AJNR Am J Neuroradiol* 2009;30:552–58 CrossRef Medline
36. Kim J, Leira EC, Callison RC, et al. **Toward fully automated processing of dynamic susceptibility contrast perfusion MRI for acute ischemic cerebral stroke.** *Comput Methods Programs Biomed* 2010;98:204–13 CrossRef Medline
37. Noch E, Khalili K. **Molecular mechanisms of necrosis in glioblastoma: the role of glutamate excitotoxicity.** *Cancer Biol Ther* 2009;8:1791–97 CrossRef Medline

Clinical and Imaging Characteristics of Diffuse Intracranial Dolichoectasia

W. Brinjikji, D.M. Nasr, K.D. Flemming, A. Rouchaud, H.J. Cloft, G. Lanzino, and D.F. Kallmes

ABSTRACT

BACKGROUND AND PURPOSE: Among patients with vertebrobasilar dolichoectasia is a subset of patients with disease affecting the anterior circulation as well. We hypothesized that multivessel intracranial dolichoectasia may represent a distinct phenotype from single-territory vertebrobasilar dolichoectasia. The purpose of this study was to characterize clinical characteristics and angiographic features of this proposed distinct phenotype termed "diffuse intracranial dolichoectasia" and compare them with those in patients with isolated vertebrobasilar dolichoectasia.

MATERIALS AND METHODS: We retrospectively reviewed a consecutive series of patients with diffuse intracranial dolichoectasia and compared their demographics, vascular risk factors, additional aneurysm prevalence, and clinical outcomes with a group of patients with vertebrobasilar dolichoectasia. "Diffuse intracranial dolichoectasia" was defined as aneurysmal dilation of entire vascular segments involving ≥2 intracranial vascular beds. Categoric and continuous variables were compared by using χ^2 and Student *t* tests, respectively.

RESULTS: Twenty-five patients had diffuse intracranial dolichoectasia, and 139 had vertebrobasilar dolichoectasia. Patients with diffuse intracranial dolichoectasia were older than those with vertebrobasilar dolichoectasia (70.9 ± 14.2 years versus 60.4 ± 12.5 years, $P = .0002$) and had a higher prevalence of abdominal aortic aneurysms (62.5% versus 14.3%, $P = .01$), other visceral aneurysms (25.0% versus 0%, $P < .0001$), and smoking (68.0% versus 15.9%, $P < .0001$). Patients with diffuse intracranial dolichoectasia were more likely to have aneurysm growth (46.2% versus 21.5%, $P = .09$) and rupture (20% versus 3.5%, $P = .007$) at follow-up. Patients with diffuse intracranial dolichoectasia were less likely to have good neurologic function at follow-up (24.0% versus 57.6%, $P = .004$) and were more likely to have aneurysm-related death (24.0% versus 7.2%, $P = .02$).

CONCLUSIONS: The natural history of patients with diffuse intracranial dolichoectasia is significantly worse than that in those with isolated vertebrobasilar dolichoectasia. Many patients with diffuse intracranial dolichoectasia had additional saccular and abdominal aortic aneurysms. These findings suggest that diffuse intracranial dolichoectasia may be a distinct vascular phenotype secondary to a systemic arteriopathy affecting multiple vascular beds.

Fusiform and dolichoectatic intracranial aneurysms are generally associated with a poor natural history with high rates of rupture, mass effect, and ischemic stroke.[1-4] These aneurysms often form secondary to circumferential loss or weakening of the internal elastic lamina of a vessel segment and can involve an entire vessel or may be limited to a single vessel segment (eg, basilar artery, cavernous or supraclinoid ICA, proximal MCA, and so forth).[5-8] Notably, most prior reports of intracranial dolichoectasia have focused on involvement of single-vessel territories, most commonly the vertebrobasilar system. These dolichoectatic aneurysms are associated with a wide range of proposed, underlying etiologies, including healed, focal arterial dissections; chronic hypertension; prior radiation therapy; connective tissue diseases; arterial tortuosity syndrome; glycogen storage diseases; infection; and myxomatous emboli.[5-8]

During the past several years, we have noticed in our clinical practice a subset of patients who have segmental aneurysmal dolichoectasia of multiple intracranial vascular territories in the absence of a known, underlying insult such as radiation, infection, genetic connective tissue disease, or dissection. We hypothesized that multivessel presentation of intracranial dolichoectasia may represent a process distinct from the frequently described single-territory dolichoectasia, potentially with distinct presentation, associations, and natural history. For this report, we have defined "diffuse intracranial dolichoectasia" as aneurysmal dilation of entire segments that involve ≥2 in-

Received August 12, 2016; accepted after revision December 13.

From the Departments of Radiology (W.B., H.J.C., G.L., D.F.K.), Neurology (D.M.N., K.D.F., G.L.), and Neurosurgery (W.B., H.J.C., G.L., D.F.K.), Mayo Clinic, Rochester, Minnesota, and Department of Interventional Neuroradiology (A.R.), Hôpital Bicêtre, Paris Sud Universite, Paris, France.

Please address correspondence to Waleed Brinjikji, MD. Mayo Clinic, 200 1st St SW, Rochester, MN 55905; e-mail: brinjikji.waleed@mayo.edu; @wbrinjikji

Indicates article with supplemental on-line table.

http://dx.doi.org/10.3174/ajnr.A5102

Table 1: Definition of vascular segments and aneurysmal dilation

Vascular Segment	Definition of Vascular Segment	Definition of Aneurysmal Dilation
Cavernous ICA	Entry point of ICA into the cavernous segment to the ophthalmic artery origin	≥8.5 mm
Supraclinoid ICA	ICA from the ophthalmic artery origin to the ICA bifurcation	≥8.0 mm
M1 segment of MCA	Origin of MCA to the MCA bifurcation	≥5.0 mm
Basilar artery	Confluence of vertebral arteries to the basilar bifurcation	≥6.0 mm

tracranial vascular beds. These criteria were chosen due to the notion that fusiform aneurysmal dilation of multiple intracranial vascular beds indicates a systemic vascular insult, while fusiform aneurysmal dilation of a single bed suggests a more localized pathologic process.

The primary purpose of this article was to fully characterize the clinical risk factors and anatomic and angiographic characteristics of this proposed distinct entity, which we term "diffuse intracranial dolichoectasia." The secondary purpose was to compare clinical risk factors and anatomic and angiographic characteristics of patients with diffuse intracranial dolichoectasia with those in a group of patients with dolichoectasia isolated to the vertebrobasilar system.

MATERIALS AND METHODS

Patient Population

Following institutional review board approval, we identified all patients with diffuse intracranial dolichoectasia evaluated at our institution from January 1, 2001, to December 31, 2014. We also identified a control group of patients with isolated vertebrobasilar dolichoectasia. To identify patients, we searched our imaging data base for reports of head MR imaging, MRA, CTA, and DSA examinations in which any one of the following terms was used in the body or conclusions of the report: "fusiform," "aneurysmal dilation," "dilation," "fusiform aneurysm," "dolichoectasia," "dolichoectatic," and "dolicho." All identified imaging examinations were then reviewed by 2 radiologists in consensus. Cases with fusiform aneurysmal dilation of multiple vascular segments were then identified for additional review to determine whether they met the diagnostic criteria for diffuse intracranial dolichoectasia. Cases in which there was fusiform aneurysmal dilation with or without tortuosity isolated to the vertebrobasilar system were defined as "isolated vertebrobasilar dolichoectasia." Of the cases that were identified for additional review as potentially representing diffuse intracranial dolichoectasia, maximum measurements were obtained of the basilar artery, supraclinoid ICAs, and bilateral M1 segments.

Diagnostic Criteria

To be included in this diffuse intracranial dolichoectasia group, patients had to meet the following diagnostic inclusion criteria: adult patients with fusiform aneurysmal dilation of entire vascular segments (ie, supraclinoid ICA, basilar artery, M1 segment of the MCA) that involved ≥2 intracranial vascular beds (ie, vertebrobasilar system, left anterior circulation, or right anterior circulation). Aneurysmal dilation of a vascular segment was defined as a diameter of at least 2 times the normal diameter of a given vascular segment as defined by an angiographic atlas.[9] Isolated vertebrobasilar dolichoectasia was defined as an aneurysmal dilation 2 times the normal diameter without a definable neck involving a portion of an arterial segment (either vertebral or basilar) with any degree of tortuosity. The criteria for aneurysmal dilation of a vessel segment are summarized in Table 1. Exclusion criteria included the following: 1) pediatric patients, 2) patients with underlying connective tissue diseases (ie, Ehlers-Danlos and Marfan syndromes, Loeys-Dietz syndrome, autosomal dominant polycystic kidney disease, neurofibromatosis type 1, and so forth), 3) patients with a history of cranial radiation, 4) patients with an underlying infectious etiology (ie, varicella zoster vasculopathy, HIV, and so forth), and 5) patients with poststenotic dilations secondary to atherosclerosis or dissection. All patients in the vertebrobasilar dolichoectasia control group and 11 patients in the diffuse intracranial dolichoectasia group were also included in a prior study on the imaging natural history of patients with vertebrobasilar, nonsaccular dolichoectatic aneurysms.[10]

Baseline Demographics and Clinical Risk Factors

We collected the following baseline patient demographic characteristics and comorbidities: age; sex; the presence of an ectatic abdominal aorta (maximum diameter, 2.6–2.9 cm) or an abdominal aortic aneurysm (maximum diameter, ≥3 cm); and the presence of other vascular ectasias/aneurysms, fibromuscular dysplasia, coronary artery disease, peripheral artery disease, hypertension, diabetes mellitus, hyperlipidemia, tobacco use (current, former, never), pack-years of tobacco use (if available), alcohol abuse, sympathomimetic abuse, and family history of abdominal aortic aneurysm, stroke, or aneurysm. In addition to baseline demographic and clinical risk factors, we collected data on presenting symptoms at the time of the discovery of the intracranial dolichoectasia (ie, incidental, stroke, subarachnoid hemorrhage, neuralgia, mass effect, headache, hemifacial spasm, other). Baseline demographic and clinical risk factors were compared between the diffuse intracranial dolichoectasia group and the isolated vertebrobasilar dolichoectasia group.

Imaging Characteristics

Among patients who met the diagnostic criteria for diffuse intracranial dolichoectasia and those in the isolated vertebrobasilar dolichoectasia control group, we collected the following information from their imaging examinations: the presence of a saccular aneurysm; the presence of other intracranial vascular dilations, subarachnoid hemorrhage, or intraparenchymal hemorrhage on presentation; white matter ischemic disease; and thrombus within the aneurysm. All measurements on CTA and MRA were obtained by using multiplanar reformatting software (Terarecon, San Mateo, California). The maximum cross-sectional diameter of the vessel perpendicular to the longitudinal axis of the vessel was obtained. For DSA images, the maximum diameter of the vessel perpendicular to the longitudinal axis of the vessel was obtained. Imaging characteristics were compared between the diffuse intracranial dolichoectasia group and the isolated vertebrobasilar dolichoectasia group.

Table 2: Summary of patient characteristics and outcomes

Variable	DID	VBD	*P* Value
No.	25	139	–
Mean age (SD) (yr)	70.9 (14.2)	60.4 (12.5)	.0002
Age group (yr)			
20–29	1 (4.0)	5 (3.6)	<.0001
30–39	0 (0.0)	6 (4.3)	
40–49	1 (4.0)	6 (4.3)	
50–59	2 (8.0)	44 (31.6)	
60–69	7 (28.0)	43 (30.9)	
70–79	6 (24.0)	30 (21.5)	
≥80	8 (32.0)	5 (3.6)	
Sex			
Male	21 (84.0)	105 (75.5)	.51
Female	4 (16.0)	34 (24.5)	
Indication for imaging			
Stroke	13 (52.0)	45 (32.7)	.10
Mass effect	5 (20.0)	25 (18.0)	.81
Other/incidental	7 (28.0)	69 (49.6)	.08
Comorbidities			
Abdominal aortic aneurysm or ectasia	10 (62.5)	12 (14.3)	.01
Other visceral aneurysms	4 (25.0)	0 (0.0)	<.0001
Fibromuscular dysplasia	0 (0.0)	0 (0.0)	1.0
Coronary artery disease	10 (40.0)	40 (29.0)	.38
Peripheral artery disease	4 (16.0)	6 (4.3)	.07
Hypertension	22 (88.0)	97 (70.3)	.11
Diabetes mellitus	3 (12.0)	22 (15.9)	.85
Hyperlipidemia	13 (52.0)	73 (52.9)	.96
Smoking	17 (68.0)	22 (15.9)	<.0001
Alcohol abuse	1 (4.0)	7 (5.0)	.82
Sympathomimetic abuse	0 (0.0)	0 (0.0)	1.0
Family history			
Abdominal aortic aneurysm	3 (12.0)	9 (6.4)	.58
Ischemic stroke	7 (28.0)	32 (23.0)	.78
Intracranial aneurysm	1 (4.0)	9 (6.4)	.98
Other saccular aneurysms present	7 (28.0)	22 (15.8)	.24
Growth on follow-up	6 (46.2)	30 (21.6)	.09
SAH on follow-up	5 (20.0)	5 (3.5)	.007
Infarct on follow-up	7 (28.0)	18 (13.0)	.10
Clinical status at last follow-up			
Good neurologic function	6 (24.0)	80 (57.6)	.004
Poor neurologic function	6 (24.0)	22 (15.8)	.48
Death	13 (52.0)	37 (26.6)	.02
Aneurysm-related death	6 (24.0)	10 (7.2)	.02

Note:—VBD indicates vertebrobasilar dolichoectasia; DID, diffuse intracranial dolichoectasia.

Outcomes Studied

In cases in which there was serial imaging, we collected data on presence of dolichoectatic aneurysm growth or rupture and new ischemic stroke. We also collected data on the clinical status of the patient at last follow-up. Clinical status was defined as no or minimal disability (mRS ≤ 2), moderate or severe disability (mRS 3–5), and death. Among patients who died, the cause of death was noted, when available. Outcomes were compared between the diffuse intracranial dolichoectasia group and the isolated vertebrobasilar dolichoectasia group.

Statistical Analysis

All categoric variables are reported as number (percentage), while continuous variables are reported as mean ± SD. Categoric variables were compared by using χ^2 tests, and continuous variables were compared by using a Student *t* test. To determine whether a diagnosis of diffuse intracranial dolichoectasia was independently associated with aneurysm growth, rupture, and new infarct, we performed a multivariate logistic regression analysis, adjusting for baseline factors that were different between groups (ie, age and smoking history). All analysis was performed by using the SAS-based statistical software package JMP 12.0 (SAS Institute, Cary, North Carolina).

RESULTS

Baseline Patient Characteristics for Diffuse Intracranial Dolichoectasia

The search of radiology reports (ie, MR imaging, MRA, CTA, and DSA) yielded 890 unique patients with the terms "fusiform," "aneurysmal dilation," "dilation," "fusiform aneurysm," "dolichoectasia," "dolichoectatic," and "dolicho" in their reports. After further review of imaging reports and radiologic images, 25 patients met the diagnostic criteria for diffuse intracranial dolichoectasia.

The mean patient age was 70.9 ± 14.2 years. Two patients were younger than 50 years of age (8.0%), and 21 patients (84.0%) were 60 years of age or older. Eighty-four percent (21/25) of patients were men. The most common clinical presentation was acute ischemic stroke or transient ischemic attack (13/25, 52%). Of the ischemic strokes, 6 affected the posterior circulation and 7 affected the anterior circulation. Five patients (20%) had symptoms due to mass effect from the aneurysmal dilations, 3 patients (12%) had dizziness, and in the remaining 4 patients (16%), the aneurysms were discovered incidentally during evaluation for loss of consciousness, syncope, or visual blurring.

Among patients with abdominal imaging, 50% (8/16) had an abdominal aortic aneurysm and an additional 13% (2/16) had aortic ectasia. Hypertension was present in 88% (22/25) of patients, and 68% (17/25) were current or former smokers. Hyperlipidemia was present in 52% (13/25) of patients, and intracranial atherosclerosis was present in 48% (12/25). These data are summarized in Table 2.

Angiographic and Anatomic Characteristics for Diffuse Intracranial Dolichoectasia

The most common distribution of disease was dilation of the basilar artery and 1 internal carotid artery (10 patients, 40%). Five patients (20%) had diffuse dilation of the basilar artery and bilateral ICAs, and 4 patients (16%) had dilation of the bilateral ICAs without dilation of the basilar artery. Two patients (8.0%) had dilation of the basilar artery and bilateral ICAs and MCAs.

The mean maximum diameter of the dilated basilar arteries was 15.2 ± 8.3 mm. The mean maximum diameter of the dilated

ICA segments was 12.7 ± 7.0 mm, and the mean maximum diameter of dilated MCA segments was 10.1 ± 4.3 mm. Seven patients (28%) had additional intracranial saccular aneurysms. These data are summarized in Table 3.

Outcomes for Diffuse Intracranial Dolichoectasia

Thirteen patients had imaging follow-up (mean, 54.1 ± 78.4 months). Of these patients, 6 (46%) had growth of at least 1 aneurysmal dolichoectasia, which occurred at a mean of 56.0 ± 54.3 months. Given a total of 63.1 patient-years of imaging follow-up, the overall growth rate was 9.5%/patient-year. Seven patients (56%) had imaging evidence of a new infarct after a mean of 60.9 ± 66.5 months of follow-up, including 2 patients with brain stem perforator infarcts, 5 patients with cerebellar or thalamic infarcts, and 4 patients with anterior circulation infarcts.

Five patients (5/25, 20.0%) had imaging evidence of subarachnoid hemorrhage at a mean of 59.0 ± 73.1 months of follow-up. Of these 5 patients, 3 had rupture of 2 basilar dolichoectatic/fusiform aneurysms, 1 had rupture of a posterior inferior cerebellar artery dissecting aneurysm, and in 1 patient, the source of the subarachnoid hemorrhage was unclear (On-line Table). Including patients without imaging follow-up, the overall rate of subarachnoid hemorrhage was 5.9%/year (5 cases over 84.9 patient-years).

The mean clinical follow-up for all 25 patients was 40.8 ± 62.3 months. At last follow-up, 13 patients (52%) had died, 6 patients (24%) had poor neurologic outcome, and 6 patients (24%) had good neurologic outcome. Among the patients who died, 4 died from aneurysm rupture, 2 died from hydrocephalus secondary to mass effect from a growing basilar artery fusiform aneurysm, and 1 patient died from intraparenchymal hemorrhage, which was not aneurysm-related. The remaining deaths were noncerebrovascular in nature, including 4 patients who died from cancer and 2 patients who died from unknown causes. In 4 of the 6 patients who had poor neurologic outcome at last follow-up, the cause of the morbidity was related to diffuse intracranial dolichoectasia. Representative case examples are provided in Figs 1–4.

Table 3: Angiographic characteristics and distribution of DID

	No. (%)
Vessels involved	
Anterior circulation only	4 (16.0)
Bilateral ICAs	4 (16.0)
Anterior and posterior circulation	21 (84.0)
Basilar artery + 1 ICA	10 (40.0)
Basilar artery + bilateral ICAs	5 (20.0)
Basilar artery + bilateral ICAs + bilateral MCAs	2 (8.0)
Basilar artery + 1 ICA/ipsilateral M1	2 (8.0)
Basilar artery + 1 ICA + bilateral MCAs	1 (4.0)
Basilar artery + 1 MCA	1 (4.0)
Mean (SD) maximum diameter of dilated (mm)	
Basilar artery	15.2 (8.3)
Internal carotid artery	12.7 (7.0)
MCA	10.1 (4.3)
Thrombus in fusiform/dolichoectatic aneurysm	7 (28.0)

Note:—DID indicates diffuse intracranial dolichoectasia.

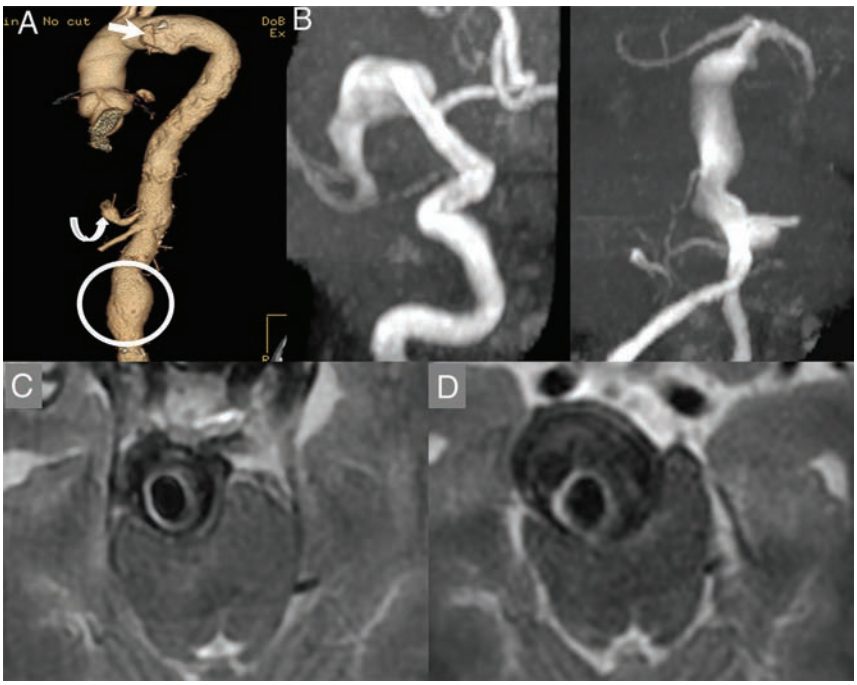

FIG 1. A 67-year-old man who is a former smoker with a history of a penetrating atheromatous ulcer of the aortic arch (*white arrow*), a 5.6-cm abdominal aortic aneurysm (*circle*), and a celiac artery aneurysm (*curved arrow*, *A*). The patient had an episode of dizziness and headache and underwent a noncontrast CT of the head, which demonstrated enlarged intracranial arteries. An MRA demonstrated fusiform aneurysmal dilation of the entire right M1 segment measuring 10 mm in maximum diameter and a largely thrombosed fusiform aneurysm of the basilar artery, which measured 18 mm in maximum diameter (*B* and *C*). Approximately 9 months later, the aneurysm grew to 25 mm in diameter and started causing obstructive hydrocephalus (*D*). The patient also had a new perforator pontine infarct at the time (not shown). A programmable ventriculoperitoneal shunt was placed; however, the patient died due to complications of hydrocephalus 3 months later.

Comparison of Diffuse Intracranial Dolichoectasia and Isolated Vertebrobasilar Dolichoectasia Groups

A total of 139 patients had vertebrobasilar dolichoectasia with a mean follow-up of 44 ± 42.9 months. A case of vertebrobasilar dolichoectasia is demonstrated in Fig 5. None of the patients with vertebrobasilar dolichoectasia progressed to the diffuse form. Patients with diffuse intracranial dolichoectasia were older (70.9 ± 14.2 years versus 60.4 ± 12.5 years, $P = .0002$), and the age distribution of patients with diffuse intracranial dolichoectasia was older ($P < .0001$). There was a predominance of males in both patient groups (84.0% versus 75.5%, $P = .51$). Patients with diffuse intracranial dolichoectasia were significantly more likely to have abdominal aortic aneurysms or ectasias (62.5% versus 14.3%, $P = .01$) as well as visceral aneurysms (25.0% versus 0.0%, $P < .0001$). Patients with diffuse intracranial dolichoectasia trended toward higher rates of peripheral artery disease (16.0% versus 4.3%, $P = .07$) and hypertension (88.0% versus 70.3%, $P = .11$). Patients with dif-

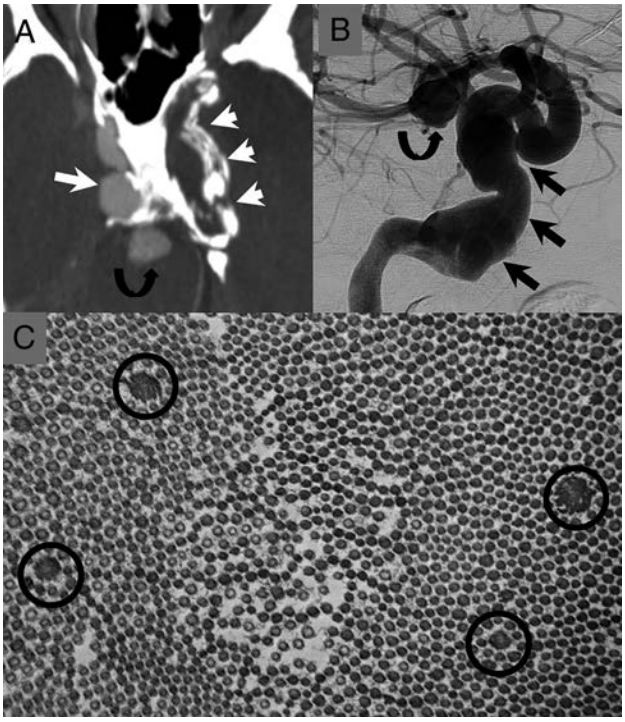

FIG 2. The patient is a 47-year-old man. He presented in his 20s with 2 large fusiform aneurysms of his cavernous carotid arteries. He later developed an aneurysm of his basilar artery and had a subarachnoid hemorrhage from a dissecting aneurysm of his PICA (not shown). *A*, CTA image demonstrates a large fusiform aneurysm of the right cavernous carotid artery (*long white arrow*) and a thrombosed/calcified aneurysm of the left cavernous carotid artery (*short white arrows*). There is also an aneurysm of the basilar tip (*curved black arrow*). *B*, Right ICA cerebral angiogram shows a large fusiform aneurysm of the right petrocavernous carotid artery (*straight black arrows*) and a basilar tip aneurysm (*curved black arrow*). *C*, There was suspicion for underlying connective tissue disease. The patient underwent a skin biopsy. Electron microscopy of the skin biopsy shows multiple abnormally enlarged collagen fibers (*black circles*) consistent with collagen flowers. These are typically seen in Ehlers-Danlos syndrome. The patient later underwent genetic testing for Loeys-Dietz, Ehlers-Danlos, and Marfan syndromes. The findings of all tests were negative.

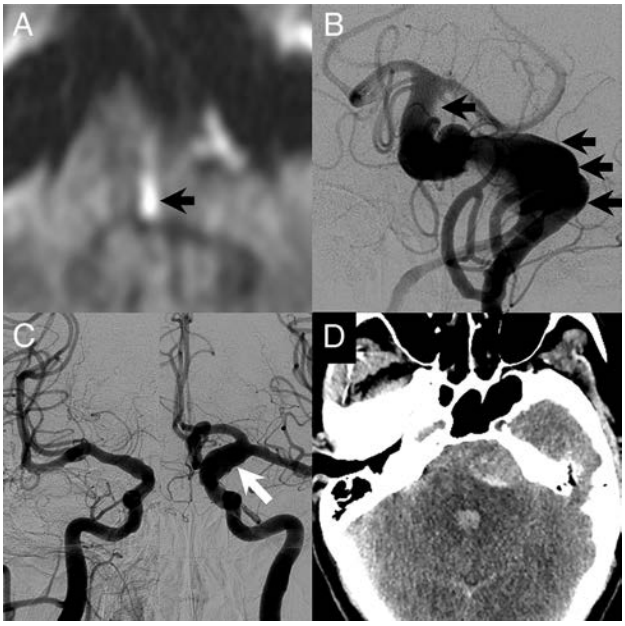

FIG 3. A 51-year-old man with a long history of headaches with associated nausea and vomiting. He had acute-onset left-sided weakness with a prominent left facial droop along with left face, arm, and leg numbness and slurred speech. The patient had no family history of cerebral aneurysms, though his father had an abdominal aortic aneurysm. *A*, MR imaging at the time of the initial evaluation showed a medial left pontine infarct (*black arrow*). There was evidence of a large dolichoectatic aneurysm of the basilar artery on MR imaging, and the patient underwent cerebral angiography for further evaluation. *B*, Cerebral angiography demonstrated a fusiform-type aneurysm of the basilar artery with a filling defect that was consistent with thrombus (*black arrows*). The patient also had diffuse arteriomegaly with dilation of the right supraclinoid ICA to 6 mm and dilation of the left supraclinoid ICA to 10 mm (*white arrow*, *C*). *D*, The day following the angiography, the patient had a 10/10 headache. Noncontrast CT at the time showed diffuse subarachnoid hemorrhage with most of the blood products surrounding the basilar artery aneurysm. He died the next day.

fuse intracranial dolichoectasia were significantly more likely to smoke (68.0% versus 15.9%, $P < .0001$).

Patients with diffuse intracranial dolichoectasia trended toward higher aneurysm growth rates (46.2% versus 21.6%, $P = .09$) and cerebral infarction rates (28.0% versus 13.0%, $P = .10$) and were more likely to have SAH on follow-up (20.0% versus 3.5%, $P = .007$). Patients with diffuse intracranial dolichoectasia were less likely to have good neurologic function at follow-up (24.0% versus 57.6%, $P = .004$), were more likely to die (52.0% versus 26.6%, $P = .02$), and were more likely to die due to aneurysm-related factors (24.0% versus 7.2%, $P = .02$). These data are summarized in Table 2.

On multivariate analysis, adjusting for age and smoking history, a diagnosis of diffuse intracranial dolichoectasia was independently associated with higher odds of aneurysm rupture (OR = 6.33; 95% CI, 1.23–35.31; $P = .02$) and higher odds of new ischemic stroke (OR = 18.62; 95% CI, 3.63–146.57; $P = .0003$). There was no significant difference in the odds of aneurysm growth on multivariate analysis (OR = 2.23; 95% CI, 0.57–8.68; $P = .24$).

DISCUSSION

Our study of 25 patients with diffuse intracranial dolichoectasia demonstrated a number of notable findings. First, this condition is a relatively rare vascular phenotype, predominantly affecting elderly male smokers with hypertension. The natural history of this disease is dismal, with only a minority surviving with good outcome at a mean follow-up of 3.5 years. Furthermore, among patients with abdominal imaging, >60% had abdominal aortic aneurysms or ectasias and nearly 30% of patients had an additional intracranial saccular aneurysm. Compared with a control group of patients with isolated vertebrobasilar dolichoectasia, patients with diffuse intracranial dolichoectasia were more likely to have aortic and visceral aneurysms, were more likely to smoke, and were more likely to experience aneurysm growth, rupture, and morbidity and mortality on both univariate and multivariate analyses. Overall, these findings suggest that diffuse intracranial dolichoectasia may represent a distinct vascular phenotype from isolated vertebrobasilar dolichoectasia and is likely the manifestation of a diffuse, systemic arteriopathy affecting multiple vascular beds. A summary of our proposed diagnostic criteria for diffuse intracranial dolichoectasia and how they compare with current definitions of vertebrobasilar dolichoectasia is provided in Table 4.

We fully acknowledge that patients with multivessel intracranial dolichoectasia have been reported previously in the literature. However, prior reports were generally quite small and did not specifically identify multivessel involvement as a distinct entity and did not provide detailed baseline demographic, imaging, and outcome data to fully characterize our proposed subgroup. In a review of 9 studies on vertebrobasilar dolichoectasia, Gutierrez et al[11] noted that approximately 45% of patients with vertebrobasilar dolichoectasia had some degree of ectasia or dilation of the anterior circulation as well. However, on closer inspection of these studies, it is apparent that the degree of dilation or tortuosity of the anterior circulation and the outcomes of patients with diffuse intracranial dolichoectasia were not reported.[3,10,12-14] For example, in a case series that our group previously published, 63 of 152 patients (41.5%) with vertebrobasilar nonsaccular dolichoectatic aneurysms had concomitant dolichoectasias in the anterior circulation by visual inspection. However, only 11 of those patients (7.2%) are included in the current study because the other 52 did not meet the size criteria set forth in Table 1. In fact, even in the large surgical series reported by Anson et al[15] and Drake et al[16] of patients with surgically treated large fusiform aneurysms, <5 percent of cases would meet the diagnostic criteria of diffuse intracranial dolichoectasia. Other small case series and case reports have reported outcomes of patients with diffuse intracranial dolichoectasia with a well-defined underlying etiology such as prior radiation, autosomal dominant polycystic kidney disease, connective tissue disease, or infection. However, findings from these studies do not necessarily apply to the patient population included in our series due to substantial differences in risk factors and etiology.[17-23]

Our comparison of the baseline clini-

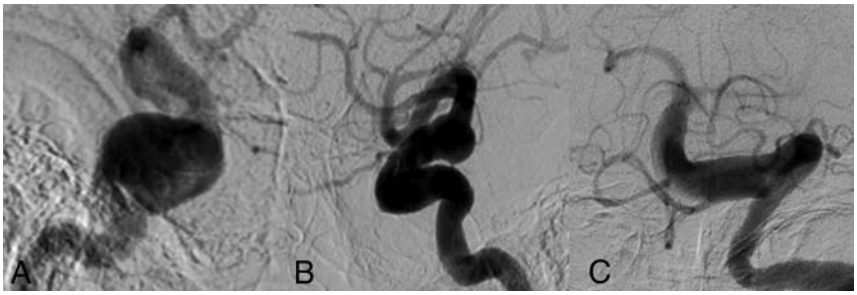

FIG 4. An 87-year-old man with a history of a right third-nerve palsy. *A*, Right ICA cerebral angiogram demonstrates a 20-mm cavernous carotid fusiform aneurysm with associated dilation of the supraclinoid ICA as well. *B*, Left ICA cerebral angiogram shows dilation of the left supraclinoid ICA to approximately 10 mm. *C*, Left vertebral artery cerebral angiogram shows diffuse dilation and tortuosity of the basilar artery measuring 9 mm in maximum diameter. The cause of the third-nerve palsy was thought to be the right cavernous aneurysm.

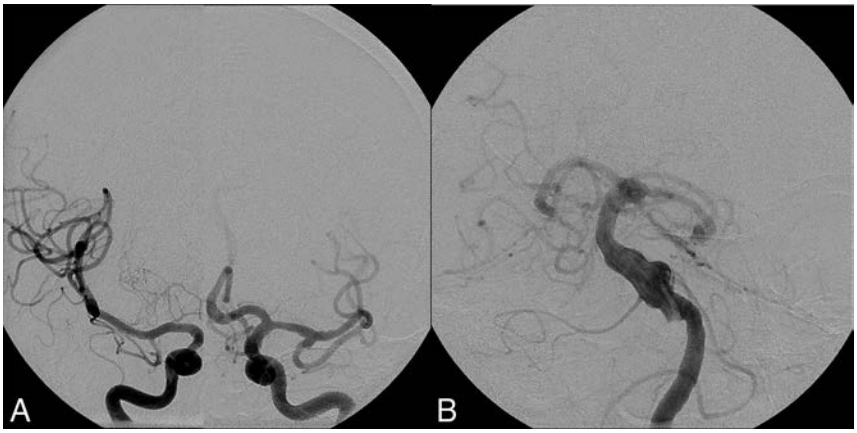

FIG 5. Vertebrobasilar dolichoectasia in a 67-year-old man. *A*, Right and left ICA cerebral angiograms demonstrate normal-caliber internal carotid arteries, MCAs, and anterior cerebral arteries bilaterally. *B*, Left vertebral artery cerebral angiogram demonstrates an irregular dolichoectatic and fusiform aneurysm involving the entirety of the basilar artery.

Table 4: Comparison of diagnostic criteria and outcomes

	Diffuse Intracranial Dolichoectasia	Vertebrobasilar Dolichoectasia[a]
Imaging appearance	Fusiform aneurysmal dilation of an entire vascular segment (ie, supraclinoid ICA, basilar artery, M1 segment of the MCA)	Fusiform: aneurysmal dilation without definable neck involving a portion of an arterial segment with any degree of tortuosity Dolichoectatic: uniform aneurysmal dilation of an artery involving the entire basilar or vertebral or both with any degree of tortuosity Transitional: uniform aneurysmal dilation of an artery with superimposed dilation of a portion of the involved arterial segment
Distribution	≥2 Intracranial vascular beds (ie, vertebrobasilar system, left anterior circulation, or right anterior circulation)	Vertebrobasilar system only
Size criteria	Cavernous ICA: ≥8.5 mm Supraclinoid ICA: ≥8.0 mm MCA: ≥5.0 mm Basilar artery: ≥6.0 mm	Basilar artery diameter of >5.0 mm
Growth rate	10%/year	7%/year[2,10]
Ischemic stroke risk	11%/year	3%/year[2,10]
Aneurysm rupture risk	6%/year	2%/year[2,10]

[a] Definitions of vertebrobasilar dolichoectasia proposed by Flemming et al.[2]

cal characteristics and outcomes of patients with diffuse intracranial dolichoectasia with patients with isolated vertebrobasilar dolichoectasia suggests that at the very least, this entity is a distinctive phenotype or a more diffuse and severe form of vertebrobasilar dolichoectasia. In general, patients with diffuse intracranial dolichoectasia were older, were more likely to have hypertension and other atherosclerotic risk factors, and were more likely to smoke. Furthermore, patients in the diffuse intracranial dolichoectasia group were significantly more likely to have intracranial, abdominal aortic, and visceral arterial aneurysms than those with isolated vertebrobasilar dolichoectasia. These differences are not only isolated to patients studied at our institution. Compared with the systematic review of the literature on vertebrobasilar dolichoectasia published by Gutierrez et al,[11] patients in our current series were generally older (71 versus 63 years), were more often male (84% versus 64%), and were more likely to have hypertension (88% versus 66%), smoke (68% versus 42%), and have other atherosclerotic risk factors. Furthermore, considering all patients in our series with abdominal imaging, 50% of patients had abdominal aortic aneurysms compared with an average of 11% in the vertebrobasilar dolichoectasia literature.[11] The rate of concomitant saccular aneurysm formation is twice as high as that reported in the literature as well (28% versus 15%).

The natural history of patients with diffuse intracranial dolichoectasia was also substantially more aggressive than that of the isolated vertebrobasilar dolichoectasia group as well as that reported in the vertebrobasilar dolichoectasia literature. Twenty percent of patients in our series had subarachnoid hemorrhage on follow-up, for a subarachnoid hemorrhage rate of 6.9%/patient-year. This compares with rupture rates of just 1%–2% per year reported for dolichoectatic and fusiform aneurysms of both the anterior and posterior circulations.[3,4,24] The growth rate for patients with diffuse intracranial dolichoectasia was also substantially higher than that reported in the literature among patients with single-vessel dolichoectatic aneurysms (9.5%/year versus 6.5%/year).[10] More than 50% of the patients in the current series had ischemic stroke after a mean of approximately 5 years of follow-up. Meanwhile, the rates of ischemic stroke among previously published large series of vertebrobasilar dolichoectasia are 3%, 11%, 16%, and 38% at 1, 5, 10, and 12 years, respectively.[11]

Limitations

Our study has limitations. First, this is a retrospective study spanning >15 years at a single institution. Therefore, there is wide variation in the type of imaging used, clinical management of these patients, and degree of follow-up. In addition, our study is prone to substantial selection bias. Patients who presented with diffuse intracranial dolichoectasia at our tertiary referral institution were more likely to have complications related to this disease, which could explain the poor natural history seen in our study. We do not have access to pathologic specimens or gene samples from the patients included in this study. Thus, we are unable to determine whether the pathologic basis of this disease is similar to that in other fusiform aneurysms and ectasias or whether the degree of vessel wall weakening is, in fact, more severe. While none of the patients in our series had a clinical diagnosis of a genetic connective tissue disease such as Marfan syndrome, Ehlers-Danlos syndrome, or Loeys-Dietz syndrome, most of the patients included in this series did not receive any genetic testing, so we cannot rule out the presence of an undiagnosed connective tissue disease. Therefore, the total number of patients or the association to secondary diseases may not be as high as that reported in our study. In our comparison of the natural history of diffuse intracranial dolichoectasia with that of vertebrobasilar dolichoectasia, we did not account for the fact that the morphology of the vertebrobasilar dolichoectatic lesions has a significant impact on their natural history. As defined in Table 4, dolichoectatic vertebrobasilar aneurysms have a much more favorable natural history than fusiform or transitional lesions.[10] Last, because this entity has not been extensively studied outside small case series and case reports, there are no well-defined diagnostic criteria. Our choice of size criteria in diagnosing diffuse intracranial dolichoectasia are somewhat arbitrary (doubling of mean values reported in the literature). Using such strict criteria could have resulted in exclusion of patients with milder or earlier forms of this disease.

CONCLUSIONS

Our study of 25 patients with diffuse intracranial dolichoectasia demonstrated that this rare disease is associated with a very poor natural history, with about 20% of patients having subarachnoid hemorrhage on follow-up, 30% of patients having ischemic stroke, and 25% of patients with aneurysm-related mass effect. Nearly two-thirds of patients with this disease have abdominal aortic aneurysms, and 25% have additional saccular intracranial aneurysms. Given the high morbidity and mortality rates associated with this disease and the high rate of concomitant intracranial saccular aneurysm and abdominal aortic aneurysms in this population, these findings suggest that diffuse intracranial dolichoectasia may represent a distinct vascular phenotype. Further research is needed to better characterize the histopathologic and genetic features of diffuse intracranial dolichoectasia and determine ideal treatment options.

Disclosures: Giuseppe Lanzino—*UNRELATED*: *Consultancy*: Covidien/Medtronic.* David F. Kallmes—*UNRELATED*: *Consultancy*: Minnetronix,* *Comments*: Data and Safety Monitoring Board; *Grants/Grants Pending*: Medtronic, MicroVention, Sequent Medical, Surmodics, Codman, NeuroSigma, *Comments*: preclinical research and clinical trials*; *Travel/Accommodations/Meeting Expenses Unrelated to Activities Listed*: Medtronic, *Comments*: FDA panel meeting.* *Money paid to the institution.

REFERENCES

1. Dispensa BP, Saloner DA, Acevedo-Bolton G, et al. **Estimation of fusiform intracranial aneurysm growth by serial magnetic resonance imaging.** *J Magn Reson Imaging* 2007;26:177–83 CrossRef Medline
2. Flemming KD, Wiebers DO, Brown RD Jr, et al. **The natural history of radiographically defined vertebrobasilar nonsaccular intracranial aneurysms.** *Cerebrovasc Dis* 2005;20:270–79 CrossRef Medline
3. Passero SG, Rossi S. **Natural history of vertebrobasilar dolichoectasia.** *Neurology* 2008;70:66–72 CrossRef Medline
4. Sacho RH, Saliou G, Kostynskyy A, et al. **Natural history and outcome after treatment of unruptured intradural fusiform aneurysms.** *Stroke* 2014;45:3251–56 CrossRef Medline
5. Mizutani T. **A fatal, chronically growing basilar artery: a new type of dissecting aneurysm.** *J Neurosurg* 1996;84:962–71 CrossRef Medline
6. Mizutani T, Aruga T. **"Dolichoectatic" intracranial vertebrobasilar**

dissecting aneurysm. *Neurosurgery* 1992;31:765–73; discussion 773 CrossRef Medline
7. Mizutani T, Kojima H. **Clinicopathological features of non-atherosclerotic cerebral arterial trunk aneurysms.** *Neuropathology* 2000; 20:91–97 CrossRef Medline
8. Mizutani T, Miki Y, Kojima H, et al. **Proposed classification of non-atherosclerotic cerebral fusiform and dissecting aneurysms.** *Neurosurgery* 1999;45:253–59; discussion 259–60 CrossRef Medline
9. Mocco J, Huston J, Fargen KM, et al. **An angiographic atlas of intracranial arterial diameters associated with cerebral aneurysms.** *J Neurointerv Surg* 2014;6:533–35 CrossRef Medline
10. Nasr DM, Brinjikji W, Rouchaud A, et al. **Imaging characteristics of growing and ruptured vertebrobasilar non-saccular and dolichoectatic aneurysms.** *Stroke* 2016;47:106–12 CrossRef Medline
11. Gutierrez J, Sacco RL, Wright CB. **Dolichoectasia-an evolving arterial disease.** *Nat Rev Neurol* 2011;7:41–50 CrossRef Medline
12. Passero SG, Calchetti B, Bartalini S. **Intracranial bleeding in patients with vertebrobasilar dolichoectasia.** *Stroke* 2005;36:1421–25 CrossRef Medline
13. Yu YL, Moseley IF, Pullicino P, et al. **The clinical picture of ectasia of the intracerebral arteries.** *J Neurol Neurosurg Psychiatry* 1982;45: 29–36 CrossRef Medline
14. Nakatomi H, Segawa H, Kurata A, et al. **Clinicopathological study of intracranial fusiform and dolichoectatic aneurysms: insight on the mechanism of growth.** *Stroke* 2000;31:896–900 CrossRef Medline
15. Anson JA, Lawton MT, Spetzler RF. **Characteristics and surgical treatment of dolichoectatic and fusiform aneurysms.** *J Neurosurg* 1996;84:185–93 CrossRef Medline
16. Drake CG, Peerless SJ. **Giant fusiform intracranial aneurysms: review of 120 patients treated surgically from 1965 to 1992.** *J Neurosurg* 1997;87:141–62 CrossRef Medline
17. Schievink WI, Torres VE, Wiebers DO, et al. **Intracranial arterial dolichoectasia in autosomal dominant polycystic kidney disease.** *J Am Soc Nephrol* 1997;8:1298–303 Medline
18. Sedat J, Alvarez H, Rodesch G, et al. **Multifocal cerebral fusiform aneurysms in children with immune deficiencies report of four cases.** *Interv Neuroradiol* 1999;5:151–56 Medline
19. Naunheim MR, Walcott BP, Nahed BV, et al. **Arterial tortuosity syndrome with multiple intracranial aneurysms: a case report.** *Arch Neurol* 2011;68:369–71 CrossRef Medline
20. Azzarelli B, Moore J, Gilmor R, et al. **Multiple fusiform intracranial aneurysms following curative radiation therapy for suprasellar germinoma: case report.** *J Neurosurg* 1984;61:1141–45 CrossRef Medline
21. Braunsdorf WE. **Fusiform aneurysm of basilar artery and ectatic internal carotid arteries associated with glycogenosis type 2 (Pompe's disease).** *Neurosurgery* 1987;21:748–49 CrossRef Medline
22. Capone PM, Mechtler LL, Bates VE, et al. **Multiple giant intracranial aneurysms associated with lymphomatoid granulomatosis: a magnetic resonance imaging and angiographic study.** *J Neuroimaging* 1994;4:109–11 CrossRef Medline
23. Siqueira Neto JI, Silva GS, De Castro JD, et al. **Neurofibromatosis associated with moyamoya arteriopathy and fusiform aneurysm: case report** [in Portuguese]. *Arq Neuropsiquiatr* 1998;56:819–23 CrossRef Medline
24. Flemming KD, Wiebers DO, Brown RD Jr, et al. **Prospective risk of hemorrhage in patients with vertebrobasilar nonsaccular intracranial aneurysm.** *J Neurosurg* 2004;101:82–87 CrossRef Medline

Detection of Focal Longitudinal Changes in the Brain by Subtraction of MR Images

N. Patel, M.A. Horsfield, C. Banahan, A.G. Thomas, M. Nath, J. Nath, P.B. Ambrosi, and E.M.L. Chung

ABSTRACT

BACKGROUND AND PURPOSE: The detection of new subtle brain pathology on MR imaging is a time-consuming and error-prone task for the radiologist. This article introduces and evaluates an image-registration and subtraction method for highlighting small changes in the brain with a view to minimizing the risk of missed pathology and reducing fatigue.

MATERIALS AND METHODS: We present a fully automated algorithm for highlighting subtle changes between multiple serially acquired brain MR images with a novel approach to registration and MR imaging bias field correction. The method was evaluated for the detection of new lesions in 77 patients undergoing cardiac surgery, by using pairs of fluid-attenuated inversion recovery MR images acquired 1–2 weeks before the operation and 6–8 weeks postoperatively. Three radiologists reviewed the images.

RESULTS: On the basis of qualitative comparison of pre- and postsurgery FLAIR images, radiologists identified 37 new ischemic lesions in 22 patients. When these images were accompanied by a subtraction image, 46 new ischemic lesions were identified in 26 patients. After we accounted for interpatient and interradiologist variability using a multilevel statistical model, the likelihood of detecting a lesion was 2.59 (95% CI, 1.18–5.67) times greater when aided by the subtraction algorithm ($P = .017$). Radiologists also reviewed the images significantly faster ($P < .001$) by using the subtraction image (mean, 42 seconds; 95% CI, 29–60 seconds) than through qualitative assessment alone (mean, 66 seconds; 95% CI, 46–96 seconds).

CONCLUSIONS: Use of this new subtraction algorithm would result in considerable savings in the time required to review images and in improved sensitivity to subtle focal pathology.

Increasingly, diagnostic radiologic assessment does not involve a single examination at 1 time point but makes use of follow-up imaging for monitoring responses during the course of treatment or to assess the progression of a condition with a view to intervention.[1-3] Manual interpretation of this type of data is burdensome and prone to errors. A challenge for medical image analysts is the development of reliable techniques to assist the radiologist.[4] Easier and faster detection of pathologic changes facilitates diagnosis and makes it more cost-effective to monitor disease evolution in the long term.

Manual analysis of medical images acquired at different time points is generally limited to a qualitative comparison. The repositioning of the patient is never identical, the scanning equipment used may be different or may have been upgraded, the acquisition parameters may have altered between scans, and local shape deformations of nonrigid anatomic structures occur. The expert radiologist compensates intuitively for some of these unwanted differences with knowledge of anatomy and the expected signal differences to identify and reject certain artifactual changes.

One of the major artifacts associated with MR imaging is caused by the spatially nonuniform transmission and reception properties of the radiofrequency coils.[5] Commonly, a large transmitter coil built into the bore of the magnet is used for radiofrequency transmission, resulting in relatively uniform transmission properties. However, to improve the signal-to-noise ratio, an array of small coils is used for signal reception, and these have very spatially nonuniform reception properties.[6] It is common to correct for this by mapping the reception properties of the coils and

Received May 11, 2015; accepted after revision December 14, 2016.

From the Department of Cardiovascular Sciences (N.P., M.A.H., M.N., J.N., E.M.L.C.), University of Leicester, Leicester Royal Infirmary, Leicester, UK; Leicester National Institute of Health Research Cardiovascular Biomedical Research Unit (N.P., E.M.L.C.), Glenfield Hospital, Leicester, UK; Departments of Radiology (A.G.T., P.B.A.) and Medical Physics (C.B., E.M.L.C.), University Hospitals of Leicester National Health Service Trust, Leicester, UK; and Neuri Beaujon (P.B.A.), University Paris Diderot, Paris, France.

This study was funded by the British Heart Foundation (FS/10/46/288350). N. Patel was funded by the National Institute of Health Research Leicester Cardiovascular Biomedical Research Unit.

Please address correspondence to Emma M.L. Chung, MD, Department of Cardiovascular Sciences, University of Leicester, Leicester Royal Infirmary, LE2 7LX, UK; e-mail: emlc1@leicester.ac.uk

http://dx.doi.org/10.3174/ajnr.A5165

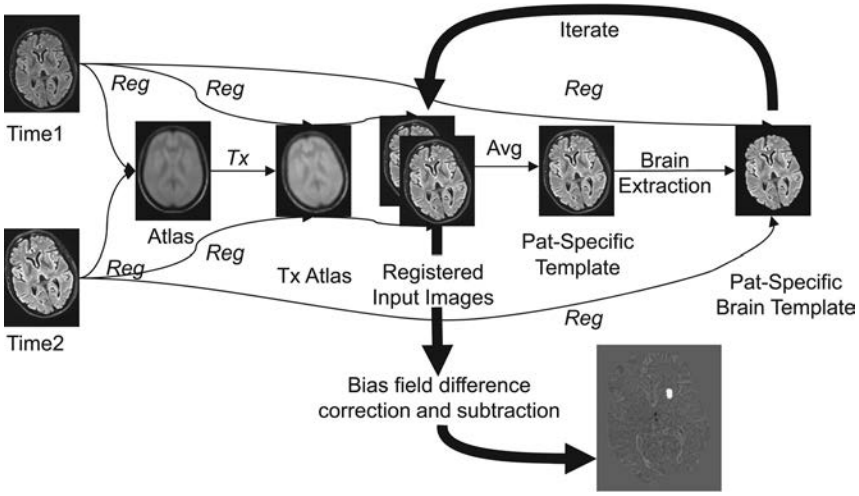

FIG 1. Flow chart illustrating the processing steps to produce a subtraction image for 2 images acquired at different time points. Registration (*Reg*) is first done with a generic atlas target to determine the average position of the input images. This atlas is transformed to the average position of the input images and serves as the registration target for the second registration. The registered input images are averaged to create a patient-specific target at the average position. This target is then refined by brain extraction and further registration of the input images to it. After the final registration, the differences in the bias field are corrected; then, a subtraction highlights any focal changes in the input images between time points. Tx indicates a transform/transformation.

rescaling the image intensities pixel by pixel.[7] This mapping, however, is based on a number of assumptions and does not remove the image-intensity shading, known as the bias field, completely. It is also possible to perform a bias field correction as a postprocessing step, but again this is based on a number of assumptions about the nature of the field and its stability.[8,9] The algorithm described in the current work circumvents these issues by correcting the bias field in subtraction images rather than in the source images themselves.

This article describes an image registration and subtraction technique that can highlight local changes in MR images of the brain acquired at ≥2 time points. It is robust to changes in the patient position and in the bias field. The technique was evaluated by using a set of 77 patients who were scanned before and after cardiac surgery, with the aim of assessing whether this algorithm could aid in the detection of small ischemic brain lesions resulting from emboli shed from the vascular system as a result of an operation.[10] The value of the system was assessed by examining the lesion detection rate and time required for the assessment of scans for radiologists examining pairs of images with and without the aid of our subtraction method.

MATERIALS AND METHODS

Registration and Subtraction

The method is based on registration of images acquired at different points in time, the correction of any differences due solely to radiofrequency reception nonuniformity, and subsequent subtraction to reveal any differences due to focal pathology. The method is described in detail elsewhere[11] and is illustrated in Fig 1. Briefly, input images are registered to a common frame of reference at the average position of all input images. Then, radiofrequency bias field variations are modeled as a smoothly varying polynomial function; then, individual registered images are corrected by pixel-wise division by the modeled field. Finally, individual pairs of registered and corrected images are subtracted (Fig 2).

Patients

We examined data from patients enrolled in a clinical study of neurologic deficits following cardiac surgery, as detailed elsewhere.[10] All clinical data were collected in accordance with local research ethics procedures. All patients provided written informed consent for their anonymized data to be used in this research.

MR Imaging

MR imaging was performed by using a 3T system (Magnetom Skyra; Siemens, Erlangen, Germany) with a 20-channel phased array head and neck coil for signal reception. MR imaging studies were performed 1–2 weeks before cardiac surgery and repeated 6–8 weeks after surgery to identify any new postoperative ischemic lesions. The same scanning protocol was used on both occasions, except that the angiogram was not obtained postsurgery. After a localizer image, the scanning protocol consisted of a diffusion-weighted image, time-of-flight angiography, a susceptibility-weighted image, and a FLAIR image.[12] The total imaging time was approximately 30 minutes.

For this study, only the FLAIR images were analyzed. The FLAIR images consisted of 48, 3-mm-thick contiguous axial sections positioned parallel to the anterior/posterior commissure line. The *k*-space matrix size was 320 × 224, zero-filled to give an image matrix of 320 × 320 and an FOV of 240 × 240 mm (TR/TE/TI, 6770/108/2170 ms).

Image Review and Analysis

Images were analyzed independently by 3 experienced neuroradiologists in 2 stages. First, for each patient, the pre- and postsurgery FLAIR images were presented side by side on a computer display and the radiologist paged through both the images section by section to identify any new ischemic lesions. The anatomic regions of any new lesions were also noted. Signal hyperintensity clearly extending outside the brain parenchyma or minor variations in ependymal signal hyperintensity (commonly encountered on FLAIR sequences) were considered artifactual. A digital timer was used by each neuroradiologist to note the time taken to review images from each patient.

Second, for each patient, the coregistered pre- and postsurgery FLAIR images along with the difference image were presented. The neuroradiologist paged through all 3 images simultaneously section by section to identify any new ischemic lesions on the difference image, with the pre- and postsurgery images used to confirm or refute the findings. Thus, it is unlikely that there were any false-positive findings. A subsequent review of the original

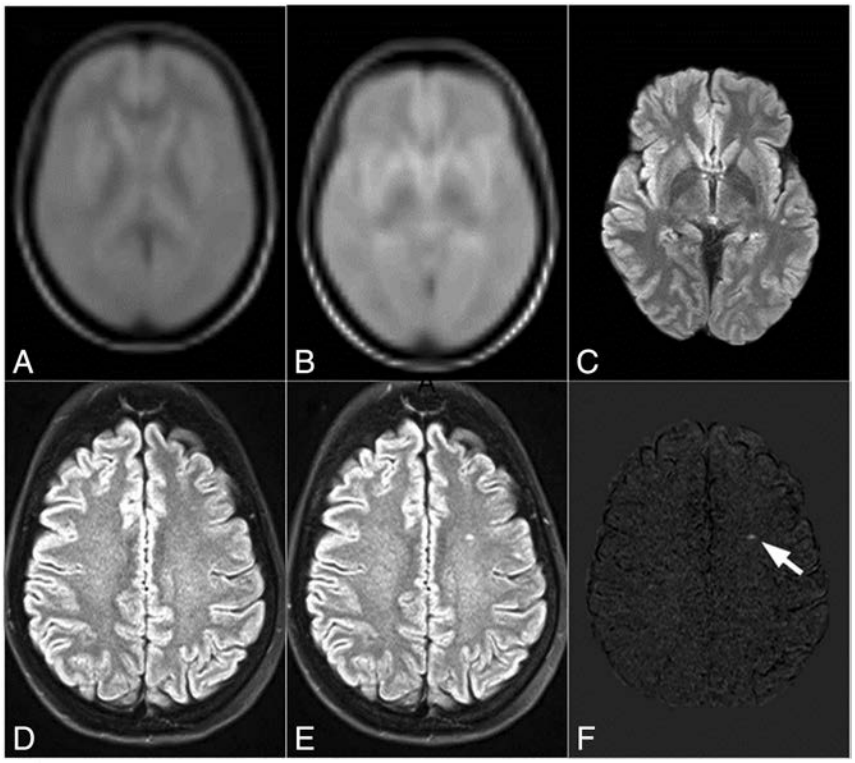

FIG 2. Images to illustrate the processing steps for registration and subtraction. *A*, Generic proton-density-weighted registration target. *B*, The generic template transformed to the average position of the input images. *C*, The final patient-specific registration target formed by intensity-averaging the input images registered to the template at the target position and after skull-stripping. More superior sections of the first (*D*) and second (*E*) input images, registered to the patient-specific registration target. *F*, The difference between the second-input image and the first-input image after correction for differences in their bias fields. The *arrow* indicates a new lesion, which was present at follow-up but absent on the baseline image.

FLAIR images confirmed that lesions originally overlooked were visible in retrospect.

The time required to perform each type of analysis was recorded. There was a gap of at least 4 weeks between the first and second analysis for any given patient, and patient scans were presented in an arbitrary order to avoid familiarity with the images.

Statistical Analysis

The total evaluation time and the number of lesions detected in 77 patients by 3 radiologists were compared for both the qualitative and subtraction-aided review methods. We assumed that the total number of lesions follows a Poisson distribution and modeled our results with a generalized linear mixed model. The model included the method of review (2 levels: qualitative- and subtraction-aided review) as a fixed effect, individual patient and radiologist as random effects, and the natural logarithm function as a link function. To assess sensitivity to detect the presence of a lesion, we created a binary variable to represent the presence or absence of a lesion with a value of 1 when the total number of lesions was greater than zero, and zero otherwise. We assumed that this binary variable follows a Bernoulli distribution and modeled the presence of lesion data by using a generalized linear mixed model approach (logistic generalized linear mixed model). The logistic generalized linear mixed model included the logit function as a link function and the same fixed and random effects structure as described for the Poisson generalized linear mixed model.

To account for increased variability with the mean review time, we transformed the data on total processing time by using the natural logarithm function, and the transformed data were analyzed by using a linear mixed model incorporating the method of review as a fixed effect and individual patient and radiologist as random effects. For all models, a predictor was considered statistically significant if the 2-sided type I error rate was $<5\%$ (ie, $P < .05$). All statistical analyses were performed by using R statistical and computing software, Version 3.3 (http://www.r-project.org/) with appropriate packages (lme4, ggplot2).

RESULTS

Pairs of images from 77 patients (72 men; mean age, 62.8 ± 10.4 years; range, 32–80 years) were evaluated independently by 3 radiologists. These 77 patients had postoperative MR imaging performed at a mean of 7 ± 1.25 weeks after surgery. Five of the 77 (7%) patients had perioperative strokes: Patients 12 and 61 had a lacunar infarct in the right corona radiata, patient 46 had a lacunar infarct in the left corona radiata, patient 18 had a lacunar infarct in the right frontal lobe, and patient 62 had 2 small lacunar infarcts in the right superior parietal lobule and the left medial percentual gyrus.

With just the pre- and postsurgery FLAIR images, on average, 37 new ischemic lesions were identified in 22 patients (median, 1 lesion per patient; range, 1–5 lesions). The anatomic locations of these new lesions were the following: left frontal WM (18 lesions); right frontal WM (9 lesions); right parieto-occipital subcortical WM (2 lesions); left corona radiata (2 lesions); left centrum semiovale (1 lesion); left anterior striatum (2 lesions); and left (1 lesion) and right (2 lesions) cerebellum. Lesions missed during qualitative assessment were frequently subsequently identified among preexisting white matter hyperintensities.

Using the difference image in combination with the pre- and postsurgery FLAIR images, we identified an average of 46 new ischemic lesions in 26 patients (median, 1 lesion per patient; range, 1–8 lesions). Therefore, the number of new ischemic lesions identified increased by 24%, and the number of patients who had new lesions increased by 18% when review was aided by a subtraction image. The anatomic locations of these new lesions were the following: left frontal WM (20 lesions); right frontal WM (9 lesions); left (1 lesion) and right (1 lesion) parieto-occipital subcortical WM; right parietal WM (1 lesion); left temporal lobe (2 lesions); left (2 lesions) and right (1 lesion) corona radiata; left centrum semiovale (2 lesions); left parietal cortex (1 lesion); left

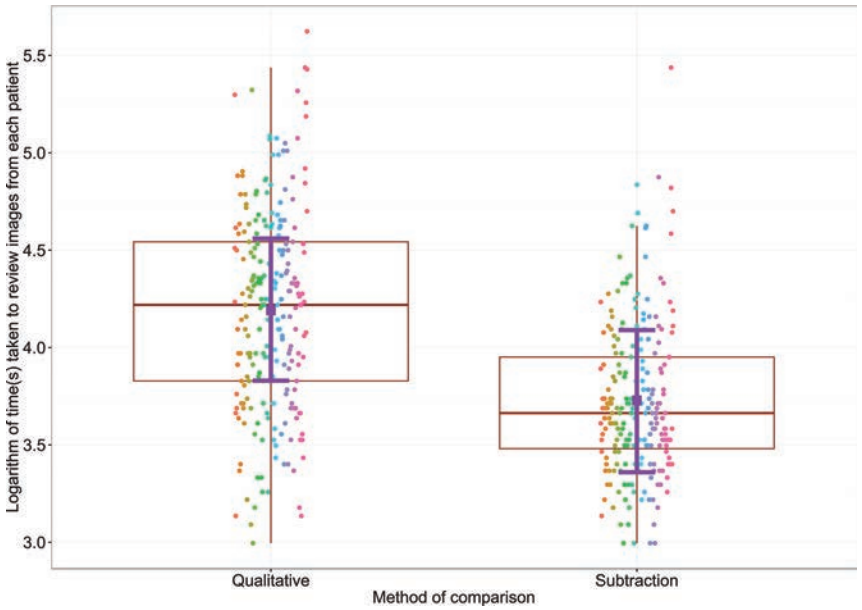

FIG 3. The logarithm of time (seconds) taken to process the data by qualitative comparison and aided by the image-subtraction algorithm. The scatterplots show the triplicate log-transformed time data (of 3 radiologists) for each patient along with boxplots presenting the median, lower, and upper quartiles for each algorithm. Points with the same color represent data from the same patient. The plot also presents the predicted mean time (square marker) along with corresponding 95% confidence intervals (*error bar*) for both methods obtained from a linear mixed model fit to the data.

anterior striatum (2 lesions); pons (1 lesion); superior vermis (1 lesion); and right (2 lesions) cerebellum.

Most lesions identified by qualitative assessment were also identified when aided by the subtraction algorithm. The exceptions were 1 lesion in the left and 2 in the right frontal WM and 1 lesion in the left and 1 in the right cerebellum. On further examination of the original FLAIR images, the lesions in the frontal white matter were very small (<1 mm) and of a level similar to that of the background "mottle." These were confirmed by only 1 of the 3 radiologists. The cerebellar lesions not appreciated on the subtraction image were larger and were definitely present on repeat viewing.

When we pooled the data over all radiologists, the mean lesion counts were 67 and 80 for the qualitative and subtractive methods, respectively, though there was no evidence that the mean lesion counts were significantly different between methods ($P = .101$). When we accounted for the variabilities between patients and radiologists, the logistic generalized regression model suggested that the likelihood of detecting the presence of a lesion was 2.59 (95% CI, 1.18–5.67) times greater with the subtraction compared with the qualitative method ($P = .017$).

When we accounted for the variability in the data between patients (interpatient variability) and between radiologists (interradiologist variability), the mean time to review the images was significantly ($P < .001$) lower with the subtraction algorithm (mean, 42 seconds; 95% CI, 29–60 seconds) compared with qualitative assessment (mean, 66 seconds; 95% CI, 46–96 seconds), reducing the processing time by 37%. Estimates of between-patient variability were slightly higher (0.27; 95% CI, 0.22–0.34) than between-radiologist variability (0.17; 95% CI, 0.07–0.42). Figure 3 presents the log-transformed time data (of 3 radiologists) for each patient alongside the predicted mean time for both algorithms obtained from the linear mixed-model fit to the data.

DISCUSSION

We have demonstrated a method for the registration, subtraction, and bias field correction of serial MR images, which can be applied in longitudinal patient studies. The subtraction image highlights the presence of new lesions, which can be confirmed or refuted on closer inspection of the source images. The method is tailored toward robust detection of focal differences in pathology that develop or resolve between scans.

Axial FLAIR imaging frequently has CSF flow-related artifacts in the posterior fossa, which necessarily result in a more heterogeneous parenchymal background on the subtraction image. On the subtraction image, the preexisting lesions were removed, but new lesions were highlighted as hyperintense, thus aiding detection. Similarly, posterior fossa lesions on FLAIR are sometimes difficult to separate from adjacent flow-related signal hyperintensity and can be easily overlooked, particularly at the periphery of the cerebellum.

Although several other studies have previously used subtraction imaging,[13-18] the procedure outlined here has several advantages. First, it can be used to analyze MR imaging data acquired serially over many time points in an unbiased fashion. Most previous studies have either selected one of the image time points as the registration target[16] or have been restricted to showing the differences between pairs of images by realigning them to a position half-way between the 2 scans.[18] By transforming all of the images to their average position, the current method allows the alignment of any number of image time points. This is achieved by first registering them to a generic atlas target to facilitate relative positioning.

Second, previous studies have incorporated bias field correction by using, for example, the N3 method,[9] in which the input images are individually bias-corrected as the first processing step. However, the N3 method is prone to errors in the bias field correction scheme, leading to residual shading artifacts in the subtracted images. The current method provides an alternative correction scheme that relies on only the assumption that in the absence of bias field differences, tissues that are not involved in focal pathologic changes should remain substantially unchanged in intensity between image acquisitions. Thus, the differences in the bias field between scans can be estimated and used to correct the subtracted images.

We believe that this method could provide a useful tool for radiologists when reviewing serially acquired MR images. First, the time required to review the images was reduced by approximately 37% when using the registered and subtracted images. All

processing was fully automatic and therefore could be performed automatically as an adjunct to the acquisition of new scans and retrieval of previous scans from a PACS system.

Second, the number of new ischemic lesions identified increased by 24%, and the number of patients who had new lesions increased by 18% when using the subtraction images compared with simply viewing the 2 scans. The likelihood of observing a lesion was also 2.6 times greater when using the new algorithm. These represent substantial increases in sensitivity in detecting new ischemic tissue damage. Although this pathology consisted of relatively small ischemic lesions and only new pathology was identified, subtle changes in tissue in other diseases, such as MS, might be equally identified and could prove important in monitoring disease progression or stability and guiding treatment decisions.[19]

On the other hand, when using the subtraction images, 2 lesions in the cerebellum were missed. On subsequent review, these lesions were clearly present in the view of the radiologists.

The 2 scans for each patient were acquired approximately 8–10 weeks apart, so there was little chance for more substantial tissue changes to develop or for cerebral atrophy to advance. We used a rigid-body (translation and rotation) registration to align the 2 scans, which proved adequate in all cases. More sophisticated nonlinear registration[20] would be required for longer follow-up periods or to account for more profound structural changes in the brain, for example, in the follow-up of patients with brain tumor and after an operation or in cases of severe atrophy.

To provide an unbiased image registration, the method uses a generic atlas in the first processing step. Because the atlas is used only to find the approximate head position for the serially acquired images, it is likely that other generic atlases[21,22] could also be used without compromising the quality of the final registration. The scan parameters were kept constant across both scans because the method is unlikely to work well when there are gross differences in contrast between the 2 images. Constraining the scan parameters was easy to do in the context of our study but might be more problematic when patients are rescanned in a routine setting, possibly with different scanner types from different manufacturers. On the other hand, particularly if a 3D acquisition is used, the method should be relatively robust to gross changes in the patient's head position because of the novel bias field correction used. However, the effects of head position and scanner settings would need to be assessed in future studies.

CONCLUSIONS

We have developed a fully automated image registration and subtraction scheme capable of highlighting small changes in serial MR imaging scans of the brain. The method should now be used in larger studies to investigate its clinical potential in monitoring progression in different diseases and for longer time periods.

Disclosures: Mark A. Horsfield—*UNRELATED*: *Stock/Stock Options*: Xinapse Systems Ltd, *Comments*: director and stock holder. Emma Chung—*RELATED*: *Grant*: British Heart Foundation, *Comments*: held an Intermediate Basic Science Research Fellowship funded by the British Heart Foundation.* *Money paid to the institution.

REFERENCES

1. Longstreth WT Jr, Arnold AM, Kuller LH, et al. **Progression of magnetic resonance imaging-defined brain vascular disease predicts vascular events in elderly: the Cardiovascular Health Study.** *Stroke* 2011;42:2970–72 CrossRef Medline
2. Rovira A, Auger C, Alonso J. **Magnetic resonance monitoring of lesion evolution in multiple sclerosis.** *Ther Adv Neurol Disord* 2013; 6:298–310 CrossRef Medline
3. Alpert NM, Berdichevsky D, Levin Z, et al. **Performance evaluation of an automated system for registration and postprocessing of CT scans.** *J Comput Assist Tomogr* 2001;25:747–52 CrossRef Medline
4. Castellino RA. **Computer aided detection (CAD): an overview.** 2005; 23;5:17–19 Medline
5. Vovk U, Pernus F, Likar B. **A review of methods for correction of intensity inhomogeneity in MRI.** *IEEE Trans Med Imaging* 2007;26: 405–21 CrossRef Medline
6. Roemer PB, Edelstein WA, Hayes CE, et al. **The NMR phased array.** *Magn Reson Med* 1990;16:192–225 CrossRef Medline
7. Vemuri P, Kholmovski EG, Parker DL, et al. **Coil sensitivity estimation for optimal SNR reconstruction and intensity inhomogeneity correction in phased array MR imaging.** *Inf Process Med Imaging* 2005;19:603–14 Medline
8. Wicks DA, Barker GJ, Tofts PS. **Correction of intensity nonuniformity in MR images of any orientation.** *Magn Reson Imaging* 1993;11: 183–96 CrossRef Medline
9. Sled JG, Zijdenbos AP, Evans AC. **A nonparametric method for automatic correction of intensity nonuniformity in MRI data.** *IEEE Trans Med Imaging* 1998;17:87–97 CrossRef Medline
10. Patel N, Horsfield MA, Banahan C, et al. **Impact of perioperative infarcts after cardiac surgery.** *Stroke* 2015;46:680–86 CrossRef Medline
11. Horsfield MA, Rocca MA, Pagani E, et al. **Estimating brain lesion volume change in multiple sclerosis by subtraction of magnetic resonance images.** *J Neuroimaging* 2016;26:395–402 CrossRef Medline
12. Taoka T, Iwasaki S, Nakagawa H, et al. **Fast fluid-attenuated inversion recovery (FAST-FLAIR) of ischemic lesions in the brain: comparison with T2-weighted turbo SE.** *Radiat Med* 1996;14:127–31 Medline
13. Bosc M, Heitz F, Armspach JP, et al. **Automatic change detection in multimodal serial MRI: application to multiple sclerosis lesion evolution.** *Neuroimage* 2003;20:643–56 CrossRef Medline
14. Meier DS, Guttmann CR. **Time-series analysis of MRI intensity patterns in multiple sclerosis.** *Neuroimage* 2003;20:1193–209 CrossRef Medline
15. Tan IL, van Schijndel RA, Fazekas F, et al. **Image registration and subtraction to detect active T(2) lesions in MS: an interobserver study.** *J Neurol* 2002;249:767–73 CrossRef Medline
16. Duan Y, Hildenbrand PG, Sampat MP, et al. **Segmentation of subtraction images for the measurement of lesion change in multiple sclerosis.** *AJNR Am J Neuroradiol* 2008;29:340–46 CrossRef Medline
17. Ganiler O, Oliver A, Diez Y, et al. **A subtraction pipeline for automatic detection of new appearing multiple sclerosis lesions in longitudinal studies.** *Neuroradiology* 2014;56:363–74 CrossRef Medline
18. Battaglini M, Rossi F, Grove RA, et al. **Automated identification of brain new lesions in multiple sclerosis using subtraction images.** *J Magn Reson Imaging* 2014;39:1543–49 CrossRef Medline
19. Fazekas F, Soelberg-Sorensen P, Comi G, et al. **MRI to monitor treatment efficacy in multiple sclerosis.** *J Neuroimaging* 2007;17(suppl 1):50S–55S CrossRef Medline
20. Sotiras A, Davatzikos C, Paragios N. **Deformable medical image registration: a survey.** *IEEE Trans Med Imaging* 2013;32:1153–90 CrossRef Medline
21. Mazziotta J, Toga A, Evans A, et al. **A probabilistic atlas and reference system for the human brain: International Consortium for Brain Mapping (ICBM).** *Philos Trans R Soc Lond B Biol Sci* 2001;356: 1293–322 CrossRef Medline
22. Xing W, Nan C, Zuo Z, et al. **Probabilistic MRI brain anatomical atlases based on 1,000 Chinese subjects.** *PLoS One* 2013;8:e50939 CrossRef Medline

Acute Cytotoxic and Vasogenic Edema after Subarachnoid Hemorrhage: A Quantitative MRI Study

J.M. Weimer, S.E. Jones, and J.A. Frontera

ABSTRACT

BACKGROUND AND PURPOSE: The mechanism of early brain injury following subarachnoid hemorrhage is not well understood. We aimed to evaluate if cytotoxic and vasogenic edema are contributing factors.

MATERIALS AND METHODS: A retrospective analysis was conducted in patients with SAH undergoing diffusion-weighted MR imaging within 72 hours of onset. Apparent diffusion coefficient values derived from DWI were evaluated by using whole-brain histograms and 19 prespecified ROIs in patients with SAH and controls with normal findings on MRI. Cytotoxic edema observed outside the ROIs was assessed in patients with SAH. The average median ADC values were compared between patients with SAH and controls and patients with SAH with mild (Hunt and Hess 1–3) versus severe early brain injury (Hunt and Hess 4–5).

RESULTS: We enrolled 33 patients with SAH and 66 controls. The overall average median whole-brain ADC was greater for patients with SAH (808×10^{-6} mm^2/s) compared with controls (788×10^{-6} mm^2/s, $P < .001$) and was higher in patients with SAH across ROIs after adjusting for age: cerebral gray matter (826 versus 803×10^{-6} mm^2/s, $P = .059$), cerebral white matter (793 versus 758×10^{-6} mm^2/s, $P = .023$), white matter tracts (797 versus 739×10^{-6} mm^2/s, $P < .001$), and deep gray matter (754 versus 713×10^{-6} mm^2/s, $P = .016$). ADC values trended higher in patients with Hunt and Hess 4–5 versus those with Hunt and Hess 1–3. Early cytotoxic edema was observed in 13 (39%) patients with SAH and was more prevalent in those with severe early brain injury (87.5% of patients with Hunt and Hess 4–5 versus 24.0% of those with Hunt and Hess 1–3, $P = .001$).

CONCLUSIONS: Age-adjusted ADC values were globally increased in patients with SAH compared with controls, even in normal-appearing brain regions, suggesting diffuse vasogenic edema. Cytotoxic edema was also present in patients with SAH and correlated with more severe early brain injury.

ABBREVIATIONS: EBI = early brain injury; HH = Hunt and Hess

Early brain injury (EBI) incurred during aneurysm rupture in spontaneous subarachnoid hemorrhage is a major predictor of poor functional outcome,[1,2] yet the mechanism for EBI is not well-understood. In both animal and human models, SAH leads to transiently elevated intracranial pressure with concomitant inadequate cerebral blood flow and, in severe cases, intracranial circulatory arrest.[3,4] This transient global hypoperfusion is associated with endothelial activation, microthrombosis, ischemia, and vasogenic edema in animal models.[5-7] As a part of routine clinical MR imaging at many institutions, diffusion-weighted imaging presents a unique opportunity for the study of patients with SAH in the acute period. Apparent diffusion coefficient values may serve as a practical and useful biomarker for the severity of EBI following SAH. In humans, we and others have demonstrated that MR imaging–detected infarctions on DWI occur acutely after SAH and before the onset of delayed cerebral ischemia/vasospasm.[8-11]

These infarctions are more common in patients with more severe EBI (Hunt and Hess [HH] 4–5); occur in unusual, nonvascular patterns (eg, corpus callosum, bilateral medial frontal lobes); and are associated with an increased risk of delayed cerebral ischemia and worse 3-month functional outcomes.[8-10] The volume of infarction associated with worse functional outcomes is small, however.[8] Thus, this finding led us to hypothesize that conventional, nonquantitative MR imaging techniques are not sensitive enough to detect the full extent of brain injury.

Received October 5, 2016; accepted after revision December 15.

From the Cerebrovascular Center of the Neurological Institute (J.M.W., J.A.F.) and the Imaging Institute (S.E.J.), Cleveland Clinic, Cleveland, Ohio.

This work was supported, in part, by the American Heart Association Student Scholarship in Cerebrovascular Disease and Stroke.

Please address correspondence to Jennifer A. Frontera, MD, FNCS, Cleveland Clinic Foundation, Cerebrovascular Center, 9500 Euclid Ave, S80, Cleveland, OH 44195; e-mail: frontej@ccf.org

Indicates article with supplemental on-line photo.

http://dx.doi.org/10.3174/ajnr.A5181

We hypothesized that patients with SAH (compared with controls) would demonstrate global reductions in apparent diffusion coefficient values, indicating diffuse cytotoxic edema presumably due to ischemia/hypoperfusion, when whole-brain ADC mapping and ROI quantitative analyses were applied. We further hypothesized that patients with SAH with evidence of severe EBI would have a greater burden of cytotoxic edema than those with mild EBI.

MATERIALS AND METHODS

Subject Enrollment and Data Collection

A retrospective review of prospectively enrolled patients with spontaneous SAH was conducted between February 2013 and March 2015 as part of the Intracranial Hemorrhage ICU Project of Cleveland Clinic and Early Status of Coagulation, Platelet Activation and Outcome after Subarachnoid Hemorrhage (Principal Investigator, J.A.F.).[1] As part of these studies, all eligible patients admitted to the neurologic intensive care unit within 72 hours of the onset of SAH symptoms were approached for enrollment. Inclusion criteria were being 18 years of age or older; SAH diagnosed by CT, MR imaging, or lumbar puncture; consent to participate in 3- and 12-month follow-up interviews; and DWI performed within 72 hours of ictus, before the clinical or radiographic onset of delayed cerebral ischemia/cerebral vasospasm (which typically occurs 3–14 days after aneurysm rupture). Exclusion criteria included SAH due to nonaneurysmal causes such as trauma, arteriovenous malformation, dural arteriovenous fistula, cavernous malformation, vasculitis, or arterial dissection. The severity of EBI due to SAH was assessed at admission by using the Hunt and Hess scale[12] and was dichotomized as mild (HH 1–3) versus severe (HH 4–5).

The control group was identified from a population of consecutive patients undergoing brain DWI on the same 1.5T inpatient scanners and were matched to patients with SAH in a 2:1 ratio. Records were queried from the hospital electronic record on inpatients 40–60 years of age (because this is the typical age range of patients with spontaneous SAH) undergoing brain MR imaging between January 2010 and December 2013 (the most recent time frame in which control data were available). Radiologists' image reports were reviewed to identify patients with normal findings on MRI and no evidence of intracranial pathology. Images were then independently reviewed by 2 reviewers (J.A.F., J.M.W.) to confirm the absence of intracranial pathology. Basic and demographic data were collected for both patients with SAH and controls. Admission clinical and radiographic data were also recorded for patients with SAH. This study was approved by our institutional review board.

MR Imaging Postprocessing and Analysis

All MRIs were performed on the same 1.5T whole-body scanners (Magnetom; Siemens, Erlangen, Germany), and diffusion-weighted images were obtained by using a standard single-shot, spin-echo, echo-planar sequence with b-values of 0 mm^2/s and 1000 mm^2/s. ADC images were automatically generated from diffusion-weighted sequences ($b=0$ and $b=1000$ series) following acquisition. To confirm their accuracy, ADC images were also reconstructed off-line by using Matlab R2013 software (MathWorks, Natick, Massachusetts). Because differences between the scanner-generated and off-line-reconstructed images were negligible, representing <1% of the maximal ADC signal, automatically generated ADC images were used for subsequent analyses.

Brain extractions were next performed on scans of all controls and patients with SAH with the FSL Brain Extraction Tool (http://fsl.fmrib.ox.ac.uk/fsl/fslwiki/BET),[13] available through FSL (http://www.fmrib.ox.ac.uk/fsl; 2015) as part of the Mango image viewing software package (http://ric.uthscsa.edu/mango; 2015). Floor and ceiling threshold filters were applied to limit the images to voxel intensities between 250 and 1250×10^{-6} mm^2/s to restrict contributions from any remaining nonparenchymal signal, such as from the extra-axial or subarachnoid space (thereby excluding blood products in the subarachnoid space and intraventricular blood). The median whole-brain ADC was calculated for each subject. Whole-brain histograms with bin widths of 10×10^{-6} mm^2/s were generated. Histograms were normalized to account for variations in brain volume among patients, and histogram peaks were calculated. Smooth curves were fit to model the histograms by applying a moving average low-pass filter. Median ADC values were compared for both patients with SAH versus control subjects and those with mild EBI (Hunt and Hess 1–3) versus severe EBI (Hunt and Hess 4–5) as performed elsewhere.[11]

Traditional regional spatial profile analysis was also performed by using standardized volumetric software in a manner similar to that previously described.[14] Images were loaded into the Medical Image Processing, Analysis, and Visualization software package (National Institutes of Health, Bethesda, Maryland; 2014), and symmetric ROIs were placed bilaterally over 19 predefined normal-appearing regions: gray matter of the frontal, parietal, occipital, and temporal lobes; white matter of the frontal, parietal, occipital, and temporal lobes; internal capsule, genu, and splenium of the corpus callosum; caudate head, lentiform nucleus, and thalamus; midbrain; hippocampus; pons; cerebellar nuclei; and white matter (On-line Figure).[14] Median ADC values were reported for each subject ROI due to the possibility of individual voxel outliers within an individual ROI. Conclusions were unchanged if mean ADC values were used during ROI analysis and therefore were not reported. Average median ADC intensity was calculated for the following ROI combinations: cerebral gray matter (frontal, parietal, occipital, and temporal); cerebral white matter (frontal, parietal, occipital, and temporal); white matter tracts (genu, splenium, and internal capsule); deep gray matter (thalamus, caudate, and lentiform nucleus); and summed ROIs (all 19 regions). Hyperintense FLAIR signal related to remote lesions (eg, old stroke) or transependymal periventricular edema was excluded from ROI analysis. Ischemic lesions were not included in summed ROI comparisons and are reported separately as their own ROI group.

For patients with SAH, DWI and ADC images were also reviewed for evidence of cytotoxic edema outside prespecified ROIs, defined qualitatively as DWI hyperintense/ADC hypointense lesions. Cytotoxic edema lesions were manually traced to calculate total volume. Procedural-related lesions, such as those along known external ventricular drain tracts or craniotomy tra-

Table 1: Summary of admission, demographic, clinical, and radiographic characteristics of patients with SAH[a]

	Patients with SAH (n = 33)	Controls (n = 66)	P Value
Basic and demographic data			
Age (yr)	59 (44.5–66)	49 (43.4–53.2)	<.001[b]
Female sex	16 (48.5%)	41 (62.1%)	.196
Race			
Caucasian	25 (75.8%)	47 (72.3%)	.343
Black	8 (24.3%)	14 (21.5%)	
Other	0	4 (6.2%)	
History of smoking	21 (63.6%)	34 (51.5%)	.253
History of alcohol abuse	7 (22.6%)	10 (15.2%)	.370
Hypertension	14 (45.2%)	33 (50.0%)	.657
Diabetes	4 (12.9%)	14 (21.2%)	.326
Hyperlipidemia	12 (38.7%)	24 (36.4%)	.824
Aspirin use	10 (31.3%)	22 (33.3%)	.837
History of ischemic stroke	1 (3.0%)	0	–
History of intracranial hemorrhage	0	0	–
History of head trauma	0	0	–
History of brain tumor	0	0	–
Family history of aneurysm	4 (13.3%)	0	–
Cocaine use within 24 hr of ictus	1 (3.0%)	0	–
Admission clinical and radiographic data			
Premorbid modified Rankin Scale score[29]	0 (0–0)		
HH grade[12]			
1	5 (15.2%)		
2	14 (42.4%)		
3	6 (18.2%)		
4	5 (15.2%)		
5	3 (9.1%)		
Glasgow Coma Score	15 (11.5–15)		
APACHE II score[30]	7 (3–10)		
Modified Fisher grade[15]			
1	4 (12.1%)		
2	2 (6.1%)		
3	18 (54.5%)		
4	9 (27.3%)		
Hijdra sum score[31]	13.5 (6–21)		
Cerebral edema on admission CT	8 (25.0%)		
External ventricular drain placed	14 (42.4%)		

Note:—APACHE II indicates Acute Physiology and Chronic Health Evaluation II.
[a] Values are reported as No. (%) or median (interquartile range). Comparative basic and demographic data are provided for controls.
[b] Statistical significance.

jectories, and lesions due to the presence of blood products were manually excluded from analysis.

Statistical Plan

Statistical analyses were performed by using the JMP 9.0 software package (SAS Institute, Cary, North Carolina; 2010). Univariate comparisons between patients with SAH and controls and between patients with SAH with severe (HH 4–5) versus mild (HH 1–3) EBI were performed by using the χ^2 test for categoric variables and the Wilcoxon rank sum test for continuous variables. Multisample comparisons were performed with the Kruskal-Wallis test. For average median ADC comparisons between patients with SAH and controls with whole-brain and combined ROI measurements (cerebral white matter, cerebral gray matter, white matter tracts, deep gray matter, and summed ROIs), multivariable logistic regression models adjusted for patient age were also performed because there were significant age differences between patients with SAH and controls. Correlations between ADC values and age, the modified Fisher score, the presence of elevated intracranial pressure, and external ventricular drainage were evaluated by using 2-sided Spearman correlation coefficients.

RESULTS

During the study period, 33 patients with SAH underwent MR imaging within 72 hours of ictus and 66 controls 40–60 years of age with normal-appearing MR imaging were evaluated. The most common indications for MR imaging in the control group were headache, altered mental status, weakness, and vertigo/dizziness/syncope. Basic and demographic data for patients with SAH and controls and SAH admission data are summarized in Table 1. The median age of patients with SAH (59 years; interquartile range, 44.5–66 years) was significantly older than that in the control cohort (49 years; interquartile range, 43.4–53.2; $P < .001$). There were no other significant baseline differences, including sex, race, history of smoking, history of alcohol abuse, hypertension, diabetes, hyperlipidemia, or aspirin use. Eight patients with SAH (24.2%) had severe EBI (HH 4–5) on admission. Most patients with SAH had either modified Fisher grade 3 (n = 18, 54.5%) or modified Fisher grade 4 bleeds (n = 9, 27.3%).[15]

The average median whole-brain ADC value was significantly higher for the SAH cohort (808×10^{-6} mm^2/s) compared with the control cohort (788×10^{-6} mm^2/s, $P < .001$). Similarly, whole-brain histograms were right-shifted toward higher ADC values in the SAH cohort compared with controls (Fig 1). The peak of the averaged SAH histogram was located at the bin centered at 780×10^{-6} mm^2/s, while the peak of the averaged control histogram was located at the bin centered at 750×10^{-6} mm^2/s.

Average median ADC values for ROIs in patients with SAH and controls are reported in Table 2. Across all ROIs, the average median ADC was higher in the SAH cohort compared with the control group (795×10^{-6} mm^2/s for patients with SAH versus 759×10^{-6} mm^2/s for controls, $P < .001$). The greatest differences were observed in the white matter tracts and the cerebral white matter of the brain, along with deep gray matter structures, while differences among gray matter ROIs were smaller.

When we compared patients with SAH with mild EBI (HH 1–3) versus severe EBI (HH 4–5), the average median whole-brain ADC values were similar between groups (808×10^{-6} mm^2/s for HH 1–3 versus 811×10^{-6} mm^2/s for HH 4–5, P = .514). However, the histogram peak for those with mild EBI

was centered at 780 × 10^{-6} mm^2/s, while the histogram peak for those with severe EBI was centered at 800 × 10^{-6} mm^2/s, resulting in the distributions shown in Fig 2. Across most individual ROIs, the average median ADC intensity was greater in patients with SAH with severe EBI compared with those with mild EBI (Table 3), though the results were not statistically significant. Similarly, there was no significant difference in average median ADC values for summed areas of cerebral gray matter ($P = .159$), cerebral white matter ($P = .147$), deep gray matter ($P = .074$), white matter tracts ($P = .916$), and total summed ROIs ($P = .200$) between patients with SAH with mild-versus-severe EBI.

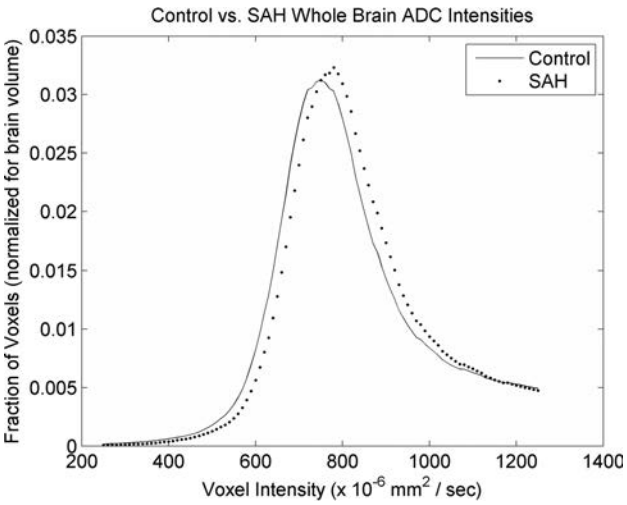

FIG 1. Composite histogram curves from all patients plotting fractions of voxels by voxel intensity in apparent diffusion coefficient maps of controls (*line*) and subjects with SAH (*dots*).

Table 2: Average median ADC values in ROIs in patients with SAH and controls[a]

ROI	ADC (×10^{-6} mm^2/s) Control (n = 66)	ADC (×10^{-6} mm^2/s) SAH (n = 33)	P Value	Age-Adjusted P Value
Cerebral gray matter	803 (36.2)	826 (37.7)	.001[b]	.059
Frontal	802 (65.2)	823 (66.4)	.137	
Parietal	820 (48.0)	843 (53.5)	.025[b]	
Occipital	798 (67.7)	814 (51.7)	.042[b]	
Temporal	791 (43.6)	822 (60.6)	.006[b]	
Cerebral white matter	758 (33.9)	793 (44.9)	.001[b]	.023[b]
Frontal	735 (53.0)	768 (55.8)	.007[b]	
Parietal	767 (50.9)	799 (51.3)	.007[b]	
Occipital	764 (36.8)	795 (47.7)	.003[b]	
Temporal	767 (45.4)	809 (61.8)	.003[b]	
White matter tracts	739 (33.5)	797 (59.3)	<.001[b]	<.001[b]
Genu	761 (45.2)	816 (69.1)	<.001[b]	
Splenium	736 (45.6)	789 (91.4)	<.001[b]	
Internal capsule	719 (53.2)	785 (96.4)	<.001[b]	
Deep gray matter	713 (27.4)	754 (59.6)	<.001[b]	.016[b]
Thalamus	730 (45.1)	777 (86.8)	.020[b]	
Caudate	705 (37.2)	739 (65.7)	.002[b]	
Lentiform	705 (45.5)	747 (67.5)	<.001[b]	
Hippocampus	854 (67.7)	878 (64.8)	.072	
Midbrain	795 (93.5)	813 (47.4)	.006[b]	
Pons	706 (50.6)	756 (54.6)	<.001[b]	
Cerebellar gray matter	756 (48.9)	796 (67.7)	.001	
Cerebellar white matter	720 (50.3)	731 (43.7)	.214	
Summed ROIs	759 (23.3)	795 (36.9)	<.00[b]	<.001[b]

[a] Values are reported as average median with SD.
[b] Statistical significance.

ADC values increased significantly with age in the combined cohort of controls and patients with SAH (Pearson correlation coefficient for median summed ROI ADC and age = 0.514, $P <$ .001), though this effect was primarily driven by patients with SAH (Pearson correlation coefficient = 0.602, $P <$ .001), while there was no correlation between age and ADC values among controls alone (Pearson correlation coefficient = 0.012, $P =$ .924). Among patients with SAH, ADC values increased as the modified Fisher score increased (median summed ROI modified Fisher score 1: 766 × 10^{-6} mm^2/s; modified Fisher score 2: 754 × 10^{-6} mm^2/s; modified Fisher score 3: 797 × 10^{-6} mm^2/s; modified Fisher score 4: 813 × 10^{-6} mm^2/s; Pearson correlation coefficient = 0.440, $P = .010$). There was no correlation between ADC values and sex, elevated intracranial pressure, or external ventricular drainage.

In multivariable analysis, after we adjusted for age, whole-brain ADC values were still significantly higher in patients with SAH compared with controls ($P = .028$). Similarly, after we adjusted for age, the average median ADC values remained higher in grouped ROIs for cerebral white matter ($P = .023$), white matter tracts ($P < .001$), deep gray matter ($P = .016$), and summed ROIs ($P < .001$, Table 2).

Evidence of cytotoxic edema was observed in 13 (39%) patients with SAH. Cytotoxic edema was more prevalent in patients with SAH with more severe EBI (87.5% of patients with HH 4–5 versus 24.0% of patients with HH 1–3, $P = .001$). The median volume of ischemia was also higher in patients with HH 4–5 than in those with HH 1–3 (0.8 mL; range, 0–88.8 versus 0 mL; range, 0–2.4; $P = .001$). The average median ADC value of ischemic lesions across all patients with SAH was 605 × 10^{-6} mm^2/s. There was no significant difference in ischemic ADC values between patients with mild and severe EBI (602 × 10^{-6} mm^2/s for HH 1–3 versus 619 × 10^{-6} mm^2/s for HH 4–5, $P =$ .721).

DISCUSSION

This study is one of the first to provide quantitative evidence of both early cytotoxic and vasogenic edema occurring within 72 hours of SAH compared with controls. On the basis of our previous work,[8] we anticipated globally decreased ADC values in patients with SAH compared with controls because we hypothesized that the abrupt increase in intracranial pressure that follows aneurysm rupture would result in inadequate cerebral blood flow and subsequent ischemia, similar to cardiac arrest models.[16] Indeed, animal studies demonstrate increased intracranial pressure followed by cerebral blood flow values below the infarction threshold immediately after SAH onset.[17] Other mechanisms may concomitantly reduce cerebral blood flow, such as primary SAH-induced vasoconstriction, as shown in preclinical

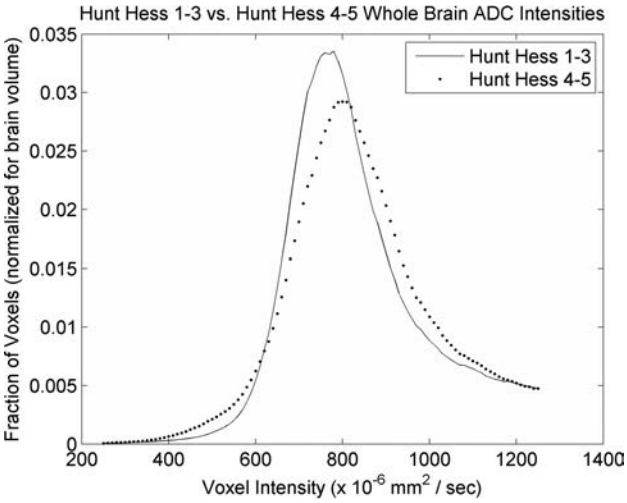

FIG 2. Composite histogram curves from all patients with SAH plotting the fraction of voxels by voxel intensity in apparent diffusion coefficient maps of patients with SAH with Hunt and Hess 1–3 (*line*) and Hunt and Hess 4–5 (*dots*).

Table 3: Average median ADC values in ROIs among patients with SAH with HH 1–3 versus 4–5[a]

ROI	ADC (×10^{-6} mm^2/s) HH 1–3 (*n* = 25)	ADC (×10^{-6} mm^2/s) HH 4–5 (*n* = 8)	*P* Value
Cerebral gray matter	823 (25.9)	833 (64.1)	.159
Frontal	821 (60.9)	831 (85.9)	.785
Parietal	844 (55.4)	843 (50.6)	.753
Occipital	813 (41.0)	819 (80.3)	.556
Temporal	816 (52.1)	840 (83.5)	.172
Cerebral white matter	787 (43.1)	811 (48.7)	.147
Frontal	764 (57.2)	781 (52.6)	.425
Parietal	801 (49.8)	792 (58.7)	1.000
Occipital	789 (45.8)	814 (51.6)	.115
Temporal	793.5 (55.4)	856 (59.7)	.014[b]
White matter tracts	796 (58.4)	798 (66.1)	.916
Genu	810 (63.5)	834 (86.6)	.401
Splenium	799 (79.1)	758 (123.8)	.950
Internal capsule	780 (103.7)	801 (71.9)	.401
Deep gray matter	748 (52.1)	773 (80.0)	.074
Thalamus	763 (81.4)	820 (94.7)	.097
Caudate	737 (57.8)	743 (90.8)	.130
Lentiform	744 (64.4)	756 (80.7)	.239
Hippocampus	881 (62.9)	870 (74.4)	1.000
Midbrain	811 (43.2)	818 (61.9)	.378
Pons	756 (50.3)	756 (70.4)	.834
Cerebellar gray matter	794 (75.5)	800 (36.8)	.324
Cerebellar white matter	730 (45.6)	732 (39.5)	.883
Summed ROIs	792 (31.7)	803 (51.7)	.200

[a] Values are reported as average median with SDs.
[b] Statistical significance.

models using laser Doppler flow analysis.[18] Hyperacute MR imaging in SAH endovascular perforation rat models has shown sharp ipsilateral declines in ADC within 2 minutes of SAH onset, followed by ADC value reductions in the contralateral cerebral cortex.[19] While we did observe evidence of cytotoxic edema (reduced ADC values, which may represent ischemia) in 87.5% of patients with SAH with severe EBI, the volume of cytotoxic edema was too small to account for the clinical differences between those with severe-versus-mild EBI.

Instead, we noted diffusely increased ADC values in normal-appearing brain parenchyma in patients with SAH compared with controls and relatively higher ADC values in patients with SAH with more severe EBI. These data suggest the early presence of diffuse vasogenic edema, which is a direct consequence of abnormal blood-brain barrier permeability. Animal models of SAH demonstrate cerebral microvessel endothelial basal lamina disruption, acute loss of collagen IV,[5] and increased microvessel permeability within minutes of SAH onset.[20] Resultant blood-brain barrier breakdown and inflammation are evidenced by the escape of platelet aggregates and neutrophils into the brain parenchyma.[6,21] Several other clinical studies have identified an increase in immunologic and inflammatory markers in patients with both unruptured intracranial aneurysms and subarachnoid hemorrhage.[1,22,23] The association of higher ADC values with higher modified Fisher scores (and hence more intracranial hemorrhage) in our study suggests that the presence of blood products may play a role in the development of vasogenic edema.

Other MR imaging studies performed in patients with SAH corroborate our findings. In one study, the volume of DWI and FLAIR hyperintensities (assessed through manual ROI segmentation and documented within 48 hours of SAH ictus) was found to correlate with worse admission neurologic status and poor 3-month functional outcomes.[24] However, much of the FLAIR signal changes in this study were related to chronic injury in addition to the evolution of DWI positive for ischemic lesions and transependymal edema, possibly due to hydrocephalus. Our data do not demonstrate a significant association of intracranial pressure or external ventricular drain use and ADC values, suggesting that hydrocephalus and transependymal edema are not the causes of higher ADC measures. Additionally, elevated ADC values occurred in ROIs that are not immediately juxtaposed to the ventricles, where transependymal edema occurs.

In another analysis, 100 patients with aneurysmal SAH underwent DWI evaluation an average of 9 days after bleed onset.[25] In this study, normal-appearing brain parenchyma had significantly higher ADC in the cerebral white matter and deep gray matter compared with healthy age-matched volunteers, while cerebral gray matter did not significantly differ between groups. Although evidence of radiographic vasospasm was not described, symptomatic vasospasm was observed in 14% of patients in this cohort. The authors also found that age was significantly associated with higher ADC values, but admission neurologic status (Hunt and Hess grades 1–2 versus 3–4, no subjects with Hunt and Hess 5 scores), treatment (surgical clipping versus endovascular coiling), and the severity of bleeding (modified Fisher grades 1–2 versus 3–4) were not significantly associated with ADC values. Limitations of this study include MRIs being performed during the vasospasm period (typically days 3–14 following aneurysm rupture) and signal change possibly representing pathology related to vasospasm rather than EBI due to aneurysm rupture.

In contrast to the above study, in which increases in ADC values were observed predominantly in the white matter and deep gray matter, we observed increases diffusely, including in the cortical gray matter, brain stem, and cerebellum. The timing of MR imaging in our study may account, in part, for this difference. Elevated ADC values have also been observed in other types of neurologic injury. In a study of traumatic brain injury, higher

whole-brain peak ADC in normal-appearing parenchyma was significantly associated with worse Glasgow Coma Scores.[26] While we found a trend toward higher ADC values in patients with SAH with worse admission neurologic status, our study was underpowered to detect a significant difference.

Although elevated ADC is typically due to increased extracellular water content, breakdown of the blood-brain barrier, and vasogenic edema, 1 additional possibility includes the pseudonormalization of ADC values during the subacute stages of ischemia. While there is some evidence of ADC heterogeneity early after acute ischemia,[27] the overall time course of ischemic ADC changes involves 2 well-defined phases: an early reduction phase lasting between 96 and 144 hours, followed by a late elevation phase in which ADC values return to normal and even exceed normative values.[28] Our study investigated an earlier time period of SAH, notably the acute phase lasting the first 72 hours. While we observed evidence of early brain ischemia in patients with SAH, ischemic lesions were often punctate and randomly distributed. The low volumes of ischemia, the presence of elevated ADC in patients with SAH without evidence of acute ischemia, and a short timeframe from ictus to imaging are inconsistent with pseudonormalization and instead are strongly supportive of the occurrence of global vasogenic edema early after SAH.

Some limitations of our study should be mentioned. Because this was a retrospective study, there is a patient selection bias. MR imaging is not routinely performed at our institution following SAH, and patients who underwent MR imaging may differ from those who did not. Furthermore, because MR imaging was performed as part of routine clinical practice, we were unable to account for possible subtle differences in patient movement or the effects of magnetic susceptibility, which may influence ADC values. Another limitation was that though the control group had normal MR imaging findings, these patients were not healthy controls but rather patients with a clinical symptom that prompted an MR imaging evaluation. It was necessary to select a control group that underwent imaging on the same inpatient MR imaging scanner to limit technical confounders. Hence, it was more expedient to use a patient group with normal-appearing MR imaging findings (based on neuroradiologist conventional assessment) rather than healthy controls who would be imaged on a different outpatient MR imaging scanner. We performed a 2:1 control to patients with SAH analysis to maximize our statistical power to detect a difference between control and SAH ADC values. Due to the low number of patients with SAH, we were unable to detect a significant association of ADC values with evidence of EBI or worse admission neurologic status. Although we did observe trends for higher ADC values in patients with HH 4–5, a larger study would be necessary to confirm this effect. Finally, our patients with SAH were older than the controls. Previous studies have demonstrated increases in ADC values with age. However, even after controlling for age, differences in ADC values remained significant.

CONCLUSIONS

We observed evidence of early cytotoxic and vasogenic edema occurring within 72 hours of SAH ictus. Patients with SAH had significantly higher whole-brain and ROI ADC values than controls. Those with more EBI had significantly more cytotoxic edema and trended toward higher ADC values (more vasogenic edema) than those with better admission neurologic status. Both cytotoxic and vasogenic edema may be related to the mechanism of EBI following SAH or may represent biomarkers for the severity of EBI. Further study is necessary to determine whether either MR imaging marker is a significant predictor of functional outcome.

Disclosures: Jonathan M. Weimer—*RELATED*: *Grant*: American Heart Association, *Comments*: research supported in part by the American Heart Association Student Scholarship in Cerebrovascular Disease and Stroke.

REFERENCES

1. Frontera JA, Provencio JJ, Sehba FA, et al. **The role of platelet activation and inflammation in early brain injury following subarachnoid hemorrhage.** *Neurocrit Care* 2017;26:48–57 CrossRef Medline
2. Wartenberg KE, Schmidt JM, Claassen J, et al. **Impact of medical complications on outcome after subarachnoid hemorrhage.** *Crit Care Med* 2006;34:617–23, quiz 624 Medline
3. Grote E, Hassler W. **The critical first minutes after subarachnoid hemorrhage.** *Neurosurgery* 1988;22:654–61 CrossRef Medline
4. Sehba FA, Bederson JB. **Mechanisms of acute brain injury after subarachnoid hemorrhage.** *Neurol Res* 2006;28:381–98 CrossRef Medline
5. Sehba FA, Mostafa G, Friedrich V Jr, et al. **Acute microvascular platelet aggregation after subarachnoid hemorrhage.** *J Neurosurg* 2005; 102:1094–100 CrossRef Medline
6. Friedrich V, Flores R, Muller A, et al. **Reduction of neutrophil activity decreases early microvascular injury after subarachnoid haemorrhage.** *J Neuroinflammation* 2011;8:103 CrossRef Medline
7. Sehba FA, Friedrich V. **Early micro vascular changes after subarachnoid hemorrhage.** *Acta Neurochir Suppl* 2011;110(Pt 1):49–55 CrossRef Medline
8. Frontera JA, Ahmed W, Zach V, et al. **Acute ischaemia after subarachnoid haemorrhage, relationship with early brain injury and impact on outcome: a prospective quantitative MRI study.** *J Neurol Neurosurg Psychiatry* 2015;86:71–78 CrossRef Medline
9. Hadeishi H, Suzuki A, Yasui N, et al. **Diffusion-weighted magnetic resonance imaging in patients with subarachnoid hemorrhage.** *Neurosurgery* 2002;50:741–47; discussion 747–48 Medline
10. Sato K, Shimizu H, Fujimura M, et al. **Acute-stage diffusion-weighted magnetic resonance imaging for predicting outcome of poor-grade aneurysmal subarachnoid hemorrhage.** *J Cereb Blood Flow Metab* 2010;30:1110–20 CrossRef Medline
11. Wartenberg KE, Sheth SJ, Michael Schmidt J, et al. **Acute ischemic injury on diffusion-weighted magnetic resonance imaging after poor grade subarachnoid hemorrhage.** *Neurocrit Care* 2011;14: 407–15 CrossRef Medline
12. Hunt WE, Hess RM. **Surgical risk as related to time of intervention in the repair of intracranial aneurysms.** *J Neurosurg* 1968;28:14–20 CrossRef Medline
13. Smith SM. **Fast robust automated brain extraction.** *Hum Brain Mapp* 2002;17:143–55 CrossRef Medline
14. Mlynash M, Campbell DM, Leproust EM, et al. **Temporal and spatial profile of brain diffusion-weighted MRI after cardiac arrest.** *Stroke* 2010;41:1665–72 CrossRef Medline
15. Frontera JA, Claassen J, Schmidt JM, et al. **Prediction of symptomatic vasospasm after subarachnoid hemorrhage: the modified Fisher scale.** *Neurosurgery* 2006;59:21–27; discussion 21–27 CrossRef Medline
16. Wijman CA, Mlynash M, Caulfield AF, et al. **Prognostic value of brain diffusion-weighted imaging after cardiac arrest.** *Ann Neurol* 2009;65:394–402 CrossRef Medline
17. Veelken JA, Laing RJC, Jakubowski J. **The Sheffield model of sub-**

arachnoid hemorrhage in rats. *Stroke* 1995;26:1279–84; discussion 1284 CrossRef Medline
18. Bederson JB, Germano IM, Guarino L. **Cortical blood flow and cerebral perfusion pressure in a new noncraniotomy model of subarachnoid hemorrhage in the rat.** *Stroke* 1995;26:1086–91; discussion 1091–92 Medline
19. Busch E, Beaulieu C, de Crespigny A, et al. **Diffusion MR imaging during acute subarachnoid hemorrhage in rats.** *Stroke* 1998;29:2155–61 CrossRef Medline
20. Friedrich V, Flores R, Muller A, et al. **Luminal platelet aggregates in functional deficits in parenchymal vessels after subarachnoid hemorrhage.** *Brain Res* 2010;1354:179–87 CrossRef Medline
21. Friedrich V, Flores R, Muller A, et al. **Escape of intraluminal platelets into brain parenchyma after subarachnoid hemorrhage.** *Neuroscience* 2010;165:968–75 CrossRef Medline
22. Hussain S, Barbarite E, Chaudhry NS, et al. **Search for biomarkers of intracranial aneurysms: a systematic review.** *World Neurosurg* 2015;84:1473–83 CrossRef Medline
23. Chen S, Feng H, Sherchan P, et al. **Controversies and evolving new mechanisms in subarachnoid hemorrhage.** *Prog Neurobiol* 2014;115:64–91 CrossRef Medline
24. De Marchis GM, Filippi CG, Guo X, et al. **Brain injury visible on early MRI after subarachnoid hemorrhage might predict neurological impairment and functional outcome.** *Neurocrit Care* 2015;22:74–81 CrossRef Medline
25. Liu Y, Soppi V, Mustonen T, et al. **Subarachnoid hemorrhage in the subacute stage: elevated apparent diffusion coefficient in normal-appearing brain tissue after treatment.** *Radiology* 2007;242:518–25 CrossRef Medline
26. Shanmuganathan K, Gullapalli RP, Mirvis SE, et al. **Whole-brain apparent diffusion coefficient in traumatic brain injury: correlation with Glasgow Coma Scale score.** *AJNR Am J Neuroradiol* 2004;25:539–44 Medline
27. Nagesh V, Welch KMA, Windham JP, et al. **Time course of ADCw changes in ischemic stroke: beyond the human eye!** *Stroke* 1998;29:1778–82 Medline
28. Schlaug G, Siewert B, Benfield A, et al. **Time course of the apparent diffusion coefficient (ADC) abnormality in human stroke.** *Neurology* 1997;49:113–19 CrossRef Medline
29. van Swieten JC, Koudstaal PJ, Visser MC, et al. **Interobserver agreement for the assessment of handicap in stroke patients.** *Stroke* 1988;19:604–07 CrossRef Medline
30. Hartley C, Cozens A, Mendelow AD, et al. **The Apache II scoring system in neurosurgical patients: a comparison with simple Glasgow coma scoring.** *Br J Neurosurg* 1995;9:179–87 CrossRef Medline
31. Hijdra A, Brouwers PJ, Vermeulen M, et al. **Grading the amount of blood on computed tomograms after subarachnoid hemorrhage.** *Stroke* 1990;21:1156–61 CrossRef Medline

Progressive Cortical Neuronal Damage and Extracranial-Intracranial Bypass Surgery in Patients with Misery Perfusion

H. Yamauchi, S. Kagawa, Y. Kishibe, M. Takahashi, and T. Higashi

ABSTRACT

BACKGROUND AND PURPOSE: Misery perfusion may cause selective neuronal damage in atherosclerotic ICA or MCA disease. Bypass surgery can improve misery perfusion and may prevent neuronal damage. On the other hand, surgery conveys a risk for neuronal damage. The purpose of this retrospective study was to determine whether progression of cortical neuronal damage in surgically treated patients with misery perfusion is larger than that in surgically treated patients without misery perfusion or medically treated patients with misery perfusion.

MATERIALS AND METHODS: We evaluated the distribution of benzodiazepine receptors twice by using PET and ^{11}C-labeled flumazenil in 18 surgically treated patients with atherosclerotic ICA or MCA disease (9 with misery perfusion and 9 without) and no perioperative stroke before and after bypass surgery; in 8 medically treated patients with misery perfusion and no intervening ischemic event; and in 7 healthy controls. We quantified abnormal decreases in the benzodiazepine receptors of the cerebral cortex within the MCA distribution and compared changes in the benzodiazepine receptor index among the 3 groups.

RESULTS: The change in the benzodiazepine receptor index in surgically treated patients with misery perfusion (27.5 ± 15.6) during 7 ± 5 months was significantly larger than that in surgically treated patients without misery perfusion (−5.2 ± 9.4) during 6 ± 4 months ($P < .001$) and in medically treated patients with misery perfusion (3.2 ± 15.4) during 16 ± 6 months ($P < .01$).

CONCLUSIONS: Progression of cortical neuronal damage in surgically treated patients with misery perfusion and no perioperative stroke may occur and may be larger than that in medically treated patients with misery perfusion and no intervening ischemic event.

ABBREVIATIONS: BZR = benzodiazepine receptor; $CMRO_2$ = cerebral metabolic rate of oxygen; FMZ = flumazenil; FMZ-BP = flumazenil-binding potential; MP = misery perfusion; OEF = oxygen extraction fraction

Chronic hemodynamic impairment, as indicated by an increased oxygen extraction fraction (OEF; misery perfusion [MP])[1] on PET, is a risk factor for subsequent ischemic stroke in patients with atherosclerotic ICA or MCA occlusive diseases.[2-4] Furthermore, MP is thought to cause cognitive impairment independent of infarction.[2,5] Extracranial-intracranial bypass surgery has been demonstrated to improve MP.[1,6] However, whether bypass surgery improves stroke risk or cognitive impairment in patients with MP is controversial.[7-10]

The Carotid Occlusion Surgery Study of patients with recently symptomatic ICA occlusion and MP failed to show that bypass surgery compared with medical therapy reduced the risk of ipsilateral ischemic stroke at 2 years.[9] Furthermore, the Randomized Evaluation of Carotid Occlusion and Neurocognition trial, an ancillary study of the Carotid Occlusion Surgery Study, showed that bypass compared with no bypass did not lead to improved cognitive function after 2 years in patients with no recurrent stroke.[8] However, in the Carotid Occlusion Surgery Study, the perioperative stroke rate was sufficiently high to nullify any benefit. Therefore, the study was criticized for the possibility that patients with MP in the bypass group may also have experienced deleterious effects on cognition (ie, silent stroke), which overshadowed any beneficial effects of improved cerebral perfusion.[11] However, no study has investigated silent stroke after bypass surgery in patients with MP, to our knowledge.

Received October 18, 2016; accepted after revision December 17.

From the Division of PET Imaging (H.Y., S.K., Y.K., M.T., T.H.), Shiga Medical Center Research Institute, Moriyama, Japan; and National Institute of Radiological Sciences (T.H.), National Institutes of Quantum and Radiological Science and Technology, Chiba, Japan.

This study was funded by the Japan Society for the Promotion of Science Grants-in-Aid for Scientific Research, grant No. 26461323 and 22613001.

None of the funding sources had any involvement in the design of the study or in the collection, analysis, and interpretation of the data.

Please address correspondence to Hiroshi Yamauchi, MD, Division of PET Imaging, Shiga Medical Center Research Institute, 5-4-30 Moriyama, Moriyama 524-8524, Japan; e-mail: yamauchi@res.med.shiga-pref.jp

http://dx.doi.org/10.3174/ajnr.A5110

MP may cause not only cerebral infarction but also selective neuronal damage in the cerebral cortex that is not detectable as an infarction on CT or MR imaging.[12] Because most cortical neurons express central-type benzodiazepine receptors (BZRs), specific imaging of these receptors has made possible the in vivo visualization of neuronal alterations induced by ischemia.[12-14] Selective neuronal damage can be detected in humans by using PET and ^{11}C-labeled flumazenil, a neuronal tracer.[15,16] Bypass surgery can improve MP and may prevent neuronal damage. Conversely, surgery conveys a risk of selective neuronal damage. However, no study has investigated changes of BZRs after bypass surgery in patients with or without MP. Carotid endarterectomy for patients with chronic hemodynamic impairment was found to result in a decrease in BZRs that was correlated with postoperative cognitive impairment associated with cerebral hyperperfusion or ischemia.[17] If this result is also the case in bypass surgery, the progression of neuronal damage in surgically treated patients with MP should be compared with that in medically treated patients with MP, in order for the procedure to prevent neuronal damage.

The purpose of this retrospective study was to determine whether the progression of cortical neuronal damage, evaluated as a decrease in BZRs, in surgically treated patients with MP is larger than that in surgically treated patients without MP or medically treated patients with MP.

MATERIALS AND METHODS

Patients

We retrospectively analyzed data collected from 18 surgically treated patients and 8 medically treated patients enrolled in an observational study that investigated the relationship between hemodynamic compromise and selective neuronal damage in patients with atherosclerotic occlusive disease of the ICA or MCA. Patients were referred to our PET unit from 2002 to 2013 for evaluation of the hemodynamic effects of ICA or MCA disease as part of a comprehensive clinical evaluation to determine the necessity of vascular reconstruction surgery.

Using PET before and after bypass surgery (anastomosis of superficial temporal artery branch to a MCA cortical branch), we studied 18 patients (12 men and 6 women; mean age, 59 ± 10 years) with atherosclerotic occlusion or stenosis of the ICA or MCA (Table 1). The interval between baseline and follow-up PET studies ranged from 2 to 16 months (mean, 6 ± 4 months). The interval between bypass surgery and follow-up PET ranged from 1 to 14 months (mean, 5 ± 4 months). Four patients with MP and 4 patients without MP were part of a previously published dataset.[16]

Inclusion criteria for the present study were as follows: 1) occlusion of the extracranial ICA or occlusion or stenosis (>50% diameter reduction) of the intracranial ICA or MCA as documented by conventional or MR angiography[18]; 2) functional independence in daily life (a modified Rankin Scale score of <3); 3) surgically treated patients with no intervening stroke since the first PET examination; 4) availability and willingness of the patients to return for a PET examination after surgery; and 5) for symptomatic patients, a history of TIA or minor completed stroke in the ICA or MCA distribution. TIA was defined as focal symptoms of presumed ischemic cerebrovascular origin lasting <24 hours. Exclusion criteria were the following: 1) cerebral-cortical, cerebellar, or brain stem infarct detectable on routine MR imaging (T1WI, T2WI, or FLAIR) or CT, 2) unilateral arterial disease with extensive white matter lesions in both hemispheres probably caused by bilateral small-vessel disease, 3) history of taking BZR agonists, and 4) the presence of potential sources of cardiogenic embolism.

Table 1: Patient characteristics

Characteristic	Surgically Treated, Misery Perfusion		Medically Treated
	Yes	No	Yes
No. of patients	9	9	8
Interval (mean) (mo)	7 ± 5	6 ± 4	16 ± 6[a]
Interval from bypass to PET (mean) (mo)	6 ± 4	4 ± 3	NA
Age (yr)	59 ± 9	59 ± 13	62 ± 9
Male sex (No.)	7	5	7
Symptomatic (No.)	8	8	6
Cerebral ischemic lesions (No.)	8	9	7
Qualifying artery (No.)			
ICA (occlusion/stenosis)	8 (8/0)	6 (4/2)	5 (5/0)
MCA (occlusion/stenosis)	1 (0/1)	3 (3/0)	3 (3/0)
Other medical illness (No.)			
Hypertension	6	7	3
Diabetes mellitus	4	2	3
Ischemic heart disease	5	2	3
Hypercholesterolemia	5	1	3
Smoking habit (current and former) (No.)	6	4	4
Antiplatelet agents	9	9	7
Statins	4	1	3
Postbypass:			
TIA	3	1	NA
Cerebral ischemic lesion	2	0	NA

Note:—NA indicates not applicable.
[a] $P < .05$ vs both surgical groups.

Follow-up PET examinations were performed in 8 medically treated patients with MP at baseline (Table 1). They were selected from a cohort of a previously published follow-up PET study for 80 medically treated patients with stenosis or occlusion of the ICA or MCA and no intervening TIA or stroke.[19] Criteria for selection were as follows: 1) occlusion of the extracranial ICA or occlusion or stenosis (>50% diameter reduction) of the intracranial ICA or MCA, and 2) MP at the baseline PET study. The interval between the first and follow-up PET studies ranged from 7 to 26 months (mean, 16 ± 6 months).

For vascular risk factors, the status of hypertension, diabetes mellitus, ischemic heart disease, hypercholesterolemia, and smoking was evaluated from patient histories recorded at the first PET examination. Hypertension, diabetes mellitus, ischemic heart disease, or hypercholesterolemia was judged to be present when there was a history of treatment.

To establish a control data base for BZR imaging, we studied 10 healthy control subjects (7 men and 3 women; mean age, 57 ± 7 years) with no previous history of a medical or psychiatric disorder or of taking BZR agonists. Among them, 7 subjects (mean age, 56 ± 8 years, including 4 men and 3 women) underwent follow-up PET examinations. The interval between the first and follow-up PET studies ranged from 38 to 45 months (mean, 41 ± 3 months). All protocols in this study were approved by the ethics

committee of Shiga Medical Center, and all subjects gave written informed consent.

PET Measurements

PET scans were performed for each subject by using a whole-body PET scanner, GE Advance (GE Healthcare, Milwaukee, Wisconsin), which permits the simultaneous acquisition of 35 image sections with an intersection spacing of 4.25 mm.[20] After a transmission scan by germanium-68/gallium-68, a series of ^{15}O-gas studies was performed.[20] Briefly, $C^{15}O_2$ and $^{15}O_2$ were delivered continuously to the patient via a mask for the duration of a 5-minute scan. CBV was measured by bolus inhalation of $C^{15}O$ with scanning for 3 minutes. Arterial samples were obtained during scanning. No subject showed substantial changes in the partial pressure of carbon dioxide in arterial blood during scanning.

The ^{15}O-gas study was followed by a study of ^{11}C-flumazenil,[16,21] which was synthesized by ^{11}C-methylation of demethylated-flumazenil (FMZ) (Hoffmann-La Roche, Basel, Switzerland). After the slow intravenous injection of ^{11}C-FMZ, a 50-minute dynamic PET scan was initiated.

We used the steady-state method to calculate CBF, the cerebral metabolic rate of oxygen ($CMRO_2$), and OEF.[22] The $CMRO_2$ and OEF were corrected on the basis of CBV. The binding potential (nondisplaceable) of ^{11}C-flumazenil was calculated by using dynamic data and Logan graphic analysis with reference tissue, with the pons as the reference region.[21,23]

Data Analysis

For ^{15}O-gas PET scanning analysis, we used a classic ROI analysis. We analyzed 10 tomographic planes, located 46.25–84.5 mm above and parallel to the orbitomeatal line.[24] The lowest plane corresponded to the level of the basal ganglia and the thalamus, and the uppermost plane corresponded to the level of the centrum semiovale. An ROI was selected for CBF images. Each image was examined by compactly placing 10–12 circular ROIs (diameter, 16 mm) over the gray matter of the outer cortex in each hemisphere. According to the atlas,[25] the ROIs in all 10 images covered the distribution of the MCA and the external borderzone regions.[24,25] The same ROIs were used for the $CMRO_2$, OEF, and CBV images. The mean hemispheric value for the hemisphere affected by ICA or MCA disease was calculated as the average of all the circular ROIs.

Normal control values of the PET variables were obtained from 7 healthy volunteers (4 men and 3 women; mean age, 47 ± 7 years) who underwent routine neurologic examinations and MR imaging. The mean OEF value in the 14 control hemispheres was 44.5% ± 3.8%. Hemispheric OEF values beyond the upper 95% limit defined in healthy subjects (>52.9%) were considered to represent increased OEF. Comparative values for CBF and CBF/CBV in healthy volunteers were 44.6 ± 4.5 mL/100 g/min and 11.4 ± 1.8/min, respectively. Hemispheric CBF and CBF/CBV values below 35.0 mL/100 g/min and 7.6/min, respectively, were considered abnormal. Patients with increased OEF, decreased CBF, and decreased CBF/CBV in hemispheres with arterial disease were categorized as having MP.[4] One investigator unaware of the clinical status categorized the patients.

Flumazenil-binding potential parametric images were analyzed by using a 3D-stereotactic surface-projection technique, as previously described.[16,26] This technique anatomically normalizes individual PET data to a standard brain and compares regional voxel data between patients and controls. In the standard stereotactic system, pixels located on the outer and medial surfaces of both hemispheres and vectors perpendicular to the 3D surface at each pixel are predetermined. For each predetermined surface pixel on an individual's anatomically standardized PET image set, the algorithm searches along the vector, 6 pixels deep into the cortex, for the highest pixel value and assigns this maximum value to the surface pixel. To correct for fluctuations in whole-brain values and to extract the changes due to ICA or MCA disease, we normalized the pixel values of an individual's image set to the mean cerebellar value before analysis. *Z* scores were calculated for each surface pixel as (Mean Normalized Pixel Value for Controls − Normalized Pixel Value for the Patient) / (SD for controls), and were used to quantify decreases in flumazenil-binding potential (FMZ-BP). Thus, a positive *z* score in a patient represented reduced FMZ-BP relative to the control group. An increased BZR index corresponded to a decreased BZR level, a decreased FMZ-BP level, and thus greater cortical neural damage.

To quantify the degree of abnormal flumazenil-binding potential reduction in each patient, we used the stereotactic extraction estimation method to calculate a BZR index, defined as (% Pixels with *z* Score >2 × Average *z* score for those pixels) for the cerebral-cortical MCA distribution affected by ICA or MCA disease.[27] This MCA distribution included the middle and inferior frontal gyri; the precentral gyrus; the superior and inferior parietal gyri; the angular, postcentral, and supramarginal gyri; the superior, middle, inferior, and transverse temporal gyri; and the superior and middle occipital gyri.[27]

At postsurgical or follow-up examinations, total change in the BZR index or the CBF, $CMRO_2$, OEF, CBV, or CBF/CBV values in the MCA distribution with arterial disease was calculated by subtracting the values obtained at the second examination from those obtained at the first examination. In controls, the calculation was performed by using the mean of the bilateral hemispheric values of the BZR index. The mean value of changes in the index in the controls was 0.94 ± 1.38. In patients, an increase of the index beyond the upper 95% limit (the mean plus 6t0.05 × SD; 6t0.05, the value of t for $P < 0.05$ and degree of freedom = 6) defined in healthy subjects (>4.32) was considered an increased BZR index (progression of neuronal damage) during follow-up.[16]

Statistical Analysis

The statistical analysis was performed by using StatView (SAS Institute, Cary, North Carolina). Comparisons of clinical backgrounds or PET values among the 3 groups were performed with 1-way ANOVA and a post hoc Scheffe analyses or Kruskal-Wallis tests and post hoc Mann-Whitney *U* tests as appropriate. PET variable values were compared between examinations by using paired *t* tests. Relationships between variables were analyzed by using simple or multiple regression analyses. A multivariable linear regression model with a forward stepwise selection procedure was used to test the independent predictive value of the presence of MP at baseline and the change in PET variables during fol-

Table 2: PET variables for surgically or medically treated patients[a]

Characteristic, MP	Surgical, Yes (n = 9)	Surgical, No (n = 9)	Medical, Yes (n = 8)
Baseline			
BZR index	53.1 ± 45.4	35.5 ± 32.2	53.2 ± 39.8
CBF (mL/100 g/min)	27.9 ± 4.1[b]	34.8 ± 4.1	25.8 ± 6.6[b]
$CMRO_2$ (mL/100 g/min)	2.73 ± 0.60	3.19 ± 0.35	2.69 ± 0.47
OEF (%)	59.9 ± 4.0	54.4 ± 4.3	60.1 ± 6.0
CBV (mL/100 g)	4.41 ± 1.08	3.96 ± 0.84	3.81 ± 0.90
CBF/CBV (min^{-1})	6.48 ± 0.97	9.08 ± 1.92	6.82 ± 0.83
Follow-up			
BZR index	80.7 ± 57.2	30.3 ± 26.8	56.4 ± 39.8
CBF (mL/100 g/min)	32.7 ± 5.5	34.0 ± 5.7	28.5 ± 6.6
$CMRO_2$ (mL/100 g/min)	2.94 ± 0.67	3.14 ± 0.39	2.82 ± 0.45
OEF (%)	56.4 ± 5.5	55.8 ± 7.3	55.9 ± 6.1
CBV (mL/100 g)	4.15 ± 1.03	3.74 ± 0.59	3.72 ± 1.01
CBF/CBV (min^{-1})	8.31 ± 2.28	9.31 ± 2.21	7.77 ± 0.78
BZR index change	27.5 ± 15.6[c]	−5.2 ± 9.4	3.2 ± 15.4
CBF change (mL/100 g/min)	4.81 ± 4.02[b]	−0.77 ± 4.23	2.67 ± 3.59
$CMRO_2$ change (mL/100 g/min)	0.21 ± 0.35	−0.05 ± 0.49	0.13 ± 0.28
OEF change (%)	−3.42 ± 4.62	1.36 ± 5.15	−4.26 ± 3.68
CBV change (mL/100 g)	−0.26 ± 1.40	−0.21 ± 0.68	−0.09 ± 0.51
CBF/CBV change (min^{-1})	1.83 ± 2.01	0.23 ± 1.56	0.95 ± 1.35

[a] Reference values for BZR index, CBF, $CMRO_2$, OEF, CBV, and CBF/CBV were 1.78 ± 1.79, 44.6 ± 4.5, 3.43 ± 0.33, 44.5 ± 3.8, 3.98 ± 0.48, and 11.4 ± 1.8, respectively. Data are means.

[b] $P < .05$ vs no group.

[c] $P < .001$ vs no group and $P < .01$ vs medical group.

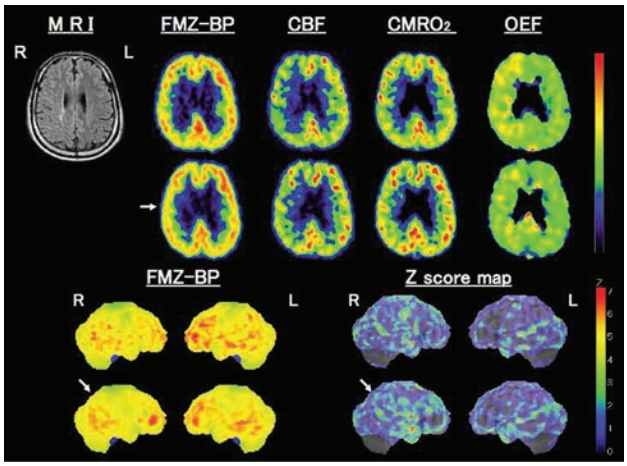

FIG 1. Representative images of ^{11}C-flumazenil PET showing decreased BZR levels in a patient with right ICA occlusion and misery perfusion. The first PET study (*first row*) shows a mild decrease in the flumazenil-binding potential in the right (R) hemisphere with ICA occlusion and subcortical or deep white matter ischemic lesions (MR imaging) in which CBF is decreased and the oxygen extraction fraction is increased (misery perfusion). Follow-up 16 months later (*second row*) (15 months after bypass to the frontal branch of the MCA) shows relative decreases in FMZ-BP (*arrow*) and OEF, with increased CBF in the right hemisphere. 3D-stereotactic surface projection images and *z* score maps from the first (*third row*) and second (*fourth row*) examinations demonstrate a decrease in FMZ-BP in the right MCA distribution, especially in the parietotemporal lobe (*arrow*). The BZR index is increased from 71.6 to 100.8 between baseline and follow-up (*arrow*). An increased BZR index corresponds to a decreased BZR level, a decreased FMZ-BP level, and thus greater cortical neural damage. An increased BZR index was apparent in the cortical regions outside the territory of the recipient vessel, which suggested that cortical neural damage could not be ascribed to technical problems of the bypass anastomosis or postoperative hyperperfusion and might be associated with sustained hemodynamic impairment.

low-up with respect to the change in the BZR index. For all analyses, statistical significance was defined as $P < .05$.

RESULTS

Four of the 18 patients who underwent bypass surgery had TIA after surgery. Two patients showed new small subcortical high-intensity lesions on follow-up MR images. Bypass was patent at follow-up in all patients on MRA.

Before the operation, 9 patients (50%) with increased OEF, decreased CBF, and decreased CBF/CBV in hemispheres with arterial disease were categorized as having MP. No patient characteristics significantly differed between the patients with MP and those without it (Table 1). The value of the BZR index at baseline was not different between the 2 groups (Table 2).

After the operation, patients with MP showed a significant increase in the BZR index (paired *t* test, $P < .001$), CBF ($P < .01$), and CBF/CBV ($P < .05$) and a tendency toward decreases in the OEF ($P = .06$), while patients without MP did not show significant changes in any PET variables (Table 2 and Fig 1). The BZR index in the MP group tended to be larger ($P = .07$) than that in the no-MP group after the operation.

The change in the BZR index in the MP group was significantly larger than that in the no-MP group ($P < .001$). Eight patients (89%) with MP showed an increase in the BZR index beyond the upper 95% limit defined in healthy subjects, while no patients without MP (0%) showed increases in the BZR index (Fisher exact test, $P = .0004$). The change in the BZR index was significantly correlated with the value of CBF ($r = -0.66$, $P < .005$) or OEF ($r = 0.47$, $P < .05$) at baseline (Fig 2).

A multivariable linear regression analysis (forward stepwise selection) was used to investigate the association of changes in the BZR index with the following: 1) the presence of MP at baseline; 2) changes in the values of CBF, $CMRO_2$, OEF, CBV, or CBF/CBV after bypass; 3) the presence of vascular risk factors; and 4) drug-treatment history (Table 1). Our analysis produced a model that included the presence of MP at baseline, changes in the OEF after surgery, and smoking habit, with a correlation coefficient of 0.905 for the changes in the BZR index after surgery ($P < .001$). In our model, the presence of MP, changes in the OEF, and smoking habit accounted for 64.5%, 8.2%, and 9.2% of the variance in changes in the BZR index, respectively. The presence of MP (coefficient, 35.2; standard error, 5.2; $t = 6.7$; $P < .0001$), changes in the OEF (coefficient, 1.2; standard error, 0.5; $t = 2.5$; $P < .05$), and smoking habit (coefficient, 13.3; standard error, 4.7; $t = 2.7$; $P < .05$) were positively correlated with changes in the BZR index.

Eight medically treated patients with MP showed a longer interval ($P < .05$) between the 2 PET examinations than 9 surgically treated patients with MP (Table 1). Other patient characteristics were not significantly different between the medically and surgi-

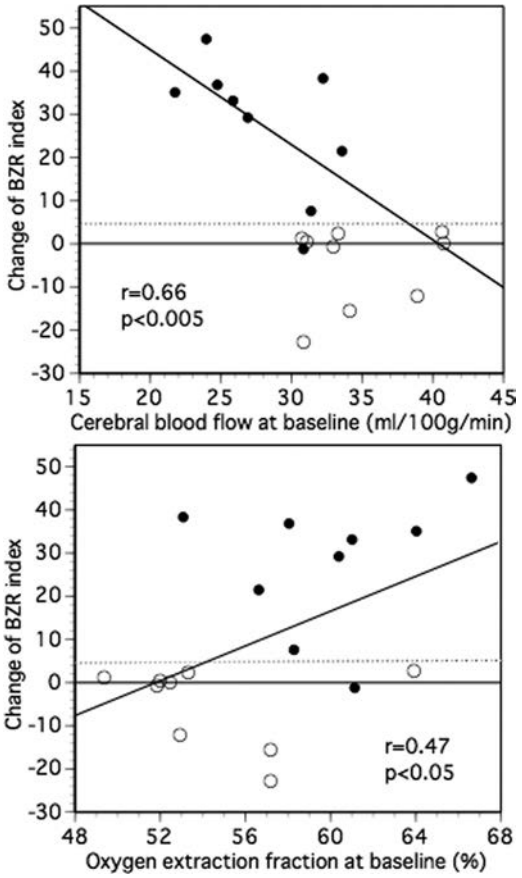

FIG 2. Scatterplots of changes in the BZR index in 18 surgically treated patients and the mean hemispheric CBF at baseline (*upper row*) or the mean hemispheric OEF at baseline (*lower row*) in the hemisphere with arterial disease. The *dashed lines* show the upper 95% limit of changes in the BZR index for the 7 controls. The *closed circles* indicate patients with misery perfusion, and the *open circles* indicate patients without misery perfusion.

cally treated patients with MP, though medically treated patients had no intervening TIA. The values of the BZR index and other PET variables at baseline or at follow-up were not significantly different between the 2 groups, while at follow-up, the BZR index in the surgically treated patients with MP had a tendency to be larger ($P = .07$) than that in the medically treated patients. The change in the BZR index in surgically treated patients was significantly larger than that in medically treated patients ($P < .01$). Three medically treated patients (37%) and 8 surgically treated patients (89%) showed an increase in the BZR index beyond the upper 95% limit defined in healthy subjects (Fisher exact test, $P < .05$). At follow-up, 3 surgically treated patients and 1 medically treated patient showed MP (Fisher exact test, $P = .57$).

DISCUSSION

This study demonstrates that the progression of cortical neuronal damage manifests as a decrease in BZRs in the normal-appearing cerebral cortex of surgically treated patients with MP and no perioperative stroke. The degree of progressive cortical neuronal damage in surgically treated patients with MP was significantly larger than that in medically treated patients with MP and no intervening ischemic event.

The precise reason for the progression of cortical neuronal damage in surgically treated patients with MP and no perioperative stroke is unclear from the present study. However, perioperative ischemia, postoperative hyperperfusion, and hemodynamic ischemia during follow-up might cause cortical neuronal damage. In patients with MP, the risk for perioperative ischemic events is reported to be high.[28,29] Patients with MP have a marginally adequate blood supply relative to metabolic demand, which increases the risk of cerebral ischemia.[1,3,4] Therefore, it is reasonable to hypothesize that fluctuations of cerebral hemodynamics during perioperative periods might have caused ischemic neuronal damage in surgically treated patients with MP. Additionally, the presence of MP is reported to be a risk factor for postoperative hyperperfusion after bypass.[29] Cerebral hyperperfusion after carotid endarterectomy was found to result in a decrease in BZRs.[17] To prevent perioperative neuronal damage, therapeutic strategies that limit selective neuronal damage, including careful perioperative management[30] and the use of neuroprotective agents,[31,32] may be needed for patients with MP. Furthermore, MP may not improve completely or immediately after bypass surgery. Thus, the risk for hemodynamic ischemia may persist during follow-up.

The progression of cortical neuronal damage in surgically treated patients with MP was larger than that in medically treated patients with MP and no intervening ischemic event. Surgically treated patients with MP showed an expected increase in CBF and CBF/CBV and a tendency for decreased OEF at postsurgical examinations, indicating hemodynamic improvement. We found that decreases in the OEF after bypass were associated with smaller increases in the BZR index after bypass. Therefore, successful bypass surgery might have reduced the risk of neuronal damage in surgically treated patients thereafter. On the other hand, medically treated patients with MP and no intervening ischemic event also showed hemodynamic improvement of a similar degree, which may be due to long-term improvement of collateral blood flow. Medically treated patients with MP have a high risk for subsequent ischemic stroke.[4,9] However, if they are successfully treated and have no intervening ischemic event, the risk for ischemic damage could be reduced. Medical treatment may play an important role in preventing progressive neuronal damage.[19] If we use BZR decreases as objective markers of neuronal damage, our findings do not support the hypothesis that bypass surgery is superior to medical therapy in patients with MP.

The Randomized Evaluation of Carotid Occlusion and Neurocognition trial failed to show that bypass can improve cognition during 2 years compared with optimal medical therapy alone in patients with symptomatic ICA occlusion and MP.[8] On the basis of the findings in the present study, we could not completely exclude the possibility that bypass surgery for patients with MP may have induced selective cortical neuronal damage that overshadowed the beneficial effects of improved cerebral perfusion. Post hoc analysis in the trial showed that cognitive improvement was associated with a less impaired PET OEF at baseline. As shown in the present study, patients with a less impaired OEF might have less perioperative neuronal damage, which, in turn, may have allowed cognitive improvement.

The findings in the present study have some implications for treatment selection and potential clinical outcomes. Reperfusion therapies could be most beneficial for patients with hemodynamic

impairment to improve clinical outcomes. However, reperfusion therapies may have a risk of neuronal damage for patients with hemodynamic impairment. Carotid endarterectomy and bypass surgery for patients with chronic hemodynamic impairment may be associated with cortical neuronal damage that may be correlated with postoperative cognitive impairment.[17] In acute stroke, selective neuronal damage may affect salvaged penumbra and hamper functional recovery following reperfusion.[12] The progression of cortical neuronal damage should be considered while treating patients with hemodynamic impairment by means of reperfusion therapy.

Limitations

This study had certain limitations, including a small sample size and a cohort with both ICA and MCA disease. It also retrospectively analyzed data from a prospective observational study. Therefore, there is a considerable risk of selection bias, though the clinical backgrounds were not significantly different among the 3 groups. For these reasons, the findings in this study should be confirmed in future randomized and blinded studies. The selection of bypass surgery was left to individual clinical judgment by attending physicians, and unknown clinical factors could have swayed treatment decisions. Nine patients with less marked hemodynamic impairment than is indicative of MP underwent bypass surgery due to regional increases in OEF in addition to other characteristics (poor collateral pathways or recurrent symptoms). Additionally, 2 patients with perioperative stroke were excluded from analysis. One patient with MP had progressing stroke after the first PET examination and underwent emergency bypass surgery, and another without MP showed multiple MR imaging lesions after aneurysm treatment performed in combination with bypass surgery. The interval time between baseline and follow-up PET for medically treated patients with MP was twice as long as that for surgically treated patients with MP, which may make it difficult to accurately compare patient groups. However, the longer interval may lead to the larger, not smaller, increase of cortical neuronal damage in medically treated patients, which may not change the conclusion. The period of patient recruitment ranged from 2002 to 2013, but the PET scan protocol had not changed, so it likely offered the same precision and accuracy. We could not systematically investigate cognitive differences among these patients. Although decreases in BZRs are objective markers of neuronal injury that may be associated with cognitive impairment,[12,17,33] the functional effect of neuronal damage should have been determined by neuropsychological testing.

CONCLUSIONS

The progression of cortical neuronal damage manifests as a decrease in BZRs in the normal-appearing cerebral cortex of surgically treated patients with MP and no perioperative stroke. The degree of progressive cortical neuronal damage in surgically treated patients with MP may be larger than that in medically treated patients with MP and no intervening ischemic event. The progression of cortical neuronal damage should be considered while treating patients with MP with bypass surgery.

REFERENCES

1. Baron JC, Bousser MG, Rey A, et al. **Reversal of focal "misery-perfusion syndrome" by extra-intracranial arterial bypass in hemodynamic cerebral ischemia: a case study with ^{15}O positron emission tomography.** *Stroke* 1981;12:454–59 CrossRef Medline
2. Klijn CJ, Kappelle LJ. **Haemodynamic stroke: clinical features, prognosis, and management.** *Lancet Neurol* 2010;9:1008–17 CrossRef Medline
3. Powers WJ. **Cerebral hemodynamics in ischemic cerebrovascular disease.** *Ann Neurol* 1991;29:231–40 CrossRef Medline
4. Yamauchi H, Higashi T, Kagawa S, et al. **Is misery perfusion still a predictor of stroke in symptomatic major cerebral artery disease?** *Brain* 2012;135:2515–26 CrossRef Medline
5. Marshall RS, Festa JR, Cheung YK, et al. **Cerebral hemodynamics and cognitive impairment: baseline data from the RECON trial.** *Neurology* 2012;78:250–55 CrossRef Medline
6. Powers WJ, Martin WRW, Herscovitch P, et al. **Extracranial-intracranial bypass surgery: hemodynamic and metabolic effects.** *Neurology* 1984;34:1168–74 CrossRef Medline
7. JET Study Group. **Japanese EC-IC Bypass Trial (JET study): the second interim analysis.** *Surgery for Cerebral Stroke* 2002;30:434–37 CrossRef
8. Marshall RS, Festa JR, Cheung YK, et al; RECON Investigators. **Randomized Evaluation of Carotid Occlusion and Neurocognition (RECON) trial: main results.** *Neurology* 2014;82:744–51 CrossRef Medline
9. Powers WJ, Clarke WR, Grubb RL Jr, et al; COSS Investigators. **Extracranial-intracranial bypass surgery for stroke prevention in hemodynamic cerebral ischemia: the Carotid Occlusion Surgery Study randomized trial.** *JAMA* 2011;306:1983–92 CrossRef Medline
10. Sasoh M, Ogasawara K, Kuroda K, et al. **Effects of EC-IC bypass surgery on cognitive impairment in patients with hemodynamic cerebral ischemia.** *Surg Neurol* 2003;59:455–60; discussion 460–63 CrossRef Medline
11. Jacobs BS, Nichols FT 3rd. **Does improving misery cerebral perfusion improve misery cognition?** *Neurology* 2014;82:738–39 CrossRef Medline
12. Baron JC, Yamauchi H, Fujioka M, et al. **Selective neuronal loss in ischemic stroke and cerebrovascular disease.** *J Cereb Blood Flow Metab* 2014;34:2–18 CrossRef Medline
13. Heiss WD, Grond M, Thiel A, et al. **Permanent cortical damage detected by flumazenil positron emission tomography in acute stroke.** *Stroke* 1998;29:454–61 CrossRef Medline
14. Sette G, Baron JC, Young AR, et al. **In vivo mapping of brain benzodiazepine receptor changes by positron emission tomography after focal ischemia in the anesthetized baboon.** *Stroke* 1993;24:2046–57; discussion 2057–58 CrossRef Medline
15. Ejaz S, Williamson DJ, Ahmed T, et al. **Characterizing infarction and selective neuronal loss following temporary focal cerebral ischemia in the rat: a multi-modality imaging study.** *Neurobiol Dis* 2013;51:120–32 CrossRef Medline
16. Yamauchi H, Kudoh T, Kishibe Y, et al. **Selective neuronal damage and chronic hemodynamic cerebral ischemia.** *Ann Neurol* 2007;61:454–65 CrossRef Medline
17. Chida K, Ogasawara K, Suga Y, et al. **Postoperative cortical neural loss associated with cerebral hyperperfusion and cognitive impairment after carotid endarterectomy: 123I-iomazenil SPECT study.** *Stroke* 2009;40:448–53 CrossRef Medline
18. Samuels OB, Joseph GJ, Lynn MJ, et al. **A standardized method for measuring intracranial arterial stenosis.** *AJNR Am J Neuroradiol* 2000;21:643–46 Medline
19. Yamauchi H, Kagawa S, Kishibe Y, et al. **Progressive cortical neuronal damage and chronic hemodynamic impairment in atherosclerotic major cerebral artery disease.** *Stroke* 2016;47:1534–41 CrossRef Medline
20. Okazawa H, Yamauchi H, Sugimoto K, et al. **Quantitative comparison of the bolus and steady-state methods for measurement of cerebral perfusion and oxygen metabolism: positron emission**

tomography study using 15O gas and water. *J Cereb Blood Flow Metab* 2001;21:793–803 Medline
21. Okazawa H, Yamauch H, Sugimoto K, et al. **Effects of metabolite correction for arterial input function on quantitative receptor images with 11C-flumazenil in clinical positron emission tomography studies.** *J Comput Assist Tomogr* 2004;28:428–35 CrossRef Medline
22. Frackowiak RS, Lenzi GL, Jones T, et al. **Quantitative measurement of regional cerebral blood flow and oxygen metabolism in man using ^{15}O and positron emission tomography: theory, procedure, and normal values.** *J Comput Assist Tomogr* 1980;4:727–36 CrossRef Medline
23. Logan J, Fowler JS, Volkow ND, et al. **Distribution volume ratios without blood sampling from graphical analysis of PET data.** *J Cereb Blood Flow Metab* 1996;16:834–40 Medline
24. Yamauchi H, Fukuyama H, Kimura J, et al. **Hemodynamics in internal carotid artery occlusion examined by positron emission tomography.** *Stroke* 1990;21:1400–06 CrossRef Medline
25. Kretschmann HJ, Weinrich W. *Neuroanatomy and Cranial Computed Tomography.* New York: Thieme; 1986:70–74
26. Minoshima S, Frey KA, Koeppe RA, et al. **A diagnostic approach in Alzheimer's disease using three-dimensional stereotactic surface projections of fluorine-18-FDG PET.** *J Nucl Med* 1995;36:1238–48 Medline
27. Mizumura S, Kumita S, Cho K, et al. **Development of quantitative analysis method for stereotactic brain image: assessment of reduced accumulation in extent and severity using anatomical segmentation.** *Ann Nucl Med* 2003;17:289–95 CrossRef Medline
28. Gibbs JM, Wise RJS, Thomas DJ, et al. **Cerebral haemodynamic changes after extracranial-intracranial bypass surgery.** *J Neurol Neurosurg Psychiatry* 1987;50:140–50 CrossRef Medline
29. Yamaguchi K, Kawamata T, Kawashima A, et al. **Incidence and predictive factors of cerebral hyperperfusion after extracranial-intracranial bypass for occlusive cerebrovascular diseases.** *Neurosurgery* 2010;67:1548–54; discussion 1554 CrossRef Medline
30. Kuroda S, Kawabori M, Hirata K, et al. **Clinical significance of STA-MCA double anastomosis for hemodynamic compromise in post-JET/COSS era.** *Acta Neurochir (Wien)* 2014;156:77–83 CrossRef Medline
31. Fujimura M, Niizuma K, Inoue T, et al. **Minocycline prevents focal neurological deterioration due to cerebral hyperperfusion after extracranial-intracranial bypass for Moyamoya disease.** *Neurosurgery* 2014;74:163–70; discussion 170 CrossRef Medline
32. Uchino H, Nakayama N, Kazumata K, et al. **Edaravone reduces hyperperfusion-related neurological deficits in adult Moyamoya disease: historical control study.** *Stroke* 2016;47:1930–32 CrossRef Medline
33. Yamauchi H, Nishii R, Higashi T, et al. **Selective neuronal damage and Wisconsin Card Sorting Test performance in atherosclerotic occlusive disease of the major cerebral artery.** *J Neurol Neurosurg Psychiatry* 2011;82:150–56 CrossRef Medline

Cognitive Implications of Deep Gray Matter Iron in Multiple Sclerosis

E. Fujiwara, J.A. Kmech, D. Cobzas, H. Sun, P. Seres, G. Blevins, and A.H. Wilman

ABSTRACT

BACKGROUND AND PURPOSE: Deep gray matter iron accumulation is increasingly recognized in association with multiple sclerosis and can be measured in vivo with MR imaging. The cognitive implications of this pathology are not well-understood, especially vis-à-vis deep gray matter atrophy. Our aim was to investigate the relationships between cognition and deep gray matter iron in MS by using 2 MR imaging–based iron-susceptibility measures.

MATERIALS AND METHODS: Forty patients with multiple sclerosis (relapsing-remitting, $n = 16$; progressive, $n = 24$) and 27 healthy controls were imaged at 4.7T by using the transverse relaxation rate and quantitative susceptibility mapping. The transverse relaxation rate and quantitative susceptibility mapping values and volumes (atrophy) of the caudate, putamen, globus pallidus, and thalamus were determined by multiatlas segmentation. Cognition was assessed with the Brief Repeatable Battery of Neuropsychological Tests. Relationships between cognition and deep gray matter iron were examined by hierarchic regressions.

RESULTS: Compared with controls, patients showed reduced memory ($P < .001$) and processing speed ($P = .02$) and smaller putamen ($P < .001$), globus pallidus ($P = .002$), and thalamic volumes ($P < .001$). Quantitative susceptibility mapping values were increased in patients compared with controls in the putamen ($P = .003$) and globus pallidus ($P = .003$). In patients only, thalamus ($P < .001$) and putamen ($P = .04$) volumes were related to cognitive performance. After we controlled for volume effects, quantitative susceptibility mapping values in the globus pallidus ($P = .03$; trend for transverse relaxation rate, $P = .10$) were still related to cognition.

CONCLUSIONS: Quantitative susceptibility mapping was more sensitive compared with the transverse relaxation rate in detecting deep gray matter iron accumulation in the current multiple sclerosis cohort. Atrophy and iron accumulation in deep gray matter both have negative but separable relationships to cognition in multiple sclerosis.

ABBREVIATIONS: DGM = deep gray matter; GP = globus pallidus; NP_{total} = composite z-score across neuropsychological tests; PASAT = Paced Auditory Serial Addition Test; QSM = quantitative susceptibility mapping; R2* = transverse relaxation rate; SDMT = Symbol Digit Modalities Test; SPART = 10/36-Spatial Recall Test; SRT = Selective Reminding Task

Cognitive problems occur in 40%–65% of individuals with multiple sclerosis, predominantly affecting information processing speed and episodic memory.[1] Subcortical atrophy, particularly in the thalamus, is well-known to predict cognitive deficits in MS.[2] Elevated levels of iron accumulation in deep gray matter (DGM) nuclei in MS have also been reported using different iron-sensitive MR imaging measures, with studies focusing particularly on the large basal ganglia nuclei (caudate, putamen, globus pallidus [GP]), and the thalamus).[3] Excess iron catalyzes production of free radicals, promoting neurodegeneration. This affects the DGM in both healthy aging and different CNS disorders.[4] DGM iron accumulation in MS may be an epiphenomenon of structural atrophy caused by cell death,[5] but others reported no relationships between DGM iron, global/regional brain volumes, or lesion load, suggesting potentially independent pathologies.[6] The functional implications of DGM iron accumulation relative to other DGM pathologies in MS need further examination. Previous studies have examined some aspects of cognitive functions and DGM iron in MS with 4 different MR techniques.[5,7-11] Among the MR imaging measures used, only the gradient-echo

Received September 9, 2016; accepted after revision December 18.

From the Departments of Psychiatry (E.F., J.A.K.), Computer Science (D.C.), Biomedical Engineering (H.S., P.S., A.H.W.), and Medicine (G.B.), Division of Neurology, University of Alberta, Edmonton, Alberta, Canada; and Northern Alberta Multiple Sclerosis Clinic (G.B.), Edmonton, Alberta, Canada.

This work was supported by the MS Society of Canada (EGID 1619) and the Canadian Institutes of Health Research (FRN MOP 102582).

Please address correspondence to A.H. Wilman, PhD, University of Alberta, Department of Biomedical Engineering, 1098 RTF, Edmonton, AB, Canada, T6G 2V2; e-mail: wilman@ualberta.ca

Indicates open access to non-subscribers at www.ajnr.org

Indicates article with supplemental on-line tables.

http://dx.doi.org/10.3174/ajnr.A5109

transverse relaxation rate (R2*) and quantitative susceptibility mapping (QSM) have been validated against postmortem iron assessment, both in non-MS[12,13] and in MS populations.[14,15]

Three MS studies assessed different aspects of cognition along with R2*.[5,10,11] In Khalil et al,[5] R2* in the basal ganglia (but not in the thalamus) was related to processing speed in patients with clinically isolated syndrome and those with MS. In Pinter et al,[10] a neuropsychological composite score of cognitive efficiency/processing speed (but not memory) of patients with clinically isolated syndrome and patients with MS was reported. This was predicted by R2* relaxation rates averaged across basal ganglia nuclei, along with caudate volume and T2 lesion load. Schmalbrock et al[11] recently cross-examined QSM and R2* measures against performance in 2 inhibitory cognitive tasks (a Stroop Task and an Eriksen Flanker Task) in patients with relapsing-remitting MS, imaged at 7T. Inhibition in the Flanker Task (but not the Stroop Task) was related to caudate and anterior putamen iron assessed with QSM, but performance in neither task was related to R2* measures. Thus, only 1 study[11] directly compared the cognitive correlates of R2* and QSM-based iron measures in MS, but it did not control for atrophy in the same DGM regions.

The objective of our study was to determine whether cognition in MS, measured by the Brief Repeatable Battery of Neuropsychological Tests, is related to DGM iron accumulation measured with R2* and QSM at a high field strength (4.7T). The core hypothesis was that iron (R2* and QSM) in DGM nuclei correlates with decreased cognitive performance in MS, irrespective of atrophy.

MATERIALS AND METHODS

Participants

This study was approved by the local research ethics board, and all participants provided written informed consent. Forty patients diagnosed with MS were recruited from the Northern Alberta Multiple Sclerosis Clinic in Edmonton, Alberta, Canada. Sixteen patients had relapsing-remitting MS, 15 patients had secondary-progressive MS, and 9 patients were diagnosed with primary-progressive MS. Patients were at least 18 years of age and were diagnosed with MS on the basis of the 2010 McDonald criteria.[16] Twenty-seven healthy controls were recruited through word of mouth, on-line (Kijiji; http://www.kijiji.ca/h-alberta/9003), and print advertising (local daily newspaper). All participants were alert, lucid, able to communicate verbally, and understood the test instructions and purpose of the testing; they had normal or corrected-to-normal vision and hearing and were fluent in English. Exclusion criteria were major neurologic or psychiatric illnesses apart from MS in the patient group (eg, stroke, encephalitis, or meningitis; head injury with loss of consciousness of >5 minutes; psychosis), diabetes, learning disabilities, and contraindications to MR imaging (pacemakers, nonremovable metal clips, major dental work, and so forth). Six participants were excluded due to MR imaging artifacts (2 patients), incomplete MR imaging data (1 control), or incomplete cognitive data (2 controls, 1 patient). The gap between MR imaging and cognitive testing was 24.48 ± 22.25 days for patients and 10.44 ± 20.01 days for controls. No patients were imaged during a time of relapse. The earliest time from relapse to imaging was 5.57 months (6.17 months to cognitive testing).

MR Imaging

Participants were imaged by using a 4.7T Varian Inova MR imaging system (Agilent Technologies, Santa Clara, California). Two MR imaging sequences were collected to enable quantitative measurements of volume, R2*, and QSM. A 3D longitudinal relaxation time (T1)-weighted sequence used inversion recovery rapid gradient-echo (84 sections; 2-mm thick; in-plane, 0.9×0.9 mm^2; acquisition time, 4.8 minutes). The R2*/QSM sequence used 3D multiecho gradient-echo (80 sections; 2-mm thick; in-plane, 1×1 mm^2; acquisition time, 9.4 minutes), with TE parameters (10 echoes; first echo, 2.9 ms; echo spacing, 4.1 ms). Both R2* and QSM were reconstructed from the same multiecho images by using previously validated methods.[17,18] Briefly, R2* used a 3D linear field gradient correction to compensate for air-tissue susceptibility effects and then a monoexponential fit.[17] For QSM, a field map was estimated from the multiecho data, followed by background field removal by using Regularization-Enabled Sophisticated Harmonic Artifact Reduction for Phase data (RESHARP),[18] and dipole inversion by using total variation regularization.[19-21] The imaging protocol also included axial T2-weighted and FLAIR imaging, both with 4-mm section thickness, which were used to estimate lesion burden.

Neuropsychological Assessment

The Brief Repeatable Battery of Neuropsychological Tests was conducted on all participants.[22] The battery includes verbal and visual memory tests: the Selective Reminding Task (SRT), the 10/36-Spatial Recall Test (SPART), information-processing speed/working memory tests (Symbol Digit Modalities Test [SDMT], and the Paced Auditory Serial Addition Test [PASAT], 2- and 3-second versions), and a phonemic fluency test (word list generation). Administration time was approximately 25 minutes. For 3 patients with limited hand or arm movement, the test administrator placed the checkers in the nontimed SPART, as directed by the patient. The PASAT was attempted but not completed in all participants due to noncompliance or fatigue.

Image Analysis

R2* and QSM data from each participant were rigidly aligned with the T1-weighted images and interpolated to the same resolution. Bias field-intensity normalization for T1 images was performed by using the N4 method[23] as part of the Advanced Normalization Tools package (stnava.github.io/ANTs/). We segmented 4 DGM nuclei (caudate, putamen, GP, and thalamus) with a multiatlas segmentation method by means of both T1 and QSM images,[24] taking advantage of the high DGM contrast available on QSM (Fig. 1), which is particularly beneficial to reliably segment the GP. Ten manually segmented volumes from healthy controls (2 controls from the current study, 8 from another ongoing study) were used as atlases. Following a standard multiatlas segmentation method,[25] the atlases from the 10 healthy controls were propagated to each individual dataset by using automatic nonlinear registration on multimodal T1, R2*, and QSM data.[26] Each of the registered anatomic labels propagated from the 10 atlases was fused by using a probabilistic label-fusion method proposed by Wang et al[27] to produce optimal segmentation of each dataset. Using these anatomic segmentation labels, we then extracted vol-

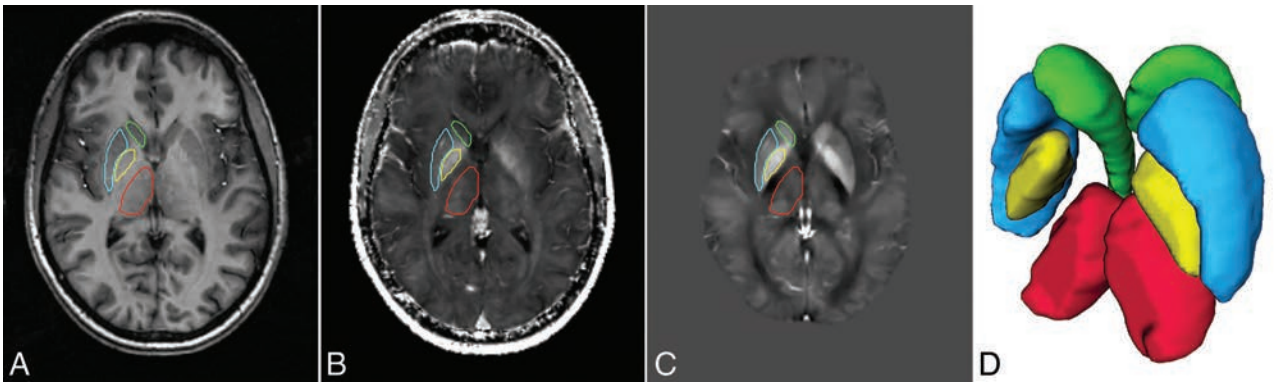

FIG 1. Sample axial images of the 3 MR imaging methods: T1-weighted image (*A*), R2* map (*B*), QSM map (*C*). *D*, Oblique view of 3D volume segmentation of the 4 deep gray matter nuclei. The ROIs within each section are shown for one side of the brain, with matching color to the 3D segmentation (caudate = green; putamen = blue; globus pallidus = yellow; thalamus = red).

Participant demographics and cognitive performance[a]

	Controls	Patients	*P* Value
Age (yr)	47.51 ± 10.09	49.08 ± 10.03	.53
Sex	18 F, 9 M	27 F, 13 M	.94
Education (yr)	17.37 ± 3.87	13.66 ± 2.05	<.001
Median Expanded Disability Status Scale score (range)	NA	5.25 (2.0–9.0)	NA
Mean disease duration	NA	14.90 ± 8.91 years	NA
Disease-modifying therapy	NA	None: *n* = 22; glatiramer acetate: *n* = 12; interferon β-1a: *n* = 6	NA
Lesion load	NA	6.23 ± 8.78 mL	NA
SRT immediate recall	56.15 ± 6.20	44.40 ± 10.77	<.001
SRT continuous long-term retrieval	42.63 ± 12.12	23.00 ± 14.66	<.001
SRT delayed recall	9.11 ± 2.10	6.70 ± 2.69	<.001
SPART immediate recall	20.37 ± 5.10	20.25 ± 5.20	.90
SPART delayed recall	7.11 ± 2.55	6.98 ± 2.39	.76
SDMT	58.74 ± 10.52	49.56 ± 16.08	.02
PASAT 3-second[b]	49.04 ± 8.51	43.94 ± 11.73	.55
PASAT 2-second[c]	36.52 ± 8.62	32.15 ± 10.78	.49
Phonemic fluency (word list generation)	30.52 ± 6.94	27.28 ± 8.57	.25

Note:—NA indicates not applicable.
[a] Group comparisons in cognition are education-adjusted. Data are means unless otherwise indicated.
[b] Available from 35 patients with MS and 26 controls.
[c] Available from 34 patients with MS and 25 controls.

umes, R2*, and QSM measurements bilaterally on each of the 4 structures in all participants. DGM volumes were normalized to intracranial volume. This method has previously been validated showing high reliability at retest and superior agreement with manual segmentation compared with conventional segmentation methods.[24] Although the size of a particular DGM region can influence segmentation results, such effects can be considered marginal (eg, concordance between T1/QSM multiatlas method and manual tracing[24]: caudate, 82%; putamen, 87%; globus pallidus, 83%; thalamus, 87%).

Total lesion volume was measured by manually tracing the outline of each lesion on T2-weighted images and multiplying by the section thickness. Lesions were defined as hyperintensities on T2-weighting, with confirmation from FLAIR. Lesion measures were made by the senior author, an imaging expert with 25 years of experience.

Statistical Analyses

We first compared patients with controls in cognitive scores and DGM parameters (volume, iron) by using ANCOVAs, controlling for age, sex, and/or education as applicable. Next, to predict cognition by the DGM parameters, we conducted nested sets of linear regression models (hierarchic regressions), successively adding predictors in blocks (see also Pinter et al[10]). Models were run separately for each of the 4 DGM structures and separately in the controls and patients. For these regressions, cognitive scores were first *z*-transformed on the basis of the control group and then combined into a composite neuropsychological *z* score (NP_{total}) comprising 6 test scores: 2 SRT measures (continuous long-term retrieval, delayed recall), 2 SPART measures (immediate and delayed recall), SDMT, and word list generation. The PASAT was excluded from NP_{total} due to excessive missing data (Table). For each of the 8 models per group, the first block of predictors included age, sex, and education. The second block added DGM volumes (age- and sex-corrected). The third block added either R2* or QSM measures (age- and sex-corrected).

RESULTS

Participant Characteristics

The Table shows that patients and healthy controls were statistically matched in age and sex distribution, but healthy controls were more educated. Our patient cohort comprised 60% patients with progressive MS with a median Expanded Disability Status Scale[28] score of 5.25 and disease duration of 14.9 ± 8.9 years. Eighteen patients (all patients with relapsing-remitting MS and 2 with progressive MS) were taking disease-modifying medications. Additional clinical details are outlined in the Table. After we controlled for the education differences, ANCOVAs on the Brief Repeatable Battery of Neuropsychological Tests subtests showed verbal memory (SRT) and processing speed reductions (SDMT) in patients compared with controls.

Medications for symptom management were prescribed to 22 patients (55%). These included antidepressants (n = 15), sleep medications (n = 3), pain medications (n = 12), and muscle relaxants (n = 6). Cognitive functions were unaffected by the

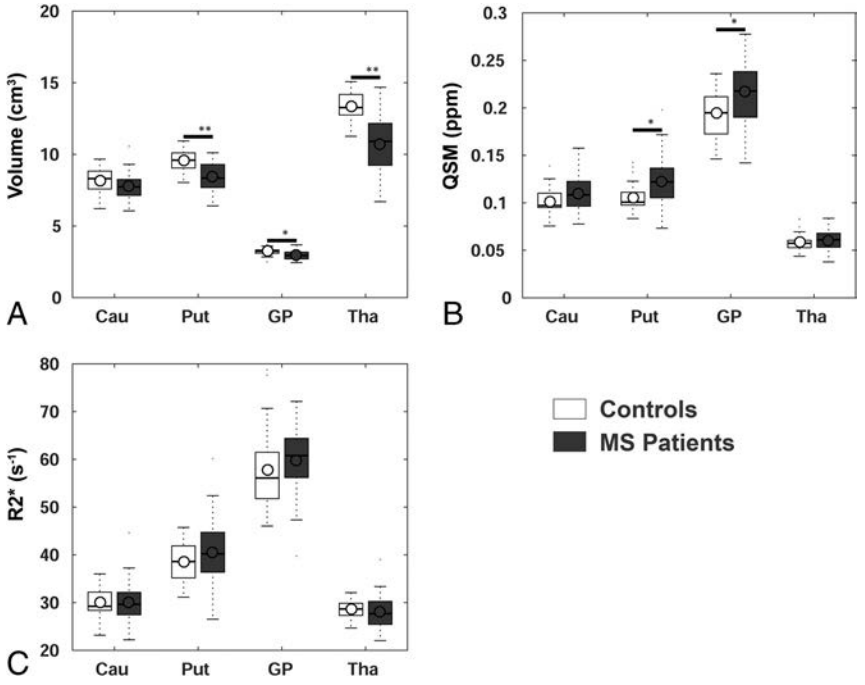

FIG 2. Group differences in age-, sex-, and intracranial volume-normalized deep gray matter volumes (*A*) and iron based on QSM (*B*) and R2* (*C*). Boxplots show ranges of the first-to-third quartiles, *circles* indicate means, *lines* inside the boxes indicate medians, *dotted lines* indicate the fence (1.5 interquartile ranges), and outliers are shown by *dots* outside the fence. Cau = caudate; Put = putamen; GP = globus pallidus; Tha = thalamus; double asterisks = $P < .001$; asterisk = $P < .01$.

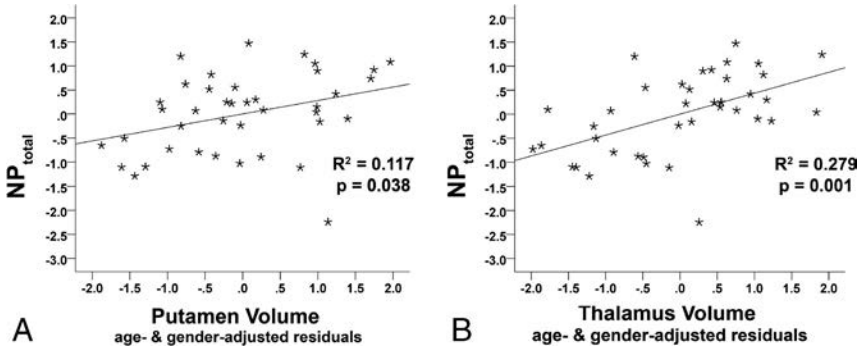

FIG 3. Prediction of cognition (NP_{total}) by age, sex, and intracranial volume-normalized putamen (*A*) and thalamus (*B*) volumes in patients with MS after correcting for age, sex, and education.

presence/absence of symptom management medications, apart from patients taking such medications showing better SRT-delayed recall ($t = 2.22$, $P = .04$).

Group Differences in DGM

Bilateral DGM volumes were correlated with age and sex in some regions; thus, age-, and sex-adjusted volumes were used. We observed volumetric reductions in patients with MS in the putamen ($P < .001$), GP ($P = .002$), and thalamus ($P < .001$) (Fig 2*A*). For QSM, patients showed higher values than controls in the putamen ($P = .003$) and GP ($P = .003$), with a trend in the caudate ($P = 0.06$) (Fig 2*B*). R2* increases in patients showed trends similar to those in QSM, but they were not significant (Fig 2*C*).

With partial correlations correcting for age and sex, measures of R2* and QSM were highly correlated with each other within each region in patients (caudate: $r = 0.66$; putamen: $r = 0.86$; GP: $r = 0.75$; thalamus: $r = 0.60$; all, $P < .001$). Except for the thalamus, these correlations were similar, albeit weaker, in the control group (caudate: $r = 0.46$, $P = .02$; putamen: $r = 0.59$, $P = .002$; GP: $r = 0.78$, $P < .001$; thalamus: $r = 0.03$, $P = .89$). Notably, R2* and QSM values were uncorrelated with structural volumes within each of the 4 DGM nuclei, both in patients and controls, permitting their use in the hierarchic regressions.

Cognition, DGM Volumes, and Iron Susceptibility

Regressions examined predictors of cognitive performance within each of the DGM regions separately for patients and controls. The first block of predictors included only demographic variables: age, sex, and education years. In the second block, DGM volumes were added. In the third block, QSM or R2* values were included.

Within the patient group, compared to a model with demographic variables alone ($R^2 = 0.15$, $P = .12$), putamen volumes significantly increased prediction of NP_{total} ($R^2 = 0.25$, $\Delta R^2 = 0.1$, model $F = 2.89$, $P = .046$; putamen $\beta = 0.32$, $t = 2.15$, $P = .04$; Fig 3*A*). These results were similar but more pronounced with thalamic volumes ($R^2 = 0.39$, $\Delta R^2 = 0.24$, model $F = 5.50$, $P = .002$; thalamus $\beta = 0.49$, $t = 3.68$, $P < .001$; Fig 3*B*). Volumetric data did not contribute significantly to relationships with NP_{total} in the healthy controls (On-line Table 1).

In a third block, QSM values were then included. In patients, after controlling for demographic influences and GP volumes, NP_{total} was related to GP QSM ($R^2 = 0.29$, $\Delta R^2 = 0.1$, model $F = 2.76$, $P = .03$; GP QSM $\beta = -0.32$, $t = 2.22$, $P = .03$; Fig 4*B*). Thus, GP QSM explained an additional 10% of variance (ΔR^2) in cognitive performance, after controlling for demographic variables and for GP volume. None of the other QSM measures were substantially related to NP_{total} in patients or in controls (see On-line Tables 1 and 2 for details). Analyses with R2* showed a similar but nonsignificant result for the GP only ($R^2 = 0.25$, $\Delta R^2 = 0.06$, model $F = 2.26$, $P = .071$; GP $\beta = -0.25$, $t = -1.70$, $P = .099$; Fig 4*A*). No other R2* measure was significantly or at trend-level related to NP_{total} in patients. Controls did not show any significant relationships between iron measures and cognition, including in the GP iron models (QSM-GP: GP $\beta = -0.077$, $t = -0.44$, $P = .663$; R2*-GP: GP $\beta = -0.15$, $t = -0.86$, $P = .399$).

When we inspected the NP_{total}, 2 tests were individually sensitive to DGM changes. Thalamic volume correlated with SPART-

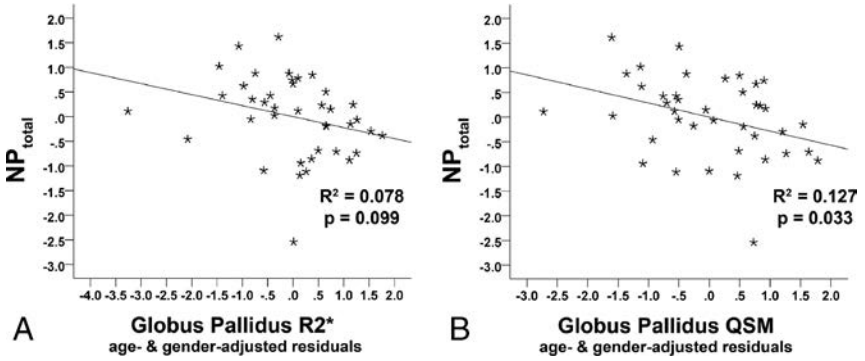

FIG 4. Prediction of cognition (NP_{total}) by age- and sex-corrected QSM (*A*) and R2* (*B*) values in the globus pallidus in patients with MS after correcting for age, sex, education, and individual DGM volumes.

delayed recall (SPART: $\beta = 0.45$, $P = .003$) and with SDMT ($\beta = 0.45$, $P = .003$). QSM in the GP was negatively related to phonemic fluency ($\beta = -0.40$, $P = .01$). Bonferroni correction by 6, the number of individual cognitive tests in the NP_{total} ($P = .05/6 = 0.008$), only retained the thalamic volume correlations with SDMT and SPART. Disability (Expanded Disability Status Scale) and disease duration were unrelated to any of the MR imaging measures in this cohort, and only trend-level correlated with NP_{total} ($r = -0.37$, $P = .07$), possibly due to limited sensitivity of the Expanded Disability Status Scale in higher ranges (focusing on motor symptoms but not cognitive symptoms) and the long duration and variability in disease durations in the current cohort.

DISCUSSION

We examined cognitive correlates of DGM atrophy and iron accumulation in a mixed cohort of patients with progressive MS and relapsing-remitting MS. Irrespective of atrophy, cognition was negatively related to iron accumulation in the GP assessed with QSM, with a similar trend in the R2* measure. In turn, volumes of the thalamus and putamen were related to cognition, replicating previous findings.[2] These correlations were also irrespective of iron accumulation in those regions. Within each investigated DGM structure, volumetric and iron measures were unrelated, suggesting that atrophic and iron-related pathologies in the DGM may exert separable influences on cognitive functions in MS.

Our findings extend the limited literature on relationships between DGM iron and cognition in MS. Only 2 previous studies concurrently accounted for regional[8] or global atrophy[10] and reported, similarly, moderate relationships between DGM iron and cognition. Modica et al[8] used susceptibility-weighted imaging to assess DGM iron. Excessive iron was indicated by the mean phase across voxels with a 2 SD+ below the normal mean phase. In the caudate, putamen, GP, and pulvinar thalamus, this iron measure predicted processing speed. However, after they adjusted for regional volumes, iron-cognition links were no longer significant. Thus, unlike in the current study using QSM and R2*, Modica et al[8] found no relationship between their iron measure and cognition when regional atrophy was controlled. Pinter et al[10] reported correlations between a processing speed ("cognitive efficiency") composite score (SDMT, PASAT) and a combined basal ganglia R2* measure, while controlling for global brain measures (normalized brain volume, lesion load, magnetization transfer ratio for normal-appearing brain tissue). Methodologic differences between the behavioral and iron measures and the normalization procedures likely caused differences among studies, but generally, these findings emphasize the importance of examining cognitive correlates of DGM iron pathology in MS vis-à-vis atrophy, as was done here.

Because iron imaging in MS is relatively new and rapidly evolving, another important aspect here was the assessment of different iron MR imaging parameters, combined with cognition. Schmalbrock et al[11] also tested both QSM and R2*, reporting a relationship between Flanker Task performance and caudate/anterior putamen iron assessed with QSM, but not R2*, in patients with relapsing-remitting MS. The Brief Repeatable Battery of Neuropsychological Tests was applied but not included, and the cognitive effects of iron accumulation were not further examined against other DGM pathologies such as atrophy. Nevertheless, the findings are comparable with ours insofar as the QSM measure was a better predictor of cognition (ie, inhibition in a Flanker Task in Schmalbrock et al) than R2*. While R2* and QSM are complementary measures, they have distinct differences. First, the iron sensitivity of R2* is highly field-dependent, with higher fields being advantageous,[29] while QSM is largely field-insensitive.[30] Second, R2* is more susceptible to water content with inflammation weakening the R2* signal but having little effect on QSM. Third, demyelination has opposing effects, with the QSM signal increasing from demyelination and R2* decreasing.[31] Thus, QSM increases by demyelinating effects adding to iron accumulation, while these 2 events oppose each other for R2*. Thus, our findings that QSM shows a tighter coupling to cognition than R2* may relate to both the dominant iron accumulation in DGM and the additive effects of DGM demyelination on QSM.

We observed a specific role of GP iron accumulation in global cognitive functions, irrespective of GP atrophy, implying that iron accumulation in the GP may have a unique role in globally affecting cognitive processes in this MS cohort. In an early study, Brass et al[9] had approximated iron accumulation by examining T2 hypointensities (at 1.5T). The authors also reported hypointensities in the GP—but no other DGM region—to be the only significant predictor of a composite cognitive score. Similar to our findings, tests that were individually related to GP hypointensities included verbal fluency and the SDMT, but not memory. The GP has the highest iron concentration in the human brain, exceeding that in all other DGM nuclei,[12,32] and it is a target region of several neurodegenerative diseases with primary brain iron accumulation etiologies.[33] Functionally, the GP is the major input region to the thalamus within all the frontostriatal-thalamic loops, including lateral prefrontal and motor/supplemental motor cortex targets and serving a range of cognitive, emotional, motor, and oculomotor functions.[34] A finer segregation within the GP would be valuable to delineate further whether specific psychomotor functions in MS are particularly vulnerable to iron accumulation

and/or regional atrophy. As it stands, our findings only speak to a relationship between GP iron and global cognitive functions in MS. Thus, future studies should extend DGM imaging and add basal ganglia–specific tasks that also probe motor functions, considering the putamen-GP iron pathology observed here.

Among the study limitations, sample size for both patients and controls was relatively small so that finer grained analyses of DGM-cognition links within MS subtypes could not be performed reliably. Combining relapsing ($n = 16$) and progressive MS subtypes ($n = 24$) in the current study may have biased the results toward patients with progressive MS. Qualitatively, the relapsing-remitting MS subgroup took an intermediate place between patients with progressive MS and controls in all of the neuropsychological measures and in most of the DGM measures. However, larger scale studies with equally sized groups of MS subtypes should be performed. These may uncover differential relationships to cognition with more dominant inflammatory (relapsing MS) or atrophic/demyelinating (progressive MS) features. Our study also did not account for lesion burden, which has shown a relationship with cognitive decline and R2* in some,[7] but not other[35] studies. None of the lesions were visible in the DGM ROIs in the current study, by using manual tracing on T2/FLAIR images. Because the focus of the current study was to disambiguate the cognitive significance of iron pathology vis-à-vis atrophy specifically in the DGM and the MR parameters were not optimized for identification of DGM lesions, potential additive or separable effects of such lesions on cognition remain to be clarified in the future.

In addition, many patients were prescribed medications for symptom management. Although we did not observe an interaction between these medications and cognitive performance here, a formal assessment of mental health and other central nervous factors would have been preferable. Finally, the healthy controls had a higher educational level than the patient group. Besides controlling for education levels in each analysis, other aspects of the data speak against a strong influence of education on the final results. For example, On-line Tables 1 and 2 show that education never emerged as a significant predictor in any of the regression models in either group. Simple correlations (not presented) between the raw neuropsychological test measures included in NP_{total} and years of education were all nonsignificant. Taken together, although there was an imbalance in educational levels between patients and controls, this is unlikely to have influenced our results.

CONCLUSIONS

Increased iron in the GP, measured by QSM, was moderately associated with a lower cognitive composite score in this MS cohort. This effect was unrelated to atrophy of the GP. Whereas thalamic atrophy was the strongest predictor of cognitive performance in patients with MS, this outcome, in turn, was not further modulated by thalamic QSM/R2* iron measures. Our findings suggest separable and negative relationships among cognition, DGM iron, and DGM atrophy in MS.

ACKNOWLEDGMENTS

We would like to thank Leah White for her help with patient recruitment and chart review.

Disclosures: Jonn A. Kmech—*RELATED*: *Grant*: MS Society of Canada (EGID 1619), Canadian Institutes of Health Research (FRN MOP 102582), *Comments*: salary as a research assistant*. Esther Fujiwara—*RELATED*: *Grant*: Canadian Institutes of Health Research, MS Society, *Comments*: operating grants to senior author Alan H. Wilman, MS Society of Canada (EGID 1619) and the Canadian Institutes of Health Research (FRN MOP 102582)*; *UNRELATED*: *Grants/Grants Pending*: MS Society, Alberta Gambling Research Institute, Canadian Institutes of Health Research, Social Sciences and Humanities Research Council of Canada, *Comments*: received an operating grant from the Social Sciences and Humanities Research Council of Canada (2010–2013) as Principal Investigator; received an operating grant from the Canadian Institutes of Health Research (2013–2017) as a team grant member*. Dana Cobzas—*RELATED*: *Grant*: MS Society of Canada (EGID 1619), Canadian Institutes of Health Research (FRN MOP 102582)*. Hongfu Sun—*RELATED*: *Grant*: MS Society of Canada (EGID 1619), Canadian Institutes of Health Research (FRN MOP 102582)*. Peter Seres—*RELATED*: *Grant*: MS Society of Canada and Canadian Institutes of Health Research, *Comments*: grant received with money paid to the institution: MS Society of Canada (EGID 1619), Canadian Institutes of Health Research (FRN MOP 102582).* Gregg Blevins—*RELATED*: *Grant*: MS Society of Canada and Canadian Institutes of Health Research*; *UNRELATED*: *Consultancy*: Biogen, Teva Pharmaceuticals, Merck Serono, Novartis, Roche, Genentech. Alan H. Wilman—*RELATED*: *Grant*: Multiple Sclerosis Society of Canada MS Society of Canada (EGID 1619), Canadian Institutes of Health Research (FRN MOP 102582).

REFERENCES

1. Ghaffar O, Feinstein A. **The neuropsychiatry of multiple sclerosis: a review of recent developments.** *Curr Opin Psychiatry* 2007;20:278–85 CrossRef Medline
2. Houtchens MK, Benedict RH, Killiany R, et al. **Thalamic atrophy and cognition in multiple sclerosis.** *Neurology* 2007;69:1213–23 CrossRef Medline
3. Stankiewicz JM, Neema M, Ceccarelli A. **Iron and multiple sclerosis.** *Neurobiol Aging* 2014;35(suppl 2):S51–58 CrossRef Medline
4. Schipper HM. **Neurodegeneration with brain iron accumulation: clinical syndromes and neuroimaging.** *Biochim Biophys Acta* 2012;1822:350–60 CrossRef Medline
5. Khalil M, Langkammer C, Ropele S, et al. **Determinants of brain iron in multiple sclerosis: a quantitative 3T MRI study.** *Neurology* 2011;77:1691–97 CrossRef Medline
6. Khalil M, Langkammer C, Pichler A, et al. **Dynamics of brain iron levels in multiple sclerosis: a longitudinal 3T MRI study.** *Neurology* 2015;84:2396–402 CrossRef Medline
7. Ge Y, Jensen JH, Lu H, et al. **Quantitative assessment of iron accumulation in the deep gray matter of multiple sclerosis by magnetic field correlation imaging.** *AJNR Am J Neuroradiol* 2007;28:1639–44 CrossRef Medline
8. Modica CM, Zivadinov R, Dwyer MG, et al. **Iron and volume in the deep gray matter: association with cognitive impairment in multiple sclerosis.** *AJNR Am J Neuroradiol* 2015;36:57–62 CrossRef Medline
9. Brass SD, Benedict RH, Weinstock-Guttman B, et al. **Cognitive impairment is associated with subcortical magnetic resonance imaging grey matter T2 hypointensity in multiple sclerosis.** *Mult Scler* 2006;12:437–44 CrossRef Medline
10. Pinter D, Khalil M, Pichler A, et al. **Predictive value of different conventional and non-conventional MRI-parameters for specific domains of cognitive function in multiple sclerosis.** *Neuroimage Clin* 2015;7:715–20 CrossRef Medline
11. Schmalbrock P, Prakash RS, Schirda B, et al. **Basal ganglia iron in patients with multiple sclerosis measured with 7T quantitative susceptibility mapping correlates with inhibitory control.** *AJNR Am J Neuroradiol* 2016;37:439–46 CrossRef Medline
12. Langkammer C, Krebs N, Goessler W, et al. **Quantitative MR imaging of brain iron: a postmortem validation study.** *Radiology* 2010;257:455–62 CrossRef Medline
13. Langkammer C, Schweser F, Krebs N, et al. **Quantitative susceptibility mapping (QSM) as a means to measure brain iron? A post mortem validation study.** *Neuroimage* 2012;62:1593–99 CrossRef Medline
14. Sun H, Walsh AJ, Lebel RM, et al. **Validation of quantitative suscep-**

tibility mapping with Perls' iron staining for subcortical gray matter. *Neuroimage* 2015;105:486–92 CrossRef Medline
15. Walsh AJ, Lebel RM, Eissa A, et al. **Multiple sclerosis: validation of MR imaging for quantification and detection of iron.** *Radiology* 2013;267:531–42 CrossRef Medline
16. Polman CH, Reingold SC, Banwell B, et al. **Diagnostic criteria for multiple sclerosis: 2010 revisions to the McDonald criteria.** *Ann Neurol* 2011;69:292–302 CrossRef Medline
17. Lebel RM, Eissa A, Seres P, et al. **Quantitative high-field imaging of sub-cortical gray matter in multiple sclerosis.** *Mult Scler* 2012;18:433–41 CrossRef Medline
18. Sun H, Wilman AH. **Background field removal using spherical mean value filtering and Tikhonov regularization.** *Magn Reson Med* 2014;71:1151–57 CrossRef Medline
19. Bilgic B, Pfefferbaum A, Rohlfing T, et al. **MRI estimates of brain iron concentration in normal aging using quantitative susceptibility mapping.** *Neuroimage* 2012;59:2625–35 CrossRef Medline
20. Liu T, Liu J, de Rochefort L, et al. **Morphology enabled dipole inversion (MEDI) from a single-angle acquisition: comparison with COSMOS in human brain imaging.** *Magn Reson Med* 2011;66:777–83 CrossRef Medline
21. Wu B, Li W, Guidon A, et al. **Whole brain susceptibility mapping using compressed sensing.** *Magn Reson Med* 2012;67:137–47 CrossRef Medline
22. Rao SM, the Cognitive Function Study Group of the National Multiple Sclerosis Society. *A Manual for the Brief Repeatable Battery of Neuropsychological Tests in Multiple Sclerosis.* Milwaukee: Medical College of Wisconsin; 1990
23. Tustison NJ, Avants BB, Cook PA, et al. **N4ITK: improved N3 bias correction.** *IEEE Trans Med Imaging* 2010;29:1310–20 CrossRef Medline
24. Cobzas D, Sun H, Walsh AJ, et al. **Subcortical gray matter segmentation and voxel-based analysis using transverse relaxation and quantitative susceptibility mapping with application to multiple sclerosis.** *J Magn Reson Imaging* 2015;42:1601–10 CrossRef Medline
25. Heckemann RA, Hajnal JV, Aljabar P, et al. **Automatic anatomical brain MRI segmentation combining label propagation and decision fusion.** *Neuroimage* 2006;33:115–26 CrossRef Medline
26. Avants BB, Tustison NJ, Song G, et al. **A reproducible evaluation of ANTs similarity metric performance in brain image registration.** *Neuroimage* 2011;54:2033–44 CrossRef Medline
27. Wang H, Suh JW, Das SR, et al. **Multi-atlas segmentation with joint label fusion.** *IEEE Trans Pattern Anal Mach Intell* 2013;35:611–23 CrossRef Medline
28. Kurtzke JF. **Rating neurologic impairment in multiple sclerosis: an expanded disability status scale (EDSS).** *Neurology* 1983;33:1444–52 CrossRef Medline
29. Mitsumori F, Watanabe H, Takaya N, et al. **Toward understanding transverse relaxation in human brain through its field dependence.** *Magn Reson Med* 2012;68:947–53 CrossRef Medline
30. Wang Y, Liu T. **Quantitative susceptibility mapping (QSM): decoding MRI data for a tissue magnetic biomarker.** *Magn Reson Med* 2015;73:82–101 CrossRef Medline
31. Deistung A, Schäfer A, Schweser F, et al. **Toward in vivo histology: a comparison of quantitative susceptibility mapping (QSM) with magnitude-, phase-, and R2*-imaging at ultra-high magnetic field strength.** *Neuroimage* 2013;65:299–314 CrossRef Medline
32. Hallgren B, Sourander P. **The effect of age on the non-haemin iron in the human brain.** *J Neurochem* 1958;3:41–51 CrossRef Medline
33. Rouault TA. **Iron metabolism in the CNS: implications for neurodegenerative diseases.** *Nat Rev Neurosci* 2013;14:551–64 CrossRef Medline
34. Alexander GE, DeLong MR, Strick PL. **Parallel organization of functionally segregated circuits linking basal ganglia and cortex.** *Annu Rev Neurosci* 1986;9:357–81 CrossRef Medline
35. Khalil M, Enzinger C, Langkammer C, et al. **Quantitative assessment of brain iron by R(2)* relaxometry in patients with clinically isolated syndrome and relapsing-remitting multiple sclerosis.** *Mult Scler* 2009;15:1048–54 CrossRef Medline

Enhancing Brain Lesions during Acute Optic Neuritis and/or Longitudinally Extensive Transverse Myelitis May Portend a Higher Relapse Rate in Neuromyelitis Optica Spectrum Disorders

G. Orman, K.Y. Wang, Y. Pekcevik, C.B. Thompson, M. Mealy, M. Levy, and I. Izbudak

ABSTRACT

BACKGROUND AND PURPOSE: Neuromyelitis optica spectrum disorders are inflammatory demyelinating disorders with optic neuritis and/or longitudinally extensive transverse myelitis episodes. We now know that neuromyelitis optica spectrum disorders are associated with antibodies to aquaporin-4, which are highly concentrated on astrocytic end-feet at the blood-brain barrier. Immune-mediated disruption of the blood-brain barrier may manifest as contrast enhancement on brain MR imaging. We aimed to delineate the extent and frequency of contrast enhancement on brain MR imaging within 1 month of optic neuritis and/or longitudinally extensive transverse myelitis attacks and to correlate contrast enhancement with outcome measures.

MATERIALS AND METHODS: Brain MRIs of patients with neuromyelitis optica spectrum disorders were evaluated for patterns of contrast enhancement (periependymal, cloudlike, leptomeningeal, and so forth). The Fisher exact test was used to evaluate differences between the proportion of contrast enhancement in patients who were seropositive and seronegative for aquaporin-4 antibodies. The Mann-Whitney test was used to compare the annualized relapse rate and disease duration between patients with and without contrast enhancement and with and without seropositivity.

RESULTS: Brain MRIs of 77 patients were evaluated; 59 patients (10 males, 49 females) were scanned within 1 month of optic neuritis and/or longitudinally extensive transverse myelitis attacks and were included in the analysis. Forty-eight patients were seropositive, 9 were seronegative, and 2 were not tested for aquaporin-4 antibodies. Having brain contrast enhancement of any type during an acute attack was significantly associated with higher annualized relapse rates ($P = .03$) and marginally associated with shorter disease duration ($P = .05$). Having periependymal contrast enhancement was significantly associated with higher annualized relapse rates ($P = .03$).

CONCLUSIONS: Brain MRIs of patients with neuromyelitis optica spectrum disorders with contrast enhancement during an acute relapse of optic neuritis and/or longitudinally extensive transverse myelitis are associated with increased annual relapse rates.

ABBREVIATIONS: AQP4 = aquaporin-4; ARR = annualized relapse rate; CE = contrast enhancement; IgG = immunoglobulin G; LETM = longitudinally extensive transverse myelitis; NMO = neuromyelitis optica; NMOSD = NMO spectrum disorders; ON = optic neuritis

Neuromyelitis optica (NMO) is an inflammatory demyelinating disorder of the central nervous system,[1] characterized by recurrent episodes of longitudinally extensive transverse myelitis (LETM) and/or optic neuritis (ON).[2] Discovery of an NMO-specific autoantibody, NMO–immunoglobulin G (IgG), and its target autoantigen, aquaporin-4 (AQP4), have differentiated NMO from multiple sclerosis as a distinct disease entity.[3] Moreover, given the high specificity of AQP4-IgG serology for clinically diagnosed NMO, such seropositivity was incorporated into the revised diagnostic criteria for NMO in 2006.[1] The term "NMO spectrum disorders" (NMOSD) was introduced in 2007 to encompass broader phenotypes, including seropositive patients with coexisting autoimmune disorders and patients with limited or inaugural

Received December 22, 2016; accepted January 14, 2017.

From the Division of Neuroradiology (G.O., Y.P., I.I.), Russell H. Morgan Department of Radiology, and Department of Neurology (M.M., M.L.), The Johns Hopkins University School of Medicine, Baltimore, Maryland; Department of Radiology (K.Y.W.), Baylor College of Medicine, Houston, Texas; and Biostatistics Center (C.B.T.), Johns Hopkins Bloomberg School of Public Health, Baltimore, Maryland.

Carol Thompson received a National Institutes of Health–Clinical and Translational Science Awards grant 1UL1TR001079 (to Johns Hopkins). Maureen Mealy received honoraria from the International Organization of Multiple Sclerosis Nurses and EMD Serono. Michael Levy received research support from the Guthy-Jackson Charitable Foundation, ViroPharma, Acorda Therapeutics, Sanofi, Neuralstem, and Genentech and serves as a consultant for Chugai Pharmaceuticals, GlaxoSmithKline, Alexion Pharmaceuticals, and MedImmune.

Paper previously presented in part as an oral presentation at: Annual Meeting of the American Society of Neuroradiology and the Foundation of the ASNR Symposium, April 25–30, 2015, Chicago, Illinois. The presentation number was O-444.

Please address correspondence to Izlem Izbudak, MD, Division of Neuroradiology, Russell H. Morgan Department of Radiology, The Johns Hopkins University School of Medicine, 600 N Wolfe St, Phipps B-126B, Baltimore, MD 21287; e-mail: iizbuda1@jhmi.edu

http://dx.doi.org/10.3174/ajnr.A5141

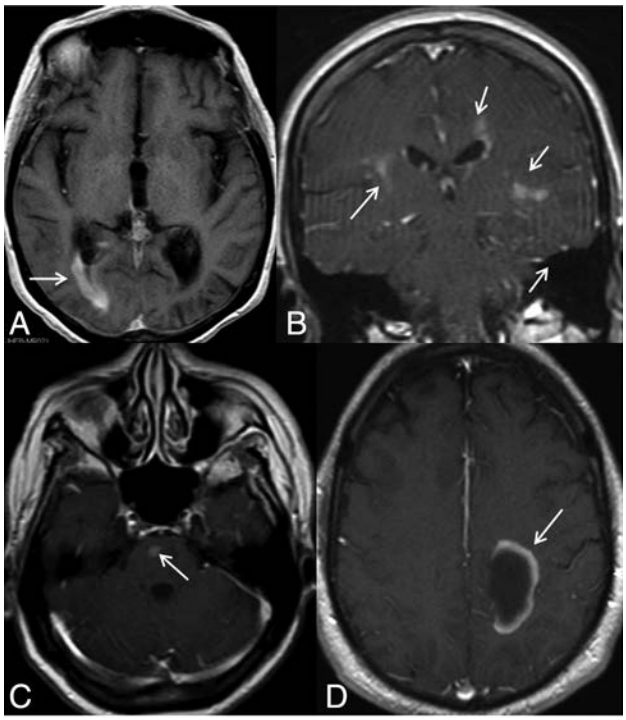

FIG 1. Different contrast-enhancement patterns are shown in this figure. *A*, A periependymal linear enhancement pattern can be seen surrounding the lateral, third or fourth ventricles, and/or cerebral aqueduct. Here we see right posterior periventricular enhancement (*arrow*). *B*, Periependymal enhancement and inhomogeneous, subtle parenchymal enhancement with ill-defined margins, so-called cloudlike enhancement (*arrows*). *C*, Isolated enhancement (*arrow*), *D*, Incomplete ring enhancement (*arrow*).

forms of NMO.[4] The terms NMO and NMOSD were unified under a revised NMOSD definition in 2015.[5] The unifying NMOSD diagnostic criteria allowed the diagnosis of NMOSD in patients without clinical involvement of the optic nerves or the spinal cord and stratified the diagnosis according to those with or without AQP4-IgG positivity.

While NMO was traditionally thought to be a disease exclusively involving the optic nerves and spinal cord, imaging abnormalities within the brain have been reported in a significant proportion of patients seropositive for AQP4-IgG, in regions with both high[6,7] and low AQP4 expression.[8] Lesions involving the diencephalon, area postrema, corpus callosum, hemispheric white matter, and corticospinal tracts have been reported.[8] Specific patterns of contrast enhancement (CE) within the brain have also been reported in NMO, including pencil-thin,[9] cloudlike,[10] leptomeningeal,[11] and perivascular enhancement (Figs 1 and 2).[12] The current literature suggests a relatively low incidence of contrast-enhancing brain lesions in NMO.[9-11,13-18]

However, in a large proportion of brain MRIs in those studies, whether they were acquired during an acute phase of the disease versus at any time point was not specified. Furthermore, the incidence of contrast-enhancing lesions in the brain during acute relapses of ON and/or LETM in patients with NMOSD has not been examined before, to our knowledge. Prior studies investigating predictors of relapse in patients with NMOSD have addressed factors that are either clinical or biochemical in nature, including AQP4-IgG seropositivity,[19] female sex,[20-22] and older age of onset.[23] In contrast, no MR imaging parameters have been shown to be associated with disease outcome.

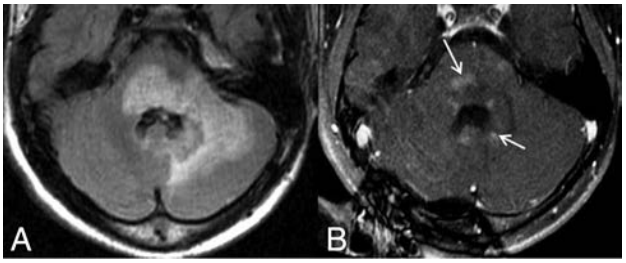

FIG 2. A 21-year-old male patient diagnosed with neuromyelitis optica. He initially presented with longitudinally extensive transverse myelitis when he was 12 years of age. MR imaging was performed at 14 years of age within 1 month of an acute LETM attack. Axial FLAIR image (*A*) shows a large region of increased signal abnormality within the pons, extending into the left middle cerebellar peduncle with expansion of the pons itself and the cerebellar hemisphere. Postcontrast T1-weighted image (*B*) shows cloudlike contrast enhancement (*arrows*).

In the current study, we aimed to delineate the extent and frequency of CE in the brain during acute attacks of ON and/or LETM. We also sought to determine whether detection of brain CE was associated with specific outcome measures, including disease duration and the annualized relapse rate (ARR).

MATERIALS AND METHODS

Patients

A retrospective chart review was performed to identify patients with contrast-enhancing brain lesions between September 2001 and November 2013 at the Johns Hopkins NMO center. All patients identified were diagnosed with NMO or NMOSD based on the Wingerchuk et al 2006[1] or 2007[4] revised criteria, respectively.[5] Institutional review board approval was obtained for the study. Electronic patient records were reviewed for demographic information, history of relapse, AQP4-IgG status, age at diagnosis, age at last follow-up, and the number of relapses.

Neuroimaging

MR imaging examinations were performed by using either 1.5T or 3T scanners (Philips Healthcare, Best, the Netherlands; GE Healthcare, Milwaukee, Wisconsin; and Siemens, Erlangen, Germany). T1WI, fast spin-echo T2WI, fast spin-echo FLAIR, and postgadolinium T1WIs were performed. A gadolinium contrast agent of 0.1 mL/kg was intravenously administered followed by a 20-mL saline injection. T1-weighted axial and coronal images were acquired without any delay after intravenous injection. The sagittal T1WIs were obtained with the following parameters: TR range = 520–696 ms, TE range = 4.6–14 ms, matrix size range = 192 × 192 to 512 × 196, FOV range = 190 × 190 mm to 240 × 240 mm, section thickness/spacing range = 1/1 to 5/7 mm. Axial T2WI was performed with the following parameters: TR range = 2500–7000 ms, TE range = 83–112 ms, matrix size range = 256 × 184 to 448 × 335, FOV range = 159 × 200 mm to 240 × 240 mm, section thickness/spacing range = 2/2 to 5/5 mm. A FLAIR sequence was obtained with the following parameters: TR = 6000 ms, TE = 120 ms, TI = 2000 ms, section thickness = 5 mm, FOV = 23 cm, matrix size = 256 × 256.

All brain MRIs were evaluated in consensus by 2 radiologists, a

Table 1: Association between the proportion of patients with CE and the presence of AQP4-IgG seropositivity[a]

AQP4-IgG	CE Present	CE Absent	No. of Patients (Total)
Positive	31 (64.6%)	17 (35.4%)	48
Negative	4 (55.6%)	5 (44.4%)	9
Total	36 (63.2%)[b]	21 (36.8%)[b]	57 (2 not tested)

[a] Fisher exact test, $P = .7$.
[b] One patient was not tested.

Table 2: Comparison of disease duration and ARR between patients with and without CE during an acute attack

	CE Present	CE Absent	*P* Value
Disease duration (mean) (yr)	4.76 ± 4.81 ($n = 21$)	7.26 ± 5.75 ($n = 38$)	.05
ARR (mean)	1.15 ± 0.73 ($n = 21$)	0.73 ± 0.52 ($n = 38$)	.03[a]

[a] $P < .05$, based on Mann-Whitney test.

board-certified neuroradiologist (I.I.) and a radiologist (G.O.), with 10 and 4 years of experience, respectively. All patients had at least 1 brain MR imaging performed at our institution. Brain MRIs acquired within 1 month of the onset of the relapse were classified as imaging during an acute LETM and/or ON attack. CE was evaluated by using postgadolinium T1-weighted images. Brain CE was categorized in 6 specific patterns of enhancement: periependymal, cloudlike, leptomeningeal, isolated, ring, or other (Figs 1 and 2).

Statistical Analysis

The Fisher exact test was used to evaluate the difference between the proportions of patients with CE who were seropositive versus seronegative. A nonparametric Mann-Whitney test was used to compare the ARR and disease duration between those with and without CE. Regression analyses of the ARR with and without CE were also performed, with and without adjusting for age, sex, race, and AQP4-status. *P* values $< .05$ were considered statistically significant and were not adjusted for multiple analyses.

RESULTS

Brain MRIs of 77 patients (11 males, 66 females) were evaluated for contrast enhancement. Fifty-nine patients (10 males, 49 females) underwent brain MR imaging within 1 month of the onset ON and/or LETM attack and were included in the final analysis. The mean age of patients was 47.8 years (range, 6–78 years). There were 35 African-American, 18 white, and 6 Hispanic (individuals from Mexico) individuals. Forty-eight patients were AQP4-IgG seropositive, 9 were seronegative, and the AQP4-IgG status was not checked in 2 of them. The ARR was not available for 1 patient.

Table 1 depicts the proportions of patients with CE in those with or without AQP4-IgG seropositivity during acute attacks. The Fisher exact test did not demonstrate significantly different proportions of CE in patients with or without AQP4-IgG seropositivity during acute attacks ($P = .7$). No significantly different proportions were noted when stratified by specific enhancement patterns ($P = .7$, data not shown).

Tables 2 and 3 depict the association between the detection of CE during an acute phase and either disease duration or ARR. When imaged during the acute phase, patients demonstrating periependymal CE had significantly higher ARRs compared with those without periependymal CE ($P = .03$). Moreover, patients demonstrating any type of CE during the acute phase had significantly higher ARRs ($P = .03$) than those without.

Table 3: Comparison of disease duration and ARR between patients with and without PCE during an acute attack

	PCE Present	PCE Absent	*P* Value
Disease duration (mean) (yr)	4.76 ± 4.81 ($n = 21$)	7.26 ± 5.75 ($n = 38$)	.05
ARR (mean)	1.30 ± 0.83 ($n = 14$)	0.74 ± 0.49 ($n = 45$)	.03[a]

Note:—PCE indicates periependymal contrast enhancement.
[a] $P < .05$, based on the Mann-Whitney test.

Table 4: Distribution of brain CE patterns among 59 patients with ON and/or LETM

Type of CE	No. of Patients
Periependymal	14
Cloudlike	7
Leptomeningeal	2
Isolated	4
Ring	2
Other	2
Absent	28

On the basis of the regression analyses, the unadjusted difference in ARRs between those with periependymal CE and those without it was 0.56 (95% CI, 0.07–1.05; $P = .03$). After we adjusted for age, sex, race, and AQP4 status, the difference was 0.60 (95% CI, 0.08–1.13; $P = .03$). The unadjusted difference in ARRs between those with any CE and without was 0.42 (95% CI, 0.04–0.80; $P = .03$). After we adjusted for age, sex, race, and AQP4 status, the difference was 0.41 (95% CI, 0.02–0.81; $P = .04$).

Table 4 shows the distribution of brain CE patterns among 59 patients who were scanned within 1 month of an ON and/or LETM attack. Brain CE was categorized and evaluated in 6 specific patterns of enhancement in the beginning of the study: periependymal, cloudlike, leptomeningeal, isolated, ring, or other (Figs 1 and 2). After excluding MRIs that were not obtained within 1 month of ON and/or LETM attack from the final analysis, we regrouped MRIs into 2 groups: a group with periependymal CE and a group with any type of CE. MRIs of 14 patients showed periependymal CE, and 21 patients showed any type of CE within 1 month of ON and/or LETM attacks.

DISCUSSION

The current literature on NMO is limited in its description of neuroimaging features that may predict the outcome of disease.[24] Most asymptomatic NMO brain lesions have not been shown to demonstrate enhancement, and the frequency of acute lesion-associated enhancement remains to be determined.[23] This study demonstrates that approximately 63% of patients during an acute attack of ON and/or LETM may also show CE within the brain parenchyma. CE within the brain, when identified during an acute phase, is associated with a significantly increased ARR. The relapse rate during the first 2 years of the disease strongly determines the risk of an unfavorable outcome as defined by severe disability or death.[25] Brain enhancement in patients during an acute ON and/or LETM may reflect a more severe underlying disease process compared with those without brain CE.

We found no significant difference in the propensity for CE in patients who were AQP4-IgG seropositive (64.6%) and seronegative (55.6%) ($P = .7$, Table 1). CE patterns of brain lesions in the

current literature were described mostly in patients seropositive for AQP4-IgG and have been reported to range from 3% to 56%, excluding small case reports.[3,7,9,10,13,16,17,26] Our study revealed a much higher proportion of CE, approximating 64.6% and 55.6% in patients seropositive and seronegative, respectively. A study investigating contrast-enhancing LETM lesions reported CE in 94% and 71% of seropositive and seronegative patients, respectively, though the authors did not specify the location of CE as within either the brain or spinal cord.[27] To our knowledge, the current study is the largest cohort to report the frequency of contrast-enhancing brain lesions in both seropositive and seronegative patients during active ON and/or LETM relapse of NMO. The small sample of patients seronegative for AQP4-IgG in the current study may be contributing to lack of detection for a significant difference in the proportion of CE seen in seropositive and seronegative patients; however, that might be the case in prior studies failing to show a difference as well. Nevertheless, the number of patients seronegative for AQP4-IgG is always low compared with those who are seropositive; therefore, multi-institutional studies are needed to increase the sample size.

That AQP4 is highly expressed on astrocytic foot processes at the BBB and contributes to the maintenance of BBB integrity is well-described.[3,28,29] Binding of AQP4-IgG to AQP4 in vitro has been shown to alter BBB permeability and astrocyte killing.[30] Disruption of the BBB manifests as CE on brain MR imaging.[31] Periependymal white matter is one of the most AQP4-rich regions of the brain; hence, the high prevalence of periependymal contrast enhancement in our cohort. Furthermore, AQP4-IgG is thought to be pathogenic only in proximity to CNS parenchyma, as evidenced by NMO-like histopathology in animal models in those that received direct administration of AQP4-IgG into the CNS. In contrast, peripheral administration had no effect.[32] The presence and levels of AQP4-IgG in CSF are associated and correlated with those in serum during acute relapses.[33,34] For example, AQP4-IgG is detectable in the CSF of most seropositive patients with serum titers of >1:250 during an acute relapse.[35] Moreover, the amount of CSF AQP4-IgG is correlated with astrocyte damage and BBB breakdown.[34] Therefore, it is possible that those with lower serum titers or those not in acute relapse in the current study may not have detectable or significant CSF levels of AQP4-IgG to lead to the BBB disruption and consequent CE. Most interesting, there have been reports of patients with NMOSD who are AQP4-IgG positive in the serum for many years before the onset of symptomatic disease.[36] The poor correlation between the presence and level of serum and CSF titers of AQP4-IgG may be contributing to the lack of significantly different proportions of CE in seropositive and seronegative patients in our study. It may also be contributing to the high interstudy variability in the reports of the percentage of CE observed in patients with NMOSD.[3,7,9,10,13,16,17,26,27]

Most important, the association between CE during the acute phase and ARR may be confounded because those who underwent brain MRIs during an acute phase may have warranted more immediate imaging because they may have been inherently sicker. Findings may be further confounded by other clinical characteristics. For example, longer intervals between the first and second attack,[37] older age at onset,[23] patients of African origin,[38] female sex,[20-22] and AQP4-IgG seropositivity[19] are associated with worse outcomes and/or higher relapse rates. However, other studies failed to find AQP4-IgG status as a predictor of outcome. Jarius et al[39] found that AQP4-IgG status did not differ significantly with regard to time to relapse or ARR. Jiao et al[40] found that the effect of seropositive status on the relapse rate and disability outcome did not differ. Responses to plasmapheresis based on AQP4-IgG were also not significantly different.[41] Regardless of the discrepant prognostic findings of AQP4-IgG in the existing literature, in our study, a periependymal pattern of CE and the presence of any pattern of CE in the acute phase remained significant predictors of higher ARRs after adjusting for AQP4 status, as well as age, sex, and race, on multivariable analysis.

Enhancement patterns of brain lesions in NMO have some unique features and sometimes, in the presence of characteristic T2 lesions, might aid in making a specific diagnosis. Patchy CE with blurred margins, so-called "cloudlike enhancement," is the most commonly reported enhancement pattern in the literature.[10] More recently, linear periependymal CE, so called "pencil-thin enhancement," and leptomeningeal CE were proposed as more specific patterns than cloudlike enhancement.[9,11] Isolated CE and ring and open-ring CE are considered specific to MS, and they are rarely seen in patients with NMOSD. However, although rare, these intense, well-defined CE patterns have been described before, especially in seronegative patients with NMOSD.[18]

The main limitation of our study is the retrospective design, and factors that have been described in the literature associated with outcomes such as seropositivity status, sex, race, and age at onset may be potential confounders and were not accounted for. There is a possible selection bias based on a group of patients with NMOSD who required brain MR imaging, which may reflect a different subpopulation than that not requiring brain MRIs. The threshold of 1 month as the criterion for an acute attack may be arbitrary, given the lack of information in records available to more accurately assess the patients' clinical statuses and may thus misrepresent these statuses in the current study. Furthermore, the current study was originally conducted before the introduction of the more inclusive revised diagnostic criteria for NMOSD of 2015.[5] Rather, included patients were based on the 2006 diagnostic criteria; therefore, the current study does not account for patients who may now qualify as diagnostic for NMOSD under the 2015 criteria.

CONCLUSIONS

Detection of CE in postgadolinium T1-weighted brain imaging within 1 month of onset of an acute ON and/or LETM is associated with higher ARRs. CE is an important marker reflecting the underlying pathogenic process of NMOSD. Although no significant association was found between CE and AQP4-IgG serostatus, the strong interplay among the BBB disruption, AQP4-IgG deposition, and CE warrants further investigation with a larger multicenter cohort to determine the prognostic role that CE may play as a predictor of outcome and its correlation with clinical severity.

Disclosures: Carol B. Thompson—*RELATED*: *Grant*: National Institutes of Health-Clinical and Translational Science Awards 1ULITR001079 to Johns Hopkins, *Comments*: The grant provides limited free statistical consultation to researchers.* Maureen Mealy—*UNRELATED*: *Payment for Lectures Including Service on Speakers*

Bureaus: Consortium of Multiple Sclerosis Centers, *Comments*: honoraria. Michael Levy—*UNRELATED*: *Grant*: National Institutes of Health, Genzyme/Sanofi, Alnylam Pharmaceuticals, Alexion Pharmaceuticals, MedImmune, Shire*; *Consulting Fee or Honorarium*: Genzyme/Sanofi, Alexion Pharmaceuticals; *Fees for Participation in Review Activities such as Data Monitoring Boards, Statistical Analysis, Endpoint Committees, and the Like*: Quest Diagnostics; *UNRELATED*: *Board Membership*: Acorda Therapeutic, Alexion Pharmaceuticals, Chugai Pharmaceuticals, Asterias Biotherapeutics; *Payment for Development of Educational Presentations*: Quest Diagnostics. Izlem Izbudak—*UNRELATED*: *Consultancy*: Alexion Pharmaceuticals, *Comments*: consulting neuroradiologist for the NMO 301 and NMO 302 PREVENT trial sponsored by Alexion Pharmaceuticals; *Grants/Grants Pending*: Siemens, *Comments*: DTI of the spinal cord in compressive myelopathy, Principal Investigator of the grant*; *Other*: Biogen, *Comments*: neuroradiologist of MS PATHS study partner institute.* *Money paid to the institution.

REFERENCES

1. Wingerchuk DM, Lennon VA, Pittock SJ, et al. **Revised diagnostic criteria for neuromyelitis optica.** *Neurology* 2006;66:1485–89 CrossRef Medline
2. Wingerchuk DM, Hogancamp WF, O'Brien PC, et al. **The clinical course of neuromyelitis optica (Devic's syndrome).** *Neurology* 1999; 53:1107–14 CrossRef Medline
3. Lennon VA, Wingerchuk DM, Kryzer TJ, et al. **A serum autoantibody marker of neuromyelitis optica: distinction from multiple sclerosis.** *Lancet* 2004;364:2106–12 CrossRef Medline
4. Wingerchuk DM, Lennon VA, Lucchinetti CF, et al. **The spectrum of neuromyelitis optica.** *Lancet Neurol* 2007;6:805–15 CrossRef Medline
5. Wingerchuk DM, Banwell B, Bennett JL, et al; International Panel for NMO Diagnosis. **International consensus diagnostic criteria for neuromyelitis optica spectrum disorders.** *Neurology* 2015;85:177–89 CrossRef Medline
6. Pittock SJ, Weinshenker BG, Lucchinetti CF, et al. **Neuromyelitis optica brain lesions localized at sites of high aquaporin 4 expression.** *Arch Neurol* 2006;63:964–68 CrossRef Medline
7. Pittock SJ, Lennon VA, Krecke K, et al. **Brain abnormalities in neuromyelitis optica.** *Arch Neurol* 2006;63:390–96 CrossRef Medline
8. Kim HJ, Paul F, Lana-Peixoto MA, et al; Guthy-Jackson Charitable Foundation NMO International Clinical Consortium & Biorepository. **MRI characteristics of neuromyelitis optica spectrum disorder: an international update.** *Neurology* 2015;84:1165–73 CrossRef Medline
9. Banker P, Sonni S, Kister I, et al. **Pencil-thin ependymal enhancement in neuromyelitis optica spectrum disorders.** *Mult Scler* 2012; 18:1050–53 CrossRef Medline
10. Ito S, Mori M, Makino T, et al. **"Cloud-like enhancement" is a magnetic resonance imaging abnormality specific to neuromyelitis optica.** *Ann Neurol* 2009;66:425–28 CrossRef Medline
11. Long Y, Chen M, Zhang B, et al. **Brain gadolinium enhancement along the ventricular and leptomeningeal regions in patients with aquaporin-4 antibodies in cerebral spinal fluid.** *J Neuroimmunol* 2014;269:62–67 CrossRef Medline
12. Pekcevik Y, Izbudak I. **Perivascular enhancement in a patient with neuromyelitis optica spectrum disease during an optic neuritis attack.** *J Neuroimaging* 2015;25:686–87 CrossRef Medline
13. Kim W, Park MS, Lee SH, et al. **Characteristic brain magnetic resonance imaging abnormalities in central nervous system aquaporin-4 autoimmunity.** *Mult Scler* 2010;16:1229–36 CrossRef Medline
14. Kim JE, Kim SM, Ahn SW, et al. **Brain abnormalities in neuromyelitis optica.** *J Neurol Sci* 2011;302:43–48 CrossRef Medline
15. Kim W, Kim SH, Lee SH, et al. **Brain abnormalities as an initial manifestation of neuromyelitis optica spectrum disorder.** *Mult Scler* 2011;17:1107–12 CrossRef Medline
16. McGraw CA, Swerdlow ML, Robbins MS. **Acute reversible periependymal ventricular enhancement in neuromyelitis optica.** *Eur J Neurol* 2012;19:57–58 CrossRef Medline
17. Cheng C, Jiang Y, Chen X, et al. **Clinical, radiographic characteristics and immunomodulating changes in neuromyelitis optica with extensive brain lesions.** *BMC Neurol* 2013;13:72 CrossRef Medline
18. Pekcevik Y, Orman G, Lee IH, et al. **What do we know about brain contrast enhancement patterns in neuromyelitis optica?** *Clin Imaging* 2016;40:573–80 CrossRef Medline
19. Weinshenker BG, Wingerchuk DM, Vukusic S, et al. **Neuromyelitis optica IgG predicts relapse after longitudinally extensive transverse myelitis.** *Ann Neurol* 2006;59:566–69 CrossRef Medline
20. Wingerchuk DM, Weinshenker BG. **Neuromyelitis optica: clinical predictors of a relapsing course and survival.** *Neurology* 2003;60: 848–53 CrossRef Medline
21. Keegan M, Pineda AA, McClelland RL, et al. **Plasma exchange for severe attacks of CNS demyelination: predictors of response.** *Neurology* 2002;58:143–46 CrossRef Medline
22. Wingerchuk DM. **Neuromyelitis optica: effect of gender.** *J Neurol Sci* 2009;286:18–23 CrossRef Medline
23. Barnett Y, Sutton IJ, Ghadiri M, et al. **Conventional and advanced imaging in neuromyelitis optica.** *AJNR Am J Neuroradiol* 2014;35: 1458–66 CrossRef Medline
24. Argyriou AA, Makris N. **Neuromyelitis optica: a distinct demyelinating disease of the central nervous system.** *Acta Neurol Scand* 2008;118:209–17 CrossRef Medline
25. Nema N, Verma A, Choudhary U, et al. **Ocular oscillations and transient oscillopsia in neuromyelitis optica.** *J Neurol Res* 2014;4:146–50
26. Tahara M, Ito R, Tanaka K, et al. **Cortical and leptomeningeal involvement in three cases of neuromyelitis optica.** *Eur J Neurol* 2012; 19:e47–e48 CrossRef Medline
27. Iorio R, Damato V, Mirabella M, et al. **Distinctive clinical and neuroimaging characteristics of longitudinally extensive transverse myelitis associated with aquaporin-4 autoantibodies.** *J Neurol* 2013; 260:2396–402 CrossRef Medline
28. Waters PJ, McKeon A, Leite MI, et al. **Serologic diagnosis of NMO: a multicenter comparison of aquaporin-4-IgG assays.** *Neurology* 2012;78:665–71; discussion 669 CrossRef Medline
29. Nicchia GP, Nico B, Camassa LM, et al. **The role of aquaporin-4 in the blood-brain barrier development and integrity: studies in animal and cell culture models.** *Neuroscience* 2004;129:935–45 CrossRef Medline
30. Vincent T, Saikali P, Cayrol R, et al. **Functional consequences of neuromyelitis optica-IgG astrocyte interactions on blood-brain barrier permeability and granulocyte recruitment.** *J Immunol* 2008; 181:5730–37 CrossRef Medline
31. Levy LM. **Exceeding the limits of the normal blood-brain barrier: quo vadis gadolinium?** *AJNR Am J Neuroradiol* 2007;28:1835–36 Medline
32. Bradl M, Lassmann H. **Experimental models of neuromyelitis optica.** *Brain Pathol* 2014;24:74–82 CrossRef Medline
33. Takahashi T, Fujihara K, Nakashima I, et al. **Anti-aquaporin-4 antibody is involved in the pathogenesis of NMO: a study on antibody titre.** *Brain* 2007;130:1235–43 CrossRef Medline
34. Sato DK, Callegaro D, de Haidar Jorge FM, et al. **Cerebrospinal fluid aquaporin-4 antibody levels in neuromyelitis optica attacks.** *Ann Neurol* 2014;76:305–09 CrossRef Medline
35. Jarius S, Franciotta D, Paul F, et al. **Cerebrospinal fluid antibodies to aquaporin-4 in neuromyelitis optica and related disorders: frequency, origin, and diagnostic relevance.** *J Neuroinflammation* 2010; 7:52 CrossRef Medline
36. Nishiyama S, Ito T, Misu T, et al. **A case of NMO seropositive for aquaporin-4 antibody more than 10 years before onset.** *Neurology* 2009;72:1960–61 CrossRef Medline
37. Bergamaschi R, Ghezzi A. **Devic's neuromyelitis optica: clinical features and prognostic factors.** *Neurol Sci* 2004;25(suppl 4):S364–67 CrossRef Medline
38. Lana-Peixoto MA. **Devic's neuromyelitis optica: a critical review.** *Arq Neuropsiquiatr* 2008;66:120–38 CrossRef Medline
39. Jarius S, Ruprecht K, Wildemann B, et al. **Contrasting disease patterns in seropositive and seronegative neuromyelitis optica: a multicentre study of 175 patients.** *J Neuroinflammation* 2012;9:14 CrossRef Medline
40. Jiao Y, Fryer JP, Lennon VA, et al. **Updated estimate of AQP4-IgG serostatus and disability outcome in neuromyelitis optica.** *Neurology* 2013;81:1197–204 CrossRef Medline
41. Bonnan M, Cabre P. **Plasma exchange in severe attacks of neuromyelitis optica.** *Mult Scler Int* 2012;2012:787630 CrossRef Medline

Can MRI Visual Assessment Differentiate the Variants of Primary-Progressive Aphasia?

S.A. Sajjadi, N. Sheikh-Bahaei, J. Cross, J.H. Gillard, D. Scoffings, and P.J. Nestor

ABSTRACT

BACKGROUND AND PURPOSE: Primary-progressive aphasia is a clinically and pathologically heterogeneous condition. Nonfluent, semantic, and logopenic are the currently recognized clinical variants. The recommendations for the classification of primary-progressive aphasia have advocated variant-specific patterns of atrophy. The aims of the present study were to evaluate the sensitivity and specificity of the proposed imaging criteria and to assess the intra- and interrater reporting agreements.

MATERIALS AND METHODS: The cohort comprised 51 patients with a root diagnosis of primary-progressive aphasia, 25 patients with typical Alzheimer disease, and 26 matched control participants. Group-level analysis (voxel-based morphometry) confirmed the proposed atrophy patterns for the 3 syndromes. The individual T1-weighted anatomic images were reported by 3 senior neuroradiologists.

RESULTS: We observed a dichotomized pattern of high sensitivity (92%) and specificity (93%) for the proposed atrophy pattern of semantic-variant primary-progressive aphasia and low sensitivity (21% for nonfluent-variant primary-progressive aphasia and 43% for logopenic-variant primary-progressive aphasia) but high specificity (91% for nonfluent-variant primary-progressive aphasia and 95% for logopenic-variant primary-progressive aphasia) in other primary-progressive aphasia variants and Alzheimer disease (sensitivity 43%, specificity 92%). MR imaging was least sensitive for the diagnosis of nonfluent-variant primary-progressive aphasia. Intrarater agreement analysis showed mean κ values above the widely accepted threshold of 0.6 (mean, 0.63 $\pm$ 0.16). Pair-wise interobserver agreement outcomes, however, were well below this threshold in 5 of the 6 possible interrater contrasts (mean, 0.41 $\pm$ 0.09).

CONCLUSIONS: While the group-level results were in precise agreement with the recommendations, semantic-variant primary-progressive aphasia was the only subtype for which the proposed recommendations were both sensitive and specific at an individual level.

ABBREVIATIONS: AD = Alzheimer disease; lvPPA = logopenic-variant PPA; nfvPPA = nonfluent-variant PPA; PPA = primary-progressive aphasia; svPPA = semantic-variant PPA

Primary-progressive aphasia (PPA) is a clinically and pathologically heterogeneous condition characterized by insidious onset and gradual worsening of language due to degeneration of brain language areas. Clinical heterogeneity, compounded by the evolution of signs and symptoms, makes accurate classification of patients a challenging task. Making a reliable clinical diagnosis, on the other hand, is important. Despite lack of a one-to-one relationship between the clinical diagnosis and the underlying pathology, previous clinicopathologic series have identified probabilistic associations among the 3 recognized clinical presentations of PPA and certain pathologies. There are established associations between semantic-variant PPA (svPPA) and frontotemporal lobar degeneration–TAR DNA binding protein 43 (TDP-43); nonfluent-variant PPA (nfvPPA) and frontotemporal lobar degeneration-tau; and logopenic-variant PPA (lvPPA) and Alzheimer pathology.[1-5]

The recommendations on clinical subtyping of PPA have proposed that clinical classification can be supported by imaging according to the pattern of regional atrophy or metabolic impairment.[6] Left posterior frontoinsular atrophy in nfvPPA, anterior temporal atrophy in svPPA, and left posterior peri-Sylvian or parietal atrophy in lvPPA are the recommended atrophy patterns.

Received August 24, 2016; accepted after revision January 2, 2017.

From the Department of Neurology (S.A.S.), University of California, Irvine, Irvine, California; Department of Radiology (N.S.-B., J.H.G.), University of Cambridge, Cambridge, UK; Department of Radiology (N.S.-B., J.C., J.H.G., D.S.), Cambridge University Hospitals, Cambridge, UK; and German Center for Neurodegenerative Diseases (P.J.N.), Magdeburg, Germany.

This work was supported by the funding from Donald Forrester Trust and the Cambridge National Institute for Health Research.

Paper previously presented in part at: Annual Meeting of the American Society of Neuroradiology and the Foundation of the ASNR Symposium; May 18–23, 2013; San Diego, California. The oral presentation was entitled, "How Sensitive Are the Proposed Criteria for the Diagnosis of the Subtypes of Frontotemporal Dementia?"

Please address correspondence to S. Ahmad Sajjadi, MD, PhD, Office 3228, Biological Sciences III, Ring Rd, Irvine, California 92617; e-mail: ssajjadi@uci.edu

Indicates open access to non-subscribers at www.ajnr.org

Indicates article with supplemental on-line table.

http://dx.doi.org/10.3174/ajnr.A5126

Remarkably, these imaging recommendations are derived from studies that either used group-averaged data—which though highly replicated,[7-10] are not necessarily valid for single-patient diagnosis—or were based on observed atrophy in convenience samples[9-14] without qualification of sensitivity, specificity, or reliability. Little is known about whether individual patients, as opposed to groups, fulfilling the clinical criteria for these variants reliably present with the prescribed patterns of atrophy and whether these patterns have sufficient reliability to be exploited to arrive at an accurate syndromic diagnosis.

The aims of the present study were the following: 1) to evaluate the utility of the proposed imaging criteria for the diagnosis of PPA variants by contrasting the patterns of atrophy in individual patients with PPA, as reported by senior neuroradiologists, with the recommendations from the criteria; and 2) to assess the neuroradiologists' intra- and interrater agreement, which, in turn, would be an indication of the robustness of the observed abnormalities.

MATERIALS AND METHODS

Participants

The cohort comprised 51 patients with a root diagnosis of PPA, 25 patients with mild typical Alzheimer disease (AD) as a neurodegenerative control group, and 26 healthy age- and education-matched control participants. The breakdown of the subjects with PPA based on clinical variants was 21 with svPPA, 14 with nfvPPA, 14 with mixed PPA, and 2 with lvPPA. Clinical diagnoses were made in accordance with the published criteria for the diagnosis of PPA[15] and probable Alzheimer disease.[16] The diagnosis of PPA variants was based on a quantitative application of the consensus recommendations[6] as detailed elsewhere.[17] No patients had pedigrees to suggest an autosomal dominant genetic cause. The mixed-PPA group, however, was designated "mixed" on the basis of strict application of the proposed clinical criteria. The patients almost certainly corresponded, however, to what others have designated lvPPA in that they had neither svPPA nor nfvPPA, and they had the same group-level atrophy pattern as in previous lvPPA cohorts.[18] Furthermore, some researchers have proposed to diagnose lvPPA through a hierarchic decision tree in which the key feature of this group is that they are neither svPPA nor nfvPPA.[19] Applying such an algorithm to the present mixed cases would also have them classified as lvPPA. The subjects with mixed PPA in this study should, therefore, be considered analogous to those with lvPPA and are referred to henceforth as such.

The study was approved by the institutional review board of Cambridge University hospitals, UK.

Neuropsychological Battery and Connected Speech Analysis

All patients underwent comprehensive neuropsychological and connected speech assessment before imaging, full details of which have been published previously.[20] The On-line Table provides a summary of some of these data.

Imaging

Image Acquisition. Study participants were scanned within an average of 1.6 ± 0.8 months from cognitive assessment. All MR imaging was performed on the same Magnetum Trio 3T system (Siemens, Erlangen, Germany). T1-weighted anatomic images were acquired by using 3D MPRAGE with the following imaging parameters: TR/TE/TI/flip angle = 2300/2.86/900 ms/9°, 144 sections, 192 × 192 matrix dimensions, and 1.25 × 1.25 × 1.25 mm^3 voxel size. Receiver bandwidth and echo spacing were 240 Hz/pixel and 6.7 ms, respectively.

Data Processing and Group-Level Data Analysis

All obtained T1 volumes were preprocessed as reported previously.[21] Preprocessing and warping procedures need reasonable initial estimates; hence, the origin of each structural volume was set manually to the anterior commissure before preprocessing. All volumes were then spatially normalized and segmented by using the unified segmentation model in statistical parametric mapping 5 (SPM5) (http://www.fil.ion.ucl.ac.uk/spm/software/spm5/).[22] The segments were also modulated to compensate for volumetric differences introduced into the warped images. Finally, gray matter segments were smoothed by using an 8-mm full width at half maximum isotropic Gaussian kernel. Total intracranial volumes were calculated by using the automated SPM technique as described elsewhere,[23] and the obtained values, along with age, were fed into the statistical models as nuisance covariates. Following these steps, a 2-sample *t* test implemented in SPM5[22] contrasted the gray matter volumes of the patient groups against those in controls. The statistical maps were thresholded at $P < .01$, corrected for multiple comparisons (false discovery rate = .01).

Visual Reporting of Individual Scans

Three senior neuroradiologists who were blinded to the clinical diagnoses of the study participants separately reported all unprocessed T1 sequences displayed by using the FMRIB Software Library (FSL, Version 4.1.2; http://www.fmrib.ox.ac.uk/fsl).[24] Thirty-five scans ($n = 7$ for each diagnostic group including controls) were duplicated, bringing the total number of scans to 137 to assess intrarater agreement.

The neuroradiologists were asked to report the scans for the presence and patterns of disproportionate regional or global atrophy in 2 stages. In the first stage, the outcome of which was used for calculations of intra- and interrater agreement and sensitivity, the radiologists were asked to report the scans in their own preferred styles. Subsequent calculations for this stage were based on the reported lobar distribution of the abnormalities. "Global atrophy" and "no atrophy" were also accepted as valid entries. In agreement with the published recommendations for AD[25] and PPA,[6] the following lobar distributions were deemed consistent with the syndromic PPA variants and Alzheimer disease: temporal lobe atrophy for svPPA; left frontal or left frontotemporal atrophy for nfvPPA; left temporal, left parietal, or left temporoparietal atrophy for lvPPA; and temporal, parietal, or temporoparietal atrophy for typical AD. Rating a scan as showing "global atrophy" was not deemed acceptable for any of the syndromic variants of PPA or for AD because the reporting radiologists had not observed "disproportionate" atrophy of a target region. In the second stage, the outcome of which was the basis for specificity and separate sensitivity and agreement calculations, however, the raters were specifically asked to comment on whether there was "disproportionate" left posterior frontoinsular atrophy (indicative of

Table 1: Demographic markers for all participant groups

Demographics	svPPA Mean (Range)	nfvPPA Mean (Range)	lvPPA Mean (Range)	AD Mean (Range)	Control Mean (Range)	Omnibus Sig *P* Value
Age at test (yr)	67 (60–79)	68.9 (53–79)	70.8 (60–83)	68 (60–79)	67.5 (51–80)	NS
Disease duration (mo)[a]	56 (24–108)	38.57 (18–60)	48.7 (24–108)	58 (24–96)	NA	NS
Education (yr)[a]	13.6 (10–18)	12.6 (10–20)	11.6 (9–16)	12.5 (10–19)	12.8 (10–20)	NS
Sex	11 M, 10 F	5 M, 9 F	6 M, 10 F	12 M, 13 F	11 M, 15 F	–
ADL-Q	1 (0–5)	0.53 (0–4)	0.68 (0–4)	2.3 (0–6)	NA	NS

Note:—ADL-Q indicates Activities of Daily Living Questionnaire; Sig, significant; NA, not applicable; NS, not significant.
[a] Nonparametric test.

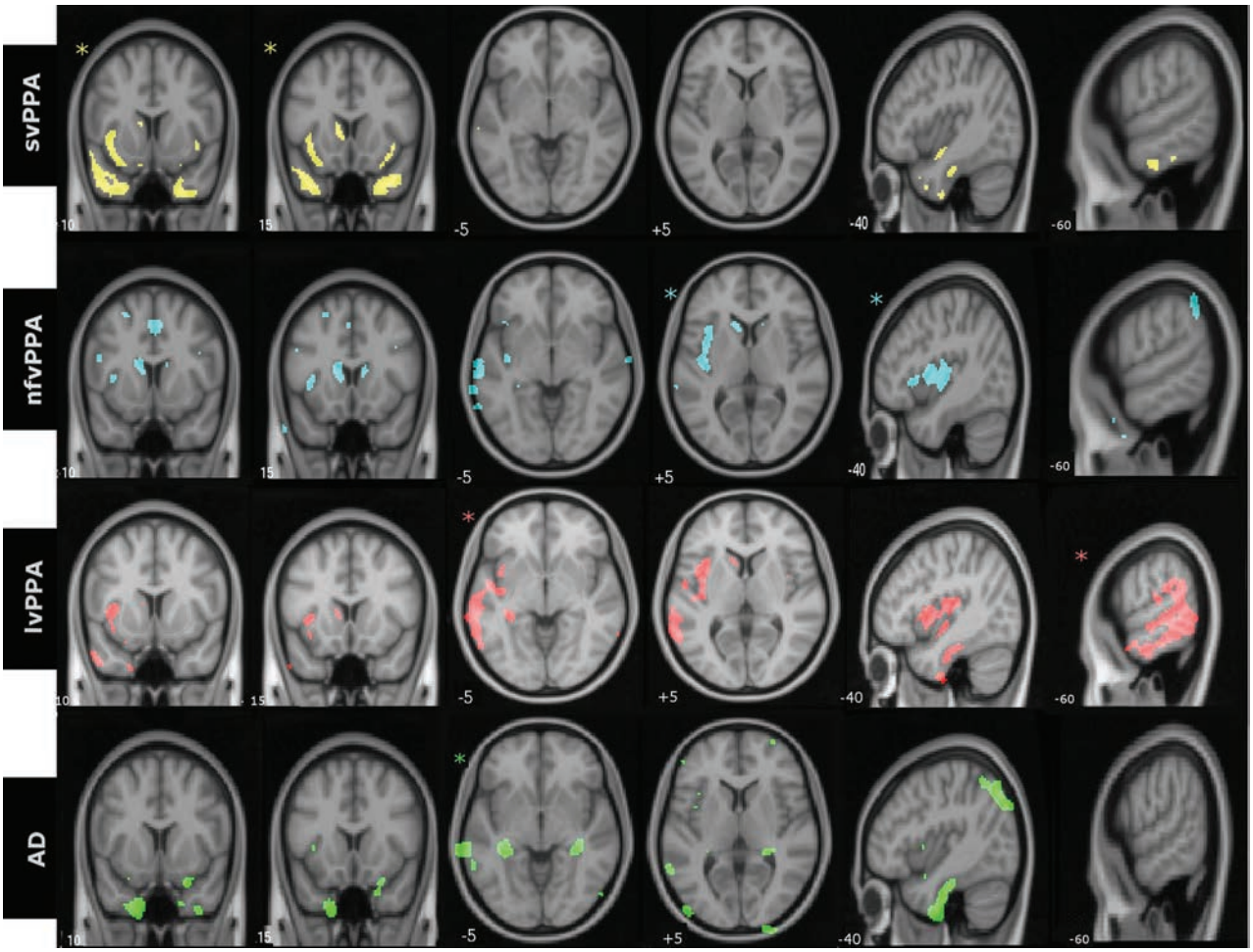

FIG 1. Group-level patterns of atrophy in identical axial, sagittal, and coronal sections of the brain. Images are displayed in neurologic orientation. *Asterisks* demonstrate the section most representative for the particular groups. All comparisons were made at false discovery rate–corrected $P < .01$.

nfvPPA), anterior temporal lobe atrophy (indicative of svPPA), left posterior peri-Sylvian or parietal lobe atrophy (indicative of lvPPA), and medial temporal or parietal atrophy (indicative of typical AD). Instructions for this second stage were only given after stage 1 was completed to ensure that the initial ratings were not biased by expected atrophy patterns.

Statistical Considerations

Predictive Analytics Software (PASW, Version 18; IBM, Armonk, New York) and SPM5 were used for statistical analysis of the data. One-way ANOVA with a 2-tailed significance level of .05 was used to compare the demographic and neuropsychological measures. A pair-wise κ was used to assess the intra- and interobserver agreement in the reports of atrophy. Group-level comparisons of the imaging data were made with a 2-sample *t* test implemented in SPM5, with age and total intracranial volume included as nuisance covariates. Group-level results are reported at a false discovery rate–corrected $P < .01$.

RESULTS

Demographic data for all participant groups are summarized in Table 1. Neuropsychological and language assessment results are presented in the On-line Table.

Figure 1 demonstrates the group-level distribution of atrophy in representative and identical coronal, axial, and sagittal sections for 3 PPA variants and AD. At a group level, svPPA was characterized by atrophy in the anterior temporal lobes; nfvPPA, by atrophy in left posterior frontal and insula and left basal ganglia;

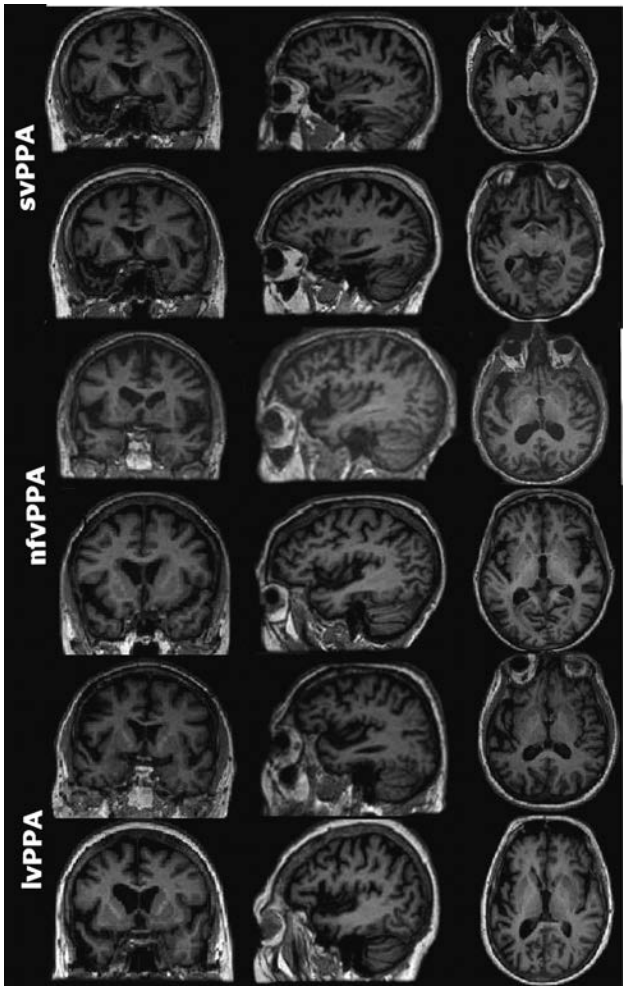

FIG 2. Representative sections of MR images of 6 patients with PPA (2 per subtype) with comparable Mini-Mental State Examination scores. Both patients with svPPA were reported by all neuroradiologists as having left anterior temporal atrophy. None of the patients with nfvPPA or lvPPA in the study had unanimous reports of the prescribed atrophy patterns (left posterior frontoinsular and posterior peri-Sylvian/inferior parietal, respectively). Images are displayed in neurologic orientation.

Table 2: Sensitivity of the proposed imaging markers for the diagnosis of PPA variants and typical AD based on the lobar distribution of the atrophy and specific consensus recommendations

	svPPA	nfvPPA	lvPPA	AD
Sensitivity based on lobar distribution				
Rater 1	100%	50%	50%	36%
Rater 2	95%	8%	57%	64%
Rater 3	100%	29%	64%	60%
Mean (SD)	98% (2.9%)	29% (21%)	57% (7%)	53% (15%)
Sensitivity based on recommendations				
Rater 1	90%	14%	50%	60%
Rater 2	92%	20%	56%	46%
Rater 3	95%	28%	42%	24%
Mean (SD)	92% (2.5%)	21% (7%)	49% (7%)	43% (18%)

Table 3: Specificity of the proposed imaging markers for the diagnosis of PPA variants and typical AD based on the specific consensus recommendations

	Specificity Based on Recommendations			
	svPPA	nfvPPA	lvPPA	AD
Rater 1	93%	92%	95%	93%
Rater 2	95%	89%	93%	92%
Rater 3	93%	92%	97%	91%
Mean (SD)	93% (0.01)	91% (0.02)	95% (0.02)	92% (0.01)

Table 4: Intraobserver agreement for the reported lobar distribution of abnormalities and recommendations

	Rater 1 (κ) (SE)	Rater 2 (κ) (SE)	Rater 3 (κ) (SE)	Mean (SD)
Lobar distribution	0.61 (0.1)	0.95 (0.04)	0.68 (0.1)	0.75 (0.18)
Recommendations	0.5 (0.09)	0.81 (0.07)	0.57 (0.1)	0.63 (0.16)

Table 5: Interobserver agreement for the reported lobar distribution of abnormalities and recommendations

	Raters 1 and 2 (κ) (SE)	Raters 1 and 3 (κ) (SE)	Raters 2 and 3 (κ) (SE)	Mean (SD)
Lobar distribution	0.56 (0.06)	0.48 (0.06)	0.64 (0.06)	0.56 (0.08)
Recommendations	0.31 (0.07)	0.47 (0.07)	0.44 (0.06)	0.41 (0.09)

lvPPA, by left posterior temporoparietal atrophy; and typical AD showed bilateral hippocampal and patchy temporoparietal atrophy.

Concerning the single-subject visual reporting outcomes, sensitivity calculations based on the lobar distribution of the abnormalities revealed almost perfect results in the svPPA group (mean sensitivity, 98% ± 2.9%) but low sensitivity of the imaging markers in the other PPA variants and the typical AD group (Table 2). The proposed imaging markers were least sensitive for the diagnosis of nfvPPA (mean, 29% ± 21%). Sensitivity values for the lvPPA and typical AD groups were modest at 57% and 53%, respectively. Sensitivity figures based on the prescribed patterns of atrophy revealed slightly lower values compared with the above figures but a similar pattern overall: high sensitivity for svPPA and low values for the other study groups (Table 2). Specificity figures were, however, consistently high for all diagnostic groups with no discernible difference (Table 3).

Tables 4 and 5 provide values for intra- and interobserver agreement for all diagnostic groups. Intraobserver agreement values for the reported lobar distribution of atrophy were consistently above the widely accepted[26] threshold of 0.6 (mean, 0.75 ± 0.18), indicating substantial agreement. The recommendation-based values, however, fell below the 0.6 threshold for 2 of the 3 reporting radiologists (mean, 0.63 ± 0.16). In the pair-wise interobserver agreement values, while κ was just below the 0.6 threshold (mean, 0.56 ± 0.08) for the reported lobar distribution of atrophy (first round), it dropped considerably to 0.41 ± 0.09 for the recommendation-based outcomes; 0.4 is generally considered the minimum threshold for moderate agreement.[26]

DISCUSSION

This study provides an objective assessment of the utility of the proposed MR imaging markers in supporting the diagnosis of various PPA variants. The group-level atrophy patterns were in precise agreement with the proposed imaging criteria for different PPA subtypes. Assessing the reliability of these measures at a single-subject level is, however, much more relevant—indeed mandatory—for determining the diagnostic utility of the proposed

imaging criteria in further classification of individual patients with PPA. In the absence of reliable automated single-subject statistical measures capable of detecting the abnormalities at an individual level, assessment of the consistency and reliability of neuroradiologists' reports along with the level of agreement constitutes a suitable substitute. Moreover, it mirrors real-life clinical practice in which visual rating of scans remains the standard reporting method.

The group-level voxel-based morphometry–based gray matter atrophy patterns for each of the PPA variants (Fig 1) were consistent with those in past studies.[7-9] This finding was important to confirm because it was precisely this group-level atrophy pattern that led to the recommendations for imaging-supported diagnoses. The results of the visual rating suggested a dichotomized pattern of high sensitivity and specificity of the proposed imaging markers for svPPA, but less reliable outcomes for the other 2 PPA subtypes, with a low sensitivity but rather high specificity. Agreement analyses for the whole group revealed substantial intrarater but only moderate interrater agreement values (mean κ, 0.63 and 0.41, respectively) for the recommendation-based atrophy patterns. This finding is now discussed in more detail for each variant.

svPPA

svPPA is characterized by an amodal loss of knowledge that consistently presents as a reduction of expressive vocabulary and word comprehension.[27] Various studies have emphasized the importance of the anterior temporal lobes as hubs of semantic knowledge.[28,29] In agreement with the proposed recommendations, group-average voxel-based morphometry analysis of the svPPA participants revealed predominant bilateral anterior temporal lobe atrophy. The high sensitivity and specificity of the proposed imaging markers (means, 0.98% and 93%, respectively) demonstrated that the presence of temporal lobe a trophy offered robust support for the diagnosis of svPPA. This finding is not unexpected because, though not always assessed systematically, atrophy of rostral-inferior temporal structures has been consistently reported in svPPA (also known as semantic dementia) both at a group level and individually.[7,10,30-35] Given the uniform pattern of atrophy seen in this consecutively recruited cohort of 21 patients with svPPA, it can be argued that the diagnosis of svPPA should be seriously questioned in the absence of this atrophy pattern. Gil-Navarro et al[36] found the same consistent presence of anterior temporal lobe atrophy in a study of 29 patients with PPA that included 5 with svPPA. As already mentioned, most patients with svPPA have frontotemporal lobar degeneration–TDP-43 pathology, but frontotemporal lobar degeneration-tau pathology is found occasionally. Previous work has indicated that the atrophy pattern does not discriminate between these 2 pathologic substrates.[31]

nfvPPA

Clinical features of nfvPPA include effortful, halting speech with sound distortions and/or grammatic errors in language production.[6] Degeneration of the left frontal operculum and rostral insula is the culprit lesion in nfvPPA. More recent studies have also highlighted involvement of premotor[32] and basal ganglia[37] regions. Like svPPA, the group-average voxel-based morphometry findings in our nfvPPA cohort were largely compatible with the proposed diagnostic recommendations. As demonstrated in Fig 1, voxel-based morphometry analysis clearly identified disproportionate left-sided atrophy in the frontal operculum and insula. There was, in addition, evidence of further atrophy in the left basal ganglia region, but no atrophy was visible in the premotor area.

Concerning the single-subject outcomes, none of the patients with nfvPPA had unanimous reports of the prescribed atrophy pattern by all 3 neuroradiologists. In fact, "left posterior frontal and insular atrophy" was only the third most commonly observed report in this group with "no atrophy" and "left posterior peri-Sylvian atrophy" being the first and second, respectively (data not shown). "No atrophy" was reported by at least one of the neuroradiologists in 10 of 14 (71%) individuals with nfvPPA and in 22 of the total 42 (14×3) reports (52%). Low sensitivity values (mean, $21\% \pm 7\%$) further corroborated the above findings. Given the abundance of no-atrophy reports, the most plausible explanation for this result seems to be that atrophy in patients with nfvPPA is often very subtle. Also, clinical heterogeneity inherent in the recommended features of nfvPPA (ie, requiring the presence of either abnormal speech or agrammatism) and more white than gray matter burden are other potential explanations for the observed discrepancies. High specificity values, however, indicated the potential utility of the prescribed pattern of atrophy in the diagnosis of nfvPPA if present.

Further evidence for the inconsistency of imaging findings in nfvPPA comes from previous single case studies reporting widely discrepant findings, ranging from no atrophy[38] to left hemispheric atrophy[39] to left frontotemporal atrophy,[14] bifrontal atrophy,[40] and generalized atrophy.[41] Even group-level findings, using parametric analysis techniques such as SPM, have been inconsistent, with different studies showing evidence of: left-sided inferior frontal and insular atrophy[42] and hypometabolism[43]; atrophy in a wide distribution comprising the left inferior frontal, superior temporal, and inferior parietal areas, with[7,9] and without[7] additional atrophy in the premotor area; and finally abnormalities in the premotor cortex and left basal ganglia.[8,32,44] One previous study reported a considerably higher sensitivity for the MR imaging–defined atrophy pattern of nfvPPA (76%).[36] The discrepancy, however, likely relates to the study design in that the raters had to expressly classify scans for the 3 proposed atrophy patterns and in a group comprising only patients with PPA (there were neither healthy controls nor controls with dementia). This difference is important, given the high prevalence of no-atrophy reports in our nfvPPA group (see above). Considering that the main challenge in the diagnosis of degenerative aphasia is at the mildest stages when it is difficult to distinguish degenerative aphasia from a normal variation, inclusion of scans with normal findings makes our study a closer reflection of real-life situations.

lvPPA

LvPPA is the PPA variant that is highly associated with Alzheimer pathology.[7] Impaired single-word retrieval in spontaneous speech and impaired sentence repetition are the recommended features. While a number of studies have failed to demonstrate the utility of these features in the diagnosis of lvPPA,[17,45] atrophy of the left

temporoparietal lobe has been consistently emphasized in Alzheimer disease—related aphasia.[17,19,45] In the "Materials and Methods" section, we mentioned our rationale for applying the lvPPA label to the group of patients with PPA whom we had previously reported as having mixed PPA. Turning to the individual visual reporting outcomes, we found low-to-moderate sensitivity (mean, 49% ± 7%) for the prescribed atrophy patterns. This was consistent with the results of the only previous study looking at the same metrics that found a sensitivity of 57% for MR imaging atrophy.[36] Given the high specificity value (mean, 95% ± 2%), it can be inferred that while the presence of the prescribed pattern of "left posterior peri-Sylvian or parietal" atrophy is highly suggestive of lvPPA, its absence does not exclude the diagnosis of lvPPA. In addition, assessment of individual reports revealed that contrary to what might be expected, a typical AD atrophy pattern (ie, medial temporal or parietal atrophy) was reported in only 8% of the ratings of patients with lvPPA; an lvPPA atrophy pattern was the most common (38%), while an nfvPPA atrophy pattern was the second most frequently reported outcome (20%). This radiologic finding resonates with the previously reported difficulty in distinguishing nfv- and lvPPA variants on clinical and neuropsychological grounds.[19,45] None of the radiologists had reported global atrophy for the $n = 16$ lvPPA cohort. This is an important negative, given possible concerns about the severity of dementia in this group.

CONCLUSIONS

This study provides an objective assessment of the utility of the proposed MRI recommendations for supporting the diagnoses of 3 PPA variants. Our findings are largely compatible with the only previous study on the subject.[36] Moreover, to our knowledge, this article is the first to report the intra- and interrater agreement of the reporting radiologists and the specificity of the MR imaging markers for the diagnosis of PPA variants. Our study provides compelling evidence for the utility of the proposed imaging recommendations for the diagnosis of svPPA. On the basis of the findings of the current and previous studies, it could even be argued that lack of anterior temporal lobe atrophy should exclude the diagnosis of svPPA. The results were less consistent in the other groups. While high specificity values observed in all groups indicate the potential utility of the recommendations for patients in whom the atrophy patterns can be identified, low sensitivity and modest agreement values suggest that absence of the proposed atrophy patterns is common in the nonsemantic PPA subtypes.

Disclosures: S. Ahmad Sajjadi—*RELATED*: *Grant*: Donald Forrester Trust, *Comments*: grant to the University of Cambridge*. Justin Cross—*RELATED*: *Grant*: National Institute for Health Research Biomedical Research Centre, *Comments*: part funding of salary.* *Money paid to the institution.

REFERENCES

1. Hodges JR, Mitchell J, Dawson K, et al. **Semantic dementia: demography, familial factors and survival in a consecutive series of 100 cases.** *Brain* 2010;133(pt 1):300–06 CrossRef Medline
2. Rohrer JD, Lashley T, Schott JM, et al. **Clinical and neuroanatomical signatures of tissue pathology in frontotemporal lobar degeneration.** *Brain* 2011;134(pt 9):2565–81 CrossRef Medline
3. Knibb JA, Xuereb JH, Patterson K, et al. **Clinical and pathological characterization of progressive aphasia.** *Ann Neurol* 2006;59:156–65 CrossRef Medline
4. Mesulam M, Wicklund A, Johnson N, et al. **Alzheimer and frontotemporal pathology in subsets of primary progressive aphasia.** *Ann Neurol* 2008;63:709–19 CrossRef Medline
5. Josephs KA, Dickson DW, Murray ME, et al. **Quantitative neurofibrillary tangle density and brain volumetric MRI analyses in Alzheimer's disease presenting as logopenic progressive aphasia.** *Brain Lang* 2013;127:127–34 CrossRef Medline
6. Gorno-Tempini ML, Hillis AE, Weintraub S, et al. **Classification of primary progressive aphasia and its variants.** *Neurology* 2011;76:1006–14 CrossRef Medline
7. Gorno-Tempini ML, Dronkers NF, Rankin KP, et al. **Cognition and anatomy in three variants of primary progressive aphasia.** *Ann Neurol* 2004;55:335–46 CrossRef Medline
8. Josephs KA, Duffy JR, Strand EA, et al. **Clinicopathological and imaging correlates of progressive aphasia and apraxia of speech.** *Brain* 2006;129(pt 6):1385–98 CrossRef Medline
9. Mesulam M, Wieneke C, Rogalski E, et al. **Quantitative template for subtyping primary progressive aphasia.** *Arch Neurol* 2009;66:1545–51 Medline
10. Galton CJ, Patterson K, Graham K, et al. **Differing patterns of temporal atrophy in Alzheimer's disease and semantic dementia.** *Neurology* 2001;57:216–25 CrossRef Medline
11. Mummery CJ, Patterson K, Price CJ, et al. **A voxel-based morphometry study of semantic dementia: relationship between temporal lobe atrophy and semantic memory.** *Ann Neurol* 2000;47:36–45 Medline
12. Rosen HJ, Kramer JH, Gorno-Tempini ML, et al. **Patterns of cerebral atrophy in primary progressive aphasia.** *Am J Geriatr Psychiatry* 2002;10:89–97 CrossRef Medline
13. Galton CJ, Patterson K, Xuereb JH, et al. **Atypical and typical presentations of Alzheimer's disease: a clinical, neuropsychological, neuroimaging and pathological study of 13 cases.** *Brain* 2000;123(pt 3):484–98 CrossRef Medline
14. Hodges JR, Patterson K. **Nonfluent progressive aphasia and semantic dementia: a comparative neuropsychological study.** *J Int Neuropsychol Soc* 1996;2:511–24 CrossRef Medline
15. Mesulam M. **Primary progressive aphasia.** *Ann Neurol* 2001;49:425–32 Medline
16. McKhann G, Drachman D, Folstein M, et al. **Clinical diagnosis of Alzheimer's disease: report of the NINCDS-ADRDA Work Group under the auspices of Department of Health and Human Services Task Force on Alzheimer's Disease.** *Neurology* 1984;34:939–44 CrossRef Medline
17. Sajjadi SA, Patterson K, Arnold RJ, et al. **Primary progressive aphasia: a tale of two syndromes and the rest.** *Neurology* 2012;78:1670–77 CrossRef Medline
18. Sajjadi SA, Patterson K, Nestor PJ. **Logopenic, mixed, or Alzheimer-related aphasia?** *Neurology* 2014;82:1127–31 CrossRef Medline
19. Leyton CE, Villemagne VL, Savage S, et al. **Subtypes of progressive aphasia: application of the International Consensus Criteria and validation using β-amyloid imaging.** *Brain* 2011;134(pt 10):3030–43 CrossRef Medline
20. Sajjadi SA, Patterson K, Tomek M, et al. **Abnormalities of connected speech in the non-semantic variants of primary progressive aphasia.** *Aphasiology* 2012;26:1219–37 CrossRef
21. Acosta-Cabronero J, Williams GB, Pereira JM, et al. **The impact of skull-stripping and radio-frequency bias correction on grey-matter segmentation for voxel-based morphometry.** *Neuroimage* 2008;39:1654–65 CrossRef Medline
22. Ashburner J, Friston KJ. **Unified segmentation.** *Neuroimage* 2005;26:839–51 CrossRef Medline
23. Pengas G, Pereira JM, Williams GB, et al. **Comparative reliability of total intracranial volume estimation methods and the influence of atrophy in a longitudinal semantic dementia cohort.** *J Neuroimaging* 2009;19:37–46 CrossRef Medline
24. Smith SM, Jenkinson M, Woolrich MW, et al. **Advances in functional**

and structural MR image analysis and implementation as FSL. *Neuroimage* 2004;23(suppl 1):S208–19 CrossRef Medline
25. Dubois B, Feldman HH, Jacova C, et al. **Research criteria for the diagnosis of Alzheimer's disease: revising the NINCDS-ADRDA criteria.** *Lancet Neurol* 2007;6:734–46 CrossRef Medline
26. Landis J, Koch G. **The measurement of observer agreement for categorical data.** *Biometrics* 1977;33:159–74 CrossRef Medline
27. Hodges JR, Patterson K. **Semantic dementia: a unique clinicopathological syndrome.** *Lancet Neurol* 2007;6:1004–14 CrossRef Medline
28. Patterson K, Nestor PJ, Rogers TT. **Where do you know what you know? The representation of semantic knowledge in the human brain.** *Nat Rev Neurosci* 2007;8:976–87 CrossRef Medline
29. Mion M, Patterson K, Acosta-Cabronero J, et al. **What the left and right anterior fusiform gyri tell us about semantic memory.** *Brain* 2010;133:3256–68 CrossRef Medline
30. Hodges JR, Patterson K, Oxbury S, et al. **Semantic dementia: progressive fluent aphasia with temporal lobe atrophy.** *Brain* 1992; 115(pt 6):1783–806 CrossRef Medline
31. Pereira JM, Williams GB, Acosta-Cabronero J, et al. **Atrophy patterns in histologic vs clinical groupings of frontotemporal lobar degeneration.** *Neurology* 2009;72:1653–60 CrossRef Medline
32. Wilson SM, Henry ML, Besbris M, et al. **Connected speech production in three variants of primary progressive aphasia.** *Brain* 2010; 133(pt 7):2069–88 CrossRef Medline
33. Mesulam M, Rogalski E, Wieneke C, et al. **Neurology of anomia in the semantic variant of primary progressive aphasia.** *Brain* 2009; 132(pt 9):2553–65 CrossRef Medline
34. Grossman M. **Primary progressive aphasia: clinicopathological correlations.** *Nat Rev Neurol* 2010;6:88–97 CrossRef Medline
35. Snowden JS, Goulding PJ, Neary D. **Semantic dementia: a form of circumscribed cerebral atrophy.** *Behavioural Neurology* 1989;2:167–82
36. Gil-Navarro S, Lladó A, Rami L, et al. **Neuroimaging and biochemical markers in the three variants of primary progressive aphasia.** *Dement Geriatr Cogn Disord* 2013;35:106–17 CrossRef Medline
37. Whitwell JL, Duffy JR, Machulda MM, et al. **Tracking the development of agrammatic aphasia: a tensor-based morphometry study.** *Cortex* 2016 Sep 30. [Epub ahead of print] CrossRef Medline
38. Caselli RJ, Jack CR Jr. **Asymmetric cortical degeneration syndromes: a proposed clinical classification.** *Arch Neurol* 1992;49:770–80 CrossRef Medline
39. Snowden JS, Neary D, Mann DM, et al. **Progressive language disorder due to lobar atrophy.** *Ann Neurol* 1992;31:174–83 CrossRef Medline
40. Mimura M, Oda T, Tsuchiya K, et al. **Corticobasal degeneration presenting with nonfluent primary progressive aphasia: a clinicopathological study.** *J Neurol Sci* 2001;183:19–26 CrossRef Medline
41. Harasty JA, Halliday GM, Xuereb J, et al. **Cortical degeneration associated with phonologic and semantic language impairments in AD.** *Neurology* 2001;56:944–50 CrossRef Medline
42. Whitwell JL, Anderson VM, Scahill RI, et al. **Longitudinal patterns of regional change on volumetric MRI in frontotemporal lobar degeneration.** *Dement Geriatr Cogn Disord* 2004;17:307–10 CrossRef Medline
43. Nestor PJ, Graham NL, Fryer TD, et al. **Progressive non-fluent aphasia is associated with hypometabolism centred on the left anterior insula.** *Brain* 2003;126(pt 11):2406–18 CrossRef Medline
44. Snowden J, Neary D, Mann D. **Frontotemporal lobar degeneration: clinical and pathological relationships.** *Acta Neuropathol* 2007;114: 31–38 CrossRef Medline
45. Mesulam MM, Wieneke C, Thompson C, et al. **Quantitative classification of primary progressive aphasia at early and mild impairment stages.** *Brain* 2012;135(pt 5):1537–53 CrossRef Medline

Entorhinal Cortex: Antemortem Cortical Thickness and Postmortem Neurofibrillary Tangles and Amyloid Pathology

A.A. Thaker, B.D. Weinberg, W.P. Dillon, C.P. Hess, H.J. Cabral, D.A. Fleischman, S.E. Leurgans, D.A. Bennett, B.T. Hyman, M.S. Albert, R.J. Killiany, B. Fischl, A.M. Dale, and R.S. Desikan

ABSTRACT

BACKGROUND AND PURPOSE: The entorhinal cortex, a critical gateway between the neocortex and hippocampus, is one of the earliest regions affected by Alzheimer disease–associated neurofibrillary tangle pathology. Although our prior work has automatically delineated an MR imaging–based measure of the entorhinal cortex, whether antemortem entorhinal cortex thickness is associated with postmortem tangle burden within the entorhinal cortex is still unknown. Our objective was to evaluate the relationship between antemortem MRI measures of entorhinal cortex thickness and postmortem neuropathological measures.

MATERIALS AND METHODS: We evaluated 50 participants from the Rush Memory and Aging Project with antemortem structural T1-weighted MR imaging and postmortem neuropathologic assessments. Here, we focused on thickness within the entorhinal cortex as anatomically defined by our previously developed MR imaging parcellation system (Desikan-Killiany Atlas in FreeSurfer). Using linear regression, we evaluated the association between entorhinal cortex thickness and tangles and amyloid-β load within the entorhinal cortex and medial temporal and neocortical regions.

RESULTS: We found a significant relationship between antemortem entorhinal cortex thickness and entorhinal cortex ($P = .006$) and medial temporal lobe tangles ($P = .002$); we found no relationship between entorhinal cortex thickness and entorhinal cortex ($P = .09$) and medial temporal lobe amyloid-β ($P = .09$). We also found a significant association between entorhinal cortex thickness and cortical tangles ($P = .003$) and amyloid-β ($P = .01$). We found no relationship between parahippocampal gyrus thickness and entorhinal cortex ($P = .31$) and medial temporal lobe tangles ($P = .051$).

CONCLUSIONS: Our findings indicate that entorhinal cortex–associated in vivo cortical thinning may represent a marker of postmortem medial temporal and neocortical Alzheimer disease pathology.

ABBREVIATIONS: AD = Alzheimer disease; EC = entorhinal cortex; SE = standard error

The human entorhinal cortex (EC) plays an integral role in memory formation and serves as the critical gateway between the hippocampus and neocortex.[1] Located in the medial temporal lobe, the EC constitutes the anterior portion of the parahip-

Received June 13, 2016; accepted after revision January 10, 2017.

From the Department of Radiology (A.A.T.), University of Colorado School of Medicine, Aurora, Colorado; Department of Radiology and Imaging Sciences (B.D.W.), Emory University Hospital, Atlanta, Georgia; Neuroradiology Section (W.P.D., C.P.H., R.S.D.), Department of Radiology and Biomedical Imaging, University of California, San Francisco, San Francisco, California; Departments of Biostatistics (H.J.C.) and Anatomy and Neurobiology (R.J.K.), Boston University School of Public Health, Boston, Massachusetts; Rush Alzheimer's Disease Center (D.A.F., S.E.L., D.A.B.), Rush University Medical Center, Chicago, Illinois; Department of Neurology (B.T.H.), Massachusetts General Hospital, Boston, Massachusetts; Department of Neurology and Division of Cognitive Neurosciences (M.S.A.), Johns Hopkins University, Baltimore, Maryland; Athinoula A. Martinos Center for Biomedical Imaging (B.F.), Department of Radiology, Massachusetts General Hospital, Charlestown, Massachusetts; Computer Science and Artificial Intelligence Laboratory (B.F.), Massachusetts Institute of Technology, Cambridge, Massachusetts; and Departments of Radiology (A.M.D.), Cognitive Sciences and Neurosciences, University of California, San Diego, La Jolla, California.

This work was supported by National Institutes of Health grants R01AG10161 and R01AG40039. R.S.D. was supported by the National Alzheimer's Coordinating Center Junior Investigator Award, ASNR Foundation Alzheimer's Imaging Research Grant Program, RSNA Resident/Scholar Award, and a National Institutes of Health/National Institute on Drug Abuse grant U24DA041123. Support for this research was provided in part by the National Institute for Biomedical Imaging and Bioengineering (P41EB015896, R01EB006758, R21EB018907, R01EB019956), the National Institute on Aging (5R01AG008122, R01AG016495), and the National Institute for Neurological Disorders and Stroke (R01NS0525851, R21NS072652, R01NS070963, R01NS083534, 5U01NS086625) and was made possible by the resources provided by Shared Instrumentation Grants 1S10RR023401, 1S10RR019307, and 1S10RR023043. Additional support was provided by the National Institutes of Health Blueprint for Neuroscience Research (5U01-MH093765), part of the multi-institutional Human Connectome Project. In addition, B.F. has a financial interest in CorticoMetrics, a company whose medical pursuits focus on brain imaging and measurement technologies. B.F.'s interests were reviewed and are managed by Massachusetts General Hospital and Partners HealthCare in accordance with their conflict of interest policies. A.M.D. is a founder and holds equity in CorTechs Labs Inc and also serves on the Scientific Advisory Board of CorTechs Labs and Human Longevity Inc. The terms of these arrangements have been reviewed and approved by the University of California, San Diego, in accordance with its conflict of interest policies.

Please address correspondence to Rahul S. Desikan, MD, PhD, Department of Radiology and Biomedical Imaging, University of California, San Francisco, 505 Parnassus Ave San Francisco, CA 94143; e-mail: rahul.desikan@ucsf.edu

http://dx.doi.org/10.3174/ajnr.A5133

pocampal gyrus and is localized in vivo laterally by the rhinal sulcus, anteriorly by the amygdala and hippocampus, and posteriorly by the posterior portion of the parahippocampal gyrus.[2,3] The EC is one of the earliest affected regions in Alzheimer disease (AD). Tau-associated neurofibrillary tangle pathology in AD follows a defined topographic and hierarchical pattern, first affecting the EC and then progressing to anatomically connected limbic and association cortices; in contrast, amyloid-β-associated pathology does not involve the EC in the earliest stages of AD but selectively affects the neocortical regions.[4,5] Most important, the association of neuronal volume loss in the EC has been shown to parallel τ-associated tangle pathology (neurofibrillary tangles and neuritic plaques) but not senile plaques seen with amyloid-β deposition.[4]

Structural MR imaging provides visualization and quantification of volume loss and has been extensively investigated in AD.[6-9] Using manually delineated assessments, early studies have shown that volumetric measures of the EC can identify individuals without dementia in the earliest stages of the AD process.[7-9] Within the past decade, rapid advances in MR imaging postprocessing have led to the development of software tools for automatic quantification of human subcortical and neocortical regions.[10] We have previously developed an MR imaging–based parcellation atlas for the human cerebral cortex, which has automatically delineated the entorhinal cortex.[11] The EC ROI from our parcellation atlas correlates with CSF levels of τ, amyloid,[12] and *Apolipoprotein E*[13] and has been used to identify cognitively healthy[14] and cognitively impaired individuals without dementia who are most likely to progress to clinical AD.[15,16] However, whether our antemortem MR imaging–based measure of the EC is associated with established postmortem measures of AD pathology is still unknown.

In this study, we evaluated the relationship between antemortem MR imaging–based automated measurements of EC thickness and postmortem measures of neurofibrillary tangle and amyloid-β pathology. To assess the specificity of our EC ROI (anterior portion of the parahippocampal gyrus), we also evaluated the relationship between the thickness of the posterior parahippocampal gyrus and EC amyloid-β and τ pathology.

MATERIALS AND METHODS

Participants

We evaluated participants from the Rush Memory and Aging Project, a community-based longitudinal study of aging, which began in 1997.[17] Details of the clinical and neuropathologic evaluations have been reported previously.[17,18] Briefly, all participants underwent a uniform structured clinical evaluation that included a medical history, physical examination with emphasis on neurologic function, and neuropsychological testing (including the Mini-Mental State Examination and 20 other tests). All participants were evaluated in person by a neuropsychologist and a physician with expertise in the evaluation of older individuals with cognitive impairment. On the basis of physician evaluation and review of the cognitive testing and the neuropsychologist's opinion, participants were classified with respect to AD and other common conditions with the potential to impact cognitive function according to the recommendations of the joint working group of the National Institute of Neurologic and Communicative Disorders and Stroke and the Alzheimer's Disease and Related Disorders Association.[19] In this article, we focused on 50 participants, clinically defined at baseline (on study entry) as being cognitively healthy ($n = 25$), having mild cognitive impairment ($n = 18$), and having probable AD ($n = 7$) (Table), with concurrent antemortem MR imaging and postmortem neuropathologic assessments. The Rush University Medical Center institutional review board approved the study, and all participants gave written informed consent and signed an Anatomic Gift.

Demographic information on participants in the current study[a]

	Healthy ($n = 25$)	MCI ($n = 18$)	AD ($n = 7$)
% Female	64%	55%	71%
Education (yr)	15.6 (3.6)	14.9 (1.2)	13.2 (1.2)
Age at MRI (yr)	87.4 (5.0)	88.3 (5.4)	85.2 (4.4)
Age at death (yr)	90.3 (4.7)	91.1 (5.4)	88.7 (4.9)
Years between MRI and death	2.8 (1.3)	2.8 (1.2)	3.6 (1.5)
Entorhinal cortex thickness	1.50 (0.30)	1.49 (0.27)	1.40 (0.41)
EC tangle density	8.9 (6.2)	12.8 (10.3)	20.1 (12.9)
EC amyloid-β load	5.5 (5.1)	7.1 (5.1)	7.5 (4.9)

Note:—MCI indicates mild cognitive impairment.
[a] All values are expressed as mean (SD).

Imaging Assessments

We assessed previously obtained T1-weighted anatomic data by using a 1.5T MR imaging scanner (GE Healthcare, Milwaukee, Wisconsin). For the current study, all antemortem MR imaging data were acquired by using a 3D magnetization-prepared rapid acquisition of gradient echo sequence with the following parameters: TE = 2.8 ms, TR = 6.3 ms, preparation time = 1000 ms, flip angle = 8°, FOV = 24 × 24 cm, 160 sections, 1-mm section thickness, a 224 × 192 acquisition matrix reconstructed to 256 × 256, and 2 repetitions. The MR imaging data were automatically segmented with FreeSurfer 5.0 (http://surfer.nmr.mgh.harvard.edu; for additional details see McKhann et al[19]). Here, we focused on intracranial volume–corrected average thickness of the entire entorhinal cortex and posterior parahippocampal gyrus (average of the left and right hemispheres) as delineated with our previously developed automated cortical parcellation atlas (Desikan-Killiany atlas in Freesurfer) (Fig 1).[11] In secondary analyses, we also evaluated baseline intracranial volume–corrected hippocampal volumes (average of the left and right hemispheres).[20]

Neuropathologic Assessments

We used results from previously obtained neuropathologic evaluations and focused on amyloid and neurofibrillary tangle pathology within the entorhinal cortex and medial temporal (entorhinal and hippocampal) regions (for additional details on neuropathologic measures from the Rush Memory and Aging Project/Rush University Medical Center, please see Bennett et al[21,22] and Barnes et al[23]). Briefly, at least 2 tissue blocks from the entorhinal cortex and hippocampus (CA1/subiculum) were dissected from 1-cm coronal slabs fixed for 48–72 hours in 4% paraformaldehyde, embedded in paraffin, and cut into 20-μm sections. Amyloid-β was labeled with MO0872 (1:100; Dako,

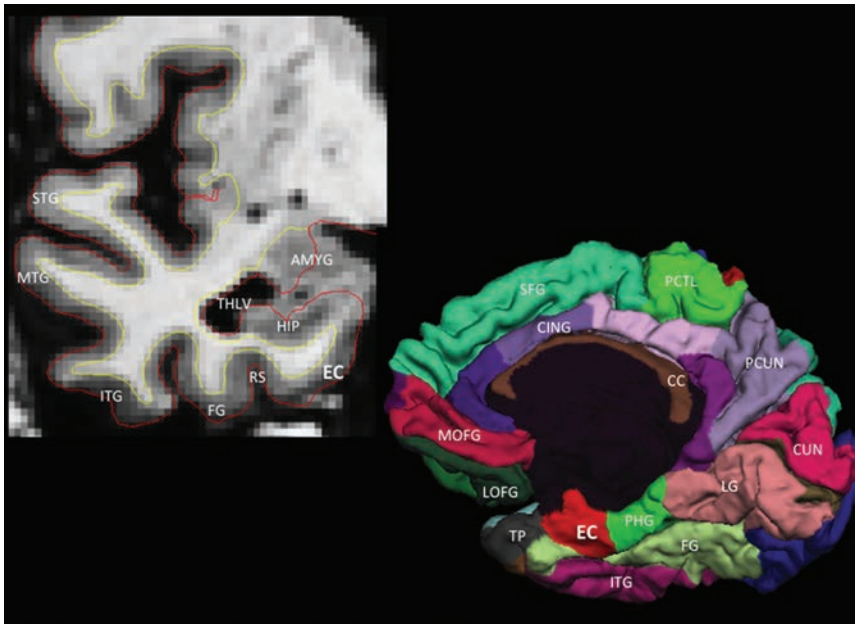

FIG 1. Coronal T1-weighted MR imaging illustrating the anatomic location of the entorhinal cortex, which is medial to the rhinal sulcus (RS) and fusiform gyrus (FG) and inferior to the hippocampus (HIP), temporal horn of the lateral ventricle (THLV), and amygdala (AMYG) (*upper left panel*). 3D cortical (pial) representation is of the right cortical (pial) surface, delineating the location of the entorhinal cortex on the medial hemisphere of the cerebral cortex (*lower right panel*). STG indicates superior temporal gyrus; MTG, middle temporal gyrus; ITG, inferior temporal gyrus; TP, temporal pole; PHG, parahippocampal gyrus; LG, lingual gyrus; CUN, cuneus cortex; PCUN, precuneus; FG, fusiform gyrus; PCTL, paracentral lobule; SFG, superior frontal gyrus; MOFG, medial orbitofrontal gyrus; LOFG, lateral orbitofrontal gyrus; CC, corpus callosum; CING, cingulate cortex.

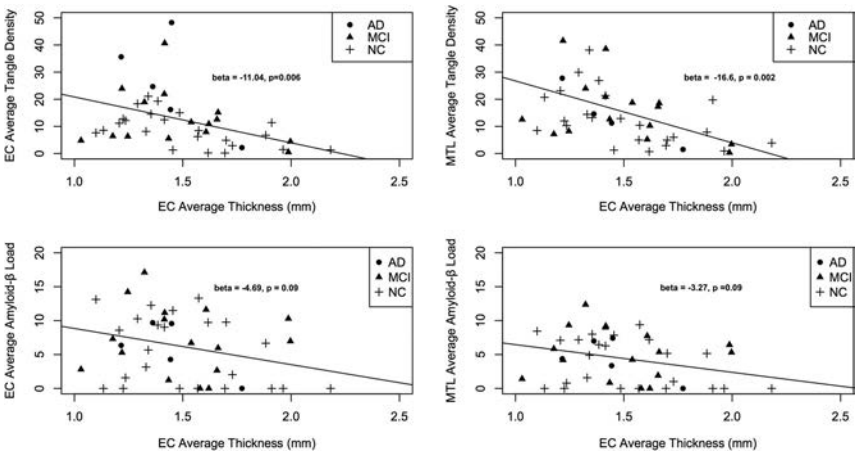

FIG 2. Scatterplots illustrating the relationship between average entorhinal cortex thickness and average tangle density within the entorhinal cortex (*upper left*) and medial temporal lobe (MTL, *upper right*), and average amyloid-β load within the EC (*lower left*) and medial temporal lobe (*lower right*). Best-fit regression line, β-coefficients, and *P* values from the logistic regression model are included (for additional details see the text).

Carpinteria, California), and paired helical filament τ was labeled with AT8 (1:800 in 4% horse serum; Innogenex, San Ramon, California), an antibody specific for phosphorylated τ. Images of amyloid-β-stained sections were captured for quantitative analysis by using a systematic random-sampling scheme, and calculation of the percentage area occupied by amyloid-β immunoreactive pixels was performed. Quantification of tangle density per square millimeter was performed with a stereologic mapping station. We used composite summary measures of the percentage area occupied by amyloid-β and the density of neurofibrillary tangles by averaging the values for each lesion within the entorhinal cortex and medial temporal regions (entorhinal cortex and hippocampus) (for additional details see Bennett et al[21,22] and Barnes et al[23]). To evaluate neuropathology within the neocortex and to minimize multiple comparisons, we used a composite measure of tangle density and amyloid-β load within the midfrontal cortex, inferior temporal gyrus, inferior parietal cortex, calcarine cortex, cingulate region, and superior frontal gyrus (cortical tangle density and cortical amyloid-β load).

Statistical Analysis

Using linear regression, we evaluated the association between entorhinal cortex thickness and average tangle and amyloid-β load within the entorhinal cortex and medial temporal regions (entorhinal cortex + hippocampus). We also evaluated the relationship between entorhinal cortex thickness and cortical tangle density and amyloid-β load. In secondary analyses, we assessed the association between (posterior) parahippocampal gyrus thickness and tangles and amyloid-β load within the entorhinal cortex and medial temporal regions. In all analyses, we controlled for the effects of age at death, sex, and clinical diagnosis.

RESULTS

We found a relationship between antemortem entorhinal cortex thickness and postmortem tangle density within the entorhinal cortex (β-coefficient = −11.04, standard error [SE] = 3.78, *P* value = .006) and medial temporal regions (β-coefficient = −16.67, SE = 5.04, *P* = .002); lower EC thickness was associated with increased EC and medial temporal lobe tangle density (Fig 2). Even after controlling for the effects of hippocampal volume, the relationship between entorhinal cortex thickness and tangle density within the entorhinal cortex (β-coefficient = −9.36, SE = 2.57, *P* = .03) and medial temporal regions (β-coefficient = −12.89, SE = 5.64, *P* = .02) remained significant. We found no relationship between entorhinal cortex thickness and amyloid-β load within the entorhinal cortex (β-coefficient = −4.69, SE = 2.70, *P* = .09) and medial temporal regions (β-coefficient = −3.27, SE = 1.90, *P* = .09) (Fig 2).

We found a relationship between entorhinal cortex thickness and both cortical tangle density (β-coefficient = −37.5, SE =

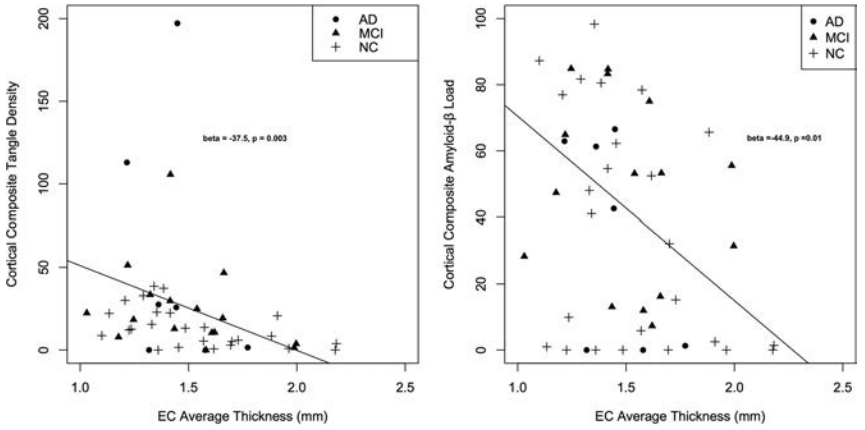

FIG 3. Scatterplots illustrating the relationship between average entorhinal cortex thickness and composite tangle density (*left*) and amyloid-β load (*right*) within the cerebral cortex (see text for details). Best-fit regression line, β-coefficients, and *P* values from the logistic regression model are included (for additional details see the text).

12.2, $P = .0003$) and amyloid-β load (β-coefficient = −44.9, SE = 17.2, $P = .01$) (Fig 3). Even after we controlled for the effects of hippocampal volume, the relationship between entorhinal cortex and both cortical tangle density (β-coefficient = −34.4, SE = 7.9, $P = .01$) and amyloid-β load (β-coefficient = −44.7, SE = 18.6, $P = .02$) remained significant.

In contrast, we found no relationship between antemortem parahippocampal gyrus thickness and postmortem tangle density within the entorhinal cortex (β-coefficient = −4.04, SE = 4.33, $P = .31$) and a trend toward significance for the medial temporal regions (β-coefficient = −11.52, SE = 5.71, $P = .051$). Similarly, we found no relationship between parahippocampal gyrus thickness and amyloid load within the entorhinal cortex (β-coefficient = 1.02, SE = 2.71, $P = .709$) and medial temporal regions (β-coefficient = 0.57, SE = 1.91, $P = .766$). We also found no relationship between parahippocampal gyrus thickness and cortical tangle density (β-coefficient = −14.2, SE = 13.5, $P = .30$) and amyloid-β load (β-coefficient = −8.7, SE = 18.6, $P = .64$).

We performed subgroup analyses within our subset of cognitively healthy older participants ($n = 25$) to evaluate the relationship between MR imaging measures of entorhinal cortex thickness and neuropathology. Similar to our main results, we found a relationship between antemortem entorhinal cortex thickness and postmortem tangle density within the entorhinal cortex (β-coefficient = −10.32, SE = 4.03, $P = .01$), medial temporal regions (β-coefficient = −14.48, SE = 6.61, $P = .04$), and cortex (β-coefficient = −16.58, SE = 7.03, $P = .02$). In contrast, we found no relationship between entorhinal cortex thickness and amyloid load either within the entorhinal cortex (β-coefficient = −5.04, SE = 3.91, $P = .23$) or cortex (β-coefficient = −32.26, SE = 22.79, $P = .12$).

DISCUSSION

Our results demonstrate that quantitative in vivo volumetric MR imaging measurements of the EC are associated with postmortem measures of entorhinal and neocortical AD pathology. Specifically, these results indicate that lower EC thickness predicts higher postmortem tangle load. We also found a similar association between EC thickness and postmortem tangle load within the medial temporal regions (EC + hippocampus). Most important, this effect remained significant after controlling for hippocampal volume. Finally, we found a robust relationship between EC thickness and cortical tangle and amyloid-β pathology. Rather than representing a specific measure of EC tangle pathology, our combined findings suggest that an antemortem MR imaging measure of the entorhinal cortex likely captures Alzheimer-associated pathology within the medial temporal and neocortical regions.

Using neuropathologic assessments from the same individuals and building on our prior work,[12,14] this study suggests that EC-associated cortical thinning in AD may represent a marker of τ-associated pathology within both the entorhinal cortex and neocortex. Consistent with the known pattern of amyloid-β deposition in AD, which heavily involves the neocortex with relative sparing of the entorhinal cortex, an association was found between EC thickness and neocortical amyloid-β load but not entorhinal amyloid pathology, compatible with the hypothesis that amyloid deposition within the neocortex, rather than the EC may represent an early component of Alzheimer pathobiology.[24,25] Our results also suggest that entorhinal cortex thickness may provide independent information about AD pathology even after accounting for hippocampal volume, further illustrating the importance of evaluating EC thickness as an early marker of in vivo Alzheimer neurodegeneration. Most interesting, even among cognitively healthy older adults, we found a selective relationship between entorhinal cortex thickness and tangle pathology but not amyloid pathology, suggesting the potential usefulness of quantitative MR imaging measures in preclinical AD.

Accumulating evidence suggests that τ pathology is closely associated with cognitive performance, particularly in the early stages of disease.[26,27] These findings suggest that automated measures of entorhinal cortex atrophy may reflect regional τ pathology, which will be clinically useful for early AD detection and disease monitoring. Additionally, quantitative measures of EC and medial temporal structures may be combined with genetic, fluid (CSF or plasma), and cognitive parameters for risk stratification, which may become increasingly relevant for AD prevention and therapeutic trials. With the advent and use of novel agents for detecting in vivo τ deposition,[28] volumetric MR imaging could be integrated with PET imaging to determine whether regional measures of entorhinal atrophy and τ deposition provide independent or complementary information. Finally, beyond AD, automated assessments of the entorhinal cortex can be useful in other disorders of the medial temporal lobe such as medial temporal sclerosis, vascular dementia, and frontotemporal lobar degeneration.

A potential limitation of our study is that our imaging and neuropathology datasets were not coregistered; thus, this drawback limits the precise correspondence between antemortem and

postmortem definitions of the EC. Another limitation is the need for validation of our results in independent, community-based samples.

CONCLUSIONS

We found a strong association between an automated, antemortem MR imaging–based measure of EC thickness and postmortem neurofibrillary tangle burden within the entorhinal cortex, medial temporal lobe, and neocortex. We additionally detected a relationship between EC thickness and neocortical amyloid-β load. Considered together, our findings serve as a validation of our automated MR imaging measure of the EC and suggest that EC-associated cortical thinning in AD may represent a marker of medial temporal and neocortical AD neuropathology.

ACKNOWLEDGMENTS

We thank the participants in the Rush Memory and Aging Project.

Disclosures: Sue E. Leurgans—*RELATED*: *Grant*: National Institutes of Health, *Comments*: P30AG010161 R01 NS078009, P20MD006886 P20MD006886-S1 RF1AG015819 U01AG046152-S1 R01AG034374 R01AG047976 R01AG033570.* David A. Bennett—*RELATED*: *Grant*: National Institutes of Health*. Bradley T. Hyman—*RELATED*: *Grant*: National Institutes of Health*; *UNRELATED*: *Board Membership:* NeuroPhage Pharmaceuticals; *Consultancy*: Genentech, Eli Lilly and Company, AbbVie, Merck, Biogen; *Grants/Grants Pending*: Merck, Denali, Spark, AbbVie, Biogen, Intellect*; *Stock/Stock Options*: Novartis, Marilyn S. Albert—*UNRELATED*: *Consultancy*: Eli Lilly and Company, Dana Foundation Scientific Advisory Board, *Comments*: member of the Eli Lilly and Company Advisory Board on preclinical Alzheimer disease, member of the Dana Foundation Scientific Advisory Board; *Grants/Grants Pending*: National Institutes of Health, Alzheimer's Association, Fidelity Biosciences, Bruce Fischl—*RELATED*: *Grant*: National Institutes of Health*; *UNRELATED*: *Grants/Grants Pending*: National Institutes of Health*; *Stock/Stock Options*: CorticoMetrics. Anders M. Dale—*RELATED*: *Grant*: National Institutes of Health, *Comments*: numerous research grants*; *UNRELATED*: *Board Membership*: CorTechs Labs Inc, *Comments*: I am a founder of and equity holder in CorTechs Labs Inc. I also serve on its scientific advisory board; *Consultancy*: Human Longevity Inc, *Comments*: I am a member of the Scientific Advisory Board of Human Longevity Inc; *Payment for Lectures Including Service on Speakers Bureaus*: GE Healthcare, *Comments*: I am the Principal Investigator of a comprehensive research agreement between the University of California, San Diego, and GE Healthcare. *Money paid to the institution.

REFERENCES

1. Squire LR, Zola-Morgan S. **The medial temporal lobe memory system.** *Science* 1991;253:1380–86 CrossRef Medline
2. Braak H, Braak E. **Neuropathological stageing of Alzheimer-related changes.** *Acta Neuropathol* 1991;82:239–59 CrossRef Medline
3. Braak H, Braak E. **Staging of Alzheimer's disease-related neurofibrillary changes.** *Neurobiol Aging* 1995;16:271–78; discussion 278–84 CrossRef Medline
4. Gómez-Isla T, Price JL, McKeel DW, et al. **Profound loss of layer II entorhinal cortex neurons occurs in very mild Alzheimer's disease.** *J Neurosci* 1996;16:4491–500 Medline
5. Arnold SE, Hyman BT, Flory J, et al. **The topographical and neuroanatomical distribution of neurofibrillary tangles and neuritic plaques in the cerebral cortex of patients with Alzheimer's disease.** *Cereb Cortex* 1991;1:103–16 CrossRef Medline
6. Desikan RS, Rafii MS, Brewer JB, et al. **An expanded role for neuroimaging in the evaluation of memory impairment.** *AJNR Am J Neuroradiol* 2013;34:2075–82 CrossRef Medline
7. Killiany RJ, Gomez-Isla T, Moss M, et al. **Use of structural magnetic resonance imaging to predict who will get Alzheimer's disease.** *Ann Neurol* 2000;47:430–39 Medline
8. Dickerson BC, Goncharova I, Sullivan MP, et al. **MRI-derived entorhinal and hippocampal atrophy in incipient and very mild Alzheimer's disease.** *Neurobiol Aging* 2001;22:747–54 CrossRef Medline
9. Killiany RJ, Hyman BT, Gomez-Isla T, et al. **MRI measures of entorhinal cortex vs hippocampus in preclinical AD.** *Neurology* 2002;58:1188–96 CrossRef Medline
10. Fischl B. **FreeSurfer.** *Neuroimage* 2012;62:774–81 CrossRef Medline
11. Desikan RS, Ségonne F, Fischl B, et al. **An automated labeling system for subdividing the human cerebral cortex on MRI scans into gyral based regions of interest.** *Neuroimage* 2006;31:968–80 CrossRef Medline
12. Desikan RS, Cabral HJ, Hess CP, et al; Alzheimer's Disease Neuroimaging Initiative. **Automated MRI measures identify individuals with mild cognitive impairment and Alzheimer's disease.** *Brain* 2009;132:2048–57 CrossRef Medline
13. Toledo JB, Da X, Weiner MW. **CSF Apo-E levels associate with cognitive decline and MRI changes.** *Acta Neuropathol* 2014;127:621–32 CrossRef Medline
14. Desikan RS, McEvoy LK, Thompson WK, et al; Alzheimer's Disease Neuroimaging Initiative. **Amyloid-β associated volume loss occurs only in the presence of phospho-tau.** *Ann Neurol* 2011;70:657–61 CrossRef Medline
15. Desikan RS, Fischl B, Cabral HJ, et al. **MRI measures of temporoparietal regions show differential rates of atrophy during prodromal AD.** *Neurology* 2008;71:819–25 CrossRef Medline
16. Desikan RS, Cabral HJ, Fischl B, et al. **Temporoparietal MR imaging measures of atrophy in subjects with mild cognitive impairment that predict subsequent diagnosis of Alzheimer disease.** *AJNR Am J Neuroradiol* 2009;30:532–38 CrossRef Medline
17. Bennett DA, Schneider JA, Buchman AS, et al. **The Rush Memory and Aging Project: study design and baseline characteristics of the study cohort.** *Neuroepidemiology* 2005;25:163–75 CrossRef Medline
18. Schneider JA, Arvanitakis Z, Bang W, et al. **Mixed brain pathologies account for most dementia cases in community-dwelling older persons.** *Neurology* 2007;69:2197–204 CrossRef Medline
19. McKhann G, Drachmann D, Folstein M, et al. **Clinical diagnosis of Alzheimer's disease: report of the NINCDS-ADRDA Work Group under the auspices of Department of Health and Human Services Task Force on Alzheimer's Disease.** *Neurology* 1984;34:939–44 CrossRef Medline
20. Fischl B, Salat DH, Busa E, et al. **Whole brain segmentation: automated labeling of neuroanatomical structures in the human brain.** *Neuron* 2002;33:341–55 CrossRef Medline
21. Bennett DA, Schneider JA, Wilson RS, et al. **Education modifies the association of amyloid but not tangles with cognitive function.** *Neurology* 2005;65:953–55 CrossRef Medline
22. Bennett DA, Wilson RS, Arvanitakis Z, et al. **Selected findings from the Religious Orders Study and Rush Memory and Aging Project.** *J Alzheimers Dis* 2013;33(suppl 1):S397–403 CrossRef Medline
23. Barnes LL, Schneider JA, Boyle PA, et al. **Memory complaints are related to Alzheimer disease pathology in older persons.** *Neurology* 2006;67:1581–85 CrossRef Medline
24. Buckner RL, Snyder AZ, Shannon BJ, et al. **Molecular, structural, and functional characterization of Alzheimer's disease: evidence for a relationship between default activity, amyloid, and memory.** *J Neurosci* 2005;25:7709–17 CrossRef Medline
25. Jack CR Jr, Barrio JR, Kepe V. **Cerebral amyloid PET imaging in Alzheimer's disease.** *Acta Neuropathol* 2013;126:643–57 CrossRef Medline
26. Brier MR, Gordon B, Friedrichsen K, et al. **Tau and Aβ imaging, CSF measures, and cognition in Alzheimer's disease.** *Sci Transl Med* 2016;8:338ra66 CrossRef Medline
27. Soldan A, Pettigrew C, Cai Q, et al. **Hypothetical preclinical Alzheimer disease groups and longitudinal cognitive change.** *JAMA Neurol* 2016;73:698–705 CrossRef Medline
28. Holtzman DM, Carrillo MC, Hendrix JA, et al. **Tau: from research to clinical development.** *Alzheimers Dement* 2016;12:1033–39 CrossRef Medline

Combined Diffusion Tensor Imaging and Apparent Transverse Relaxation Rate Differentiate Parkinson Disease and Atypical Parkinsonism

G. Du, M.M. Lewis, S. Kanekar, N.W. Sterling, L. He, L. Kong, R. Li, and X. Huang

ABSTRACT

BACKGROUND AND PURPOSE: Both diffusion tensor imaging and the apparent transverse relaxation rate have shown promise in differentiating Parkinson disease from atypical parkinsonism (particularly multiple system atrophy and progressive supranuclear palsy). The objective of the study was to assess the ability of DTI, the apparent transverse relaxation rate, and their combination for differentiating Parkinson disease, multiple system atrophy, progressive supranuclear palsy, and controls.

MATERIALS AND METHODS: A total of 106 subjects (36 controls, 35 patients with Parkinson disease, 16 with multiple system atrophy, and 19 with progressive supranuclear palsy) were included. DTI and the apparent transverse relaxation rate measures from the striatal, midbrain, limbic, and cerebellar regions were obtained and compared among groups. The discrimination performance of DTI and the apparent transverse relaxation rate among groups was assessed by using Elastic-Net machine learning and receiver operating characteristic curve analysis.

RESULTS: Compared with controls, patients with Parkinson disease showed significant apparent transverse relaxation rate differences in the red nucleus. Compared to those with Parkinson disease, patients with both multiple system atrophy and progressive supranuclear palsy showed more widespread changes, extending from the midbrain to striatal and cerebellar structures. The pattern of changes, however, was different between the 2 groups. For instance, patients with multiple system atrophy showed decreased fractional anisotropy and an increased apparent transverse relaxation rate in the subthalamic nucleus, whereas patients with progressive supranuclear palsy showed an increased mean diffusivity in the hippocampus. Combined, DTI and the apparent transverse relaxation rate were significantly better than DTI or the apparent transverse relaxation rate alone in separating controls from those with Parkinson disease/multiple system atrophy/progressive supranuclear palsy; controls from those with Parkinson disease; those with Parkinson disease from those with multiple system atrophy/progressive supranuclear palsy; and those with Parkinson disease from those with multiple system atrophy; but not those with Parkinson disease from those with progressive supranuclear palsy, or those with multiple system atrophy from those with progressive supranuclear palsy.

CONCLUSIONS: DTI and the apparent transverse relaxation rate provide different but complementary information for different parkinsonisms. Combined DTI and apparent transverse relaxation rate may be a superior marker for the differential diagnosis of parkinsonisms.

ABBREVATIONS: CN = caudate nucleus; FA = fractional anisotropy; MD = mean diffusivity; MoCA = Montreal Cognitive Assessment; MSA = multiple system atrophy; MSA-P = MSA parkinsonian subtype; PD = Parkinson disease; PSP = progressive supranuclear palsy; PUT = putamen; R2* = apparent transverse relaxation rate; ROC = receiver operating characteristic; RN = red nucleus; SN = substantia nigra; STN = subthalamic nucleus; UPDRS-III = Unified Parkinson's Disease Rating Scale, Part III (motor part)

Parkinson disease (PD), multiple system atrophy (MSA), and progressive supranuclear palsy (PSP) are the 3 most common parkinsonian syndromes with overlapping clinical manifestations. Differentiating these diseases on the basis of clinical symptoms alone can be challenging.[1,2] Despite similar clinical symptoms, each

Received September 22, 2016; accepted after revision January 11, 2017.

From the Departments of Neurology (G.D., M.M.L., N.W.S., L.H., X.H.), Radiology (S.K., X.H.), Pharmacology (M.M.L., X.H.), Neurosurgery (X.H.), Kinesiology (X.H.), Bioengineering (X.H.), and Public Health Sciences (L.K.), Pennsylvania State University–Milton S. Hershey Medical Center, Hershey, Pennsylvania; Department of Public Health (L.H.), Shanxi Medical University, Taiyuan, China; and Department of Statistics (R.L.), Pennsylvania State University, University Park, Pennsylvania.

This work was supported in part by the National Institute of Neurological Disorders and Stroke (NS082151), the Hershey Medical Center General Clinical Research Center (National Center for Research Resources, grant UL1 RR033184, which is now at the National Center for Advancing Translational Sciences, grant UL1 TR000127), the National Institute on Drug Abuse (P50 DA039838 and P50 DA036107), the National Nature Science Foundation of China (11690014 and 11690015), the Pennsylvania Department of Health Tobacco CURE Funds, the Michael J. Fox Foundation for Parkinson's Research, the Alzheimer's Association, Alzheimer's Research UK, and the Weston Brain Institute.

Please address correspondence to Guangwei Du, MD, PhD, Department of Neurology, 500 University Dr, Hershey, PA 17033; e-mail: guangweidu@hmc.psu.edu; Xuemei Huang, MD, PhD, Department of Neurology, 500 University Dr, Hershey, PA 17033; e-mail: xuemei@psu.edu

Indicates open access to non-subscribers at www.ajnr.org
Indicates article with supplemental on-line appendix and table.
Indicates article with supplemental on-line photos.
http://dx.doi.org/10.3174/ajnr.A5136

disorder has distinct gross and microscopic pathologies. PD is marked by the loss of dopamine neurons in the substantia nigra (SN).[3] MSA is characterized neuropathologically by glial and neuronal cytoplasmic inclusions in many basal ganglia and cerebellar related structures,[4] whereas PSP has neuronal loss, gliosis, and neurofibrillary tangles in both the basal ganglia and cerebellum that may extend to limbic areas.[5,6]

Two MR imaging modalities, diffusion tensor imaging and the apparent transverse relaxation rate (R2*), have been studied intensively in recent decades with the goal of detecting the distinct pathologic patterns in PD, MSA, and PSP and differentiating them from each other.[7-13] DTI has been suggested to reflect the disruption of microstructural integrity (eg, cell death and associated myelin changes), whereas R2* has been used to estimate iron accumulation in brain tissue.[14,15] There has been little effort, however, to directly compare DTI and R2* in the differential diagnosis of PD and atypical parkinsonism, and in testing whether they can provide complementary information regarding pathology and/or discriminability of those diseases.[10,14]

In the current study, we compared the pattern of DTI and R2* changes among the different parkinsonian diseases and a control group in multiple ROIs that included striatal-, midbrain-, limbic-, and cerebellar-related structures. The performance of DTI, R2*, and their combination to discriminate controls from patient groups and patient groups from each other also was assessed by using an Elastic-Net machine learning approach with a nested 10-fold cross-validation.

MATERIALS AND METHODS

Subjects

A total of 106 individuals (16 with MSA parkinsonian subtype [MSA-P], 19 with PSP [13 with Richardson subtype and 6 with parkinsonian subtype], 35 with PD, and 36 healthy controls) were included in this study from an ongoing longitudinal case-control cohort established in 2012. Patients were recruited from a tertiary movement disorders clinic, and controls were recruited from the spouse population of the clinic or the local community. All patients were free of major neurologic/medical issues other than PD, MSA-P, or PSP, and all controls were free of any known neurologic/psychiatric diagnoses. Patient diagnoses were initially established according to published criteria[16-18] by a movement disorder specialist and updated (August 2016) before the analysis of the current data according to the most recent clinical assessment and postmortem pathology if available (5 PD and 3 PSP cases were confirmed by postmortem pathology results). Two subjects (1 with PD and 1 with PSP) were excluded from later analyses due to severe motion artifacts. Disease duration was defined as the number of years between the date when a parkinsonian syndrome was first diagnosed by a medical professional and the study visit date. All participants were administered the Movement Disorder Society Unified Parkinson's Disease Rating Scale part III (UPDRS-III) for motor function assessment and the Montreal Cognitive Assessment (MoCA) for global cognitive function.[19] UPDRS-III and MoCA scores and MR imaging scans were collected for patients in an "on" state. The study was approved by the institutional review board at the Pennsylvania State University-Milton S. Hershey Medical Center. All subjects provided written informed consent.

MR Imaging Data Acquisition

Brain MRIs were obtained from all participants by using a 3T MR imaging system (Magnetom Trio; Siemens, Erlangen, Germany) with an 8-channel phased array head coil. The MR imaging examination included multi-gradient-echo (for R2*) and diffusion tensor imaging sequences, along with high-resolution T1-weighted and T2-weighted images for segmentation. Detailed imaging parameters are described in the On-line Appendix.

DTI and R2* Maps

Diffusion tensor images were processed using DTIPrep (Neuro Image Research and Analysis Laboratory, University of North Carolina, Chapel Hill, North Carolina). In DTIPrep, a thorough quality control for diffusion-weighted images was performed by intersection and intervolume correlation analysis, eddy currents, and motion artifact correction. Fractional anisotropy (FA) and mean diffusivity (MD) maps were then estimated for subsequent analysis.

For R2*, an affine registration was used to align 6 magnitude images to an averaged mean magnitude image for potential head motion correction in multi-gradient-echo images. The R2* maps then were generated by using a voxelwise nonlinear Levenberg-Marquardt algorithm to fit a monoexponential function ($s = s_0 e^{-\mathrm{TE} \times \mathrm{R2^*}}$) by using an in-house Matlab (MathWorks, Natick, Massachusetts) tool.

ROI Segmentation

The segmentation of ROIs was performed by using the Advanced Normalization Tools software package (ANTs; http://stnava.github.io/ANTs/)[20] and an atlas-based segmentation pipeline implemented in AutoSeg (http://www.nitrc.org/projects/autoseg/),[21] along with an in-house atlas. An unbiased, age-appropriate template was generated from T1-weighted images from all controls with ANTs.[22] The following 13 ROIs, including striatal and related structures (putamen [PUT], caudate nucleus [CN], and globus pallidus), midbrain (anterior SN, posterior SN, red nucleus [RN], and subthalamic nucleus [STN]), limbic (hippocampus and amygdala), and cerebellar structures (dentate nucleus, cerebellar hemisphere, superior cerebellar peduncle, and middle cerebellar peduncle) were defined on the cohort-specific T1-weighted and T2-weighted templates by an experienced neuroimager (G.D.). Segmented ROIs are illustrated in On-line Fig 1. ROIs for each subject were then parcellated by using AutoSeg with ANTs as a warping option[21,23] (see the On-line Appendix for details regarding the segmentation process). On-line Fig 3 illustrates the segmentation quality for small structures (SN, RN, and superior cerebellar peduncle).

B0 images for DTI and mean magnitude images for R2* then were coregistered to individual T2-weighted images using ANTs. The resulting transformations were then applied to FA, MD, and R2* maps by using a B-spline interpolation to bring FA, MD, and R2* images into the same space as the segmented ROIs, where the mean values of FA, MD, and R2* for each ROI were calculated for subsequent analyses.

Statistical Analysis and Modeling

The difference in sex frequency among groups was evaluated by using the χ^2 test. Age and disease duration were compared by using 1-way analysis of variance. MoCA and UPDRS-III scores

Table 1: Demographic and clinical data for control and patient groups[a]

	Control	PD	MSA-P	PSP	*P* Value
No. of subjects	36	35	16	19	
Female/male	13:23	12:23	8:8	4:15	.356[b]
Age (yr)	70.0 ± 7.5	70.3 ± 7.9	68.0 ± 7.5	74.9 ± 8.7	.057[c]
Disease duration (yr)	–	3.4 ± 3.6	3.9 ± 3.3	3.2 ± 2.8	.812[c]
MoCA	25 ± 2.3	22.8 ± 4.5	23.9 ± 2.7	20.1 ± 4.9	.002,[d] .120[e]
UPDRS III	4.6 ± 3.6	36.6 ± 27.3	51.5 ± 20.0	46.6 ± 23.4	<.0001,[d] .145[e]

[a] Data are sums or mean ± SD.
[b] Group difference in sex was compared among all 4 groups using the χ^2 test.
[c] Group differences in age and disease duration were compared using 1-way ANOVA.
[d] Group differences in MoCA and UPDRS-III were compared among all 4 groups using ANCOVA with adjustments for age and sex.
[e] Group differences in MoCA and UPDRS-III were compared among the 3 patient groups, using ANCOVA with adjustments for age and sex.

among groups were assessed by using 1-way analyses of covariance with adjustments for age and sex.

Each MR imaging measurement in patients with PD, MSA-P, and PSP was compared with that of controls by using univariate ANCOVAs with age and sex as covariates for each of the 13 ROIs. For MR imaging measurements, the Bonferroni method was used to correct for multiple comparisons, with a resulting *P* value ≤ .0038 (0.05/13 independent tests) considered significant.

One major challenge for multimodal MR imaging studies is the high dimensionality of potential predictors generated from different MR imaging measurements and brain structures, which can result in overfitting and collinearity among variables, causing traditional analyses to fail. In this study, we used an Elastic Net regularized logistic regression approach with a nested 10-fold cross-validation scheme to unravel the high-dimensional problem. Two hyperparameters need to be defined in Elastic-Net regularized regression. In our study, α was fixed to 0.2 empirically and λ was selected by an inner layer 10-fold cross-validation that was independent of the outer layer 10-fold cross-validation used for performance evaluation. This nested cross-validation setting was implemented to alleviate potential overfitting.[24]

Regularized logistic models were built from all ROI measurements including R2*, DTI (including both FA and MD), and the combined measures (R2*, FA, and MD) for discriminating the following: 1) controls from those with PD/MSA-P/PSP, 2) those with PD from those with MSA-P/PSP, 3) controls from those with PD, 4) those with PD from those with MSA-P, 5) those with PD from those with PSP, and 6) those with MSA-P from those with PSP. Receiver operating characteristic (ROC) curves were generated by using outer layer 10-fold cross-validation models for each MR imaging technique and their combination. A bootstrap approach was used to test the differences among ROC curves.[25] ROC curve comparisons were performed between the combined marker and DTI because DTI was better or equal to R2* in all 6 scenarios mentioned above. Sensitivity, specificity, positive predictive value, and negative predictive value were generated by using the Youden method.

Statistical analyses were performed by using the open-source statistical software package R (Version 3.0.3; http://www.r-project.org). Elastic-Net regularized logistic regression was conducted by using the R package glmnet (http://web.stanford.edu/~hastie/glmnet/glmnet_alpha.html),[26] whereas the ROC curve analyses were performed by using the R package pROC (https://cran.r-project.org/web/packages/pROC/index.html).[27]

RESULTS

Demographic Data

Demographic characteristics for subjects are shown in Table 1. No significant overall differences in sex distribution or age were detected among the control, PD, PSP, and MSA-P groups. Post hoc pair-wise analysis showed trending differences between MSA-P and PSP in both sex ($P = .072$) and age ($P = .065$). Thus, both age and sex were entered as covariates for group comparisons. Logistic regression on age and sex showed no comparable discriminability among PD, MSA-P, and PSP (area under the curve < 0.66). Although patients had significantly lower MoCA and higher UPDRS-III scores compared with controls, there were no significant differences among the patient groups on the clinical measures (disease duration, MoCA, or UPDRS-III).

DTI and R2* Comparison between Parkinsonian Disease and Control Groups

Compared with controls, patients with PD showed changes in the posterior SN and RN in both DTI and R2*, though only the R2* value in the RN survived correction for multicomparisons. Patients with both MSA and PSP showed more widespread changes (after correction for multicomparisons) involving structures both within and outside the midbrain. The pattern of changes, however, was different between the 2 groups. Namely, patients with MSA-P showed increased MD values in the PUT, globus pallidus, cerebellum, and middle cerebellar peduncle, a decreased FA value in the STN, and increased R2* values in the STN and middle cerebellar peduncle. Patients with PSP, however, showed increased MD and R2* values in the posterior substantia nigra but no changes in the STN or any other basal ganglia structures. Patients with PSP had significantly increased MD values in the dentate nucleus, cerebellum, and superior cerebellar peduncle, but not in the middle cerebellar peduncle (Table 2 and On-line Table).

Discriminative Analysis

We compared the discriminative ability of DTI and R2* measures and their combination under 6 different scenarios by using Elastic-Net regularized logistic regression and ROC curves (Table 3 and On-line Fig 2). The combined models (DTI+R2*) were better than DTI or R2* alone (*P*s < .05) in discriminating controls from those with PD/MSA-P/PSP, controls from those with PD, those with PD from those with MSA-P/PSP, and those with PD from those with MSA-P. When we considered the separation of controls from subjects with PD, the combined model was improved dramatically compared with either measure alone (from area under the curve = 0.82 to area under the curve = 0.91, $P = .001$).

The DTI model, however, showed strong discriminability when differentiating PD from PSP (area under the curve = 0.97) or MSA-P from PSP (area under the curve = 0.96), and adding R2* did not significantly improve the performance of the model. Nevertheless, R2* alone showed decent discriminative ability

Table 2: Individual MRI measurements in PD, MSA-P, and PSP compared with controls in different structures

	PD			MSA-P			PSP		
	FA	MD	R2*	FA	MD	R2*	FA	MD	R2*
Striatal and related structures									
PUT					↑ ↑[a]			↑	
CN									
GP					↑ ↑ ↑[a]	↑	↑	↑	
Midbrain structures									
antSN				↓		↑		↑ ↑	↑
postSN	↓ ↓	↑	↑ ↑	↓		↑		↑ ↑ ↑ ↑[a]	↑ ↑
RN			↑ ↑[a]	↓	↑			↑	↑ ↑[a]
STN				↓ ↓[a]	↑	↑ ↑ ↑[a]			↑
Limbic structures									
Hipp							↓	↑ ↑ ↑ ↑[a]	↓
AM				↓			↓	↑ ↑	
Cerebellar structures									
DN							↓	↑ ↑[a]	
CB				↓ ↓	↑ ↑ ↑[a]		↓ ↓[a]	↑ ↑[a]	
SCP							↓ ↓ ↓ ↓[a]	↑ ↑ ↑ ↑[a]	
MCP				↓	↑ ↑ ↑[a]	↓ ↓ ↓[a]		↑ ↑[a]	

Note:—antSN indicates anterior substantia nigra; postSN, posterior substantia nigra; Hipp, hippocampus; AM, amygdala; CB, cerebellum; DN, dentate nucleus; GP, globus pallidus; MCP, middle cerebellar peduncle; SCP, superior cerebellar peduncle.

[a] Statistical significance after Bonferroni correction ($P < .0038$, considering 13 independent tests). Upward arrows indicate increased MRI measures compared with controls, and downward arrows indicate decreased MRI measures compared with controls. ↑ represents $P < .05$, ↑ ↑ represents $P < .01$, ↑ ↑ ↑ represents $P < .001$, and ↑ ↑ ↑ ↑ represents $P < 0.0001$.

Table 3: ROC analysis of individual and combined MRI modalities

	AUC	Sens	Spec	PPV	NPV	*P* Value[a]
C vs PD/MSA-P/PSP						.013
DTI+R2*	0.88	0.80	0.83	0.82	0.81	
DTI[b]	0.80	0.81	0.71	0.60	0.87	
R2*	0.75	0.69	0.69	0.55	0.81	
C vs PD						.001
DTI+R2*	0.91	0.86	0.80	0.82	0.89	
DTI	0.82	0.74	0.76	0.75	0.76	
R2*	0.78	0.71	0.75	0.71	0.74	
PD vs MSA-P/PSP						.038
DTI+R2*	0.94	0.86	0.87	0.88	0.84	
DTI	0.89	0.83	0.80	0.82	0.81	
R2*	0.87	0.87	0.77	0.87	0.77	
PD vs MSA-P						.006
DTI+R2*	0.99	0.97	1.00	1.00	0.93	
DTI	0.89	0.83	0.86	0.79	0.86	
R2*	0.91	0.86	0.86	0.94	0.70	
PD vs PSP						.156
DTI+R2*	0.99	0.97	1.00	1.00	0.94	
DTI	0.97	0.94	0.94	0.97	0.89	
R2*	0.87	0.80	0.83	0.82	0.81	
MSA-P vs PSP						.435
DTI+R2*	0.98	0.94	1.00	1.00	0.93	
DTI	0.96	0.94	0.92	0.94	0.92	
R2*	0.89	0.86	0.80	0.82	0.81	

Note:—Sens indicates sensitivity; Spec, specificity; PPV, positive predictive value; NPV, negative predictive value; AUC, area under the curve; C, controls.

[a] ROC curves were compared between the models, including all MRI measurements and that with DTI measurements only.

[b] Models for DTI measurements were generated by including both FA and MD features.

when differentiating PD from PSP (area under the curve = 0.87) and MSA-P from PSP (area under the curve = 0.89).

DISCUSSION

First, we confirmed that DTI and R2* differentiate parkinsonian syndromes and controls. In addition, our studies demonstrated that DTI and R2* can capture the distinct pathologic patterns of the different parkinsonian syndromes and may provide complementary information about each disease. Individually, DTI showed better discriminability among the disease groups, whereas R2 added significant value in separating controls from those with parkinsonian syndromes and those with PD from those with MSA-P/PSP or MSA-P.

DTI and R2 Changes in PD*

The pathologic hallmark of PD is neuronal loss in the SN pars compacta. Our study may capture this pathology by demonstrating decreased FA and increased R2* in the posterior SN.[28,29] The inclusion of additional ROIs in our study, however, requires a rather conservative Bonferroni correction; thus, the detected difference did not reach statistical significance. Future studies are needed to confirm these findings in light of a recent meta-analysis suggesting that nigral FA changes in patients with PD vary widely.[30] In the current study, patients with PD also demonstrated increased R2* values in the RN. This result is consistent with the notion that the RN may be involved in the primary cerebellar motor pathway, which has been shown to be affected in PD.[31,32]

DTI and R2 Changes in MSA-P*

We also found significantly increased MD values in the PUT, globus pallidus, cerebellum, and middle cerebellar peduncle of patients with MSA-P, consistent with previous neuroimaging results.[7,8,12,33,34] On the basis of previous studies, DTI MD changes in the CN have been controversial. For example, Seppi et al[35] reported significantly increased MD values in the CN, whereas others have found no changes in CN MD values.[12,34] We did not find significant MD changes in the CN, consistent with these later reports. One study reported MD changes in the SN of patients with MSA-P[12]; however, we could not replicate this finding. Pathology studies have reported robust changes in the PUT but more variable changes in other basal ganglia regions.[4,36] This varying pathology may contribute partly to the inconsistent DTI findings in the CN and SN in the current study and previous ones.[9,12,13,34,35]

Patients with MSA-P consistently demonstrated increased R2* values in the PUT.[10-12] The current study, however, failed to detect R2* changes in the PUT of these patients. Although the exact reason for the discrepancy is unknown, we postulate the following 2 possibilities: First, heterogeneous cohort characteristics may have contributed to the different results. For example, previous studies had significantly younger patients with MSA (mean ages, 58–62 years) compared with our cohort (mean age, 68 years). Age significantly affects iron and R2* values in basal ganglia structures.[37] Thus, these age effects may mask the disease-related changes in the PUT. Second, the different R2* techniques used among the studies may influence the results.[10,12,38] For example, Lee et al[11] used 8 echoes and a TR = 24 ms, whereas Barbagallo et al[12] used 6 echoes with repetition and a TR = 100 ms; and we used 6 echoes and a TR = 54 ms. In addition to imaging parameters, each study used different curve-fitting techniques: Lee et al[11] used linear fitting after log-transformation of the original signal, whereas the current study used nonlinear curve-fitting to a monoexponential function similar to that in Barbagallo et al.[12]

Most interesting, we detected a decreased FA value in the STN of patients with MSA-P, along with an increased R2* value, which has not been reported by any previous MR imaging studies, to our knowledge. It is unclear whether the lack of significant STN findings arises from a lack of focus on this structure or whether no differences were found. The neuronal/glial cytoplasmic inclusions that typically are found in basal ganglia regions are less common in the STN of patients with MSA.[4] One pathology study, however, noted increased microglia in the STN of patients with MSA-P,[36] which may reflect a reactive or compensatory process instead of the primary pathology. Thus, the STN changes we detected may reflect these reactive or compensatory changes, though future studies focused on the STN are warranted to verify this.

DTI and R2* Changes in PSP

Consistent with previous studies, we found significant DTI (MD) changes in midbrain (posterior SN and cerebellar [cerebellum and superior cerebellar peduncle]) structures of patients with PSP, with the most robust change seen in the superior cerebellar peduncle.[7,8,35,39] Whereas most studies reported increased MD values in the PUT of patients with PSP,[35,39,40] we did not detect MD changes in the PUT or other basal ganglia structures (CN and globus pallidus) in the current study. Consistent with our findings, Tsukamoto et al[34] reported no MD changes in the PUT of patients with PSP. Additional studies are needed to clarify the discrepancies.

In the past, both pathologic and neuroimaging studies with free-water imaging suggested changes in the STN of patients with PSP.[6,13] Pathologic studies also reported both neuronal and oligodendroglia loss in the STN of patients with PSP. Using traditional DTI measures (FA and MD), the current study did not detect significant changes in the STN of patients with PSP. It is possible that the mixed microscopic pathology may have complex or opposing effects on these traditional DTI measurements at the macroscopic level. Change in the STN of patients with PSP by means of the free-water measure derived from a bi-tensor model[13] suggests that free-water may be a more sensitive marker for PSP-related pathology in the STN. Future studies are needed to further confirm the links between PSP-related pathology and different MR imaging contrasts.

In the current study, we also detected an increased MD value in the dentate nucleus of patients with PSP. Although this finding is new, it is in line with pathologic results of neuronal loss in the dentate nucleus of patients with PSP.[6] In addition, patients with PSP demonstrated significantly increased MD values in the hippocampus and a trending change in the amygdala. These results are consistent with previous volumetric studies suggesting pathologic involvement of the hippocampus in PSP[5,41] and early cognitive issues that often are detected in patients with PSP clinically. These findings are inconsistent, however, with previous pathologic studies indicating that the hippocampus and amygdala are spared from τ pathology in patients with PSP.[42] A growing literature supports the heterogeneity of PSP and mixed pathologic findings across different tauopathies[39,43]; thus, the value of using differential imaging patterns to subtype the patient with PSP will be evaluated in the future.

Previous studies on R2* in the PUT, CN, and globus pallidus in patients with PSP have been controversial because some studies showed significantly increased R2* values in these structures,[11,44] whereas others did not.[10] The current results are consistent with no R2* changes in the PUT, CN, and globus pallidus. Patients with PSP, however, had significantly increased R2* values in the SN and RN. This finding is consistent with previous PSP pathologic studies indicating that τ pathology–related neuronal and oligodendroglia loss is involved in both the SN and RN.[42]

Discriminative Analysis

Many promising MR imaging markers have been suggested to differentiate patients with PD from those with atypical parkinsonism.[8,9,13,45,46] Systematic comparison and validation of those markers in the same subjects are needed before translating these findings into a clinical setting. The current study is the first to systematically compare DTI, R2*, and their combination by using Elastic-Net regularized logistic regression. When we compared DTI and R2* measures under 6 clinically relevant scenarios, our results suggested the following: 1) that DTI measures overall are better or comparable with R2* values in differentiating parkinsonisms, and 2) that R2* provides complementary information in most scenarios except when differentiating PD from PSP or MSA-P from PSP.

Limitations

The current study has some limitations. First, among 70 patients with parkinsonism, only 8 cases were confirmed by postmortem pathology. Despite updating the clinical diagnosis by integrating more longitudinal clinical information right before conducting the current analysis, diagnosis error inevitably exists and might bias the results. Additionally, we included controls with positive UPDRS-III scores as high as 14. It is possible that controls with high UPDRS-III scores have a preclinical parkinsonian syndrome. Nonetheless, a recent study has demonstrated that parkinsonian signs are common in older adults, even without a clinical diagnosis of disease.[47] Second, this study is case-control in nature and does not simulate clinical practice, which would include other diseases potentially confused with PD such as essential tremor,

corticobasal degeneration, dementia with Lewy bodies, and psychogenic disorders. In addition, we did not separate PSP subtypes.[43] Re-analyzing the data to include only patients with PSP Richardson subtype ($n = 13$) did not change the results demonstrably from those including the entire PSP cohort. Finally, in the current study, all data were collected while patients were on antiparkinsonian medications, and the MR imaging measures may be affected by the drugs. Further prospective studies that mimic clinical practice are warranted to further test the potential of these markers in clinical practice.

Technically, recent advances in MR imaging markers for PD and atypical parkinsonism have suggested that 2 new measures (free-water and quantitative susceptibility) may be useful for discriminating patient groups and are derived from the same MR imaging data (DTI and R2*, respectively). Quantitative susceptibility has been suggested to improve the R2* signal by reducing potential confounders of the iron measurement,[48] whereas free-water may provide additional information above traditional FA or MD values.[49] The current study did not include these new measures, and future work validating and comparing them is warranted. Finally, this study did not compare our models with conventional MR imaging clues used by radiologists in these disorders, such as the "hummingbird" and "hot cross bun" signs, midbrain atrophy, and putaminal T2-weighted hypointensity.[50-52] Notably, Reiter et al,[51] with visual rating of dorsolateral nigral hyperintensity in susceptibility-weighted images, showed promising discriminability in differentiating those with parkinsonian syndromes from controls. It will be important to discern the additional value a quantitative MR imaging marker derived from combining DTI and R2* provides compared with the best medical knowledge. In this study, we adopted an Elastic-Net regularized regression as the multivariate classification method. Even though we used a nested 10-fold cross-validation for model selection and performance evaluation, the models still may be overly optimistic due to the small sample size.[24]

CONCLUSIONS

Our findings are consistent with those in previous neuroimaging and postmortem pathologic studies reporting significant involvement of striatal-, midbrain-, and cerebellar-related structures in PD and atypical parkinsonism.[4,6,8,10,12,14,15,29,34,35,39] The exact location and MR imaging measures in striatal and midbrain-related structures between previous studies and the current study, however, vary.[34,35,39] This study demonstrated that DTI and R2* reflect different-yet-complementary information that can be used for discriminating controls and patients with PD, MSA, and PSP. Further refinement of this approach, including the use of novel measures that assess other aspects of disease pathology and the extension to whole-brain feature space, could lead to an optimized tool that can diagnose and differentiate PD from atypical parkinsonism. We envision applying this approach to a large prospective cohort, including a more diverse patient population (PD, MSA, PSP, essential tremor, corticobasal degeneration, and dementia with Lewy bodies), that simulates a real clinical setting to further test its utility in clinical practice.

ACKNOWLEDGMENTS

We thank the MR imaging technical support of Jeffery Vesek and the assistance of study coordinators Melissa Santos and Raghda Clayiff.

Disclosures: Guangwei Du—*RELATED*: *Grant*: National Institute of Neurological Disorders and Stroke and Michael J. Fox Foundation for Parkinson's Research.* Mechelle M. Lewis—*RELATED*: *Grant*: National Institute of Neurological Disorders and Stroke, and Michael J. Fox Foundation for Parkinson's Research *UNRELATED*: *Grants/Grants Pending*: National Institute of Environmental Health Sciences*; *Travel/Accommodations/Meeting Expenses Unrelated to Activities Listed*: Parkinson's Disease Biomarkers Program (PDBP) Annual Consortium Meeting, *Comments*: every year, the PDBP meets in Bethesda, Maryland, for 1.5 days. The PDBP pays for hotel accommodations, travel, and per diem meals for me to attend the meeting. Nicholas W. Sterling—*UNRELATED*: *Support for Travel to Meetings for the Study or Other Purposes*: American Neurological Association, *Comments*: travel grant.* Lan Kong—*RELATED*: *Grant*: National Institutes of Health and Michael J. Fox Foundation for Parkinson's Research, *Comments*: I am the coinvestigator on the following grants: National Institutes of Health grant: Multimodal MRI Markers of Nigrostriatal Pathology in Parkinson's Disease; Michael J. Fox Foundation for Parkinson's Research: Benchmark Structural MRI Markers for Parkinsonian Syndromes.* Runze Li—*RELATED*: *Grant*: National Science Foundation and National Institutes of Health*; *UNRELATED*: *Grants/Grants Pending*: National Science Foundation and National Institutes of Health.* Xuemei Huang—*RELATED*: *Grant*: National Institutes of Health, *Comments*: National Institute of Neurological Disorders and Stroke, and Michael J. Fox Foundation for Parkinson's Research*; *UNRELATED*: *Consultancy*: National Institute of Environmental Health Sciences, *Comments*: This is payment for my consultation for the National Institute of Environmental Health Sciences about Parkinson disease diagnosis; *Grants/Grants Pending*: National Institute of Environmental Health Sciences, *Comments*: NIEHS-ES019672.* *Money paid to the institution.

REFERENCES

1. Hughes AJ, Daniel SE, Ben-Shlomo Y, et al. **The accuracy of diagnosis of parkinsonian syndromes in a specialist movement disorder service.** *Brain* 2002;125:861–70 CrossRef Medline
2. Joutsa J, Gardberg M, Röyttä M, et al. **Diagnostic accuracy of parkinsonism syndromes by general neurologists.** *Parkinsonism Relat Disord* 2014;20:840–44 CrossRef Medline
3. Fearnley JM, Lees AJ. **Ageing and Parkinson's disease: substantia nigra regional selectivity.** *Brain* 1991;114(pt 5):2283–301 CrossRef Medline
4. Cykowski MD, Coon EA, Powell SZ, et al. **Expanding the spectrum of neuronal pathology in multiple system atrophy.** *Brain* 2015;138:2293–309 CrossRef Medline
5. Padovani A, Borroni B, Brambati SM, et al. **Diffusion tensor imaging and voxel based morphometry study in early progressive supranuclear palsy.** *J Neurol Neurosurg Psychiatry* 2006;77:457–63 CrossRef Medline
6. Dickson DW, Rademakers R, Hutton ML. **Progressive supranuclear palsy: pathology and genetics.** *Brain Pathol* 2007;17:74–82 CrossRef Medline
7. Blain CR, Barker GJ, Jarosz JM, et al. **Measuring brain stem and cerebellar damage in parkinsonian syndromes using diffusion tensor MRI.** *Neurology* 2006;67:2199–205 CrossRef Medline
8. Nicoletti G, Rizzo G, Barbagallo G, et al. **Diffusivity of cerebellar hemispheres enables discrimination of cerebellar or parkinsonian multiple system atrophy from progressive supranuclear palsy-Richardson syndrome and Parkinson disease.** *Radiology* 2013;267:843–50 CrossRef Medline
9. Prodoehl J, Li H, Planetta PJ, et al. **Diffusion tensor imaging of Parkinson's disease, atypical parkinsonism, and essential tremor.** *Mov Disord* 2013;28:1816–22 CrossRef Medline
10. Focke NK, Helms G, Pantel PM, et al. **Differentiation of typical and atypical Parkinson syndromes by quantitative MR imaging.** *AJNR Am J Neuroradiol* 2011;32:2087–92 CrossRef Medline
11. Lee JH, Han YH, Kang BM, et al. **Quantitative assessment of subcortical atrophy and iron content in progressive supranuclear palsy and parkinsonian variant of multiple system atrophy.** *J Neurol* 2013;260:2094–101 CrossRef Medline

12. Barbagallo G, Sierra-Peña M, Nemmi F, et al. **Multimodal MRI assessment of nigro-striatal pathway in multiple system atrophy and Parkinson disease.** *Mov Disord* 2016;31:325–34 CrossRef Medline
13. Planetta PJ, Ofori E, Pasternak O, et al. **Free-water imaging in Parkinson's disease and atypical parkinsonism.** *Brain* 2016;139(pt 2): 495–508 CrossRef Medline
14. Péran P, Cherubini A, Assogna F, et al. **Magnetic resonance imaging markers of Parkinson's disease nigrostriatal signature.** *Brain* 2010; 133:3423–33 CrossRef Medline
15. Du G, Lewis MM, Styner M, et al. **Combined R2* and diffusion tensor imaging changes in the substantia nigra in Parkinson's disease.** *Mov Disord* 2011;26:1627–32 CrossRef Medline
16. Hughes AJ, Daniel SE, Kilford L, et al. **Accuracy of clinical diagnosis of idiopathic Parkinson's disease: a clinico-pathological study of 100 cases.** *J Neurol Neurosurg Psychiatry* 1992;55:181–84 CrossRef Medline
17. Gilman S, Wenning GK, Low PA, et al. **Second consensus statement on the diagnosis of multiple system atrophy.** *Neurology* 2008;71: 670–76 CrossRef Medline
18. Litvan I, Agid Y, Calne D, et al. **Clinical research criteria for the diagnosis of progressive supranuclear palsy (Steele-Richardson-Olszewski syndrome): report of the NINDS-SPSP international workshop.** *Neurology* 1996;47:1–9 CrossRef Medline
19. Nasreddine ZS, Phillips NA, Bédirian V, et al. **The Montreal Cognitive Assessment, MoCA: a brief screening tool for mild cognitive impairment.** *J Am Geriatr Soc* 2005;53:695–99 CrossRef Medline
20. Avants BB, Tustison NJ, Song G, et al. **A reproducible evaluation of ANTs similarity metric performance in brain image registration.** *Neuroimage* 2011;54:2033–44 CrossRef Medline
21. Wang J, Vachet C, Rumple A, et al. **Multi-atlas segmentation of subcortical brain structures via the AutoSeg software pipeline.** *Front Neuroinform* 2014;8:7 CrossRef Medline
22. Avants BB, Yushkevich P, Pluta J, et al. **The optimal template effect in hippocampus studies of diseased populations.** *Neuroimage* 2010;49: 2457–66 CrossRef Medline
23. Avants BB, Epstein CL, Grossman M, et al. **Symmetric diffeomorphic image registration with cross-correlation: evaluating automated labeling of elderly and neurodegenerative brain.** *Med Image Anal* 2008;12:26–41 CrossRef Medline
24. Cawley GC, Talbot NL. **On over-fitting in model selection and subsequent selection bias in performance evaluation.** *J Mach Learn Res* 2010;11:2079–107
25. Venkatraman ES. **A permutation test to compare receiver operating characteristic curves.** *Biometrics* 2000;56:1134–38 CrossRef Medline
26. Friedman J, Hastie T, Tibshirani R. **Regularization paths for generalized linear models via coordinate descent.** *J Stat Softw* 2010;33: 1–22 Medline
27. Robin X, Turck N, Hainard A, et al. **pROC: an open-source package for R and S+ to analyze and compare ROC curves.** *BMC Bioinformatics* 2011;12:77 CrossRef Medline
28. Vaillancourt DE, Spraker MB, Prodoehl J, et al. **High-resolution diffusion tensor imaging in the substantia nigra of de novo Parkinson disease.** *Neurology* 2009;72:1378–84 CrossRef Medline
29. Du G, Lewis MM, Sen S, et al. **Imaging nigral pathology and clinical progression in Parkinson's disease.** *Mov Disord* 2012;27:1636–43 CrossRef Medline
30. Schwarz ST, Abaei M, Gontu V, et al. **Diffusion tensor imaging of nigral degeneration in Parkinson's disease: a region-of-interest and voxel-based study at 3 T and systematic review with meta-analysis.** *Neuroimage Clin* 2013;3:481–88 CrossRef Medline
31. Lewis MM, Du G, Kidacki M, et al. **Higher iron in the red nucleus marks Parkinson's dyskinesia.** *Neurobiol Aging* 2013;34:1497–503 CrossRef Medline
32. He N, Ling H, Ding B, et al. **Region-specific disturbed iron distribution in early idiopathic Parkinson's disease measured by quantitative susceptibility mapping.** *Hum Brain Mapp* 2015;36: 4407–20 CrossRef Medline
33. Schocke MF, Seppi K, Esterhammer R, et al. **Diffusion-weighted MRI differentiates the Parkinson variant of multiple system atrophy from PD.** *Neurology* 2002;58:575–80 CrossRef Medline
34. Tsukamoto K, Matsusue E, Kanasaki Y, et al. **Significance of apparent diffusion coefficient measurement for the differential diagnosis of multiple system atrophy, progressive supranuclear palsy, and Parkinson's disease: evaluation by 3.0-T MR imaging.** *Neuroradiology* 2012;54:947–55 CrossRef Medline
35. Seppi K, Schocke MF, Esterhammer R, et al. **Diffusion-weighted imaging discriminates progressive supranuclear palsy from PD, but not from the parkinson variant of multiple system atrophy.** *Neurology* 2003;60:922–27 CrossRef Medline
36. Salvesen L, Ullerup BH, Sunay FB, et al. **Changes in total cell numbers of the basal ganglia in patients with multiple system atrophy: a stereological study.** *Neurobiol Dis* 2015;74:104–13 CrossRef Medline
37. Betts MJ, Acosta-Cabronero J, Cardenas-Blanco A, et al. **High-resolution characterisation of the aging brain using simultaneous quantitative susceptibility mapping (QSM) and R2* measurements at 7T.** *Neuroimage* 2016;138:43–63 CrossRef Medline
38. Minnerop M, Specht K, Ruhlmann J, et al. **Voxel-based morphometry and voxel-based relaxometry in multiple system atrophy-a comparison between clinical subtypes and correlations with clinical parameters.** *Neuroimage* 2007;36:1086–95 CrossRef Medline
39. Rizzo G, Martinelli P, Manners D, et al. **Diffusion-weighted brain imaging study of patients with clinical diagnosis of corticobasal degeneration, progressive supranuclear palsy and Parkinson's disease.** *Brain* 2008;131:2690–700 CrossRef Medline
40. Zanigni S, Calandra-Buonaura G, Manners DN, et al. **Accuracy of MR markers for differentiating progressive supranuclear palsy from Parkinson's disease.** *Neuroimage Clin* 2016;11:736–42 CrossRef Medline
41. Stutzbach LD, Xie SX, Naj AC, et al. **The unfolded protein response is activated in disease-affected brain regions in progressive supranuclear palsy and Alzheimer's disease.** *Acta Neuropathol Commun* 2013;1:31 CrossRef Medline
42. Dickson DW. **Parkinson's disease and parkinsonism: neuropathology.** *Cold Spring Harb Perspect Med* 2012;2:a009258 Medline
43. Agosta F, Pievani M, Svetel M, et al. **Diffusion tensor MRI contributes to differentiate Richardson's syndrome from PSP-parkinsonism.** *Neurobiol Aging* 2012;33:2817–26 CrossRef Medline
44. Boelmans K, Holst B, Hackius M, et al. **Brain iron deposition fingerprints in Parkinson's disease and progressive supranuclear palsy.** *Mov Disord* 2012;27:421–27 CrossRef Medline
45. Massey LA, Jäger HR, Paviour DC, et al. **The midbrain to pons ratio: a simple and specific MRI sign of progressive supranuclear palsy.** *Neurology* 2013;80:1856–61 CrossRef Medline
46. Focke NK, Helms G, Scheewe S, et al. **Individual voxel-based subtype prediction can differentiate progressive supranuclear palsy from idiopathic Parkinson syndrome and healthy controls.** *Hum Brain Mapp* 2011;32:1905–15 CrossRef Medline
47. Buchman AS, Leurgans SE, Yu L, et al. **Incident parkinsonism in older adults without Parkinson disease.** *Neurology* 2016;87:1036–44 CrossRef Medline
48. Wang Y, Liu T. **Quantitative susceptibility mapping (QSM): Decoding MRI data for a tissue magnetic biomarker.** *Magn Reson Med* 2015;73:82–101 CrossRef Medline
49. Ofori E, Pasternak O, Planetta PJ, et al. **Increased free water in the substantia nigra of Parkinson's disease: a single-site and multi-site study.** *Neurobiol Aging* 2015;36:1097–104 CrossRef Medline
50. Massey LA, Micallef C, Paviour DC, et al. **Conventional magnetic resonance imaging in confirmed progressive supranuclear palsy and multiple system atrophy.** *Mov Disord* 2012;27:1754–62 CrossRef Medline
51. Reiter E, Mueller C, Pinter B, et al. **Dorsolateral nigral hyperintensity on 3.0T susceptibility-weighted imaging in neurodegenerative Parkinsonism.** *Mov Disord* 2015;30:1068–76 CrossRef Medline
52. Scherfler C, Göbel G, Müller C, et al. **Diagnostic potential of automated subcortical volume segmentation in atypical parkinsonism.** *Neurology* 2016;86:1242–49 CrossRef Medline

Performance Assessment for Brain MR Imaging Registration Methods

J.S. Lin, D.T. Fuentes, A. Chandler, S.S. Prabhu, J.S. Weinberg, V. Baladandayuthapani, J.D. Hazle, and D. Schellingerhout

ABSTRACT

BACKGROUND AND PURPOSE: Clinical brain MR imaging registration algorithms are often made available by commercial vendors without figures of merit. The purpose of this study was to suggest a rational performance comparison methodology for these products.

MATERIALS AND METHODS: Twenty patients were imaged on clinical 3T scanners by using 4 sequences: T2-weighted, FLAIR, susceptibility-weighted angiography, and T1 postcontrast. Fiducial landmark sites (n = 1175) were specified throughout these image volumes to define identical anatomic locations across sequences. Multiple registration algorithms were applied by using the T2 sequence as a fixed reference. Euclidean error was calculated before and after each registration and compared with a criterion standard landmark registration. The Euclidean effectiveness ratio is the fraction of Euclidean error remaining after registration, and the statistical effectiveness ratio is similar, but accounts for dispersion and noise.

RESULTS: Before registration, error values for FLAIR, susceptibility-weighted angiography, and T1 postcontrast were 2.07 ± 0.55 mm, 2.63 ± 0.62 mm, and 3.65 ± 2.00 mm, respectively. Postregistration, the best error values for FLAIR, susceptibility-weighted angiography, and T1 postcontrast were 1.55 ± 0.46 mm, 1.34 ± 0.23 mm, and 1.06 ± 0.16 mm, with Euclidean effectiveness ratio values of 0.493, 0.181, and 0.096 and statistical effectiveness ratio values of 0.573, 0.352, and 0.929 for rigid mutual information, affine mutual information, and a commercial GE registration, respectively.

CONCLUSIONS: We demonstrate a method for comparing the performance of registration algorithms and suggest the Euclidean error, Euclidean effectiveness ratio, and statistical effectiveness ratio as performance metrics for clinical registration algorithms. These figures of merit allow registration algorithms to be rationally compared.

ABBREVIATIONS: ANTs = advanced normalization tools; AOI = algorithm of interest; CC = cross-correlation; EER = Euclidean effectiveness ratio; LM = landmarks; MI = mutual information; SER = statistical effectiveness ratio; SWAN = susceptibility-weighted angiography; T1C = T1 postcontrast; TRE = target-to-registration error

Image registration is an essential step in the analysis of brain MR imaging data from multiple images because it ensures the spatial correspondence of anatomy across complementary information sources for diagnosis and treatment. Most commercially available MR image–analysis software packages have some implementation of image registration, and such techniques have a thorough, well-documented grounding in the literature.[1-6]

Research publications about new registration methods for MR images of the brain nearly always include quantitative assessments of their performance, while commercial registration solutions are often released without disclosing the performance metrics of the vendor. Furthermore, due to the proprietary nature of these commercial algorithms, the explicit transformations are often not disclosed; thus, there are relatively few publicly available figures of

Received September 1, 2016; accepted after revision December 12.

From the Department of Bioengineering (J.S.L.), Rice University, Houston, Texas; Departments of Imaging Physics (J.S.L., D.T.F., A.C., J.D.H.), Neurosurgery (S.S.P., J.S.W.), Biostatistics (V.B.), Diagnostic Radiology (D.S.), and Cancer Systems Imaging (D.S.), University of Texas M.D. Anderson Cancer Center, Houston, Texas; and Molecular Imaging and Computed Tomography Research (A.C.), GE Healthcare, Milwaukee, Wisconsin.

This work was supported, in part, by the National Cancer Institute (Cancer Center Support Grant CA016672 and Training Grant 5T32CA119930) and by M.D. Anderson internal funding sources (Diagnostic Imaging Clinical Research Committee, Clinical Research Finance Molecular Evaluation and Biopsy Support, Internal Research Grant). J.S.L. acknowledges support from the Baylor College of Medicine Medical Scientist Training Program and the Cullen Trust for Higher Education Physician/Scientist Fellowship Program.

Please address correspondence to Dawid Schellingerhout, MD, Department of Diagnostic Radiology and Cancer Systems Imaging, University of Texas M.D. Anderson Cancer Center, 1881 East Rd, Unit 1482, Houston, TX 77054; e-mail: Dawid.schellingerhout@mdanderson.org

Indicates open access to non-subscribers at www.ajnr.org
Indicates article with supplemental on-line tables.
Indicates article with supplemental on-line photos.
http://dx.doi.org/10.3174/ajnr.A5122

merit to assess the performance of these heavily used commercial solutions that are essential to clinical neuroimaging.

Performance assessments of these products from commercial vendors would be clinically useful, however, such information is seldom available. In a study that used a widely accepted, neurosurgical commercial package, Hoelper et al[7] placed 25 anatomic landmarks in T1 and T2 brain volumes to test the registration error for 39 patients, a rare example of a publicly available assessment for a commercial registration solution. They demonstrated that whole-brain volume registrations could have errors ranging from 0.7 to 2 mm, depending on the region of the brain, and they therefore recommended using a volume of interest to improve local registrations when a particular area was important.[7] Such knowledge of the behavior of a commercial product can improve its use in the clinic, but if commercial vendors do not use objective metrics to characterize thoroughly the performance of their products and then make these results available, rational choices and improvements cannot be made. This situation is to the ultimate detriment of the patient undergoing treatments that rely on these algorithms being highly accurate.

Within the academic research world, various prior methods have been used to assess the performance of registration algorithms. External, invasive skull-implanted markers have been used as fiducial landmarks to assess CT-MR imaging and PET-MR imaging registrations,[4] the 8 corner voxels of a box around the head have been used to assess MR-MR brain registrations,[8] and 256 anatomic landmarks throughout the brain have been used to assess intersubject MR-MR registrations.[9] An on-line data base of MR imaging and sonography brain volumes also contains 19–40 landmarks per patient to assess registration accuracy.[10]

In addition to fiducial landmarks, other quantitative and semi-quantitative methodologies for assessment have been used. Examples include tissue edge distances as measured by the Hausdorff distance,[11] comparing the resulting transformations with the criterion standard reference transformations,[12] using the amount of tissue overlap for equivalent regions,[6,13] using image-similarity measures calculated between images,[14] and using visual assessments by human observers.[15] Extensive neuroimaging algorithm comparison studies have shown that registration performance is minimally affected by the many variations of labeling protocols and overlap measures.[6]

In light of these examples, there is a real need for simple, objective metrics to serve as figures of merit for clinically used registration algorithms from academic and commercial vendors. The aim of this project was therefore to demonstrate the feasibility of a performance-testing methodology for modern registration algorithms by using fiducial landmark sites in routinely used clinical images. This method was then used to assess the performance of both commercial and open-source registration algorithms as applied to a set of intrasubject, multisequence, MR images of the brain. Internal, anatomic landmark-based fiducials served as the criterion standard against which to measure performance. By calculating several objective metrics of performance from the results of these registrations on clinically acquired data, we show how various methods of registration can be meaningfully compared by end users. We use a limited set of algorithms in demonstration, but any registration algorithm could be substituted and similarly assessed (the authors could be contacted to arrange this).

MATERIALS AND METHODS

This study was a retrospective analysis of data acquired as part of a Health Insurance Portability and Accountability Act–compliant, institutional review board–approved clinical protocol that required signed consent from study participants.

Images

Patients were consecutively recruited on the basis of specific criteria for inclusion (18 years of age or older, candidate for cerebral tumor resection with suspected or biopsy-proved primary brain tumor) and exclusion (prior brain tumor treatment, including surgical resection, radiation therapy, or chemotherapy). From February 2013 to October 2015, 20 patients (mean age, 45.3 years; range, 21–75 years) were imaged for surgical-planning purposes on Signa HDxt 3T or Discovery MR750 3T clinical scanners (GE Healthcare, Milwaukee, Wisconsin). This cohort included 11 women (mean, 40.7 years; range, 21–75 years) and 9 men (mean, 50.9 years; range, 28–67 years). The imaging protocol (On-line Table 1) included a high-resolution T2-weighted scan (voxel size, $0.5469 \times 0.5469 \times 2$ mm), a FLAIR scan (voxel size, $0.5 \times 0.5 \times 1$ mm), a susceptibility-weighted angiography (SWAN) scan (voxel size, $0.3906 \times 0.3906 \times 1$ mm), and a T1 postcontrast (T1C) scan (voxel size, $0.4688 \times 0.4688 \times 3.5$ mm) obtained after injecting 0.1 mmol/kg of either gadopentetate dimeglumine or gadobutrol (Magnevist; Bayer HealthCare Pharmaceuticals, Wayne, New Jersey; or Gadavist; Bayer Schering Pharma, Berlin, Germany, respectively) at 5 mL/s, followed by 30 mL of saline at 5 mL/s. Because 2 separate contrast doses were needed for the scanning session, the total dosage was 20 mL of Magnevist or Gadavist and 60 mL saline. DICOM image files were converted into the NIfTI file format (https://nifti.nimh.nih.gov/nifti-1) with functions from the Insight ToolKit (https://lhncbc.nlm.nih.gov/project/insight-toolkit).[16] Images were skull-stripped by using the Brain Extraction Tool (http://fsl.fmrib.ox.ac.uk/fsl/fslwiki/BET)[17] from the FMRIB Software Library (fsl.fmrib.ox.ac.uk), followed by manual refinement of the mask with Amira3D (Version 6.0; FEI, Hillsboro, Oregon) and application of the mask by using Matlab (MathWorks, Natick, Massachusetts). These clinically acquired imaging sequences, with nonisotropic voxel sizes, different section thicknesses, and different contrast mechanisms, were intentionally used for this study to emphasize its real-world applicability, because such images would be registered to each other in the clinic for various purposes.

Landmarks

Fifteen landmarks (LMs) were manually specified per patient sequence, meaning that 60 independent landmark sites were specified across the 4 imaging sequences. For the entire set of 20 patients, 1200 LM points were planned. Landmarks were placed at anatomically distinct locations across the entire brain volume (Fig 1, On-line Fig 1, and On-line Table 2) by using the Amira3D software. All fiducial sites were reviewed by multiple observers (J.S.L., D.S.) with expertise in neuroanatomy, including a neuroradiologist with 15 years' clinical experience (D.S.).

Landmark fiducial sites were chosen for their unambiguous appearance across imaging sequences (ie, vessel intersections, bifurcations, inflection points, and unique geometries), so as to

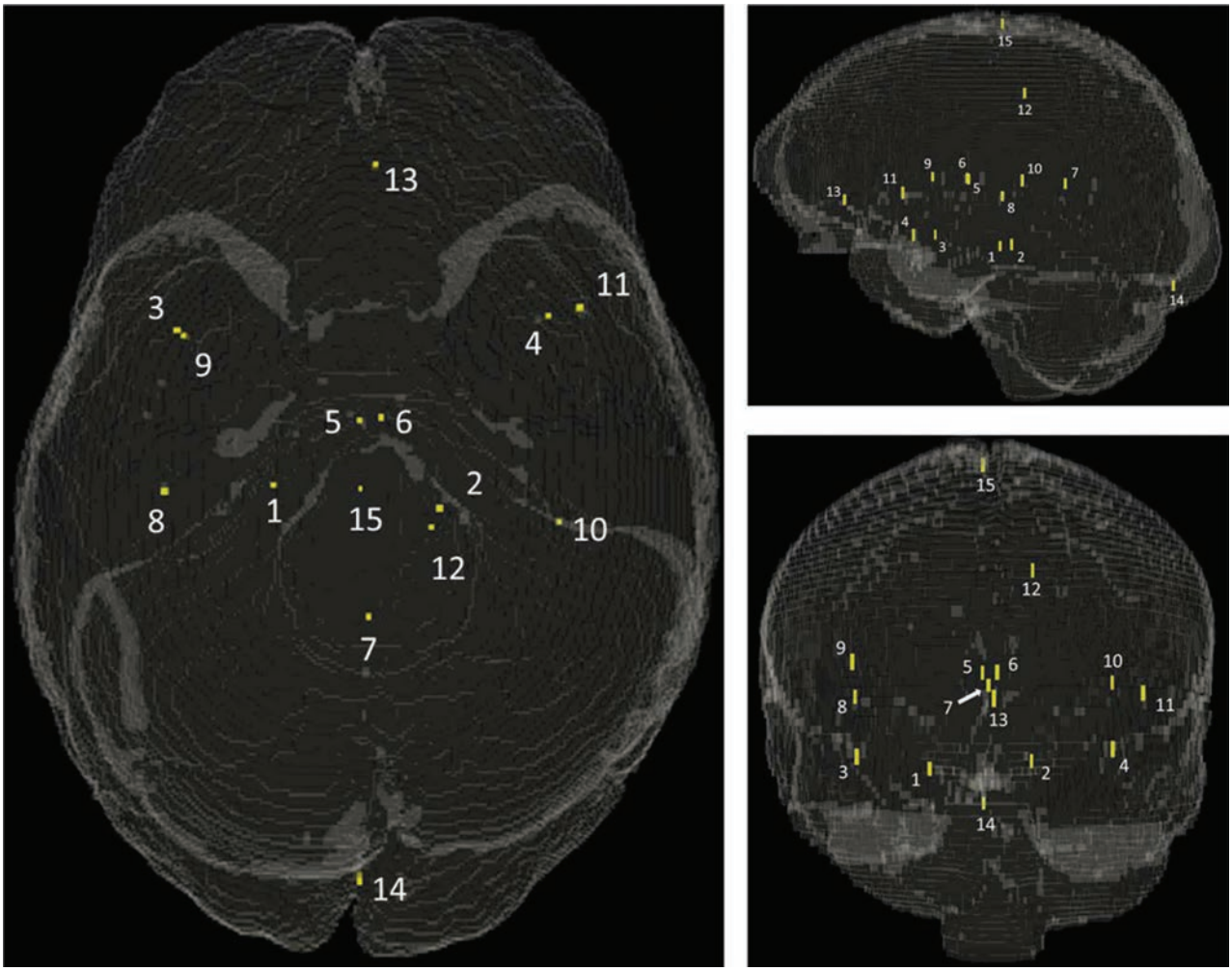

FIG 1. Fiducial landmark locations in a synthetic 3D head volume model. Refer to On-line Table 2 for descriptions and coordinates.

ensure correspondence between homologous sites (On-line Fig 2). The general locations of landmarks were similar across patients, but the exact placements differed from patient to patient because of natural anatomic variations. Landmarks were intended to be spatially distributed within the brain, to capture registration error in many different regions. However, most suitable fiducial sites ended up being in the midaxial area of the brain, due to plentiful, easily identifiable anatomy being located there. Key sites were therefore chosen in extreme anterior, posterior, inferior, and superior locations to round out the placement of landmarks.

The standardized landmark coordinates shown in On-line Table 2 were obtained by registering the T2 volume to the International Consortium for Brain Mapping 152 Nonlinear Symmetric 2009b template,[18] thereby generating coordinates in the right-anterior-superior convention with the anterior commissure as the origin. This template volume was only used for determining these coordinates and was not part of the actual registration experiments.

Registrations

Each patient's T2 image volume served as the fixed image, and the FLAIR, SWAN, and T1C images served as the moving image for registration procedures.

Landmark registration was performed as a criterion standard reference. Rigid (6 *df*) and affine (12 *df*) transformations with the fiducial LM sites as input were performed by using convert3D (c3d).[19] These registrations disregarded all imaging content and focused only on minimizing the gap between corresponding landmarks, thereby creating a lower bound for target-to-registration error (TRE), defined as the Euclidean distance between 2 points in space.

The Volume Viewer software package (Version 11.3 Ext. 14; GE Healthcare) available on the Advantage Workstation Server (Version 2; GE Healthcare) was used for its Integrated Registration module with its specialized Neuro Registration mode. Registrations for GE were performed on a stand-alone server dedicated to this software.

The open-source Advanced Normalization Tools software package (ANTs; http://stnava.github.io/ANTs/[20]) was used to perform multiple registrations for each of the FLAIR-T2, SWAN-T2, and T1C-T2 image pairs, by using both different similarity measures (cross-correlation [CC] versus mutual information [MI]) and different *df*s for image movement (rigid versus affine). All registrations were performed on a Linux workstation (Xeon X5675 CPU @ 3.07GHz with 24 cores, 96 GB RAM; Intel, Santa Clara, California).

Analysis

Euclidean TRE values between fixed and moving images were calculated at baseline (preregistration) and for 7 different registration experiments (Table 1). To create independent TRE measurements for analysis, we averaged together multiple TRE values within each patient by sequence. For location-dependent analyses, TRE values were averaged across patients on the basis of coordinate locations.

Baseline TRE values were analyzed on the basis of the time of image acquisition and location in space. Postregistration TRE values were also analyzed, with Shapiro-Wilk test results used to determine the appropriate ANOVA test for comparing means of groups for main effects (On-line Fig 3). When we compared TRE values of 8 different groups for a single sequence, if all groups passed the Shapiro-Wilk test, the repeated measures ANOVA was used, with post hoc testing with the Tukey test to adjust P values for multiple comparisons ($\alpha = .05$). Otherwise, the Friedman nonparametric ANOVA was used, with post hoc testing by using the Dunn test ($\alpha = .05$). Pair-wise comparisons were also performed between the best-performing algorithm for each sequence and its runners-up (On-line Fig 4), with the paired t test used if results for both groups passed the Shapiro-Wilk test. Otherwise, the Wilcoxon signed-rank test was used. All statistical testing was performed by GraphPad Prism software (Version 6.07, 2015; GraphPad Software, San Diego, California) with $P < .05$ denoting significance.

The Euclidean effectiveness ratio (EER, On-line Fig 5) represents the fraction of Euclidean error remaining after registration, defined as 1 TRE gap (between the results of an algorithm of interest and the affine LM algorithm [LM12]) divided by another TRE gap (between baseline and LM12 results). The EER scale will always be between 0 and 1 with values at the boundary interpreted accordingly. The statistical effectiveness ratio (SER, On-line Fig 5) is similar to the EER, but accounts for statistical noise. It is defined as the ratio of 1 Cohen d (between an algorithm of interest [AOI] and the LM12 results) divided by another Cohen d (between baseline and LM12 results). The Cohen effect size d was calculated between algorithms by using

$$d_{A-B} = \frac{\Delta TRE_{\overline{A}-\overline{B}}}{s_{A-B}}$$

where the 2 algorithms being compared are A and B, the pooled SD, $s_{A-B} = \sqrt{\frac{(n_A-1)s_A^2 + (n_B-1)s_B^2}{n_A+n_B-2}}$, s_A is the SD of group A, and n_A is the number of samples in group A.

RESULTS

Images

Table 2 contains demographic information about patients from this clinical trial. The "high movers" and "low movers" subgroups are defined in "Baseline TRE as a Function of Time."

Landmarks

Of the 1200 fiducial LM sites planned, 1175 were realized. Because SWAN volumes in 17 of 20 patients had limited superior/inferior head coverage, LM sites 14 and/or 15 had to be omitted, depending on the patient, for a deficit of 25 SWAN landmark sites ($n = 10$ omitted for LM site 14, and $n = 15$ omitted for LM site 15). The resulting 1175 points translated to 875 LM pairs (300 for FLAIR-T2, 275 for SWAN-T2, and 300 for T1C-T2). In 3 of 20 patients, the SWAN imaging volume was located too superiorly to include the normal locations of LM sites 1–4 (the next most inferior landmarks, after LM site 14). In these cases, alternative fiducial sites were chosen, superior enough to still allow a valid site pairing with the T2 volume.

Registrations and Analysis

Baseline TRE as a Function of Time. Baseline TRE increased as a function of time in the magnet for the entire population (Fig 2, *left*), with a best-fit line significantly different from the zero slope ($F = 17.80$, $P < .0001$, $R^2 = 0.2348$). Using z scores based on T1C TRE values, we dichotomized patients into high movers ($z > 0.35$) and low movers ($z < 0.35$). The line for the high movers was significantly different from the zero slope (Fig 2, *right*; $F = 33.64$, $P < .0001$), but the line for the low movers was not ($F = 0.004419$, $P = .9474$).

Baseline TRE as a Function of Location. We analyzed the high movers group, and found that their predominant motion appeared to be rotatory in nature, around an axis passing through the dens (On-line Fig 6). TRE values were therefore plotted against their distance from a point on this fulcrum axis (Fig 3). For the T1C sequence (Fig 3, *lower row*), the baseline TRE increased with the distance from this point, with a

Table 1: Registration experiment inputs, parameters, and outputs

Registration Experiment	Inputs	Software	Similarity Measure	*df*	Outputs
Pre-registration	NA	NA	NA	NA	TRE, EER, SER
GE	Images	GE	Proprietary	Proprietary	TRE, EER, SER
Rigid CC	Images	ANTs	CC	6	TRE, EER, SER
Rigid MI	Images	ANTs	MI	6	TRE, EER, SER
Affine CC	Images	ANTs	CC	12	TRE, EER, SER
Affine MI	Images	ANTs	MI	12	TRE, EER, SER
Rigid LM	LM	c3d	LM	6	TRE, EER, SER
Affine LM	LM	c3d	LM	12	TRE, EER, SER

Note:—NA indicates not applicable; c3d, Convert3D; GE, GE Volume Viewer.

Table 2: Age, race, and frontal lobe tumor involvement of patient groups

	All (n = 20)	Female (n = 11)	Male (n = 9)	High Movers (n = 9)	Low Movers (n = 11)
Age (mean)	45.3 ± 16.4	40.7 ± 17.7	50.9 ± 14.3	38.1 ± 15.3	51.2 ± 15.5
Age range (yr)	21–75	21–75	28–67	21–66	29–75
Race (White/Black/Hispanic/Asian) (No.)	15/2/2/1	8/2/1/0	7/0/1/1	6/1/1/1	9/1/1/0
No. of patients with tumor with frontal lobe involvement	11 (55%)	7 (64%)	4 (44%)	8 (89%)	3 (27%)

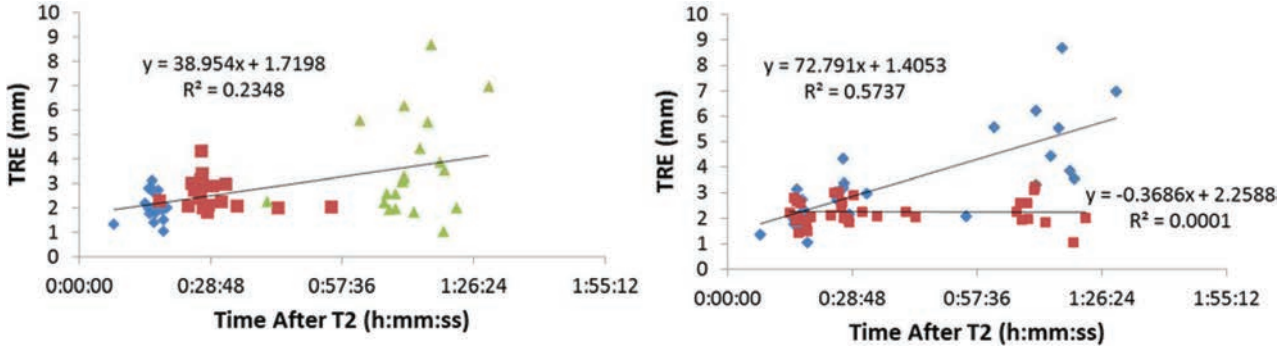

FIG 2. Plot of baseline TRE versus time, sorted by image sequence (*left*, FLAIR: *blue diamonds*, SWAN: *red squares*, T1C: *green triangles*) and by patient movement (*right*, high movers: *blue diamonds*; low movers: *red squares*) ($n = 15$ for FLAIR and T1C, $n = 12$–15 for SWAN per data point).

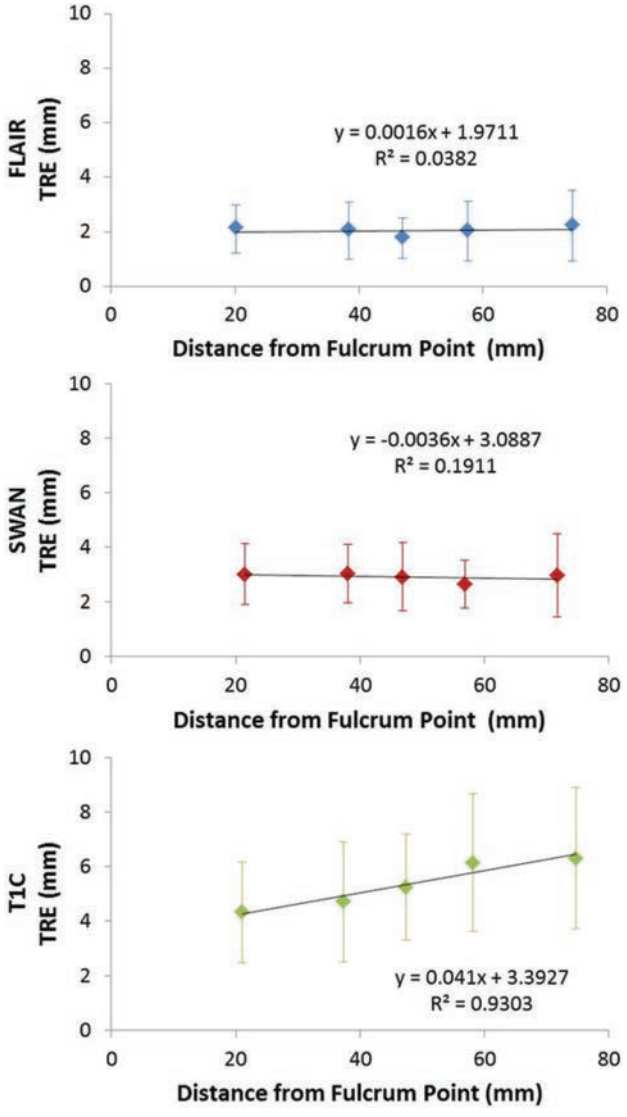

FIG 3. Plots of TRE versus distance from the fulcrum point for FLAIR (*upper row*), SWAN (*middle row*), and T1C (*lower row*). All TRE values shown are from the high movers subpopulation ($n = 27$ for FLAIR and T1C; $n = 25$–26 for SWAN per data point).

best-fit line significantly different from the zero slope ($F = 42.12$, $P = .0074$). However, the best-fit lines for FLAIR ($F = 8.311$, $P = .0634$) and SWAN ($F = 1.331$, $P = .3322$) were not significantly different from the zero slope, suggesting a threshold effect for movement as time increases.

TRE and Euclidean Effectiveness Ratio after Registration. For FLAIR TRE and EER values (Fig 4 *upper row* and On-line Table 3), the rankings were the following: rigid MI < rigid CC < affine CC < GE < affine MI. Pair-wise TRE comparisons between the best algorithm and its runners-up did not reveal significant differences for the rigid MI–rigid CC pair ($P = .0552$ paired t, effect size $d = 0.1492$) or the rigid MI–affine CC pair ($P = .0532$ paired t, effect size $d = 0.3620$). Significant differences did exist for the rigid MI–GE pair ($P = .0323$ paired t, effect size $d = 0.4627$).

For SWAN TRE and EER values (Fig 4 *middle row* and On-line Table 3), the rankings were the following: affine MI < GE < rigid MI < affine CC < rigid CC. Pair-wise TRE comparisons between the best algorithm and its runners-up revealed significant differences for the affine MI–GE pair ($P = .0136$, Wilcoxon signed-rank test, effect size $d = 0.4969$) and the affine MI–rigid MI pair ($P = .0121$, Wilcoxon signed-rank test, effect size $d = 0.6454$).

For T1C, TRE, and EER values (Fig 4 *lower row* and On-line Table 3), the rankings were: GE < affine MI < affine CC < rigid MI < rigid CC. Pair-wise TRE comparisons between the best algorithm and its runners-up did not reveal significant differences for the GE–affine MI pair ($P = .6640$ paired t, effect size $d = 0.0669$), but they did reveal significant differences for the GE–affine CC pair ($P = .0042$ Wilcoxon signed-rank test, effect size $d = 0.7720$).

The SER rankings were the same as rankings based on TRE and EER for the FLAIR and SWAN sequences. For the T1C sequence, the SER ranking was different, selecting rigid CC as the top algorithm (On-line Table 4).

TRE Values before Registration: FLAIR versus SWAN versus T1C. Before registration, the mean TRE rankings were as follows: FLAIR < SWAN < T1C. Differences among these 3 groups were statistically significant (Friedman ANOVA, $F = 9.300$, $P = .0096$), and post hoc testing showed significant differences for the FLAIR-T1C pair, but not for the FLAIR-SWAN or SWAN-T1C pairs ($P = .0133$, $P = .0531$, and $P > .9999$, respectively; Dunn test).

TRE Values after the Affine LM Registration: FLAIR versus SWAN versus T1C. Affine LM results, representing the criterion standard minimum possible TRE, consistently had the smallest TRE values

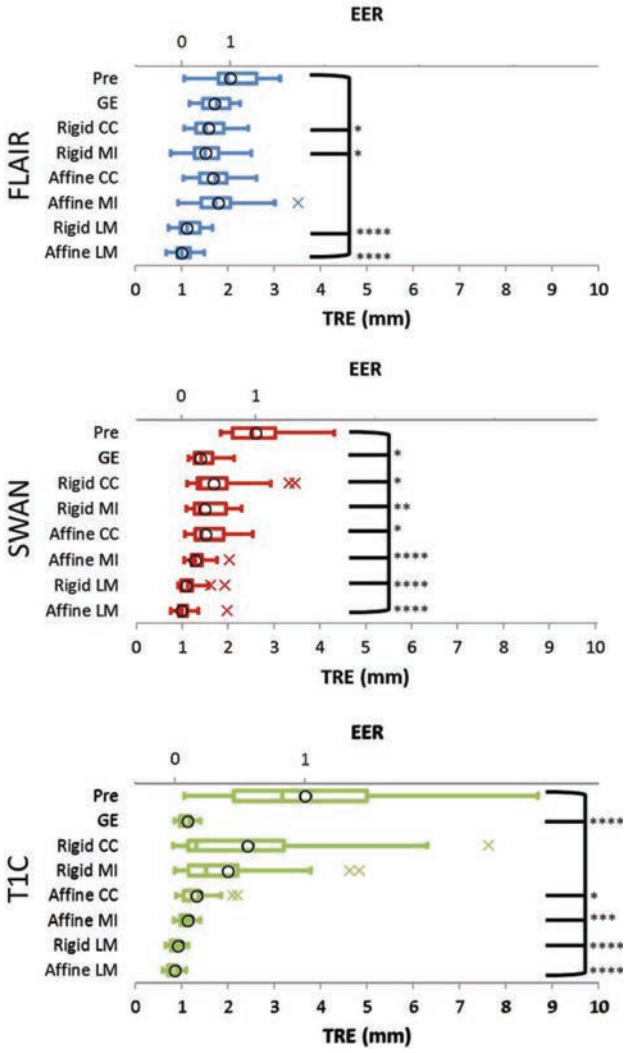

FIG 4. TRE and EER values (*boxplots* and *circles*, respectively; $n = 20$) for FLAIR (*upper row*), SWAN (*middle row*), and T1C (*lower row*). TRE differences among the 8 groups are statistically significant for FLAIR (repeated measures ANOVA, $F = 19.22$, $P < .0001$), SWAN (Friedman ANOVA, $F = 103.5$, $P < .0001$), and T1C (Friedman ANOVA, $F = 108.5$, $P < .0001$). *Asterisks* indicate statistically significant TRE differences from baseline. *Asterisk* indicates $P \leq .05$; *2 asterisks*, $P \leq .01$; *3 asterisks*, $P \leq .001$; *4 asterisks*, $P \leq .0001$; FLAIR: Dunnett test; SWAN, T1C: Dunn test).

for each sequence, with rankings as follows: T1C < FLAIR < SWAN. Differences among the 3 sequences were significant (Friedman ANOVA, $F = 12.40$, $P = .0020$), with post hoc testing showing significant differences for the SWAN-T1C pair, but not the FLAIR-SWAN or FLAIR-T1C pairs ($P = .0015$, $P = .6177$, and $P = .0806$, respectively; Dunn test).

TRE Differences by Landmark: Preregistration and Affine LM Registration. Baseline TRE differences between landmarks (On-line Fig 7, *left*) were significant (Friedman ANOVA, $F = 30.23$, $P = .0071$), but post hoc testing with the Dunn test revealed significant differences only for the LM site 5 to LM site 13 pair ($P = .0191$), suggesting mainly random, not systematic, differences among landmark locations. Differences among landmarks after the affine LM registration (On-line Fig 7, *right*) were not significant (Friedman ANOVA, $F = 23.13$, $P = .0581$).

DISCUSSION

The main findings from this study were the following:

1) The FLAIR, SWAN, and T1C image volumes, on average, all had lower TRE values after registrations that corrected for spatial errors due to patient motion. For open-source methods, MI outperformed CC registrations and affine usually outperformed rigid registrations.
2) Spatial error values after registration were comparable with or better than values found in the literature.
3) The unregistered spatial error increased as a function of time in the magnet, and a subpopulation of patients, most with frontal lobe tumor involvement, was responsible for most of the time-dependence of the spatial error.
4) Better correction was possible between sequences with similar planes of acquisition. If images are acquired in different planes, out-of-plane distortion corrections should be applied.
5) The best algorithms with the EER metric were the same as the best algorithms by TRE values.

The FLAIR, SWAN, and T1C image volumes, on average, all had lower TRE values after registrations that corrected for spatial errors due to patient motion, a finding that is compatible with conventional wisdom regarding spatially aligning images before analysis.[21,22] For open-source methods, MI generally outperformed CC registrations, given the same *df* and image sequence; this outcome agrees with existing literature.[23] Affine usually outperformed rigid transformations, given the same similarity measure and image sequence; this finding makes sense, given that the latter is a special case of the former.[22]

The smallest TRE values for FLAIR (1.55 mm), SWAN (1.34 mm), and T1C (1.06 mm) were comparable with error values from a commercial vendor that performed rigid, whole-volume registrations on brain MR images (1.6 mm[7]). They were also comparable with or better than average nonlinear registration errors for other body parts and imaging modalities, including CT-CT lung (1.0 mm,[24] 2.05 mm[25]), CT-CT liver (1.8 mm[24]), MR-CT liver (3.9 mm[24]), and MR-MR prostate (2.3 mm[24]).

Spatial error increased as a function of time in the magnet; this finding supports previous observations about image misalignments increasing with time during a scanning session[26] and which likely occurs due to patient restlessness expressed by repositioning of the head. The high movers subpopulation, responsible for most of the time-dependent error, was younger than the overall cohort (38.1 versus 45.3 years), and 8 of 9 patients had tumors with involvement in the frontal lobe, an area of the brain associated with motor impulse control.[27] Analysis of error versus location suggests that most head movement during the scanning session occurs as rotation about a fulcrum that is in line with the dens.

Better spatial corrections were possible between sequences with similar planes of acquisition, because differences in native orientations lead to differences in residual, out-of-plane distortions. Specifically, FLAIR had left/right distortions (with the brain pinched along the left/right axis, especially near the superior/inferior edges of the volume), while T2, SWAN, and T1C did not have such distortions (because reverse-pin-cushion-shaped corrections had restored the brain to its proper shape and size, On-line Fig 8). As a result, the smallest TRE value for FLAIR was larger

than the smallest TRE values for SWAN and T1C. Rigid also outperformed affine registrations for the FLAIR sequence, because affine transformations attempted to recreate the nonlinear effects of distortion correction and unintentionally worsened FLAIR-T2 matching. Out-of-plane distortion corrections should therefore be applied by MR imaging scanners, whenever available, to counter this problem.

The best algorithms by EER values (FLAIR, rigid MI; SWAN, affine MI; T1C, GE) were the same as the best algorithms by TRE values, which makes sense given that the EER is a normalization of TRE that preserves the relative rankings of different algorithms while facilitating comparisons across different sequences. The SER, however, gave different rankings for T1C and is a less intuitive metric to interpret but attractive from a statistical perspective due to its incorporation of noise.

Both single-voxel landmarks and labeled regions have been used to assess registration accuracy for various purposes, with the best assessment method ultimately dictated by the application area and, to some degree, the resources available for the time-intensive, manual label, and/or landmark dataset curation process to create the criterion standard control. We believe that single-voxel landmarks were an appropriate choice for our study, relative to labeled regions and their derived metrics. First, volume and surface overlap metrics, as used in other literature, are well-known to be biased by the total volume/surface and also ignore misregistrations within the labeled regions themselves because no landmarks exist inside those areas to assess correspondence.[6] Also, using volume size as a metric is reasonable in the context of nonlinear registration algorithms that can locally deform the image volume and change the size of labeled anatomic regions, but our affine registrations create minimal regional size changes, making volume size an inappropriate metric and further motivating the use of pinpoint, single-voxel landmarks in a manner that extends prior work.[7] Additionally, surface distance, which describes registration success by using the average distance between points on one surface to the closest points on another surface,[6] disregards whether homologous points are being compared and highlights a possible lack of spatial precision.

This article targets the radiologic clinic, where patient care involves the affine registration of a single patient's images across modalities and/or techniques to assess pathology. Because of the guaranteed anatomic correspondence across these images, single-voxel landmarks can be successfully used to assess registration performance. Additionally, spatially precise landmarks are preferred over a labeled region overlap measure in this context because the use of a single person's images guarantees that a homologous point can be found. Moreover, if wisely distributed throughout the brain volume, these single-voxel landmarks can give a sense of the regional registration error not obtainable by using labeled regions. However, if the registration goal is to spatially align the images from different patients (as is frequently the case in the grouping of functional MR imaging data), it makes sense to use volume overlap as the metric of success, particularly given anatomic variations among patients.

Multiple limitations existed for this study. The placement of fiducial landmark sites was subject to user error, voxel size limitations, and image deformations caused by patient motion. A neuroanatomic expert therefore evaluated all landmark sites, followed by adjustments, if needed. Fiducial sites were also limited to those locations that could be reliably identified across images with widely different contrast mechanisms, with most sites ending up in the central region of the brain. To help compensate for this limitation, we sought a well-rounded distribution of landmarks in the anatomy that was usable and also placed landmarks at extreme anterior, posterior, superior, and inferior locations. Measurement precision was limited by using voxels (discretized representations of anatomy) to measure spatial error on a continuous scale. All voxel sizes and error values as originally calculated are therefore reported, to allow readers to form their own judgments. Our patient number was low and focused on a treatment-naïve patient population with gliomas. Further studies are needed to investigate biases in the registration accuracy that may be influenced by the major disease phenotypes seen in a general patient population, including brain metastases, stroke, neurodegeneration, postsurgery, and postradiation.

CONCLUSIONS

In summary, we developed and evaluated a methodology to quantify the registration accuracy of registration algorithms. The method could be used to test any algorithm, providing easy-to-interpret figures of merit that allowed meaningful comparisons with other algorithms in clinical practice. We advocate the publication of figures of merit such as these for all clinical registration algorithms, to better inform the choices of clinical users and allow the future development of improved algorithms for clinical use.

Disclosures: Adam Chandler—*UNRELATED*: *Employment:* GE Healthcare, *Comments*: I am a salaried GE Healthcare employee. Veera Baladandayuthapani—*RELATED*: *Grant*: University of Texas M.D. Anderson Cancer Center Support Grant (CCSG) (P30 CA016672).* *Money paid to the institution.

REFERENCES

1. Maes F, Collignon A, Vandermeulen D, et al. **Multimodality image registration by maximization of mutual information.** *IEEE Trans Med Imaging* 1997;16:187–98 CrossRef Medline
2. Studholme C, Hill DL, Hawkes DJ. **An overlap invariant entropy measure of 3D medical image alignment.** *Pattern Recognition* 1999; 32:71–86 CrossRef
3. Wells WM 3rd, Viola P, Atsumi H, et al. **Multi-modal volume registration by maximization of mutual information.** *Med Image Anal* 1996;1:35–51 CrossRef Medline
4. West J, Fitzpatrick JM, Wang MY, et al. **Comparison and evaluation of retrospective intermodality brain image registration techniques.** *J Comput Assist Tomogr* 1997;21:554–66 CrossRef Medline
5. Woods RP, Grafton ST, Holmes CJ, et al. **Automated image registration, I: general methods and intrasubject, intramodality validation.** *J Comput Assist Tomogr* 1998;22:139–52 CrossRef Medline
6. Klein A, Andersson J, Ardekani BA, et al. **Evaluation of 14 nonlinear deformation algorithms applied to human brain MRI registration.** *Neuroimage* 2009;46:786–802 CrossRef Medline
7. Hoelper BM, Soldner F, Lachner R, et al. **Enhancing accuracy of magnetic resonance image fusion by defining a volume of interest.** *Neuroradiology* 2003;45:804–09 CrossRef Medline
8. Nyúl LG, Udupa JK, Saha PK. **Incorporating a measure of local scale in voxel-based 3-D image registration.** *IEEE Trans Med Imaging* 2003;22:228–37 CrossRef Medline
9. Grachev ID, Berdichevsky D, Rauch SL, et al. **A method for assessing the accuracy of intersubject registration of the human brain using anatomic landmarks.** *Neuroimage* 1999;9:250–68 Medline

10. Mercier L, Del Maestro RF, Petrecca K, et al. **Online database of clinical MR and ultrasound images of brain tumors.** *Med Phys* 2012; 39:3253–61 CrossRef Medline
11. Archip N, Clatz O, Whalen S, et al. **Non-rigid alignment of pre-operative MRI, fMRI, and DT-MRI with intra-operative MRI for enhanced visualization and navigation in image-guided neurosurgery.** *Neuroimage* 2007;35:609–24 CrossRef Medline
12. Skerl D, Likar B, Pernus F. **A protocol for evaluation of similarity measures for rigid registration.** *IEEE Trans Med Imaging* 2006;25: 779–91 CrossRef Medline
13. So RW, Tang TW, Chung AC. **Non-rigid image registration of brain magnetic resonance images using graph-cuts.** *Pattern Recognition* 2011;44:2450–67 CrossRef
14. Siddiqui AM, Masood A, Saleem M. **A locally constrained radial basis function for registration and warping of images.** *Pattern Recognition Letters* 2009;30:377–90 CrossRef
15. Saad ZS, Glen DR, Chen G, et al. **A new method for improving functional-to-structural MRI alignment using local Pearson correlation.** *Neuroimage* 2009;44:839–48 CrossRef Medline
16. McCormick M, Liu X, Jomier J, et al. **ITK: enabling reproducible research and open science.** *Front Neuroinform* 2014;8:13 CrossRef Medline
17. Smith SM. **Fast robust automated brain extraction.** *Hum Brain Mapp* 2002;17:143–55 CrossRef Medline
18. Fonov V, Evans AC, Botteron K, et al; Brain Development Cooperative Group. **Unbiased average age-appropriate atlases for pediatric studies.** *Neuroimage* 2011;54:313–27 CrossRef Medline
19. Yushkevich PA, Piven J, Hazlett HC, et al. **User-guided 3D active contour segmentation of anatomical structures: significantly improved efficiency and reliability.** *Neuroimage* 2006;31:1116–28 CrossRef Medline
20. Avants BB, Tustison NJ, Stauffer M, et al. **The Insight ToolKit image registration framework.** *Front Neuroinform* 2014;8:44 CrossRef Medline
21. Hill DL, Batchelor PG, Holden M, et al. **Medical image registration.** *Phys Med Biol* 2001;46:R1–45 CrossRef Medline
22. Maintz JB, Viergever MA. **A survey of medical image registration.** *Med Image Anal* 1998;2:1–36 Medline
23. Avants BB, Tustison NJ, Song G, et al. **A reproducible evaluation of ANTs similarity metric performance in brain image registration.** *Neuroimage* 2011;54:2033–44 CrossRef Medline
24. Brock KK; Deformable Registration Accuracy Consortium. **Results of a multi-institution deformable registration accuracy study (MIDRAS).** *Int J Radiat Oncol Biol Phys* 2010;76:583–96 CrossRef Medline
25. Castillo R, Castillo E, Guerra R, et al. **A framework for evaluation of deformable image registration spatial accuracy using large landmark point sets.** *Phys Med Biol* 2009;54:1849–70 CrossRef Medline
26. Li G, Xie H, Ning H, et al. **Correction of motion-induced misalignment in co-registered PET/CT and MRI (T1/T2/FLAIR) head images for stereotactic radiosurgery.** *J Appl Clin Med Phys* 2010;12: 58–67 CrossRef Medline
27. Bechara A, Van Der Linden M. **Decision-making and impulse control after frontal lobe injuries.** *Curr Opin Neurol* 2005;18:734–39 CrossRef Medline

Quantitative Assessment of Variation in CT Parameters on Texture Features: Pilot Study Using a Nonanatomic Phantom

K. Buch, B. Li, M.M. Qureshi, H. Kuno, S.W. Anderson, and O. Sakai

ABSTRACT

SUMMARY: Our aim was to evaluate changes in texture features based on variations in CT parameters on a phantom. Scans were performed with varying milliampere, kilovolt, section thickness, pitch, and acquisition mode. Forty-two texture features were extracted by using an in-house-developed Matlab program. Two-tailed *t* tests and false-detection analyses were performed with significant differences in texture features based on detector array configurations (*Q* values = 0.001–0.006), section thickness (*Q* values = 0.0002–0.001), and acquisition mode (*Q* values = 0.003–0.006). Variations in milliampere and kilovolt had no significant effect.

ABBREVIATIONS: GLCM = gray-level co-occurrence matrix; GLGM = gray-level gradient matrix; GLRL = gray-level run length; MDCT = multidetector row CT; RP = run percentage

Image texture describes a complex visual pattern within an image that consists of simpler subpatterns with characteristic features that may be evaluated through quantitative analysis known as a texture analysis.[1] Texture analysis is a set of quantitative, postprocessing, image-analysis algorithms that are being increasingly used within the field of radiology.[1-9] The texture analysis may be applied to any imaging technique including CT, MR imaging, and sonography, among others. The texture analysis is composed of a series of mathematic algorithms that extract texture descriptors from an image, thus allowing the mathematic detection of subtle changes in pixel intensity throughout an image.[1]

Within radiology, texture analysis has been used to detect subtle pathologic changes in an image that are not easily quantifiable by the human eye in a variety of areas of the body such as the liver, brain, and cartilage.[2-8] One of the most prevalent areas for use of texture analysis within radiology is for tumor evaluation and characterization.[8-18] Despite a growing number of publications on the use of texture analysis for tumor imaging, direct correlations between texture analysis features and histopathologic analysis are still being investigated.[18,19]

Recently, the upsurge in genomic discoveries and advanced imaging technologies on publicly available data bases, such as The Cancer Imaging Archive (http://www.cancerimagingarchive.net/) and The Cancer Genomic Atlas (https://cancergenome.nih.gov/), large, multi-institutional, quantitative genomic and imaging-based studies, are becoming areas of increased interest.[20,21] Particularly, within the field of tumor imaging, texture analysis is becoming increasingly used[8-18]; however, the lack of standardized scanning protocols poses a significant limitation to the use of texture analysis in these instances.

The purpose of this study was to evaluate how changes in CT parameters (milliampere, kilovolt[peak], section thickness, pitch, and acquisition mode) could affect variations in the texture analysis features irrespective of the internal architecture of the item being scanned.

MATERIALS AND METHODS

This study used a phantom for all image acquisitions, precluding the requirement for institutional review board approval.

Phantom Development

A nonanatomic phantom was constructed to investigate whether texture analysis features change with various CT parameters (milliampere, kilovolt[peak], section thickness, pitch, and acquisition mode). The phantom was constructed from a composition of cereal (Cheerios; General Mills, Minneapolis, Minnesota) and commercially available mayonnaise (Hellmann's; Unilever US, Englewood Cliffs, New Jersey). The content of the phantom was chosen on the basis of a regularly repeating geometric pattern composed of different internal densities, including air, fat, and grain (of

Received November 18, 2016; accepted after revision January 9, 2017.

From the Departments of Radiology (K.B., B.L., M.M.Q., H.K., S.W.A., O.S.), Radiation Oncology (M.M.Q., O.S.), and Otolaryngology–Head and Neck Surgery (O.S.), Boston Medical Center, Boston University School of Medicine, Boston, Massachusetts.

Please address correspondence to Osamu Sakai, MD, PhD, Department of Radiology, Boston Medical Center, Boston University School of Medicine, FGH Building, 3rd Floor, 820 Harrison Ave, Boston, MA 02118; e-mail: osamu.sakai@bmc.org

Indicates article with supplemental on-line appendix and tables.

http://dx.doi.org/10.3174/ajnr.A5139

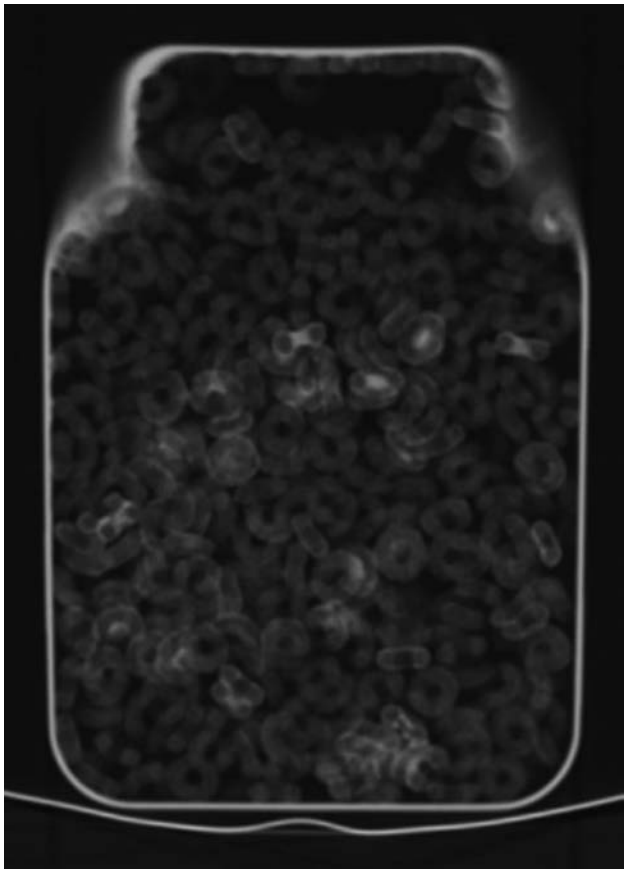

FIG 1. CT scan of the phantoms comprising Hellman's mayonnaise, Cheerios cereal, and air, housed in an acrylic container (15.88 × 23.50 × 31.75 cm).

slightly higher density). The phantom measured 15.88 × 23.50 × 31.75 cm (Fig 1).

CT Protocol

Noncontrast CT scans were obtained on the phantom on a 64–detector row CT scanner (Lightspeed VCT; GE Healthcare, Milwaukee, Wisconsin) and a 16–detector row CT scanner (LightSpeed, 16 section; GE Healthcare). In addition to scanning the phantom on different detector-row CT scanners, we also scanned the phantom with different CT parameters, including variations in the milliampere, kilovolt(peak), section thickness, and acquisition mode.

Each of the aforementioned CT scanning parameters was altered one at a time, while the remaining 5 texture features were held constant as shown in the Table.

The variations for the acquisition mode included an axial scan compared with a helical scan. Variations in milliampere ranged from 80 mA to 140 mA in increments of 20 mA. Similarly, variations in the kV ranged from 80 kV up to 140 kV in increments of 20 kV. Serial scans were obtained with variations in the thickness of the reconstructed axial datasets of 0.625, 1.25, 2.5, and 5 mm. Changes in helical pitch were also investigated by using pitches of 0.51, 0.98, 1.37, and 1.75.

Image Segmentation and Texture Analysis

The internal content of the phantom was manually contoured on an equal number of sections by a fourth-year diagnostic radiology resident on each CT scan. Segmentation was performed by using a dedicated workstation (Advantage Workstation; GE Healthcare) with a semiautomated graphical user interface.

Each contour was then imported into in-house-developed Matlab (MathWorks, Natick, Massachusetts) texture analysis software. The texture analysis software was developed by the coauthor (B.L.), and the use of this texture analysis program has been previously reported in the literature.[7,8] In total, 42 texture features, including 13 histogram features, 5 gray-level co-occurrence matrix (GLCM) features, 11 gray-level run-length (GLRL) features, 4 gray-level gradient matrix (GLGM) features, and 9 Law's features, were computed and averaged over the images per dataset.

The use of this in-house-developed Matlab program and the specific details of the texture analysis features calculated in this program have been previously published.[8] For additional details on the mathematic equations proposed by Haralick et al[1] and the GLRL matrix defined by Tang,[22] please refer to the On-line Appendix.

Outline of CT scanning protocol[a]

Varying Parameters	Scan No.	MDCT	Scan Type	Scan mA	Scan kV	Section Thickness	Pitch
MDCT	1	16	Axial	140	120	5	0.98
	2	64	Axial	140	120	5	0.98
	3	64	Axial	140	120	5	0.98
	4	64	Helical	140	120	5	0.98
Acquisition Mode	5	64	Helical	80	120	5	0.98
	6	64	Helical	100	120	5	0.98
Milliampere	7	64	Helical	120	120	5	0.98
	8	64	Helical	140	120	5	0.51
	9	64	Helical	140	80	5	0.98
	10	64	Helical	140	100	5	0.98
Kilovolt	11	64	Helical	140	120	5	0.98
	12	64	Helical	140	140	5	0.98
	13	64	Helical	140	120	5	0.51
	14	64	Helical	140	120	5	0.98
Pitch	15	64	Helical	140	120	5	1.37
	16	64	Helical	140	120	5	1.75
	17	64	Helical	140	120	0.625	0.98
	18	64	Helical	140	120	1.25	0.98
Section thickness	19	64	Helical	140	120	2.5	0.98
	20	64	Helical	140	120	5	0.98

[a] Eight CT scanning parameters were varied during serial CT acquisitions.

Statistical Analysis

The CT scanning parameters were incrementally changed, and the textures features were compared among the scans by using the Student *t* test for independent samples. To adjust for multiple comparisons, we performed a false discovery rate correction and calculated the false discovery rate–corrected *P* values (termed *Q* values) in addition to raw *P* values with the Benjamini-Hochberg method described in the literature.[23] Statistical computations were performed by using SAS 9.1.3 software (SAS Institute, Cary, North Carolina). The PROC MULTTEST function in SAS was used to calculate the *Q* values. A 2-tailed *P* value of $< .05$ was used to evaluate statistical significance.

RESULTS

The results of the texture analysis features with variations in CT parameters are shown in On-line Tables 1–8.

Multidetector Row CT Scanner

Significantly larger values were seen in the histogram features of second deviation ($P = .0042$, $Q = 0.018$) and range ($P = .0046$, $Q = 0.018$) as shown in On-line Table 1. There were no significant differences in the GLCM texture features with the exception of the texture feature correlation, which demonstrated lower values for the 64–multidetector row CT (MDCT) compared with 16–MDCT ($P = .012$, $Q = 0.039$). Overall, higher texture features were seen in all the Law's features for the 64–MDCT scanner compared with the 16–MDCT scanner (for all Law's features, $P < .0001$, $Q = 0.0005$). No statistically significant differences were seen in the GLRL or GLGM texture features.

Changes in Milliampere

All CT parameters except for milliampere were held constant on a 64–MDCT scanner. The milliampere varied from 80 to 140 mA in increments of 20 mA. For all included texture features, there were no statistically significant differences between the texture features based on the variations in the milliampere, as shown in On-line Table 1.

Changes in Kilovolt

All CT parameters except for kilovolt were held contrast for these serial scans of the phantom on the 64–MDCT scanner. Kilovolt varied from 80 to 140 kV in increments of 20 kV. For all included texture features, there were no statistically significant differences between the texture features based on the variations in kilovolt as shown in On-line Table 1.

Changes in Section Thickness

All CT parameters except for the section thickness were held constant for serial scans of the phantom on the 64–MDCT scanner. Serial helical acquisitions of the phantom were performed by using section thicknesses of 0.625, 1.25, 2.5, and 5 mm.

While there was no statistically significant difference in the histogram feature of mean ($P = .86$, $Q = 0.86$), statistically significant differences were seen in the other histogram features, including median ($P = .0004$, $Q = 0.0005$), SD ($P = .0006$, $Q = 0.0008$), second SD ($P < .0001$, $Q = 0.0002$), geometric mean ($P = .0013$, $Q = 0.0016$), and harmonic mean ($P < .0001$, $Q = 0.0002$), as shown in On-line Table 1. Additionally, all the GLCM texture features demonstrated statistically significant differences with variations in the section thicknesses.

Changes in Pitch

For variations in the pitch of helical scans, there were several significant differences in the Law's features of L5, L6, and L7 ($P = .021$, $P = .001$, $P = .0014$, respectively); however, after false discovery rate correction only the L6 feature remained statistically significant ($Q = 0.034$). No statistically significant differences were seen in the histogram, GLCM, GLRL, or GLGM texture features as shown in On-line Table 1.

Changes in Acquisition

Statistically significant differences were seen in the histogram features of second SD ($P = .0015$, $Q = 0.0045$) and range ($P = .0016$, $Q = 0.0045$), which exhibited lower values in an axial acquisition compared with a helical acquisition. No significant differences were seen in the GLCM features in an axial-versus-helical scan. Lower GLRL values were seen in the axial acquisition compared with the helical acquisition, with significant differences in the GLRL features of short-run emphasis ($P = .0024$, $Q = 0.63$), long-run emphasis ($P = .0006$, $Q = 0.0028$), gray-level nonuniformity ($P = .0011$, $Q = 0.0042$), and run-length nonuniformity ($P = .0007$, $Q = 0.0029$). No statistically significant differences were seen in the Law features or GLGM texture features shown in On-line Table 1.

DISCUSSION

The results of this study demonstrate statistically significant changes in the texture features based on the use of different CT parameters. CT texture features were not dependent on variations in milliampere and kilovolt. Variations in section thickness resulted in significant differences in the largest number of texture features, most of which were histogram texture features. To a lesser extent, the histogram features of second SD and range were both significantly affected by changes in the MDCT and an axial-versus-helical scan. Differences in CT texture features based on variations in scanning protocols have been suggested by the work of Fave et al[9]; however, to date, there remains no standardization for CT texture analysis or a comprehensive study investigating how CT parameters may influence the various texture parameters.

The use of texture analysis has been increasing in prevalence throughout the radiology literature, particularly as an adjunct aiding in diagnosis, lesion characterization, and even in the evaluation for treatment-related response.[10-14,19,24] Preliminary works investigating the use of a texture analysis to detect and characterize stages of hepatic fibrosis have been reported in the literature.[7,25,26] Similarly, texture analysis has also been used for examining potential differences in tissue architecture on CT in oropharyngeal squamous cell carcinomas and for help in evaluating changes in cartilage.[8,27] In these studies, a single CT protocol scanning algorithm has been used, limiting potential variations in the texture analysis feature related to scanning technique. This has future implications in multi-institutional research, such as for the imaging-based studies from The Cancer Imaging Archive, in which different scanning techniques could potentially reflect quantitative differences related to scanning techniques across different equipment manufacturers.

The GLCM texture features were most affected by changes in slice thickness. This dependency may be related to an increase in the likelihood of partial volume effect as the section thickness increases. Partial volume effect occurs when a structure partially intrudes the x-ray beam. With thicker sections, due to the volume-averaging effect, the contrast of the anatomy with its background decreases (ie, decreased GLCM contrast) and, visually, the image becomes more "homogeneous" (ie, increased GLCM homogeneity). Clinically, this is an important consideration because several GLCM features, particularly the GLCM texture feature of entropy, have been described as being important for tumor imaging.[15,16]

Multiple prior studies have highlighted the potential importance and ease of use of a quantitative texture analysis to evaluate

subtle changes in pixel intensity, which may not be evident to the human eye. The potential clinical applications of CT texture analysis include disease and lesion characterization, prognosis and treatment prediction, and treatment-response evaluation. However, a precise relationship between texture analysis features and a histopathologic understanding of correlative changes in tissue microstructure is less well-defined. Additionally, a prior study noted changes in texture features based on changes in CT parameters thought to reflect a degree of image heterogeneity.[17] In this study, we developed a physically heterogeneous phantom simulating varying densities to closely investigate how changes in CT scanning parameters influence texture analysis features. The impact of CT acquisition parameters on texture analysis features is an important consideration for the development and understanding of texture-based features when applied to CT images of clinical patients or research subjects. This is particularly important in cases in which texture analysis is used to evaluate treatment-related responses, longitudinal studies, and cross-institutional studies whereby the CT scanning parameters may vary, therefore further complicating the texture analysis results because measurements of image heterogeneity may be confused with biologic responses.

A previous study used a water phantom with no internal structural heterogeneity and concluded that the CT texture features were relatively insensitive to CT parameters such as tube voltage, tube current, and section thickness.[18] The results of this study also demonstrated that all examined texture analysis features were insensitive to tube voltage and tube current, but not scanning parameters or section thickness. The observed insensitivity of the texture features to changes in the tube voltage and current may reflect the phantom used in our study comprising similar material densities. Future investigation will be directed at using a more complex phantom with a greater variation in material densities. This study serves as an initial pilot investigation using a nonanatomic phantom looking into how differences in texture analysis features change with variations in CT parameters. The construction of additional phantoms with greater architectural complexity and composed of higher attenuation materials such as iodine, bone, and so forth is the next step in furthering our understanding of how material composition and CT techniques contribute to variations in texture analysis.

There are several limitations to this study. First, it used a nonanatomic phantom constructed of varying internal architecture of relatively low-density material. The texture results of this study would be most applicable to low-density soft-tissue and fat-attenuating structures. Higher attenuation material such as bone was not reflected in the design of this phantom. Future investigations will pursue an anatomic internal architecture, following this initial, pilot study. Second, a discrete range of varying milliampere, kilovolt, section thickness, and pitch was interrogated in this study; however, the ranges investigated may not be broad enough to cover a comprehensive range of all milliampere, kilovolt, section thickness, and pitch values used in radiology practices. Additionally, we chose to manually contour the internal content of our phantom for every study; that introduces a source of destandardization. Future work on this subject matter will entail an investigation into automated contouring to reduce any potential variation from manual contouring.

CONCLUSIONS

While texture analysis represents an increasingly popular, postprocessing, quantitative evaluation technique that can potentially be used as an adjunct in diagnostic imaging as a possible biomarker, standardization of CT parameters for the use of texture analysis is crucial to prevent features of intrinsic image heterogeneity from being confused with biologic features.

Disclosures: Hirofumi Kuno—*UNRELATED*: *Grants/Grants Pending*: Grant-in-Aid for Young Scientists (B) KAKEN (No. 26861033); *Payment for Lectures Including Service on Speakers Bureaus*: Toshiba Medical Systems. Osamu Sakai—*UNRELATED*: *Consultancy*: Guerbet, LLC, *Comments*: consulting fee; *Payment for Lectures Including Service on Speakers Bureaus*: Bracco Diagnostics.

REFERENCES

1. Haralick R, Shanmugam K, Dinstein I. **Textural features for image classification.** *IEEE Trans Syst Man Cybern A Syst Hum* 1973;SMC-3:610–21
2. de Carvalho Alegro M, Valotta Silva A, Yumi Bando S, et al. **Texture analysis of high-resolution MRI allows discrimination between febrile and afebrile initial precipitating injury in mesial temporal sclerosis.** *Magn Reson Med* 2012;68:1647–53 CrossRef Medline
3. Mayerhoefer ME, Stelzeneder D, Bachbauer W, et al. **Quantitative analysis of lumbar intervertebral disc abnormalities at 3.0 Tesla: value of T(2) texture features and geometric parameters.** *NMR Biomed* 2012;25:866–72 CrossRef Medline
4. Risse F, Pesic J, Young S, et al. **A texture analysis approach to quantify ventilation changes in hyperpolarised ^{3}He MRI of the rat lung in an asthma model.** *NMR Biomed* 2012;25:131–41 CrossRef Medline
5. Fujimoto K, Tonan T, Azuma S, et al. **Evaluation of the mean and entropy of apparent diffusion coefficient values in chronic hepatitis C: correlation with pathologic fibrosis stage and inflammatory activity grade.** *Radiology* 2011;258:739–48 CrossRef Medline
6. Jirák D, Dezortová M, Taimr P, et al. **Texture analysis of human liver.** *J Magn Reson Imaging* 2002;15:68–74 CrossRef Medline
7. Barry B, Buch K, Soto JA, et al. **Quantifying liver fibrosis through the application of texture analysis to diffusion weighted imaging.** *Magn Reson Imaging* 2014;32:84–90 CrossRef Medline
8. Buch K, Fujita A, Li B, et al. **Using texture analysis to determine human papillomavirus status of oropharyngeal squamous cell carcinomas on CT.** *AJNR Am J Neuroradiol* 2015;36:1343–48 CrossRef Medline
9. Fave X, Cook M, Frederick A, et al. **Preliminary investigation into sources of uncertainty in quantitative imaging features.** *Comput Med Imaging Graph* 2015;44:54–61 CrossRef Medline
10. Fried DV, Tucker SL, Zhou S, et al. **Prognostic value and reproducibility of pretreatment CT texture features in stage III non-small cell lung cancer.** *Int J Radiat Oncol Biol Phys* 2014;90:834–42 CrossRef Medline
11. Cunliffe AR, Armato SG 3rd, Straus C, et al. **Lung texture in serial thoracic CT scans: correlation with radiologist-defined severity of acute changes following radiation therapy.** *Phys Med Biol* 2014;59:5387–98 CrossRef Medline
12. Ba-Ssalamah A, Muin D, Schernthaner R, et al. **Texture-based classification of different gastric tumors at contrast-enhanced CT.** *Eur J Radiol* 2013;82:e537–43 CrossRef Medline
13. Ng F, Ganeshan B, Kozarski R, et al. **Assessment of primary colorectal cancer heterogeneity by using whole-tumor texture analysis: contrast-enhanced CT texture as a biomarker of 5-year survival.** *Radiology* 2013;266:177–84 CrossRef Medline
14. Schieda N, Thornhill RE, Al-Subhi M, et al. **Diagnosis of sarcomatoid renal cell carcinoma with CT: evaluation by qualitative imag-**

ing features and texture analysis. *AJR Am J Roentgenol* 2015;204:1013–23 CrossRef Medline
15. Lubner MG, Stabo N, Lubner SJ, et al. **CT textural analysis of hepatic metastatic colorectal cancer: pre-treatment tumor heterogeneity correlates with pathology and clinical outcomes.** *Abdom Imaging* 2015;40:2331–37 CrossRef Medline
16. Ahn SY, Park CM, Park SJ, et al. **Prognostic value of computed tomography texture features in non-small cell lung cancers treated with definitive concomitant chemoradiotherapy.** *Invest Radiol* 2015;50:719–25 CrossRef Medline
17. Ganeshan B, Miles KA. **Quantifying tumour heterogeneity with CT.** *Cancer Imaging* 2013;13:140–49 CrossRef Medline
18. Miles KA, Ganeshan B, Griffiths MR, et al. **Colorectal cancer: texture analysis of portal phase hepatic CT images as a potential marker of survival.** *Radiology* 2009;250:444–52 CrossRef Medline
19. Paniagua B, Ruellas AC, Benavides E, et al. **Validation of CBCT for the computation of textural biomarkers.** *Proc SPIE Int Soc Opt Eng* 2015;9417 CrossRef
20. Colen RR, Vangel M, Wang J, et al; TCGA Glioma Phenotype Research Group. **Imaging genomic mapping of an invasive MRI phenotype predicts patient outcome and metabolic dysfunction: a TCGA glioma phenotype research group project.** *BMC Med Genomics* 2014;7:30 CrossRef Medline
21. Kalpathy-Cramer J, Freymann JB, Kirby JS, et al. **Quantitative Imaging Network: data sharing and competitive algorithm validation leveraging The Cancer Imaging Archive.** *Transl Oncol* 2014;7:147–52 CrossRef Medline
22. Tang X. **Texture information in run-length matrices.** *IEEE Trans Image Process* 1998;7:1602–09 CrossRef Medline
23. Benjamini Y, Hochberg Y. **Controlling the false discovery rate: a practical and powerful approach to multiple testing.** *Journal of the Royal Statistical Society* 1995;57:289–300
24. Hodgdon T, McInnes MD, Schieda N, et al. **Can quantitative CT texture analysis be used to differentiate fat-poor renal angiomyolipoma from renal cell carcinoma on unenhanced CT images?** *Radiology* 2015;276:787–96 CrossRef Medline
25. Daginawala N, Li B, Buch K, et al. **Using texture analyses of contrast enhanced CT to assess hepatic fibrosis.** *Eur J Radiol* 2016;85:511–17 CrossRef Medline
26. Yu H, Buch K, Li B, et al. **Utility of texture analysis for quantifying hepatic fibrosis on proton density MRI.** *J Magn Reson Imaging* 2015;42:1259–65 CrossRef Medline
27. MacKay JW, Murray PJ, Kasmai B, et al. **MRI texture analysis of subchondral bone at the tibial plateau.** *Eur Radiol* 2016;26:3034–45 CrossRef Medline

Quantifying Intracranial Internal Carotid Artery Stenosis on MR Angiography

H. Baradaran, P. Patel, G. Gialdini, K. Al-Dasuqi, A. Giambrone, H. Kamel, and A. Gupta

ABSTRACT

BACKGROUND AND PURPOSE: Intracranial atherosclerosis is a common cause of ischemic stroke. Intracranial stenosis is most commonly quantified by the Warfarin-Aspirin Symptomatic Intracranial Disease method, which involves calculating a ratio of luminal diameter measurements on conventional angiography. Our purpose was to determine whether a single linear measurement of the narrowest caliber of the intracranial ICA on MRA can accurately predict Warfarin-Aspirin Symptomatic Intracranial Disease stenosis measurements.

MATERIALS AND METHODS: We identified patients from a prospective stroke registry who had undergone head MRAs to quantitatively evaluate the degree of Warfarin-Aspirin Symptomatic Intracranial Disease–derived stenosis in each intracranial ICA. We also made a single linear millimeter measurement at the site of maximal narrowing of the ICA. We calculated a correlation coefficient between the lumen diameter in millimeters and percentage Warfarin-Aspirin Symptomatic Intracranial Disease stenosis. We performed receiver operating characteristic analysis to determine optimal luminal diameter cutoff values.

RESULTS: In 386 unique intracranial ICAs, we found a strong linear relationship between single lumen measurements and Warfarin-Aspirin Symptomatic Intracranial Disease–style stenosis measurements ($R = -0.84$, $P < .0001$). We found that ICA lumen diameters of ≤2.1 and ≤1.3 mm were optimal cutoffs for identifying patients with ≥50% stenosis and ≥70% stenosis, respectively (area under the curve = 0.96 and 0.99, respectively).

CONCLUSIONS: There is a strong linear relationship between the narrowest lumen diameter of the intracranial ICA and percentage stenosis. Our results suggest that a single lumen diameter measurement on MRA allows accurate estimation of Warfarin-Aspirin Symptomatic Intracranial Disease stenosis, which may affect risk stratification and treatment decisions.

ABBREVIATIONS: CAESAR = Cornell AcutE Stroke Academic Registry; WASID = Warfarin-Aspirin Symptomatic Intracranial Disease

Intracranial atherosclerotic disease is a major risk factor for ischemic stroke. As one of the most common causes of stroke worldwide,[1] intracranial atherosclerosis is generally assessed by measuring the degree of luminal stenosis on angiography.[2,3] Accurate assessment of the degree of luminal stenosis of the cerebral vasculature is important to assign stroke etiology because most stroke classification schemes require a luminal stenosis of ≥50% for a stroke to be attributed to large-vessel atherosclerosis.[4] In addition, given trial data showing that aggressive medical therapy is an effective approach to reduce recurrent stroke risk in patients with ≥70% stenosis of a major intracranial artery,[5] reliable and accurate stenosis measurements are critical for appropriate patient selection for preventative therapy.[4] Similarly, studies have shown that patients with ≥70% stenosis are at an elevated risk of stroke recurrence compared with those with 50%–69% stenosis.[3]

The most commonly used method for calculating intracranial stenosis severity is the Warfarin-Aspirin Symptomatic Intracranial Disease (WASID) method, which has been the basis of several randomized controlled trials for the treatment of major intracranial stenosis.[5-7] The measurement is performed by calculating a ratio of luminal diameters obtained from angiographic images. Although the WASID technique has high reproducibility with experienced readers and meticulous technique, the practical imple-

Received July 12, 2016; accepted after revision December 14.

From the Department of Radiology (H.B., P.P., K.A.-D., A. Gupta), Clinical and Translational Neuroscience Unit (H.B., G.G., H.K., A. Gupta), Feil Family Brain and Mind Research Institute, Department of Healthcare Policy and Research (A. Giambrone), and Department of Neurology (H.K.), Weill Cornell Medicine, New York, New York.

Dr Ajay Gupta is supported by National Institutes of Health/National Center for Advancing Translational Sciences grant No. KL2TR000458; and Dr Hooman Kamel is supported by National Institutes of Health/National Institute of Neurological Disorders and Stroke grant No. K23NS082367.

Please address correspondence to Ajay Gupta, MD, Department of Radiology, Weill Cornell Medicine, 525 East 68th St, Box 141 Starr 8A, New York, NY 10065; e-mail: ajg9004@med.cornell.edu

http://dx.doi.org/10.3174/ajnr.A5113

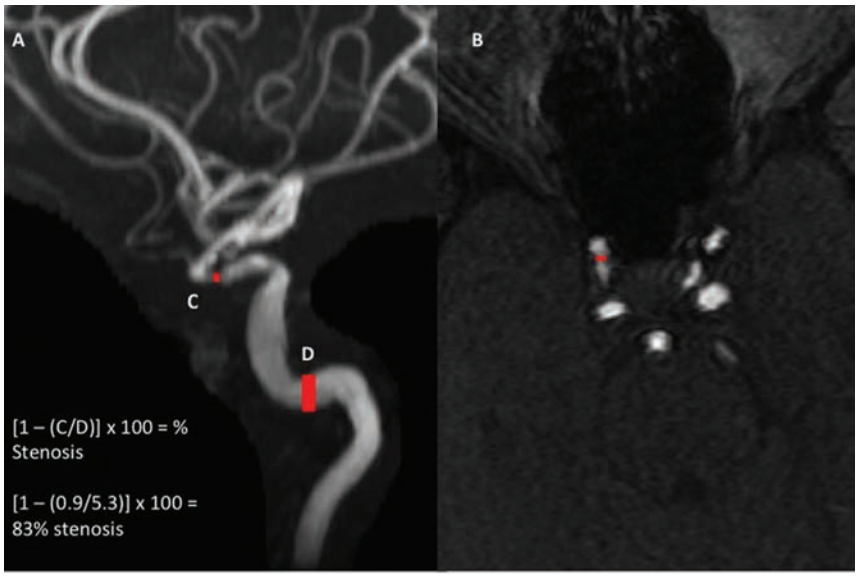

FIG 1. MRA MIP (*A*) and axial source (*B*) images demonstrating high-grade stenosis of the right intracranial ICA. For an accurate measurement of the degree of Warfarin-Aspirin Symptomatic Intracranial Disease stenosis, we made a linear measurement of the most stenotic portion of the ICA on either the MIP or axial source image, in this case 0.9 mm (*C*). A second "normal" measurement was made at the widest, nontortuous, normal portion of the petrous ICA that had margins parallel with the site of stenosis, in this case 5.3 mm (*D*). If the petrous ICA was also diseased, the most distal, parallel part of the extracranial ICA was measured. The ratio of these 2 measurements was then used to calculate the WASID stenosis, in this case $[1 - (0.9/5.30)] \times 100 = 83\%$ stenosis. Alternatively, we could use the single linear measurement at the site of greatest stenosis, 0.9 mm (*C*), which correlates with a stenosis of >70%.

mentation of WASID measurements can be cumbersome and prone to error, especially in the ICA where multiple vascular segments and an anatomically tortuous course can complicate measurement. For these reasons, strictly defined WASID stenosis measurements are not routinely performed in day-to-day practice, especially with noninvasive vascular imaging modalities. Thus, having a rapid and accurate method of estimating luminal stenosis measurements by using only single-diameter measurements obtained on cross-sectional images would be beneficial, similar to prior work done in the extracranial carotid artery.[8] The purpose of our study was therefore to test the hypothesis that a single luminal measurement on MRA images of the ICA can accurately approximate the WASID-determined intracranial ICA stenosis in a cohort of patients with acute ischemic stroke.

MATERIALS AND METHODS

Patients admitted to New York Presbyterian Hospital/Weill Cornell Medical Center with acute ischemic stroke in 2013 were included in the prospectively maintained Cornell AcutE Stroke Academic Registry (CAESAR). We retrospectively included all patients with MRA of the head because we were interested in characterizing the degree of intracranial arterial stenosis. We excluded any patients with complete occlusion of their intracranial ICAs and any patients with images that were too motion-degraded for accurate interpretation and measurement. The Weill Cornell Medicine institutional review board approved this data collection and waived the need for informed consent, given the retrospective nature of the analysis and minimal risk to subjects.

As part of the CAESAR registry, data on patient demographics, National Institutes of Health Stroke Scale score on admission, and vascular risk factors (including atrial fibrillation, tobacco use, diabetes mellitus, hypertension, dyslipidemia, peripheral vascular disease, and cardiac valvular disease) were prospectively collected by trained hospital personnel. Retrospectively, 2 neurologists used available medical records to independently identify stroke etiology by using the Trial of Org 10172 in Acute Stroke Treatment classification scheme,[4] with a third neurologist to independently resolve disagreements.

All included patients underwent noncontrast MRA examinations on either a 1.5T or 3T Signa (GE Healthcare, Milwaukee, Wisconsin) scanner. 3D-TOF acquisitions of the head were performed with an FOV of 20 cm, 1.4-mm section thickness, TR = 25, TE = 3, and matrices of 320 × 192 and 3210 × 224 on 1.5T and 3T scanners, respectively. Maximum intensity projections of each intracranial ICA were created.

We measured the degree of ICA narrowing by using the WASID method[6] and single luminal measurements.

WASID Measurement Technique

To calculate WASID stenosis, we obtained 2 measurements for each intracranial ICA: 1) a linear measurement at the site of the most severe stenosis on either the MIP or axial source images; and 2) a linear measurement at the widest, nontortuous, normal portion of the petrous ICA parallel to the site of stenosis. Using these measurements, we calculated the degree of WASID stenosis by using the following equation: Percentage Stenosis = $[(1 - [D_{stenosis}/D_{normal}])] \times 100$, where $D_{stenosis}$ is the diameter of the artery at the site of most severe degree of stenosis and D_{normal} is the diameter of the proximal artery at its widest, nontortuous, normal segment.[6]

Single Luminal Measurement Technique

For the single luminal measurement calculations, a single luminal measurement was made at the site of the most severe stenosis within the intracranial ICA.

The stenosis measurements for both techniques were obtained in either the cavernous or supraclinoid segments of the ICA. In cases of no measurable stenosis, linear measurements were made in the normal-caliber cavernous segment of the intracranial ICA. Stenosis was evaluated and measurements were made by using a combination of the MIP and axial source MRA images. Linear measurements were obtained on the MIP projection or axial source image showing the greatest degree of stenosis (Fig 1 and On-line Fig 1). Measurements were made from outer lumen to outer lumen in all arteries. A second radiologist independently calculated WASID stenosis measurements of the first 50 consecutive intracranial ICAs ordered by admission date to evaluate interobserver reproducibility.

Statistical Analysis

Categoric data are presented as number (percentage); and continuous data, as mean ± SD. Pearson correlation coefficients were used to determine the strength of the linear relationship between millimeter stenosis and percentage WASID stenosis followed by linear regression to determine 95% confidence intervals for the percentage stenosis predicted values at each millimeter stenosis.

Table 1: Patient demographics

Variable	No. (%)
Age (yr) (mean)	71.9 ± 14.0
Female	91 (47.2)
Race	
White	173 (89.6)
Black	11 (5.7)
Other	9 (4.7)
Atrial fibrillation	27 (14.0)
Coronary artery disease	37 (19.2)
Carotid artery disease	7 (3.6)
Diabetes	55 (28.5)
Hypertension	132 (68.4)
Dyslipidemia	103 (53.4)
NIHSS quartile	
1	54 (28.0)
2	48 (24.9)
3	22 (11.4)
4	69 (35.8)
Prior stroke	63 (32.6)
Peripheral vascular disease	13 (6.7)
Active tobacco use	18 (9.3)
Stroke subtype	
Cardioembolic	62 (32.1)
Cryptogenic	77 (39.9)
Large-artery atherosclerosis	25 (13.0)
Small-vessel occlusion	20 (10.4)
Other	9 (4.7)
IV tPA administered	16 (8.3)
Valvular disease	4 (2.1)

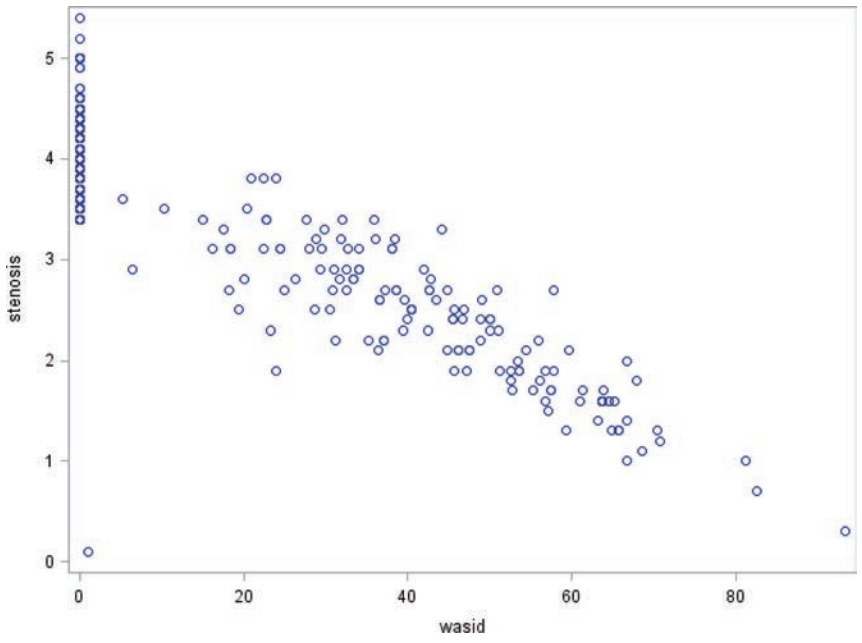

FIG 2. Correlation scatterplot demonstrating a linear relationship between millimeter stenosis measurements and percentage WASID stenosis for all included patients with $R = -0.84$ ($P < .0001$).

Pearson correlation coefficients were also performed on subgroups stratified by magnet field strength (1.5T versus 3T). WASID and millimeter stenosis measurements were each divided into 3 groups (<50% stenosis, 50%–69% stenosis, and ≥70% stenosis) to determine the number of arteries falling into each category. Sensitivity, specificity, positive predictive value, and negative predictive value were calculated for the millimeter stenosis measurement in discriminating between 50% and 70% stenosis, respectively. The optimal threshold for both 50% and 70% stenosis was determined by using the Youden index and receiver operating characteristic curves. All *P* values were 2-sided and were evaluated at the .05 α level. All analyses were performed by using SAS, Version 9.3 (SAS Institute, Cary, North Carolina).

RESULTS

Of the 335 patients included in the 2013 CAESAR stroke registry, 134 patients were excluded because they did not have an MRA examination of their head; 7 patients, because they had complete occlusion of their intracranial ICA; and 1 patient, because his MRA was too motion-degraded for accurate measurement. Of the 193 patients (386 arteries) who were ultimately included, the mean age was 71.9 years (Table 1).

Measures of single lumen diameter taken at the narrowest point of the intracranial ICA and the percentage WASID stenosis showed a linear relationship with excellent correlation ($R = -0.84$, $P < .0001$) (Fig 2). A subset analysis demonstrated similar correlation coefficients across 1.5T and 3T machines with $R = -0.85$ ($P < .001$) and -0.82 ($P < .001$), respectively. We also calculated the WASID percentage stenosis corresponding to the narrowest ICA lumen diameter in increments of 0.1 mm (Table 2).

Using receiver operating curve analysis on the 139 arteries (36%) with detectable WASID stenosis (Table 3), we determined that a millimeter measurement of 2.1 mm predicts >50% stenosis (area under the curve = 0.96, sensitivity = 89.9, specificity = 86.0) and a millimeter measurement of 1.3 mm predicts >70% stenosis (area under the curve = 0.99, sensitivity = 95.5, specificity = 100) (Fig 3 and On-line Table).

Of the 247 arteries without measurable WASID stenosis, the mean millimeter measurement was 3.97 ± 0.3 mm (range, 2.6–5.4 mm) and a median of 3.9 mm (interquartile range, 3.8–4.2).

Measures of interobserver reproducibility showed a κ coefficient of 0.85 (range, 0.72–0.98) for millimeter stenosis measurements.

DISCUSSION

In our analysis, we found a strong linear relationship with excellent correlation between millimeter measurement of the narrowest point of the ICA and percentage WASID stenosis. Additionally, we were able to determine optimal millime-

Table 2: WASID percentage stenosis estimates from millimeter measurements of the most stenotic portion of the intracranial ICA

Stenosis (mm)	% WASID Stenosis (95% CI)
3.0–3.8	14–30
2.2–2.9	31–48
1.3–2.2	50–65
<1.3	>65

Table 3: Breakdown of the millimeter measurements of the 139 arteries with detectable WASID stenosis

Stenosis Measurement	<50%	50%–69%	70%+	Total
>2.1 mm	75	6	0	81
1.4–2.1 mm	14	32	0	46
≤1.3 mm	0	6	6	12
Total	89	44	6	139

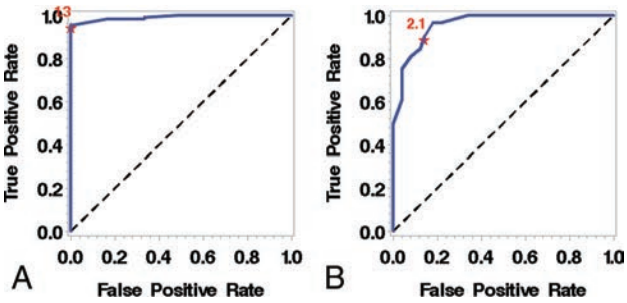

FIG 3. *A*, Receiver operating characteristic curve for predicting >70% stenosis demonstrates an optimal cutoff of 1.3 mm. *B*, Receiver operating characteristic curve for predicting >50% stenosis demonstrates that a measurement of 2.1 mm is an ideal cutoff.

ter cutoffs of 2.1 and 1.3 mm to identify those with ≥50% and ≥70% stenosis respectively by WASID methods, which demonstrated excellent accuracy. These findings are important because they suggest that accurate luminal stenosis measurements for the intracranial ICA can be obtained without calculating ratios, which are cumbersome and may be prone to error. We believe that a single luminal diameter measurement offers a simple and rapid approach to ICA stenosis measurement that can be readily integrated into clinical practice. Accurate quantification of intracranial ICA stenosis is important because it allows clinicians to determine whether patients exceed specific stenosis thresholds above which intensive medical therapies are warranted, according to existing evidence-based guidelines.

We used MR angiographic studies to evaluate the degree of stenosis. Although the original WASID measurements were performed on conventional angiography, the high radiation exposure, need to administer iodinated contrast, stroke risk, and risks of arterial puncture have reduced the role of conventional angiography in screening for atherosclerosis.[9] Conversely, MRA is an attractive technique for screening intracranial stenosis for several reasons: First, MR angiographic studies are obtained relatively quickly and are often performed concurrently with brain MR imaging in the evaluation of patients with potential stroke. At many institutions, including our own, cross-sectional imaging is almost exclusively used for the evaluation of intracranial stenosis and to inform treatment decisions, including whether to initiate more intensive medical therapy for stroke prevention. Second, using MIPs from MRA studies simulates the appearance of conventional angiography, thereby allowing measurements to be obtained in the same locations and projections, similar to those for the original WASID measurements. Third, recent studies have shown that MRA performs well, with sensitivities and specificities ranging from 80% to 100% and 89% to 95%, respectively, compared with conventional angiography when assessing intracranial stenosis.[10-13] Furthermore, MRA is not subject to the challenge of separating a high-density contrast-enhanced lumen from adjacent calcification and bone inherent in the evaluation of CTA of the head.

Our study had some limitations. First, time-of-flight MR angiography is sensitive to flow disturbances caused by stenosis[14] and is known to overestimate the degree of stenosis compared with CT and conventional angiography.[13] By evaluating both the MIP and axial source images to measure the degree of stenosis, according to established methods[15] shown to be highly accurate, we attempted to minimize the degree of overestimation of stenosis.[10-13] Second, obtaining measurements on MR angiograms can be subject to error, given the lack of precise spatial resolution. We used a uniform method for making all WASID measurements, including measuring from outer lumen to outer lumen. Additionally, we had excellent interobserver reliability between our 2 readers. Last, we had a relatively small number of ICAs demonstrating high-grade intracranial stenosis, with an overall prevalence of 12.9% for a stenosis of ≥50% and 1.6% for a stenosis of ≥70%. The relatively low prevalence of high-grade stenosis likely contributed to the positive predictive value of 50% for the cutoff for >70% stenosis.

We believe that by focusing on all ICAs in our cohort regardless of stenosis severity, our results are more generalizable, especially given that our data are consistent with the prevalence data of high-grade intracranial ICA stenosis derived from population-based studies.[16] Because we did not limit our study sample exclusively to patients with high-grade stenosis, the precision of our cutoff values to estimate exact degrees of high-grade WASID stenosis values is somewhat limited. We believe that our cutoff values are most useful as a practical and rapid approach to screen for potentially clinically relevant intracranial atherosclerotic stenosis, whose identification may warrant more detailed evaluation and possible treatment. Validating these cutoff values further in a separate prospective cohort would also be valuable.

CONCLUSIONS

We found a strong linear relationship between a simple measurement of the narrowest point of the intracranial ICA and the percentage WASID stenosis. Our results allow a direct estimation of WASID stenosis via a single-diameter measurement on MRA. We found an optimal cutoff measurement of 2.1 mm for identifying patients with ≥50% stenosis and 1.3 mm for identifying patients with ≥70% stenosis and that there is a strong linear relationship between the narrowest lumen diameter of the intracranial ICA and WASID-derived percentage stenosis, allowing a single linear measurement to provide accurate WASID stenosis estimates, which are useful in guiding treatment decisions.

Disclosures: Ajay Gupta—*RELATED*: *Grant*: National Institutes of Health, *Comments*: KL2 TR000458 supporting Dr Gupta, administered through Weill Cornell Clinical and Translational Science Center.* *Money paid to the institution.

REFERENCES

1. Holmstedt CA, Turan TN, Chimowitz MI. **Atherosclerotic intracranial arterial stenosis: risk factors, diagnosis, and treatment.** *Lancet Neurol* 2013;12:1106–14 CrossRef Medline
2. Gorelick PB, Wong KS, Bae HJ, et al. **Large artery intracranial occlusive disease a large worldwide burden but a relatively neglected frontier.** *Stroke* 2008;39:2396–99 CrossRef Medline
3. Kasner SE, Chimowitz MI, Lynn MJ, et al; Warfarin Aspirin Symptomatic Intracranial Disease Trial Investigators. **Predictors of ischemic stroke in the territory of a symptomatic intracranial arterial stenosis.** *Circulation* 2006;113:555–63 CrossRef Medline
4. Adams HP Jr, Bendixen BH, Kappelle LJ, et al. **Classification of subtype of acute ischemic stroke: definitions for use in a multicenter clinical trial—TOAST. Trial of Org 10172 in Acute Stroke Treatment**. *Stroke* 1993;24:35–41 CrossRef Medline
5. Chimowitz MI, Lynn MJ, Derdeyn CP, et al; SAMMPRIS Trial Investigators. **Stenting versus aggressive medical therapy for intracranial arterial stenosis.** *N Engl J Med* 2011;365:993–1003 CrossRef Medline
6. Samuels OB, Joseph GJ, Lynn MJ, et al. **A standardized method for measuring intracranial arterial stenosis.** *AJNR Am J Neuroradiol* 2000;21:643–46 Medline
7. Chimowitz MI, Lynn MJ, Howlett-Smith H, et al; Warfarin-Aspirin Symptomatic Intracranial Disease Trial Investigators. **Comparison of warfarin and aspirin for symptomatic intracranial arterial stenosis.** *N Engl J Med* 2005;352:1305–16 CrossRef Medline
8. Bartlett ES, Walters TD, Symons SP, et al. **Quantification of carotid stenosis on CT angiography.** *AJNR Am J Neuroradiol* 2006;27:13–19 Medline
9. Willinsky RA, Taylor SM, terBrugge K, et al. **Neurologic complications of cerebral angiography: prospective analysis of 2,899 procedures and review of the literature.** *Radiology* 2003;227:522–28 CrossRef Medline
10. Oelerich M, Lentschig GM, Zunker P, et al. **Intracranial vascular stenosis and occlusion: comparison of 3D time-of-flight and 3D phase-contrast MR angiography.** *Neuroradiology* 1998;40:567–73 CrossRef Medline
11. Choi CG, Lee DH, Lee JH, et al. **Detection of intracranial atherosclerotic steno-occlusive disease with 3D time-of-flight magnetic resonance angiography with sensitivity encoding at 3T.** *AJNR Am J Neuroradiol* 2007;28:439–46 Medline
12. Hirai T, Korogi Y, Ono K, et al. **Prospective evaluation of suspected stenoocclusive disease of the intracranial artery: combined MR angiography and CT angiography compared with digital subtraction angiography.** *AJNR Am J Neuroradiol* 2002;23:93–101 Medline
13. De Marco J, Nesbit G, Wesbey G, et al. **Prospective evaluation of extracranial carotid stenosis: MR angiography with maximum-intensity projections and multiplanar reformation compared with conventional angiography.** *AJR Am J Roentgenol* 1994;163:1205–12 CrossRef Medline
14. Bash S, Villablanca JP, Jahan R, et al. **Intracranial vascular stenosis and occlusive disease: evaluation with CT angiography, MR angiography, and digital subtraction angiography.** *AJNR Am J Neuroradiol* 2005;26:1012–21 Medline
15. Korogi Y, Takahashi M, Nakagawa T, et al. **Intracranial vascular stenosis and occlusion: MR angiographic findings.** *AJNR Am J Neuroradiol* 1997;18:135–43 Medline
16. Suri MF, Qiao Y, Ma X, et al. **Prevalence of intracranial atherosclerotic stenosis using high-resolution magnetic resonance angiography in the general population: the Atherosclerosis Risk in Communities Study.** *Stroke* 2016;47:1187–93 CrossRef Medline

Risk of Thrombus Fragmentation during Endovascular Stroke Treatment

J. Kaesmacher, T. Boeckh-Behrens, S. Simon, C. Maegerlein, J.F. Kleine, C. Zimmer, L. Schirmer, H. Poppert, and T. Huber

ABSTRACT

BACKGROUND AND PURPOSE: Periprocedural thrombus fragmentation is a relevant risk in endovascular stroke treatment. Because factors influencing its occurrence are largely unknown, this study addresses a potential relationship between thrombus histology and clot stability.

MATERIALS AND METHODS: Eighty-five patients with anterior circulation stroke treated with thrombectomy were included in this retrospective study. The number and location of emboli after retrieving the primary thrombus, the number of maneuvers, and TICI scores were evaluated. H&E and neutrophil elastase staining of retrieved clots was performed, and semiquantitative measurements of thrombus components were correlated with procedural parameters.

RESULTS: An inverse correlation between maneuvers required for thrombus retrieval and the number of distal and intermediate emboli was observed (Spearman *r*, −0.23; $P = .032$). Younger patients were at higher risk for periprocedural thrombus fragmentation (Spearman *r*, −0.23; $P = .032$). Bridging thrombolysis tended to be associated with fewer maneuvers (2 vs 3, $P = .054$) but more emboli (1 vs 0, $P = .067$). While no consistent correlation between procedural parameters and red/white blood cells and fibrin-/platelet fractions could be found, higher amounts of neutrophil elastase–positive cells within the thrombus were independently associated with the occurrence of multiple emboli (adjusted OR, 4.6; 95% CI, 1.1–19.7; $P = .041$) and lower rates of complete recanalization (adjusted OR, 0.3; 95% CI, 0.1–0.9; $P = .050$).

CONCLUSIONS: Younger age, easy-to-retrieve thrombi, and bridging thrombolysis may be risk factors for periprocedural thrombus fragmentation. Findings from standard histologic stains did not provide insight into thrombectomy-relevant thrombus stability. However, higher neutrophil levels in the thrombus tissue were related to an increased risk of periprocedural thrombus fragmentation. This observation aligns with the proposed thrombolytic capacity of neutrophil elastase and points to its potential clinical relevance in the context of stroke thrombectomy.

ABBREVIATIONS: ACA = anterior cerebral artery; F/P = fibrin-/platelet accumulations; IQR = interquartile range; MT = mechanical thrombectomy, NE = neutrophil elastase; POS = primary occlusion site; PTF = periprocedural thrombus fragmentation; RBC = red blood cells; WBC = white blood cells

Mechanical thrombectomy (MT) of large-vessel occlusion has evolved as a safe and effective procedure that plays an indispensable role in modern therapeutic management of acute ischemic stroke.[1-5] In recent randomized trials, high rates of successful recanalization (range, 59%–88%) were considered a key element in achieving excellent rates of good functional outcome (range, 33%–71%).[6] However, not all successfully treated patients showed complete (TICI 3) recanalization; this outcome potentially limits therapeutic benefit.

In general, all endovascular MT techniques are accompanied by the risk of periprocedural thrombus fragmentation (PTF) and subsequent downstream embolism,[7-9] preventing complete recanalization. Because the neurologic outcome of patients with complete (TICI 3) recanalization is significantly better compared with patients with "almost complete" (TICI 2b)[10] or incomplete recanalization (TICI 1–2a),[11] understanding the factors contributing to PTF may prove beneficial in achieving maximal therapeutic benefit. Previous reports demonstrated that thrombus stability[12] may influence the incidence of PTF, and analyses of cellular thrombus composition have revealed a possible associa-

Received September 12, 2016; accepted after revision December 12.

From the Departments of Neuroradiology (J.K., T.B.-B., C.M., J.F.K., C.Z., T.H.) and Neurology (S.S., L.S., H.P.), Klinikum rechts der Isar, Technical University of Munich, Munich, Germany.

Paper previously presented at: World Stroke Congress, October 26–29, 2016; Hyderabad, India.

Please address correspondence to Thomas Huber, MD, Department of Neuroradiology, Klinikum rechts der Isar, Technical University of Munich, Ismaninger Str 22, 81675 Munich, Germany; e-mail: Thomas-huber@tum.de

Indicates article with supplemental on-line table.

Indicates article with supplemental on-line photos.

http://dx.doi.org/10.3174/ajnr.A5105

tion between thrombus histology and thrombus etiology[13,14] as well as clinical outcome.[15,16] Discrepant results in previous studies[17] might be primarily explained by low patient numbers and the risk of clot fragmentation. The latter may bias the representative character of the analyzed fragment.

While the main cellular components of a thrombus are known to be fibrin-/platelet accumulations (F/P) as well as red (RBC) and white blood cells (WBC),[15,17] a higher fraction of RBC has been associated with increased rates of successful endovascular recanalization as noninvasively measured by whole-thrombus density (CT)[13,18] and corresponding blooming artifacts (MR imaging).[16,18-21] Besides common thrombus characteristics obtained from H&E staining, new evidence has emerged that the degree of inflammatory cell invasion, particularly by neutrophils, may alter the stability and degradation of a thrombus.[22,23] This finding is of particular interest because neutrophils exhibit fibrinolytic activity, which may weaken clot stability.[24] Nevertheless, the impact of inflammatory cells on the mechanical properties of a thrombus remains uncertain, especially in the context of stroke thrombectomy. Potential knowledge of the clot composition before MT may be a further valuable tool to aid in the selection of the most appropriate devices and techniques to avoid PTF.

To this end, this is the first study investigating the dependency of procedural thrombectomy characteristics on anatomic and immune-histochemical thrombus histology, to our knowledge.

MATERIALS AND METHODS

Subjects and Outcome

All consecutive patients presenting with a stroke due to large-vessel occlusion in the anterior circulation between July 2010 and September 2012 at a tertiary care center were included in this retrospective single-center study. Parts of this cohort and histologic analyses have been previously published.[14,15] All patients underwent MT at the Department of Neuroradiology, and thrombus material was preserved. All patients in whom no thrombus material could be retrieved were excluded. Under this premise, 85 patients (45 women; median age, 73 years) formed the final study cohort. This study was approved by the local ethics committee at the Klinikum rechts der Isar of the Technical University of Munich, Germany, in accordance with the ethical standards of the 1964 Declaration of Helsinki and its later amendments.[25] Clinical outcomes were measured as NIHSS at the day of discharge. Substantial neurologic improvement was defined as either NIHSS at day of discharge $\leq$1 or the difference between NIHSS on admission and NIHSS at the day discharge $\geq$8.[26] This definition was based on previous studies that have shown this criterion to be a sensitive outcome measure.[26]

Image Analysis

The primary occlusion site (POS) was defined as the location and extent of the initial thrombus as evaluated on a synopsis of admission CT/CTA and initial DSA. After recanalization of the POS, any vessel occlusions distal from the POS were considered emboli due to PTF. This simplified definition is based on previous findings, which have shown that >90% of intracranial vessel occlusions are caused by a single thrombus.[27] Hence, most vessel occlusions after POS recanalization are due to PTF. Emboli following PTF were further categorized into proximal, intermediate, and distal, according to their localization in lateral and corresponding anteroposterior DSA projections (On-line Fig 1). Emboli involving the M1 or M2 segment were always defined as proximal emboli, whereas those located distal to the pericallosal artery (on lateral projections) were considered distal emboli (see examples of emboli in Figs 1 and 2). The remaining vessel occlusions were assigned to the group of intermediate emboli. A schematic classification of emboli locations in cases of initial MCA or carotid-T occlusions is presented in On-line Fig 1. The success of POS recanalization (TICI-POS) as well as after additional rescue maneuvers (TICI-FINAL) was rated according to the original TICI scale, with TICI 2b defined as reperfusion of more than two-thirds of the initial occluded territory.[25] Note that TICI-POS and TICI-FINAL may be the same (ie, if no additional maneuvers were performed). All images were evaluated in consensus by 2 experienced neuroradiologists.

Endovascular Procedure

Patients underwent angiography if groin puncture could be performed within 6 hours after symptom onset, clinical presentation was severe (NIHSS $\geq$4), and no early infarct signs involving more than one-third of the MCA territory were present on cranial CT on admission. IV rtPA was administered as "bridging therapy" in the absence of contraindication (n = 58, 68.2%). All stent-retriever passages were counted, and the number of maneuvers was registered after POS recanalization and at the end of the procedure. All procedures were performed by using a distal access catheter (MCA/anterior cerebral artery [ACA]) or proximal flow arrest by balloon occlusion (carotid-T) and one of the following stent retrievers (maneuvers with the respective device): Solitaire (n = 45; Covidien, Irvine, California), pREset 4–20 (n = 58; Phenox, Bochum, Germany), Trevo (n = 29; Stryker, Kalamazoo, Michigan), Revive (n = 2; Codman Neurovascular, Raynham, Massachusetts), Pulse (n = 4; Penumbra, Almeda, California), and Separator 3D (n = 6, Penumbra). Aspiration techniques, applied as stand-alone approach, were not performed in this study.

Thrombus Histology

After clot retrieval, thrombus material was fixed in phosphate-buffered 4% formalin. H&E staining and subsequent quantitative analysis of WBC, RBC, and F/P content were performed as described previously.[14,15] To assess the prevalence of neutrophils within the thrombus, we stained the samples immunohistochemically by using an anti-neutrophil elastase monoclonal mouse antibody (clone NP57, M0752; Dako Denmark, Glostrup, Denmark). The number of neutrophil elastase (NE)-positive cells was semiquantitatively evaluated by 2 independent raters (NE index) who were blinded to the clinical data. Discrepancies were rated in consensus in a separate session. Evaluation was performed by using a 5-step grading scale: 0 (none), 1 (scattered), 2 (intermediate), 3 (clustered), 4 (high, >50% of all cells) (Fig 3).

Statistical Analysis and Illustrations

The Shapiro-Wilk test was applied to analyze data for normal distribution. Because all variables, except NIHSS on admission (P = .322 in Shapiro-Wilk test), were non-normally distributed,

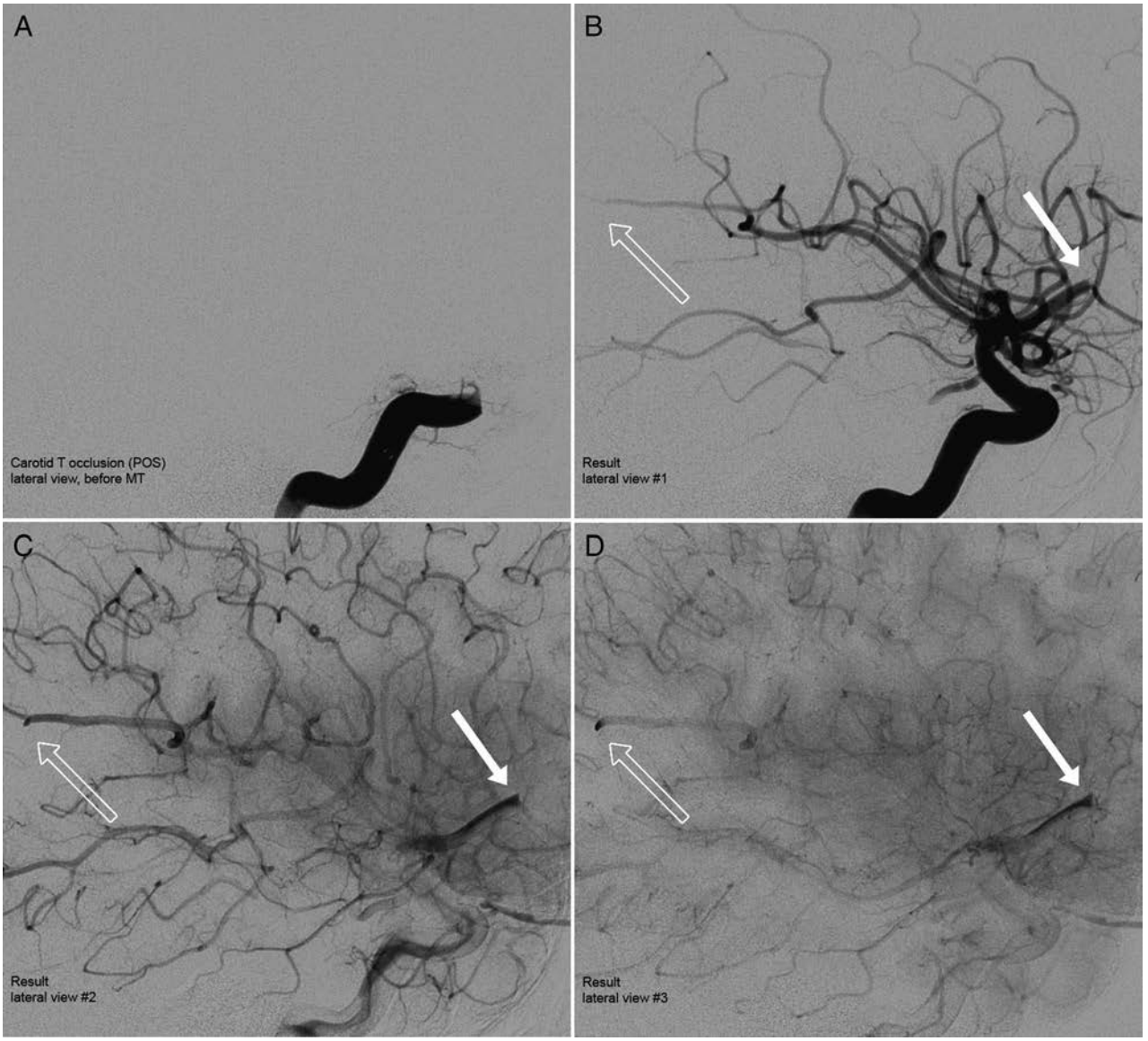

FIG 1. DSA images in a lateral projection in a case of initial carotid-T occlusion (*A*). Dynamic images (delay = 1 second) after successful POS recanalization resulting in 1 proximal (*filled arrow*) and 1 intermediate embolus (*open arrow*) due to PTF (*B–D*).

bivariate correlation analysis with the 2-sided Spearman correlation was performed. Frequency counts and median/mean comparison were evaluated by using standard statistical measures (Fisher exact test, Mann-Whitney *U* test). For median values, the interquartile range (IQR) is shown; for mean values, the SD is shown. Because PTF was shown to be a multifactorial process (eg, age, MCA/ACA versus ICA occlusion, bridging therapy; see "Results"), we adjusted the analysis of histologic clot characteristics for these potential confounders by using a multivariate logistic regression. For statistical analysis, SPSS statistics, release 23.0 (IBM, Armonk, New York), was used. Illustrations were prepared by using Adobe Photoshop CS4 (Adobe Systems, Mountain View, California).

RESULTS

Study Population and Outcomes

Inclusion criteria were met by 85 patients (mean age, 70.2 ± 14.6 years; 45 women) (Table). Approximately one-third (n = 26, 30.6%) of patients presented with a carotid-T occlusion, while the rest had isolated occlusions of the MCA/ACA (n = 57, 67.1%, and n = 2, 2.3%, respectively). The median NIHSS score at presentation was 15 (IQR, 10.5–18) and improved to 5.5 (IQR, 2–14) by the day of discharge. The median symptom-onset-to-treatment-time of 225 minutes (IQR, 165–278.75 minutes) could be sufficiently determined for 72 patients. Following recanalization of the POS, 36 patients (42.2%) showed no peripheral emboli, corresponding to an instant TICI 3 recanalization. Rescue therapy, namely retrieving downstream thrombi due to PTF, was successful in 27 cases. A median of 1 (IQR, 1–3.5) additional stent-retriever maneuver was required to perform the rescue therapy. The final rate of successful recanalization was 91.7%.

When a single device type was used, distribution of final reperfusion success and the number of emboli did not differ among different stent-retriever types (P = .442 for final reperfusion success and P = .931 for the number of all emboli; On-line Fig 2). Use

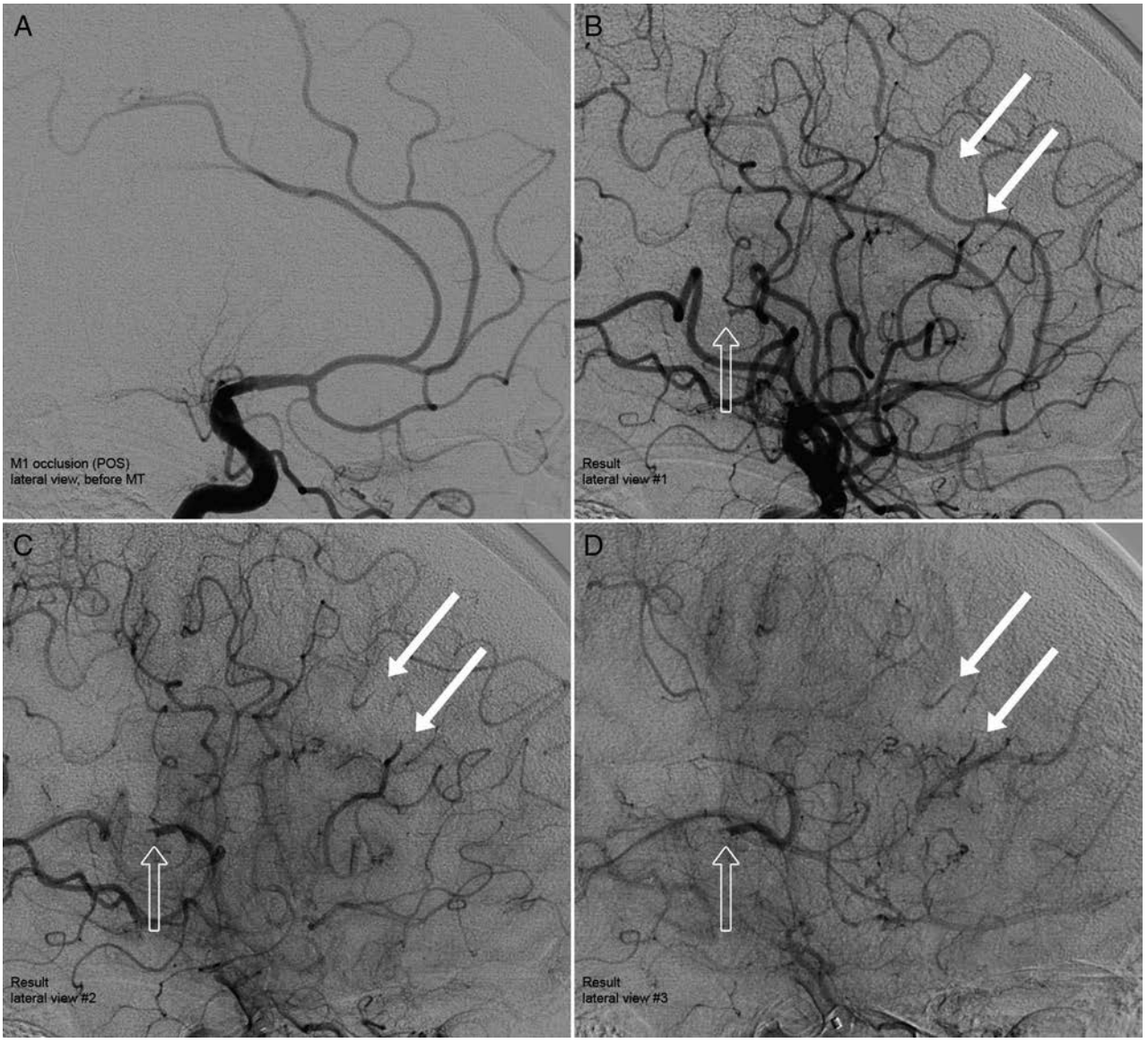

FIG 2. DSA images in a lateral projection in a case of initial M1 occlusion (*A*). Dynamic images (delay = 1 second) after successful recanalization of the POS, resulting in 1 intermediate (*open arrow*) and 2 distal emboli (*filled arrows*) due to PTF (*B–D*).

of multiple device types during a solitary thrombectomy was associated with lower rates of successful recanalization ($P = .042$). Occurrence of proximal and intermediate emboli after recanalization of the POS was associated with poorer neurologic outcome (NIHSS-proximal emboli: Spearman *r*, 0.279; $P = .013$; NIHSS-intermediate emboli: Spearman *r*, 0.223; $P = .049$), whereas patients showing a substantial neurologic improvement had fewer proximal ($P = .029$) and intermediate emboli ($P = .018$).

Physical Clot Properties

A consistent, inverse trend could be observed between the ease of the procedure and the risk of PTF: An easier procedure, namely requiring fewer stent-retriever maneuvers and less time to POS recanalization, was associated with a higher risk of distal and intermediate embolization (On-line Table). We also noted an age dependency of emboli occurrence because younger patients were at higher risk for PTF, resulting in higher numbers of intermediate and overall thrombus fragments distal to the POS. No correlation could be found between the time from symptom onset to groin puncture and the risk of embolization or maneuvers required. Administration of preinterventional IV rtPA tended to be associated with fewer endovascular maneuvers (2 versus 3, $P = .054$), shorter time to POS recanalization (30 minutes versus 47 minutes, $P = .051$), but a higher sum of overall emboli (1 versus 0, $P = .067$). In carotid-T occlusions as opposed to isolated MCA/ACA occlusions, more device passages were required to retrieve the primary thrombus (3 versus 2, $P = .006$), resulting in longer times for POS recanalization (66 versus 33 minutes, $P < .001$). However, no difference could be found regarding the location or number of occurring emboli (all $P > .5$).

Thrombus Histology

The mean fraction of RBC, F/P, and WBC was 42% (IQR, 22%–57%), 49% (IQR, 36%–69%), and 7% (IQR, 5%–11%), respectively. The median NE index, as determined for 42 patients, was 2 (IQR, 1–3). Clot histology characteristics did not differ between

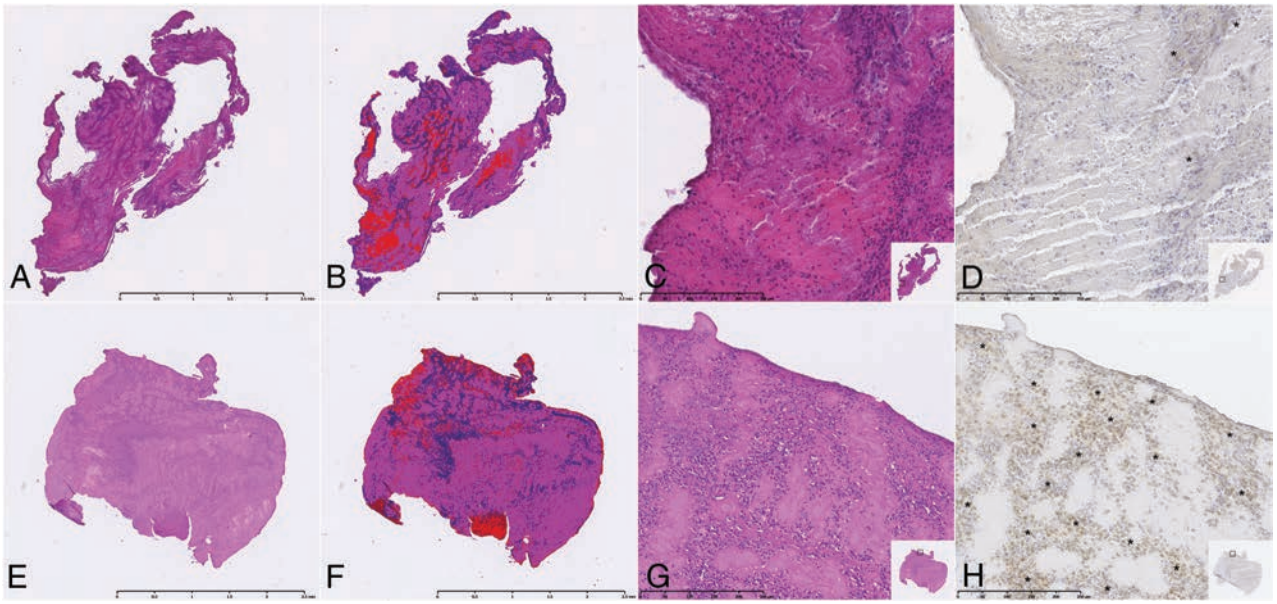

FIG 3. Histologic specimens of 2 different clots with H&E staining (magnification ×30) (*A* and *E*), segmentation of RBC (red), F/P (purple), WBC (blue), and staining artifacts (brown) for composite quantification (*B* and *F*). H&E staining (magnification ×200) (*C* and *G*) and NE staining (magnification ×200) (*D* and *H*) with accumulation of NE-positive cells marked (*asterisks*). Clot composition is the following: upper row: 30% RBC, 51% F/P, 19% WBC; NE index 1; lower row: 7% RBC, 84% F/P, 9% WBC, NE index 4.

Patient characteristics, clot histology, and procedural parameters

	No. or Median with Interquartile Range
Patients (No.)	85
Male/female (No.)	40/45 (47%/53%)
Age (median) (yr)	73 (65–80)
POS (No.)	
ICA/carotid-T	26 (30.6%)
ACA	2 (2.3%)
MCA	57 (67.1%)
IV rtPA bridging therapy (No.)	58 (68%)
Maneuvers (No.)	2 (1–4)
Procedure time for POS recanalization (min)	37 (21–64)
TICI after POS recanalization (No.)	
1	1 (1%)
2a	27 (32%)
2b	21 (25%)
3	36 (42%)
Occlusions due to PTF (n = 101)	
Proximal	26 (26%)
Intermediate	50 (50%)
Distal	25 (25%)
Clot histology (fraction in %)	
RBC	37 (27–48)
F/P	57 (47–67)
WBC	5 (4–7)

patients receiving bridging therapy and patients who did not (all, $P > .3$). Except for a higher NE index in carotid-T thrombi (median 2; IQR, 2–3.5, versus 2; IQR, 1–2; $P = .008$), no difference in histologic clot characteristics could be found when comparing MCA and carotid-T occlusions (all, $P > .3$). We could not observe a correlation between the time from symptom onset to recanalization or age and fraction of RBC, F/P, and WBC (all, $P > .5$). No consistent association between procedural parameters and RBC, F/P, or WBC content within the clot could be found (all, $P > .1$; On-line Table). This was also true when restricting analysis to different stent-retriever types (all, $P > .2$). However, the fraction of RBC (median RBC fraction, 50% [IQR, 28%–59%], versus 39% [IQR, 21%–57%]; $P = .183$) and the degree of neutrophil invasion (median NE index, 2 [IQR, 2–3] versus 2 [IQR, 1–3]; $P = .192$) tended to be higher in patients with multiple embolizations. The effect of neutrophil invasion on the occurrence of multiple emboli remained statistically tangible (without case restriction) when adjusting for age, site of occlusion (carotid-T versus MCA/ACA), and bridging therapy in a multivariate logistic regression model with multiple (>1) emboli defined as dependent variables (adjusted OR, 4.6; 95% CI, 1.1–19.7 for every NE index grade increase; $P = .041$; pseudo-$R^2 = 0.568$). In contrast, the fraction of RBC was not a significant factor associated with the occurrence of multiple emboli by using the same logistic regression model (OR, 1.0; 95% CI, 0.9–1.0; $P = .390$). Pursuant to the first finding, the median NE index was lower in successfully recanalized patients (2 versus 3; $P = .033$, On-line Fig 3). Furthermore, the NE index was an independent predictor of unsuccessful recanalization (TICI-FINAL < 2b, [see above for the logistic regression used]; adjusted OR, 0.3; 95% CI, 0.1–0.9; $P = .050$; pseudo-$R2 = 0.322$).

DISCUSSION

PTF during MT in acute stroke is common and was observed in more than half of the patients. This study shows 3 major findings: 1) In vivo clots differ regarding their MT-relevant mechanical properties, 2) common histologic clot characteristics do not consistently correlate with the mechanical clot properties, and 3) neutrophil invasion of the clot is linked to PTF and might serve as a novel surrogate for clot stability.

Our results show that easily retractable clots are generally prone to small/intermediate fragment dissociation, while those retracted with considerable effort are usually more stable and less

susceptible to PTF. During endovascular stroke treatment, the use of stent retrievers and aspiration devices has a risk of thrombus fragmentation, which can lead to an "embolic shower."[28,29] Smaller fragments (<200 μm) constitute, by far, the highest percentage of occurring emboli.[28] They usually dissolve due to spontaneous thrombolysis or revascularization as achieved by embolus extravasation.[30] However, those emboli are usually undetected by conventional DSA, and their true clinical impact remains unclear.[31] Larger emboli (>200 μm) cause clinically relevant cerebral occlusion[32] and lead to angiographically defined incomplete recanalization (TICI < 3). We have found those emboli to be clinically important because intermediate and proximal emboli were associated with lower NIHSS scores at discharge. Occurrence and "rescue" removal of those emboli are of important clinical relevance because patients with complete recanalization have fewer neurologic deficits.[10]

The beneficial effects of preinterventional systemic rtPA administration concur with our assessment; this finding suggests a facilitating effect of bridging therapy.[33-35] Patients receiving rtPA needed fewer maneuvers and had shorter procedure times. However, the presumed bridging therapy–related thrombus softening came with the risk of PTF, which has been reported previously.[36]

Thrombus characteristics have been shown to predict technical outcome in endovascular stroke therapy. Particularly, thrombi with higher Hounsfield units are associated with higher rates of successful recanalization.[19,21] Given prior histologic analyses, it seems reasonable to assume that those thrombi are RBC rich and have low F/P content.[18] In the present study, thrombi prone to dissociate into multiple emboli tended to have a higher RBC fraction. However, this association was inconsistent and statistically irrelevant when correcting for possible confounders. Our data regarding the true success rate of thrombectomy are particularly limited because we only analyzed cases in which thrombus material could be retrieved (usually TICI > 1–2a). Hence, the true impact of RBC on the capability of retrieving the clot and POS recanalization cannot finally be assessed in the presented cohort.

To the best of our knowledge, this is the first study that establishes a possible link between procedurally relevant thrombus stability and the content of neutrophils. Neutrophils invade newly formed thrombi through recruitment due to adherent activated platelets.[37] Adhesion triggers activation of neutrophils and subsequent release of neutrophil elastase.[38] Initially, proinflammatory mediators promote fibrin cross-linking and the formation of neutrophil extracellular traps, which promote a procoagulatory state.[39] However, activated neutrophils in the later phase also seem to restrict growth and promote thrombus degradation by NE-dependent fibrinolysis ("cell-dependent thrombolysis").[22] Komorowicz et al[24] could indeed show that NE triggers the release of thrombus fragments in the soluble phase when incubated under shear stress conditions. Beyond altering the stability properties of thrombi, experimental data further suggest that NE seems to be involved in inflammatory reperfusion damage,[40] and a recent study proposed an association between the presence of $CD4^+$ T-cells and $CD68^+$-monocytes/macrophages within the thrombus and stroke severity.[41] However, the true impact of "thromboinflammation" has yet to be evaluated in further studies.[42] In this context, the presented data underscore the need for considering and correcting for potential effects of inflammatory cells on thrombus stability, when evaluating its effect on clinical outcome in patients with stroke who were endovascularly treated.

Our study has several limitations beyond the common ones of a retrospective study design. Due to our inclusion criteria, the cohort exhibits a selection bias for successfully recanalized patients because histologic analysis was feasible only in cases in which the thrombus could be retrieved. Thus, results regarding the effects of histologic parameters on the true success rates of MT should be interpreted cautiously. Second, assessing the rate and location of emboli by using midprocedural DSA is a simplification and might not be as sensitive as susceptibility-weighted imaging for thrombus detection.[43] However, it is the only feasible method of PTF detection during the procedure and has the advantage of assessing the hemodynamic relevance of emboli due to PTF. Third, this technique is not capable of differentiating peri- and preprocedural thrombus fragmentation (distal to the POS). However, because previous studies have found a low frequency of preprocedural fragmentation (<10%),[27,43] the rate of false-positive classification is expected to be rather low. Fourth, the grading of the NE of the clot is based on a semiquantitative scale and was performed visually. Subjective analysis may, in the future, be overcome by ensuring comparable staining intensity and following threshold-based software quantification (comparable with the algorithm used for the analysis of H&E staining). Fifth, because we analyzed the thrombus retrieved from the POS, the histologic characteristics of the fragments causing distal emboli remain uncertain and might differ from the clot composition of the retrieved thrombus. One may speculate that dissolvable tissue islands or additional apposition thrombi might accumulate at the clot margins. These areas may be more prone to fragmenting during endovascular manipulation than the main thrombus and might show a different histology. Finally, because different stent retrievers were used, recanalization success and subsequent risk of PTF might be influenced by the choice of the device.

CONCLUSIONS

Younger age, easy-to-retrieve thrombi, and bridging thrombolysis are factors that may have a higher risk of PTF. Conventional histologic characteristics (RBC, WBC, F/P) do not seem to influence MT-relevant thrombus stability. However, higher amounts of clot-infiltrating neutrophils were related to an increased risk of PTF. This observation aligns well with the proposed thrombolytic capacity of neutrophilic enzymes and may implicate them as a novel marker for clot stability, which should be addressed in future clot studies.

Disclosures: Claus Zimmer—*UNRELATED*: *Board Membership*: Philips Healthcare and Bayer Schering Pharma, *Comments*: scientific advisory boards*; *Payment for Lectures including Service on Speakers Bureaus*: Bayer Schering Pharma and Philips Healthcare, *Comments*: speaker honoraria; *Other*: Biogen Idec, Quintiles, MSD Sharp & Dome, Boehringer Ingelheim, Inventive Health Clinical UK Ltd, advanceCOR, BrainsGate, Pfizer, Bayer Schering Pharma, Novartis, Roche, Servier, Penumbra, WCT GmbH, Syngis, SSS International Clinical Research, PPD Germany GmbH, Worldwide Clinical Trials Ltd, phenox, Covidien, Actelion, Medivation, Medtronic, Harrison Clinical Research, Concentric, pharmtrace, Reverse Medical Corp, Premier Research Germany Ltd, Surpass Medical Ltd, and GlaxoSmithKline, *Comments*: research support and investigator fees for clinical studies.* Lucas Schirmer—*UNRELATED*: *Patents (Planned, Pending, or Issued)*: WO2015166057A1; *Comments*: I filed a patent for the detection of antibodies against KIR4.1 in a subpopulation of patients with MS; the

patent has been published, however, payments have not been made yet; *Travel/Accommodations/Meeting Expenses Unrelated to Activities Listed*: Genzyme, *Comments*: travel support. Holger Poppert—*UNRELATED*: *Consultancy*: Bayer HealthCare, Daiichi Sankyo Pharmaceuticals; *Grants/Grants Pending:* Deutsche Stiftung Neurologie*; *Payment for Lectures including Service on Speakers Bureaus*: Bayer HealthCare, Daiichi Sankyo Pharmaceuticals, Boehringer Ingelheim, Bristol-Myers Squibb, Pfizer, DEGUM, RG Gesellschaft für Information und Organisation, Medkom Akademie, CVA-Cardio Vascular Academy gemeinnützige GmbH. Thomas Huber—*UNRELATED*: *Consultancy*: Brainlab, Feldkirchen, Germany, *Comments*: consultancy for atlas-based segmentation techniques. *Money paid to the institution.

REFERENCES

1. Berkhemer OA, Fransen PS, Beumer D, et al. **A randomized trial of intraarterial treatment for acute ischemic stroke.** *N Engl J Med* 2015; 372:11–20 CrossRef Medline
2. Goyal M, Demchuk AM, Menon BK, et al; ESCAPE Trial Investigators. **Randomized assessment of rapid endovascular treatment of ischemic stroke.** *N Engl J Med* 2015;372:1019–30 CrossRef Medline
3. Jovin TG, Chamorro A, Cobo E, et al; REVASCAT Trial Investigators. **Thrombectomy within 8 hours after symptom onset in ischemic stroke.** *N Engl J Med* 2015;372:2296–306 CrossRef Medline
4. Campbell BC, Mitchell PJ, Kleinig TJ, et al; EXTEND-IA Investigators. **Endovascular therapy for ischemic stroke with perfusion-imaging selection.** *N Engl J Med* 2015;372:1009–18 CrossRef Medline
5. Saver JL, Goyal M, Bonafe A, et al; SWIFT PRIME Investigators. **Stent-retriever thrombectomy after intravenous t-PA vs. t-PA alone in stroke.** *N Engl J Med* 2015;372:2285–95 CrossRef Medline
6. Manning NW, Chapot R, Meyers PM. **Endovascular stroke management: key elements of success.** *Cerebrovasc Dis* 2016;42: 170–77 CrossRef Medline
7. Gralla J, Schroth G, Remonda L, et al. **Mechanical thrombectomy for acute ischemic stroke: thrombus-device interaction, efficiency, and complications in vivo.** *Stroke* 2006;37:3019–24 CrossRef Medline
8. Gralla J, Schroth G, Remonda L, et al. **A dedicated animal model for mechanical thrombectomy in acute stroke.** *AJNR Am J Neuroradiol* 2006;27:1357–61 Medline
9. Penumbra Pivotal Stroke Trial Investigators. **The Penumbra Pivotal Stroke Trial: safety and effectiveness of a new generation of mechanical devices for clot removal in intracranial large vessel occlusive disease.** *Stroke* 2009;40:2761–68 CrossRef Medline
10. Kleine JF, Wunderlich S, Zimmer C, et al. **Time to redefine success? TICI 3 versus TICI 2b recanalization in middle cerebral artery occlusion treated with thrombectomy.** *J Neurointerv Surg* 2016 Feb 17. [Epub ahead of print] Medline
11. Jayaraman MV, Grossberg JA, Meisel KM, et al. **The clinical and radiographic importance of distinguishing partial from near-complete reperfusion following intra-arterial stroke therapy.** *AJNR Am J Neuroradiol* 2013;34:135–39 CrossRef Medline
12. Machi P, Jourdan F, Ambard D, et al. **Experimental evaluation of stent retrievers' mechanical properties and effectiveness.** *J Neurointerv Surg* 2016 Mar 25. [Epub ahead of print] CrossRef Medline
13. Niesten JM, van der Schaaf IC, van Dam L, et al. **Histopathologic composition of cerebral thrombi of acute stroke patients is correlated with stroke subtype and thrombus attenuation.** *PLoS One* 2014;9:e88882 CrossRef Medline
14. Boeckh-Behrens T, Kleine JF, Zimmer C, et al. **Thrombus histology suggests cardioembolic cause in cryptogenic stroke.** *Stroke* 2016;47: 1864–71 CrossRef Medline
15. Boeckh-Behrens T, Schubert M, Förschler A, et al. **The impact of histological clot composition in embolic stroke.** *Clin Neuroradiol* 2016;26:189–97 CrossRef Medline
16. Kim SK, Yoon W, Kim TS, et al. **Histologic analysis of retrieved clots in acute ischemic stroke: correlation with stroke etiology and gradient-echo MRI.** *AJNR Am J Neuroradiol* 2015;36:1756–62 CrossRef Medline
17. Marder VJ, Chute DJ, Starkman S, et al. **Analysis of thrombi retrieved from cerebral arteries of patients with acute ischemic stroke.** *Stroke* 2006;37:2086–93 CrossRef Medline
18. Liebeskind DS, Sanossian N, Yong WH, et al. **CT and MRI early vessel signs reflect clot composition in acute stroke.** *Stroke* 2011;42: 1237–43 CrossRef Medline
19. Mokin M, Morr S, Natarajan SK, et al. **Thrombus density predicts successful recanalization with Solitaire stent retriever thrombectomy in acute ischemic stroke.** *J Neurointerv Surg* 2015;7:104–07 CrossRef Medline
20. Froehler MT, Tateshima S, Duckwiler G, et al; UCLA Stroke Investigators. **The hyperdense vessel sign on CT predicts successful recanalization with the Merci device in acute ischemic stroke.** *J Neurointerv Surg* 2013;5:289–93 CrossRef Medline
21. Moftakhar P, English JD, Cooke DL, et al. **Density of thrombus on admission CT predicts revascularization efficacy in large vessel occlusion acute ischemic stroke.** *Stroke* 2013;44:243–45 CrossRef Medline
22. Imamura T, Kaneda H, Nakamura S. **New functions of neutrophils in the arthus reaction: expression of tissue factor, the clotting initiator, and fibrinolysis by elastase.** *Lab Invest* 2002;82:1287–95 CrossRef Medline
23. Michel JB, Ho-Tin-Noé B. **Thrombi and neutrophils.** *Circ Res* 2015; 116:1107–08 CrossRef Medline
24. Komorowicz E, Kolev K, Léránt I, et al. **Flow rate-modulated dissolution of fibrin with clot-embedded and circulating proteases.** *Circ Res* 1998;82:1102–08 CrossRef Medline
25. Higashida RT, Furlan AJ, Roberts H, et al; Technology Assessment Committee of the American Society of Interventional and Therapeutic Neuroradiology, Technology Assessment Committee of the Society of Interventional Radiology. **Trial design and reporting standards for intra-arterial cerebral thrombolysis for acute ischemic stroke.** *Stroke* 2003;34:e109–37 CrossRef Medline
26. Kerr DM, Fulton RL, Lees KR, et al; VISTA Collaborators. **Seven-day NIHSS is a sensitive outcome measure for exploratory clinical trials in acute stroke: evidence from the Virtual International Stroke Trials Archive.** *Stroke* 2012;43:1401–03 CrossRef Medline
27. Gratz PP, Schroth G, Gralla J, et al. **Whole-brain susceptibility-weighted thrombus imaging in stroke: fragmented thrombi predict worse outcome.** *AJNR Am J Neuroradiol* 2015;36:1277–82 CrossRef Medline
28. Chueh JY, Kühn AL, Puri AS, et al. **Reduction in distal emboli with proximal flow control during mechanical thrombectomy: a quantitative in vitro study.** *Stroke* 2013;44:1396–401 CrossRef Medline
29. Gobin YP, Starkman S, Duckwiler GR, et al. **MERCI 1: a phase 1 study of Mechanical Embolus Removal in Cerebral Ischemia.** *Stroke* 2004; 35:2848–54 CrossRef Medline
30. Yoo AJ, Simonsen CZ, Prabhakaran S, et al; Cerebral Angiographic Revascularization Grading Collaborators. **Refining angiographic biomarkers of revascularization: improving outcome prediction after intra-arterial therapy.** *Stroke* 2013;44:2509–12 CrossRef Medline
31. Rapp JH, Pan XM, Sharp FR, et al. **Atheroemboli to the brain: size threshold for causing acute neuronal cell death.** *J Vasc Surg* 2000;32: 68–76 CrossRef Medline
32. Sorimachi T, Nishino K, Shimbo J, et al. **Routine use of debris aspiration before retrieval of distal filter protection devices in carotid arterial stenting: analysis of captured debris and evaluation of clinical results.** *Neurosurgery* 2010;67:1260–67; discussion 1267 CrossRef Medline
33. Behme D, Kabbasch C, Kowoll A, et al. **Intravenous thrombolysis facilitates successful recanalization with stent-retriever mechanical thrombectomy in middle cerebral artery occlusions.** *J Stroke Cerebrovasc Dis* 2016;25:954–59 CrossRef Medline
34. Leker RR, Pikis S, Gomori JM, et al. **Is bridging necessary? A pilot study of bridging versus primary Stentriever-based endovascular reperfusion in large anterior circulation strokes.** *J Stroke Cerebrovasc Dis* 2015;24:1163–67 CrossRef Medline
35. Pfefferkorn T, Holtmannspötter M, Patzig M, et al. **Preceding intravenous thrombolysis facilitates endovascular mechanical recanalization in large intracranial artery occlusion.** *Int J Stroke* 2012;7: 14–18 CrossRef Medline

36. Kaesmacher J, Kleine JF. **Bridging therapy with i. v. rtPA in MCA occlusion prior to endovascular thrombectomy: a double-edged sword?** *Clin Neuroradiol* 2016 Aug 19. [Epub ahead of print] Medline
37. Kirchhofer D, Riederer MA, Baumgartner HR. **Specific accumulation of circulating monocytes and polymorphonuclear leukocytes on platelet thrombi in a vascular injury model.** *Blood* 1997;89:1270–78 Medline
38. Rainger GE, Rowley AF, Nash GB. **Adhesion-dependent release of elastase from human neutrophils in a novel, flow-based model: specificity of different chemotactic agents.** *Blood* 1998;92:4819–27 Medline
39. Massberg S, Grahl L, von Bruehl ML, et al. **Reciprocal coupling of coagulation and innate immunity via neutrophil serine proteases.** *Nat Med* 2010;16:887–96 CrossRef Medline
40. Nicolini FA, Mehta JL, Nichols WW, et al. **Leukocyte elastase inhibition and t-PA-induced coronary artery thrombolysis in dogs: beneficial effects on myocardial histology.** *Am Heart J* 1991;122:1245–51 CrossRef Medline
41. Schuhmann MK, Gunreben I, Kleinschnitz C, et al. **Immunohistochemical analysis of cerebral thrombi retrieved by mechanical thrombectomy from patients with acute ischemic stroke.** *Int J Mol Sci* 2016;17:298 CrossRef Medline
42. De Meyer SF, Denorme F, Langhauser F, et al. **Thromboinflammation in stroke brain damage.** *Stroke* 2016;47:1165–72 CrossRef Medline
43. Klinger-Gratz PP, Schroth G, Gralla J, et al. **Protected stent retriever thrombectomy prevents iatrogenic emboli in new vascular territories.** *Neuroradiology* 2015;57:1045–54 CrossRef Medline

Selective-versus-Standard Poststent Dilation for Carotid Artery Disease: A Systematic Review and Meta-Analysis

O. Petr, W. Brinjikji, M.H. Murad, B. Glodny, and G. Lanzino

ABSTRACT

BACKROUND: The safety and efficacy of standard poststent angioplasty in patients undergoing carotid artery stent placement have not been well-established.

PURPOSE: We conducted a systematic review of the literature to evaluate the safety and efficacy of carotid artery stent placement and analyzed outcomes of standard-versus-selective poststent angioplasty.

DATA SOURCES: A systematic search of MEDLINE, EMBASE, Scopus, and the Web of Science was performed for studies published between January 2000 and January 2015.

STUDY SELECTION: We included studies with >30 patients describing standard or selective poststent angioplasty during carotid artery stent placement.

DATA ANALYSIS: A random-effects meta-analysis was used to pool the following outcomes: periprocedural stroke/TIA, procedure-related neurologic/cardiovascular morbidity/mortality, bradycardia/hypotension, long-term stroke at last follow-up, long-term primary patency, and technical success.

DATA SYNTHESIS: We included 87 studies with 19,684 patients with 20,378 carotid artery stenoses. There was no difference in clinical ($P = .49$) or angiographic outcomes ($P = .93$) in carotid artery stent placement treatment with selective or standard poststent balloon angioplasty. Both selective and standard poststent angioplasty groups had a very high technical success of >98% and a low procedure-related mortality of 0.9%. There were no significant differences between both groups in the incidence of restenosis ($P = .93$) or procedure-related complications ($P = .37$).

LIMITATIONS: No comparison to a patient group without poststent dilation could be performed.

CONCLUSIONS: Our meta-analysis demonstrated no significant difference in angiographic and clinical outcomes among series that performed standard poststent angioplasty and those that performed poststent angioplasty in only select patients.

ABBREVIATION: CAS = carotid artery stent placement

Endovascular therapy of carotid artery disease has advanced during the past decade and is now considered a valuable treatment alternative to surgery in appropriately selected patients.[1-5] The indications for carotid endarterectomy were initially established in the North American Symptomatic Carotid Endarterectomy Trial[6] in 1991, which expanded treatment indications to patients with symptomatic severe or moderate carotid stenoses. Formerly, patients who were not eligible for surgery were treated with percutaneous transluminal balloon angioplasty,[7,8] first described by Kerber et al in 1980.[9] Although procedure-related complication rates were similar/comparable for both treatment modalities,[7,8,10] some potential drawbacks and specific problems occurred due to the endovascular approach, including luminal compromise from catheters and guidewires crossing the stenotic lesions and/or during balloon inflation (temporary carotid occlusion by a balloon and/or wire catheter), intraprocedural thromboembolic events, elastic vessel recoil, or intimal dissection.[11] Af-

Received August 29, 2016; accepted after revision December 12.

From the Departments of Neurologic Surgery (O.P., G.L.) and Radiology (W.B., G.L.) and Division of Preventive Medicine (M.H.M.), Mayo Clinic, Rochester, Minnesota; and Departments of Radiology (B.G.) and Neurosurgery (O.P.), Medical University Innsbruck, Innsbruck, Austria.

Please address correspondence to Ondra Petr, MD, Mayo Clinic, 200 1st St SW, Rochester, MN 55905; e-mail: petr.ondra@mayo.edu; ondra.petr@yahoo.com

Indicates article with supplemental on-line tables.

http://dx.doi.org/10.3174/ajnr.A5103

ter the carotid artery stent placement technique was developed, stent-assisted balloon angioplasty showed better results in event-free survival and even lower repeat angioplasty rates.[11] The primarily used balloon-expandable stents were increasingly replaced by self-expanding stents,[11,12] exhibiting an intrinsic radial expansion force with memory on the stenotic vessel wall. Poststent balloon angioplasty may then be performed to closely appose the stent and intima and, moreover, to expand regions of residual stent narrowing.[11]

Supporters of standard poststent balloon angioplasty (per protocol) indicated that poststent ballooning decreased the incidence of restenosis by re-establishing the normal luminal diameter. However, numerous studies[13-15] have suggested that poststent balloon dilation increases the likelihood of postprocedural emboli. Moreover, poststent ballooning can increase the probability of reflex bradycardia and hypotension, which might be associated with higher rates of periprocedural and postprocedural complications.[16-19]

Some authors claim that poststent dilation should be performed on a selective, case-by-case basis to maximize patient benefits and limit complications. However, to the best of our knowledge, there is no evidence in the recently published literature supporting the superiority of either of these techniques. Standard poststent balloon angioplasty has become the standard of care in many vascular centers,[20-35] and only some interventionalists[19,36-41] prefer performing poststent angioplasty on a selective base. On the basis of the latter studies, standard poststent balloon angioplasty may be associated with additional risks in patients with acceptable angiographic results, without additional post–carotid artery stent placement (CAS) angioplasty.

To evaluate the safety and efficacy of standard poststent angioplasty versus selective poststent angioplasty, we conducted a systematic review and meta-analysis and analyzed outcomes by a series that performed standard poststent balloon angioplasty per protocol on all patients versus those that performed selective poststent balloon angioplasty on only a subset of patients.

MATERIALS AND METHODS

Study Selection

A comprehensive review of the literature was performed by using the keywords "carotid stenosis," "carotid artery disease," "revascularization," "carotid," "stent," "angioplasty," and "endarterectomy" in both "AND" and "OR" combinations to search PubMed, Ovid MEDLINE, Ovid EMBASE, Scopus, and the Web of Science. Inclusion criteria were the following: English language; >30 patients; studies published between January 2000 and January 2015; studies that performed poststent angioplasty regardless of patient selection for this procedure; and studies with adequate data on periprocedural and postprocedural complications, outcome and technical success, and primary patency. The exclusion criteria were the following: case reports; in vitro, cadaveric or animal studies; studies with no poststent angioplasty; review articles, guidelines, and technical notes. In case of any inconsistencies or differences with regard to study inclusion/exclusion into the meta-analysis, the senior author decided on inclusion or exclusion (G.L.).

The electronic search was supplemented by contacting experts in the field and reviewing the bibliographies of included studies for relevant publications. Abstracts, methods, results, figures, and tables of full text for detailed review were searched by 2 independent reviewers (neurosurgeon O.P. and radiologist W.B.) for data on poststent balloon angioplasty selection, technical success, long-term primary patency, procedure-related morbidity and mortality, and possible selection-related complications such as periprocedural hypotension and bradycardia. The reference lists of retrieved articles were also screened for additional studies. Furthermore, in case of multiple publications from the same institution and/or the same authors, only the most recent and updated study was considered to avoid inclusion of overlapping patients.

Definition of Treatment Groups

The objective of this study was to determine whether there was any difference in angiographic and clinical outcomes among series in which standard poststent angioplasty was performed and those in which poststent angioplasty was performed in only select cases. Studies were categorized as either a "standard poststent balloon angioplasty" series or a "selective poststent balloon angioplasty" series. Standard poststent balloon angioplasty series were defined as those in which poststent angioplasty was reportedly performed in all patients, whereas selective poststent balloon angioplasty series were defined as those in which poststent balloon angioplasty was performed in select cases (ie, residual stenosis, poor wall apposition, and so forth).

Data Abstraction

For each study, we extracted the following descriptive clinical and anatomic information: patient demographics, initial clinical status, and the type of patient selection for the poststent balloon angioplasty (standard versus selective). We studied the following outcomes: periprocedural stroke rates with differentiation of minor and major stroke, periprocedural TIA, procedure-related neurologic or cardiovascular morbidity and mortality, periprocedural myocardial infarction, bradycardia and hypotension rates in all patients distinguishing between hemodynamic changes requiring intervention, long-term stroke rate at last follow-up, long-term primary patency, and technical success. Periprocedural complications were defined as those occurring within 30 days of the carotid artery stent placement.

Statistical Analysis

We estimated from each study the cumulative incidence (event rate) and 95% confidence interval for each outcome. Event rates for each intervention were pooled in the meta-analysis across studies by using the random-effects model.[42] Consequently, there was no need for establishing a hierarchy of analyzed outcomes. Subgroup interactions were conducted by using an interaction test as described by Altman and Bland.[43] For all outcomes, we quantified between-study heterogeneity by calculating the I^2 statistics.[44,45] Anticipating heterogeneity between studies, we chose this model a priori because it incorporates within-study variance and between-study variance. We were unable to test for publication bias due to the noncomparative nature of these studies.

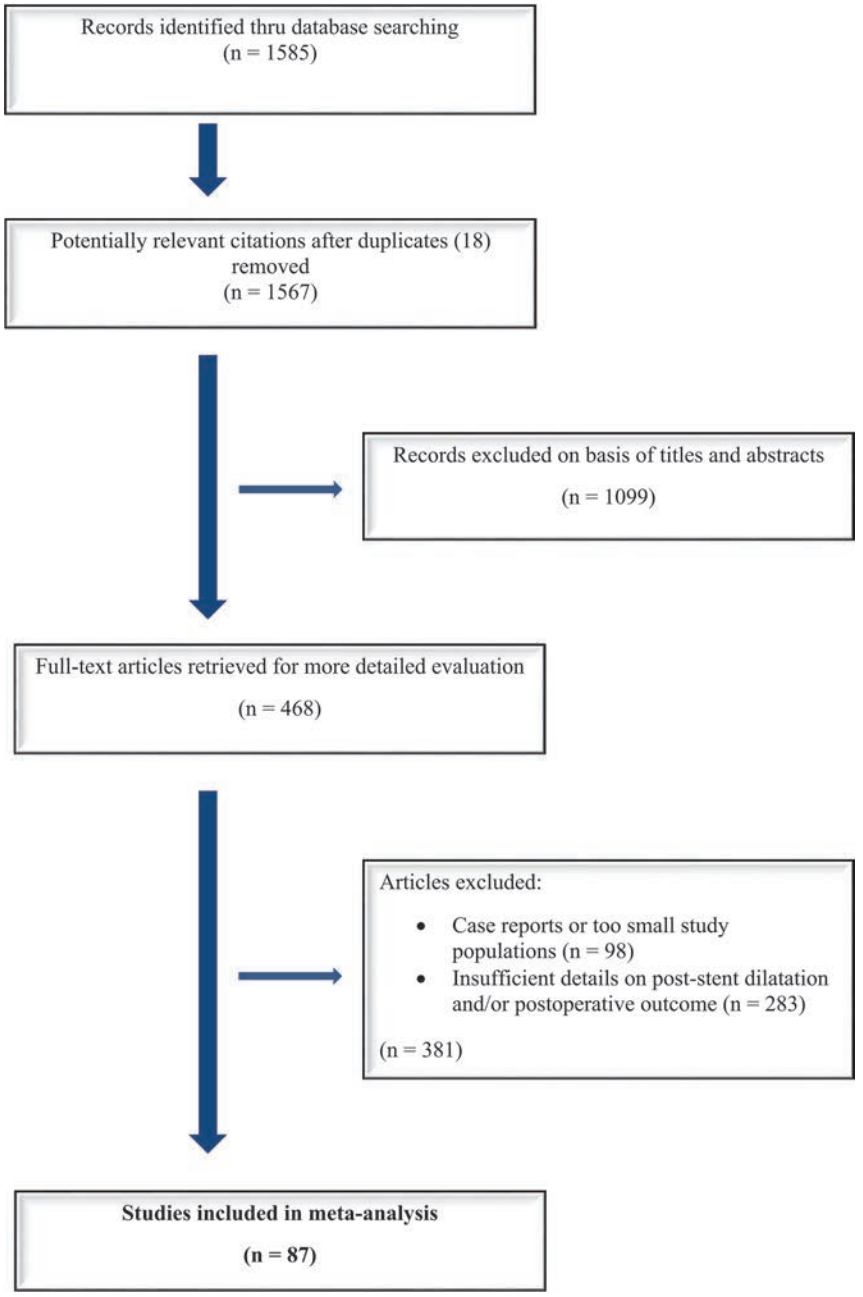

FIG 1. A flow diagram describing our comprehensive literature search.

RESULTS

Literature Review

An initial comprehensive literature search yielded 1585 articles. Eighteen studies were removed as duplicates. On the initial abstract and title review, 1099 were excluded because they were deemed not relevant to the current study. Four hundred sixty-eight studies were reviewed in additional detail; 283 studies were irrelevant because they lacked information about the use of poststent balloon angioplasty and/or postprocedural outcome/complications of patients. Ninety-eight additional studies were excluded because they were either case reports or had too few patients. In total, 87 studies with 19,684 patients with 20,378 carotid artery stenoses were included. Series reporting standard poststent angioplasty included 16,983 procedures (83.3%), and series reporting selective poststent angioplasty included 3395 procedures (16.7%). Sixty included studies had ≥100 patients. Eleven studies were prospective, and 76 were retrospective. Data are summarized in On-line Table 1. Methodologic characteristics of included studies are listed in On-line Table 2. A flow diagram describing our literature search process is provided in Fig 1.

Complication Rates by Type of Poststent Angioplasty

There were no statistically significant differences in any of the periprocedural and long-term complication rates by type of poststent angioplasty. Studies reporting selective poststent balloon angioplasty had similar rates of periprocedural stroke (2.3%; 95% CI, 1.8%–3.0%) compared with those reporting standard poststent balloon angioplasty (2.6%; 95% CI, 2.2%–3.1%) ($P = .36$). The same was true for long-term stroke rates (1.3% versus 1.6%, $P = .49$). Major stroke rates were similar in the selective poststent angioplasty group compared with the standard poststent angioplasty group (1.2% versus 1.0%, $P = .44$). There was no difference in minor stroke rates in the selective poststent angioplasty group (1.3% versus 1.7%, $P = .19$). There was no difference in periprocedural TIA rates either (1.7% versus 2.2%, $P = .43$). The periprocedural myocardial infarction rate was 0.6% (95% CI, 0.4%–1.1%) in the selective poststent angioplasty group versus 0.7% (95% CI, 0.5%–1.1%) in the standard poststent angioplasty group ($P = .66$). These data are summarized in On-line Table 3.

Periprocedural Hemodynamic Changes by Type of Poststent Angioplasty

Studies reporting selective poststent balloon angioplasty had significantly higher rates of bradycardia/hypotension (25.3%; 95% CI, 16.9%–36.3%) compared with those undergoing standard poststent angioplasty (13.3%; 95% CI, 8.0%–21.4%) ($P = .04$). The same was true for bradycardia/hypotension rates requiring interventions (18.7% versus 8.6%, $P = .01$). Data are summarized in On-line Table 3.

Angiographic Long-Term Results by Type of Poststent Angioplasty

There were no statistically significant differences in any of the long-term primary patency rates or technical success by type of

poststent angioplasty. Studies reporting selective poststent angioplasty had similar long-term primary patency rates (94.3%; 95% CI, 90.7%–96.6%) compared with those undergoing standard poststent angioplasty (94.5%; 95% CI, 92.5%–95.9%) ($P = .93$). Technical success was 98.7% (95% CI, 97.1%–99.5%) in the selective poststent angioplasty group versus 99.0% (95% CI, 98.6%–99.3%) in the standard poststent angioplasty group ($P = .61$). These data are summarized in On-line Table 3.

Study Heterogeneity and Characteristics

Significant heterogeneity (I^2 value $> 50\%$ and P value for the Cochrane Q test $< .05$) was noted in the analyses of 2 outcomes: bradycardia/hypotension and bradycardia/hypotension requiring intervention. Therefore, confidence in a pooled summary estimate for these 2 outcomes is limited. I^2 values are summarized in On-line Table 3. Methodologic characteristics of included studies are listed in On-line Table 2.

DISCUSSION

This systematic review and meta-analysis of 87 studies with 19,684 patients reporting either selective and standard poststent balloon angioplasty following carotid artery stent placement demonstrated no difference in clinical or angiographic outcomes in the CAS treatment with selective or standard poststent balloon angioplasty. In our study, we also found that both selective and standard poststent angioplasty groups had very high technical success rates of >98% and very low procedure-related mortality rates of 0.9%. Furthermore, there were no statistically significant differences between both groups in the incidence of restenosis or in procedure-related complication rates. Last, despite the selective poststent balloon angioplasty being associated with higher rates of periprocedural bradycardia/hypotension events, there was a very slight trend toward lower rates of periprocedural TIAs in these patients. These findings are important because they suggest that standard poststent angioplasty is not required during carotid stent placement. The similar rates of primary patency between groups suggest that the addition of standard poststent angioplasty does not provide any definite benefit.

Comparisons of clinical and angiographic outcomes between standard and selective poststent dilations in the literature are limited largely due to the small sizes of most case series. Numerous transcranial Doppler studies[14,15,46] demonstrate the presence of emboli with each passage across a stenosis with a guidewire, embolic protection device, balloon, or stent, with the highest potential for embolization occurring during poststent dilation when the balloon pushes the stent struts against the atheromatous plaque. Ackerstaff et al[47] reported in a series of 550 patients that multiple microemboli (>5 showers) at poststent angioplasty were independently associated with neurologic deficits. While our study found no statistically significant differences between the selective and the standard poststent angioplasty groups in terms of risk of stroke and TIA, the standard poststent angioplasty producing no benefit in primary patency suggests that this additional procedure may not always be necessary.

There has been considerable debate in the literature with regard to hemodynamic depression as a possible predictor of adverse events. Some studies[16,17,19,48] suggested that hypotension may result in a greater incidence of periprocedural complications, and even death. To our knowledge, in the largest study to date of 103 patients evaluating the effect of poststent ballooning on hemodynamic stability during and after carotid stent placement, Qazi et al[19] demonstrated that poststent balloon angioplasty was a significant predictor of hemodynamic depression (OR, 3.8; 95% CI, 1.3–11; $P < .01$) with increased risk of major adverse cardiovascular events. Gupta et al[16] showed that patients with persistent hypotension are at a higher risk of developing an adverse clinical event such as stroke or death after CAS. On the other hand, our study found higher rates of bradycardia/hypotension in patients treated with selective poststent angioplasty compared with standard poststent angioplasty; however, there was no impact on procedure-related complications. The reasons behind this surprising finding in our study are not known. Presumably, patients who undergo selective post-CAS dilation are more likely to have rigid stenoses or insufficient alignment of the stent with the vessel wall compared with those undergoing standard post-CAS angioplasty. Consequently, selective post-CAS dilation is then performed in these cases. During this procedure, relevant hemodynamic events such as bradycardia and/or hypotension can occur, reflecting forced opening of the rigid stenosis.

Limitations

We acknowledge that our meta-analysis has several limitations. Studies reporting only carotid artery stent placement without subsequent angioplasty were excluded. With this design, no comparison with a group without poststent dilation could be performed. There was a paucity of studies comparing outcomes of patients who received no poststent angioplasty and those who did. Our results should not be interpreted as saying that poststent angioplasty is ineffective because it is likely useful on a case-by-case basis. Rather, our results should be interpreted to say that there is no difference in angiographic and clinical outcomes among patients undergoing standard poststent angioplasty and those undergoing selective poststent angioplasty.

Ecologic bias (eg, comparisons are made across studies and not within studies), the possibility of publication bias, and statistical heterogeneity are important limitations that affect inferences derived from this study. None of the included studies were randomized or included control groups. There was no detailed information regarding the indications for selective poststent angioplasty. Similarly, there was no information about residual stent narrowing before performing balloon angioplasty. However, given the contemporary and widely accepted literature evidence for treatment of carotid artery disease, all included studies most likely had similar strict indications for carotid artery stent placement.

CONCLUSIONS

This meta-analysis of >87 series reporting selective and standard poststent balloon angioplasty following carotid artery stent placement demonstrated that both standard and selective approaches were associated with low rates of procedure-related neurologic or cardiovascular morbidity and high rates of long-term primary patency of >94%. There were no statistically

significant differences in clinical or angiographic outcomes between series reporting standard and selective poststent angioplasty. Comparative prospective studies are needed to confirm our findings.

Disclosures: Giuseppe Lanzino—*UNRELATED*: *Consultancy*: Covidien/Medtronic.*
*Money paid to the institution.

REFERENCES

1. Ricotta JJ 2nd, Piazza M. **Carotid endarterectomy or carotid artery stenting? Matching the patient to the intervention.** *Perspect Vasc Surg Endovasc Ther* 2010;22:124–36 CrossRef Medline
2. Ederle J, Bonati LH, Dobson J, et al; CAVATAS Investigators**. Endovascular treatment with angioplasty or stenting versus endarterectomy in patients with carotid artery stenosis in the Carotid and Vertebral Artery Transluminal Angioplasty Study (CAVATAS): long-term follow-up of a randomised trial.** *Lancet Neurol* 2009;8:898–907 CrossRef Medline
3. Ederle J, Dobson J, Featherstone RL, et al; International Carotid Stenting Study investigators. **Carotid artery stenting compared with endarterectomy in patients with symptomatic carotid stenosis (International Carotid Stenting Study): an interim analysis of a randomised controlled trial.** *Lancet* 2010;375:985–97 CrossRef Medline
4. Yadav JS, Wholey MH, Kuntz RE, et al; Stenting and Angioplasty with Protection in Patients at High Risk for Endarterectomy Investigators. **Protected carotid-artery stenting versus endarterectomy in high-risk patients.** *N Engl J Med* 2004;351:1493–501 CrossRef Medline
5. Brott TG, Hobson RW 2nd, Howard G, et al; CREST Investigators. **Stenting versus endarterectomy for treatment of carotid-artery stenosis.** *N Engl J Med* 2010;363:11–23 CrossRef Medline
6. North American Symptomatic Carotid Endarterectomy Trial Collaborators. **Beneficial effect of carotid endarterectomy in symptomatic patients with high-grade carotid stenosis.** *N Engl J Med* 1991;325:445–53 CrossRef Medline
7. Kachel R. **Results of balloon angioplasty in the carotid arteries.** *J Endovasc Surg* 1996;3:22–30 Medline
8. Gil-Peralta A, Mayol A, Marcos JR, et al. **Percutaneous transluminal angioplasty of the symptomatic atherosclerotic carotid arteries: results, complications, and follow-up.** *Stroke* 1996;27:2271–73 CrossRef Medline
9. Kerber CW, Cromwell LD, Loehden OL. **Catheter dilatation of proximal carotid stenosis during distal bifurcation endarterectomy.** *AJNR Am J Neuroradiol* 1980;1:348–49 Medline
10. Ferguson GG, Eliasziw M, Barr HW, et al. **The North American Symptomatic Carotid Endarterectomy Trial: surgical results in 1415 patients.** *Stroke* 1999;30:1751–58 CrossRef Medline
11. Phatouros CC, Higashida RT, Malek AM, et al. **Carotid artery stent placement for atherosclerotic disease: rationale, technique, and current status.** *Radiology* 2000;217:26–41 CrossRef Medline
12. Mathur A, Dorros G, Iyer SS, et al. **Palmaz stent compression in patients following carotid artery stenting.** *Cathet Cardiovasc Diag* 1997;41:137–40 Medline
13. Martin JB, Pache JC, Treggiari-Venzi M, et al. **Role of the distal balloon protection technique in the prevention of cerebral embolic events during carotid stent placement.** *Stroke* 2001;32:479–84 Medline
14. Manninen HI, Räsänen HT, Vanninen RL, et al. **Stent placement versus percutaneous transluminal angioplasty of human carotid arteries in cadavers in situ: distal embolization and findings at intravascular US, MR imaging and histopathologic analysis.** *Radiology* 1999;212:483–92 CrossRef Medline
15. Vos JA, van den Berg JC, Ernst SM, et al. **Carotid angioplasty and stent placement: comparison of transcranial Doppler US data and clinical outcome with and without filtering cerebral protection devices in 509 patients.** *Radiology* 2005;234:493–99 CrossRef Medline
16. Gupta R, Abou-Chebl A, Bajzer CT, et al. **Rate, predictors, and consequences of hemodynamic depression after carotid artery stenting.** *J Am Coll Cardiol* 2006;47:1538–43 CrossRef Medline
17. Howell M, Krajcer Z, Dougherty K, et al. **Correlation of periprocedural systolic blood pressure changes with neurological events in high-risk carotid stent patients.** *J Endovasc Ther* 2002;9:810–16 CrossRef Medline
18. Park BD, Divinagracia T, Madej O, et al. **Predictors of clinically significant postprocedural hypotension after carotid endarterectomy and carotid angioplasty with stenting.** *J Vasc Surg* 2009;50:526–33 CrossRef Medline
19. Qazi U, Obeid TE, Enwerem N, et al. **The effect of ballooning following carotid stent deployment on hemodynamic stability.** *J Vasc Surg* 2014;59:756–60 CrossRef Medline
20. Ghandehari K, Edraki K, Karimi M, et al. **Complications of angioplasty and stenting of cervicocerebral arteries in Iran.** *Asian Cardiovasc Thorac Ann* 2010;18:49–53 CrossRef Medline
21. Ielasi A, Latib A, Godino C, et al. **Clinical outcomes following protected carotid artery stenting in symptomatic and asymptomatic patients.** *J Endovasc Ther* 2010;17:298–307 CrossRef Medline
22. Micari A, Stabile E, Cremonesi A, et al. **Carotid artery stenting in octogenarians using a proximal endovascular occlusion cerebral protection device: a multicenter registry.** *Catheter Cardiovasc Interv* 2010;76:9–15 CrossRef Medline
23. Montorsi P, Galli S, Ravagnani P, et al. **Randomized trial of predilation versus direct stenting for treatment of carotid artery stenosis.** *Int J Cardiol* 2010;138:233–38 CrossRef Medline
24. Stabile E, Salemme L, Sorropago G, et al. **Proximal endovascular occlusion for carotid artery stenting: results from a prospective registry of 1,300 patients.** *J Am Coll Cardiol* 2010;55:1661–67 CrossRef Medline
25. Almekhlafi MA, Couillard PL, Pandya A, et al. **Outcomes after carotid angioplasty and stenting in symptomatic octogenarians.** *Can J Neurol Sci* 2011;38:446–51 CrossRef Medline
26. Satya K, Dougherty K, Lee VV, et al. **Determinants and outcomes of asystole during carotid artery stenting.** *J Endovasc Ther* 2011;18:513–17 CrossRef Medline
27. Kimiagar I, Gur AY, Auriel E, et al. **Long-term follow-up of patients after carotid stenting with or without distal protective device in a single tertiary medical center.** *Vasc Endovasc Surg* 2012;46:536–41 CrossRef Medline
28. Mazzaccaro D, Occhiuto MT, Stegher S, et al. **Long-term results of carotid artery stenting in patients 80 years and older.** *Perspect Vasc Surg Endovasc Ther* 2012;24:49–54 CrossRef Medline
29. Mohammadian R, Sohrabi B, Mansourizadeh R, et al. **Unprotected carotid artery stenting: complications in 6 months follow-up.** *Neuroradiology* 2012;54:225–30 CrossRef Medline
30. Dumont TM, Wach MM, Mokin M, et al. **Perioperative complications after carotid artery stenting: a contemporary experience from the University at Buffalo neuroendovascular surgery team.** *Neurosurgery* 2013;73:689–93; discussion 693–94 CrossRef Medline
31. Lago A, Parkhutik V, Tembl JI, et al. **Diabetes does not affect outcome of symptomatic carotid stenosis treated with endovascular techniques.** *Eur Neurol* 2013;69:263–69 CrossRef Medline
32. Ullery BW, Orlova K, Shang EK, et al. **Results of carotid angioplasty and stenting are equivalent for critical versus high-grade lesions in patients deemed high risk for carotid endarterectomy.** *J Surg Res* 2013;185:21–26 CrossRef Medline
33. Biggs NG, Rangarajan S, McClure DN. **Has carotid artery stenting found its place? A 10-year regional centre perspective.** *ANZ J Surg* 2016;86:179–83 CrossRef Medline
34. Hernández-Fernández F, Parrilla G, Garcia-Villalba B, et al. **Comparison between proximal versus distal protection devices in 287 cases of carotid revascularization using angioplasty and stenting: periprocedure complications, morbidity, and mortality.** *Cardiovasc Intervent Radiol* 2014;37:639–45 CrossRef: Medline

35. Morgan CE, Lee CJ, Chin JA, et al. **High-risk anatomic variables and plaque characteristics in carotid artery stenting.** *Vasc Endovascular Surg* 2014;48:452–59 CrossRef Medline
36. Cohen JE, Gomori JM, Itshayek E, et al. **Ischemic complications after tailored carotid artery stenting in different subpopulations with high-grade stenosis: feared but rare.** *J Clin Neurosci* 2015;22:189–94 CrossRef Medline
37. Ogata A, Sonobe M, Kato N, et al. **Carotid artery stenting without post-stenting balloon dilatation.** *J Neurointerv Surg* 2014;6:517–20 CrossRef Medline
38. Oteros Fernandez R, Jimenez-Gomez E, Bravo-Rodriguez F, et al. **Unprotected carotid artery stenting in symptomatic patients with high-grade stenosis: results and long-term follow-up in a single-center experience.** *AJNR Am J Neuroradiol* 2012;33:1285–91 CrossRef Medline
39. Tallarita T, Rabinstein AA, Cloft H, et al. **Are distal protection devices 'protective' during carotid angioplasty and stenting?** *Stroke* 2011;42:1962–66 CrossRef Medline
40. Mansour OY, Weber J, Niesen W, et al. **Carotid angioplasty and stenting without protection devices: safety and efficacy concerns–single center experience.** *Clin Neuroradiol* 2011;21:65–73 CrossRef Medline
41. González A, Gil-Peralta A, Mayol A, et al. **Internal carotid artery stenting in patients with near occlusion: 30-day and long-term outcome.** *AJNR Am J Neuroradiol* 2011;32:252–58 CrossRef Medline
42. DerSimonian R, Laird N. **Meta-analysis in clinical trials.** *Control Clin Trials* 1986;7:177–88 CrossRef Medline
43. Altman DG, Bland JM. **Interaction revisited: the difference between two estimates.** *BMJ* 2003;326:219 CrossRef Medline
44. Higgins JP, Thompson SG, Deeks JJ, et al. **Measuring inconsistency in meta-analyses.** *BMJ* 2003;327:557–60 CrossRef Medline
45. Higgins JP, Thompson SG. **Quantifying heterogeneity in a meta-analysis.** *Stat Med* 2002;21:1539–58 CrossRef Medline
46. Rubartelli P, Brusa G, Arrigo A, et al. **Transcranial Doppler monitoring during stenting of the carotid bifurcation: evaluation of two different distal protection devices in preventing embolization.** *J Endovasc Ther* 2006;13:436–42 CrossRef Medline
47. Ackerstaff RG, Suttorp MJ, van den Berg JC, et al; Antonius Carotid Endarterectomy, Angioplasty, and Stenting Study Group. **Prediction of early cerebral outcome by transcranial Doppler monitoring in carotid bifurcation angioplasty and stenting.** *J Vasc Surg* 2005;41:618–24 CrossRef Medline
48. Park B, Shapiro D, Dahn M, et al. **Carotid artery angioplasty with stenting and postprocedure hypotension.** *Am J Surg* 2005;190:691–95 CrossRef Medline
49. Morrish W, Grahovac S, Douen A, et al. **Intracranial hemorrhage after stenting and angioplasty of extracranial carotid stenosis.** *AJNR Am J Neuroradiol* 2000;21:1911–16 Medline
50. Ahmadi R, Schillinger M, Lang W, et al. **Carotid artery stenting in older patients: is age a risk factor for poor outcome?** *J Endovasc Ther* 2002;9:559–65 CrossRef Medline
51. Criado FJ, Lingelbach JM, Ledesma DF, et al. **Carotid artery stenting in a vascular surgery practice.** *J Vasc Surg* 2002;35:430–34 CrossRef Medline
52. Hobson RW 2nd, Lal BK, Chakhtoura EY, et al. **Carotid artery closure for endarterectomy does not influence results of angioplasty-stenting for restenosis.** *J Vasc Surg* 2002;35:435–38 CrossRef Medline
53. Kao HL, Lin LY, Lu CJ, et al. **Long-term results of elective stenting for severe carotid artery stenosis in Taiwan.** *Cardiology* 2002;97:89–93 CrossRef Medline
54. Antonius Carotid Endaterectomy, Angioplasty, and Stenting Study Group. **Transcranial Doppler monitoring in angioplasty and stenting of the carotid bifurcation.** *J Endovasc Ther* 2003;10:702–10 CrossRef Medline
55. Cernetti C, Reimers B, Picciolo A, et al. **Carotid artery stenting with cerebral protection in 100 consecutive patients: immediate and two-year follow-up results.** *Ital Heart J* 2003;4:695–700 Medline
56. Cremonesi A, Manetti R, Setacci F, et al. **Protected carotid stenting: clinical advantages and complications of embolic protection devices in 442 consecutive patients.** *Stroke* 2003;34:1936–41 CrossRef Medline
57. Tsuura M, Terada T, Matsumoto H, et al. **Clinical results of stenting for cervical internal carotid stenoses.** *Interv Neuroradiol* 2003;9:133–36 Medline
58. Wholey MH, Wholey MH, Tan WA, et al. **A comparison of balloon-mounted and self-expanding stents in the carotid arteries: immediate and long-term results of more than 500 patients.** *J Endovasc Ther* 2003;10:171–81 CrossRef Medline
59. Eskandari MK, Longo GM, Vijungco JD, et al. **Does carotid stenting measure up to endarterectomy? A vascular surgeon's experience.** *Arch Surg* 2004;139:734–38 CrossRef Medline
60. Faries PL, Dayal R, Clair DG, et al. **Continuity in the treatment of carotid artery disease: results of a carotid stenting program initiated by vascular surgeons.** *Ann Vasc Surg* 2004;18:669–76 CrossRef Medline
61. Kastrup A, Schulz JB, Raygrotzki S, et al. **Comparison of angioplasty and stenting with cerebral protection versus endarterectomy for treatment of internal carotid artery stenosis in elderly patients.** *J Vasc Surg* 2004;40:945–51 CrossRef Medline
62. Sadato A, Satow T, Ishii A, et al. **Use of a large angioplasty balloon for predilation is a risk factor for embolic complications in protected carotid stenting.** *Neurol Med Chir (Tokyo)* 2004;44:337–42; discussion 343 CrossRef Medline
63. Bonaldi G, Aiazzi L, Baruzzi F, et al. **Angioplasty and stenting of the cervical carotid bifurcation under filter protection: a prospective study in a series of 53 patients.** *J Neuroradiol* 2005;32:109–17 CrossRef Medline
64. Cayne NS, Faries PL, Trocciola SM, et al. **Carotid angioplasty and stent-induced bradycardia and hypotension: impact of prophylactic atropine administration and prior carotid endarterectomy.** *J Vasc Surg* 2005;41:956–61 CrossRef Medline
65. Coppi G, Moratto R, Silingardi R, et al. **PRIAMUS: proximal flow blockage cerebral protection during carotid stenting—results from a multicenter Italian registry.** *J Cardiovasc Surg (Torino)* 2005;46:219–27 Medline
66. Eskandari MK, Longo GM, Matsumura JS, et al. **Carotid stenting done exclusively by vascular surgeons: first 175 cases.** *Ann Surg* 2005;242:431–36; discussion 436–38 Medline
67. Kadkhodayan Y, Derdeyn CP, Cross DT 3rd, et al. **Procedure complications of carotid angioplasty and stent placement without cerebral protection devices.** *Neurosurg Focus* 2005;18:e1 Medline
68. Li SM, Li D, Ling F, et al. **Carotid artery stenting: experience of a single institute in China.** *Interv Neuroradiol* 2005;11:205–12 Medline
69. Lin PH, Bush RL, Peden EK, et al. **Carotid artery stenting with neuroprotection: assessing the learning curve and treatment outcome.** *Am J Surg* 2005;190:850–57 CrossRef Medline
70. Longo GM, Kibbe MR, Eskandari MK. **Carotid artery stenting in octogenarians: is it too risky?** *Ann Vasc Surg* 2005;19:812–16 CrossRef Medline
71. Reimers B, Sievert H, Schuler GC, et al. **Proximal endovascular flow blockage for cerebral protection during carotid artery stenting: results from a prospective multicenter registry.** *J Endovasc Ther* 2005;12:156–65 CrossRef Medline
72. Chaer RA, Derubertis BG, Trocciola SM, et al. **Safety and efficacy of carotid angioplasty and stenting in high-risk patients.** *Am Surg* 2006;72:694–98; discussion 698–99 Medline
73. Faries PL, Trocciola SM, De Rubertis B, et al. **Hemodynamic instability after carotid artery angioplasty and stening is associated with increased age and female gender.** *Vas Dis Management* 2006;3:200–05
74. Gröschel K, Ernemann U, Schulz JB, et al. **Statin therapy at carotid angioplasty and stent placement: effect on procedure-related**

stroke, myocardial infarction, and death. *Radiology* 2006;240:145–51 CrossRef Medline
75. Halabi M, Gruberg L, Pitchersky S, et al. **Carotid artery stenting in surgical high-risk patients.** *Catheter Cardiovasc Interv* 2006;67:513–18 CrossRef Medline
76. Kwon BJ, Han MH, Kang HS, et al. **Protection filter-related events in extracranial carotid artery stenting: a single-center experience.** *J Endovasc Ther* 2006;13:711–22 CrossRef Medline
77. Nano G, Dalainas I, Bianchi P, et al. **Ballooning-induced bradycardia during carotid stenting in primary stenosis and restenosis.** *Neuroradiology* 2006;48:533–36 CrossRef Medline
78. Cotroneo AR, Iezzi R. **Cutting balloon angioplasty (CBA) versus conventional balloon angioplasty (PTA) in the pre-dilatation of carotid artery stenosis: our preliminary experience.** *Cardiovasc Intervent Radiol* 2007;30:1210–17 CrossRef Medline
79. Criado E, Fontcuberta J, Orgaz A, et al. **Transcervical carotid stenting with carotid artery flow reversal: 3-year follow-up of 103 stents.** *J Vasc Surg* 2007;46:864–69 CrossRef Medline
80. Kawarada O, Yokoi Y, Takemoto K, et al. **Double-wire technique in balloon-protected carotid artery stenting.** *J Interv Cardio* 2007;20:55–62 CrossRef Medline
81. Lin PH, Zhou W, Kougias P, et al. **Factors associated with hypotension and bradycardia after carotid angioplasty and stenting.** *J Vasc Surg* 2007;46:846–53; discussion 853–54 CrossRef Medline
82. Maynar M, Baldi S, Rostagno R, et al. **Carotid stenting without use of balloon angioplasty and distal protection devices: preliminary experience in 100 cases.** *AJNR Am J Neuroradiol* 2007;28:1378–83 CrossRef Medline
83. Van der Heyden J, Suttorp MJ, Bal ET, et al. **Staged carotid angioplasty and stenting followed by cardiac surgery in patients with severe asymptomatic carotid artery stenosis: early and long-term results.** *Circulation* 2007;116:2036–42 CrossRef Medline
84. Younis GA, Gupta K, Mortazavi A, et al. **Predictors of carotid stent restenosis.** *Catheter Cardiovasc Interv* 2007;69:673–82 CrossRef Medline
85. AbuRahma AF, Bates MC, Eads K, et al. **Safety and efficacy of carotid angioplasty/stenting in 100 consecutive high surgical risk patients: immediate and long-term follow-up.** *Vasc Endovasc Surg* 2008;42:433–39 CrossRef Medline
86. Bussière M, Pelz DM, Kalapos P, et al. **Results using a self-expanding stent alone in the treatment of severe symptomatic carotid bifurcation stenosis.** *J Neurosurg* 2008;109:454–60 CrossRef Medline
87. Bussière M, Lownie SP, Lee D, et al. **Hemodynamic instability during carotid artery stenting: the relative contribution of stent deployment versus balloon dilation.** *J Neurosurg* 2009;110:905–12 CrossRef Medline
88. Buszman P, Debiński M, Gruszka A, et al. **Early and late outcomes of percutaneous transluminal angioplasty of cephalad arteries.** *Kardiol Pol* 2008;66:233–42, discussion 243 Medline
89. Castriota F, de Campos Martins EC, Setacci C, et al. **Cutting balloon angioplasty in percutaneous carotid interventions.** *J Endovasc Ther* 2008;15:655–62 CrossRef Medline
90. Cieri E, De Rango P, Maccaroni MR, et al. **Is haemodynamic depression during carotid stenting a predictor of peri-procedural complications?** *Eur J Vasc Endovasc Surg* 2008;35:399–404 CrossRef Medline
91. Diehm N, Katzen BT, Dick F, et al. **Influence of stent type on hemodynamic depression after carotid artery stent placement.** *J Vasc Interv Radiol* 2008;19:23–30 CrossRef Medline
92. Henry M, Henry I, Polydorou A, et al. **Carotid angioplasty and stenting in octogenarians: is it safe?** *Catheter Cardiovasc Interv* 2008;72:309–17 CrossRef Medline
93. Pieniazek P, Musialek P, Kablak-Ziembicka A, et al. **Carotid artery stenting with patient- and lesion-tailored selection of the neuroprotection system and stent type: early and 5-year results from a prospective academic registry of 535 consecutive procedures (TARGET-CAS).** *J Endovasc Ther* 2008;15:249–62 CrossRef Medline
94. Roffi M, Greutmann M, Schwarz U, et al. **Flow impairment during protected carotid artery stenting: impact of filter device design.** *J Endovasc Ther* 2008;15:103–09 CrossRef Medline
95. Velez CA, White CJ, Reilly JP, et al. **Carotid artery stent placement is safe in the very elderly (> or =80 years).** *Catheter Cardiovasc Interv* 2008;72:303–08 CrossRef Medline
96. Brown KE, Usman A, Kibbe MR, et al. **Carotid stenting using tapered and nontapered stents: associated neurological complications and restenosis rates.** *Ann Vasc Surg* 2009;23:439–45 CrossRef Medline
97. Goldstein LJ, Khan HU, Sambol EB, et al. **Carotid artery stenting is safe and associated with comparable outcomes in men and women.** *J Vasc Surg* 2009;49:315–23; discussion 323–24 CrossRef Medline
98. Simonetti G, Gandini R, Versaci F, et al. **Carotid artery stenting: findings based on 8 years' experience** [in English, Italian]. *Radiol Med* 2009;114:95–110 CrossRef Medline
99. Theron J, Venturi C, Reul J, et al. **Immediate and 30-day clinical outcome of patients treated with the TwinOne cerebral protection system: multicenter experience in 217 cases.** *Cardiovasc Intervent Radiol* 2009;32:1139–45 CrossRef Medline
100. Veselka J, Cerná D, Zimolová P, et al. **Feasibility, safety, and early outcomes of direct carotid artery stent implantation with use of the FilterWire EZ Embolic Protection System.** *Catheter Cardiovasc Interv* 2009;73:733–38 CrossRef Medline
101. Chung C, Cayne NS, Adelman MA, et al. **Improved hemodynamic outcomes with glycopyrrolate over atropine in carotid angioplasty and stenting.** *Perspect Vasc Surg Endovasc Ther* 2010;22:164–70 CrossRef Medline
102. Shabaneh B, Dougherty K, Hernandez E, et al. **Catheter aspiration thrombectomy during carotid stenting is safe and potentially efficacious: a pilot retrospective study.** *J Cardiovasc Surg (Torino)* 2010;51:865–72 Medline
103. Knur R. **Carotid artery stenting with distal filter protection: single-center experience in high-surgical-risk patients.** *Heart Vessels* 2011;26:125–30 CrossRef Medline
104. Mak CS, Chambers BR, Clark DJ, et al. **Multidisciplinary approach to carotid stenting.** *Intern Med J* 2011;41:789–94 CrossRef Medline
105. Mendiz OA, Sampaolesi AH, Londero HF, et al. **Initial experience with transradial access for carotid artery stenting.** *Vasc Endovasc Surg* 2011;45:499–503 CrossRef Medline
106. Rizwan Khalid M, Khalid F, Farooqui FA, et al. **Can experienced physicians with high peripheral interventional volume but low carotid artery stenting (CAS) volume achieve low complication rates during CAS?** *EuroIntervention* 2011;6:744–47 CrossRef Medline
107. Wu YM, Wong HF, Chen YL, et al. **Carotid stenting of asymptomatic and symptomatic carotid artery stenoses with and without the use of a distal embolic protection device.** *Acta Cardiol* 2011;66:453–58 CrossRef Medline
108. Harada K, Morioka J, Higa T, et al. **Significance of combining distal filter protection and a guiding catheter with temporary balloon occlusion for carotid artery stenting: clinical results and evaluation of debris capture.** *Ann Vasc Surg* 2012;26:929–36 CrossRef Medline
109. Moratto R, Veronesi J, Silingardi R, et al. **Urgent carotid artery stenting with technical modifications for patients with transient ischemic attacks and minor stroke.** *J Endovasc Ther* 2012;19:627–35 CrossRef Medline
110. Kessler I, Gory B, Macian F, et al. **Carotid artery stenting in patients with symptomatic carotid stenosis: a single-center series.** *J Neuroradiol* 2013;40:38–44 CrossRef Medline
111. Miyawaki S, Maeda K. **Surgical treatment for cervical carotid artery stenosis in the elderly: importance of perioperative management of ischemic cardiac complications.** *Neurol Med Chir (Tokyo)* 2014;54:120–25 CrossRef Medline
112. Shinozaki N, Ogata N, Ikari Y. **Plaque protrusion detected by intravascular ultrasound during carotid artery stenting.** *J Stroke Cerebrovasc Dis* 2014;23:2622–25 CrossRef Medline

Presurgical Brain Mapping of the Ventral Somatomotor Network in Patients with Brain Tumors Using Resting-State fMRI

N. Yahyavi-Firouz-Abadi, J.J. Pillai, M.A. Lindquist, V.D. Calhoun, S. Agarwal, R.D. Airan, B. Caffo, S.K. Gujar, and H.I. Sair

ABSTRACT

BACKGROUND AND PURPOSE: Resting-state fMRI readily identifies the dorsal but less consistently the ventral somatomotor network. Our aim was to assess the relative utility of resting-state fMRI in the identification of the ventral somatomotor network via comparison with task-based fMRI in patients with brain tumor.

MATERIALS AND METHODS: We identified 26 surgically naïve patients referred for presurgical fMRI brain mapping who had undergone both satisfactory ventral motor activation tasks and resting-state fMRI. Following standard preprocessing for task-based fMRI and resting-state fMRI, general linear model analysis of the ventral motor tasks and independent component analysis of resting-state fMRI were performed with the number of components set to 20, 30, 40, and 50. Visual overlap of task-based fMRI and resting-state fMRI at different component levels was assessed and categorized as full match, partial match, or no match. Rest-versus-task-fMRI concordance was calculated with Dice coefficients across varying fMRI thresholds before and after noise removal. Multithresholded Dice coefficient volume under the surface was calculated.

RESULTS: The ventral somatomotor network was identified in 81% of patients. At the subject level, better matches between resting-state fMRI and task-based fMRI were seen with an increasing order of components (53% of cases for 20 components versus 73% for 50 components). Noise-removed group-mean volume under the surface improved as component numbers increased from 20 to 50, though ANOVA demonstrated no statistically significant difference among the 4 groups.

CONCLUSIONS: In most patients, the ventral somatomotor network can be identified with an increase in the probability of a better match at a higher component number. There is variable concordance of the ventral somatomotor network at the single-subject level between resting-state and task-based fMRI.

ABBREVIATIONS: BOLD = blood oxygen level–dependent; ICA = independent component analysis; rs-fMRI = resting-state fMRI; tb-fMRI = task-based fMRI; VSMN = ventral somatomotor network; VUS = volume under the surface

Functional MRI is widely used as a noninvasive tool for presurgical localization of the eloquent cortex, typically involving somatomotor and language mapping. Mapping of these eloquent brain areas with fMRI correlates well with invasive methods such as intraoperative electrocortical stimulation[1] and can result in reduced surgical time, increased extent of resection, and decreased craniotomy size.[2] In addition, postoperative morbidity correlates with the distance of the resection margin from fMRI-identified eloquent cortex.[3] In current clinical practice, changes in blood oxygen level–dependent (BOLD) signal are measured across time as the patient performs a specific task (ie, task-based fMRI [tb-fMRI]).[4] These BOLD signal changes reflect characteristic hemodynamic responses to neural activity. However, tb-fMRI has several limitations. Primarily, accurate localization of function is dependent on the patient's cooperation and ability to

Received June 5, 2016; accepted after revision December 25.

From the Department of Radiology (N.Y.-F.-A.), Mid-Atlantic Permanente Medical Group of Kaiser Permanente, Kensington, Maryland; Division of Neuroradiology, (N.Y.-F.-A., J.J.P., S.A., R.D.A., S.K.G., H.I.S.), The Russell H. Morgan Department of Radiology and Radiological Sciences, Johns Hopkins University School of Medicine, Baltimore, Maryland; Department of Biostatistics (M.A.L., B.C.), Johns Hopkins University, Baltimore, Maryland; and The Mind Research Network (S.A., V.D.C.), Departments of Electrical and Computer Engineering, University of New Mexico, Albuquerque, New Mexico.

This work was supported in part by the Radiological Society of North America Research and Education Foundation–Carestream Health/RSNA Research Scholar Grant to H.I.S. (grant No. RSCH1420).

Previously presented in part at: Annual Meeting of the American Society of Neuroradiology and the Foundation of the ASNR Symposium, April 25–30, 2015; Chicago, Illinois.

Please address correspondence to Noushin Yahyavi-Firouz-Abadi, MD, Division of Neuroradiology, The Russell H. Morgan Department of Radiology and Radiological Sciences, Johns Hopkins University School of Medicine, 600 North Wolfe St, Phipps B-112, Baltimore, MD 21287; e-mail: nyahyavi@gmail.com; @nyahyavi

Indicates article with supplemental on-line table.

http://dx.doi.org/10.3174/ajnr.A5132

adequately perform the task, which can be an important limitation in those with physical or mental debilitation or those who cannot understand the instructions such as children. The patient must be awake and cooperative during the task; therefore, sedation cannot be used; this feature is a limitation in the pediatric population. Furthermore, due to the inherently low signal-to-noise ratio of this technique, long and repeated acquisitions are often required to ensure adequate data sampling for analysis.[5,6]

Resting state fMRI (rs-fMRI) is a promising method of assessing brain function that can overcome some of the limitations of tb-fMRI. In rs-fMRI, spontaneous fluctuations in BOLD signal are measured across time while no specific task is performed. Temporal correlations of these spontaneous fluctuations can be organized into spatially distinct intrinsic networks.[5] These networks are now described as resting-state networks, many of which have topography similar to that of networks engaged in sensory, motor, and cognitive tasks.[7] These intrinsic resting-state networks persist, though somewhat modified, in states of decreased awareness such as sleep[8] or sedation.[9] Rs-fMRI has thus gained interest as a potential viable alternative to tb-fMRI, especially in pediatric or cognitively/neurologically impaired patients. Multiple studies have investigated the potential role of rs-fMRI in presurgical mapping of somatomotor[5,10-12] and language[2,6,13] networks. In a limited number of subjects, moderate overlap between rs-fMRI and tb-fMRI was found for mapping of the motor cortex.[5,11,12] Furthermore, there is good qualitative concordance between intraoperative cortical stimulation and rs-fMRI in the localization of the eloquent motor cortex.[10] With quantitative analysis, rs-fMRI and tb-fMRI perform comparably, but the shortest distance to stimulation points is observed for tb-fMRI.[11] Rs-fMRI has been shown to identify a larger pattern of the motor network compared with tb-fMRI.[11,14] In addition, localization by rs-fMRI and tb-fMRI may include different parts of the sensorimotor network.[11,15] While the motor system at large has been the target of most prior investigations, distinct subnetworks of the motor network exist. We narrowed our focus to the ventral motor area, which largely reflects oral somatomotor function. Three recent studies evaluated the concordance of rs-fMRI and tb-fMRI in the localization of the face representation area of the primary motor cortex in addition to limb motor areas in a limited number of patients with a variety of brain lesions in different locations.[11,12,16]

To our knowledge, no study has specifically investigated the concordance between tb-fMRI activation and the rs-fMRI-derived ventral somatomotor network (VSMN) maps in a large cohort of patients with lesions close to or involving the VSMN. We hypothesized that the ventral motor network can be identified in patients with brain tumors and that there is good concordance with tb-fMRI with a tongue motor paradigm. In addition, we hypothesized that a higher number of components in independent component analysis (ICA) may yield a better concordance between rs-fMRI and tb-fMRI.

MATERIALS AND METHODS

Study Subjects

The institutional review board approved this retrospective study. Searching the Radiology Information Systems, we identified patients who underwent fMRI for presurgical brain mapping between January 1, 2009, and July 31, 2014. Fifty-eight patients underwent rs-fMRI in addition to tb-fMRI during the same imaging session. Seventeen patients had a prior history of a brain operation (including biopsy) and were excluded. One patient had imaging features characteristic of an arteriovenous malformation and was excluded. At the Johns Hopkins Hospital, tb-fMRI for presurgical mapping is tailored for each patient, predominantly based on the location of their tumor and the relation of eloquent regions along the expected surgical trajectory and in the immediate vicinity of the lesion. Among the remaining 40 patients, 26 with brain tumors involving or in close proximity to the ventral somatomotor network who had undergone both tb-fMRI for localization of the VSMN and rs-fMRI were included for final analysis (age range, 21–69 years; mean age, 43.6 years; 15 men and 11 women).

Brain Tumor Characterization

Tumor location, volume (in cubic millimeters), pathology, and World Health Organization histologic grade (when available) were recorded by a subspecialty board-certified neuroradiologist for each patient. Lesion volume was measured by manually drawing the ROI on FLAIR images in the Medical Image Processing, Analysis, and Visualization application software (MIPAV; National Institutes of Health, Bethesda, Maryland; http://mipav.cit.nih.gov). For high-grade brain tumors, we assessed the entire region of T2 signal abnormality, which represents a combination of infiltrative neoplasm and vasogenic edema.

MR Imaging

A 3T Tim Trio system (Siemens, Erlangen, Germany) with a 12-channel head matrix coil was used. Structural images included a 3D T1 sequence (TR = 2300 ms, TI = 900 ms, TE = 3.5 ms, flip angle = 9°, FOV = 24 cm, acquisition matrix = 256 × 256 × 176, section thickness = 1 mm) and a 2D T2 FLAIR sequence (TR = 9310 ms, TI = 2500 ms, TE = 116 ms, flip angle = 141°, FOV = 24 cm, acquisition matrix = 320 × 240 × 50, section thickness = 3 mm). Functional T2*-weighted BOLD images for both tb-fMRI and rs-fMRI were acquired by using 2D gradient-echo echo-planar imaging (TR = 2000 ms, TE = 30 ms, flip angle = 90°, FOV = 24 cm, acquisition matrix = 64 × 64 × 33, section thickness = 4 mm, section gap = 1 mm, interleaved acquisition). Instructions for rs-fMRI were the following: try to keep still, keep your eyes closed, and do not fall asleep. For rs-fMRI, 180 volumes were acquired (6 minutes).

Tongue Motor Task

The face representation area of the primary motor cortex was mapped by using the vertical tongue movement task as a robust and spatially extensive representative of the ventral/face motor network.[17,18] The duration of the task is 3 minutes and consists of 3 cycles of 30-second blocks of rest alternating with 30-second blocks of repetitive vertical tongue movement. For each patient, a board-certified neuroradiologist with experience in fMRI provided instructions and practice sessions on the tongue motor task outside the scanner. The quality of the tb-fMRI maps was monitored in real-time by the neuroradiologist monitoring the session. Per protocol, if real-time maps dem-

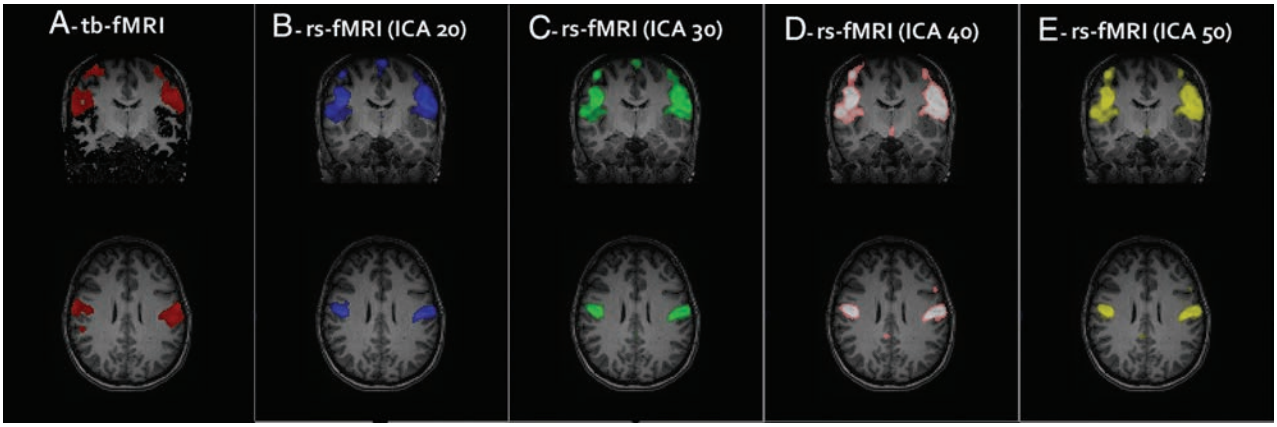

FIG 1. Task-based fMRI map demonstrating activation of the VSMN with the vertical tongue movement task in a single subject (*A*). Rs-fMRI maps with the best visual correlates to tb-fMRI at different ICA groups (*B–E*) were selected.

onstrated suboptimal activation or excessive noise, the task was repeated. Tasks were presented with the environment implemented in the Prism Acquire software (Prism Clinical Imaging, Elm Grove, Wisconsin). Only runs that met quantitative quality control criteria (<2-mm net head displacement along any axis) were considered.

Image Processing

fMRI data were processed by using Statistical Parametric Mapping, Version 8 (SPM8 software; http://www.fil.ion.ucl.ac.uk/spm/software/spm12) and custom Matlab (MathWorks, Natick Massachusetts) scripts. Processing of tb-fMRI included section-timing correction, motion correction, normalization to a Montreal Neurological Institute 152 template, and spatial smoothing included a 6-mm full width at half maximum Gaussian kernel.

For processing the rs-fMRI data, section-timing correction and motion correction were performed. The motion-correction step included registration of tb-fMRI and rs-fMRI to each other. The ArtRepair toolbox (http://cibsr.stanford.edu/tools/human-brain-project/artrepair-software.html)[19] was used to detect volumes with large shifts in global average signal intensity, which include contributions from scan-to-scan motion. The outlier volumes and additional volumes recommended for deweighting in ArtRepair were tagged for subsequent removal from analysis (ie, scrubbing). The rs-fMRI data were then linearly detrended. Rs-fMRI and T1-weighted images were coregistered and normalized to perform physiologic nuisance regression of rs-fMRI with the component-based noise-correction method.[20] The same transformation matrix was used for normalization between tb-fMRI and rs-fMRI to ensure that spatial comparison between these 2 was valid for each subject. Bandpass filtering from 0.01 to 0.1 Hz and smoothing were performed with a 6-mm full width at half maximum Gaussian kernel. At the end, previously tagged images by ArtRepair were scrubbed.

Statistical Analysis

Tb-fMRI Analysis. We used a general linear model analysis for tb-fMRI implemented in SPM8 with the canonical hemodynamic response function convolved with the boxcar function for each task with standard parameters previously described.[6] High-pass filtering was performed at the default setting to remove drift. The hemodynamic response function-convolved task vectors were input into a design matrix, and a contrast was created to target the associated parameter comparing the hemodynamic response function-weighted time engaged in the task with rest. The SPM t-contrast maps were generated without clustering because these activation maps were subsequently thresholded across multiple levels for comparison as previously described.[6] Activation maps were reviewed to ensure that ventral motor activation was present.

Rs-fMRI Analysis. Rs-fMRI was analyzed with the Group ICA of the fMRI Toolbox Software (GIFT; http://mialab.mrn.org/software/gift/). Independent component analysis was performed separately for each subject by using the InfoMax algorithm with ICASSO (http://research.ics.aalto.fi/ica/icasso/) set at 5 repeats,[21] including selection of the "best run" to ensure consistent estimates. ICA maps were generated for 20, 30, 40, and 50 components, designated here as ICA20, ICA30, ICA40, and ICA50, respectively. Following scrubbing, 1 subject had only slightly >50 volumes left; therefore, the maximum number of components was limited to 50. For each ICA group, the component that best represented the VSMN based on overlap with tb-fMRI was selected visually (Fig 1). Any component whose spatial map was specific and limited to the ventral perirolandic cortices corresponding to the tb-fMRI activation maps was considered a "full match." If the component included additional networks outside these regions, it was considered a "partial match," indicating that the VSMN was present but not separated from other networks. If no VSMN was identified, a "no match" designation was assigned to that ICA group for that subject. A mixed-effects logistic regression analysis was performed to see whether there was a significant increase in the probability of getting a full match as a function of the number of ICA components.

Comparison of tb-fMRI and rs-fMRI. The level of tb-fMRI T-map thresholding may affect the degree of rs-tb fMRI concordance. At low thresholds, there will be artificially high concordance due to the introduction of a higher percentage of voxels, many of which may not represent true activation but rather statistical noise that

exceeds this threshold. Although there are strategies to determine the level of optimum fMRI thresholding, there is no consensus for reproducible results at a subject level.[18] To minimize this issue, we used a multithresholding technique to compare concordance across a wide range of thresholds as previously described (Fig 2).[6,22] We calculated Dice coefficients as a quantitative measure of overlap across each threshold to generate a matrix of rs-versus-tb overlap (left map, Fig 3).[6] Dice coefficients vary between 0 and 1 and give an objective evaluation of similarity or concordance between 2 sets of data. At very low thresholds, high Dice coefficients result from overlap of random noise as can be seen in Fig 2. We used a previously described noise-removal method[6] briefly described here.

For calculation of noise, an ICA component representing the anterior ventricular signal was selected for each subject. After removing negative values, we normalized image maps in value from 0 to 1, and we subsequently used multiple thresholds of this normalized map to calculate Dice coefficients between ventricular "noise" and task maps (middle map, Fig 3). The resultant noise-versus-task Dice map was subtracted from the resting-versus-task Dice map (right map, Fig 3).[6] Noise-corrected resting state-versus-task-based Dice map volume under the surface (VUS) was calculated across different ICA orders. The VUS measurement collapses this multithresholded dice map into a single variable that can be used as a metric; the VUS is equivalent to the area under the curve in a 2D graph (such as a receiver operating characteristic curve); however, because the multithresholded dice map has 3 dimensions (the rs-fMRI threshold, the task-threshold, and value), a volume under the surface is computed. One-way ANOVA was performed to determine significant differences in VUS across the 4 ICA orders. Maximum Dice coefficient values at the group level and subject level were calculated.

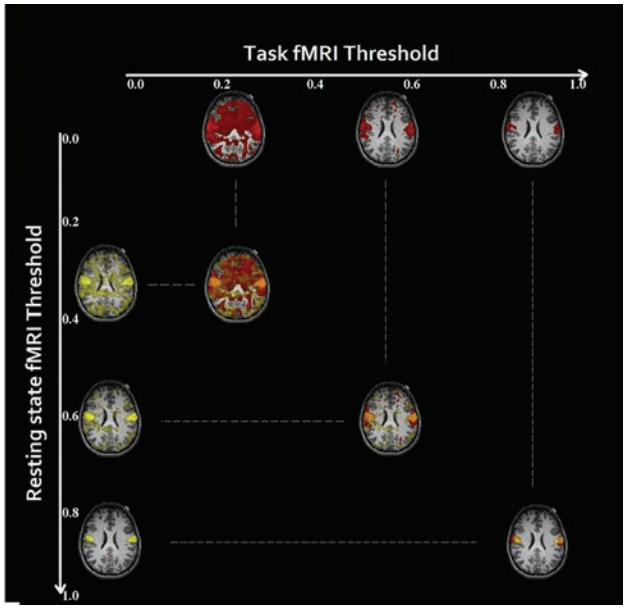

FIG 2. Rs-fMRI ICA maps (yellow) and Tb-fMRI T-maps (red) were thresholded, and 100 threshold maps were generated for each in a single subject. At a low threshold, there is artificially higher overlap (orange) between the maps due to noise. At a very high threshold, the overlap is smaller.

RESULTS

Tumors

The On-line Table summarizes the patients' demographic data, location and volume of lesions, pathology, World Health Organization grade (if applicable), and the distance from the edge of the lesion to the edge of the ventral somatomotor activation cluster based on the clinical task-fMRI maps. Brain lesions were mainly centered in the left cerebral hemisphere (19 patients), and 4 lesions were primarily located in the right cerebral hemisphere. Tumor size ranged from 0.84 to 159.05 cm^3 (mean, 41.82 cm^3).

FMRI Comparison

Twenty-six patients met the inclusion criteria and were included for analysis. In 21 patients (81%), rs-fMRI successfully identified a VSMN (Fig 4). Among these, 2 patients were considered a partial match because the VSMN was not distinct from the dorsal somatomotor network. There was an increase in the number of full matches with an increase in the ICA order (14 patients at ICA 20 and 19 patients at ICA 50). In 14 patients, a separate VSMN was identified at all ICA groups. Mixed-effect logistic regression demonstrated a significant increase in the probability of getting a full match as a function of the number of components ($P < .00001$). This probability is shown in Table 1.

In 5 patients, rs-fMRI failed to identify a VSMN at any of the ICA levels. In 3 of these 5 patients, only the dorsal somatomotor

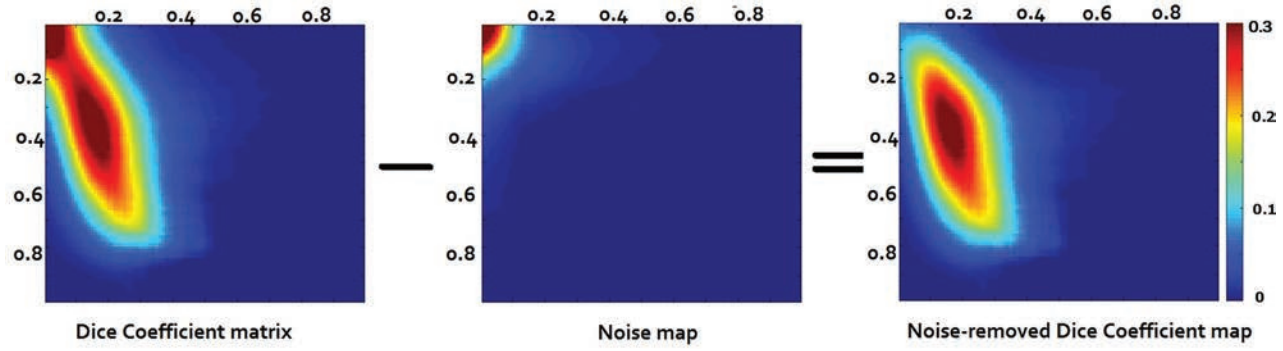

FIG 3. The Dice coefficient matrix at different thresholds at the subject level between the rs-fMRI (x-axis) at ICA 20 and tb-fMRI (y-axis). An artificially high Dice coefficient is seen in the top left corner of the left map due to overlap of noise. A noise matrix was generated (*middle map*) and was subtracted (*right map*). Noise-removed Dice coefficient maps were generated for all the subjects across 4 different ICA orders.

network was identified. In the remaining 2 patients, no somatomotor network was identified.

Group mean Dice maps for each ICA order are shown in Fig 5. Group mean Dice VUS overall increased with the ICA order (Fig 6); however, 1-way ANOVA demonstrated no significant differences among the 4 ICA groups (P value =.4). The range of Dice coefficient values at the subject level is shown in Table 2. Negative Dice values in these noise-subtracted maps may occur when the concordance between the noise maps and tb-fMRI at low thresholds is greater than the concordance between rs-fMRI and tb-fMRI due to the randomness of noise at low thresholds.

DISCUSSION

A growing number of studies have explored the feasibility of rs-fMRI as a substitute or complement to tb-fMRI for presurgical mapping of the eloquent somatomotor cortex in patients with brain tumor. Previous studies have demonstrated the reliability of rs-fMRI for localization of the hand motor area in comparison with tb-fMRI in a limited number of patients, with seed-based[10,23] or ICA analysis.[12] Concordance of rs-fMRI with intraoperative cortical stimulation was assessed in a few patients.[10,11,24] In addition, investigators have assessed the entire somatomotor cortex by using hand, foot, and face paradigms, with evaluation of the face motor area in a small subset of patients.[11,16,24] A novel data-driven algorithm for mapping the functional cortex in preoperative planning of motor and language networks in a small group of patients with tumor and epilepsy has been reported.[25] The existing data predominantly evaluate the usefulness of rs-fMRI in localization of the hand representation area of the somatomotor cortex, but there has been very limited evaluation of the ventral somatomotor cortex to date. In addition, there is wide variation in analysis methods, and most studies have only qualitatively compared tb-fMRI and rs-fMRI. To our knowledge, our study represents a relatively large cohort of patients with brain tumors involving or in close spatial proximity to the VSMN. In addition, we evaluated the overlap quantitatively by using multithresholding at different ICA levels.

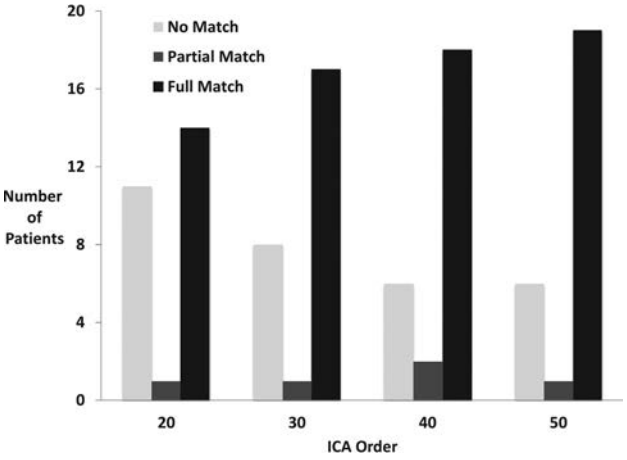

FIG 4. fMRI comparison among the patients. The number of patients with full, partial, and no match between tb- and rs-fMRI at different ICA levels is demonstrated.

Table 1: Probability of getting a full match between rs-fMRI and tb-fMRI maps as a function of number of ICA components

	ICA 20	ICA 30	ICA 40	ICA 50
Probability	0.53	0.65	0.69	0.73

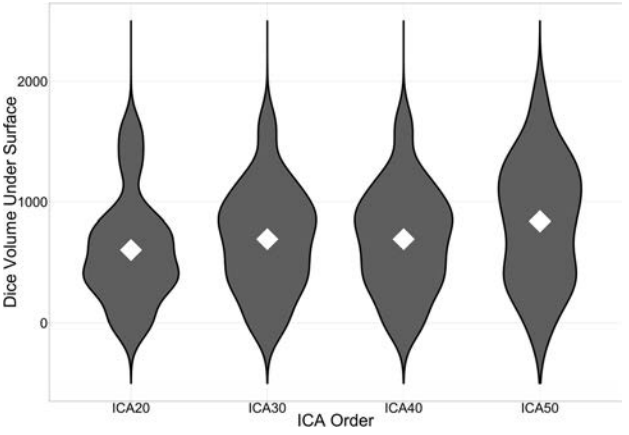

FIG 6. Violin plots of Dice VUS across ICA orders. The mean Dice VUS for each ICA order is denoted by *white diamonds*. As the ICA order increases, there are larger numbers of subjects with higher Dice VUS values as reflected in the greater width of the violin plots corresponding to kernel densities.

Table 2: Dice coefficient values range, median, and mean at the subject level across different ICA orders

	Minimum	Maximum	Median	Mean
ICA 20	−0.214	0.528	0.009	0.062
ICA 30	−0.134	0.540	0.015	0.071
ICA 40	−0.056	0.587	0.024	0.085
ICA 50	−0.368	0.616	0.024	0.086

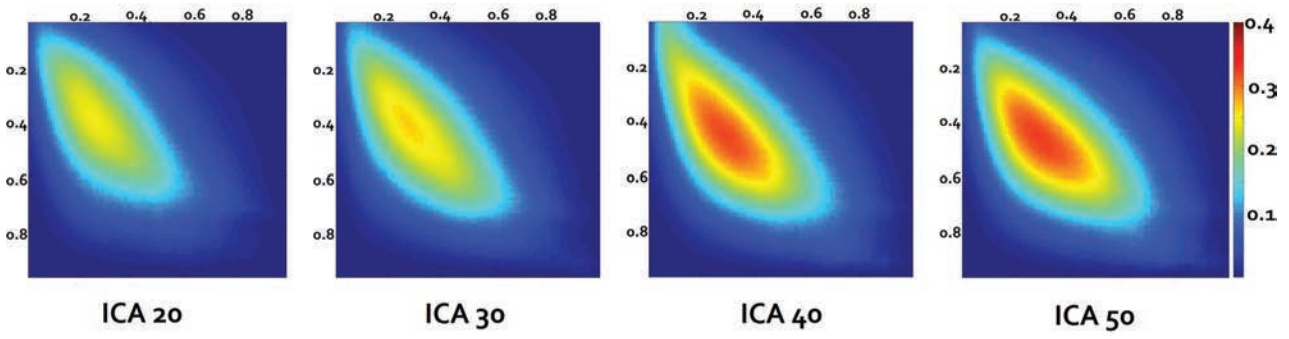

FIG 5. Group mean Dice coefficient maps across all the subjects at each ICA order calculated from subject-level noise-removed Dice coefficient maps. The x-axis depicts the rs-fMRI threshold levels, and the y-axis depicts the tb-fMRI threshold levels with the color bar demonstrating the Dice coefficient value.

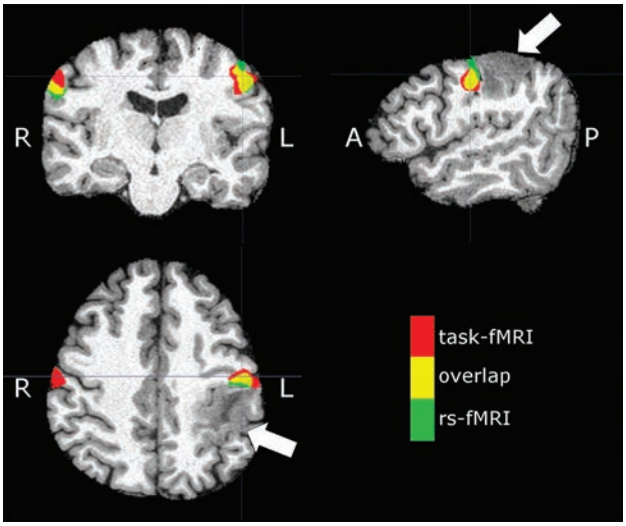

FIG 7. Sample subject (patient 23 in the On-line Table) demonstrating an expansile mass lesion centered in the postcentral gyrus (*arrows*). Signal abnormality is extended to the subcortical white matter of the precentral gyrus. Red denotes tongue motor task activation, green denotes the VSMN network identified from rs-fMRI (ICA 50), and yellow denotes areas of overlap between tb- and rs-fMRI.

Our data demonstrate the ability of rs-fMRI to successfully identify the VSMN in most patients (81%). There was a significant increase in the number of rs- versus tb-fMRI full matches, with an increase in the number of ICA orders from 20 to 50. In addition, there was an increase in the mean Dice VUS and maximum Dice coefficient values, with an increasing number of independent components; however, this effect did not reach statistical significance, potentially due to intersubject variability. The choice of an ideal number of informative components for ICA analysis is challenging due to the spatial and temporal dependence of the BOLD signal.[26] Using a higher number of target components could result in fragmentation of networks to subnetworks; conversely, using a lower number of target components may result in merging different brain networks.[7] Concordantly, we qualitatively saw better separation of the VSMN and dorsal somatomotor network subnetworks at higher ICA orders. Therefore, using a higher number of target components in ICA analysis may be suggested in cases in which localizing a specific subnetwork is desired for preoperative planning, though this needs to be further balanced by the risk of further subsegmenting the networks with even higher ICA orders.

Our results show a strong concordance between the rs-fMRI and tb-fMRI in some of the subjects, demonstrating the potential utility of rs-fMRI as a viable preoperative mapping tool (Fig 7); however, there is significant variability across subjects. In particular, if rs-fMRI is to be used without a tb-fMRI acquisition, one must ensure that a reliability estimate of rs-fMRI can be calculated from the data itself. Improvement in technique and data analysis may overcome some of these limitations in the future. Increasing the scan time may improve the quality of rs-fMRI[27] and thus potentially decrease such intersubject variability. Alternative methods of analysis such as seed-based analysis that have shown some promise in localizing the motor network in patients with brain tumors[11,28] may also be considered. However, in the current study population of patients with brain tumors, accurate placement of seeds may be limited due to anatomic gyral distortion or compression. Therefore, an unbiased method such as ICA may be preferable. In addition, ICA remains an attractive choice due to availability of easy-to-use software such as the MELODIC tool in FSL (http://fsl.fmrib.ox.ac.uk/fsl/fslwiki/MELODIC) or the GIFT toolbox.

Several limitations in this study should be addressed. rs-fMRI was performed after tb-fMRI in this clinical cohort of patients to ensure that the patients tolerated the lengthy scan and performed well on their tb-fMRI, which was critical for clinical presurgical mapping. Thus, there may have been an inadvertent task effect on the observed functional connectivity.[29] Another limitation is the inability to ensure that patients did not fall asleep during rs-fMRI. We instructed the patients to stay awake during the rs-fMRI and confirmed that they stayed awake during a postscan interview; however, the accuracy of their statements could not be verified by physiologic measures indicating sleep during the acquisition. While this inability poses a potential limitation because changes in functional connectivity have been reported in sleep or altered consciousness,[30] functional connectivity in the somatomotor network has been shown to be preserved during different states of arousal.[8] Nevertheless, the effect of sleep or altered arousal on rs-fMRI concordance with tb-fMRI could be further investigated. In addition, we used tb-fMRI T-maps to find the best candidate ICA map to represent the VSMN. However, brain tumors may cause alteration of somatomotor network organization, and brain tumor–induced neurovascular uncoupling may further compromise our ability to accurately detect the VSMN. Therefore, using only rs-fMRI data to identify the best somatomotor map may be challenging with brain tumors. The use of a data-driven neural network algorithm to identify the eloquent cortex in 7 patients with brain tumor with distorted anatomy has shown some promise.[25]

CONCLUSIONS

We demonstrate variable concordance of rs- and tb-fMRI at the single-subject level for detection of the VSMN in patients with brain tumor. We demonstrate improved reliability of rs-fMRI VSMN maps with higher ICA orders. Failure of rs-fMRI to identify the VSMN in about one-fifth of patients in our study limits the ability of rs-fMRI to completely substitute for tb-fMRI for presurgical assessment, though it may be considered as a supplement for tb-fMRI, for example, when task activation is suboptimal. Further improvements in technique, processing, and analysis methods may enhance the potential of using rs-fMRI as a substitute or complement to tb-fMRI in mapping of the VSMN.

Disclosures: Jay J. Pillai—*UNRELATED*: *Royalties*: Springer Science and Business Media, Elsevier, *Comments*: royalties for books published; *Board Membership*: Prism Clinical Imaging, *Comments*: unpaid medical advisory board member. Raag Airan—*UNRELATED*: *Grants/Grants Pending*: Philips Healthcare, *Comments*: limited grant research support*; *Stock/Stock Options*: Lumos labs, *Comments*: stock options received as member of the Scientific Advisory Board. Brian Caffo—*UNRELATED*: *Grant*: National Institutes of Health, *Comments*: standard National Institutes of Health support.* Haris I. Sair—*RELATED*: *Grant*: Radiological Society of North America–Carestream Health Research Scholar Grant*; *UNRELATED*: *Grants/Grants Pending*: ImmunArray, *Comments*: grant support for research.* *Money paid to the institution.

REFERENCES

1. Lehéricy S, Duffau H, Cornu P, et al. **Correspondence between functional magnetic resonance imaging somatotopy and individual brain anatomy of the central region: comparison with intraoperative stimulation in patients with brain tumors.** *J Neurosurg* 2000;92:589–98 CrossRef Medline
2. Petrella JR, Shah LM, Harris KM, et al. **Preoperative functional MR imaging localization of language and motor areas: effect on therapeutic decision making in patients with potentially resectable brain tumors.** *Radiology* 2006;240:793–802 CrossRef Medline
3. Vlieger EJ, Majoie CB, Leenstra S, et al. **Functional magnetic resonance imaging for neurosurgical planning in neurooncology.** *Eur Radiol* 2004;14:1143–53 CrossRef Medline
4. Ogawa S, Menon RS, Tank DW, et al. **Functional brain mapping by blood oxygenation level-dependent contrast magnetic resonance imaging: a comparison of signal characteristics with a biophysical model.** *Biophys J* 1993;64:803–12 CrossRef Medline
5. Shimony JS, Zhang D, Johnston JM, et al. **Resting-state spontaneous fluctuations in brain activity: a new paradigm for presurgical planning using fMRI.** *Acad Radiol* 2009;16:578–83 CrossRef Medline
6. Sair HI, Yahyavi-Firouz-Abadi N, Calhoun VD, et al. **Presurgical brain mapping of the language network in patients with brain tumors using resting-state fMRI: comparison with task fMRI.** *Hum Brain Mapp* 2016;37:913–23 CrossRef Medline
7. Smith SM, Fox PT, Miller KL, et al. **Correspondence of the brain's functional architecture during activation and rest.** *Proc Natl Acad Sci U S A* 2009;106:13040–45 CrossRef Medline
8. Larson-Prior LJ, Zempel JM, Nolan TS, et al. **Cortical network functional connectivity in the descent to sleep.** *Proc Natl Acad Sci U S A* 2009;106:4489–94 CrossRef Medline
9. Mhuircheartaigh RN, Rosenorn-Lanng D, Wise R, et al. **Cortical and subcortical connectivity changes during decreasing levels of consciousness in humans: a functional magnetic resonance imaging study using propofol.** *J Neurosci* 2010;30:9095–102 CrossRef Medline
10. Zhang D, Johnston JM, Fox MD, et al. **Preoperative sensorimotor mapping in brain tumor patients using spontaneous fluctuations in neuronal activity imaged with functional magnetic resonance imaging: initial experience.** *Neurosurgery* 2009;65(6 suppl):226–36 Medline
11. Rosazza C, Aquino D, D'Incerti L, et al. **Preoperative mapping of the sensorimotor cortex: comparative assessment of task-based and resting-state FMRI.** *PLoS One* 2014;9:e98860 CrossRef Medline
12. Kokkonen SM, Nikkinen J, Remes J, et al. **Preoperative localization of the sensorimotor area using independent component analysis of resting-state fMRI.** *Magn Reson Imaging* 2009;27:733–40 CrossRef Medline
13. Tie Y, Rigolo L, Norton IH, et al. **Defining language networks from resting-state fMRI for surgical planning: a feasibility study.** *Hum Brain Mapp* 2014;35:1018–30 CrossRef Medline
14. Kristo G, Rutten GJ, Raemaekers M, et al. **Task and task-free FMRI reproducibility comparison for motor network identification.** *Hum Brain Mapp* 2014;35:340–52 CrossRef Medline
15. Hou BL, Bhatia S, Carpenter JS. **Quantitative comparisons on hand motor functional areas determined by resting state and task BOLD fMRI and anatomical MRI for pre-surgical planning of patients with brain tumors.** *Neuroimage Clin* 2016;11:378–87 CrossRef Medline
16. Schneider FC, Pailler M, Faillenot I, et al. **Presurgical assessment of the sensorimotor cortex using resting-state fMRI.** *AJNR Am J Neuroradiol* 2016;37:101–07 CrossRef Medline
17. Zacà D, Jovicich J, Nadar SR, et al. **Cerebrovascular reactivity mapping in patients with low grade gliomas undergoing presurgical sensorimotor mapping with BOLD fMRI.** *J Magn Reson Imaging* 2014;40:383–90 CrossRef Medline
18. Voyvodic JT. **Reproducibility of single-subject fMRI language mapping with AMPLE normalization.** *J Magn Reson Imaging* 2012;36:569–80 CrossRef Medline
19. Mazaika PK. **Methods and software for fMRI analysis of clinical subjects.** *Neuroimage* 2009;47:S58 CrossRef
20. Behzadi Y, Restom K, Liau J, et al. **A component based noise correction method (CompCor) for BOLD and perfusion based fMRI.** *Neuroimage* 2007;37:90–101 CrossRef Medline
21. Himberg J, Hyvärinen A, Esposito F. **Validating the independent components of neuroimaging time series via clustering and visualization.** *Neuroimage* 2004;22:1214–22 CrossRef Medline
22. Branco P, Seixas D, Deprez S, et al. **Resting-state functional magnetic resonance imaging for language preoperative planning.** *Front Hum Neurosci* 2016;10:11 CrossRef Medline
23. Qiu T, Yan C, Tang W, et al. **Localizing hand motor area using resting-state fMRI: validated with direct cortical stimulation.** *Acta Neurochir (Wien)* 2014;156:2295–302 CrossRef Medline
24. Liu H. **Task-free presurgical mapping using functional magnetic resonance imaging intrinsic activity.** *J Neurosurg* 2009;111:746–54 CrossRef Medline
25. Mitchell TJ, Hacker CD, Breshears JD, et al. **A novel data-driven approach to preoperative mapping of functional cortex using resting-state functional magnetic resonance imaging.** *Neurosurgery* 2013;73:969–82; discussion 982–83 CrossRef Medline
26. Li YO, Adali T, Calhoun VD. **Estimating the number of independent components for functional magnetic resonance imaging data.** *Hum Brain Mapp* 2007;28:1251–66 CrossRef Medline
27. Birn RM, Molloy EK, Patriat R, et al. **The effect of scan length on the reliability of resting-state fMRI connectivity estimates.** *Neuroimage* 2013;83:550–58 CrossRef Medline
28. Agarwal S, Sair HI, Yahyavi-Firouz-Abadi N, et al. **Neurovascular uncoupling in resting state fMRI demonstrated in patients with primary brain gliomas.** *J Magn Reson Imaging* 2016;43:620–26 CrossRef Medline
29. Wang Z, Liu J, Zhong N, et al. **Changes in the brain intrinsic organization in both on-task state and post-task resting state.** *Neuroimage* 2012;62:394–407 CrossRef Medline
30. Tagliazucchi E, Laufs H. **Decoding wakefulness levels from typical fMRI resting-state data reveals reliable drifts between wakefulness and sleep.** *Neuron* 2014;82:695–708 CrossRef Medline

Prognostic Predictors of Visual Outcome in Open Globe Injury: Emphasis on Facial CT Findings

U.K. Bodanapally, H. Addis, D. Dreizin, A.K. Reddy, J.A. Margo, K.L. Archer-Arroyo, S. Feldman, B. Saboury, K. Sudini, and O. Saeedi

ABSTRACT

BACKGROUND AND PURPOSE: The present prognostic models for open globe injuries have a limited ability to predict visual outcome before a comprehensive ophthalmologic examination or operation because they depend on the data derived from the ophthalmologic examination and intraoperative findings. The purpose of our study was to determine the specific CT and preoperative clinical data that can predict the prognosis of open globe injury.

MATERIALS AND METHODS: We analyzed the relationship of 29 variables derived from clinical and CT data from 97 globe injuries with visual acuity at 1 month. A prediction model was derived from 49 globe injuries by regression analysis, followed by receiver operating characteristic curve analysis of the best CT predictor.

RESULTS: Four variables with significance on a regression model were the following: posterior segment hemorrhage ($\beta = -0.93$, $P < .0001$), presenting visual acuity ($\beta = 0.28$, $P = .042$), orbital emphysema ($\beta = 0.46$, $P = .0018$), and complex facial fracture ($\beta = -0.43$, $P = .009$). Receiver operating characteristic analysis of the posterior segment hemorrhage predicted profound vision loss (light perception or no light perception) with an area under the curve of 0.97. The receiver operating characteristic table indicated that grade III posterior segment hemorrhage has a strong positive predictive value of 100% for profound vision loss. On the other hand, the absence of posterior segment hemorrhage has a strong positive predictive value of 93% for mild-to-severe vision loss (visual acuity better than light perception).

CONCLUSIONS: Radiologists, with the help of CT and preoperative clinical data, can predict visual acuity after open globe injury.

ABBREVIATIONS IOP = intraocular pressure; LP = light perception; logMAR = logarithm of the minimum angle of resolution; NLP = no light perception; PPV = positive predictive value; RAPD = relative afferent pupillary defect; VA = visual acuity

Open globe injury is described as a full-thickness injury of the eye wall resulting from either blunt or penetrating trauma.[1] It is a vision-threatening injury, and primary surgical repair is the standard practice to restore the structural and physiologic integrity of the globe, regardless of the extent of the injury and the presenting visual acuity (VA).[2,3] Prompt diagnosis and surgical repair of the injury are crucial to optimize visual outcome.[4,5]

There are only 2 predictive models of poor visual outcome after open globe injury, the Ocular Trauma Score system[6] and the Classification and Regression Tree model, that were developed to guide both clinicians and patients in clinical decision-making.[7] The Ocular Trauma Score is derived from presenting VA, globe rupture, endophthalmitis, perforating injury, retinal detachment, and relative afferent pupillary defect (RAPD) as predictors of poor visual outcome. The Classification and Regression Tree model identifies RAPD, presenting VA, lid laceration, and posterior wound location at surgery as predictors of poor outcome. Both models depend on data derived from a comprehensive ophthalmologic examination and intraoperative findings. This requirement limits the ability of the models to consistently provide prognostic information before ophthalmologic examination or an operation. The time between the injury and surgery is crucial because that is when clinicians need the most prognostic information to reduce the patient's anxiety and assist in informed decision-making regarding treatment choices.[6] A comprehensive ophthalmologic assessment is challenging and is often delayed in the acute trauma setting due to periorbital soft-tissue swelling, poor patient co-

Received October 28, 2016; accepted December 13.

From the Department of Radiology, R Adams Cowley Shock Trauma Center (U.K.B., D.D., K.L.A.-A., B.S.), and Department of Ophthalmology and Visual Sciences (J.A.M., O.S.), University of Maryland Medical Center, Baltimore, Maryland; University of Maryland School of Medicine (H.A., S.F.), Baltimore, Maryland; University of Iowa Carver College of Medicine (A.K.R.), Iowa City, Iowa; and Department of Environmental Health Sciences (K.S.), Bloomberg School of Public Health, Johns Hopkins University, Baltimore, Maryland.

Please address correspondence to Uttam K. Bodanapally, MBBS, Department of Radiology, University of Maryland Medical Center, 22S Greene St, Baltimore, MD 21201; e-mail: ubodanapally@umm.edu

Indicates article with supplemental on-line tables.

http://dx.doi.org/10.3174/ajnr.A5107

operation, and altered mental status due to concomitant head trauma or the use of mind-altering medications.[5,8] Subjecting patients with globe rupture to an aggressive ophthalmologic examination can even worsen the initial injury.[9]

In contemporary trauma care, CT has evolved as the imaging technique of choice for evaluating orbital trauma, especially in patients with difficult ophthalmologic examinations.[4,5,8-10] Various studies have shown the sensitivities and specificities of CT, ranging from 56% to 76% and 79% to 100%, respectively, in detecting open globe injuries.[4,5,8-10] CT offers the additional benefit of detecting concomitant intraorbital soft-tissue injuries and orbitofacial fractures.[8] Objective preoperative prognostic data that can be derived from CT findings and limited clinical data obtainable in acute trauma settings would be of great clinical value. Such information could facilitate effective communication and counseling of patients.

Our purpose was to determine the specific CT and preoperative clinical data that can predict the prognosis of open globe injury. VA at 1 month after surgery was used as the reference standard for visual outcome in this study.

MATERIALS AND METHODS

The study was compliant with the Health Insurance Portability and Accountability Act, and permission was obtained from the University of Maryland, Baltimore (UMB) institutional review board. The study was conducted at a level 1 trauma center. The inclusion criteria for this retrospective study were the following: 1) a history of open globe injury and subsequent surgical repair between July 2005 and January 2014, 2) CT of the face performed before surgical repair, 3) subject at least 18 years of age, and 4) clinical follow-up with determination of VA at 1 month after globe repair.

Subjects

A search of the trauma data base of our institution from July 2005 to January 2014 yielded 132 patients with 138 globe repairs; 6 patients sustained bilateral injuries. Only 1 globe was randomly selected from patients with bilateral injuries. One-month VA was available in 97 globes and constituted the study group. CT of the face was performed in 85 of the 97 patients. Figure 1 shows the patient selection flowchart. In the study group, there were 72 men and 25 women (mean age, 41.4 years; range, 18–94 years). The mechanism of injury was blunt trauma in 44% (43 of 97), gunshot wound in 25% (24 of 97), and stab wounds/penetrating injuries by sharp objects in 15% (15 of 97); and in 15% (15 of 97) of patients, the mechanism could not be determined.

Clinical information regarding the complete ophthalmic/pupil examination, if performed, was obtained. The data included presenting VA, RAPD, and intraocular pressure (IOP) measurements. Clinical information was obtained from the initial consultation note, progress notes, and operative reports. A senior ophthalmology resident (J.A.M.) reviewed the medical records.

Imaging Technique

Protocols for multidetector row CT are shown in On-line Table 1. Admission multidetector row CT was performed with a 16-, 40-, or 64 section CT system (Brilliance 16-, 40-, and 64-channel system; Philips Healthcare, Best, the Netherlands). Facial CT was performed from the frontal sinuses through the mental symphysis. The CT images included 2-mm axial sections and reformatted sagittal and coronal images (2-mm thickness, obtained at 1-mm intervals through the face).

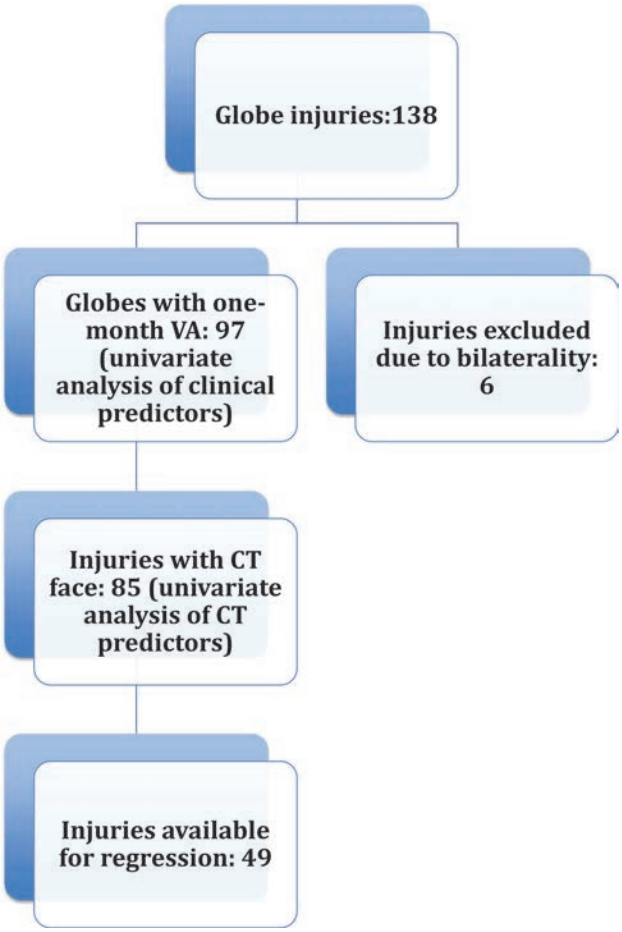

FIG 1. Flowchart shows the patient selection process.

Table 1: Correlation between continuous predictor variables and VA at 1 month

Variable	No. of Globes with Variable	Spearman ρ	*P* Value
Age	97/97	−0.02	.84
IOP	29/97	−0.48	.008[a]
Presenting VA	59/97	0.84	<.0001[a]
Fractional decrease in globe volume	53/85	−0.36	.0074[a]
Fractional increase in globe volume	32/85	0.4	.026[a]

[a] Statistical significance ($P < .05$).

Variable Construction

We analyzed the relationship of 29 study variables derived from demographic, clinical, and CT imaging data (Table 1 and On-line Table 2). Predictors of visual outcome identified in the literature were also included, in addition to the CT variables most commonly related to intraorbital soft-tissue injuries and craniofacial fractures.[8,12]

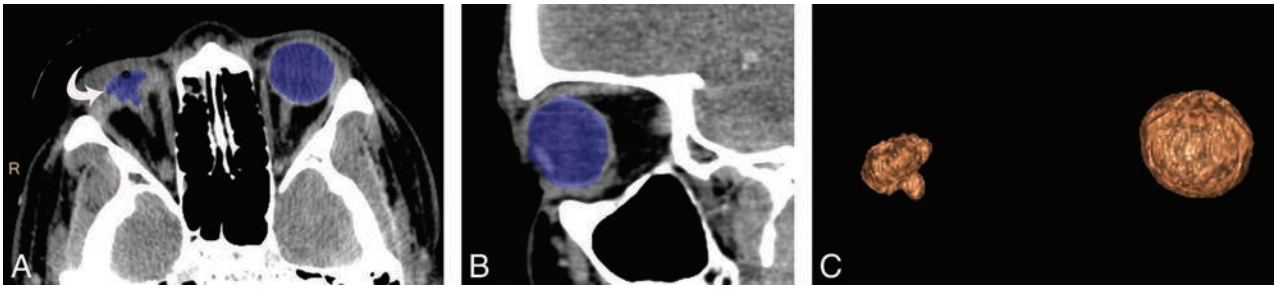

FIG 2. A 30-year-old man with a stab wound to the right eye. Axial (*A*) and coronal (*B*) CT images demonstrate the ROI drawn by 3D segmentation on the thin-client server. The ruptured right globe resulted in decompression (*curved arrow*) due to vitreous and uveal prolapse. *C*, Segmented volume-rendered image of both the ruptured globe and the normal contralateral globe. Based on the calculated volumes, there was a fractional decrease in globe volume of 0.89.

Image Analysis and Definitions

CT studies were loaded onto the thin-client server of our institution (IntelliSpace Portal; Philips Healthcare) to facilitate postprocessing of multiplanar reconstruction images in additional planes. Three trauma attending radiologists (reviewer 1, 5 years of experience; reviewer 2, 8 years of experience; reviewer 3, 10 years of experience), blinded to the clinical data, performed independent reviews of each CT study on the PACS of our institution with additional use of the thin-client software. For all the CT variables, discrepancies between the assessments of 2 reviewers were resolved by adjudication by a third reviewer.

The reviewers assessed and recorded the presence of the CT variables of globe and orbitofacial trauma. All the variables were given nominal scores based on the presence (score of 1) versus the absence (score of 0) of each variable. Apart from the qualitative analysis, a quantitative analysis was performed for posterior segment hemorrhage, fractional decrease in globe volume, and fractional increase in globe volume. Reviewer 3 measured globe volumes on the thin-client server by using semiautomated 3D segmentation. ROIs were drawn on axial sections with the use of sagittal sections to exclude unwanted surrounding bone and soft tissues from the ROIs (Fig 2). Volumes of both globes were obtained in all patients. In patients with lens destruction or severe intraocular hemorrhage too dense to allow visualization of the lens on CT, evaluation for lens subluxation and dislocation and assessment of the anterior chamber depth were not performed. It is quite difficult to distinguish hemorrhage into the vitreous chamber and subretinal or suprachoroidal subtypes in globes with severe injury. Hence, we considered it more appropriate to refer to them collectively as posterior segment hemorrhage (Fig 3).

Study Term Definitions

Grade of Posterior Segment Hemorrhage. Posterior segment hemorrhage was graded from 0 to III, based on the amount of blood in the posterior segment: grade 0 (no posterior hemorrhage), grade I (<25% of posterior segment filled with blood), grade II (25%–75% filled), and grade III (>75% filled) (Fig 3).

Fractional Change in Globe Volume. Fractional increase or fractional decrease in the globe volume was obtained by using the contralateral normal globe volume as a reference (Fig 2). In patients with bilateral globe injuries, the mean volume of all the normal globes included in the study was used as reference.

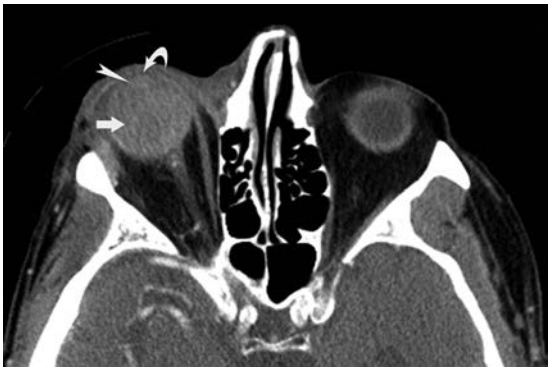

FIG 3. CT image shows a grade III posterior segment hemorrhage (*arrow*) in a 77-year-old man with right-sided open globe injury after blunt force trauma. The image shows intraocular hemorrhage that was too dense; however, the lens can be delineated from the hemorrhage (*arrowhead*) along with shallow anterior chamber (*curved arrow*). The right eye had a relative afferent pupillary defect with a measured intraocular pressure (IOP = 44 mm Hg) and a fractional increase in globe volume of 0.27.

Intraorbital Hemorrhage and Emphysema. Intraorbital hemorrhage and emphysema were further divided into extraconal and intraconal components.

Facial and Orbital Fractures. Simple facial fractures were defined as fractures without involvement of facial buttresses. Complex facial fractures, defined as buttress fractures, included naso-orbitoethmoid fractures, zygomaticomaxillary complex fractures, and Le Fort fractures. Orbital fractures included isolated wall fractures and also those commonly associated with posterior propagation of complex midfacial fractures.

Perforating Injury. Injuries caused by stab wounds and gunshot wounds were divided into penetrating injury (only entry wound) and perforating injury (both entry and exit wounds present).[1]

Profound Vision Loss. Profound vision loss was defined as VA of light perception (LP) or no light perception (NLP). Mild-to-severe vision loss was further defined as VA better than LP.

Statistical Analysis

Statistical analysis was performed by K.S., by using statistical software (R statistical and computing software, Version 3.3.1; http://www.r-project.org/; and JMP 12 software; SAS Institute, Cary, North Carolina). Univariate analysis was performed by the Spearman rank correlation for continuous variables. Categoric vari-

Table 2: Logistic regression analysis for the variables related to VA

Variable	β Regression Coefficient	Standard Error	Accumulated Model Adjusted R^2	P Value
Posterior segment hemorrhage	−0.93	0.15	0.627	<.0001
Presenting VA	0.28	0.13	0.789	.042
Orbital emphysema	0.46	0.14	0.8	.0018
Complex facial fracture	−0.43	0.16	0.827	.009

ables were compared by 1-way ANOVA. After testing for homogeneous variance (Levene test), a post hoc analysis was performed by using the Welch and Wilcoxon tests. All significant predictor variables in univariate analysis were incorporated into a multivariate logistic regression model. A backward selection model was used. Variables thought to be of infrequent incidence were excluded to result in a model with less overfitting and greater generalizability. Missing data were dealt with by pair-wise deletion for univariate analysis and by a list-wise deletion for multivariate analysis. The regression equation was derived from a continuous dependent variable (ie, VA). The variance inflation factor and adjusted R^2 were also obtained from regression analysis. A P value of .05 was significant. To examine the degree of overfitting of the prediction model, we performed a k-fold × 10 cross-validation. First, the sample was partitioned into 10 equal-sized subsamples. Of the 10 subsamples, 9 were used to develop the regression model and the resulting prediction equation was applied to the left-out sample. This procedure was repeated 10 times, each time rotating the cross-validation subset to derive the root mean square error and standard error for the root mean square error.

VA was converted into a logarithm of the minimum angle of resolution (logMAR) units (On-line Table 3) to provide a numeric scale for statistical analysis.[11,12] Diagnostic performance of the strongest CT predictor derived from the regression analysis was further analyzed by receiver operating characteristic curves after converting the visual outcome into a binary variable (VA ≤ LP and VA ≥ LP). The data excluded from regression analysis were used as a test set to validate the results because all the patients had admission facial CT scans. Contingency tables were used to obtain sensitivities, specificities, positive predictive values (PPVs), and negative predictive values. The κ statistic was used to test interobserver reliability in assessing CT variables by the radiologists.

RESULTS

Of the 97 globe injuries that constituted the study group, IOP could be measured in 29 globe injuries, only 41 eyes could be evaluated for the presence of RAPD, and preoperative VA could be measured in 59 eyes. Patients who had IOP, RAPD, and presenting VA measured on the initial examination were compared with those who did not. Patients with measured IOP had a mean logMAR of −3.38 (difference = 0.2, P = .5), the RAPD evaluated had a mean logMAR of −3.1 (difference = 0.68, P = .06), and those with presenting VA had a logMAR of −3.1 (difference = 1.15, P = .0002). The data indicate that patients with poor outcomes were less likely to have had a complete ophthalmologic examination, mainly a VA test.

Univariate Analysis

Univariate analysis showed that penetrating injuries with stabs/sharp objects predicted a favorable VA at 1 month (P = .03), while penetrating injuries caused by gunshot wounds predicted unfavorable VA (P < .0001), with no significant difference in outcome between penetrating and perforating injuries (P = .4) (On-line Table 2).

The ophthalmologic examination data associated with poor VA include higher IOP (Spearman $\rho = -0.48$, P = .008), the presence of RAPD (P = .008), and poor presenting VA (Spearman ρ = 0.84, P < .0001) (Table 1 and On-line Table 2).

The CT findings that predicted poor 1-month VA included the presence of posterior segment hemorrhage (P < .0001) (Fig 3), fractional decrease in globe volume (P = .007) (Fig 2), fractional increase in globe volume (P = .026) (Fig 3), hyphema (P < .0001), intraorbital hemorrhage (P = .0001), extraconal hemorrhage (P < .0001), intraconal hemorrhage (P < .0001), intraorbital emphysema (P < .0001), extraconal emphysema (P < .0001), intraconal emphysema (P < .0001), intraocular gas (P < .0001), lens subluxation (P = .0018), orbital fractures (P < .0001), complex facial fractures (P < .0001), and a shallow anterior chamber (P = .04) (Fig 3). A visible lens (P = .0054) on CT predicted a favorable VA at 1 month (Table 1 and On-line Table 2).

There was fair-to-very good agreement among the reviewers (On-line Table 2), except for traumatic cataract and lens subluxation, which had poor agreement.

Multivariate Analysis

Statistically significant variables such as IOP, RAPD, lens subluxation, and shallow anterior chamber were excluded from multivariate analysis as part of a list-wise deletion and due to their infrequent availability; this elimination resulted in a model with less overfitting and greater generalizability. Forty-nine globe injuries were selected to derive the regression model. The remaining 36 globe injuries, which were excluded from regression analysis due lack of adequate clinical data, were retained as test samples to validate the value of the strongest CT variable. The regression model identified 4 predictor variables with significance (Table 2): posterior segment hemorrhage, presenting VA, orbital emphysema, and complex facial fractures. The 4 variables resulted in an adjusted R^2 of 0.827 and P < .0001 (root mean square error = 0.71). The variance inflation factor was <4 for the variables. On internal k-fold cross-validation with 10-fold analysis, the results were consistent in all the folds and the average root mean square error was 0.75 (standard error, 0.02).

Receiver operating characteristic analysis of posterior segment hemorrhage in predicting profound vision loss yielded an area under the curve value of 0.97 in the derivation sample of 49 globes. The result was further validated on the test sample of 36 globes, which yielded a comparable area under the curve of 0.98. The addition of presenting VA to the model already containing posterior segment hemorrhage increased the area under the curve from 0.97 to 0.98 in the derivation sample.

The sensitivities, specificities, positive predictive values, and negative predictive values of various grades of posterior segment

Table 3: Sensitivities, specificities, PPVs, and NPVs of various grades of posterior segment hemorrhage in predicting profound vision loss

Posterior Segment Hemorrhage	Sensitivity (95% CI)	Specificity (95% CI)	PPV (95%CI)	NPV (95% CI)
PSH ≥ grade I	98 (62/63) (91–100)	64 (14/22) (41–83)	89 (62/70) (19–95)	93 (14/15) (68–100)
PSH ≥ grade II	86 (54/63) (75–93)	91 (20/22) (71–99)	96 (54/56) (88–100)	69 (20/29) (49–85)
PSH grade III	78 (49/63) (65–87)	100 (22/22) (85–100)	100 (49/49) (93–100)	61 (22/36) (43,77)

Note:—PSH indicates posterior segment hemorrhage; NPV, negative predictive value.

hemorrhage in predicting profound vision loss (LP or NLP) are shown in Table 3. The absence of posterior segment hemorrhage predicted a 1-month VA better than LP (mild-to-severe vision loss) with sensitivity, specificity, PPV, and negative predictive values of 64%, 98%, 93%, and 89%, respectively. The results indicate that grade III posterior segment hemorrhage has a strong PPV for profound vision loss (LP or NLP) at 1-month follow-up, with all 49 injured globes with grade III hemorrhage resulting in profound vision loss. On the other hand, the absence of posterior segment hemorrhage has a strong PPV for VA better than LP (mild-to-severe vision loss), with 14 of 15 patients without hemorrhage having a VA of better than LP on follow-up.

DISCUSSION

In this study, we systematically analyzed the CT findings of open globe injuries, intraorbital soft-tissue injuries, orbitofacial skeletal injuries, and limited clinical data that are possible to obtain in the acute trauma setting to determine the predictors of VA at 1 month. According to our results, posterior segment hemorrhage, presenting VA, orbital emphysema, and complex facial fractures are the independent predictors of poor VA. The developed model has a good predictive performance, and the strengths of the model are the following: 1) Most of the predictors can be assessed on admission CT, 2) it requires a minimum amount of clinical data, and 3) the prediction model does not depend on surgical findings or postsurgical outcomes. Posterior segment hemorrhage was found to be the strongest predictor of VA at 1 month. Moreover, grade III posterior segment hemorrhage had a strong PPV (100%) for profound vision loss (LP or NLP) at 1 month, while absence of hemorrhage had a strong PPV (93%) for mild-to-severe vision loss (VA better than LP).

The Ocular Trauma Score model predicted profound vision loss with a sensitivity of 100% and specificity of 91%, respectively.[13] On the other hand, Classification and Regression Tree analysis has shown a sensitivity of 82% and specificity of 86%.[13] Our results showed that grade III posterior segment hemorrhage, which can be easily derived from facial CT, alone has a sensitivity of 78% and specificity of 100% in predicting profound vision loss. The absence of posterior segment hemorrhage, on the other hand, had a sensitivity of 64% and a specificity of 98% in predicting mild-to-severe vision loss. The best predictor from Classification and Regression Tree analysis was RAPD. In contrast, RAPD was not incorporated into the logistic regression model due to listwise deletion, though RAPD was significant on univariate analysis. The other disadvantage of depending on RAPD as a predictor was that only 42% of our injuries could be evaluated for the presence of RAPD in the acute trauma setting.

Joseph et al[9] have reported that nearly 90% of globes with moderate-to-severe deformity had poor visual outcomes and 64% underwent enucleation, while no globes without scleral deformity underwent enucleation.[9] Yuan et al[5] showed that scleral deformities are associated with a decompressed globe in 36% of their studied globe ruptures and 15% showed enlarged globes. Decompression of the globe results from vitreous or uveal prolapse through the defect.[4,5,9,14] Enlargement of the globe has been ascribed to intraocular hemorrhage, which can also contribute to increased IOP.[3-5,9,14] To increase the quantitative precision of the degree of scleral deformity, we measured the globe volumes and calculated the fractional decrease or fractional increase in the volume of the ruptured globe. Our results showed that neither fractional decrease nor fractional increase in the globe volume was significant on regression analysis, though both variables were significant on univariate analysis. Margo et al,[3] in a recent study, showed a correlation between high IOP and poor visual prognosis. Increased IOP, which had collinearity with posterior segment hemorrhage (Spearman $\rho = 0.015$), was associated with poor visual outcome. Joseph et al[9] showed that 60% of patients with vitreous hemorrhage end up with enucleation and 75% of those with blood occupying >50% of the vitreous chamber end up with enucleation. Although our study did not evaluate the rates of enucleation, the results confirmed high sensitivity (98%; 95% CI, 91–100) of posterior segment hemorrhage in predicting profound vision loss.

Limitations

Our study has several limitations. First, it is a retrospective design with inherent biases. Second, some significant CT variables may have been excluded from analysis because CT variable selection was performed on the basis of the previously identified risk factors and some of the variables were selected by the study team members on the basis of their clinical experience. Simultaneous review of all signs may have resulted in some degree of bias in determining their individual performance. Finally, a direct comparison of our model with either the Ocular Trauma Score or the Classification and Regression Tree model was not performed because we did not record the surgical data that were the major components of those models, in keeping with the purpose of our study (ie, to derive a predictive model before surgery).

CONCLUSIONS

Previously known prognostic prediction models after open globe injury depend on data derived from ophthalmologic examination and surgical findings. However, ophthalmologic examination or even testing for RAPD, the best predictor in the Classification and Regression Tree model, may not be possible or reliable in some patients as seen from our results, due to nonreactive pupils frequently encountered in patients with associated traumatic brain injury, coma, or raised intracranial pressures. In this context, our

results may have clinical implications when radiologists, with the help of CT and limited preoperative clinical data that is realistically possible to obtain in acute trauma settings, can predict VA after open globe injury. Such information reduces anxiety in patients and helps informed decision-making regarding treatment choices.

Disclosures: Osamah Saeedi—*UNRELATED*: *Grant*: National Institutes of Health, *Comments*: K23 National Institutes of Health career development award.* *Money paid to the institution.

REFERENCES

1. Kuhn F, Morris R, Witherspoon CD. **Birmingham Eye Trauma Terminology (BETT): terminology and classification of mechanical eye injuries.** *Ophthalmol Clin North Am* 2002;15:139–43, v CrossRef Medline
2. Rahman I, Maino A, Devadson D, et al. **Open globe injuries: factors predictive of poor outcome.** *Eye (Lond)* 2006;20:1336–41 CrossRef Medline
3. Margo JA, Feldman S, Addis H, et al. **Open globe injuries presenting with normal or high intraocular pressure.** *Eye Contact Lens* 2016;42:256–61 CrossRef Medline
4. Kim SY, Lee JH, Lee YJ, et al. **Diagnostic value of the anterior chamber depth of a globe on CT for detecting open-globe injury.** *Eur Radiol* 2010;20:1079–84 CrossRef Medline
5. Yuan WH, Hsu HC, Cheng HC, et al. **CT of globe rupture: analysis and frequency of findings.** *AJR Am J Roentgenol* 2014;202:1100–07 CrossRef Medline
6. Kuhn F, Maisiak R, Mann L, et al. **The Ocular Trauma Score (OTS).** *Ophthalmol Clin North Am* 2002;15:163–65, vi CrossRef Medline
7. Schmidt GW, Broman AT, Hindman HB, et al. **Vision survival after open globe injury predicted by classification and regression tree analysis.** *Ophthalmology* 2008;115:202–09 CrossRef Medline
8. Bodanapally UK, Van der Byl G, Shanmuganathan K, et al. **Traumatic optic neuropathy prediction after blunt facial trauma: derivation of a risk score based on facial CT findings at admission.** *Radiology* 2014;272:824–31 CrossRef Medline
9. Joseph DP, Pieramici DJ, Beauchamp NJ. **Computed tomography in the diagnosis and prognosis of open-globe injuries.** *Ophthalmology* 2000;107:1899–906 CrossRef Medline
10. Arey ML, Mootha VV, Whittemore AR, et al. **Computed tomography in the diagnosis of occult open-globe injuries.** *Ophthalmology* 2007;114:1448–52 CrossRef Medline
11. Bodanapally UK, Shanmuganathan K, Shin RK, et al. **Hyperintense optic nerve due to diffusion restriction: diffusion-weighted imaging in traumatic optic neuropathy.** *AJNR Am J Neuroradiol* 2015;36:1536–41 CrossRef Medline
12. Reddy RP, Bodanapally UK, Shanmuganathan K, et al. **Traumatic optic neuropathy: facial CT findings affecting visual acuity.** *Emerg Radiol* 2015;22:351–56 CrossRef Medline
13. Yu Wai Man C, Steel D. **Visual outcome after open globe injury: a comparison of two prognostic models—the Ocular Trauma Score and the Classification and Regression Tree.** *Eye* 2010;24:84–89 CrossRef Medline
14. Weissman JL, Beatty RL, Hirsch WL, et al. **Enlarged anterior chamber: CT finding of a ruptured globe.** *AJNR Am J Neuroradiol* 1995;16:936–38 Medline

MRI-Based Texture Analysis to Differentiate Sinonasal Squamous Cell Carcinoma from Inverted Papilloma

S. Ramkumar, S. Ranjbar, S. Ning, D. Lal, C.M. Zwart, C.P. Wood, S.M. Weindling, T. Wu, J.R. Mitchell, J. Li, and J.M. Hoxworth

ABSTRACT

BACKGROUND AND PURPOSE: Because sinonasal inverted papilloma can harbor squamous cell carcinoma, differentiating these tumors is relevant. The objectives of this study were to determine whether MR imaging–based texture analysis can accurately classify cases of noncoexistent squamous cell carcinoma and inverted papilloma and to compare this classification performance with neuroradiologists' review.

MATERIALS AND METHODS: Adult patients who had inverted papilloma or squamous cell carcinoma resected were eligible (coexistent inverted papilloma and squamous cell carcinoma were excluded). Inclusion required tumor size of >1.5 cm and preoperative MR imaging with axial T1, axial T2, and axial T1 postcontrast sequences. Five well-established texture analysis algorithms were applied to an ROI from the largest tumor cross-section. For a training dataset, machine-learning algorithms were used to identify the most accurate model, and performance was also evaluated in a validation dataset. On the basis of 3 separate blinded reviews of the ROI, isolated tumor, and entire images, 2 neuroradiologists predicted tumor type in consensus.

RESULTS: The inverted papilloma ($n = 24$) and squamous cell carcinoma ($n = 22$) cohorts were matched for age and sex, while squamous cell carcinoma tumor volume was larger ($P = .001$). The best classification model achieved similar accuracies for training (17 squamous cell carcinomas, 16 inverted papillomas) and validation (7 squamous cell carcinomas, 6 inverted papillomas) datasets of 90.9% and 84.6%, respectively ($P = .537$). For the combined training and validation cohorts, the machine-learning accuracy (89.1%) was better than that of the neuroradiologists' ROI review (56.5%, $P = .0004$) but not significantly different from the neuroradiologists' review of the tumors (73.9%, $P = .060$) or entire images (87.0%, $P = .748$).

CONCLUSIONS: MR imaging–based texture analysis has the potential to differentiate squamous cell carcinoma from inverted papilloma and may, in the future, provide incremental information to the neuroradiologist.

ABBREVIATIONS: DOST = Discrete Orthonormal Stockwell Transform; GFB = Gabor Filter Banks; GLCM = Gray-Level Co-occurrence Matrix; IP = inverted papilloma; LBP = local binary patterns; LoGHist = Laplacian of Gaussian histogram; PC = principal component; SCC = squamous cell carcinoma; T1 = axial T1-weighted MRI pulse sequence; T2 = axial T2-weighted MRI pulse sequence with frequency-selective fat suppression; T1C = axial T1-weighted postcontrast MRI pulse sequence with frequency-selective fat suppression

Inverted papilloma (IP) is an uncommon sinonasal tumor of ectodermal origin that most commonly arises from the lateral nasal wall.[1,2] In addition to its pattern of locally aggressive behavior and a propensity for postoperative recurrence, there is an association with malignancy, mostly squamous cell carcinoma (SCC). Reports vary widely in frequency, but the rate of carcinoma is on the order of 10%–15%, and approximately 60%–70% of these are synchronous.[3,4] Although office-based endoscopic incisional biopsy is safe, the sensitivity for the diagnosis of malignancy has been called into question due to sampling errors.[5]

It can be useful to preoperatively identify SCC when coexistent with IP to guide biopsy, expedite surgery, and plan an oncologically sound resection. Although bone thinning and remodeling without large areas of erosion on CT are more characteristic of IP than SCC, this finding is imperfect because IP may also aggressively destroy

Received October 12, 2016; accepted after revision December 13.

From the School of Computing, Informatics, and Decision Systems Engineering (S.Ramkumar, S.N., T.W., J.L.) and Department of Biomedical Informatics (S.Ranjbar), Arizona State University, Tempe, Arizona; Departments of Otolaryngology (D.L.) and Radiology (C.M.Z., J.M.H.), Mayo Clinic, Phoenix, Arizona; Department of Radiology (C.P.W.), Mayo Clinic, Rochester, Minnesota; Department of Radiology (S.M.W.), Mayo Clinic, Jacksonville, Florida; and Department of Research (J.R.M.), Mayo Clinic, Scottsdale, Arizona.

S. Ramkumar and S. Ranjbar are co-first authors.

This work was supported by the Arizona State University/Mayo Clinic Seed Grant Program.

Paper previously presented at: Annual Meeting of the North American Skull Base Society, February 12–14, 2016; Scottsdale, Arizona.

Please address correspondence to Joseph M. Hoxworth, MD, Department of Radiology, Mayo Clinic, 5777 E Mayo Blvd, Phoenix, AZ 85054; e-mail: hoxworth.joseph@mayo.edu

http://dx.doi.org/10.3174/ajnr.A5106

bone, particularly when contacting the walls of the sphenoid sinuses and floor of the anterior cranial fossa.[6,7] Not surprising, FDG-PET has shown a higher mean standard uptake value for SCC compared with IP, but overlap limits the clinical utility of PET.[8] To date, MR imaging has the most promise in differentiating SCC from IP. Although early work initially found no signature appearance on MR imaging for IP, alternating hypointense and hyperintense bands on T2-weighted and contrast-enhanced T1-weighted sequences have become recognized as a distinctive feature of IP and have been described as a convoluted cerebriform pattern.[6,9-11] As with any subjective finding, interpretive errors can occur, especially when tumors are small or incompletely express the convoluted cerebriform pattern. Hence, a more objective form of image analysis is desirable.

Texture analysis is a form of image processing that seeks to characterize complex visual patterns by quantitatively identifying simpler but characteristic subpatterns. Within the field of head and neck radiology, texture analysis has shown applicability in predicting the p53 status of SCC, classifying SCC as human papilloma virus–related, predicting treatment response in head and neck cancer, differentiating benign from malignant thyroid nodules, and characterizing parotid tumors and structural changes after radiation therapy.[12-19] Because a large volume of data is generated when multiple texture analysis algorithms are applied to MR imaging sequences, the statistical comparison of individual texture features is of limited practical value; instead, a multifactorial data-driven analysis is necessary (ie, "radiomics"). Therefore, the objective of this study was to determine whether MR imaging–based texture analysis can differentiate sinonasal SCC from IP by using a multiparametric machine-learning model. Model performance was additionally compared against qualitative neuroradiologists' interpretation to determine its potential for added clinical value.

MATERIALS AND METHODS

Subject Enrollment

The Mayo Clinic Institutional Review Board approved this retrospective study, and the need for informed consent was waived. The pathology data base was queried to identify adult patients (18 years of age or older) who underwent resection of sinonasal IP or SCC. Subjects enrolled from January 1, 2009, to December 31, 2014, were included in the training dataset for model development, while those enrolled between January 1, 2015, and July 1, 2016, composed the validation dataset. To ensure that only a single histologic tumor type would be used for texture analysis, we excluded cases of coexistent IP and SCC. Potential subjects were screened to determine which of them had preoperative face MR imaging available for review. The MRIs, which were performed on numerous scanners within the authors' institution and at external facilities, had to be of diagnostic image quality. At a minimum, the imaging had to include an axial T1-weighted MRI pulse sequence (T1), an axial T2-weighted pulse sequence with frequency-selective fat-suppression (T2), and an axial T1-weighted postcontrast MRI pulse sequence with frequency-selective fat suppression (T1C) for texture analysis, with a section thickness of ≤5 mm, an FOV of ≤ 22 cm, and a matrix size of at least 256 × 192. No restrictions on additional MR imaging technical parameters or type of gadolinium-based intravenous contrast were imposed, and studies were included whether they were performed at 1.5T or 3T field strength. The electronic medical record was reviewed for each potential case, and subjects were excluded if they had an intervention for the sinonasal tumor, including biopsy, surgery, chemotherapy, or radiation therapy before imaging. Subjects were further eliminated if the tumor did not have orthogonal transaxial dimensions greater than 1.5 × 1.5 cm on at least 1 axial image.

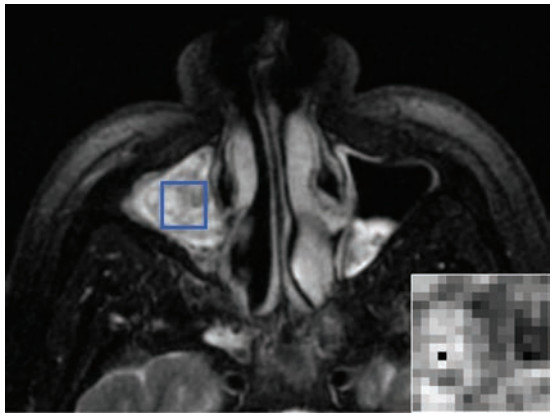

FIG 1. ROI placement. A 51-year-old man with an IP involving the right maxillary sinus. Axial T2-weighted fat-suppressed MR imaging pulse sequence demonstrates the manual placement of the largest rectangular ROI that would fit within the tumor margins on the axial image with the greatest tumor cross-sectional area. The inset image in the lower right corner is representative of the final 16 × 16 matrix that was derived from the ROI isocenter and served as the input for texture analysis.

Image Preparation and Texture Analysis

DICOM files containing the T1, T2, and T1C pulse sequences (also referred to as "contrasts" for the purpose of texture analysis) were anonymized and encoded so that all subsequent image analysis was blinded. To ensure uniformity for texture analysis, we performed resampling and/or zero-padding to generate images with an 18-cm FOV and a 256 × 256 pixel array and normalized image intensities to a dynamic range of 0–255. The studies were then reviewed by a board-certified neuroradiologist with OsiriX (Version 6.5; http:// www.osirix-viewer.com). The borders of the tumor were manually traced on all T1C images on which tumor was visible to generate an ROI-based cross-sectional area for each image and an estimated tumor size by using the ROI Volume function in OsiriX. On the axial image with the greatest tumor cross-sectional area, the neuroradiologist inserted the largest possible rectangular ROI that would fit within the tumor for all 3 sequences (Fig 1). To prevent the 2D texture analysis from being biased by tumor size, a computer script determined the maximal square ROI that could fit within all manually drawn rectangular ROIs across all subjects and automatically positioned this smallest common square ROI at the isocenter of each of the rectangular ROIs. The contents of this square ROI, with 16 × 16 pixels, served as the input for texture analysis.

Texture analysis of each ROI consisted of 3 first-order intensity-based features (mean, SD, and range of gray-level intensities) and features computed by using 5 widely available texture algorithms (all implemented in Python 2.7 programming language [https:// www.python.org/downloads/], by using either custom-written code based on publications or open-source libraries as noted):

1) Gray-Level Co-occurrence Matrix (GLCM) is a widely applied method that uses second-order statistics to assess the ar-

Table 1: Patient demographic characteristics and tumor features[a]

Study Group	Sample Size	Sex (Female/Male)	Age (yr)	Tumor Volume (cm^3)	Tumor Stage[b]			
					T1	T2	T3	T4
IP training	16	4:12	58.0 ± 12.1	21.2 ± 17.7	1	3	10	2
IP validation	6	1:5	58.2 ± 15.3	22.0 ± 6.9	1	1	3	1
IP combined	22	5:17[c]	58.1 ± 13.1[d]	21.4 ± 15.5[e]	2	4	13	3
SCC training	17	4:13	54.0 ± 13.5	55.8 ± 40.5	0	1	4	12
SCC validation	7	1:6	54.6 ± 9.4	43.5 ± 27.9	0	1	2	4
SCC combined	24	5:19[c]	54.2 ± 12.5[d]	52.2 ± 37.7[e]	0	2	6	16

[a] Data are presented separately for the training and validation sets and also as a single combined cohort for each tumor type. Age and tumor volume are presented as means.
[b] Tumor stage represents the Krouse staging system[39] for IP and the American Joint Committee on Cancer staging[40] for SCC.
[c] Fisher exact test, $P = .578$.
[d] Two-sample t test, $P = .317$.
[e] Two-sample t test, $P = .001$.

rangement of similar gray-scale intensities within an ROI.[20] GLCM evaluates how frequently a pair of intensity levels is identified in an orientation based on a specified angle and radius. In the current study, the co-occurrence matrix was determined for a distance of 1 pixel over 4 angular directions (0°, 45°, 90°, and 135°). The mean and range for 13 rotationally invariant features (including measures of homogeneity, entropy, angular second moment, correlation, and dissimilarity) were computed at each ROI for each MR imaging contrast.[20]

2) Local binary patterns (LBP) evaluates the set of points within a fixed radius of a specified voxel to determine in a binary fashion whether they are higher or lower in intensity than neighboring voxels.[21] Depending on the number of bitwise transitions across this interrogated region, the LBP can be classified as uniform or nonuniform, and histograms of these data provide a measure of ROI uniformity. A 3-voxel radius was selected to complement the smaller scale patterns already assessed by GLCM. A 12-bin histogram was used, resulting in 12 LBP texture features being calculated at each ROI for each MR imaging contrast.

3) Discrete Orthonormal Stockwell Transform (DOST) provides a rotationally invariant multiresolution spatial-frequency representation of an image based on dyadic sampling of the Fourier representation of the image.[22] Ten DOST features were calculated at each ROI for each MR imaging contrast.

4) Laplacian of Gaussian Histogram (LoGHist) is a convolution-based method to capture the spectral composition of an image in intermediate scales not achievable with first- and second-order statistics. Through the use of varying sizes of bandpass filters, different scales of texture ranging from fine to coarse are highlighted.[23] Gaussians with 3 different values of σ (2.0, 4.0, and 6.0) were used to cover the range of fine-to-medium-scale textures, and 18 LoGHist features were generated at each ROI for each MR imaging contrast.

5) The Gabor Filter Banks (GFB) technique uses localized and linear filters to capture details in various frequency resolutions.[24] Four different Gabor filters were rendered by using 2 σ levels (1.0 and 3.0) and 2 frequency levels (0.6 and 1.0). By calculating the mean and SD of the filtered ROI, we computed 8 GFB features at each ROI for each MR imaging contrast.

Neuroradiologists' Review

Using OsiriX, 2 neuroradiologists with 25 and 28 years of experience, respectively, performed a blinded review to reach a consensus diagnosis of IP or SCC for each case. This was performed during 3 separate rounds of image review, each of which was randomized and completed in the following order:

1) ROI: For the T1, T2, and T1C series, the neuroradiologists exclusively reviewed the 16 × 16 square ROIs that had been used for texture analysis.

2) Tumor: On all images in the T1, T2, and T1C series, the data outside the tumor margins were zero-filled so that the neuroradiologists could only base their assessment on the intrinsic appearance of the tumor without information regarding tumor location and invasive behavior.

3) Image: The neuroradiologists were able to review the unaltered T1, T2, and T1C imaging datasets in their entirety.

Machine Learning and Statistical Analysis

Open-source R statistical and computing software (http://www.r-project.org) was used to perform the analyses and classification. Hypothesis tests were 2-sided, and statistical significance was defined as $P < .05$. The comparison of subject demographics and tumor size between IP and SCC was performed by using a 2-sample t test for subject age and tumor volume and a Fisher exact test for sex. The 2-sample t test was used for a univariate comparison of texture features between IP and SCC before the application of machine-learning methodology, and P values were corrected for multiple comparisons by using the false discovery rate.[25]

A total of 231 texture features were calculated for each case (77 texture features per MR imaging contrast × 3 contrasts). To reduce the dimensionality of the texture features and increase the generalizability of the predictive model for the training dataset, we used principal component (PC) analysis.[26-28] PCs, which are linear combinations of features, were identified separately for each texture algorithm and MR imaging contrast. Those PCs that sufficiently accounted for 90% of the texture feature variability were selected for further processing. Three commonly described classification algorithms, Diagonal Linear Discriminate Analysis, Support Vector Machines, and Diagonal Quadratic Discriminate Analysis, were conducted on the basis of the selected PCs in an attempt to differentiate SCC from IP.[29-31] Sequential forward-feature selection identified the image-based PCs that yielded the greatest accuracy.[26,27] In developing the classification model, we initially selected the PC with the largest discriminatory power and incorporated additional PCs that improved model accuracy in an iterative fashion until incremental gains in accuracy were <1%.

Classification accuracy was determined by using leave-one-out cross-validation, in which all samples except for 1 were used, while the left-out sample served as the test case with which to assess classification accuracy.[32] This process was repeated until all samples in the training dataset had served as the test case, and the overall cross-validation accuracy was the averaged accuracy. The most accurate classification model was applied in a blinded fashion to the validation dataset, and the diagnostic performance of the model was assessed. Model performance accuracies between

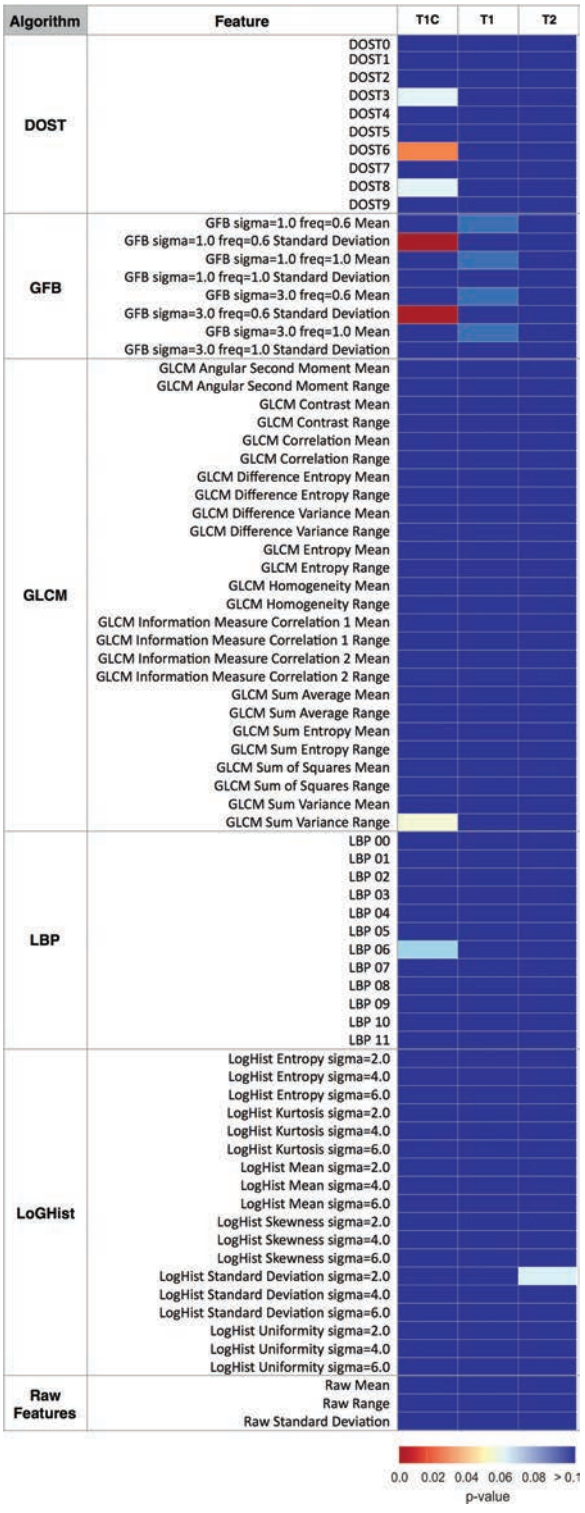

FIG 2. Heat map showing MR imaging texture feature significance in distinguishing tumor type. Univariate analysis compared the pathology status (SCC versus IP) with MR imaging–texture features. Color maps show the false discovery rate–adjusted *P* values of a 2-sample *t* test. MR imaging contrasts (pulse sequences) are listed above the columns, and MR imaging–based texture features are listed in rows. DOST features 0–9 correspond with low-to-high frequency patterns. LBP 0–11 are the normalized bin counts in the LBP histogram. The reader is referred to the "Materials and Methods" section for additional details about the features.

Table 2: Diagnostic performance of machine-learning classification in training and validation datasets

	Tumor Type (Pathologic Diagnosis)		Diagnostic Performance	
	SCC	IP		
Model prediction for training dataset				
SCC	16	2	Accuracy	90.9%[a]
			Sensitivity	94.1%
IP	1	14	Specificity	87.5%
			PPV	88.9%
Total	17	16	NPV	93.3%
Model prediction for validation dataset				
SCC	6	1	Accuracy	84.6%[a]
			Sensitivity	85.7%
IP	1	5	Specificity	83.3%
			PPV	85.7%
Total	7	6	NPV	83.3%
Model prediction for entire cohort				
SCC	22	3	Accuracy	89.1%
			Sensitivity	91.7%
IP	2	19	Specificity	86.4%
			PPV	88.0%
Total	24	22	NPV	90.5%

Note:—NPV indicates negative predictive value; PPV, positive predictive value.
[a] With a 2-tailed test of population proportion, the accuracies for the training and validation datasets were not significantly different ($P = .537$).

the training and validation datasets and between the best classification model and neuroradiologists' review were compared by using a 2-tailed test of population proportion.

RESULTS

Thirty-three subjects were included in the training set, 16 IPs and 17 SCCs, while the validation set consisted of 6 IPs and 7 SCCs (Table 1). The patients were similarly matched for age and male-predominant sex. Mean tumor volume was larger for SCC than IP ($P = .001$).

Individual features derived from the 5 different texture analyses across all 3 MR imaging contrasts (T1, T2, T1C) were initially evaluated in a univariate fashion to look for significant differences between the IP and SCC groups (Fig 2). The greatest number of texture features showing statistically significant differences were derived from the DOST and GFB texture analyses.

Model performance for the training and validation datasets is presented in Table 2. Following PC analysis and machine-learning classification, the predictive classifier with the best classification result was Support Vector Machines, yielding 90.9% accuracy for the training dataset. The 84.6% accuracy of the validation dataset did not significantly differ from that achieved in the training dataset ($P = .537$). When we combined the training and validation cohorts ($n = 46$), the accuracy achieved by texture analysis (89.1%) was significantly better than that of the ROI-based neuroradiologists' review (Table 3, 56.5%, $P = .0004$) and showed a trend toward improved accuracy over neuroradiologists' review of the entire tumor (73.9%, $P = .060$). Texture-analysis accuracy was not significantly different from that of the neuroradiologists reviewing the entire unaltered images (87.0%, $P = .748$).

Table 3: Diagnostic performance of texture analysis with machine learning compared with neuroradiologists' review for the differentiation of SCC from IP[a]

Analysis Method	Accuracy[b]	Sensitivity	Specificity	PPV	NPV
Texture analysis with machine learning	89.1%	91.7%	86.4%	88.0%	90.5%
Neuroradiologists' review, ROI	56.5% ($P = .0004$)	54.2%	59.1%	59.1%	54.2%
Neuroradiologists' review, tumor	73.9% ($P = .060$)	75.0%	72.7%	75.0%	72.7%
Neuroradiologists' review, image	87.0% ($P = .748$)	91.7%	81.8%	84.6%	90.0%

Note:—NPV indicates negative predictive value; PPV, positive predictive value.

[a] Results are shown for the entire cohort (22 IPs, 24 SCCs) and reflect the best classification model. The labels for the neuroradiologists' assessment indicate whether they reviewed the 16 × 16 ROI (ROI), tumor alone (tumor), or entire images (image).

[b] *P* values represent comparison of texture analysis with machine learning against each neuroradiologist's review using a 2-tailed test of population proportion.

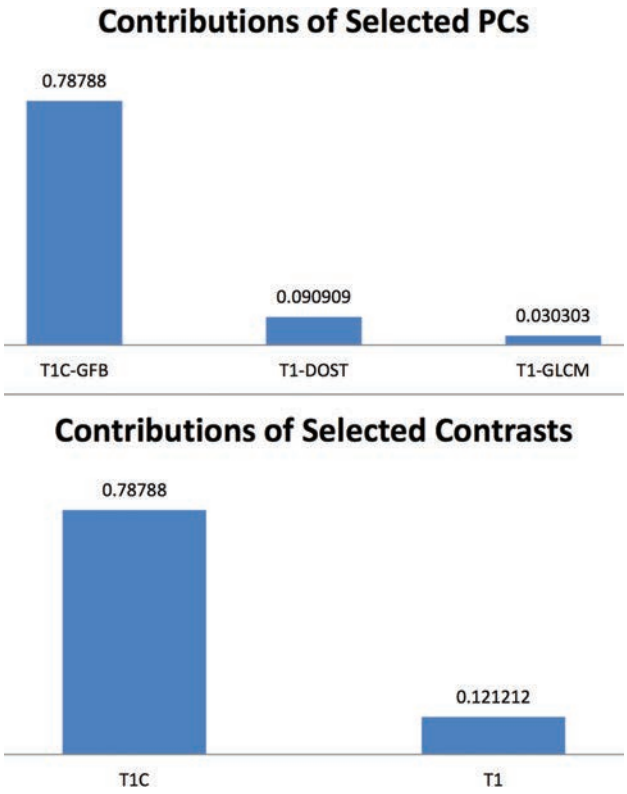

FIG 3. Relative contributions to model accuracy. Of the 90.9% overall model accuracy for the training dataset, the bar graph demonstrates the accuracy attributable to PCs derived from T1C-GFB, T1-DOST, and T1-GLCM (*upper panel*). Across all texture algorithms, the contribution to total model accuracy was derived predominantly from T1C, with minor contributions from T1 and no input from T2 (*lower panel*).

Relative contributions to model accuracy from each texture analysis algorithm and MR imaging contrast are presented (Fig 3). The most significant texture features were derived from T1C-GFB, T1-GLCM, and T1-DOST (Fig 4).

DISCUSSION

MR imaging has long been recognized as the most useful technique with which to distinguish sinonasal SCC from IP. Most of the prior work focused on a qualitative imaging appearance known as the "convoluted cerebriform pattern."[6,9-11,33,34] Although this pattern has a high level of sensitivity for IP, it is not entirely specific. As an example, Jeon et al[9] evaluated the performance of the convoluted cerebriform pattern in 30 patients with IP relative to 128 patients with sinonasal malignancies and reported a sensitivity of 100%, specificity of 87%, positive predictive value of 64%, negative predictive value of 100%, and accuracy of 89%.

Texture analysis integrated into a machine-learning model was able to classify SCC and IP with an accuracy on par with the previously published results based on the convoluted cerebriform pattern.[9] It is also similar to the best consensus neuroradiologists' interpretation in the current study. However, this technology is meant to supplement a neuroradiologist's interpretive skills rather than compete with them. In clinical practice, a diagnosis is rendered by synthesizing all available data that include not only intrinsic tumor appearance but also other imaging features such as site of origin, tumor size, extrasinonasal extension, and tumor margins. Indeed, the current results support a neuroradiologist's accuracy improving for differentiating sinonasal IP and SCC as more imaging information is made available. On the basis of a 16 × 16 ROI, the texture-based machine-learning model outperformed the accuracy of the neuroradiologists ($P = .0004$). In terms of assessing the intrinsic tumor appearance, texture analysis stands to provide incremental benefit when human pattern recognition becomes most limited, and this can occur with a small tumor. For example, Maroldi et al[6] found it more challenging to recognize the convoluted cerebriform pattern on T2-weighted images for tumors of <2 cm. While tumors smaller than 1.5 × 1.5 cm were excluded from enrollment in the current study, the final processed ROIs were only 1.125 × 1.125 cm.

Because small noninvasive sinonasal tumors are not universally imaged with MR imaging, the greatest potential benefit for texture analysis might be in detecting a small focus of SCC within a larger IP to expedite patient management. Accurately assessing small regions would be a prerequisite for the detection of such tumor heterogeneity. The potential for interpretive error is greatest when a small focus of SCC exists within a much larger IP and goes unrecognized because a convoluted cerebriform pattern is still present. Indeed, this pattern of a "partial" convoluted cerebriform pattern has been described.[6,9,35] Likewise, necrosis, recognized as nonenhancing tissue on contrast-enhanced MR imaging, is associated with SCC but may not be apparent when a small focus of SCC coexists with an IP.[9,10,35] A future goal for texture analysis of a mixed tumor containing both IP and SCC is to assist with interpretation by highlighting areas that are most suspicious for SCC.

Texture analysis can also extract useful features from images that have been traditionally neglected by the human eye. The convoluted cerebriform pattern has been historically described on T1-weighted postcontrast and T2-weighted sequences.[6,9-11,33-35] However, noncontrast T1-weighted MR imaging has received no attention to date, to our knowledge. The texture analysis in the current study found more significant features for T1 than T2 on a univariate basis (Fig 2). Although T1-DOST and T1-GLCM made a minority contribution to the final model, no T2 features contributed to final model accuracy (Fig 3).

For MR imaging, it has been suggested that texture analysis models may not effectively translate across different imaging pro-

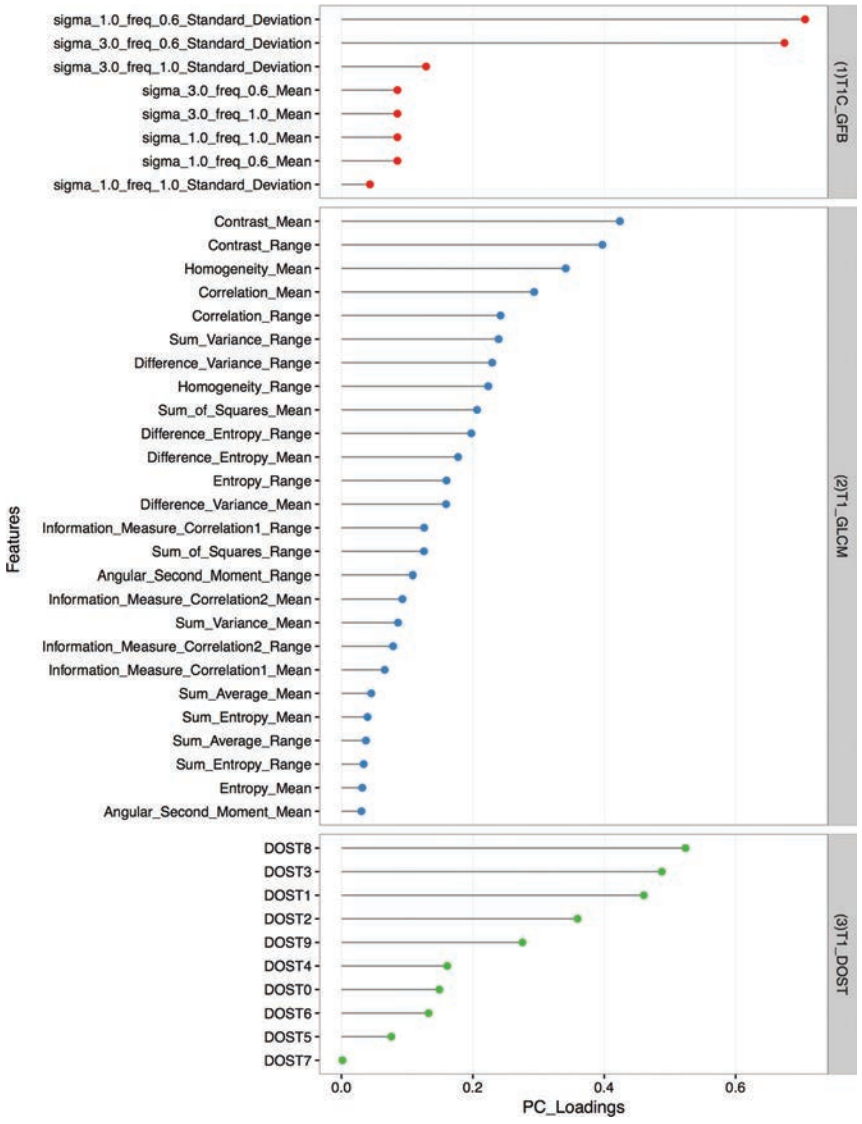

FIG 4. PC loading. The model with the greatest accuracy for discriminating SCC from IP was derived from T1C-GFB, T1-GLCM, and T1-DOST texture features (*right*). For the individually specified texture features (*left*), PC loadings are graphically represented, and larger values in the PC loading indicate greater significance in the final model.

tocols and scanner platforms.[36,37] Certainly, this possibility would make such results clinically meaningless because a new model would have to be created for each scanner running a unique protocol. Fruehwald-Pallamar et al[38] concluded that texture analysis is not practical for differentiating malignant and benign tumors of the head and neck when using different protocols on different MR imaging scanners. However, their cohort was very heterogeneous, containing numerous types of benign and malignant lesions. The subjects for the current study were accrued during a long period and were not imaged with a common scanner and protocol. Nevertheless, an accurate texture-based model was achieved that performed similarly in the training and validation datasets. At least for the context of sinonasal IP and SCC, this outcome holds promise for reproducibility across scanner platforms.

The current study is limited, given its retrospective nature and small sample size. Hence, the high accuracy for the differentiation of SCC from IP with texture analysis is not meant to represent the performance of an established diagnostic imaging test. Instead, these results merely confirm the feasibility of this technique for distinguishing these 2 tumor types. In showing proof of concept, a 2D ROI-based analysis was used to confirm discriminatory ability with a limited data sample. Moreover, because SCC tends to be a larger tumor than IP on average, this approach eliminated the potential for falsely finding texture differences on the basis of relative oversampling of a larger tumor. Future directions will include the refinement of the texture analysis pipeline into a volumetric tool with the objective of highlighting foci of SCC when it is coexistent with IP. This will need to be studied prospectively to ensure that the histopathologic analysis can be accurately coregistered to MR imaging.

CONCLUSIONS

With MR imaging–based texture analysis, a machine-learning model for the differentiation of sinonasal SCC and IP achieved accuracy comparable with both neuroradiologists' interpretation and previously published reports on the convoluted cerebriform pattern. Because the classification model was significantly more accurate than the neuroradiologists' interpretation for a small ROI, texture analysis has the potential to provide incremental benefit to the neuroradiologists' interpretation, particularly in cases of small or heterogeneous tumors.

Disclosures: Shreya Ramkumar—*RELATED*: *Grant*: Arizona State University/Mayo Clinic Seed Grant, *Comments*: A $40,000 intramural research grant funding was awarded to foster collaborative research between Arizona State University and Mayo Clinic.* Sara Ranjbar—*RELATED*: *Grant*: Arizona State University/Mayo Clinic Seed Grant, *Comments*: A $40,000 intramural research grant funding was awarded to foster collaborative research between Arizona State University and Mayo Clinic.* Devyani Lal—*UNRELATED*: *Board Membership*: American Rhinologic Society, *Comments*: not for profit; *Employment*: Mayo Clinic; *Grants/Grants Pending*: Flinn Foundation, Sanofi. Joseph Ross Mitchell—*UNRELATED*: *Employment*: Mayo Clinic; *Grants/Grants/Grants Pending*: National Institutes of Health*; *Patents (Planned, Pending, or Issued)*: Mayo Clinic, *Comments*: Provisional patents were filed relating to texture analysis of medical imaging data.* Joseph Hoxworth—*RELATED*: *Grant*: Arizona State University/Mayo Clinic Seed Grant, Comments: A $40,000 intramural research grant funding was awarded to foster collaborative research between Arizona State University and Mayo Clinic.* *Money paid to the institution.

REFERENCES

1. Anari S, Carrie S. **Sinonasal inverted papilloma: narrative review.** *J Laryngol Otol* 2010;124:705–15 CrossRef Medline
2. Sauter A, Matharu R, Hörmann K, et al. **Current advances in the**

basic research and clinical management of sinonasal inverted papilloma (review). *Oncol Rep* 2007;17:495–504 Medline
3. Barnes L. **Diseases of the nasal cavity, paranasal sinuses, and nasopharynx.** In: Barnes L, ed. *Surgical Pathology of the Head and Neck.* 3rd ed. New York: Informa Healthcare; 2008:361–71
4. Mirza S, Bradley PJ, Acharya A, et al. **Sinonasal inverted papillomas: recurrence, and synchronous and metachronous malignancy.** *J Laryngol Otol* 2007;121:857–64 Medline
5. Han MW, Lee BJ, Jang YJ, et al. **Clinical value of office-based endoscopic incisional biopsy in diagnosis of nasal cavity masses.** *Otolaryngol Head Neck Surg* 2010;143:341–47 CrossRef Medline
6. Maroldi R, Farina D, Palvarini L, et al. **Magnetic resonance imaging findings of inverted papilloma: differential diagnosis with malignant sinonasal tumors.** *Am J Rhinol* 2004;18:305–10 Medline
7. Som PM, Lawson W, Lidov MW. **Simulated aggressive skull base erosion in response to benign sinonasal disease.** *Radiology* 1991;180:755–59 CrossRef Medline
8. Jeon TY, Kim HJ, Choi JY, et al. **18F-FDG PET/CT findings of sinonasal inverted papilloma with or without coexistent malignancy: comparison with MR imaging findings in eight patients.** *Neuroradiology* 2009;51:265–71 CrossRef Medline
9. Jeon TY, Kim HJ, Chung SK, et al. **Sinonasal inverted papilloma: value of convoluted cerebriform pattern on MR imaging.** *AJNR Am J Neuroradiol* 2008;29:1556–60 CrossRef Medline
10. Ojiri H, Ujita M, Tada S, et al. **Potentially distinctive features of sinonasal inverted papilloma on MR imaging.** *AJR Am J Roentgenol* 2000;175:465–68 CrossRef Medline
11. Yousem DM, Fellows DW, Kennedy DW, et al. **Inverted papilloma: evaluation with MR imaging.** *Radiology* 1992;185:501–05 CrossRef Medline
12. Brown AM, Nagala S, McLean MA, et al. **Multi-institutional validation of a novel textural analysis tool for preoperative stratification of suspected thyroid tumors on diffusion-weighted MRI.** *Magn Reson Med* 2016;75:1708–16 CrossRef Medline
13. Buch K, Fujita A, Li B, et al. **Using texture analysis to determine human papillomavirus status of oropharyngeal squamous cell carcinomas on CT.** *AJNR Am J Neuroradiol* 2015;36:1343–48 CrossRef Medline
14. Dang M, Lysack JT, Wu T, et al. **MRI texture analysis predicts p53 status in head and neck squamous cell carcinoma.** *AJNR Am J Neuroradiol* 2015;36:166–70 CrossRef Medline
15. Fruehwald-Pallamar J, Czerny C, Holzer-Fruehwald L, et al. **Texture-based and diffusion-weighted discrimination of parotid gland lesions on MR images at 3.0 Tesla.** *NMR Biomed* 2013;26:1372–79 CrossRef Medline
16. Fujita A, Buch K, Li B, et al. **Difference between HPV-positive and HPV-negative non-oropharyngeal head and neck cancer: texture analysis features on CT.** *J Comput Assist Tomogr* 2016;40:43–47 CrossRef Medline
17. Liu J, Mao Y, Li Z, et al. **Use of texture analysis based on contrast-enhanced MRI to predict treatment response to chemoradiotherapy in nasopharyngeal carcinoma.** *J Magn Reson Imaging* 2016;44:445–55 CrossRef Medline
18. Scalco E, Fiorino C, Cattaneo GM, et al. **Texture analysis for the assessment of structural changes in parotid glands induced by radiotherapy.** *Radiother Oncol* 2013;109:384–87 CrossRef Medline
19. Zhang H, Graham CM, Elci O, et al. **Locally advanced squamous cell carcinoma of the head and neck: CT texture and histogram analysis allow independent prediction of overall survival in patients treated with induction chemotherapy.** *Radiology* 2013;269:801–09 CrossRef Medline
20. Haralick RM, Shanmugam K, Dinstein I. **Textural features for image classification.** *IEEE Transactions on Systems, Man, and Cybernetics* 1973;SMC-3:610–21
21. Ojala T, Pietikainen M, Mäenpää T. **Multiresolution gray-scale and rotation invariant texture classification with local binary patterns.** *IEEE Transactions on Pattern Analysis and Machine Intelligence* 2002;24:971–87 CrossRef
22. Drabycz S, Stockwell RG, Mitchell JR. **Image texture characterization using the discrete orthonormal S-transform.** *J Digit Imaging* 2009;22:696–708 CrossRef Medline
23. Davnall F, Yip CS, Ljungqvist G, et al. **Assessment of tumor heterogeneity: an emerging imaging tool for clinical practice?** *Insights Imaging* 2012;3:573–89 CrossRef Medline
24. Jain AK, Farrokhnia F. **Unsupervised texture segmentation using Gabor filters.** *Pattern Recognition* 1991;24:1167–86 CrossRef
25. Benjamini Y, Hochberg Y. **Controlling the false discovery rate: a practical and powerful approach to multiple testing.** *Journal of the Royal Statistical Society. Series B (Methodological)* 1995;57:289–300
26. Eyal E, Bloch BN, Rofsky NM, et al. **Principal component analysis of dynamic contrast enhanced MRI in human prostate cancer.** *Invest Radiol* 2010;45:174–81 CrossRef Medline
27. Jolliffe I. 2014. Principal Component Analysis. Wiley StatsRef: Statistics Reference Online. CrossRef
28. Yeung TP, Dekaban M, De Haan N, et al. **Improving quantitative CT perfusion parameter measurements using principal component analysis.** *Acad Radiol* 2014;21:624–32 CrossRef Medline
29. Dixon SJ, Brereton RG. **Comparison of performance of five common classifiers represented as boundary methods: Euclidean Distance to Centroids, Linear Discriminant Analysis, Quadratic Discriminant Analysis, Learning Vector Quantization and Support Vector Machines, as dependent on data structure.** *Chemometrics and Intelligent Laboratory Systems* 2009;95:1–17 CrossRef
30. Lin GC, Wang WJ, Wang CM, et al. **Automated classification of multi-spectral MR images using Linear Discriminant Analysis.** *Comput Med Imaging Graph* 2010;34:251–68 CrossRef Medline
31. Zacharaki EI, Wang SM, Chawla S, et al. **Classification of brain tumor type and grade using MRI texture and shape in a machine learning scheme.** *Magn Reson Med* 2009;62:1609–18 CrossRef Medline
32. Drabycz S, Roldán G, de Robles P, et al. **An analysis of image texture, tumor location, and MGMT promoter methylation in glioblastoma using magnetic resonance imaging.** *Neuroimage* 2010;49:1398–405 CrossRef Medline
33. Fujima N, Nakamaru Y, Sakashita T, et al. **Differentiation of squamous cell carcinoma and inverted papilloma using non-invasive MR perfusion imaging.** *Dentomaxillofac Radiol* 2015;44:20150074 CrossRef Medline
34. Wang X, Zhang Z, Chen X, et al. **Value of magnetic resonance imaging including dynamic contrast-enhanced magnetic resonance imaging in differentiation between inverted papilloma and malignant tumors in the nasal cavity.** *Chin Med J (Engl)* 2014;127:1696–701 Medline
35. Miyazaki Y, Ikeda K, Uemura Y, et al. **Non-necrotic invasive squamous cell carcinoma associated with an inverted papilloma: MRI features.** *Radiat Med* 2006;24:143–46 CrossRef Medline
36. Lerski RA, Schad LR, Luypaert R, et al. **Multicentre magnetic resonance texture analysis trial using reticulated foam test objects.** *Magn Reson Imaging* 1999;17:1025–31 CrossRef Medline
37. Mayerhoefer ME, Szomolanyi P, Jirak D, et al. **Effects of MRI acquisition parameter variations and protocol heterogeneity on the results of texture analysis and pattern discrimination: an application-oriented study.** *Med Phys* 2009;36:1236–43 CrossRef Medline
38. Fruehwald-Pallamar J, Hesselink JR, Mafee MF, et al. **Texture-based analysis of 100 MR examinations of head and neck: is it possible to discriminate between benign and malignant masses in a multicenter trial?** *Rofo* 2016;188:195–202 CrossRef Medline
39. Krouse JH. **Development of a staging system for inverted papilloma.** *Laryngoscope* 2000;110:965–68 CrossRef Medline
40. Edge SB; American Joint Committee on Cancer. *AJCC Cancer Staging Manual.* 7th ed. New York: Springer-Verlag; 2010:69–78

Trochlear Groove and Trochlear Cistern: Useful Anatomic Landmarks for Identifying the Tentorial Segment of Cranial Nerve IV on MRI

P.M. Bunch, H.R. Kelly, D.A. Zander, and H.D. Curtin

ABSTRACT

BACKGROUND AND PURPOSE: The trochlear groove and trochlear cistern are anatomic landmarks closely associated with the tentorial segment of cranial nerve IV. The purposes of this study were to describe the MR imaging appearances of the trochlear groove and trochlear cistern and to test our hypothesis that knowledge of these anatomic landmarks facilitates identification of cranial nerve IV in routine clinical practice.

MATERIALS AND METHODS: For this retrospective study, consecutive MR imaging examinations of the sinuses performed in 25 patients (50 sides) at our institution were reviewed. Patient characteristics and study indications were recorded. Three readers performed independent assessments of trochlear groove, cistern, and nerve visibility on coronal images obtained by using a T2-weighted driven equilibrium radiofrequency reset pulse sequence.

RESULTS: Interobserver agreement was 78% for visibility of the trochlear groove, 56% for the trochlear cistern, and 68% for cranial nerve IV. Following consensus review, the trochlear groove was present in 44/50 sides (88%), the trochlear cistern was present in 25/50 sides (50%), and cranial nerve IV was identified in 36/50 sides (72%). When the trochlear groove was present, cranial nerve IV was identified in 35/44 sides (80%), in contrast to 1/6 sides (17%) with no groove ($P = .0013$). When the trochlear cistern was present, cranial nerve IV was identified in 23/25 sides (92%), in contrast to 13/25 sides (52%) with no cistern ($P = .0016$).

CONCLUSIONS: The trochlear groove and trochlear cistern are anatomic landmarks that facilitate identification of cranial nerve IV in routine clinical practice.

ABBREVIATION: coronal T2 DRIVE = coronal 2D T2-weighted driven equilibrium radiofrequency reset pulse

Historically, imaging of cranial nerve IV has been difficult.[1,2] These difficulties likely relate to the small size of the nerve and the presence of numerous adjacent blood vessels in the quadrigeminal and ambient cisterns.[3,4] These difficulties are compounded by the fact that MR images are often acquired in the axial plane, nearly parallel to the cisternal course of the nerve.

In research settings, high-resolution MR images have reliably demonstrated cranial nerve IV in healthy volunteers; however, long acquisition times ranging from 7 to 26 minutes make these sequences impractical for routine clinical use.[3,5,6] Acknowledging the perceived impracticality of consistently identifying cranial nerve IV in routine practice, more recently published work has proposed using volumetric analyses of the superior oblique muscles as a correlate for the presence or absence of cranial nerve IV in patients with congenital superior oblique palsy.[7] However, the ability to reliably identify the nerve itself can be important in identifying underlying pathology and can aid in treatment and surgical planning.[3,8]

Various segments and subsegments have been proposed to describe the course of cranial nerve IV distal to its exit from the dorsal midbrain and proximal to its entrance into the cavernous sinus.[3,4,6,9-11] Some authors consider the tentorial segment to be the distal subdivision of the cisternal segment,[3,6,9,10] and others describe the tentorial segment as distinct from the cisternal segment of cranial nerve IV.[4,11] However, there is generally agreement that the tentorial segment of cranial nerve IV begins when the nerve becomes closely associated with the inferior aspect of the cerebellar tentorium and ends at the entrance of the nerve to the cavernous sinus.

Received November 16, 2016; accepted after revision December 19.

From the Department of Radiology (P.M.B., H.R.K.), Division of Neuroradiology, Massachusetts General Hospital, Boston, Massachusetts; and Department of Radiology (H.R.K., D.A.Z., H.D.C.), Massachusetts Eye and Ear, Boston, Massachusetts.

Paper previously represented, in part, as an oral scientific presentation entitled "The Trochlear Groove: A Useful Anatomic Landmark for Identifying Cranial Nerve IV" at: Annual Meeting of the American Society of Head and Neck Radiology, September 7–11, 2016; Washington, DC.

Please address correspondence to Paul M. Bunch, MD, Department of Radiology, Division of Neuroradiology, Massachusetts General Hospital, Gray 2, Room 273A, 55 Fruit St, Boston, MA 02114; e-mail: paul.m.bunch@gmail.com; @pbunchmd

http://dx.doi.org/10.3174/ajnr.A5117

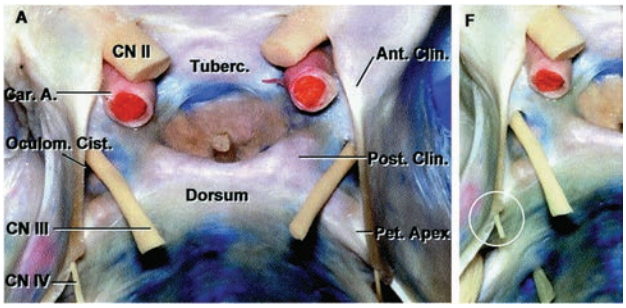

FIG 1. Labeled (*A*) and unlabeled (*F*) anterosuperior views of the sella and suprasellar region demonstrate cranial nerve IV passing into the trochlear groove (*circle*, *F*). Car.A. indicates carotid artery; Oculom., oculomotor; Post., posterior; Ant., anterior; Cist., cistern; Tuberc., tuberculum; Clin., clinoid; Pet. Apex, petrous apex. Modified with permission from Rhoton AL Jr. The sellar region. *Neurosurgery* 2002;51(4 suppl):S335–74.[12]

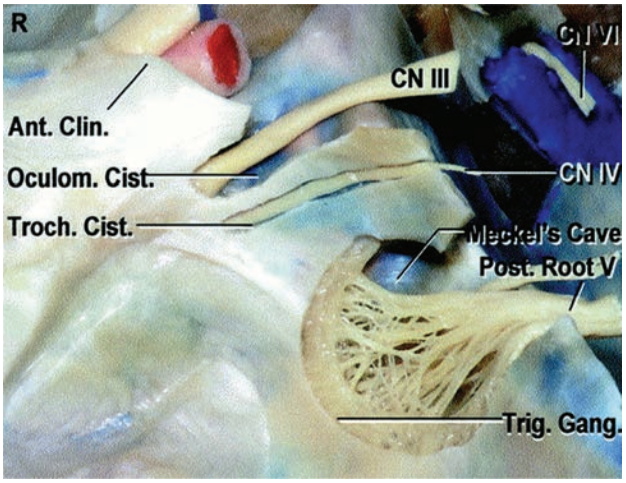

FIG 2. Lateral view of the right cavernous sinus demonstrates cranial nerve IV traveling within the trochlear cistern immediately proximal to entering the cavernous sinus. The trochlear cistern is located inferior to the oculomotor cistern and superior to the Meckel cave. Troch. indicates trochlear; Trig. Gang., trigeminal ganglion. Modified with permission from Rhoton AL Jr. The cavernous sinus, the cavernous venous plexus, and the carotid collar. *Neurosurgery* 2002;51(4 suppl):S375–410.[16]

Cadaveric dissections have shown that the tentorial segment of cranial nerve IV travels within a shallow groove (Fig 1) inferolateral to the free tentorial edge en route to the cavernous sinus, and this shallow groove has been referred to as the "trochlear groove."[4,9,10,12] After passing through the trochlear groove but before entering the cavernous sinus, the tentorial segment of cranial nerve IV pierces the tentorium to course a short distance through the posterior petroclinoid fold.[4,13] The space through which cranial nerve IV passes in the posterior petroclinoid fold may contain CSF and has been referred to as the "trochlear cistern" (Fig 2).[4] These findings are consistent with the common progression of the cranial nerves through a transitional "dural cave segment" in their course from the intracranial to the extracranial compartment.[14]

Coronal 2D T2-weighted driven equilibrium radiofrequency reset pulse (coronal T2 DRIVE) is a fluid-sensitive MR sequence commonly performed during sinus MR imaging examinations at our institution. We have observed cranial nerve IV within both the trochlear groove (Fig 3) and the trochlear cistern (Fig 4) on clinical images obtained with this sequence. With respect to the more easily identifiable cranial nerve V, the trochlear groove is typically seen on coronal images at the level of the trigeminal nerve cisternal segment and the trochlear cistern is seen at the level of the Meckel cave.

We hypothesized that knowledge of these anatomic landmarks will facilitate identification of the tentorial segment of cranial nerve IV in routine clinical practice.

The purposes of this study were to describe the MR imaging appearances of the trochlear groove and trochlear cistern and to test our hypothesis regarding the utility of these landmarks for identifying cranial nerve IV.

MATERIALS AND METHODS

Subjects

For this Health Insurance Portability and Accountability Act–compliant, institutional review board–approved study, all sinus MR imaging examinations performed at Massachusetts Eye and Ear between December 1, 2015, and April 1, 2016, were retrospectively reviewed. Inclusion criteria were the following: 1) older than 18 years of age, 2) coronal T2 DRIVE sequence performed, and 3) no superior oblique palsy documented in the patient's electronic medical record. Twenty-five MR imaging examinations in 25 patients met the inclusion criteria and were included in the study. Patient characteristics and study indications were recorded.

To maximize generalizability and to best simulate routine clinical practice, we did not exclude examinations containing motion, pulsation, and other MR imaging artifacts from our study.

Image Acquisition

All examinations were performed on a 3T scanner (Achieva; Philips Healthcare, Best, the Netherlands) by using an 8-channel head coil (SENSE Flex M coil; Philips Healthcare).

The coronal T2 DRIVE sequence acquisition parameters for the study group were as follows: TR, 3369–6355 ms; TE, 100 ms; echo-train length, 11; FOV, 120–160 mm; matrix, 324 × 300 to 456 × 454; voxel size, from 0.3 × 0.35 × 3.0 to 0.4 × 0.44 × 3.0; gap, 0.3 ($n = 12$) or 1 mm ($n = 13$); NEX, 1 ($n = 15$) or 2 ($n = 10$). These acquisition parameters resulted in a mean sequence acquisition time of 3 minutes 54 seconds ± 37 seconds (range, 2 minutes 54 seconds–5 minutes).

Reader Assessment

Anatomic Structures. After a brief self-guided training session based on 10 sinus MR imaging examinations not included in the study group, 3 radiologists independently reviewed the coronal T2-DRIVE sequences for the 25 patients in the study group with the Massachusetts Eye and Ear PACS. The radiologists included 2 fellowship-trained neuroradiologists (6 and 3 years' subspecialty experience) and 1 neuroradiology fellow. They were asked to determine whether the trochlear groove, trochlear cistern, and cranial nerve IV were identifiable on each side in all patients, and discrepancies were resolved by consensus review. To be considered "identifiable," the tentorial segment of cranial nerve IV had to be identified by the

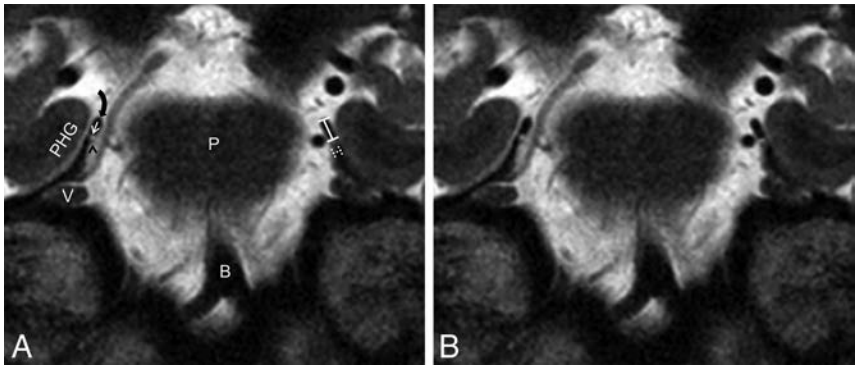

FIG 3. Labeled (*A*) and unlabeled (*B*) coronal T2 DRIVE images demonstrate cranial nerve IV (*black arrowhead* on the patient's right) in cross-section traveling along the bilateral trochlear grooves (*straight white arrow* on the patient's right). The right tentorial free edge (*curved black arrow*), right cranial nerve V (V), right parahippocampal gyrus (PHG), belly of the pons (P), and basilar artery (B) are labeled for orientation. The *dashed lines* on the patient's left illustrate the measurement of the maximum trochlear groove depth, and the *solid lines* on the patient's left illustrate the measurement of the shortest distance between the free tentorial edge and the medial border of the trochlear groove.

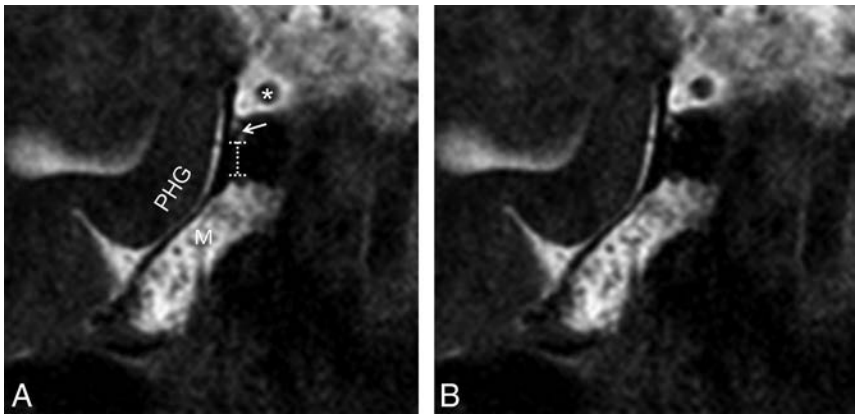

FIG 4. Labeled (*A*) and unlabeled (*B*) coronal T2 DRIVE images demonstrate cranial nerve IV (*white arrow*) in cross-section within the right trochlear cistern. The right cranial nerve III (*asterisk*), right Meckel cave (M), and right parahippocampal gyrus (PHG) are labeled for orientation. The *dashed lines* illustrate the measurement of the vertical distance between the inferior margin of the trochlear cistern and the superior margin of the Meckel cave.

Characteristics of the study group

Characteristics	No. (%)
Sex	
Male	9 (36%)
Female	16 (64%)
Age (yr)	
Mean	56.2
SD	13.8
Max	85
Min	30
Indication	
Sinonasal carcinoma	6
Inverted papilloma	4
Adenoid cystic carcinoma	2
Other (n = 1 each)	13

Note:—Max indicates maximum; Min, minimum.

radiologist on at least 2 images for a given side, though the images did not have to be contiguous.

Artifacts. Potential confounding effects of MR imaging artifacts (motion, pulsation, and so forth) on cranial nerve IV visibility were assessed by consensus. Sequences were designated as containing artifacts that would "not preclude nerve identification," "possibly preclude nerve identification," or "likely preclude nerve identification." This consensus review was performed 3 weeks following the anatomic structure identification consensus review to minimize potential for recall bias.

Measurements

When the anatomic structures of interest were identified, related measurements were obtained. For the trochlear groove, the maximum groove depth and the shortest distance between the free tentorial edge and the medial border of the groove were measured (Fig 3*A*). For the trochlear cistern, the vertical distance between the inferior margin of the trochlear cistern and the superior margin of the Meckel cave was measured (Fig 4*A*). For the tentorial segment of cranial nerve IV, the cross-sectional nerve diameter was measured.

Statistical Analysis

Mean, SD, and range are reported for continuous variables. Absolute and relative frequencies are reported for categoric variables. The Pearson χ^2 test was used to compare proportions. For statistical analysis, consensus opinion regarding the identification of the trochlear groove and trochlear cistern was taken to indicate the "presence" or "absence" of these landmarks. Consensus opinion regarding identification of cranial nerve IV indicated whether the nerve was "identifiable" or "not identifiable." JMP Pro, Version 12 (SAS Institute, Cary, North Carolina) was used for all analyses, and a P value $< .05$ indicated a statistically significant difference.

RESULTS

Subjects

To reach a study group of 25 patients and 50 sides, we reviewed 32 examinations. Seven examinations were excluded for not containing the coronal T2 DRIVE sequence of interest. Patient age and sex and study indication data are provided in the Table.

Reader Assessment

Anatomic Structures. Interobserver agreement was 78% for identification of the trochlear groove, 56% for the trochlear cistern, and 68% for cranial nerve IV.

Following consensus review, the trochlear groove was present in 44/50 sides (88%), and the trochlear cistern was present in 25/50 sides (50%). In 46/50 sides (92%), either the trochlear groove or trochlear cistern was present. The tentorial segment of

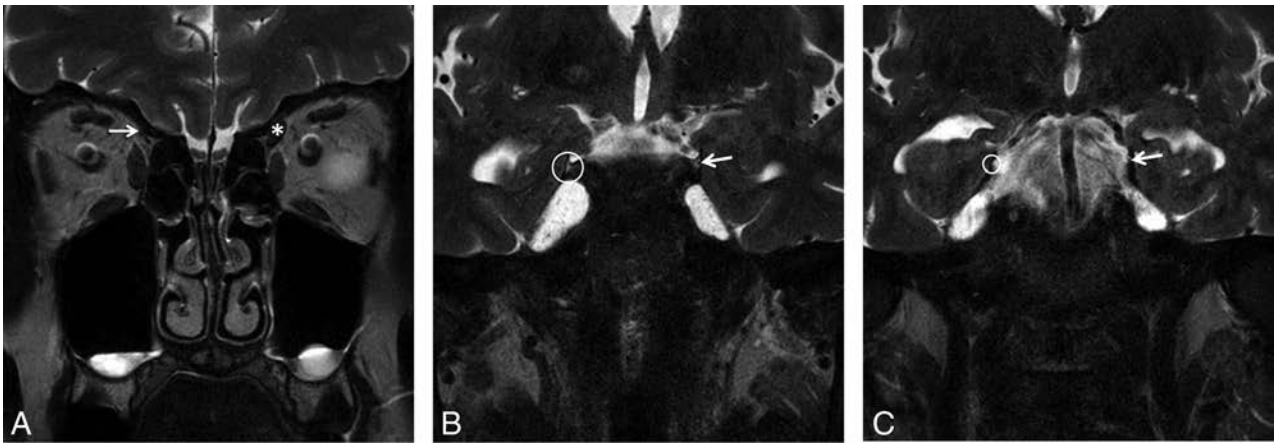

FIG 5. *A*, Coronal T2 DRIVE image obtained in a 47-year-old woman with clinically suspected congenital right trochlear palsy demonstrates a markedly diminutive right superior oblique muscle (*arrow*). The left superior oblique muscle (*asterisk*) is normal. Coronal T2 DRIVE images obtained in the same patient demonstrate the presence of the trochlear nerve within the trochlear groove (*arrow*, *B*) and trochlear cistern (*arrow*, *C*) on the normal left side. On the symptomatic right side, the trochlear groove (*circle*, *B*) and trochlear cistern (*circle*, *C*) can be seen clearly; however, no nerve can be identified.

cranial nerve IV was identified in 36/50 sides (72%). When the trochlear groove was present, cranial nerve IV was identified in 35/44 sides (80%), in contrast to 1/6 sides (17%) with no groove. This observed difference in proportions was statistically significant ($P = .0013$). When the trochlear cistern was present, cranial nerve IV was identified in 23/25 sides (92%), in contrast to 13/25 sides (52%) with no cistern. This observed difference in proportions was also statistically significant ($P = .0016$).

When neither the trochlear groove nor trochlear cistern was present, cranial nerve IV was identified in 0/4 sides (0%), in contrast to 36/46 sides (78%) with at least 1 landmark present ($P = .0008$).

Artifacts. None of the coronal T2 DRIVE sequences were considered to contain artifacts that would "likely preclude nerve identification," and 4 examinations (8 sides) were thought to contain artifacts that would "possibly preclude nerve identification." Among these 4 examinations with artifacts that would possibly preclude nerve identification, cranial nerve IV was identified in 5/8 sides (63%). If these 8 sides had been initially excluded, the observed differences in proportions between cranial nerve IV identification in the presence and absence of the trochlear groove and trochlear cistern would have remained statistically significant ($P = .0196$ and .0082, respectively).

Measurements

When present, the trochlear groove was located a mean distance of 1.4 ± 0.44 mm inferolateral to the free tentorial edge (range, 0.7–2.4 mm), and the mean maximum groove depth was 0.5 ± 0.15 mm (range, 0.2–0.8 mm). When present, the trochlear cistern was located a mean distance of 3.7 ± 1.8 mm superior to the Meckel cave (range, 1.2–7.0 mm). When identified, the mean diameter of the tentorial segment of cranial nerve IV was 0.4 ± 0.07 mm (range. 0.2–0.6 mm).

DISCUSSION

This study describes the MR imaging appearances of the trochlear groove and trochlear cistern on a fluid-sensitive sequence used in our routine clinical practice and demonstrates that successfully identifying these anatomic landmarks facilitates identification of the tentorial segment of cranial nerve IV.

Recent neurosurgical studies report that the trochlear groove and trochlear cistern are present in up to 100% of cadaver specimens and represent reliable anatomic landmarks for intraoperative nerve identification.[9,11] We identified the trochlear groove in 88% of sides and the trochlear cistern in 50% of sides, with at least 1 of these landmarks seen in 92% of sides. The discrepancy in rates of landmark identification between the current MR imaging–based study and previous cadaveric studies likely reflects limitations of the coronal T2 DRIVE sequence for resolving these small structures, with the increased length of the trochlear groove relative to the trochlear cistern likely contributing to its relatively increased visibility.

We identified the tentorial segment of cranial nerve IV in 72% of total sides, 80% of sides in which the trochlear groove was present, and 92% of sides in which the trochlear cistern was present. Although these results for the tentorial segment of cranial nerve IV do not match those previously reported by Kanoto et al,[6] who used a high-resolution motion-sensitized driven equilibrium sequence with a 26-minute acquisition time in a population of healthy volunteers, the coronal T2 DRIVE sequence investigated in our study with an average acquisition time of <4 minutes is more likely to be of practical benefit when daily MR imaging volume imposes sequence acquisition time constraints. Additionally, patients being evaluated for cranial nerve deficits may be less likely to remain motionless during longer sequence acquisitions than healthy volunteers; this scenario may result in image-quality degradation. Image-acquisition parameters were not the focus of this study, and it is possible that the coronal T2 DRIVE sequence or a similar fluid-sensitive sequence could be modified to improve visualization of the trochlear groove, trochlear cistern, and cranial nerve IV without meaningfully prolonging the acquisition.

Regardless of the particular sequence used, there are multiple clinical scenarios in which it is important for the radiologist to provide an accurate imaging assessment of cranial nerve IV, in-

cluding suspected congenital absence of the nerve, involvement of the nerve by schwannoma or perineural spread of malignancy, trauma to the nerve related to penetrating injury or shear forces, and extrinsic compression of the nerve by a skull base mass, aneurysm, or crossing vessel.

Operative planning for skull base mass resection likely represents the scenario in which the radiologist has the greatest opportunity to positively impact patient care, because cranial nerve IV palsy is the most frequent complication following meningioma surgery in the region of the tentorial incisura.[15] The frequency of this complication has been hypothesized to reflect difficulty in identifying and preserving the nerve at the time of the operation related to the small diameter of the nerve and displacement and distortion of the nerve along its lengthy intracranial course.[9-11]

The relatively low interobserver agreement for the presence of the trochlear groove, trochlear cistern, and cranial nerve IV likely reflects both the difficulty of confidently identifying these small structures noninvasively and the relatively limited self-guided training of the readers before completing the study interpretations. Interobserver agreement may have been improved with a more extensive group training session before performing the study, and given that consensus was easily reached in all discrepant cases, we expect interobserver agreement to improve with continued experience.

A limitation of this study is that we were not able to confirm the presence of cranial nerve IV along its entire cisternal length, though the nerve had to be present on at least 2 images to be considered "identifiable." In the evaluation of patients with trochlear nerve palsy at our institution, we have observed cases in which the nerve could be reliably identified along most of its course on the normal side but could not be seen within the trochlear groove or trochlear cistern on the contralateral, symptomatic side (Fig 5). Although anecdotal, the "empty" trochlear groove and "empty" trochlear cistern in such patients may represent important imaging findings.

An additional weakness of this study is the exclusion of pediatric patients, who represent a substantial proportion of patients being evaluated for suspected cranial nerve IV pathology and most patients with suspected congenital palsy.

Additional work could optimize sequence acquisition parameters for the visualization of the trochlear groove, trochlear cistern, and tentorial segment of cranial nerve IV; determine whether the trochlear groove and trochlear cistern are present in patients with congenital absence of cranial nerve IV; and assess whether the trochlear groove and trochlear cistern in combination with the coronal T2 DRIVE sequence or a sequence similar to it could be used for the following: 1) to identify cranial nerve IV in pediatric patients, 2) to reliably determine the presence or absence of cranial nerve IV, 3) to facilitate preoperative identification of cranial nerve IV in patients with skull base masses, or 4) to have a measurable effect on the historically high cranial nerve IV palsy complication rate following resection of tentorial meningiomas.

CONCLUSIONS

The trochlear groove and trochlear cistern are anatomic landmarks with which the tentorial segment of cranial nerve IV is closely associated en route to the cavernous sinus. These landmarks can be reliably identified by using a fluid-sensitive MR sequence and may improve the chances of identifying cranial nerve IV in routine clinical practice. These findings are expected to improve diagnostic confidence and diagnostic accuracy in the MR imaging evaluation of patients with suspected cranial nerve IV pathology.

REFERENCES

1. Fischbach F, Müller M, Bruhn H. **High-resolution depiction of the cranial nerves in the posterior fossa (N III-N XII) with 2D fast spin echo and 3D gradient echo sequences at 3.0 T.** *Clin Imaging* 2009;33:169–74 CrossRef Medline
2. Yousry I, Camelio S, Schmid UD, et al. **Visualization of cranial nerves I-XII: value of 3D CISS and T2-weighted FSE sequences.** *Eur Radiol* 2000;10:1061–67 CrossRef Medline
3. Yousry I, Moriggl B, Dieterich M, et al. **MR anatomy of the proximal cisternal segment of the trochlear nerve: neurovascular relationships and landmarks.** *Radiology* 2002;223:31–38 CrossRef Medline
4. Joo W, Rhoton AL. **Microsurgical anatomy of the trochlear nerve.** *Clin Anat* 2015;28:857–64 CrossRef Medline
5. Choi BS, Kim JH, Jung C, et al. **High-resolution 3D MR imaging of the trochlear nerve.** *AJNR Am J Neuroradiol* 2010;31:1076–79 CrossRef Medline
6. Kanoto M, Toyoguchi Y, Hosoya T, et al. **Visualization of the trochlear nerve in the cistern with use of high-resolution turbo spin-echo multisection motion-sensitized driven equilibrium.** *AJNR Am J Neuroradiol* 2013;34:1434–37 CrossRef Medline
7. Yang HK, Lee DS, Kim JH, et al. **Association of superior oblique muscle volumes with the presence or absence of the trochlear nerve on high-resolution MR imaging in congenital superior oblique palsy.** *AJNR Am J Neuroradiol* 2015;36:774–78 CrossRef Medline
8. Blitz AM, Macedo LL, Chonka ZD, et al. **High-resolution CISS MR imaging with and without contrast for evaluation of the upper cranial nerves: segmental anatomy and selected pathologic conditions of the cisternal through extraforaminal segments.** *Neuroimaging Clin N Am* 2014;24:17–34 CrossRef Medline
9. Herlan S, Hirt B, Tatagiba M, et al. **Focus on the lateral incisural space: where is the trochlear nerve?** *J Neurol Surg B Skull Base* 2013;74:271–73 CrossRef Medline
10. Ammirati M, Musumeci A, Bernardo A, et al. **The microsurgical anatomy of the cisternal segment of the trochlear nerve, as seen through different neurosurgical operative windows.** *Acta Neurochir (Wien)* 2002;144:1323–27 CrossRef Medline
11. Gupta T, Gupta SK, Sahni D. **Anatomy of the tentorial segment of the trochlear nerve in reference to its preservation during surgery for skull base lesions.** *Surg Radiol Anat SRA* 2014;36:967–71 CrossRef Medline
12. Rhoton AL Jr. **The sellar region.** *Neurosurgery* 2002;51(4 suppl):S335–74 Medline
13. Iaconetta G, de Notaris M, Benet A, et al. **The trochlear nerve: microanatomic and endoscopic study.** *Neurosurg Rev* 2013;36:227–37; discussion 237–38 CrossRef Medline
14. Blitz AM, Choudhri AF, Chonka ZD, et al. **Anatomic considerations, nomenclature, and advanced cross-sectional imaging techniques for visualization of the cranial nerve segments by MR imaging.** *Neuroimaging Clin N Am* 2014;24:1–15 CrossRef Medline
15. Samii M, Carvalho GA, Tatagiba M, et al. **Meningiomas of the tentorial notch: surgical anatomy and management.** *J Neurosurg* 1996;84:375–81 CrossRef Medline
16. Rhoton AL Jr. **The cavernous sinus, the cavernous venous plexus, and the carotid collar.** *Neurosurgery* 2002;51(4 suppl):S375–410 Medline

Hindbrain Herniation in Chiari II Malformation on Fetal and Postnatal MRI

U.D. Nagaraj, K.S. Bierbrauer, B. Zhang, J.L. Peiro, and B.M. Kline-Fath

ABSTRACT

BACKGROUND AND PURPOSE: As the practice of in utero repair of myelomeningoceles becomes more prevalent, knowledge of the expected MR imaging findings has become increasingly important. Our aim was to examine neuroimaging findings with a focus on hindbrain herniation and ventricular size in fetuses with open spinal dysraphism and to compare them with postnatal imaging features in groups undergoing prenatal-versus-postnatal repair.

MATERIALS AND METHODS: Single-center retrospective analysis was performed on MRIs of fetuses with open spinal dysraphism from January 2004 through July 2015 with available postnatal imaging. One hundred two fetuses were included. Reports from available fetal ultrasound were also examined. Images were reviewed by 2 board-certified fellowship-trained pediatric neuroradiologists. Descriptive analyses were performed to demonstrate the distribution of the imaging findings.

RESULTS: Thirty-two of 102 (31.3%) fetuses underwent in utero repair of open spinal dysraphism; 68.6% (70/102) underwent postnatal repair. Ninety-four of 102 (92.2%) fetuses had cerebellar ectopia. Of those who underwent prenatal repair (26 grade 3, 6 grade 2), 81.3% (26/32) had resolved cerebellar ectopia postnatally. Of those who had severe cerebellar ectopia (grade 3) that underwent postnatal repair, 65.5% (36/55) remained grade 3, while the remaining 34.5% (19/55) improved to grade 2. The degree of postnatal lateral ventriculomegaly in those that underwent prenatal repair (20.3 ± 5.6 mm) was not significantly different from that in those that underwent postnatal repair (21.5 ± 10.2 mm, $P = .53$). Increased Chiari grade was significantly correlated with decreased head size for gestational age on fetal sonography ($P = .0054$).

CONCLUSIONS: In fetuses with open spinal dysraphism and severe Chiari II malformation that do not undergo prenatal repair, most have no change in the severity of cerebellar ectopia/Chiari grade. However, in fetuses that undergo in utero repair, most have resolved cerebellar ectopia postnatally.

ABBREVIATION: OSD = open spinal dysraphism

Since the Management of Myelomeningocele (MOMS) trial revealed that prenatal surgery for myelomeningocele reduces the need for ventricular shunting and improves motor outcomes in infants with Chiari II malformation, the practice has become more widely available and is being offered and performed with increasing frequency.[1] Fetal MR imaging continues to play an essential role in evaluating fetuses prenatally not only to determine which candidates may potentially benefit from the procedure but also to evaluate associated anomalies to shed some light on prognostic information that will aid in counseling.[2]

Ample literature describes postnatal MR imaging findings of Chiari II malformation after postnatal repair of myelomeningoceles.[3-5] However, the literature describing imaging findings in Chiari II malformation on fetal MR imaging is somewhat limited, mostly comprised of review articles with a few small studies.[6-10] There are even fewer articles in the literature comparing neuroimaging findings between pre- and postnatal brain MRIs in patients with Chiari II malformation.[2,11,12] In order to improve our understanding of the disease and improving outcomes, studies evaluating the neuroimaging findings in these patients both pre- and postnatally are becoming increasingly important, particularly studies that describe imaging parameters that can be easily implemented in clinical practice.

Received September 19, 2016; accepted after revision December 19.

From the Department of Radiology and Medical Imaging (B.Z., B.M.K.-F.), Department of Pediatric Neurosurgery (K.S.B.), Division of Biostatistics and Epidemiology (B.Z.), and Department of Pediatric Surgery (J.L.P.), Cincinnati Children's Hospital Medical Center, Cincinnati, Ohio; and University of Cincinnati College of Medicine (U.D.N., K.S.B., B.Z., J.L.P., B.M.K.-F.), Cincinnati, Ohio.

Preliminary findings were presented as an oral presentation (O-307) at: Annual Meeting of the American Society of Neuroradiology and the Foundation of the ASNR Symposium, May 21–26, 2016; Washington, DC.

Please address correspondence to Usha D. Nagaraj, MD, Department of Radiology and Medical Imaging, Cincinnati Children's Hospital Medical Center, 3333 Burnet Ave, Cincinnati, OH 45229-3026; e-mail: usha.nagaraj@cchmc.org; @CincyKidsRad

http://dx.doi.org/10.3174/ajnr.A5116

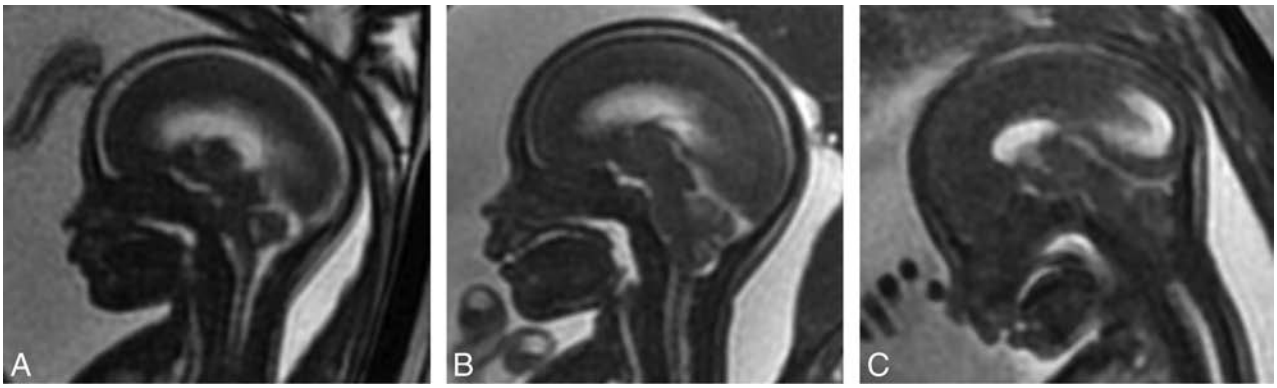

FIG 1. Grading of cerebellar ectopia on fetal MR imaging on sagittal FIESTA images of the brain. Grade 1 (*A*) has no cerebellar ectopia with a patent cisterna magna and fourth ventricle. Grade 2 (*B*) has cerebellar ectopia with an effaced fourth ventricle but a patent cisterna magna. Grade 3 (*C*) has cerebellar ectopia with an effaced fourth ventricle and cisterna magna.

Our aim was to evaluate neuroimaging findings in fetuses with open spinal dysraphism (OSD) and to compare them with the postnatal imaging findings, with a focus on hindbrain herniation and ventricular size.

MATERIALS AND METHODS

Study Design

This study was a single-center, retrospective review. The case list was compiled from all of the fetal MRIs performed between 2004 and 2015. Inclusion criteria encompassed fetuses with diagnostic-quality fetal MRIs for OSD (either myelomeningocele or myelocele).[13] Patients underwent either immediate postnatal repair or open in utero repair of OSD. Fetuses without cerebellar ectopia (grade 1) underwent postnatal repair only. Only fetuses with adequate available postnatal neuroimaging and clinical/neurosurgical follow-up were included. Criteria for adequate postnatal neuroimaging for this study included a diagnostic-quality MR imaging of the brain within the first 3 months of life. Determination of diagnostic-quality imaging was made at the neuroradiologists' discretion. A chart review was performed to obtain relevant clinical data, including reports from level II obstetric ultrasound when available. This study was compliant with the Health Insurance Portability and Accountability Act and approved by the institutional review board. The requirement for informed consent was waived.

Scanning Parameters

All fetuses included in our study were scanned prenatally on a 1.5T magnet at Cincinnati Children's Hospital Medical Center by using a Ingenia 1.5T (Philips Healthcare, Best, the Netherlands) or a 1.5T Signa HDxt (GE Healthcare, Milwaukee, Wisconsin) system. T2 single-shot FSE images of the brain were obtained in 3 planes: axial, sagittal, and coronal. Three-millimeter-section thickness no-gap interleaved images at $\leq$24 weeks gestational age and 4-mm no-gap interleaved images at $>$24 weeks were used. Although this imaging protocol did not change during the study period, the TRs and TEs varied between each scanner and were changed at times of scanner upgrades to optimize image quality. At least 2 stacks in each plane were obtained to the radiologist's satisfaction. The smallest FOV possible was used. Axial DWI and T1 spoiled gradient-recalled images of the fetal brain were inconsistently implemented at the radiologist's discretion at the time of imaging. The postnatal imaging parameters varied because 1 of 6 available clinical magnets was used, and the routine use of volume T1 3D spoiled gradient-recalled imaging was not implemented until 2009.

Image Interpretation

All images were reviewed by 2 board-certified radiologists (U.D.N., B.M.K.-F.), both with added qualifications in pediatric radiology and fellowship training in pediatric neuroradiology, one (B.M.K.-F.) with $>$10 years of postfellowship attending experience in pediatric neuroradiology in a large academic center, the other (U.D.N.) with 2 years of experience. The images were viewed on a PACS workstation. Only diagnostic-quality MRIs for the assessment of the fetal brain were included in our study; image quality was a subjective assessment made by the neuroradiologists. All patients included in our analysis also had diagnostic-quality postnatal brain MRIs available for interpretation, as determined by the neuroradiologists (6 patients were excluded for this reason). The readers were blinded to the pre- and postnatal reported imaging findings at the time of interpretation and were also blinded to therapy (prenatal-versus-postnatal repair). Differences were resolved by consensus.

The degree of Chiari II malformation was determined by a grading scale in the fetus so that grade 1 was either normal or had a downward sloping tentorium and a normal patent fourth ventricle and cisterna magna without cerebellar ectopia; grade 2 had cerebellar ectopia with effacement of the fourth ventricle but a patent cisterna magna; and grade 3 had cerebellar ectopia and effacement of both the cisterna magna and fourth ventricle (Fig 1). This grading system was slightly modified from a previously reported system by Sutton et al[2] in that we did not differentiate normal (grade 0) from grade 1 because the described difference was difficult to objectify. The same grading system was applied postnatally except that cerebellar ectopia with patency of the fourth ventricle or cisterna magna was considered grade 2. The grading system was modified postnatally because unlike fetal MR imaging in which we did not see cerebellar ectopia when the fourth ventricle was patent, we frequently observed varying degrees of fourth ventricle and cisterna magna patency with cerebellar ectopia, so to maintain 3 groups, we modified the grading scale.

Lateral ventricular size was measured in transverse dimensions in the axial plane at the level of the frontal horns or in the coronal plane at the level of the glomus of the choroid plexus, analogous to previously established fetal sonography guidelines. Fetal ventricular size was considered normal at <10 mm, mild-moderate ventriculomegaly at 10–15 mm, and severe ventriculomegaly at >15 mm.[14] Postnatal ventricular size was considered normal at <10 mm, mild-moderate at 10–15 mm, severe at 16–25 mm, and extreme at >25 mm. Third ventricle size was measured in the transverse dimension in the coronal plane and was considered enlarged in the fetus if it was >3 mm.[15]

Extra-axial CSF spaces over the cerebral hemispheres were described as either completely patent or effaced (including both partial and complete effacement). The presence or absence of ventricular rupture/dehiscence was determined, with rupture being defined as the presence of direct communication between the lateral ventricle and the extra-axial CSF space over the cerebral convexity.

Statistical Analysis

Descriptive analyses were performed to demonstrate the distribution of the imaging findings. Continuous variables were presented as mean ± SD, and categoric variables were presented as number (percentage). A 2-sample *t* test or 1-way ANOVA was used to detect the differences of continuous variables between different groups. The correlation between categoric variables was assessed by the χ^2 or Fisher exact test when appropriate. All analyses were performed by using SAS, Version 9.4 (SAS Institute, Cary, North Carolina). A *P* value of <.05 was considered statistically significant.

RESULTS

Description of the Cohort

A total of 102 fetuses (45 male, 57 female) met the criteria and were included in this analysis. Average gestational age at fetal MR imaging was 23.9 ± 3.7 weeks in the cohort as a whole, 24.6 ± 4.2 weeks in the postnatal repair group, and 22.4 ± 1.5 weeks in the prenatal repair group ($P = .004$). Thirty-two of 102 (31.3%) fetuses underwent open in utero repair of OSD, while the remaining 68.6% (70/102) underwent postnatal repair. The average gestational age at delivery was significantly lower in the prenatal (31.5 ± 4 weeks) versus the postnatal (37.5 ± 1.6 weeks) repair group ($P < .0001$). Eighty-five of 102 (83.3%) had a level II obstetric sonogram performed within a week of the fetal MR imaging, with images and/or a detailed report available for review. The average age at postnatal brain MR imaging was 19.7 ± 21.9 days.

Posterior Fossa

Imaging findings in the cohort as a whole are summarized in Tables 1 and 2. Seventy of 102 (68.6%) fetuses underwent postnatal repair. Of these, 78.6% (55/70) had grade 3 and 10% (7/70) had grade 2 Chiari II malformation on fetal MR imaging. Of the 55 that were grade 3, 65.5% (36/55) remained grade 3 (Fig 2), while the remaining 34.5% (19/55) improved to grade 2 postnatally. Of the 12.7% (7/55) that were fetal grade 2, 2 progressed to grade 3, 3 remained at grade 2, and 2 had resolved ectopia (grade 1) postnatally. Fetuses without cerebellar ectopia (grade 1) underwent postnatal repair only. Of the 11.4% (8/70) that did not have fetal cerebellar ectopia (grade 1), most 87.5% (7/8) did not progress to a higher grade postnatally (Figs 1*A* and 3).

Table 1: Summary of imaging findings on fetal MR in the cohort as a whole

Imaging Findings	% of Cohort
Cerebellar ectopia	92.2% (94/102)
Fetal Chiari grade	
1	7.8% (8/102)
2	12.7% (13/102)
3	79.4% (81/102)
Effacement of prepontine cistern	92.2% (94/102)
Lateral ventricular size	
Normal	20.6% (21/102)
Mild-moderate ventriculomegaly	57.8% (59/102)
Severe ventriculomegaly	21.6% (22/102)
Third ventriculomegaly	9.8% (10/102)
Lateral ventricular rupture	1% (1/102)
Extra-axial CSF effacement	92.1% (94/102)

Table 2: Summary of imaging findings on postnatal MR imaging in the cohort as a whole

Imaging Finding	% of Cohort
Cerebellar ectopia	63.7% (65/102)
Postnatal Chiari grade	
1	36.3% (37/102)
2	26.5% (27/102)
3	37.3% (38/102)
Effacement of prepontine cistern	14.7% (15/102)
Lateral ventricular size	
Normal	4.9% (5/102)
Mild-moderate ventriculomegaly	21.6% (22/102)
Severe ventriculomegaly	51% (52/102)
Extreme ventriculomegaly	22.5% (23/102)
Lateral ventricular rupture	2.9% (3/102)
Extra-axial CSF effacement	22.5% (23/102)

Thirty-two of 102 (31.4%) fetuses underwent open in utero repair of OSD, 81.3% (26/32) with grade 3 and 18.8% (6/32) with grade 2 Chiari II malformation. Of those with grade 3, 76.9% (20/26) had resolved (grade 1) cerebellar ectopia (Fig 4), 11.5% (3/26) had improved ectopia (grade 2), and 11.5% (3/26) had persistent grade 3 Chiari II malformation postnatally. Of those with grade 2, 100% (6/6) had resolved cerebellar ectopia postnatally after prenatal repair.

Ventricle Size and Extra-Axial CSF Spaces

Imaging findings, including the degree of ventriculomegaly, the presence of at least partial effacement of the extra-axial CSF spaces over the cerebral convexities, and lateral ventricular rupture/dehiscence in the cohort as a whole, are summarized in Tables 1 and 2.

The degree of postnatal lateral ventriculomegaly in those that underwent prenatal repair (20.3 ± 5.6 mm) was not significantly different from that in those that underwent postnatal repair (21.5 ± 10.2 mm, $P = .53$). The difference between the mean postnatal third ventricle size for the prenatal repair group (4.7 ± 2.8 mm) and the postnatal repair group (4.2 ± 1.5 mm) was also not statistically significant ($P = .29$). Postnatal lateral ventricular size in the 8 patients with grade 1 Chiari II malformation on fetal

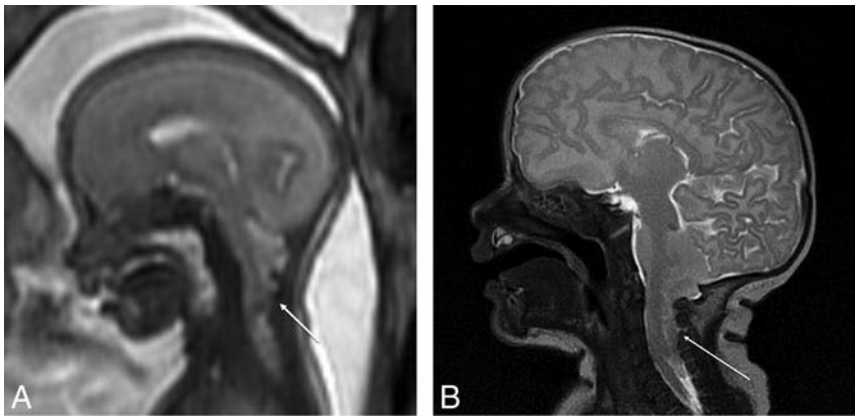

FIG 2. *A* and *B*, Sagittal T2 SSFSE from fetal MR imaging performed at 24 weeks' and 5 days' gestational age (*A*) demonstrates severe cerebellar ectopia or grade 3 Chiari II malformation (*arrow*). Note that there is also effacement of the prepontine cistern and extra-axial CSF spaces over the cerebral hemispheres. Sagittal T2 FSE from postnatal MR imaging of the same patient at 2 weeks of age after postnatal repair of OSD shows a persistent grade 3 Chiari II malformation (*arrow*).

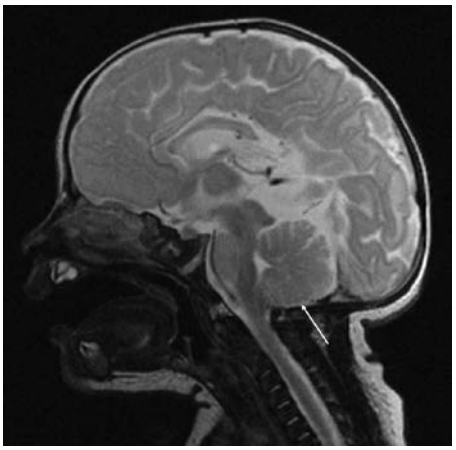

FIG 3. Sagittal T2 FSE from postnatal MR imaging in the same patient as in Fig 1*A*, status post postnatal repair of OSD at 11 days of age again demonstrates no cerebellar ectopia (*arrow*). Note the presence of other intracranial findings of a Chiari II malformation, including callosal hypogenesis/dysgenesis, a thickened massa intermedia, and tectal beaking.

MR imaging (15.6 ± 4.3 mm) was significantly less than that in the remaining patients (21.6 ± 9.2 mm, $P = .005$). When we examined the change between the pre- and postnatal imaging findings, the prenatal lateral and third ventricle size was significantly smaller than the postnatal ventricular size in both the prenatal and postnatal repair groups ($P < .001$). The Fisher exact test (for Chiari grade) and 1-way ANOVA (for ventricle size) showed a significant correlation between the prenatal Chiari grade and postnatal third ventricle size, with a *P* value of .0443. There was no significant correlation between prenatal Chiari grade and prenatal ventricular size (lateral and third ventricle) or postnatal lateral ventricular size. There was also no statistically significant relationship between lateral ventricular size and the presence of improved hindbrain herniation in either the pre- or postnatal repair groups.

Thirty-four of 102 (33.3%) fetuses had a ventricular drainage catheter/shunt in place at the time of postnatal MR imaging, 47.1% (33/70) of the postnatal repair group and 3.1% (1/32) of the prenatal repair group. Of the 22 fetuses, 1 in the prenatal repair and 21 in the postnatal repair group, with severe lateral ventriculomegaly (>15 mm), 54.5% (12/22) had a shunt at the time of postnatal MR imaging, compared with 27.5% (22/80) with a fetal lateral ventricular size of ≤15 mm. All except 2 (94.1%, 32/34) of the patients with a shunt on postnatal MR imaging had a grade 3 Chiari II malformation on fetal MR imaging. Only 12.5% (1/8) of patients with grade 1 Chiari II malformation on fetal MR imaging had a shunt on postnatal MR imaging. The Fisher exact test showed a significant correlation between increased Chiari grade and the presence of prenatal extra-axial CSF space effacement, with a *P* value of < .0001. There was no significant correlation between Chiari grade and postnatal extra-axial CSF space effacement.

Sonographic Findings

Reports from fetal ultrasound performed within 1 week of fetal MR imaging were available in 84 of the fetuses, 81 of which included amniotic fluid measurements. Of these, 96.3% (78/81) had reported normal amniotic fluid, 2.5% (2/81) had decreased amniotic fluid (deepest vertical pocket, ≤2 cm), and 1.2% (1/81) had increased amniotic fluid (deepest vertical pocket, ≥8 cm).[16,17] Head circumference measurements were available in all 84 fetuses. Of these, 35.7% (30/84) had normal head circumference, 61.9% (52/84) had decreased head circumference (<10th percentile), and 2.4% (2/84) of fetuses had increased head circumference (>90th percentile) for gestational age.[18] The Fisher exact test showed that an increased Chiari grade was significantly correlated with decreased head size, with a *P* value of .0054.

DISCUSSION

We describe pre- and postnatal MR imaging brain findings in patients with OSD with a focus on hindbrain herniation. We found that 92.2% (94/102) of fetuses had, prenatally and presurgically, cerebellar ectopia (grade 2 or 3), while 7.8% (8/102) did not. In those with severe/grade 3 cerebellar ectopia who underwent postnatal repair, 65.5% (36/55) remained grade 3, while the remaining 34.5% (19/55) improved to grade 2. Of those who underwent prenatal repair, 81.3% (26/32) had resolved cerebellar ectopia postnatally (Table 3). We found a significant correlation between increased fetal Chiari grade and the presence of prenatal extra-axial CSF space effacement. We also found that the degree of postnatal lateral ventriculomegaly in those that underwent prenatal repair was not significantly different from that in those that underwent postnatal repair. Finally, we observed that an increased fetal Chiari grade was significantly correlated with decreased head size on fetal sonography.

The MOMS trial, in addition to describing the reduced need for shunting and improved motor outcomes in fetuses that undergo prenatal repair of a myelomeningocele, also reported improved hindbrain herniation.[1] Smaller clinical studies in other centers have had similar results.[19-21] Our findings are in keeping

with these studies because we found that 81% of fetuses that underwent prenatal repair had resolved cerebellar ectopia postnatally, a result that was not observed in any of the fetuses that underwent postnatal repair. Our study adds to the clinical literature by describing in more detail the imaging findings on both pre- and postnatal MR imaging by adapting the grading system used by Sutton et al[2] on fetal MR imaging, which can be applied to clinical practice. It seems clear that prenatal repair, by preventing leakage of CSF through the open neural tube defect, can progressively remodel the posterior fossa and revert the Chiari malformation to different degrees as we saw in the MR imaging studies of our patients. We also describe the evolution of the Chiari grade in the patients with postnatal repair in the cohort, including the 35% of fetuses with grade 3 Chiari who underwent postnatal repair and improved to grade 2; this improvement has not been previously described, to our knowledge.

The association between OSD and Chiari II malformation in infants has been long established and is accepted as a constant by many.[4,3,13] The widely accepted unified theory of McLone and Dias[22] and McLone and Knepper[23] describes how defective occlusion caused by an open neural tube defect precludes CSF accumulation and pressure within the developing cerebral ventricles, causing the findings of Chiari II malformation, including a small posterior fossa with hindbrain herniation. However, in our study, 8% of fetuses with postnatally confirmed OSD did not have cerebellar ectopia on fetal MR imaging. Although there is little in the literature describing this phenomenon, one other study described an incidence as high as 23%.[10] Our findings support the idea that not all fetuses with OSD have cerebellar ectopia. In addition, our study adds the finding that nearly all of these fetuses (7/8) did not develop cerebellar ectopia in the postnatal period after repair, which suggests that hindbrain malformation in Chiari is unlikely to worsen. This suggestion may be helpful for prenatal counseling.

There is very little in the literature analyzing ventricle size in fetuses with OSD. One study found that on fetal MR imaging ventriculomegaly (>10 mm) was associated with the presence of cerebellar ectopia in fetuses with OSD.[10] However, we demonstrate not only that there was no significant association between Chiari grade and ventricle size on fetal MR imaging but also that there was no statistically significant difference in postnatal ventricle size between the pre- and postnatal repair groups. This finding questions the role of ventricular size in shunt placement, because the MOMS trial and our own data illustrate a decreased need for shunting in patients who undergo prenatal repair. The decision to place a shunt does not rely on ventricle size alone, and other clinical factors are taken under consideration.[1] In addition, our study only examines the initial postnatal brain MR imaging, so it is possible that differences in ventricular size may develop later and that the patients with prenatal repair may have stabilization of ventricular dilation that was previously obstructive. Evaluation of ventricle size may be clinically relevant because an update to the MOMS trial suggests that larger lateral ventricle size at initial screening is associated with an increased need for shunting and prenatal repair may not improve outcomes in fetuses with ventricles of >15 mm.[24] In our study, only 1 fetus of 32 that underwent prenatal repair had severe ventriculomegaly (>15 mm). However, we observed that of the 22 fetuses with severe lateral ventriculomegaly in both groups combined, 54.5% (12/22) had a shunt at the time of postnatal MR imaging, compared with 27.5% (22/80) with a fetal lateral ventricular size of ≤15 mm. This finding may suggest that in fetuses with a ventricle size of >15 mm, there may be a degree of obstruction that is more prone to progressively worsen.

Also very little in the literature exists describing the extra-axial CSF spaces over the cerebral convexities in fetuses with Chiari II, with only 1 study describing the depth of this space being lower in patients with Chiari II than in controls.[10] Our study adds to the literature by not only describing a high association between CSF effacement and higher Chiari grade in fetuses but also showing that this association does not persist in the postnatal period after repair. When we examined head size, 62% of the fetuses in our study had decreased head circumference

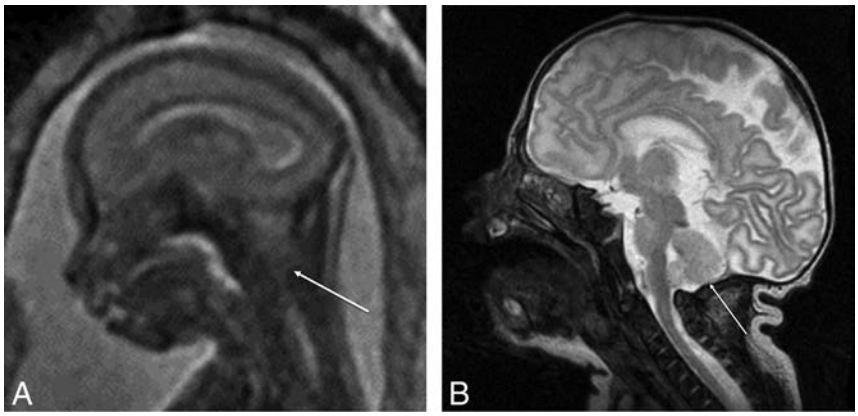

FIG 4. Sagittal T2 SSFSE from fetal MR imaging at 23 weeks' and 3 days' gestational age (*A*) with severe or grade 3 Chiari II malformation (*arrow*). Sagittal T2 FSE image from postnatal MR imaging in the same patient at 2 weeks of age after in utero repair of OSD (*B*) demonstrates resolved cerebellar ectopia (*arrow*).

Table 3: Benefits of prenatal-versus-postnatal repair by imaging

	Prenatal Repair Group (*n* = 32)	Postnatal Repair Group (*n* = 70)
% of fetal grade 3 Chiari II malformation that remained grade 3 postnatally	11.5% (3/26)	65.5% (36/55)
% of fetal grade 3 Chiari II malformation that improved or resolved postnatally	88.5% (23/26)	34.5% (19/55)
% of fetal grade 2 Chiari II malformation that resolved postnatally (grade 1)	100% (6/6)	28.6% (2/7)
% that had a ventricular shunt catheter on postnatal MRI	3.1% (1/32)	47.1% (33/70)

on fetal sonography, which is consistent with previously published literature.[18] We also found that an increased Chiari grade on fetal MR imaging is associated with decreased head size on fetal ultrasound, which has not been previously described. This finding may suggest that decreased head size is a reflection of effaced extra-axial CSF spaces and that fetuses with decreased head circumference may have more benefit from in utero repair than those with normal or increased head circumference. It may be interesting to perform further studies examining head size in utero after prenatal repair to see whether head size has the potential to normalize with this procedure.

Our study does have some limitations. First, the retrospective nature of this study limits its internal validity. Second, given that this is a single-institution study performed within a certain timeframe, the external validity may be limited as well. Along those same lines, our study likely has some degree of selection bias, given that these data are from one of the largest referral centers for fetal repair of OSD in the country, which we started performing at our institution in 2011. This may explain why the gestational age at fetal MR imaging is significantly less in the prenatal repair group compared with the postnatal repair group, as prenatal repair is typically performed before 26 weeks gestational age. However, differences in gestational age are unlikely to substantially affect our ventricular size data because it has been documented in the literature that lateral ventricular size remains relatively constant throughout gestation.[25] Given that imaging studies were acquired during a 10-year period on multiple different clinical magnets with periodic upgrades, the heterogeneity of scanning parameters may affect our results as well.

CONCLUSIONS

We describe imaging parameters on pre- and postnatal brain MR imaging in patients with OSD and find that in fetuses with severe Chiari II malformation that do not undergo prenatal repair, most (65.5%) have no change in the severity of cerebellar ectopia/Chiari grade postnatally. In fetuses that undergo in utero repair, most (81.3%) have resolved cerebellar ectopia postnatally. We also describe how cerebellar ectopia is not always present in fetuses with OSD on fetal MR imaging. We found no significant difference in the degree of postnatal lateral ventriculomegaly between those that underwent prenatal repair and those that underwent postnatal repair ($P = .53$). Finally, we found a relationship between the degree of cerebellar ectopia with head size on fetal ultrasound and effacement of extra-axial CSF spaces on fetal MR imaging. The exact clinical implications of these findings are yet to be determined, and long-term clinical follow-up of these patients will be essential.

REFERENCES

1. Adzick NS, Thom EA, Spong CY, et al. **A randomized trial of prenatal versus postnatal repair of myelomeningocele.** *N Engl J Med* 2011;364:993–1004 CrossRef Medline
2. Sutton LN, Adzick NS, Bilaniuk LT, et al. **Improvement in hindbrain herniation demonstrated by serial fetal magnetic resonance imaging following fetal surgery for myelomeningocele.** *JAMA* 1999;282:1826–31 CrossRef Medline
3. Wolpert M, Anderson M, Scott RM, et al. **Chiari II malformation: MR imaging evaluation.** *AJR Am J Roentgenol* 1987;149:1033–42 CrossRef Medline
4. el Gammal T, Mark EK, Brooks BS. **MR imaging malformation of Chiari II.** *AJR Am J Roentgenol* 1988;150:163–70 CrossRef Medline
5. Geerdink N, van der Vliet T, Rotteveel JJ, et al. **Interobserver reliability and diagnostic performance of Chiari II malformation measures in MR imaging, part 2.** *Childs Nerv Syst* 2012;28:987–95 CrossRef Medline
6. Glenn OA, Barkovich J. **Magnetic resonance imaging of the fetal brain and spine: an increasingly important tool in prenatal diagnosis, part 2.** *AJNR Am J Neuroradiol* 2006;27:1807–14 Medline
7. Glenn OA. **MR imaging of the fetal brain.** *Pediatr Radiol* 2010;40:68–81 CrossRef Medline
8. Righini A, Zirpoli S, Mrakic F, et al. **Early prenatal MR imaging diagnosis of polymicrogyria.** *AJNR Am J Neuroradiol* 2004;25:343–46 Medline
9. Mignone Philpott C, Shannon P, Chitayat D, et al. **Diffusion-weighted imaging of the cerebellum in the fetus with Chiari II malformation.** *AJNR Am J Neuroradiol* 2013;34:1656–60 CrossRef Medline
10. Batty R, Vitta L, Whitby EH, et al. **Is there a causal relationship between open spinal dysraphism and Chiari II deformity? A study using in utero magnetic resonance imaging of the fetus.** *Neurosurgery* 2012;70:890–98; discussion 898–99 CrossRef Medline
11. Papadias A, Miller C, Martin WL, et al. **Comparison of prenatal and postnatal MRI findings in the evaluation of intrauterine CNS anomalies requiring postnatal neurosurgical treatment.** *Childs Nerv Syst* 2008;24:185–92 CrossRef Medline
12. Adzick NS. **Fetal surgery for spina bifida: past, present, future.** *Semin Pediatr Surg* 2013;22:10–17 CrossRef Medline
13. Tortori-Donati P, Rossi A, Cama A. **Spinal dysraphism: a review of neuroradiological features with embryological correlations and proposal for a new classification.** *Neuroradiology* 2000;42:471–91 CrossRef Medline
14. Melchiorre K, Bhide A, Gika AD, et al. **Counseling in isolated mild fetal ventriculomegaly.** *Ultrasound Obstet Gynecol* 2009;34:212–24 CrossRef Medline
15. Sari A, Ahmetoglu A, Dinc H, et al. **Fetal biometry: size and configuration of the third ventricle.** *Acta Radiol* 2005;46:631–35 CrossRef Medline
16. Magann EF, Sandlin AT, Ounpraseuth ST. **Amniotic fluid and the clinical relevance of the sonographically estimated amniotic fluid volume: oligohydramnios.** *J Ultrasound Med* 2011;30:1573–85 CrossRef Medline
17. Sandlin AT, Chauhan SP, Magann EF. **Clinical relevance of sonographically estimated amniotic fluid volume: polyhydramnios.** *J Ultrasound Med* 2013;32:851–63 CrossRef Medline
18. Coleman BG, Langer JE, Horii SC. **The diagnostic features of spina bifida: the role of ultrasound.** *Fetal Diagn Ther* 2015;37:179–96 CrossRef Medline
19. Moldenhauer JS, Soni S, Rintoul NE, et al. **Fetal myelomeningocele repair: the post-MOMS experience at the Children's Hospital of Philadelphia.** *Fetal Diagn Ther* 2015;37:235–40 CrossRef Medline
20. Faria TC, Cavalheiro S, Hisaba WJ, et al. **Improvement of motor function and decreased need for postnatal shunting in children who had undergone intrauterine myelomeningocele repair.** *Arq Neuropsiquiatr* 2013;71:604–08 CrossRef Medline
21. Hisaba WJ, Cavalheiro S, Almodim CG, et al. **Intrauterine myelomeningocele repair postnatal results and follow-up at 3.5 years of age: initial experience from a single reference service in Brazil.** *Childs Nerv Syst* 2012;28:461–67 CrossRef Medline
22. McLone DG, Dias MS. **The Chiari II malformation: cause and impact.** *Childs Nerv Syst* 2003;19:540–50 CrossRef Medline
23. McLone DG, Knepper PA. **The cause of Chiari II malformation: a unified theory.** *Pediatr Neurosci* 1989;15:1–12 CrossRef Medline
24. Tulipan N, Wellons JC 3rd, Thom EA, et al; MOMS Investigators. **Prenatal surgery for myelomeningocele and the need for cerebrospinal fluid shunt placement.** *J Neurosurg Pediatr* 2015;16:613–20 CrossRef Medline
25. Almog B, Gamzu R, Achiron R, et al. **Fetal lateral ventricular width: what should be its upper limit? A prospective cohort study and reanalysis of the current and previous data.** *J Ultrasound Med* 2003;22:39–43 CrossRef Medline

Brain Development in Fetuses of Mothers with Diabetes: A Case-Control MR Imaging Study

F.C. Denison, G. Macnaught, S.I.K. Semple, G. Terris, J. Walker, D. Anblagan, A. Serag, R.M. Reynolds, and J.P. Boardman

ABSTRACT

BACKGROUND AND PURPOSE: Offspring exposed to maternal diabetes are at increased risk of neurocognitive impairment, but its origins are unknown. With MR imaging, we investigated the feasibility of comprehensive assessment of brain metabolism (^{1}H-MRS), microstructure (DWI), and macrostructure (structural MRI) in third-trimester fetuses in women with diabetes and determined normal ranges for the MR imaging parameters measured.

MATERIALS AND METHODS: Women with singleton pregnancies with diabetes ($n = 26$) and healthy controls ($n = 26$) were recruited prospectively for MR imaging studies between 34 and 38 weeks' gestation.

RESULTS: Data suitable for postprocessing were obtained from 79%, 71%, and 46% of women for ^{1}H-MRS, DWI, and structural MRI, respectively. There was no difference in the NAA/Cho and NAA/Cr ratios (mean [SD]) in the fetal brain in women with diabetes compared with controls (1.74 [0.79] versus 1.79 [0.64], $P = .81$; and 0.78 [0.28] versus 0.94 [0.36], $P = .12$, respectively), but the Cho/Cr ratio was marginally lower (0.46 [0.11] versus 0.53 [0.10], $P = .04$). There was no difference in mean [SD] anterior white, posterior white, and deep gray matter ADC between patients and controls (1.16 [0.12] versus 1.16 [0.08], $P = .96$; 1.54 [0.16] versus 1.59 [0.20], $P = .56$; and 1.49 [0.23] versus 1.52 [0.23], $P = .89$, respectively) or volume of the cerebrum (243.0 mL [22.7 mL] versus 253.8 mL [31.6 mL], $P = .38$).

CONCLUSIONS: Acquiring multimodal MR imaging of the fetal brain at 3T from pregnant women with diabetes is feasible. Further study of fetal brain metabolism in maternal diabetes is warranted.

ABBREVIATIONS: T1DM = type 1 diabetes mellitus; T2DM = type 2 diabetes mellitus; GDM = gestational diabetes; sMRI = structural MRI

Diabetes is the most common medical disorder of pregnancy with the prevalence of type 1 (T1DM), type 2 (T2DM), and gestational diabetes (GDM) all increasing among women of childbearing age in resource-rich settings. The perinatal complications of maternal diabetes, which reflect altered metabolic function in utero, include major congenital malformations, macrosomia, and stillbirth.[1] Long-term, children born to mothers with diabetes are at increased risk for cognitive impairment,[2,3] inattentiveness,[4] impaired working memory,[5] and altered language development.[6] These adverse outcomes are not fully explained by postnatal events; this question focuses research attention on the vulnerability of the developing brain during fetal life. Identification of the nature and timing of alterations to brain structure and function that underlie neurocognitive impairment could help the development of strategies designed to improve the long-term outcome of children of diabetic mothers.

During fetal life, the predominant source of brain energy is glucose, which crosses the placenta by facilitated diffusion.[7] While severe perturbations in glucose homeostasis after birth are associated with neonatal brain injury, the effect of chronic fluctuant glucose concentration experienced by fetuses of women with diabetes on in utero brain development has not been investigated, to our knowledge. Maternal diabetes is also associated with disturbances in fatty acid metabolism: Umbilical venous blood docosahexaenoic acid concentration is reduced; this reduction reflects lower docosahexaenoic acid transfer to the fetus.[8] Docosahexaenoic acid accumulates in the brain in abundance from the

Received September 28, 2016; accepted December 20.

From the Medical Research Council Centre for Reproductive Health (F.C.D., D.A., A.S., J.P.B.), University of Edinburgh, Queen's Medical Research Institute, Edinburgh, UK; Clinical Research Imaging Centre (G.M., S.I.K.S.), University/British Heart Foundation Centre for Cardiovascular Science (S.I.K.S., R.M.R.), and Centre for Clinical Brain Sciences (D.A., J.P.B.), University of Edinburgh, Edinburgh, UK; and Simpson Centre for Reproductive Health (G.T., J.W.), Royal Infirmary, Edinburgh, UK.

This work was supported by Theirworld (www.theirworld.org) and was undertaken in the Medical Research Council Centre for Reproductive Health, which is funded by an Medical Research Council Centre grant (Medical Research Council G1002033). We acknowledge the support of the British Heart Foundation.

Please address correspondence to Fiona C. Denison, MD, Medical Research Council Centre for Reproductive Health, University of Edinburgh, Queen's Medical Research Institute, 47 Little France Crescent, Edinburgh EH16 4TJ, UK; e-mail: Fiona.Denison@ed.ac.uk; @MRC_CRH

http://dx.doi.org/10.3174/ajnr.A5118

third trimester and is essential for neurogenesis, neurotransmission, and protection from oxidative stress. Reduced bioavailability of this key metabolite has been suggested as a putative mechanism for programming altered neurodevelopment.[8,9]

Advances in proton MR spectroscopy (^{1}H-MRS) and diffusion-weighted and structural MR imaging (sMRI) have led to the development of objective and sensitive measures of fetal brain structure and metabolism. Use of these technologies has revealed alterations in the cerebral NAA:choline ratio and gyrification in fetuses with congenital heart disease,[10] temporal lobe volumes in fetuses with congenital cytomegalovirus infection,[11] and ADC values and parenchymal volume in antenatal ventriculomegaly.[12,13] Historically, most fetal imaging studies have been undertaken at 1.5T. However, although an increasing number of studies have been performed at 3T field strength,[14-20] which has benefits over 1.5T due to improved signal-to-noise and is likely to be advantageous for depicting fetal anatomy,[21] to date, there have been no studies assessing the feasibility of recruiting women with diabetes for fetal neuroimaging.

Early-life metrics derived from ^{1}H-MRS, DWI, and sMRI are associated with function in childhood. After preterm birth, NAA/Cho and Cho/Cr ratios are associated with neurodevelopmental outcome at 2 years of age,[22] lactate/NAA predicts outcome following hypoxic-ischemic encephalopathy,[23] and abnormalities in the NAA/Cr and Cho/Cr ratios in neonates[24] and older children[25] predict developmental delay. Increased ADC values in white matter are associated with diffuse white matter injury following preterm birth[26] and with poor outcome after hypoxic-ischemic encephalopathy in term infants.[27,28] Finally, reduced regional and whole-brain volumes are associated with specific preterm comorbidities,[29,30] and structural alteration predicts long-term impairment after preterm birth.[31,32]

On the basis of disturbances to fetal glucose and fatty acid metabolism associated with maternal diabetes and the neurocognitive profile of offspring, we aimed to investigate the feasibility of comprehensive fetal brain assessment by acquiring measurements of NAA/Cho, NAA/Cr, and Cho/Cr ratios; regional apparent diffusion coefficient measurements; and volume of the cerebrum during the third trimester of pregnancy from women with diabetes and from healthy controls by using 3T MR imaging. The secondary aim was to determine normal values for these measures for future studies designed to investigate the effect of maternal disease on fetal brain development and in utero origins of neurodevelopmental impairment.

MATERIALS AND METHODS

Study Population

Ethics approval was obtained from the National Research Ethics Committee (South East Scotland Research Ethics Committee), and written informed consent was obtained. Women with a pregnancy complicated by diabetes ($n = 26$) and healthy controls ($n = 26$) were recruited prospectively from antenatal diabetes clinics at the Simpson Centre for Reproductive Health at the Royal Infirmary, Edinburgh, UK. The inclusion criteria were a singleton pregnancy and a fetal anomaly scan with normal findings at 20 weeks' gestation. Women with diabetes were eligible to participate if they had gestational diabetes, diagnosed by using the Scottish Intercollegiate Guideline Network diagnostic criteria[33] as a fasting venous plasma glucose of ≥5.1 mmol/l or 2-hour glucose of ≥8.5 mmol/l after a 75-g oral glucose tolerance test or pregestational type 1 or type 2 diabetes. Exclusion criteria were serious coexisting maternal systemic disease other than maternal diabetes and women with any contraindications to MR imaging, including metal implants and pacemakers.

MR Image Acquisition

MR imaging studies were performed at the Clinical Research Imaging Centre in the Queen's Medical Research Institute, University of Edinburgh, UK, by using a Magnetom Verio 3T MR imaging clinical scanner (Siemens, Erlangen, Germany). To avoid vena-cava compression, we placed women in a left-lateral tilt, with blood pressure being constantly monitored by using a Veris MR imaging vital signs monitor (Medrad, Indianola, Pennsylvania). No fetal sedation was used, women were limited to spending 45 minutes in the scanner, and data were acquired with women free-breathing throughout. MR images were obtained between 34 and 38 weeks' gestation. A radiologist with experience in MR imaging reported all images.

T2-weighted half-Fourier-acquisition single-shot turbo spin-echo images were acquired of the fetal brain in sagittal, coronal, and transverse orientations (HASTE: TR/TE = 1800/86 ms, FOV = 400 × 400 mm, matrix = 192 [phase] × 256 [frequency], section thickness = 8 mm, acquisition time = 18 seconds). These images were used to plan the position of the single 20-mm^3 spectroscopy voxel within the fetal brain. The scanner bed was moved to ensure that the fetal brain was positioned at the isocenter, and the voxel was positioned within 1 hemisphere of the fetal brain, avoiding ventricles and contaminant signal from surrounding tissue. An optimized semiautomated shimming protocol was systematically applied until the full width at half maximum of the water peak was <20 Hz. A single-voxel point-resolved spectroscopy technique was applied with TR/TE = 1500/30 ms, 96 signal averages, bandwidth = 2000 Hz, and a water suppression bandwidth = 50 Hz. The spectral acquisition took 2 minutes 30 seconds. Signal was received from selected elements of the spine matrix coil and body matrix surface coils positioned to allow adequate coverage of the fetal brain. A postspectroscopy 3-plane HASTE acquisition was then compared with the prespectroscopy HASTE images to allow visual assessment of fetal movement during the spectral acquisition. If the expert operator observed evidence of movement between HASTE acquisitions, then the spectroscopy voxel was repositioned and the spectral acquisition was repeated. No additional filtering or quality-control limiting of data was applied during the processing stage. We therefore processed all the MR spectroscopy data that were acquired. An example of voxel positioning for the MR spectroscopy acquisition is shown in Fig 1*A*.

Transverse DWIs of the whole fetal brain (TR/TE = 7300/106 ms, FOV = 400 × 400 mm, matrix = 128 × 128, section thickness = 3 mm, b-values = 0, 500, and 1000 s/mm^2) were acquired. DWI was checked at the point of acquisition for obvious signs of fetal motion and was repeated if required. ADC maps were generated automatically from the diffusion-weighted images.

Finally, additional transverse HASTE images were acquired with identical coverage to the DWIs to aid subsequent ROI anal-

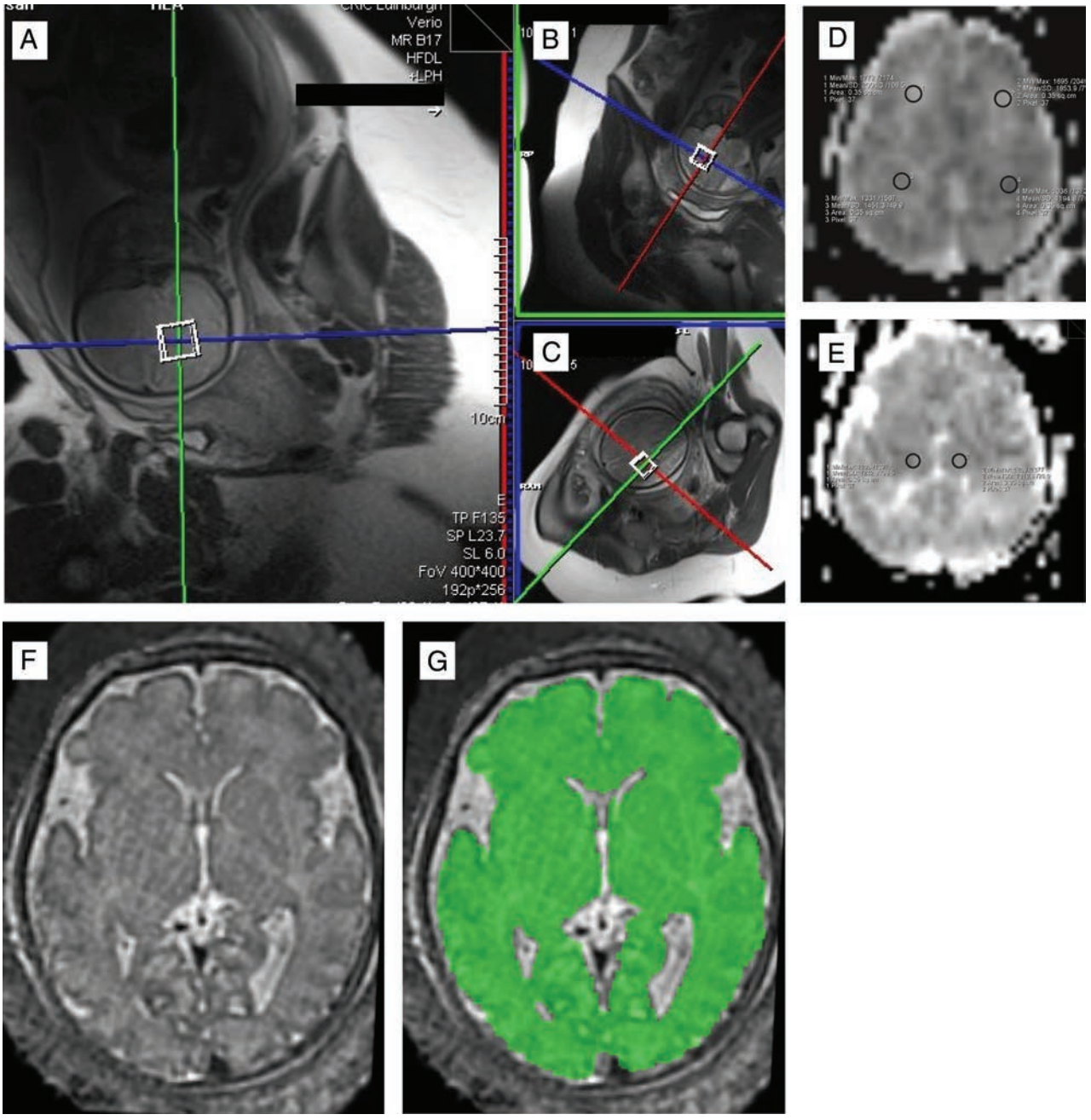

FIG 1. Examples of MR spectroscopy voxel placement in the fetal brain (*A–C*). ROIs for DWI in anterior white matter and posterior white matter (right and left) (*D*) and deep gray matter (right and left) (*E*), and tissue segmentation in the brain, highlighted in green (*F–G*).

ysis and to enable construction of the 3D motion-corrected brain volumes.

Data Analysis: ^{1}H-MRS

Spectral analysis was performed by using the QUEST algorithm available in jMRUI (www.mrui.uab.es/mrui/mrui_download/).[34] This technique estimates metabolite amplitudes by using a nonlinear least-squares fit of simulated metabolite signals to the acquired spectrum. A metabolite basis set was generated by using the NMR-Scope function available in jMRUI[35] and included contributions from NAA (2.01, 2.49, and 2.70 ppm), Cho (3.20, 3.53, and 4.08 ppm), and Cr (3.04 and 3.93 ppm). We then calculated the following ratios: NAA/Cho, NAA/Cr, and Cho/Cr.[36,37] The QUEST algorithm calculates errors associated with the estimated metabolite amplitudes by using an extended version of the Cramer–Rao lower bounds calculation.[35] The errors for each of the calculated metabolite ratios were derived through error propagation of the jMRUI output.

Data Analysis: Diffusion and sMRI

Apparent Diffusion Coefficients. ROI analysis was performed on ADC maps by using standard software on the 3T Magnetom Verio MR imaging system (Siemens). First, ROIs within white matter and gray matter were identified from the HASTE images acquired in the same plane and with the same coverage as the diffusion-

Table 1: Demographics, MRI details, and delivery outcomes

		Diabetes			
	Control (*n* = 26)	All (*n* = 26)	GDM (*n* = 13)	T1DM (*n* = 12)	T2DM (*n* = 1)
Maternal demographics					
Maternal age (mean) (SD) (yr)	31 (5)	31 (5)	32 (5)	30 (6)	34
Parity (median) (range)	0 (0–3)	0 (0–3)	1 (0–2)	0 (0–3)	0
Current smoker (No.) (%)	1 (4)	3 (12)	1 (8)	2 (17)	
Deprivation (No.) (%)					
SIMD 1–3	13 (50)	13 (50)	6 (46)	6 (50)	1
SIMD 4–5	13 (50)	13 (50)	7 (54)	6 (50)	
MRI details					
Gestation at MRI (mean) (SD) (wk)	36.1 (0.9)	36.0 (0.8)	36.0 (0.8)	36.0 (0.9)	36.7
MRI-to-delivery interval (mean) (SD) (wk)	3.6 (1.6)	2.1 (1.2)	2.6 (1.2)	1.6 (1.1)	15
Neonatal outcome					
Gestation delivery (mean) (SD) (wk)	39.7 (1.5)	38.1 (1.4)	38.6 (1.1)	37.6 (1.5)	38.9
Birthweight (mean) (SD) (g)	3372 (467)	3551 (627)	3629 (483)	3508 (780)	3040
Sex (male/female)	13:13	9:17	6:7	2:10	Male
Occipitofrontal circumference (mean) (SD) (cm)	34.4 (1.4)	34.8 (1.8)	35 (1.6)	35 (2.2)	36

Note:—SIMD indicates Scottish Index of Multiple Deprivation; SIMD 1, most deprived; SIMD 5, most affluent.

weighted images. A section above the ventricles was identified as white matter, and a section at the level of the thalami was identified as deep gray matter by using landmarks described in Boardman et al.[38] The identical sections were then identified on the corresponding ADC map; 4 ROIs were positioned in the white matter (2 posterior and 2 anterior) and 2 were positioned in the gray matter. Due to differences in fetal brain volume, we used an anatomically appropriate ROI size for each individual brain, taking care to avoid partial volume effects from adjacent structures and artifacts. The mean (SD) ADC value for each ROI was recorded. The mean white matter ROI size was 0.30 ± 0.12, and the mean gray matter ROI size was 0.32 ± 0.13. Sample ROI placements for white and gray matter are shown in Fig 1*B*. Interrater agreement was checked by 2 independent investigators (D.A., G.M.).

sMRI. For each participant, a single 3D motion-corrected brain volume was reconstructed by using a section-to-volume registration method (Fig 1*C*).[39] The fetal brain was extracted from surrounding fetal and maternal tissue by using an atlas-based approach.[40] All reconstructed images were nonlinearly aligned to the closest age-matched template from a publicly available 4D fetal brain atlas.[41] Then, an automatic method based on an expectation-maximization framework for brain tissue segmentation was used, in which the priors of brain tissues were propagated by using prior probabilities provided by the 4D atlas. Finally, binary masks of the cerebrum (intracranial contents excluding intraventricular CSF, extra-axial CSF, and the choroid plexus, brain stem, cerebellum, and pons structures) and the intracranial volume (GM, WM, and CSF) were deformed to the subject's native space, and volumes were calculated.

Statistical Analysis

This was a feasibility study, so a formal power calculation for sample size was not required.[42,43] For normally distributed data, the mean and SD are reported, and for non-normally distributed data, the median and interquartile range are reported. For group-wise comparisons of normally distributed variables, an independent-sample *t* test was used, and for skewed data, the Mann-Whitney *U* test was used. To analyze regional ADC values, we first tested for evidence of laterality in the anterior and posterior white matter and deep gray matter values with a paired-samples *t* test, and if there were no significant differences between left and right, the values were averaged to compute mean anterior white matter ADC, mean posterior white matter ADC, and mean deep gray matter ADC per individual. The distributions were assessed for normality, and an independent-samples *t* test was used for group-wise comparisons of regional ADC. Interobserver agreement in ADC measurements was assessed for each region in a randomly selected subset of 20 participants by using Bland-Altman statistics. For group-wise analysis of NAA/Cho, NAA/Cr, and Cho/Cr ratios and cerebral and intracranial volumes, an independent-samples *t* test was used after assessing the equality of variance between groups. Statistical analyses were performed by using SPSS 21 (IBM, Armonk, New York) with statistical significance defined as $P < .05$.

RESULTS

Participants

The maternal demographics and delivery outcomes of the study population are shown in Table 1. All women tolerated the MR imaging well, and no scan had to be abandoned due to maternal discomfort or claustrophobia. Of the women with diabetes, 13 were diagnosed with GDM during pregnancy, 12 had T1DM, and 1 had T2DM. In women with GDM, the median gestation at diagnosis and diagnosis-to-scan interval were 27.1 weeks (interquartile range, 12.0–31.0 weeks) and 8.9 weeks (interquartile range, 4.4–23.6 weeks), respectively. Only 1 woman with GDM was treated with diet alone. The other 12 were treated with metformin ($n = 9$) or metformin and insulin ($n = 3$) to achieve glycemic control. All women with T1DM were insulin-treated, and the 1 woman with T2DM was treated with insulin and metformin. The hemoglobin A1c (glycolated hemoglobin) at booking (11–13 weeks' gestation) for women with T1DM and T2DM was 51.9 mmol/mol (16.6 mmol/mol). Two women with GDM, 4 women with T1DM, and 1 control had antenatal steroids for fetal lung maturation before MR imaging. Three neonates of women with T1DM were admitted to the neonatal unit for <72 hours. The reasons for admission were suspected sepsis (culture negative

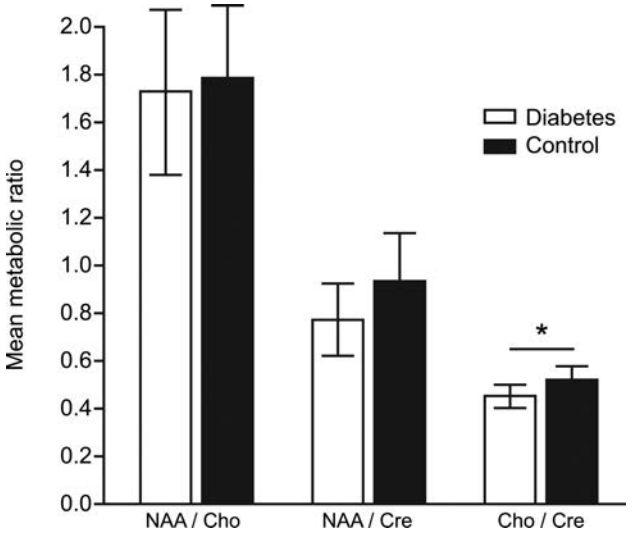

FIG 2. Metabolite ratios for NAA/Cho, NAA/Cr, and Cho/Cr in the fetal brain in women with diabetes and healthy controls. Data are presented as mean ± SD.

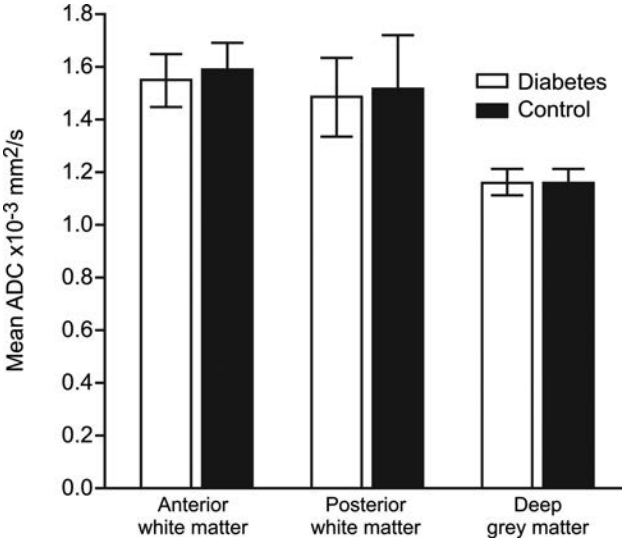

FIG 3. ADC values in the anterior white matter, posterior white matter, and deep gray matter in the fetal brain in women with diabetes and healthy controls. Data are presented as mean ± SD.

for bacteria) and transient low blood glucose ($n = 1$), a fractured clavicle sustained during a forceps delivery with shoulder dystocia, and a duplication cyst that was not diagnosed antenatally. No neonates born to healthy controls required admission. All neonates were discharged home alive and well.

There was no difference in the gestation in weeks at MR imaging between women with diabetes and healthy controls (mean [SD]) (36.0 weeks [0.8 weeks] versus 36.1 weeks [0.9 weeks], $P = .69$). No adjustment was therefore made for gestational age in the statistical analysis. No congenital anomalies, acquired brain injuries, or incidental findings were detected by MR imaging.

MR Spectroscopy

In utero ^{1}H-MRS of the fetal brain of suitable quality for analysis was obtained in 41/52 (79%) women in the study population, 22/26 (85%) with diabetes and 19/26 (73%) healthy controls. There was no difference in the clinical characteristics of women in whom interpretable data were acquired compared with those in whom they were not (data not shown). There was no difference in the NAA/Cho and NAA/Cr ratios in the fetal brain in women with diabetes compared with controls (1.74 [0.70] versus 1.79 [0.64], $P = .81$; and 0.78 [0.28] versus 0.94 [0.36], $P = .12$, respectively). The Cho/Cr ratio was marginally lower in the fetal brain in women with diabetes compared with controls (0.46 [0.11] versus 0.53 [0.10], $P = .04$) (Fig 2).

Diffusion-Weighted Imaging: ADC

DWIs amenable to ADC computation were available for 37/52 (71%) women in the study population, 18/26 (69%) with diabetes and 19/26 (73%) healthy controls. Fetal motion or maternal size prevented interpretable data from being obtained from 9/52 (17%) of the study population. There was no difference in the clinical characteristics of women in whom interpretable data were acquired compared with those in whom they were not (data not shown).

There was no evidence of laterality in the anterior white matter, posterior white matter, or deep gray matter ADC values (all $P > .05$). Data were therefore combined to 3 variables: mean anterior white matter, mean posterior white matter, and mean deep gray matter ADC. There was no difference in mean (SD) ADC values for anterior white matter, posterior white matter, and deep gray matter in women with diabetes mellitus compared with controls (1.16 [0.12] versus 1.16 [0.08], $P = .96$; 1.54 [0.16] versus 1.59 [0.20], $P = .56$; and 1.49 [0.23], versus 1.52 [0.23], $P = .89$, respectively) (Fig 3).

There was good interrater agreement between the 2 independent investigators for ADC values. The mean difference and 95% confidence intervals between investigators for anterior white matter, posterior white matter, and deep gray matter measurements are reported in Table 2.

Brain Volumes

Tissue segmentation data suitable for analysis were used to assess the macrostructure of the fetal brain in 24/52 (46%) of the study population (9/26 [35%] women with diabetes, 15/26 [58%] healthy controls). Fetal motion or data quality prevented interpretable data from being obtained from 28/52 (54%) women of the study population. There was no difference in mean cerebrum volume/milliliter in women with diabetes compared with controls (243.0 ± 22.7 mL^3 versus 253.8 ± 31.6 mL^3, $P = .39$). There was no difference in mean intracranial volume in fetuses of women with diabetes compared with controls (265.0 ± 22.5 mL^3 versus 274.5 ± 32.3 mL^3, $P = .47$).

DISCUSSION

In this study, we demonstrated that it is feasible to recruit pregnant women with diabetes to undergo MR imaging at 3T during the third trimester of pregnancy for measurements of NAA/Cho, NAA/Cr, and Cho/Cr ratios; regional ADC measurements; and cerebrum and intracranial volumes. We chose to acquire ^{1}H-MRS, DWI, and sMRI because of their use as markers of tissue injury/altered metabolism in the neonatal period and their relationships with long-term outcome. The values we acquired con-

Table 2: Bland-Altman statistics for ADC measurements recorded by 2 observers[a]

	Mean Difference	Mean + (1.96 × SD)	Mean − (1.96 × SD)
Gray matter ADC	-0.073×10^{-3} mm^2/s	0.108×10^{-3} mm^2/s	-0.253×10^{-3} mm^2/s
Anterior white matter ADC	-0.033×10^{-3} mm^2/s	0.175×10^{-3} mm^2/s	-0.241×10^{-3} mm^2/s
Posterior white matter ADC	-0.028×10^{-3} mm^2/s	0.225×10^{-3} mm^2/s	-0.281×10^{-3} mm^2/s

[a] Data are presented as mean difference ± 95% confidence intervals 91.96 × SD.

tribute useful normative data for future fetal brain studies performed with 3T systems.

Although this feasibility study was not powered to detect group differences, we observed a marginal-but-significant reduction in Cho/Cr in the brains of fetuses of diabetic mothers during the third trimester. The MR spectroscopy choline peak included free choline, phosphocholine, and glycerophosphocholine, so these data raise the possibility that brain metabolism and neuronal membrane phospholipid turn-over are altered in pregnancies with women with diabetes. While this finding requires confirmation in a larger study, alterations in the Cho/Cr ratio in brains of adults with type 2 diabetes have been reported.[44]

A strength of our study is that we recruited a cohort of women with well-characterized diabetes with all participants being scanned within a 4-week time window and gestation matched to our control group. This feature is important because ^{1}H-MRS spectra and ADC values are dynamic during this period of brain development.[45-47] We also acquired sMRI suitable for conventional clinical reporting, which was possible for all participants. A limitation of our study is that we were unable to acquire data amenable to quantitative analysis on all fetuses scanned. Despite ensuring the comfort of the women in a large-bore scanner, data could not be processed from ^{1}H-MRS in 21% of cases: DWI in 29% of cases and sMRI in 54% of cases. The low data yield for sMRI was partly because acquisition of ^{1}H-MRS and DWI was prioritized over sMRI. For future study designs that require fetal brain segmentation, yield may be increased by modifications to the acquisition protocol such as the increasing the number of stacks per plane and accepting the idea that time constraints required for safety may curtail other acquisitions (we capped imaging at 45 minutes). sMRI suitable for conventional clinical reporting was available for all participants.

We chose to recruit a heterogeneous population of women with diabetes to assess the feasibility of dissecting the effect of different in utero exposure to T1DM, T2DM, and GDM in a future study. Recruitment of women with T1DM and GDM was relatively easy; thus, recruitment to a future study assessing the effect of in utero exposure of T1DM and GDM on the fetal brain would be feasible. In contrast, we were able to recruit only 1 woman with T2DM, due to the lower prevalence of this condition. Thus, targeting recruitment of women with T2DM to a future study will not be practical unless recruitment occurs across multiple sites.

Our data were acquired by using a 3T system as opposed to 1.5T. For the advanced imaging techniques used in this study, there are advantages of acquiring data with the higher field strength of 3T.[48] Compared with lower field strengths, imaging at higher field strengths increases the signal-to-noise ratio. This increase improves the spectral quality obtained in ^{1}H-MRS and the ability to differentiate closely located metabolites, particularly at short TEs. The inability to complete data acquisition within the time available due to fetal movement is a major limitation of MR imaging in pregnancy. Acquiring data more rapidly by using more advanced imaging methodologies, using methods of motion correction to compensate for fetal movement, and using alternative sampling techniques such as compressed sensing is likely to greatly increase data yield in the future. Finally, one advantage of 3T is the ability to acquire images with higher spatial resolution (depending on the imaging coil used), potentially increasing diagnostic accuracy.[49]

Perinatal image metrics are sensitive to tissue injury and neuroprotective treatment strategies. They are therefore increasingly used to address the "gap in translation" in perinatal neuroscience to assess therapies that show promise in preclinical studies at lower economic and opportunity costs than randomized controlled trials powered on clinical outcomes.[50] The normative data provided here may inform the development of fetal brain biomarkers for use in interventional perinatal neuroprotective outcome studies.

CONCLUSIONS

The data provide proof-of-concept that comprehensive assessment of the fetal brain using measures derived from images acquired at 3T from women with diabetes and healthy controls is achievable. In addition, they suggest that fetal brain MR spectroscopy may provide a promising image marker of altered brain development in maternal diabetes. Finally, although we studied fetuses of mothers with diabetes, this research pipeline and the normative values obtained could be applied to any paradigm in which fetal origins of brain development are being investigated by using 3T MR imaging.

ACKNOWLEDGMENTS

We are grateful to the women who consented to take part in the study, to the research midwives, and to the nursing and radiography staff at the Clinical Research Imaging Centre, University of Edinburgh (http://www.cric.ed.ac.uk) who participated in scanning the women.

Disclosures: Fiona C. Denison—*RELATED*: *Grant*: TheirWorld, *Comments*: block grant, research funded by TheirWorld to cover work undertaken and reported in the article*; *UNRELATED*: *Board Membership*: Vice-Chair of the National Institute of Clinical Excellence Committee, *Comments*: I am Vice-Chair of the National Institute of Clinical Excellence Medical Technologies Advisory Committee. My travel expenses are paid to attend this monthly meeting. I am not paid directly to attend; *Grants/Grants Pending*: National Institute for Health and Care Excellence, Medical Research Council, Edinburgh and Lothians Health Foundation, and Tommy's, *Comments*: I am Co-Investigator or Principal Investigator of several research grants funded by the National Institute for Health and Care Excellence, Medical Research Council, Edinburgh, and Lothians Health Foundation. All of these grants fund separate studies, and there is no overlap with the work undertaken in article. Gillian Macnaught—*UNRELATED*: *Employment*: GlaxoSmithKline, *Comments*: Forty percent of my previous post was paid by GlaxoSmithKline; however, they were not involved in this submitted work.* Scott I.K. Semple—*UNRELATED*: *Other:* GlaxoSmithKline, *Comments*: GlaxoSmithKline sponsored a research fellow in my group, not connected to this work.* Jane

Walker—*RELATED*: *Grant*: TheirWorld.* James P. Boardman—*RELATED*: *Grant*: TheirWorld.* *Money paid to the institution.

REFERENCES

1. Mitanchez D, Yzydorczyk C, Siddeek B, et al. **The offspring of the diabetic mother: short- and long-term implications.** *Best Pract Res Clin Obstet Gynaecol* 2015;29:256–69 CrossRef Medline
2. Bolaños L, Matute E, Ramírez-Dueñas Mde L, et al. **Neuropsychological impairment in school-aged children born to mothers with gestational diabetes.** *J Child Neurol* 2015;30:1616–24 CrossRef Medline
3. Stehbens JA, Baker GL, Kitchell M. **Outcome at ages 1, 3, and 5 years of children born to diabetic women.** *Am J Obstet Gynecol* 1977;127:408–13 CrossRef Medline
4. Nomura Y, Marks DJ, Grossman B, et al. **Exposure to gestational diabetes mellitus and low socioeconomic status: effects on neurocognitive development and risk of attention-deficit/hyperactivity disorder in offspring.** *Arch Pediatr Adolesc Med* 2012;166:337–43 CrossRef Medline
5. Temple RC, Hardiman M, Pellegrini M, et al. **Cognitive function in 6- to 12-year-old offspring of women with Type 1 diabetes.** *Diabet Med* 2011;28:845–48 CrossRef Medline
6. Dionne G, Boivin M, Séguin JR, et al. **Gestational diabetes hinders language development in offspring.** *Pediatrics* 2008;122:e1073–79 CrossRef Medline
7. Kalhan S, Parimi P. **Gluconeogenesis in the fetus and neonate.** *Semin Perinatol* 2000;24:94–106 CrossRef Medline
8. Pagán A, Prieto-Sánchez MT, Blanco-Carnero JE, et al. **Materno-fetal transfer of docosahexaenoic acid is impaired by gestational diabetes mellitus.** *Am J Physiol Endocrinol Metab* 2013;305:E826–33 CrossRef Medline
9. Larqué E, Demmelmair H, Gil-Sánchez A, et al. **Placental transfer of fatty acids and fetal implications.** *Am J Clin Nutr* 2011;94(6 suppl):1908S–13S CrossRef Medline
10. Limperopoulos C, Tworetzky W, McElhinney DB, et al. **Brain volume and metabolism in fetuses with congenital heart disease: evaluation with quantitative magnetic resonance imaging and spectroscopy.** *Circulation* 2010;121:26–33 CrossRef Medline
11. Hoffmann C, Grossman R, Bokov I, et al. **Effect of cytomegalovirus infection on temporal lobe development in utero: quantitative MRI studies.** *Eur Neuropsychopharmacol* 2010;20:848–54 CrossRef Medline
12. Erdem G, Celik O, Hascalik S, et al. **Diffusion-weighted imaging evaluation of subtle cerebral microstructural changes in intrauterine fetal hydrocephalus.** *Magn Reson Imaging* 2007;25:1417–22 CrossRef Medline
13. Pier DB, Levine D, Kataoka ML, et al. **Magnetic resonance volumetric assessments of brains in fetuses with ventriculomegaly correlated to outcomes.** *J Ultrasound Med* 2011;30:595–603 CrossRef Medline
14. Egaña-Ugrinovic G, Sanz-Cortes M, Figueras F, et al. **Fetal MRI insular cortical morphometry and its association with neurobehavior in late-onset small-for-gestational-age fetuses.** *Ultrasound Obstet Gynecol* 2014;44:322–29 CrossRef Medline
15. Masoller N, Sanz-Cortés M, Crispi F, et al. **Severity of fetal brain abnormalities in congenital heart disease in relation to the main expected pattern of in utero brain blood supply.** *Fetal Diagn Ther* 2016;39:269–78 CrossRef Medline
16. Sanz Cortes M, Bargallo N, Arranz A, et al. **Feasibility and success rate of a fetal MRI and MR spectroscopy research protocol performed at term using a 3.0-Tesla scanner.** *Fetal Diagn Ther* 2016 May 27. [Epub ahead of print] CrossRef Medline
17. Sanz-Cortes M, Egaña-Ugrinovic G, Simoes RV, et al. **Association of brain metabolism with sulcation and corpus callosum development assessed by MRI in late-onset small fetuses.** *Am J Obstet Gynecol* 2015;212:804 e1–8 CrossRef Medline
18. Sanz-Cortes M, Simoes RV, Bargallo N, et al. **Proton magnetic resonance spectroscopy assessment of fetal brain metabolism in late-onset 'small for gestational age' versus 'intrauterine growth restriction' fetuses.** *Fetal Diagn Ther* 2015;37:108–16 CrossRef Medline
19. Simões RV, Sanz-Cortes M, Muñoz-Moreno E, et al. **Feasibility and technical features of fetal brain magnetic resonance spectroscopy in 1.5 T scanners.** *Am J Obstet Gynecol* 2015;213:741–42 CrossRef Medline
20. Taylor-Clarke M. **Re: mid-gestation brain Doppler and head biometry in fetuses with congenital heart disease predict abnormal brain development at birth. N. Masoller, M. Sanz-Cortés, F. Crispi, O. Gómez, M. Bennasar, G. Egaña-Ugrinovic, N. Bargalló, J. M. Martínez and E. Gratacós. Ultrasound Obstet Gynecol 2016; 47: 65–73.** *Ultrasound Obstet Gynecol* 2016;47:15 CrossRef Medline
21. Victoria T, Johnson AM, Edgar JC, et al. **Comparison between 1.5-T and 3-T MRI for fetal imaging: is there an advantage to imaging with a higher field strength?** *AJR Am J Roentgenol* 2016;206:195–201 CrossRef Medline
22. Van Kooij BJ, Benders MJ, Anbeek P, et al. **Cerebellar volume and proton magnetic resonance spectroscopy at term, and neurodevelopment at 2 years of age in preterm infants.** *Dev Med Child Neurol* 2012;54:260–66 CrossRef Medline
23. Hanrahan JD, Cox IJ, Azzopardi D, et al. **Relation between proton magnetic resonance spectroscopy within 18 hours of birth asphyxia and neurodevelopment at 1 year of age.** *Dev Med Child Neurol* 1999;41:76–82 CrossRef Medline
24. Amess PN, Penrice J, Wylezinska M, et al. **Early brain proton magnetic resonance spectroscopy and neonatal neurology related to neurodevelopmental outcome at 1 year in term infants after presumed hypoxic-ischaemic brain injury.** *Dev Med Child Neurol* 1999;41:436–45 Medline
25. Filippi CG, Uluğ AM, Deck MD, et al. **Developmental delay in children: assessment with proton MR spectroscopy.** *AJNR Am J Neuroradiol* 2002;23:882–88 Medline
26. Counsell SJ, Allsop JM, Harrison MC, et al. **Diffusion-weighted imaging of the brain in preterm infants with focal and diffuse white matter abnormality.** *Pediatrics* 2003;112(1 pt 1):1–7 CrossRef Medline
27. Cavalleri F, Lugli L, Pugliese M, et al. **Prognostic value of diffusion-weighted imaging summation scores or apparent diffusion coefficient maps in newborns with hypoxic-ischemic encephalopathy.** *Pediatr Radiol* 2014;44:1141–54 CrossRef Medline
28. Rutherford M, Biarge MM, Allsop, et al. **MRI of perinatal brain injury.** *Pediatr Radiol* 2010;40:819–33 CrossRef Medline
29. Boardman JP, Counsell SJ, Rueckert D, et al. **Early growth in brain volume is preserved in the majority of preterm infants.** *Ann Neurol* 2007;62:185–92 CrossRef Medline
30. Inder TE, Warfield SK, Wang H, et al. **Abnormal cerebral structure is present at term in premature infants.** *Pediatrics* 2005;115:286–94 CrossRef Medline
31. Boardman JP, Craven C, Valappil S, et al. **A common neonatal image phenotype predicts adverse neurodevelopmental outcome in children born preterm.** *Neuroimage* 2010;52:409–14 CrossRef Medline
32. Ullman H, Spencer-Smith M, Thompson DK, et al. **Neonatal MRI is associated with future cognition and academic achievement in preterm children.** *Brain* 2015;138(pt 11):3251–62 CrossRef Medline
33. Scottish Intercollegiate Guidelines Network. Management of diabetes: a national clinical guideline, 2014. Edinburgh. http://www.sign.ac.uk/pdf/sign116.pdf. Accessed May 30, 2016
34. Macnaught G, Gray C, Walker J, et al. **(1)H MRS: a potential biomarker of in utero placental function.** *NMR Biomed* 2015;28:1275–82 CrossRef Medline
35. Ratiney H, Sdika M, Coenradie Y, et al. **Time-domain semi-parametric estimation based on a metabolite basis set.** *NMR Biomed* 2005;18:1–13 CrossRef Medline
36. Horton MK, Margolis AE, Tang C, et al. **Neuroimaging is a novel tool to understand the impact of environmental chemicals on neurodevelopment.** *Curr Opin Pediatr* 2014;26:230–36 CrossRef Medline
37. Spader HS, Ellermeier A, O'Muircheartaigh J, et al. **Advances in myelin imaging with potential clinical application to pediatric imaging.** *Neurosurg Focus* 2013;34:E9 CrossRef Medline

38. Boardman JP, Counsell SJ, Rueckert D, et al. **Abnormal deep grey matter development following preterm birth detected using deformation-based morphometry.** *Neuroimage* 2006;32:70–78 CrossRef Medline
39. Rousseau F, Oubel E, Pontabry J, et al. **BTK: an open-source toolkit for fetal brain MR image processing.** *Comput Methods Programs Biomed* 2013;109:65–73 CrossRef Medline
40. Serag A, Aljabar P, Ball G, et al. **Construction of a consistent high-definition spatio-temporal atlas of the developing brain using adaptive kernel regression.** *Neuroimage* 2012;59:2255–65 CrossRef Medline
41. Serag A, Kyriakopoulou V, Rutherford MA, et al. **A multi-channel 4D probabilistic atlas of the developing brain: application to fetuses and neonates.** *Ann BMVA* 2012;2012:1–14. http://www.bmva.org/annals/2012/2012-0003.pdf
42. Billingham SA, Whitehead AL, Julious SA. **An audit of sample sizes for pilot and feasibility trials being undertaken in the United Kingdom registered in the United Kingdom Clinical Research Network database.** *BMC Med Res Methodol* 2013;13:104 CrossRef Medline
43. Whitehead AL, Julious SA, Cooper CL, et al. **Estimating the sample size for a pilot randomised trial to minimise the overall trial sample size for the external pilot and main trial for a continuous outcome variable.** *Stat Methods Med Res* 2016;25:1057–73 CrossRef Medline
44. Santhakumari R, Reddy IY, Archana R. **Effect of type 2 diabetes mellitus on brain metabolites by using proton magnetic resonance spectroscopy: a systematic review.** *Int J Pharma Bio Sci* 2014;5:1118–23 Medline
45. Cannie M, De Keyzer F, Meersschaert J, et al. **A diffusion-weighted template for gestational age-related apparent diffusion coefficient values in the developing fetal brain.** *Ultrasound Obstet Gynecol* 2007;30:318–24 CrossRef Medline
46. Kok RD, van den Berg PP, van den Bergh AJ, et al. **Maturation of the human fetal brain as observed by 1H MR spectroscopy.** *Magn Reson Med* 2002;48:611–16 CrossRef Medline
47. Righini A, Bianchini E, Parazzini C, et al. **Apparent diffusion coefficient determination in normal fetal brain: a prenatal MR imaging study.** *AJNR Am J Neuroradiol* 2003;24:799–804 Medline
48. Wardlaw JM, Brindle W, Casado AM, et al; SINAPSE Collaborative Group. **A systematic review of the utility of 1.5 versus 3 Tesla magnetic resonance brain imaging in clinical practice and research.** *Eur Radiol* 2012;22:2295–303 CrossRef Medline
49. Alvarez-Linera J. **3T MRI: advances in brain imaging.** *Eur J Radiol* 2008;67:415–26 CrossRef Medline
50. Azzopardi D, Robertson NJ, Bainbridge A, et al. **Moderate hypothermia within 6 h of birth plus inhaled xenon versus moderate hypothermia alone after birth asphyxia (TOBY-Xe): a proof-of-concept, open-label, randomised controlled trial.** *Lancet Neurol* 2015 Dec 18. [Epub ahead of print] CrossRef Medline

Spectrum of Spinal Cord, Spinal Root, and Brain MRI Abnormalities in Congenital Zika Syndrome with and without Arthrogryposis

M.F.V.V. Aragao, A.M. Brainer-Lima, A.C. Holanda, V. van der Linden, L. Vasco Aragão, M.L.M. Silva Júnior, C. Sarteschi, N.C.L. Petribu, and M.M. Valença

ABSTRACT

BACKGROUND AND PURPOSE: Arthrogryposis is among the malformations of congenital Zika syndrome. Similar to the brain, there might exist a spectrum of spinal cord abnormalities. The purpose of this study was to explore and describe in detail the MR imaging features found in the spinal cords, nerve roots, and brains of children with congenital Zika syndrome with and without arthrogryposis.

MATERIALS AND METHODS: Twelve infants with congenital Zika syndrome (4 with arthrogryposis and 8 without) who had undergone brain and spinal cord MR imaging were retrospectively selected. Qualitative and quantitative analyses were performed and compared between groups.

RESULTS: At visual inspection, both groups showed reduced thoracic spinal cord thickness: 75% (6/8) of the group without arthrogryposis and 100% (4/4) of the arthrogryposis group. However, the latter had the entire spinal cord reduced and more severely reduced conus medullaris anterior roots (respectively, $P = .002$ and .007). Quantitative differences were found for conus medullaris base and cervical and lumbar intumescences diameters (respectively, $P = .008$, .048, .008), with more prominent reduction in arthrogryposis. Periventricular calcifications were more frequent in infants with arthrogryposis ($P = .018$).

CONCLUSIONS: Most infants had some degree of spinal cord thickness reduction, predominant in the thoracic segment (without arthrogryposis) or in the entire spinal cord (with arthrogryposis). The conus medullaris anterior roots were reduced in both groups (thinner in arthrogryposis). A prominent anterior median fissure of the spinal cord was absent in infants without arthrogryposis. Brain stem hypoplasia was present in all infants with arthrogryposis, periventricular calcifications, in the majority, and polymicrogyria was absent.

ABBREVIATIONS: AACD = Association for Assistance of Disabled Children; GRE = gradient recalled-echo; IgM = immunoglobulin M

The Zika virus infection is transmitted by a bite from an infected mosquito, with *Aedes aegypti* being the main vector.[1] Zika virus was first discovered in 1947 in monkeys in the Zika forest in Uganda,[2] and human infection was identified in 1952.[3] The first epidemic of Zika virus occurred only in 2007 in Micronesia and the Yap Islands.[4] The second epidemic was found in 2013, in French Polynesia,[5] and the third began in Brazil,[6,7] where it was initially detected in Bahia, Northeast Brazil, in March 2015.[6,8]

In September 2015, a substantial increase in the incidence of infants with microcephaly was detected in northeast Brazil.[8] For the first time, a strong increase of evidence suggested the association between the Zika virus infection outbreak and microcephaly by congenital infection.[9] In Brazil, on December 31, 2016, there were 2366 cases of microcephaly and other central nervous system malformations suggestive of congenital Zika syndrome.[10] There are 2 major lineages of Zika virus, the African, reported recently in Guinea-Bissau, and the Asian, reported from Asia and the West Pacific region to the Americas and Cabo Verde, which is the strain currently in Brazil.[10] Neurologic complications have been related only to the Asian strains after 2007.[10] The explanation as to why

Received November 2, 2016; accepted after revision December 22.

From the Centro Diagnostico Multimagem (M.F.V.V.A.), Recife, Brazil; PROCAPE (A.M.B.-L.), University of Pernambuco, Recife, Brazil; Mauricio de Nassau University (M.F.V.V.A., A.M.B.-L.), Recife, Brazil; Federal University of Pernambuco (A.C.H., M.L.M.S.J., M.M.V.), Recife, Brazil; Association for Assistance of Disabled Children (V.v.d.L.), Recife, Brazil; Barão de Lucena Hospital (V.v.d.L., N.C.L.P.), Recife, Brazil; Prof Fernando Figueira Integral Medicine Institute (L.V.A.), Recife, Brazil; and Fundação Oswaldo Cruz–Fiocruz/PE (C.S.), Recife, Brazil.

Please address correspondence to M.F.V.V. Aragao, MD, Centro Diagnostico Multimagem, Rua Frei Matias Teves, 194-Ilha do Leite, Recife-PE, Brazil 50070-45; e-mail: fatima.vascoaragao@gmail.com

Indicates open access to non-subscribers at www.ajnr.org

Indicates article with supplemental on-line table.

http://dx.doi.org/10.3174/ajnr.A5125

and how the Brazilian Zika virus strain could have developed this neurotropism for the central nervous system is still unknown.

The disease has already spread and, according to the World Health Organization, 76 countries and territories, particularly in Latin America, have reported evidence of transmission of the Zika virus by mosquitoes. Cases of microcephalic infants have been reported in 29 countries.[10]

In addition to microcephaly, other serious brain abnormalities were observed, especially brain calcifications, predominantly in the cortical and subcortical white matter junction, associated with malformations of cortical development (often polymicrogyria or pachygyria with predominant frontal lobe involvement) and a simplified cortical gyral pattern. Other frequent imaging findings are ventriculomegaly; decrease in brain, brain stem, and cerebellar volumes; enlargement of the cisterna magna and the extra-axial subarachnoid space; corpus callosum abnormalities (hypogenesis and hypoplasia); and delayed myelination.[11]

The congenital Zika syndrome is an entity without a well-known clinical spectrum, probably with only the most severe cases of the spectrum recognized. Other malformations have been described in some infants, such as ophthalmologic alterations[12,13] and arthrogryposis.[11,13,14] Currently, 8% of the children with presumed congenital Zika virus infection followed by the Association for Assistance of Disabled Children (AACD) in Recife, Brazil have arthrogryposis. Among the children with CSF immunoglobulin M (IgM) who tested positive for Zika virus, 6.6% have arthrogryposis.

Arthrogryposis multiplex congenita, often known simply as arthrogryposis, is a syndrome characterized by joint contractures, present since birth, affecting ≥2 areas of the body.[15-20] These joint malformations can be attributed to different disorders, such as defects of uterine environment, disorders of connective tissues, muscular dystrophies, and other abnormalities or conditions that affect the central or peripheral nervous systems in at least one of the components of the motor pathways from the spinal cord to muscles.[16,18] Regardless of the cause, children affected by arthrogryposis have onset and severe weakness early in intrauterine life, with immobilization of joints at different developmental stages.[16]

No study has yet analyzed qualitatively and quantitatively MR imaging of the spinal cord of children with congenital Zika syndrome, to our knowledge. Because there is a spectrum of congenital Zika syndrome for brain abnormalities, a similar spectrum might occur in the spinal cord. Therefore, the aim of this study was to explore and describe in detail the MR imaging features found in the spinal cord and nerve roots of infants with congenital Zika syndrome with or without arthrogryposis.

MATERIALS AND METHODS

This retrospective series included 12 infants diagnosed with congenital Zika syndrome, based on the Brazilian government protocol,[8] who had or did not have arthrogryposis and met the following inclusion criteria: 1) brain imaging suggestive of any congenital infection; 2) a complete investigation with negative findings, including laboratory testing, of the other 6 main infectious causes of primary microcephaly (toxoplasmosis, cytomegalovirus, rubella, syphilis, herpes simplex, and HIV); 3) negative results of an investigation, through clinical examination and family history, for causes of microcephaly and brain calcifications such as prenatal and perinatal complications; exposure to licit and illicit drugs, toxic substances, and ionizing radiation; genetic and metabolic diseases; and congenital infections; and 4) the existence of previously performed brain and spinal cord MR imaging.

Since October 2015, infants with suspected microcephaly born in Pernambuco are reported on a government Web site (cievspe.com/microcefalia) by health professionals. The criterion for microcephaly up to December 2015 was a head circumference of ≤33 cm. Therefore, all the infants born before December 2015, including all the ones included in this study, were referred for investigation of congenital Zika syndrome because they had a head circumference of up to 33 cm (currently, the criterion for microcephaly is based on the International Fetal and Newborn Growth Consortium for the 21st Century [INTERGROWTH-21st]). Once microcephaly was detected, the infants in this study were referred to the AACD, where they were evaluated, as needed, by a multidisciplinary team. The AACD has become one of the major referral centers in Pernambuco for the diagnosis and follow-up of children with microcephaly and congenital Zika syndrome.

Besides a noncontrast brain CT scan, obtained in all suspected cases of microcephaly as part of the government protocol, all infants in this study also underwent MR imaging, based on clinical evaluation. The major indications for brain MR imaging were the presence of refractory seizures or suspicion of hydrocephalus, while the major indications for spinal cord MR imaging were suspicions of arthrogryposis or the presence of early-onset abnormal posture of the limbs. A reduced essential protocol for neuroaxis MR imaging was created in our service with a reduced sedation time.

This retrospective study was approved by the Federal University of Pernambuco Research Ethical Committee, and the children's mothers or guardians gave their consent for the publication of the results and images. Infants included in this study were chosen by convenience, following the inclusion criteria. Up to the beginning of the study, 12 infants with congenital Zika syndrome (4 with arthrogryposis and 8 without it) had undergone, postnatally, brain and spinal cord MR imaging at our service.

Inclusion of controls was not possible because the techniques and section thickness of spinal MR imaging of infants up to 1 year found retrospectively at our service (5 cases) were different from the 12 already-included cases, making comparison very difficult. Nevertheless, a brief qualitative comparison, by visual inspection, was still performed (Fig 1).

MR imaging of the whole spinal cord was performed in all 12 children. All the images were T2-weighted. The protocol was optimized to decrease the examination time. Therefore, T1 was not performed in the spinal cord, and the duration of an MR imaging procedure for the brain and spinal cord was 50 minutes, approximately. Of the 12 children, 2 underwent MR imaging in a 1.5T scanner (Intera; Philips Healthcare, Best, the Netherlands); and 10, in a 1.5T scanner (Signa HDxt; GE Healthcare, Milwaukee, Wisconsin). The 2 examinations performed in the Philips MR imaging scanner had technical parameters similar to those of the GE scanner, while measurements were performed on balanced fast-field echo sequences. No contrast was used in any of the infants, while sedation was necessary for all of them. Table 1 shows

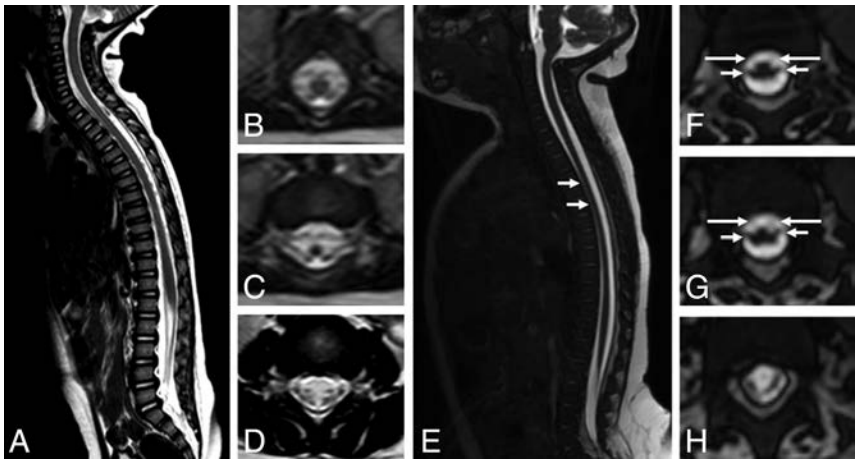

FIG 1. Comparison of spinal cord MR imaging between a control 12-month-old child (*A–D*) and a 4-month-old infant with presumed congenital Zika syndrome and arthrogryposis (*E–H*). Sagittal T2 (*A*) shows a normal-sized spinal cord and conus medullaris and no abnormal signal. Axial reformatted T2 reveals symmetric and normal-sized anterior and posterior nerve roots in the conus medullaris (*B* and *C*) and cauda equina (*D*). Meanwhile, sagittal T2-weighted volumetric GRE image (*E*) shows reduced spinal cord thickness, especially in the thoracic region (*short white arrows*). On the axial reconstruction of T2-weighted volumetric GRE (*F–H*), we can observe reduction of the conus medullaris anterior roots (*long arrows*) compared with posterior roots (*short arrows*).

Table 1: MR imaging parameters for brain and spinal cord image acquisition for all of the participants

	Brain			Spinal Cord		
MRI Parameters	Axial 3D SWAN	Axial 3D FSPGR	Axial T2*GRE	Sagittal 3D Volumetric GRE	Coronal T2	Axial T2
TE (ms)	50	Minimum	645	Minimum	120	110
TR (ms)	78.3	–	25	–	3700	5934
Flip angle	15°	12°	15°	45°	–	–
Bandwidth (kHz)	41.67	31.25	31.25	50	41	31.25
FOV (cm)	20	20	24	30	25	18
Section thickness (mm)	3	2	5	0.8	4.5	4
Spacing (mm)	–	–	0.5	–	0.5	1
Frequency (Hz)	288	256	288	320	384	320
Phase	224	256	192	320	224	224
NEX	–	1	1	1	1	3
Frequency direction	AP	AP	AP	AP	R-L	AP

Note:—AP indicates anteroposterior; R-L, right-left; FSPGR, fast-spoiled gradient recalled; SWAN, susceptibility-weighted angiography.

the parameters used for brain and spinal cord MR imaging. The images were analyzed and measured by 2 experienced neuroradiologists (M.F.V.V.A. and A.M.B.-L.), with the final interpretation determined by a consensus between them. Discrepancies between observers were not common, and when they occurred, they were resolved jointly after further review of the images.

Measurements of the spinal cord and spinal canal of these infants were taken by using the PACS software. To account for the spinal cord and spine curvatures, we performed all the measurements on sagittal images, as shown in Fig 2 (sagittal T2 volumetric gradient recalled-echo [GRE] image and balanced fast-field echo, respectively, in the GE Healthcare and Philips scanners).

The anatomic references for measurements of the spinal cord were the following: the smallest anteroposterior diameter of cervical, thoracic, and lumbar segments; and the largest anteroposterior diameter of the cervical and lumbar segments (ie, cervical and lumbar intumescences in adults are from about C4 to T1 and from T9 to T12, respectively)[21] determined by visual inspection. The anteroposterior diameter of the conus medullaris base was also measured. It is defined as the inferior portion of the spinal cord, at the location where the spinal cord begin to reduce its thickness to form the conus medullaris. The medullaris cone is usually located, in infants, in the level of L2–L3 or above.[22] Similarly, the vertebral canal was measured at approximately the same levels as the spinal cord measurements, to obtain a spinal cord/vertebral canal ratio for each measure of the spinal cord. These measurements were compared between children with and without arthrogryposis.

Other features of the spinal cord were qualitatively evaluated and compared between the 2 groups on axial T2 FSE or volumetric GRE and balanced fast-field echo reconstructions. The features evaluated in the axial plane were reduction of conus medullaris roots (graded as mild, moderate, and severe) and prominence of the anterior median fissure of the spinal cord (absent or present). On the sagittal plane, the thickness for each spinal cord segment (normal or decreased) was evaluated. The hip joints were assessed for developmental dysplasia on coronal FSE T2WI.

Additionally, brain MR imaging findings were compared between the 2 groups. We reviewed the MR images for the following: decreased brain volume (graded as mild, moderate, and severe); cerebral ventricular enlargement due to white matter hypoplasia; malformations of cortical development and sulcation and their locations; abnormalities of the corpus callosum (classified as agenesis, hypogenesis, and hypoplasia); myelination (normal or delayed, based on a previous study); the presence and location of brain calcifications; decreased brain stem and cerebellar volume; an enlarged cisterna magna; an enlarged anterior supratentorial subarachnoid space; and the presence of intraparenchymal cysts.

Symmetry of brain damage was also evaluated. It was determined by visual comparison between the cerebral hemispheres. The criteria used to describe pathologic asymmetry were those used in clinical practice, mainly ventricle size, sulci enlargement, cerebral lobe size, and spatial displacement of the left and right hemispheres with respect to each other. When the differences between the hemispheres were according to the normal pattern, even though they were not equally sized, the damage was considered symmetric.

Statistical Analysis

Absolute and percentage values were calculated to describe the qualitative variables and median and interquartile ranges for con-

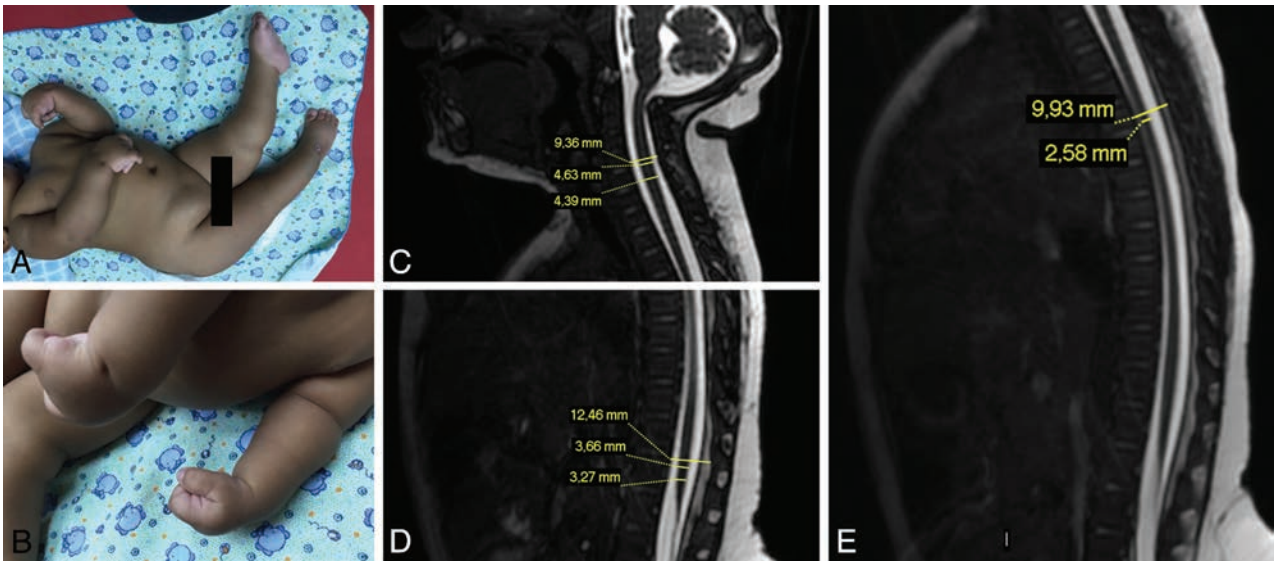

FIG 2. An infant with congenital Zika syndrome and arthrogryposis (*A* and *B*), with flexion contracture of the superior limbs, mainly of the wrists, hyperextension contracture of the lower limbs, and right hip deformity. Spinal cord MR imaging of an infant with arthrogryposis, showing spinal cord measurements (*C–E*). Sagittal T2-weighted fast imaging using steady-state acquisition (volumetric GRE) shows the cervical (*C*, from superior to inferior, vertebral canal diameter, largest cervical cord diameter, and smallest cervical cord diameter), lumbar (*D*, from superior to inferior, vertebral canal diameter, largest lumbar cord diameter, and smallest lumbar cord diameter), and thoracic (*E*, from superior to inferior, vertebral canal diameter and smallest thoracic cord diameter) segments. There is apparently reduced spinal cord thickness, especially in the thoracic region (*E*), and an enlarged cisterna magna (*C*).

Table 2: Individual clinical data of the 12 infants, 8 without and 4 with arthrogryposis, included in the study

No.	Sex	Gestational Age (wk)	HC at Birth (cm)	Mother's Rash during Pregnancy	Joints Affected	IgM ZIKV CSF Status[a]
Congenital Zika syndrome without arthrogryposis						
1	F	35	29.5	2 mo		Positive
2	M	36	31.5	4 mo		No data
3	F	40	30	No rash		No data
4	M	39	26	3 mo		Positive
5	M	39	31	3 mo		Positive
6	F	39	28.5	2.5 mo		Positive
7	M	39 wk 5 days	32	4 mo		Positive
8	M	39 wk 5 days	28	3 mo		Positive
Congenital Zika syndrome with arthrogryposis						
9	F	37	29	No rash	Feet, knees, hips, elbows, wrists, fingers	Positive
10	M	37	26	4 mo	Feet, knees, hips, wrists, fingers	No data
11	M	40	27	No rash	Feet, knees, hips	No data
12	F	38	30	2 mo	Feet, hips, wrists, fingers	Positive

Note:—HC indicates head circumference; ZIKV, Zika virus.
[a] Test performed on the infant.

tinuous variables. For association, we used the Fisher exact test. The Mann-Whitney test was applied to compare continuous variables. A P value $< .05$ was significant, while a P value $< .1$ was considered a statistical trend. The authors opted to include the data with a statistical trend because it points to the possibility of finding statistically significant results if the sample size is increased. The statistical analyses were performed with the Statistical Package for Social Sciences software, Version 21.0 (IBM, Armonk, New York).

RESULTS

Of the analyzed sample of 12 children, 7 (58%) were boys, and of the total, 4 (33%) had arthrogryposis. Maternal mean age was 27.4 ± 8.5 years. Gestational age ranged from 35 to 40 weeks, with an average of 38.2 ± 1.6 weeks. Nine of the mothers reported a rash, 6 (66.7%) in the first trimester and 3 (33.3%) in the second trimester. Forty percent of girls in this study had arthrogryposis, while 29% of boys had arthrogryposis, with no statistical difference ($P = 1.000$). Table 2 shows the individual clinical data of the 12 children and the IgM CSF status positive for Zika virus for all 8 children tested. The mean age at MR imaging was 135.83 days (131.25 days for the arthrogryposis group and 138.16 days for the group without arthrogryposis). The On-line Table shows the individual radiologic data of the 12 children.

At visual inspection, both groups showed reduction of high thoracic spinal cord thickness: 75% (6/8) without arthrogryposis and 100% (4/4) with arthrogryposis. The thoracic spinal cord

segment was frequently the one most severely reduced, as shown in Table 3. Indeed, all children with arthrogryposis had more segments of the spinal cord affected and had severe reduction of the anterior nerve roots of the conus medullaris compared with the children without arthrogryposis, with statistical significance (respectively, $P = .002$ and .007). However, 6 of the children without arthrogryposis also had reductions of the anterior conus medullaris roots (4 had mild and 2 had moderate reduction), and 6 had congenital hip dysplasia. The groups were also found to be different, with a statistical trend ($P = .091$), regarding the prominence of the anterior median fissure of the spinal cord, with none of the children without arthrogryposis having this feature.

Thus, in summary, the 4 infants with congenital Zika syndrome and arthrogryposis had, at visual inspection, reduced thickness of all segments of the spinal cord, with the thoracic segment its most compromised portion. All of them also had a severe reduction of the anterior nerve roots of the conus medullaris and congenital hip dysplasia. In addition, half of these infants had a prominent anterior median fissure, a feature not identified in any of the children without arthrogryposis.

Overall, the anteroposterior diameters of different levels of the spinal cord were smaller in infants with arthrogryposis compared with those without (Table 4). Statistically significant differences were found between the children with and without arthrogryposis regarding the conus medullaris base and lumbar and cervical intumescence measurements (respectively, $P = .008$, .008, .048). In addition, a statistical trend was observed regarding the smallest cervical spinal cord diameter ($P = .073$). No statistical difference was found in the smallest high thoracic spinal cord anteroposterior diameters between the 2 groups.

The anteroposterior diameter of the vertebral canal was statistically similar between the 2 groups. The ratio between the spinal cord diameters and these vertebral canal measurements, at similar levels of the spinal cord, revealed statistically significant differences in the conus medullaris base and the lumbar intumescence between children with and without arthrogryposis (respectively, $P = .016$ and .008) (Table 4).

Figures 3 and 4 show children with congenital Zika syndrome with arthrogryposis, while Fig 5 shows a child with congenital Zika syndrome without arthrogryposis. Reduced spinal cord thickness (Figs 3*D* and 4*C*), severe reduction of anterior conus medullaris roots (Figs 3*E–G* and 4*G*, *-H*), and congenital hip dysplasia (Fig 3*I*) were found in all children with arthrogryposis.

Statistically significant differences between the groups with and without arthrogryposis were found only in periventricular calcifications ($P = 0.018$) when brain abnormalities were compared, and only a statistical trend was observed for cerebellar or brain stem hypoplasia, cerebellar calcifications, and brain stem calcifications (Table 5); those findings were more frequent in infants with arthrogryposis than without it, being brain stem hypoplasia found in all 4 infants, and cerebellar hypoplasia in 2 of them. The cerebral damage was severe in all the children with arthrogryposis, while only 3 without

Table 3: Comparison between groups with and without arthrogryposis of features identified on MRI by visual inspection[a]

	Ag (*n* = 4)	No Ag (*n* = 8)	*P*[b]
Sites with spinal cord reduction			
Absent	0 (0.0%)	2 (25.0%)	.002[c]
Thoracic	0 (0.0%)	5 (62.5%)	
Cervical, thoracic	0 (0.0%)	1 (12.5%)	
Cervical, thoracic, conus medullaris	4 (100.0%)	0 (0.0%)	
Site of most severe spinal cord reduction			
Absent	0 (0.0%)	2 (25.0%)	<.999
Thoracic	4 (100.0%)	6 (75.0%)	
Prominence of the anterior median fissure of the spinal cord			
Absent	2 (50.0%)	8 (100.0%)	.091
Present	2 (50.0%)	0 (0.0%)	
Reduction of the anterior nerve roots of the conus medullaris			
No reduction	0 (0.0%)	2 (25.0%)	.007[c]
Mild	0 (0.0%)	4 (50.0%)	
Moderate	0 (0.0%)	2 (25.0%)	
Severe	4 (100.0%)	0 (0.0%)	
Congenital hip dysplasia			
Absent	0 (0.0%)	2 (25.0%)	.515
Present	4 (100.0%)	6 (75.0%)	

Note:—Ag indicates arthrogryposis.
[a] Data are number of patients (%).
[b] *P* = Fisher Exact test.
[c] Statistically significant.

Table 4: Comparison between groups with and without arthrogryposis regarding the anteroposterior diameter at different levels of the spinal cord and as the ratio between the spinal cord and vertebral canal anteroposterior diameters[a]

	Spinal Cord Measures			Spinal Cord/Vertebral Canal Ratio		
AP Diameters (mm)	Ag (*n* = 4)	No Ag (*n* = 8)	*P*[b]	Ag (*n* = 4)	No Ag (*n* = 8)	*P*[b]
Smallest spinal cord diameters						
Cervical	4.5 (4.4–4.9)	5.4 (4.7–5.9)	.073	0.44 (0.41–0.47)	0.57 (0.44–0.60)	.154
High thoracic	3.6 (2.8–4.2)	3.9 (3.6–4.5)	.214	0.39 (0.29–0.41)	0.39 (0.34–0.46)	.570
Conus medullaris base	4.3 (3.5–4.8)	6.3 (5.7–6.5)	.008[c]	0.44 (0.41–0.47)	0.57 (0.44–0.60)	.016[c]
Largest spinal cord diameters						
Cervical intumescence	4.7 (4.5–5.0)	5.6 (5.4–6.2)	.048[c]	0.46 (0.41–0.49)	0.58 (0.47–0.63)	.109
Lumbar intumescence	5.0 (3.9–5.8)	7.3 (7.1–7.5)	.008[c]	0.44 (0.32–0.51)	0.59 (0.56–0.64)	.008[c]

Note:—AP indicates anteroposterior; Ag, arthrogryposis.
[a] Data are median (25th–75th percentile).
[b] *P* = Mann-Whitney test.
[c] Statistically significant.

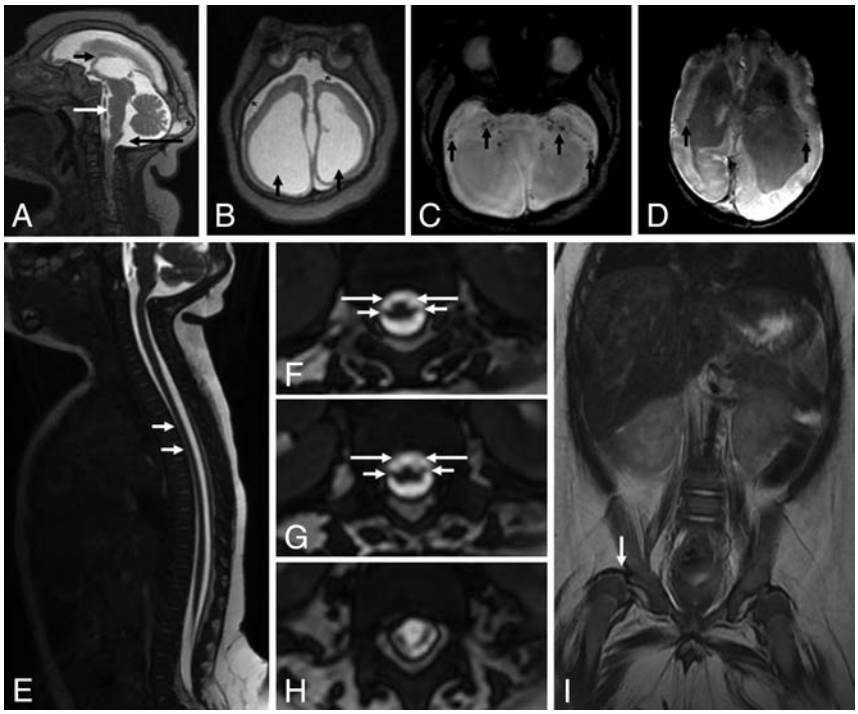

FIG 3. MR imaging of the brain and the spinal cord of an infant with microcephaly probably caused by congenital Zika virus infection, who has arthrogryposis. Sagittal T2-weighted image (*A*) shows craniofacial disproportion, a hypogenetic corpus callosum (*short black arrow*), pons hypoplasia (*white arrow*), and a slightly enlarged cisterna magna (*long black arrow*). Note the lush external occipital protuberance (*star*). Axial T2-weighted image (*B*) shows an extremely simplified gyral pattern, a thin cortex with minimal sulcation, enlargement of the subarachnoid space (*stars*), and severe ventriculomegaly, mainly at the posterior horn (*black arrows*). Note small dystrophic calcifications, mainly at the basal ganglia and thalamus and in the junction between the cortical and subcortical white matter, and periventricular calcifications (*black arrows*) on T2-weighted SWI (*C* and *D*). Sagittal T2-weighted volumetric GRE (*E*) shows reduced spinal cord thickness, especially in the thoracic region (*white arrows*). On the axial reconstruction of T2-weighted volumetric GRE (*F–H*), we can observe reduction of the conus medullaris anterior roots (*long arrows*) compared with the posterior roots (*short arrows*), suggesting increased damage in the anterior-versus-posterior horns of the spinal cord. Coronal T2-weighted imaging (*I*) reveals congenital hip dysplasia, especially on the right side (*white arrow*).

arthrogryposis had severe damage, though there were no statistical differences between the groups.

Regarding malformations of cortical development, no statistical differences were found. None of the infants with arthrogryposis had polymicrogyria, while this malformation was present in 2 children without arthrogryposis ($P = .515$). Pachygyria and a simplified gyral pattern were more often seen among the infants with arthrogryposis (both $P = .576$): One had diffuse pachygyria, one had diffuse simplified gyral pattern, and the other 2 had both malformations, with frontal pachygyria and a simplified parieto-occipital gyral pattern.

DISCUSSION

We analyzed the spinal cords of children with microcephaly with congenital Zika syndrome with and without arthrogryposis. One-third of our sample had arthrogryposis, a figure that is not representative of the entire sample of patients with congenital Zika syndrome in the AACD.

By visual inspection, the arthrogryposis group had significant qualitative reduction of the entire spinal cord and severe reduction in the anterior conus medullaris roots. However, most of the children without arthrogryposis also had mild reduction of the anterior conus medullaris roots, and often just the thoracic spinal cord was reduced. This finding could explain the lack of statistical differences in the thoracic spinal cord segment between the groups evaluated in quantitative analysis.

Significant quantitative differences were found between the groups, with arthrogryposis showing a thinner conus medullaris base, lumbar intumescence, and cervical intumescence. The arthrogryposis group was also significantly thinner at the conus medullaris base and at the lumbar intumescence by the evaluation of ratios with the canal diameter (anteroposterior diameters of the spinal cord/vertebral canal).

These findings support the hypothesis that the congenital Zika syndrome has a disease-severity spectrum. The spectrum is not restricted to the brain, but a disease spectrum is also present in the spinal cord and spinal roots. Clinically, this spectrum would range from absent or mild manifestations to arthrogryposis. Thus, arthrogryposis would be the most severe extreme of the spectrum of spinal cord damage, with thinner thickness of the entire spinal cord and severe anterior nerve root reduction. However, the MRIs of infants without arthrogryposis have also demonstrated some grade of damage in the spinal cord, mainly in the thoracic segment, with some mild anterior spinal root reduction.

Our study has no control group for quantitative analysis. In addition, we have found no references in the literature to normal spinal cord measurements in infants. The control group is a group difficult to obtain retrospectively, especially with the same MR imaging technique for accurate comparison.

Arthrogryposis has been associated with microcephaly in the spectrum of congenital Zika virus infection.[11,13,14] Schuler-Faccini et al[14] identified arthrogryposis in 4 of 27 children, while Oliveira Melo et al[13] mentioned 1 child with the condition. In addition, Melo et al[23] also described 3 neonates who died shortly after birth. The MR imaging findings in arthrogryposis were recently reported, but that series of cases did not evaluate the spinal cord of infants without arthrogryposis.[24] This study identified apparently reduced spinal cord thickness and reduced ventral roots in comparison with the dorsal roots.[24] Regarding neurogenic arthrogryposis in patients without congenital Zika virus infection, Fedrizzi et al[17] described brain and spinal cord MR imaging findings in 10 patients without an identified etiology.

The histopathologic changes in neurogenic arthrogryposis are dysgenesis of the anterior medullary horns and cytoarchitectural disorganization, which are more prominent in cervical and lum-

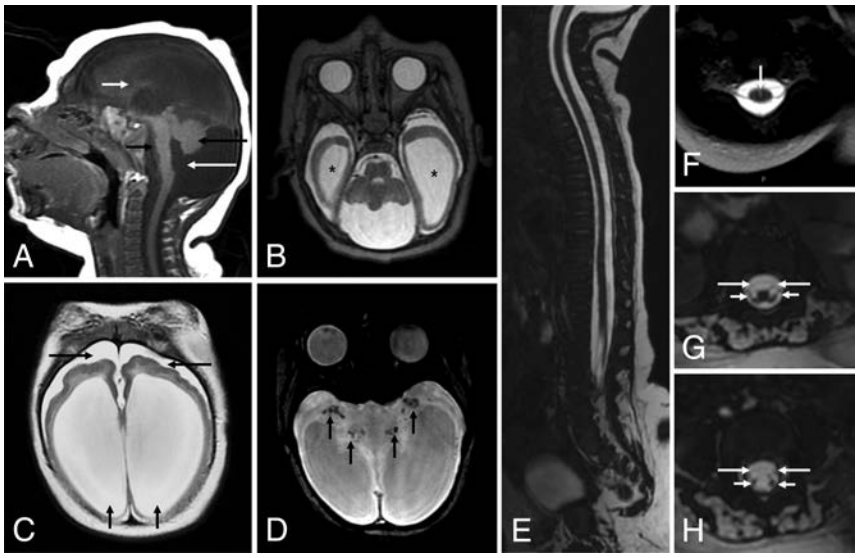

FIG 4. MR imaging of the brain and the spinal cord of an infant with microcephaly probably caused by congenital Zika virus infection who has arthrogryposis. Sagittal T1-weighted image (*A*) shows severe microcephaly, brain stem (*short black arrow*) and severe cerebellar (*long black arrow*) hypoplasia, and an enlarged posterior fossa with a very enlarged cisterna magna communicating with the fourth ventricle (*long white arrow*). Note the extremely hypogenetic corpus callosum (*small white arrow*). Axial T2-weighted images (*B* and *C*) show severe ventriculomegaly and enlargement of temporal horns (*stars*) and other parts of the lateral ventricles, mainly at the posterior horn and ventricular atrium (*short black arrows*). Note the bulging walls of the ventricle and a simplified gyral pattern with minimal sulcation and slight enlargement of the subarachnoid space (*long black arrows*). Also, note small dystrophic calcifications mainly seen at the basal ganglia and thalamus (*black arrows*) on T2-weighted SWI (*D*). Sagittal T2-weighted volumetric GRE (*E*) shows thin spinal cord thickness, and axial reconstruction of T2-weighted volumetric GRE reveals a prominent anterior median fissure of the spinal cord (*F*) and symmetric reduction of the conus medullaris anterior roots (*long arrows*) compared with posterior roots (*short arrows*), with damage affecting the anterior cord, preferentially (*G* and *H*).

bosacral intumescences associated with motor function.[16] Histopathologic evaluation of the spinal cord of an infant with congenital Zika syndrome and arthrogryposis revealed fewer motor neurons than expected, even though transverse spinal cord sections could not be obtained.[23] In addition, the brain stem had nerve cell degeneration and coarse and filamentous calcifications, while the cerebellum was hypoplastic and had focal cortical dysplasia.[23]

The above-mentioned features were previously suggested by brain and spinal MR imaging evaluation of infants with arthrogryposis and reported by the authors[24] and are consistent with what was found in the present study, reinforcing MR imaging being able to demonstrate the physiopathology of the congenital Zika syndrome. In this context, Zika virus probably has a tropism for the brain and also for the motor spinal cord neurons, which could occur initially in the thoracic region and achieve cervical and lumbar intumescences and conus medullaris in more severe cases.

Tropism of the Zika virus for neurons, leading eventually to their death, has been shown in the literature.[23] The morphologic brain alterations with multiple calcifications, mainly in the junction between the cortical and subcortical white matter, induced by the Zika virus, suggest serious damage that may cause sudden arrest in the development of the nervous system, resulting in a simplified pattern of cortical circumvolutions, malformations of cortical development (mainly in the frontal lobes), associated with ventriculomegaly, and corpus callosum and brain stem hypoplasia.[11,13,25,26] Long tract and spinal cord neuron alterations may occur in congenital Zika virus infection, even in patients without arthrogryposis. This hypothesis is supported by Mlakar et al,[26] who described infant brain abnormalities and Wallerian degeneration in the descending tracts of the brain stem and spinal cord, while the ascending tracts of the dorsal columns were well-preserved, in a 32-week-old fetus with confirmed real-time polymerase chain reaction for Zika virus infection without arthrogryposis.

In our study, the arthrogryposis group showed significantly more frequent periventricular calcifications and a trend toward more frequent cerebellar and brain stem hypoplasia and calcifications. One hypothesis that could be taken from these data is that the Zika virus damage to the human neural progenitor cells[27] in the periventricular zone will be more pronounced in children with arthrogryposis. Another possible explanation is major damage in the basal ganglia and pyramidal tracts, which could lead to or be associated with brain stem and cerebellar hypoplasia and spinal cord abnormalities. We hypothesized that both primary and secondary damage to the spinal cord are possible. We observed that the virus probably has great tropism for motor neurons, both in the brain (frontal lobes) and spinal cord (ventral spinal cord). In this context, MR imaging is important in understanding the physiopathology of congenital Zika syndrome and clarifying that the joint malformations found in these children are due to the virus tropism for specific motor neurons in related areas of the brain stem, cerebellum, and spinal cord and not to direct action of the virus in the osteoarticular system.

Although without significance, the overall brain damage caused by the Zika virus was more pronounced in the arthrogryposis group. Another interesting observation is that polymicrogyria was absent in the 4 children with arthrogryposis, while pachygyria was present in almost all the infants with arthrogryposis. Polymicrogyria is a feature related to an interruption in the late stages of neuronal migration and cortical organization that originates only after the twentieth gestational week,[28] while pachygyria is believed to originate in the early phase of pregnancy, between the twelfth and sixteenth gestational weeks.[28] These data can indicate that congenital Zika syndrome with arthrogryposis is more often associated with earlier fetal infection, further supported by the more severe damage found in these infants. However, we did not find an association of the type of malformation of cortical development with the time of the mother's rash.

Nevertheless, the literature has shown that there is an interval between the maternal infection and the sonographic evidence of fetal abnormalities from 2 to 27 weeks.[23] We suppose that the month of the mother's rash does not necessarily indicate exactly

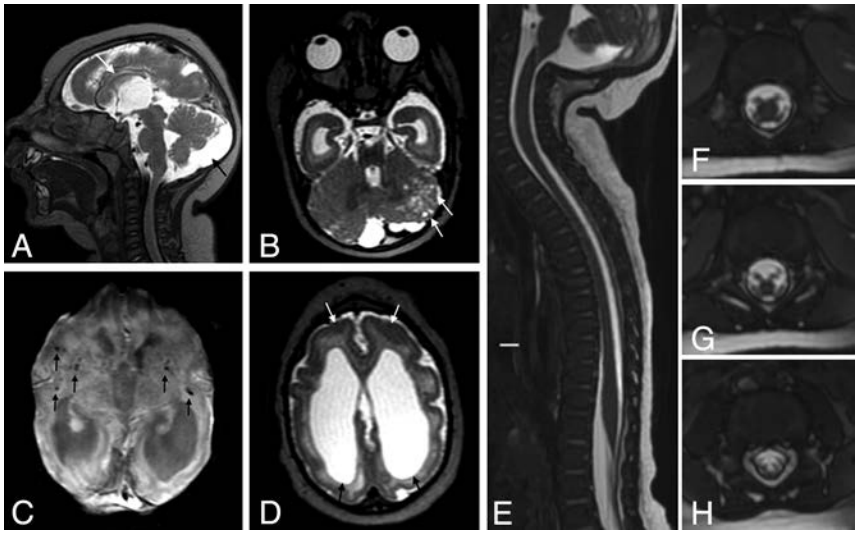

FIG 5. MR imaging of the brain and the spinal cord of an infant with microcephaly confirmed to be caused by the Zika virus without arthrogryposis. Sagittal T2-weighted images (*A*) shows hypogenesis of the corpus callosum (*white arrow*) and an enlarged cisterna magna (*black arrow*). Coronal T2-weighted image (*B*) shows left cerebellar hemisphere hypoplasia, with cortical malformation and microcysts (*white arrows*). Axial SWI (*C*) shows small dystrophic calcifications in the junction between the cortical and subcortical white matter and in the basal ganglia (*black arrows*). Axial T2-weighted image (*D*) shows a simplified gyral pattern, bilateral cortical thickness in the pachygyric frontal lobe (*white arrows*), and ventriculomegaly (*black arrows*). The spinal cord and conus medullaris are normal-sized and show no abnormal signal on the sagittal T2-weighted volumetric GRE (*E*). Axial reformatted T2-weighted volumetric GRE reveals normal-sized anterior and posterior nerve roots in the conus medullaris (*F* and *G*) and cauda equina (*H*).

Table 5: Comparison between children with and without arthrogryposis regarding some of the brain abnormalities found on MRI[a]

Variables	Arthrogryposis		P^b
	No (n = 8)	Yes (n = 4)	
Decreased brain volume	6 (75.0%)	4 (100.0%)	.515
Grade of brain volume decrease			
Mild	1 (20.0%)	0 (0.0%)	.876
Moderate/severe	4 (80.0%)	3 (100.0%)	
Degree of cerebral damage			.394
Absent	1 (12.5%)	0 (0.0%)	
Mild	2 (25.0%)	0 (0.0%)	
Moderate	2 (25.0%)	0 (0.0%)	
Severe	3 (37.5%)	4 (100.0%)	
Symmetry	6 (75.0%)	3 (75.0%)	>.999
Cortical development abnormalities			
Pachygyria	3 (37.5%)	3 (75.0%)	.545
Polymicrogyria	2 (25.0%)	0 (0.0%)	.515
Simplified gyral pattern	4 (50.0%)	3 (75.0%)	.576
Corpus callosum			>.999
Normal	2 (25.0%)	0 (0.0%)	
Hypogenesis	5 (62.5%)	3 (75.0%)	
Hypoplasia	1 (12.5%)	1 (25.0%)	
Cortical and subcortical junction calcifications	7 (85.5%)	4 (100.0%)	>.999
Basal ganglia calcifications	3 (37.5%)	3 (75.0%)	.545
Periventricular calcifications	0 (0.0%)	3 (75.0%)	.018[c]
Brain stem calcifications	1 (12.5%)	3 (75.0%)	.067
Cerebellum calcifications	0 (0.0%)	2 (50.0%)	.091
Cerebellum or brain stem hypoplasia	2 (25.0%)	4 (100.0%)	.061
Increased cisterna magna	8 (100.0%)	4 (100.0%)	–
Delayed myelination	5 (50.0%)	4 (100.0%)	.208

[a] Data are number of patients (%).
[b] P = Fisher Exact test.

when the embryo or fetus was infected, whether early or late during infection of the mother in the pregnancy.

On the basis of the findings described in this study, it is important to consider Zika virus infection in the differential diagnosis of congenital spinal cord and anterior nerve root diseases if the infant and mother have a positive epidemiologic context. This is especially important in mild cases in which microcephaly is absent and the only clinical manifestation is, for example, abnormal joints. On the other hand, health professionals should pay close attention during the follow-up of children from an epidemic area with mild or no clinical signs of spinal cord and anterior nerve root damage because they could possibly have future problems in their neuropsychomotor development. This can also be true for children without microcephaly, born in regions with the Zika virus epidemic.

It is difficult to determine the prognosis of the different degrees of the congenital Zika syndrome due to the lack of follow-up studies[29]; however, congenital Zika virus infection with severe brain damage should have a poor prognosis.[29] Knowledge of the spectrum of this syndrome can be helpful in identifying which cases could have higher chances of worse outcomes. It is probable that infants with arthrogryposis will have worse prognoses, especially in motor development, even if they do not have severe brain lesions or microcephaly.

Despite the limitations, especially regarding the small number of patients and lack of a control group for quantitative analysis, this study is the first to analyze spinal cord MR imaging abnormalities in children with congenital Zika virus infection without arthrogryposis. In addition, this study raises the alarming hypothesis that children without clear signs of impairment (eg, microcephaly and arthrogryposis) can have brain and spinal cord imaging abnormalities probably caused by the Zika virus, a possibility that is starting to be seen in clinical practice.

The 8 children with congenital Zika syndrome without arthrogryposis did not have this major clinical manifestation of spinal cord impairment but had mild radiologic spinal cord abnormalities, such as a qualitative decrease in

spinal cord thickness, especially at the thoracic segment, and mildly reduced anterior nerve roots at the conus medullaris. Therefore, we can suppose that there are, currently unidentified in the normal population of the epidemic area, more children with a mild degree of damage not only in the brain but also in the spinal cord. The identified cases could correspond to only the "tip of the iceberg," represented by microcephaly and arthrogryposis, of the congenital Zika syndrome.

CONCLUSIONS

Most of the infants with congenital Zika syndrome had some degree of spinal cord thickness reduction, which is predominant in the thoracic segment in cases without arthrogryposis and in the entire spinal cord in cases with arthrogryposis. In addition, there is thickness reduction of anterior nerve roots of the conus medullaris in both groups, being more severe in infants with arthrogryposis. With regard to brain lesions, periventricular calcifications were more frequent in infants with arthrogryposis. Although without statistical significance, the prominence of the anterior median fissure of the spinal cord was found only in infants with arthrogryposis; brain stem hypoplasia was present in all infants with arthrogryposis; brain stem and cerebellum calcifications were more frequent; and polymicrogyria was absent in this group.

ACKNOWLEDGMENTS

We are especially grateful to the anesthesiology staff, Drs Antonio Monteiro and Cristovam A. de Lira Terceiro; the neuropediatrician, Dr Ana van der Linden; the medical student, Julia Sales Machado; the MR imaging technician, Edineide Cristina Leite Lopes; and the Centro Diagnostico Multimagem for their help.

REFERENCES

1. Dick GW, Kitchen SF, Haddow AJ. **Zika virus. I: isolations and serological specificity.** *Trans R Soc Trop Med Hyg* 1952;46:509–20 CrossRef Medline
2. Dick GW. **Zika virus, II: pathogenicity and physical properties.** *Trans R Soc Trop Med Hyg* 1952;46:521–34 CrossRef Medline
3. Macnamara FN. **Zika virus: a report on three cases of human infection during an epidemic of jaundice in Nigeria.** *Trans R Soc Trop Med Hyg* 1954;48:139–45 CrossRef Medline
4. Duffy MR, Chen TH, Hancock WT, et al. **Zika virus outbreak on Yap Island, Federated States of Micronesia.** *N Engl J Med* 2009;360:2536–43 CrossRef Medline
5. Cauchemez S, Besnard M, Bompard P, et al. **Association between Zika virus and microcephaly in French Polynesia, 2013–15: a retrospective study.** *Lancet* 2016;387:2125–32 CrossRef Medline
6. Campos GS, Bandeira AC, Sardi SI. **Zika virus outbreak, Bahia, Brazil.** *Emerg Infect Dis* 2015;21:1885–86 CrossRef Medline
7. Cardoso CW, Paploski IA, Kikuti M, et al. **Outbreak of exanthematous illness associated with Zika, Chikungunya, and Dengue Viruses, Salvador, Brazil.** *Emerg Infect Dis* 2015;21:2274–76 CrossRef Medline
8. Ministério da Saúde (Brazil). Protocolo de vigilância e resposta à ocorrência de microcefalia e/ou alterações do sistema nervoso central (SNC). March 10, 2016. http://combateaedes.saude.gov.br/images/sala-de-situacao/Microcefalia-Protocolo-de-vigilancia-e-resposta-10mar2016–18h.pdf. Accessed December 19, 2016
9. Brito C. **Zika virus: a new chapter in the history of medicine.** *Acta Med Port* 2015;28:679–80 Medline
10. World Health Organization. Situation Report. Zika virus, microcephaly, Guillain-Barre syndrome. February 2, 2017. http://apps.who.int/iris/bitstream/10665/254507/1/zikasitrep2Feb17-eng.pdf. Accessed February 8, 2017
11. de Fatima Vasco Aragao M, van der Linden V, Brainer-Lima AM, et al. **Clinical features and neuroimaging (CT and MRI) findings in presumed Zika virus related congenital infection and microcephaly: retrospective case series study.** *BMJ* 2016;353:i1901 CrossRef Medline
12. Ventura CV, Maia M, Ventura BV, et al. **Ophthalmological findings in infants with microcephaly and presumable intra-uterus Zika virus infection.** *Arq Bras Oftalmol* 2016;79:1–3 CrossRef Medline
13. Oliveira Melo AS, Malinger G, Ximenes R, et al. **Zika virus intrauterine infection causes fetal brain abnormality and microcephaly: tip of the iceberg?** *Ultrasound Obstet Gynecol* 2016;47:6–7 CrossRef Medline
14. Schuler-Faccini L, Ribeiro EM, Feitosa IM, et al; Brazilian Medical Genetics Society–Zika Embryopathy Task Force. **Possible association between Zika virus infection and microcephaly: Brazil, 2015.** *MMWR Morb Mortal Wkly Rep* 2016;65:59–62 CrossRef Medline
15. Bamshad M, Van Heest AE, Pleasure D. **Arthrogryposis: a review and update.** *J Bone Joint Surg Am* 2009;91(suppl 4):40–46 CrossRef Medline
16. Banker BQ. **Arthrogryposis multiplex congenita: spectrum of pathologic changes.** *Hum Pathol* 1986;17:656–72 CrossRef Medline
17. Fedrizzi E, Botteon G, Inverno M, et al. **Neurogenic arthrogryposis multiplex congenita: clinical and MRI findings.** *Pediatr Neurol* 1993;9:343–48 CrossRef Medline
18. Gordon N. **Arthrogryposis multiplex congenita.** *Brain Dev* 1998;20:507–11 CrossRef Medline
19. Kalampokas E, Kalampokas T, Sofoudis C, et al. **Diagnosing arthrogryposis multiplex congenita: a review.** *ISRN Obstet Gynecol* 2012:264918 CrossRef Medline
20. Mennen U, van Heest A, Ezaki MB, et al. **Arthrogryposis multiplex congenita.** *J Hand Surg Br* 2005;30:468–74 CrossRef Medline
21. Yousem D, Grossman R. **Anatomy and degenerative diseases of the spine.** In: *Neuroradiology: The Requisites.* 3rd ed. Philadelphia: Mosby/Elsevier; 2010:515–42
22. Wilson DA, Prince JR. **John Caffey award. MR imaging determination of the location of the normal conus medullaris throughout childhood.** *AJR Am J Roentgenol* 1989;152:1029–32 CrossRef Medline
23. Melo AS, Aguiar RS, Amorim MM, et al. **Congenital Zika virus infection: beyond neonatal microcephaly.** *JAMA Neurol* 2016;73:1407–16 CrossRef Medline
24. van der Linden V, Filho EL, Lins OG, et al. **Congenital Zika syndrome with arthrogryposis: retrospective case series study.** *BMJ* 2016;354:i3899 CrossRef Medline
25. Hazin AN, Poretti A, Turchi Martelli CM, et al. **Computed tomographic findings in microcephaly associated with Zika virus.** *N Engl J Med* 2016;374:2193–95 CrossRef Medline
26. Mlakar J, Korva M, Tul N, et al. **Zika virus associated with microcephaly.** *N Engl J Med* 2016;374:951–58 CrossRef Medline
27. Tang H, Hammack C, Ogden SC, et al. **Zika virus infects human cortical neural progenitors and attenuates their growth.** *Cell Stem Cell* 2016;18:587–90 CrossRef Medline
28. Barkovich AJ, Gressens P, Evrard P. **Formation, maturation, and disorders of brain neocortex.** *AJNR Am J Neuroradiol* 1992;13:423–46 Medline
29. Vouga M, Baud D. **Imaging of congenital Zika virus infection: the route to identification of prognostic factors.** *Prenat Diagn* 2016;36:799–811 CrossRef Medline

Intraforaminal Location of Thoracolumbar Radicular Arteries Providing an Anterior Radiculomedullary Artery Using Flat Panel Catheter Angiotomography

L. Gregg, D.E. Sorte, and P. Gailloud

ABSTRACT

BACKGROUND AND PURPOSE: Flat panel catheter angiotomography performed during the selective injection of intersegmental arteries offers a multiplanar assessment of the intraforaminal course of the radicular arteries providing an anterior radiculomedullary artery. Injury of anterior radiculomedullary arteries during transforaminal epidural steroid injections can result in spinal cord damage. Evaluations of the intraforaminal location of these arteries have so far been limited to anteroposterior views or the examination of cadaveric material. This study documents the in vivo intraforaminal location of thoracolumbar arteries providing an anterior radiculomedullary artery with flat panel catheter angiotomography.

MATERIALS AND METHODS: Ninety-four flat panel catheter angiotomography acquisitions obtained during the selective injection of intersegmental arteries providing an anterior radiculomedullary artery were reviewed. Measurements obtained from sagittal reconstructions were converted into a scatterplot visualization. Patients' age, sex, and side and level of the injection were recorded.

RESULTS: The location of radicular arteries could be ascertained in 78 of 94 flat panel catheter angiotomography acquisitions (33 women and 45 men, 22–82 years of age). Fifty-three acquisitions (67.9%) were on the left side, and 25 (32.1%), on the right, between T2 and L3. The arteries were found in the anterosuperior quadrant of the neural foramen in 75 cases (96.2%), in the posterosuperior quadrant in 2 cases (2.6%), and in the anteroinferior quadrant in 1 case (1.3%). None were located in the posteroinferior quadrant. No differences in location were observed with age, sex, side of injection, or vertebral level.

CONCLUSIONS: Avoiding needle placement in the superior half of the neural foramen, specifically the anterosuperior quadrant, can reduce the risk of spinal cord injury during transforaminal epidural steroid injection.

ABBREVIATIONS: ARMA = anterior radiculomedullary artery; FPCA = flat panel catheter angiotomography; ISA = intersegmental arteries; NF = neural foramen; TFESI = transforaminal epidural steroid injection

Flat panel catheter angiotomography (FPCA) is a recently developed angiographic technique in which rotational datasets are used to generate high-resolution multiplanar reconstructions. FPCA performed during the injection of the thoracolumbar intersegmental arteries (ISA) allows documenting with precision the intraforaminal course of radicular branches providing an anterior radiculomedullary artery (ARMA). The location of these vessels within the neural foramen (NF) is relevant to needle placement during transforaminal epidural steroid injection (TFESI), a commonly performed image-guided procedure consisting of the injection of corticosteroids at the NF. Inadvertent injection or injury of branches contributing to the supply of the anterior spinal artery during TFESI can result in spinal cord damage[1] and can lead to paralysis and death.[2,3] Although several cases of paralysis after TFESI have now been published,[3,4] such complications are likely under-reported.[1,5]

Targeting the "safe triangle," an area located between the pedicle and the nerve root, has been recommended to avoid nerve injury during needle placement (Fig 1).[6] However, this approach does not take into account the position of branches providing an ARMA. Evaluations of the intraforaminal location of these arteries critical to the spinal cord vascularization have so far been limited to anteroposterior views only[7] or to the examination of ca-

Received September 1, 2016; accepted after revision December 12.

From the Division of Interventional Neuroradiology (L.G., D.E.S., P.G.), and Department of Art as Applied to Medicine (L.G.), The Johns Hopkins University School of Medicine, Baltimore, Maryland.

This work was supported by a Siemens Medical Research Grant (P.G.) paid to the institution.

Paper previously presented, in part, at: Annual Meeting of the American Society of Neuroradiology and the Foundation of the ASNR Symposium, May 21–26, 2016; Washington, DC.

Please address correspondence to Philippe Gailloud, MD, Division of Interventional Neuroradiology, The Johns Hopkins Hospital, 1800 Orleans St, Bloomberg Building, Room 7218, Baltimore, MD 21287; e-mail: phg@jhmi.edu; @JohnsHopkinsINR

Indicates article with supplemental on-line video.

http://dx.doi.org/10.3174/ajnr.A5104

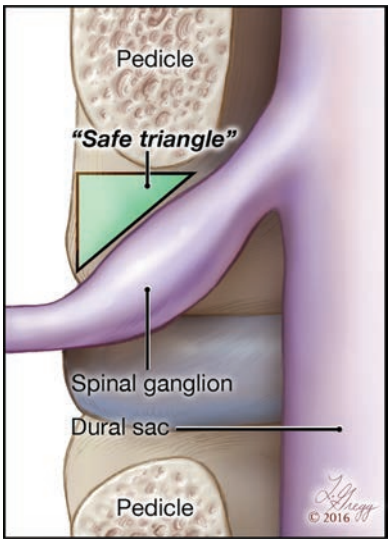

FIG 1. Illustration of the safe triangle for needle placement during the subpedicular TFESI approach. The safe triangle sides are defined in the anteroposterior projection as the inferior edge of the corresponding pedicle, the superior edge of the nerve, and the lateral margin of the neural foramen. Copyright 2016 Lydia Gregg.

daveric material.[8,9] The purpose of this study was to document with precision the intraforaminal course of branches providing a thoracolumbar ARMA by using FPCA.

MATERIALS AND METHODS

FPCA studies performed during routine spinal angiography between November 2009 and September 2015 were collected retrospectively from an institutional review board–approved clinical data base. Additional approval for publication was granted. Ninety-four datasets obtained during the selective injection of the thoracolumbar ISAs providing an ARMA were reviewed. Acquisitions documenting a radicular branch and the ARMA course within the NF were included, while those with pathologies that obscured or distorted the vessel of interest were excluded. The patient's age, sex, and side and level of injection were recorded.

Datasets generated by a 20-second nonsubtracted rotational acquisition (DynaCT, Artis Zee; Siemens, Erlangen, Germany) were reconstructed on a dedicated workstation (0.1^3- to 0.4^3-mm voxel size, depending on the size of the FOV selected for reconstruction) and were studied with MIP rendering. Measurements were obtained by using commercially available software (OsiriX 64-bit Imaging Software; http://www.osirix-viewer.com). In a sagittal view of the injected ISA, the working projection was adjusted medially to follow the radicular artery and/or ARMA until the osseous borders of the NF were in view (On-line Video) (Fig 2). Measurements included the NF height, defined as the longest distance between the superior and inferior osseous NF borders (Fig 2*C*, B to B′), and the NF width, measured perpendicular to and at the midpoint of the height line (Fig 2*C*, C to C′). The NF was then divided into quadrants based on the divisions created by the height and width measurement lines (Fig 2*C*). When osteophytes were present, the NF width was measured from the estimated original NF boundaries.

The intraforaminal location of branches providing an ARMA was evaluated by measuring the distance from the center of the artery to the inferior edge of the corresponding pedicle (Fig 2*C*, D), the posterior edge of the vertebral body (Fig 2*C*, E), the horizontal NF division line (Fig 2*C*, F), and the vertical NF division line (Fig 2*C*, G). These data were used to generate a scatterplot representation. The NF height measurement was used to normalize the measurement data, thus providing a comparable point of reference for ARMAs located in NFs of various sizes.

RESULTS

The intraforaminal location of branches providing an ARMA could be ascertained in 78 of the 94 reviewed FPCA acquisitions (83.0%), including 33 women (42.3%) and 45 men (57.7%) with an average age of 53 years (range, 22–82 years). Precise analysis of the ARMA course was prevented by the presence of a vascular malformation (2 cases), technical artifacts (4 cases), anatomic distortion by a tumor or prior surgery (4 cases), or incomplete documentation of the NF (6 cases).

Of the 78 FPCA acquisitions included in the study, 53 (67.9%) were on the left side and 25 (32.1%) were on the right. Acquisitions included vertebral levels extending from T2 to L3 (Table 1). The branches providing an ARMA were found in the anterosuperior quadrant of the NF in 75 cases (96.2%), in the posterosuperior quadrant in 2 cases (2.6%), and in the anteroinferior quadrant in 1 case (1.3%) (Fig 3). Branches providing an ARMA were not found in the posteroinferior quadrant.

Most arteries providing an ARMA were close to the bone near the subpedicular notch, at the inferior border of the junction of the pedicle and the vertebral body. The center point of the arteries in 51 cases (65.4%) was located ≤2 mm from the osseous borders of the anterosuperior quadrant of the NF.

The scatterplot of the raw data (Fig 3*A*) was comparable with that of the normalized data (Fig 3*B*), both of which documented a close association of branches providing an ARMA with the anterosuperior quadrant of the NF near the junction of the pedicle and the vertebral body.

The mean caliber of arteries providing an ARMA was 1 mm (range, 0.6–1.7 mm). A summary of the NF and artery caliber measurements is shown in Table 2. No differences in artery location were observed with age, sex, side of injection, or vertebral level. Illustrative cases are shown in Figs 4 and 5.

DISCUSSION

Methodologic Considerations

To assess the location of the branches providing an ARMA in a clinically relevant manner, our measurements were performed in a sagittal reconstruction of the FPCA datasets matching the fluoroscopic landmarks used during TFESI (ie, a lateral projection perpendicular to the entrance of the NF).[10] The vessel measured can be considered as either a radicular artery or an ARMA because the exact point of transition from one to the other remains difficult to assess by imaging and nomenclatures show slight variations.[11,12] All the branches investigated for this study continued intradurally as contributors to the anterior spinal arterial axis.

The NF variability in size between patients and vertebral levels was accounted for by adopting the NF height as the normalization

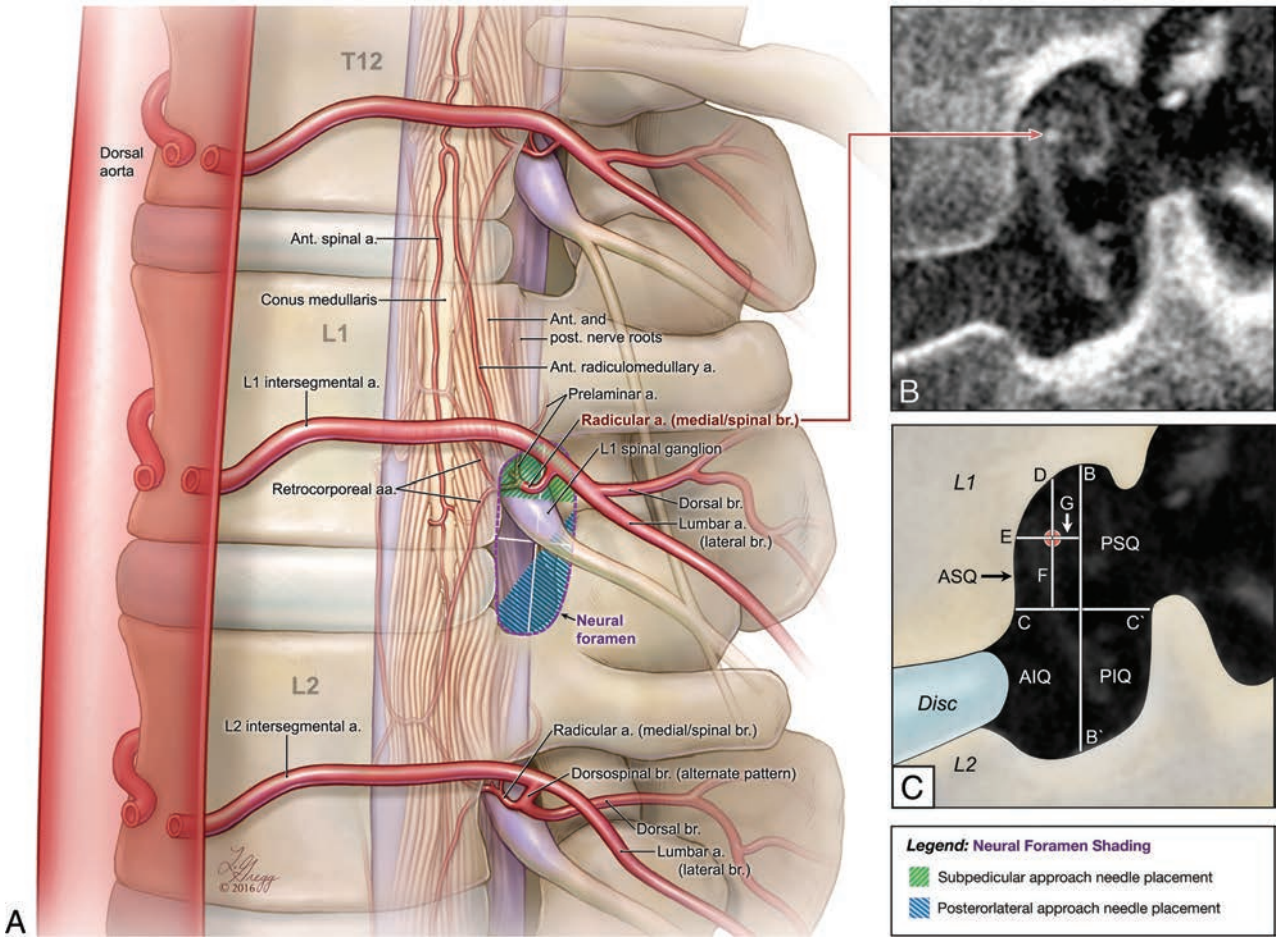

FIG 2. Depiction of the arterial anatomy of the NF showing the measurements used in this study. *A*, Illustration of ISA anatomy including the principal supply to the thoracolumbar spinal cord from an anterior oblique view. The ISA originates from the aorta and divides into medial, dorsal, and lateral branches. A complete spinal branch is shown entering the NF at the left L1 vertebral level and providing a retrocorporeal artery, a prelaminar artery, and a radicular artery; the latter crosses the dura to continue as an ARMA and anastomoses with the anterior spinal artery. The shaded regions and quadrant grids depicted at the L1 NF clarify the working projection and measurement definitions depicted in *B* and *C*. *B*, FPCA, left L1 ISA injection, sagittal reconstruction (thickness = 0.2 mm) demonstrates the working projection used to take measurements. The image documents the location of an ARMA within the NF (*red arrow*) in a 59-year-old women investigated for acute onset paraplegia. Spinal angiography and FPCA revealed severe stenosis of the left proximal L1 ISA, resulting in an episode of spinal cord ischemia. Measurements were performed with the anterior surface to the left side. *C*, Measurements included the NF height (*B* to *B′*), which was defined as the long axis from the posterior edge of the vertebral pedicle to the superior edge of the pedicle below. The NF was divided into quadrants by measuring the width (*C* to *C′*) at the midpoint of the height. The ARMA location was evaluated by measuring the distance from the center of the artery to the superior (D) and anterior (E) walls of the NF and the vertical (F) and horizontal (G) distances to the quadrant divisions. ASQ indicates anterosuperior quadrant; PSQ, posterosuperior quadrant; PIQ, posteroinferior quadrant; AIQ, anteroinferior quadrant. Copyright 2016 Lydia Gregg.

Table 1: Vertebral level and side of included FPCA acquisitions documenting a radicular branch and the ARMA course within the NF

Vertebral Level	L Side (No.)	L Side	R Side (No.)	R Side	L and R Sides, Total (No.)	L and R Sides, Total
T2	1	1.3%	–	–	1	1.3%
T3	–	–	–	–	–	–
T4	–	–	1	1.3%	1	1.3%
T5	1	1.3%	1	1.3%	2	2.6%
T6	–	–	–	–	–	–
T7	4	5.1%	–	–	4	5.1%
T8	5	6.4%	3	3.8%	8	10.3%
T9	10	12.8%	5	6.4%	15	19.2%
T10	2	2.6%	5	6.4%	7	9.0%
T11	6	7.7%	1	1.3%	7	9.0%
T12	7	9.0%	3	3.8%	10	12.8%
L1	14	17.9%	5	6.4%	19	24.4%
L2	2	2.6%	1	1.3%	3	3.8%
L3	1	1.3%	–	–	1	1.3%
Total	53	67.9%	25	32.1%	78	100.0%

Note:— L indicates left; R, right.

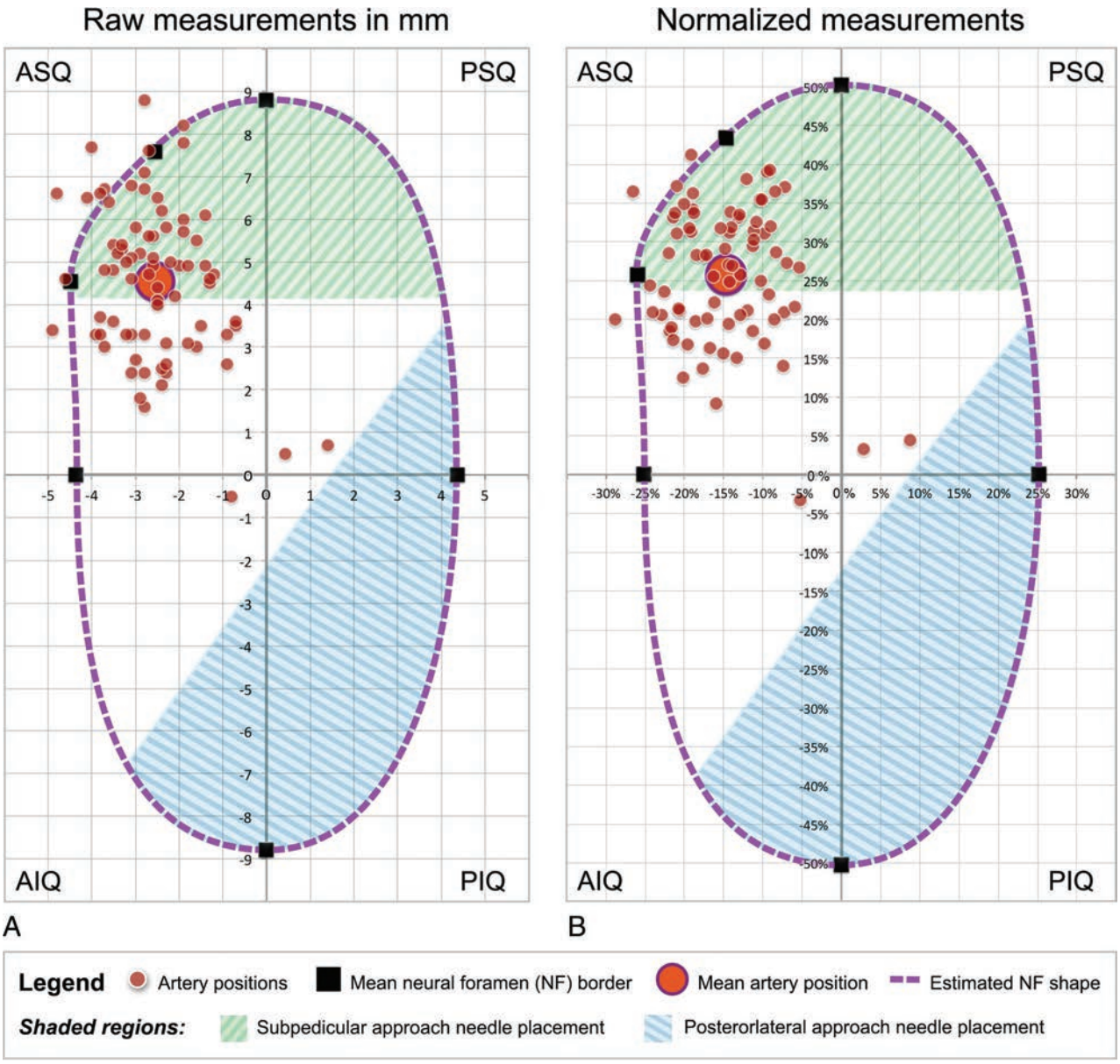

FIG 3. Scatterplots visualizing the location within the NF of arteries that provide a thoracolumbar ARMA. *A*, Raw measurements in millimeters. Zero values for the x- and y-axes represent the approximate center of the neural foramina in 78 patients. *B*, Normalized measurements, shown as a percentage of the height of the NF (NF height = 100%) to compare the relative location of the artery within the foramina of different sizes (Measurements / NF Height × 100 = Percentage NF Height) in 78 patients.

Table 2: NF and radicular branches providing ARMA lumen diameter measurements[a]

Vertebral Level	No.	Measurement	Mean	Range	SD
Thoracic ARMAs	55	NF height	16.2	9.7–21.2	2.4
		NF width	8.0	5.4–12.7	1.8
		ARMA diameter	1.0	0.6–1.4	0.2
Lumbar ARMAs	23	NF height	20.6	14.8–25	2.3
		NF width	10.3	8.1–13.6	1.4
		ARMA diameter	1.1	0.7–1.7	0.3
All ARMAs	78	NF height	17.5	9.7–25	3.1
		NF width	8.7	5.4–13.6	2.0
		ARMA diameter	1.0	0.6–1.7	0.2

[a] Data are in millimeters.

standard, considering, in particular, the relative paucity of osteophytes that form on the superior and inferior borders of the vertebral pedicles.[13] No major differences in artery locations were noted between the raw measurement data and the normalized data (Fig 3).

Intraforaminal Location of Branches Providing an ARMA

The ISA consists of an aortic stem that divides into medial (or spinal), dorsal, and lateral branches; depending on the level considered, the lateral branch takes the name of posterior intercostal, subcostal, or lumbar artery (Fig 2*A*). The medial branch, when complete, enters the neural foramen and provides the retrocorporeal and prelaminar arteries, which contribute to the vertebral vascularization and the radicular artery.[14] A radicular artery that supplies the spinal cord crosses the dura to continue as an anterior or posterior radiculomedullary artery or both, which, respectively, contribute to the anterior or posterior spinal arterial chains. Supply to the anterior thoracolumbar spinal cord is typi-

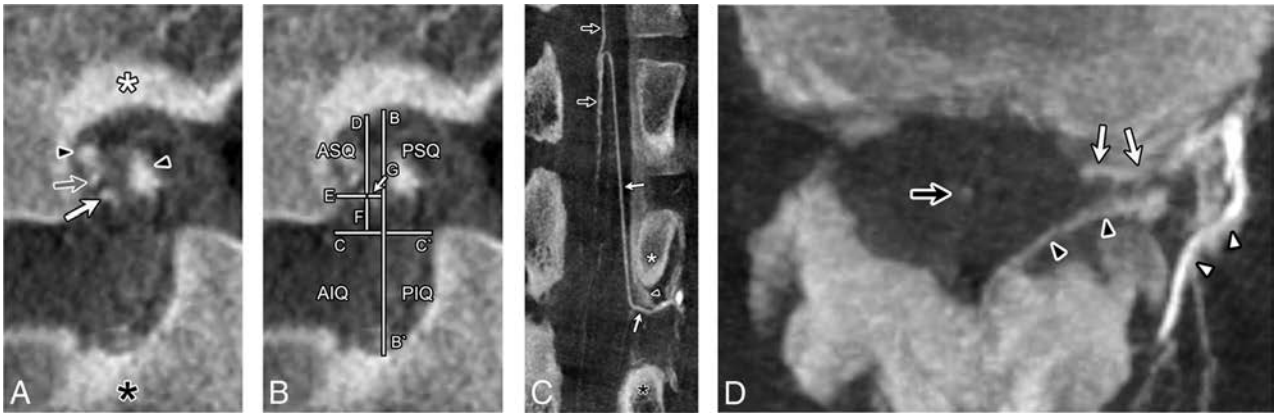

FIG 4. FPCA, left L2 ISA injection. This case illustrates the intraforaminal course of an ARMA in a 42-year-old woman investigated for progressive myelopathy. Spinal angiography and FPCA findings were unremarkable. *A*, Sagittal MIP reconstruction (thickness = 0.2 mm) documents the location of an ARMA (*white arrow*) within the NF. The retrocorporeal artery (*gray arrow*), L2 (*white asterisk*) and L3 pedicles (*black asterisk*), and portions of the internal vertebral venous plexus (*black arrowheads*) are also visible. *B*, The same sagittal MIP reconstruction with graphics indicates recorded measurements, including the NF height (B to B′), NF width (C to C′), distance of the ARMA to the inferior border of the L2 pedicle (D), the posterior wall of the L2 vertebral body (E), and the vertical (F) and horizontal (G) distances to the quadrant divisions. *C*, Coronal-oblique MIP reconstruction (thickness = 1.7 mm) documents the same ARMA (*white arrows*) within the NF and its anastomosis with the anterior spinal artery (*black arrows*). The L2 (*white asterisk*) and L3 pedicles (*black asterisk*) and a portion of the internal vertebral venous plexus (*black arrowhead*) are also visible. *D*, Axial MIP reconstruction (thickness = 9.3 mm) documents the same L2 ARMA (*white arrows*), the anterior spinal artery (*black arrow*), portions of the internal vertebral venous plexus (*black arrowheads*), and the dorsal branch of the L2 ISA (*white arrowheads*).

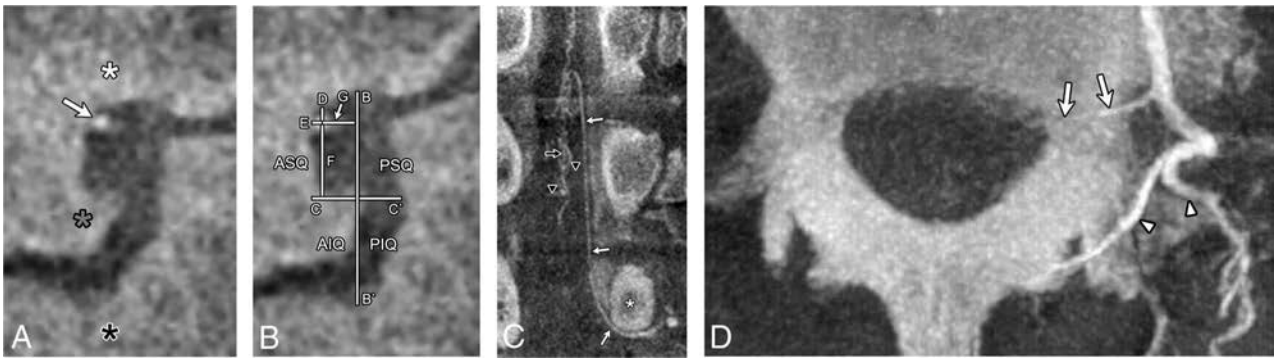

FIG 5. FPCA, left L1 ISA injection, in a 77-year-old man with severe spinal canal stenosis investigated for myelopathy. Spinal angiography and FPCA findings were normal. This case illustrates how NF width estimates were derived from abnormal foramina. *A*, Sagittal MIP reconstruction (thickness = 0.2 mm) documents the location of a branch providing an ARMA (*white arrow*) within the NF. An osteophyte (*gray asterisk*) on the L1 vertebral body distorts the width of the NF between the L1 (*white asterisk*) and L2 pedicles (*black asterisk*), while the NF height appears unaffected. *B*, The same sagittal MIP reconstruction with graphics indicating recorded measurements includes the following: the NF height (B to B′), estimated NF width (C to C′), distance of the artery to the inferior border of the L1 pedicle (D), the estimated posterior wall of the L1 vertebral body (E), and the vertical (F) and horizontal (G) distances to the quadrant divisions. *C*, Coronal-oblique MIP reconstruction (thickness = 1.8 mm) documents the same branch providing an ARMA (*white arrows*) within the NF and its anastomoses with the anterior spinal artery (*black arrow*). The L1 (*white asterisk*) pedicle and a dilated anterior median spinal vein (*black arrowheads*) are also visible. *D*, Axial MIP reconstruction (thickness = 9.0 mm) documents the same branch providing an ARMA (*white arrows*) and dorsal branches of the L1 ISA (*white arrowheads*).

cally limited to a dominant thoracolumbar ARMA, the artery of Adamkiewicz, and a smaller upper thoracic ARMA, the artery of von Haller.[15] Reports of paralysis resulting from vascular injuries during TFESI spurred previous studies on the location of these vessels within the NF. The investigation of Murthy et al,[7] based on anteroposterior views only, concluded that the radicular segment most often crosses the superior aspect of the NF. Two cadaveric studies reported that branches providing an ARMA are generally located anterosuperior to the dorsal nerve root within the NF.[8,9] Our multiplanar analysis of high-resolution angiographic datasets acquired during routine clinical practice confirms and extends these observations by plotting the precise distribution of branches providing an ARMA within the NF (Fig 3).

The caliber of radicular branches that provide an ARMA measured in our study (average, 1.0 mm; range, 0.6–1.7 mm) was comparable with that in prior investigations, which have reported diameters ranging from 1.2 to 2.5 mm (average, 1.9 mm)[8] and from 0.8 to 1.9 mm (average, 1.2 mm)[9] (measurements obtained in anatomic specimens, including the vessel wall thickness).

Clinical Implications for Arterial Injury

Despite being associated with severe complications related to the intraforaminal location of radicular branches that provide an ARMA,[3] TFESI has seen its rate of use steadily increase due to its purported superiority over alternative techniques, such as the caudal or interlaminar approaches.[1] Spinal cord ischemia and stroke occurring during TFESI may result from arterial embolization with air or particulate steroids[1] or from direct vessel

injuries such as spasm, laceration, and dissection.[16] The close association between branches providing an ARMA and the subpedicular notch documented in our study emphasizes the danger in making contact between the needle and the pedicle, as is typical with the subpedicular approach.[1] Multiple attempts at repositioning the needle tip, as reported in several cases of paralysis,[16,17] likely increase the risk of vessel damage.

The Role of Particulate Steroids

All 19 observations of paralysis reported so far have involved the injection of particulate steroids during TFESI.[3,4] With particle sizes ranging from 1 to 100 μm, an intra-arterial injection could result in the embolization of spinal arterioles.[18] Direct arterial injection of particulate steroids has caused permanent neurologic damage in animal models, while nonparticulate steroids such as dexamethasone[19,20] and prednisolone[20] produced no injuries. Although it has been suggested that particulate steroids are more effective than nonparticulate steroids, no significant difference in efficacy after lumbar TFESI has been reported.[21,22] It is possible that the small number of reported complications and the widespread use of particulate steroids[21] falsely suggest a causative relationship between particulate injectate and the risk of paralysis. Nonetheless, dexamethasone became the recommended injectate for TFESI in 2010.[21]

Posterolateral Approach

Positioning the needle in the region of the NF known as the Kambin triangle[23] has been recommended as a safer alternative to the subpedicular approach.[1] In this posterior triangle or posterolateral approach, the targeted area is defined by the posterior margin of the exiting nerve root, the endplate of the caudal vertebral level, and the articular facet of the cranial vertebral level.[23] This approach was proposed for arthroscopic discectomy,[23] which requires the transforaminal placement of large-caliber instrumentation.[1] TFESI via the posterolateral approach has shown pain reduction scores similar to the those with the subpedicular approach,[24] while decreasing both the amount of periprocedural pain and the risk of nerve damage.[25] Considering that the posterolateral approach targets the posteroinferior quadrant of the NF, where branches providing an ARMA are least likely encountered, and that it has not yet been associated with reports of paralysis suggests that it should be the preferred technique for TFESI.[1]

Misconceptions Regarding Spinal Vascular Anatomy and the "Safe Triangle"

Several misconceptions have led to a slow rejection of the subpedicular approach,[1] notably the incorrect notions that the "safe triangle" helps prevent vascular injuries in addition to nerve damage and that arterial opacification is reliably detected during contrast injections performed before steroid instillation.[1] Intra-arterial needle tip placement during TFESI can, in fact, not be excluded with certainty by using intermittent fluoroscopy,[26,27] aspiration,[27-30] contrast injection,[1] or even digital subtraction angiography.[1,31] In addition, none of these imaging methods would help avoid other injury mechanisms such as arterial transection or dissection. A limited understanding of spinal vascular anatomy, which is often overlooked or misrepresented,[10] also plays a role.

Simon et al[32] reported the presence of arteries both in the subpedicular region and the posterolateral triangle on contrast-enhanced CT scans, but the vessels observed with that technique cannot be clearly identified as branches providing an ARMA or osteomeningeal branches or even venous structures such as radiculomedullary veins or the emissary veins linking the internal and external venous plexuses at each vertebral level. Figures 4 and 5 illustrate the advantage offered by a high-resolution imaging technique to reliably distinguish such minute vascular elements on the basis of their morphology (ie, termination of the radiculomedullary veins into the epidural plexus) or opacification pattern. A similar lack of specificity is found in a report of apparent retrograde flow into a T6 spinal artery noted during a posterolateral approach,[33] which prompted Simon et al[32] to suggest that the injection of any artery near the NF carries potential clinical consequences. However, the images documenting that observation only show the opacification of the external epidural venous plexus with retrograde filling of a basivertebral and intraosseous venous system. An analysis of reports of paralysis following TFESI in which the needle position was mentioned shows that spinal cord damage only occurred in association with the subpedicular approach,[3] a fact weakening the role of retrograde injections and the notion that any artery in the vicinity of the NF has clinical consequences comparable with those supplying ARMAs when performing TFESI.

Study Limitations

The goal of our study was to describe the typical location of radicular branches providing an ARMA in the NF based on FPCA datasets acquired in patients principally investigated for myelopathy. This patient group may have a lower incidence of degenerative osteodiscal pathology than the population typically treated with TFESI, leading to a more stable distribution of contributors of ARMAs within the NF.

CONCLUSIONS

Thoracolumbar radicular branches providing an ARMA were located in the anterosuperior quadrant of the NF in 75 of 78 patients (96.2%), suggesting that needle placement in that area should be avoided during TFESI. Unlike the subpedicular approach, the posterolateral approach allows placing the needle tip away from the documented position of ARMA contributors within the NF, reducing the risk of intra-arterial injection or injury to the spinal vascularization.

Disclosures: Lydia Gregg—*UNRELATED*: *Board Membership*: Association of Medical Illustrators Board of Governors. Danielle Eckart Sorte—*UNRELATED*: *Travel/Accommodations/Meeting Expenses Unrelated to Activities Listed*: Stryker Neurovascular, Penumbra, *Comments*: Fellows courses, user courses. Philippe Gailloud—*RELATED*: *Grant*: Siemens, *Comments*: grants for the development of low-dose angiography protocols*; *UNRELATED*: *Consultancy*: Codman Neurovascular; *Stock/Stock Options*: ArtVentive Medical.* *Money paid to the institution.

REFERENCES

1. Glaser SE, Shah RV. **Root cause analysis of paraplegia following transforaminal epidural steroid injections: the 'unsafe' triangle.** *Pain Physician* 2010;13:237–44 Medline

2. Gharibo C, Koo C, Chung J, et al. **Epidural steroid injections: an update on mechanisms of injury and safety.** *Techniques in Regional Anesthesia and Pain Management* 2009;13:266–71 CrossRef
3. Atluri S, Glaser SE, Shah R, et al. **Needle position analysis in cases of paralysis from transforaminal epidurals: consider alternative approaches to traditional technique.** *Pain Physician* 2013;16:321–34 Medline
4. AbdeleRahman KT, Rakocevic G. **Paraplegia following lumbosacral steroid epidural injections.** *J Clin Anesth* 2014;26:497–99 CrossRef Medline
5. Bogduk N, Dreyfuss P, Baker R, et al. **Complications of spinal diagnostic and treatment procedures.** *Pain Med* 2008;9(suppl 1):S11–34 CrossRef
6. Bogduk N, Aprill C, Derby R. **Selective nerve root blocks.** In: Wilson DJ, ed. *Practical Interventional Radiology of the Musculoskeletal System*. London: Edward Arnold; 1995:121–32
7. Murthy NS, Maus TP, Behrns CL. **Intraforaminal location of the great anterior radiculomedullary artery (artery of Adamkiewicz): a retrospective review.** *Pain Med* 2010;11:1756–64 CrossRef Medline
8. Alleyne CH Jr, Cawley CM, Shengelaia GG, et al. **Microsurgical anatomy of the artery of Adamkiewicz and its segmental artery.** *J Neurosurg* 1998;89:791–95 CrossRef Medline
9. Kroszczynski AC, Kohan K, Kurowski M, et al. **Intraforaminal location of thoracolumbar anterior medullary arteries.** *Pain Med* 2013;14:808–12 CrossRef Medline
10. La Barge DV, Shah LM. *Specialty Imaging: Essentials of Image-Guided Procedures—Pain Management.* Salt Lake City: Amirsys; 2011
11. Djindjian R. *Angiography of the Spinal Cord.* Baltimore: University Park Press; 1970
12. Federative Committee on Anatomical Terminology. *Terminologia Anatomica: International Anatomical Terminology*. Stuttgart: Thieme; 1998
13. Rauschning W, Eysel P, Hopf C, et al. **Pathoanatomy of lumbar disc degeneration and stenosis.** *Acta Orthop Scand Suppl* 1993;64:3–12
14. Hovelacque A. *Le thorax, anatomie médico-chirurgicale.* Paris: Maloine; 1937
15. Gailloud P. **The artery of von Haller: a constant anterior radiculomedullary artery at the upper thoracic level.** *Neurosurgery* 2013;73:1034–43 CrossRef Medline
16. Glaser SE, Falco F. **Paraplegia following a thoracolumbar transforaminal epidural steroid injection.** *Pain Physician* 2005;8:309–14 Medline
17. Lyders E, Morris P. **A case of spinal cord infarction following lumbar transforaminal epidural steroid injection: MR imaging and angiographic findings.** *AJNR Am J Neuroradiol* 2009;30:1691–93 CrossRef Medline
18. Thefenne L, Dubecq C, Zing E, et al. **A rare case of paraplegia complicating a lumbar epidural infiltration.** *Ann Phys Rehabil Med* 2010;53:575–83 CrossRef Medline
19. Dawley JD, Moeller-Bertram T, Wallace MS, et al. **Intra-arterial injection in the rat brain: evaluation of steroids used for transforaminal epidurals.** *Spine* 2009;34:1638–43 CrossRef Medline
20. Okubadejo GO, Talcott MR, Schmidt RE, et al. **Perils of intravascular methylprednisolone injection into the vertebral artery: an animal study.** *J Bone Joint Surg Am* 2008;90:1932–38 CrossRef Medline
21. El-Yahchouchi C, Geske JR, Carter RE, et al. **The noninferiority of the nonparticulate steroid dexamethasone vs the particulate steroids betamethasone and triamcinolone in lumbar transforaminal epidural steroid injections.** *Pain Med* 2013;14:1650–57 CrossRef Medline
22. Kennedy DJ, Plastaras C, Casey E, et al. **Comparative effectiveness of lumbar transforaminal epidural steroid injections with particulate versus nonparticulate corticosteroids for lumbar radicular pain due to intervertebral disc herniation: a prospective, randomized, double-blind trial.** *Pain Med* 2014;15:548–55 CrossRef Medline
23. Kambin P, O'Brien E, Zhou L, et al. **Arthroscopic microdiscectomy and selective fragmentectomy.** *Clin Orthop Rel Res* 1998;347:150–67 Medline
24. Park KD, Lee J, Jee H, et al. **Kambin triangle versus the supraneural approach for the treatment of lumbar radicular pain.** *Am J Phys Med Rehabil* 2012;91:1039–50 CrossRef Medline
25. Lee IS, Kim SH, Lee JW, et al. **Comparison of the temporary diagnostic relief of transforaminal epidural steroid injection approaches: conventional versus posterolateral technique.** *AJNR Am J Neuroradiol* 2007;28:204–08 Medline
26. Smuck M, Fuller BJ, Yoder B, et al. **Incidence of simultaneous epidural and vascular injection during lumbosacral transforaminal epidural injections.** *Spine J* 2007;7:79–82 CrossRef Medline
27. Furman MB, O'Brien EM, Zgleszewski TM. **Incidence of intravascular penetration in transforaminal lumbosacral epidural steroid injections.** *Spine* 2000;25:2628–32 CrossRef Medline
28. Sullivan WJ, Willick SE, Chira-Adisai W, et al. **Incidence of intravascular uptake in lumbar spinal injection procedures.** *Spine* 2000;25:481–86 CrossRef Medline
29. Ho K. **Vascular uptake of contrast despite negative aspiration in interlaminar cervical epidural injection.** *Pain Physician* 2006;9:267–68 Medline
30. Manchikanti L, Cash KA, Pampati V, et al. **Evaluation of lumbar transforaminal epidural injections with needle placement and contrast flow patterns: a prospective, descriptive report.** *Pain Physician* 2004;7:217–23 Medline
31. Chang CG, Candido KD, Knezevic NN. **Digital subtraction angiography does not reliably prevent paraplegia associated with lumbar transforaminal epidural steroid injection.** *Pain Physician* 2012;15:515–23 Medline
32. Simon JI, McAuliffe M, Smoger D. **Location of radicular spinal arteries in the lumbar spine from analysis of CT angiograms of the abdomen and pelvis.** *Pain Med* 2016;17:46–51 CrossRef Medline
33. Yin W, Bogduk N. **Retrograde filling of a thoracic spinal artery during transforaminal injection.** *Pain Med* 2009;10:689–92 CrossRef Medline

Quantitative Measurement of CSF in Patients with Spontaneous Intracranial Hypotension

H.-C. Chen, P.-L. Chen, Y.-H. Tsai, C.-H. Chen, C.C.-C. Chen, and J.-W. Chai

ABSTRACT

BACKGROUND AND PURPOSE: CSF hypovolemia is a core feature of spontaneous intracranial hypotension. Spontaneous intracranial hypotension is characterized by orthostatic headache and radiologic manifestations, including CSF along the neural sleeves, diffuse pachymeningeal enhancement, and/or venous engorgement. However, these characteristics are only qualitative. Quantifying intraspinal CSF volumes could improve spontaneous intracranial hypotension diagnosis and evaluation of hypovolemic statuses in patients with spontaneous intracranial hypotension. The purpose of this study was to compare intraspinal CSF volumes across spontaneous intracranial hypotension stages and to test the clinical applicability of these measures.

MATERIALS AND METHODS: A cohort of 23 patients with spontaneous intracranial hypotension and 32 healthy controls was subjected to brain MR imaging and MR myelography with 1.5T imaging. An automatic threshold-based segmentation method was used to calculate intraspinal CSF volumes at initial hospitalization (spontaneous intracranial hypotension-initial), partial improvement (spontaneous intracranial hypotension-intermediate), and complete recovery (spontaneous intracranial hypotension-recovery) stages.

RESULTS: The mean intraspinal CSF volumes observed were the following: 95.31 mL for healthy controls, 72.31 mL for spontaneous intracranial hypotension-initial, 81.15 mL for spontaneous intracranial hypotension-intermediate, and 93.74 mL for spontaneous intracranial hypotension-recovery. Increased intraspinal CSF volumes were related to disease recovery ($P < .001$). The intraspinal CSF volumes of patients before complete recovery were significantly lower than those of healthy controls. With the estimated intradural CSF volumes as a reference, the intraspinal CSF volume percentage was lower in patients with spontaneous intracranial hypotension with venous engorgement than in those without it ($P = .058$).

CONCLUSIONS: With a threshold-based segmentation method, we found that spinal CSF hypovolemia is fundamentally related to spontaneous intracranial hypotension. Intraspinal CSF volumes could be a sensitive parameter for the evaluation of treatment response and follow-up monitoring in patients with spontaneous intracranial hypotension.

ABBREVIATIONS: BH = body height; BMI = body mass index; BW = body weight; 3D-SPACE = 3D sampling perfection with application-optimized contrasts by using different flip angle evolution; ECSF = estimated intradural CSF volume; DPE = diffuse pachymeningeal enhancement; HC = healthy control; MRM = MR myelography; SIH = spontaneous intracranial hypotension

Spontaneous intracranial hypotension (SIH) has been diagnosed increasingly as an important cause of headaches. Orthostatic headache is the characteristic symptom of SIH caused by CSF leakage in the spine. Despite the term "SIH," CSF hypovolemia may be the core of the condition.[1] About 18% of patients with symptoms typical of SIH have normal CSF opening pressure.[2,3] The diagnosis of SIH depends on various imaging characteristics and clinical symptoms. The commonly reported findings indicating CSF leakage are epidural fluid accumulation with a dilated epidural venous plexus, a triangular-shaped expansion of the neural sleeve, and an irregular linear signal lateral to the neural sleeve on spinal MR imaging or MR myelography (MRM).[4,5] Conventional brain MR imaging has demonstrated diffuse pachymeningeal enhancement (DPE), venous engorgement, and pituitary hyperemia in patients with SIH.[4] However, DPE and other brain MR imaging abnormalities are not observed in all patients with SIH, especially in early-stage SIH.[6]

As the amount of CSF decreases, the buoyant force from in-

Received September 23, 2016; accepted after revision December 29.

From the Departments of Radiology (H.-C.C., C.-H.C., C.C.-C.C., J.-W.C.) and Neurology (P.-L.C.), Taichung Veterans General Hospital, Taichung, Taiwan; Department of Medicine (H.-C.C.), National Yang-Ming University, Taipei, Taiwan; and College of Medicine (Y.-H.T., J.-W.C.), China Medical University, Taichung, Taiwan.

Please address correspondence to Jyh-Wen Chai, MD PhD, Department of Radiology, Taichung Veterans General Hospital, Taichung 407, Taiwan, 1650 Taiwan Blvd, Section 4, Taichung, Taiwan 407; e-mail: hubt@vghtc.gov.tw

Indicates article with supplemental on-line table.

http://dx.doi.org/10.3174/ajnr.A5134

tracranial CSF is reduced and the brain descends while patients are standing. This results in stretching of pain-sensitive structures on the brain surface and causes orthostatic headaches. However, CSF hypovolemia has only been linked indirectly as a causative factor of SIH in the literature.[1] Researchers have used imaging signs to determine the severity of CSF hypovolemia, such as the number of vertebral bodies over which leaked CSF had spread in spine MR imaging and DPE in brain MR imaging.[1] Therefore, in addition to morphologic alterations in the brain and spine, we hypothesized that quantifying intraspinal CSF volumes would be crucial to evaluating the hypovolemic status of patients with SIH. This important issue of direct monitoring of CSF volume depletion has not been discussed in the SIH literature, to our knowledge.

The aim of this study was to apply an automatic segmentation method to measure the entire CSF volume in the spine and detect CSF hypovolemia in patients with SIH. Furthermore, we compared intraspinal CSF volumes across SIH stages and tested the clinical applicability of these measures.

MATERIALS AND METHODS

Subjects

Between January 2012 and February 2016, 23 patients diagnosed with SIH (according to the criteria of Schievink et al[7] or the "International Classification of Headache Disorders," 3rd ed[8]) and treated in the neurology department at our hospital (Taichung Veterans General Hospital, Taichung, Taiwan) were enrolled in our study. During their hospital stays, patients received conservative treatment and a targeted epidural blood patch. Whole-spine MRM and conventional brain MR imaging were performed on patients simultaneously at 3 different time points. All patients underwent MR imaging on presentation/enrollment that was defined as SIH-initial. Some patients received a second MR imaging for an additional epidural blood patch when their clinical symptoms improved but did not resolve completely. These measurements are the SIH-intermediate. The mean time of MR imaging for SIH-intermediate measurement was 8.41 ± 4.34 days. If complete recovery was achieved following treatment, patients received another MR imaging, the SIH-recovery measurement. Complete recovery was defined as patients having no more headaches or other associated clinical orthostatic symptoms and no CSF leakage or other abnormalities detected in MRM or MR imaging. The mean time of MR imaging for SIH-recovery was 104.67 ± 94.00 days.

Thirty-two healthy volunteers with no known neurologic disorders, spine malformations, or previous spine operations were recruited as healthy controls (HCs). Whole-spine MRM was performed for each subject, and the only pathologic finding acceptable for inclusion was minor degenerative changes of the spine. Before enrollment, written informed consent was obtained from all subjects. This study was approved by the institutional review board of Taichung Veterans General Hospital.

MR Imaging Acquisition

Subjects underwent MRM and brain MR imaging on a 1.5T MR imaging scanner (Magnetom Aera; Siemens, Erlangen, Germany). Whole-spine MRM was performed with a 3D sampling perfection with application-optimized contrasts by using different flip angle evolution (3D-SPACE) sequence (Siemens). The MR imaging parameters were as follows: TR = 3000 ms, TE = 560 ms, isotropic voxel size = 0.9 mm^3, matrix size = 320 × 320 pixels, and FOV = 200 mm. Fat suppression and a generalized autocalibrating partially parallel acquisition imaging reconstruction with an acceleration factor of 2 were used. Images were acquired volumetrically in the coronal plane of the cervical-to-thoracic and thoracic-to-lumbar regions of the spine, parallel to the spinal curve with some overlapping. The acquisition time was 7 minutes 58 seconds for each segment. Conventional brain MR imaging included axial spin-echo T1-weighted images (TR/TE, 500/10 ms) (2 minutes 12 seconds); axial fast-spin-echo T2-weighted images (TR/TE, 3200/115 ms) (2 minutes 39 seconds); and gadolinium-enhanced spin-echo T1WI in the axial (2 minutes 25 seconds), sagittal (2 minutes 10 seconds), and coronal planes (1 minute 56 seconds). The contrast-enhanced study was performed by using 1.0 mol/L of gadolinium chelate (gadobutrol, Gadovist 1.0; Bayer Schering Pharma, Berlin, Germany) with 0.1 mmol per kilogram of body weight.

Intraspinal CSF Volume Measurement and Data Segmentation

Before segmentation, a preprocessing of bias field correction was performed to reduce intensity inhomogeneity in 2 sets of 3D-SPACE whole-spine MRM studies. The threshold-based algorithm of relative entropy has been proposed for use in clinical applications to enable reproducible and facile image segmentation.[9-12] With the advantages of selecting an optimal threshold value with local neighborhood information, the method could extract hyperintense CSF voxels from other hypointense background tissue automatically and robustly in 3D-SPACE whole-spine MRM. After processing, we calculated CSF volumes by identifying all CSF-specific voxels from the tip of the odontoid process to the end of the dural sac. The volumes obtained were defined as intraspinal CSF volumes, including intra- and extradural CSF in the spinal canal at SIH-initial and SIH-intermediate measurements. For SIH-recovery measurements and HCs, intraspinal CSF volumes would be equal to intradural CSF because no CSF leakage occurred. Intraspinal CSF volumes were evaluated by using absolute data. We also estimated each subject's intradural CSF volumes by correlated parameters. The intraspinal CSF volume percentage was defined as the following: Intraspinal CSF Volumes of SIH-Initial / Estimated Intradural CSF Volumes.

Brain Imaging Measurements

Some qualitative indications in brain images were evaluated, including the following: pituitary volumes (in cubic centimeters) defined as the half-value of the product of the gland height, length, and width; venous engorgement, which appears as a convex upper surface of the sinus confluence on a sagittal view of postcontrast T1WI; and any DPE, defined as continuously enhanced dural matter.

Statistical Analyses

All data were analyzed in SPSS software (Version 18; IBM, Armonk, New York). Demographic data, intraspinal CSF volumes,

Table 1: Demographic data

Parameter	Patients with SIH	HCs	*P* Value
Age, y (mean)[a]	38.83 ± 11.83	35.56 ± 10.02	.393
Range	23–58	20–59	
BMI, kg/m^2 (mean)[a]	24.97 ± 5.80	22.07 ± 4.24	.078
BH, m (mean)[a]	1.67 ± 0.098	1.67 ± 0.078	.942
BW, kg (mean)[a]	72.22 ± 20.72	61.48 ± 12.79	.077
Sex[b]			.598
Male (No.)	8	10	
Female (No.)	15	22	

[a] Mann-Whitney *U* test.
[b] Two-sample *t* test.

Table 2: Spinal MR imaging parameters and brain MRI findings from HCs and patients with SIH at initial, intermediate, and recovery stages

		Intraspinal CSF Volumes (mL)	Pituitary Volumes (cm^3)
HCs (n = 32)		95.31 ± 15.48	
SIH	Ini (n = 23)	72.31 ± 19.35	0.60 ± 0.20
	Int (n = 18)	81.15 ± 25.41	0.47 ± 0.15
	Rec (n = 18)	93.74 ± 20.33	0.36 ± 0.14
P value[a]	HCs vs SIH_{Ini}	<.001[b]	
	HCs vs SIH_{Int}	<.05[b]	
	HCs vs SIH_{Rec}	.731	
P value[c]	SIH_{Ini} vs SIH_{Int}	<.001[b]	<.001[b]
	SIH_{Ini} vs SIH_{Rec}	<.001[b]	<.001[b]
	SIH_{Int} vs SIH_{Rec}	<.001[b]	.155

Note:—Ini indicates initial; Int, intermediate, Rec, recovery.
[a] Mann-Whitney *U* test.
[b] Significant.
[c] Paired *t* test.

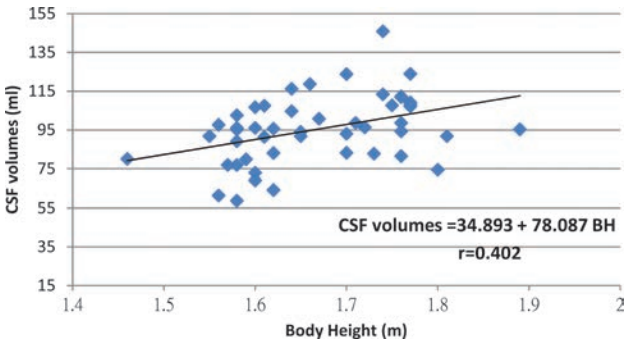

FIG 1. Linear regression equation and figure of intraspinal CSF volumes with BH.

and brain MR imaging findings were compared between HCs and the SIH-initial, SIH-intermediate, and SIH-recovery measurements of patients. We used Kolmogorov-Smirnov tests to verify normal distribution of continuous variables. The age, body mass index (BMI), body height (BH), body weight (BW), and intraspinal CSF volume data for subjects with SIH and HCs were not normally distributed and were therefore analyzed with nonparametric Mann-Whitney tests. The sexes between patients with SIH and HCs were analyzed by using a 2-sample *t* test. The difference among SIH-initial, SIH-intermediate, and SIH-recovery measurements was analyzed with the paired *t* test. The relationships between intraspinal CSF volumes of the HCs and SIH-recovery measurements with age, BMI, BH, BW, and sex were subjected to the Spearman rank-based correlation coefficient. For estimated intradural CSF volumes (ECSF), we used linear regression to fit parameters that correlated with the intraspinal CSF volumes in SIH-recovery measurements of patients and HCs. All tests were 2-tailed with statistical significance at $P < .05$.

RESULTS

Patient demographics and baseline characteristics are summarized in Table 1. There were no statistical differences in age, sex, BMI, BH, or BW between the patients with SIH and HCs. Most of our patients had a significant amount CSF leakage at the spinal nerve roots with epidural fluid accumulation. The extent of CSF leakage for each patient is summarized in the On-line Table. All patients received at least 1 targeted epidural blood patch without any complications. Five patients did not have follow-up MR imaging at symptoms partially improved. Five patients were found to not have achieved complete recovery. Comparisons of spinal and brain MR imaging data between HCs and patients with SIH are reported in Table 2.

Intraspinal CSF Volumes

The mean intraspinal CSF volumes obtained for the SIH-initial (72.31 mL) and SIH-intermediate (81.15 mL) stages differed significantly from those of the HCs (95.31 mL; $P < .001$ and $P < .05$, respectively). However, the mean intraspinal CSF volumes obtained for the SIH-recovery stage (93.74 mL) were similar to those of the HCs ($P = .731$). Intraspinal CSF volumes increased stepwise ($P < .001$) in patients with SIH from SIH-initial to SIH-intermediate to SIH-recovery.

Estimated Intradural CSF Volumes

Intraspinal CSF volumes of HCs and SIH-recovery measurements correlated moderately well and significantly with BH (correlation coefficient = 0.444, $P = .002$), but not with BMI (correlation coefficient = −0.033, $P = .822$), BW (correlation coefficient = 0.073, $P = .622$), age (correlation coefficient = −0.215, $P = .134$), or sex (correlation coefficient = −0.233, $P = .164$). Because intradural CSF volumes varied across individuals, we estimated each subject's intradural CSF volumes by using a linear regression equation according to BH to see whether it could provide useful clinical information for diagnosis and treatment (Fig 1).

Relative to ECSF values, intraspinal CSF volumes in the SIH-initial ($P < .001$) and SIH-intermediate ($P < .05$) groups, but not the SIH-recovery group ($P = .772$), were significantly reduced (Table 3).

Diffuse Pachymeningeal Enhancement

Among the 23 patients with SIH, 15 had DPE (Table 4). The mean intraspinal CSF volumes of patients with SIH and DPE (70.14 ± 18.74 mL) did not differ significantly from those of patients with SIH without DPE (76.36 ± 21.10 mL, $P = .388$). The intraspinal CSF volume percentage (ie, quotient of the initial intraspinal CSF volumes and ECSF volumes) also did not differ significantly between patients with SIH with and without DPE ($P = .274$).

Venous Engorgement

Among the 23 patients with SIH, 13 showed venous engorgement and the other 10 did not (Table 4). The intraspinal CSF volumes of

patients with SIH with venous engorgement (66.24 ± 16.40 mL) did not differ from those of patients without venous engorgement (80.19 ± 20.84 mL, $P = .128$). Although the intraspinal CSF volume percentage of patients with SIH with venous engorgement did not differ from that of those without venous engorgement ($P = .058$), there seemed to be a trend toward patients with SIH with venous engorgement having a lower intraspinal CSF volume percentage.

Pituitary Volumes

As shown in Table 2, pituitary volumes were significantly larger in the SIH-initial than in the SIH-intermediate and SIH-recovery measurements (both $P < .001$). However, there was no significant difference in the SIH-intermediate and SIH-recovery pituitary volumes ($P = .155$). Pituitary volumes did not differ significantly between patients with SIH with and without DPE ($P = .747$, Table 4). However, the pituitary volumes of patients with SIH with venous engorgement were significantly greater than those of patients with SIH without venous engorgement ($P < .05$, Table 4).

Case Illustration

MR imaging and MRM images obtained for a 57-year-old woman who was diagnosed with CSF leakage into the spine are shown in Fig 2. The initial brain MR imaging showed no evidence of DPE, venous engorgement, or pituitary hyperemia. The calculated intraspinal CSF volume for this patient was 68.36 mL in the initial stage. The estimated intradural CSF for this patient was 79.11 mL, with an intraspinal CSF volume percentage of 86.5%. The intradural CSF volume at complete recovery was 80.04 mL.

MR imaging and MRM images obtained for a 34-year-old man who had orthostatic headache and was shown to have CSF leakage into the spine are shown in Fig 3. The calculated intraspinal CSF volume for this patient was 88.11 mL in the initial stage. DPE, venous engorgement, and pituitary hyperemia were noted in the patient's initial brain MR imaging. The estimated intradural CSF for this patient was 103.32 mL, with an intraspinal CSF volume percentage of 85.3%. The intradural CSF volume at complete recovery was 109.15 mL.

DISCUSSION

In this study, we obtained direct measurements of intraspinal CSF volumes in patients with SIH at 3 clinical stages and compared them with those of HCs. Although the intraspinal CSF volumes in the SIH-initial and SIH-intermediate measurements included leaked CSF in the extradural space and intradural CSF, stepwise increases in intraspinal CSF volumes were observed during the disease recovery. Furthermore, the mean intraspinal CSF volume was significantly lower in the SIH-initial and -intermediate disease stages than in the SIH-recovery stage or in HCs. These findings support the hypothesis that CSF hypovolemia is a core feature of SIH syndrome.

The normal intraspinal CSF volume range for healthy subjects has not been well-documented. In subjects without CSF leakage, intraspinal CSF volumes should be equal to intradural CSF volumes. Hogan et al[13] reported 2 healthy volunteers with intradural CSF volumes of the spine plus nerve roots of 95 and 120 mL. The only large-scale report was a study of 22 healthy volunteers having a mean intradural CSF volume of 81 ± 13 mL (range, 52–103 mL).[14] In that study, the original images were obtained with 3D balanced turbo-field echo pulse sequences and the regions for measurement were drawn on the images manually. For CSF volume calculation, the original images were transformed to an axial image of 1.9-mm thickness with a 0.7-mm spacing covering the whole spine. Manually drawing the outline of the spinal cord, spinal canal, and nerve root on every 10th axial image was performed. The intradural CSF volume of the spine was calculated as the following: Area of Spinal Canal − Nerve Roots and Spinal Cord × Interslice Distance.

Here, we used automatic threshold-based segmentation methods for CSF analysis to estimate the mean intradural CSF volumes of 32 HCs. Slightly larger intradural CSF volumes were observed in our study. The reason for the volume differences might be from the imaging sequences and analytic methods. In our experiment, a heavily T2-weighted 3D-SPACE sequence was used to acquire whole spinal MRM, which provided higher isotropic spatial resolution and tissue contrast of CSF in whole spinal

Table 3: Comparison of intraspinal CSF volumes at each SIH stage relative to the ECSF value

		SIH		
Parameter	ECSF ($n = 23$)	Ini ($n = 23$)	Int ($n = 18$)	Rec ($n = 18$)
Intraspinal CSF volumes (mL)	93.03 ± 13.23	72.31 ± 19.35	81.15 ± 25.41	93.74 ± 20.33
P values, ECSF vs SIH[a]	–	<.001[b]	<.05[b]	.772

Note:—Ini indicates initial; Int, intermediate, Rec, recovery.
[a] Paired *t* test.
[b] Significant.

Table 4: Comparison of MR imaging parameters between patients with SIH versus those without DPE and venous engorgement

	Volume (Mean)					
	SIH with Ini DPE ($n = 15$)	SIH without Ini DPE ($n = 8$)	*P* Value[a]	SIH with Ini Venous Engorgement ($n = 13$)	SIH without Ini Venous Engorgement ($n = 10$)	*P* Value[a]
Spinal						
Intraspinal CSF volumes (mL)	70.14 ± 18.74	76.36 ± 21.10	.388	66.24 ± 16.40	80.19 ± 20.84	.128
Intraspinal CSF volume percentage	78.59 ± 29.27	81.75 ± 19.64	.274	70.87 ± 17.74	91.16 ± 30.99	.058
Brain						
Pituitary volumes (cm^3)	0.61 ± 0.20	0.58 ± 0.19	.747	0.67 ± 0.15	0.51 ± 0.22	<.05[b]

Note:—Ini indicates initial; Int, intermediate, Rec, recovery.
[a] Mann-Whitney *U* test.
[b] Significant.

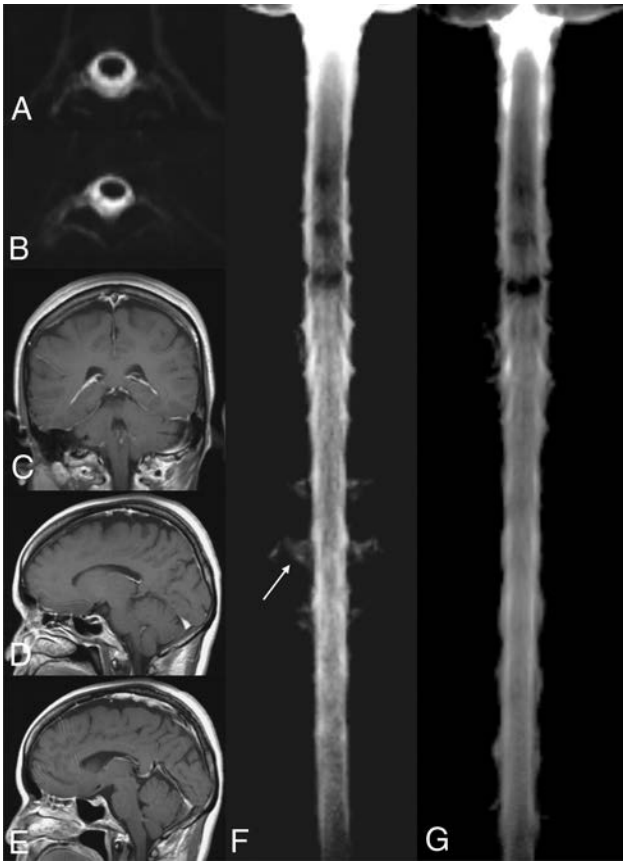

FIG 2. A 57-year-old woman diagnosed with CSF leakage in the spine with epidural fluid accumulation (*A*) and CSF signals along the neural sleeve (*B*) at the patient's initial MRM. The patient's initial brain MR imaging showed no evidence of DPE (*C*), venous engorgement (*D*), or pituitary hyperemia (*E*). 3D maximum intensity projection of the initial MRM (*F*) revealed CSF leakage along the neural sleeves at the T-spine (*arrow*) and reduced CSF volumes with lower CSF intensities of the dural sac compared with 3D MIP of her recovery MRM (*G*).

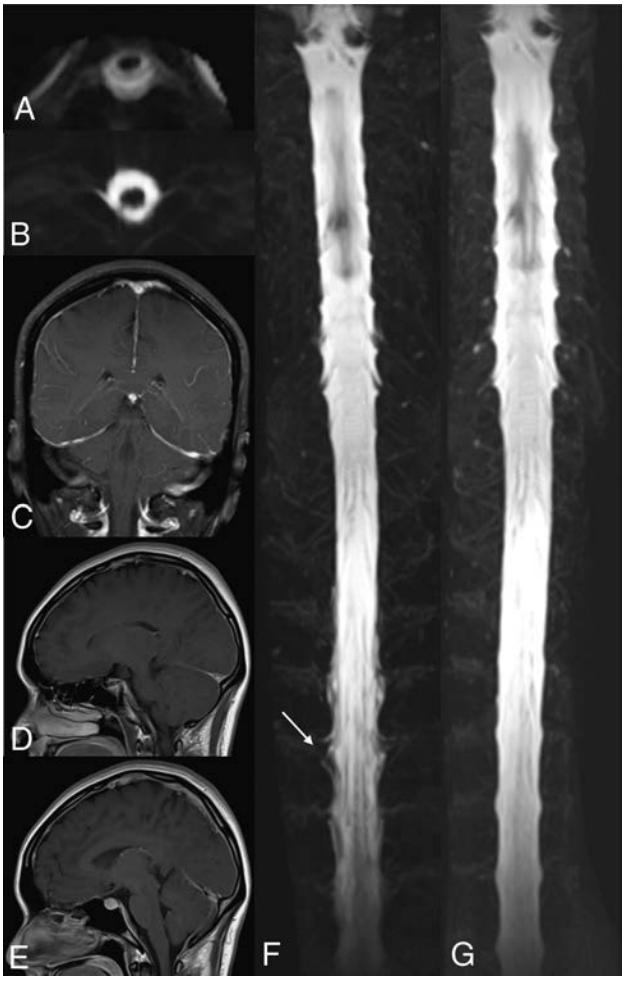

FIG 3. A 34-year-old man with orthostatic headache. CSF leakage at the spine with epidural fluid accumulation (*A*) and CSF signals along the neural sleeve (*B*) were seen at the patient's initial MRM. DPE (*C*), venous engorgement (*D*), and pituitary hyperemia (*E*) were noted at the initial brain MR imaging. 3D maximum intensity projection of the initial MRM (*F*) revealed an irregular contour along the neural sleeves at the T-spine, indicating CSF leakage (*arrow*) and reduced CSF volumes with lower CSF intensities of the dural sac compared with the 3D MIP of his recovery MRM (*G*).

images.[15] We believed that sequence would be more sensitive for detecting the CSF voxels than using a balanced turbo-field echo sequence because the SPACE sequence has less susceptibility artifact–related image blurring and better contrast-to-noise ratio.[16,17] Additionally, the automatic threshold-based segmentation method could effectively eliminate the discrepancy from intra- and interoperator variability and increase the reliability in clinical applicability. Our cohort was younger (range, 39–59 years) than those in prior studies. For example, in Edsbagge et al,[14] all participants were older than 64 years of age. Degenerative spinal changes, such as spurs or stenosis, might reduce intradural CSF volumes. However, we did observe a wide variation of intradural CSF volumes across individuals.

Using ECSF volumes as a reference to predict individual intraspinal CSF volumes, we discovered that patients with SIH had significantly lower intraspinal CSF volumes at their initial and intermediate measurements. No significant differences in intraspinal CSF volumes were found between the recovery measurements and the ECSF values. We presented 2 cases of SIH with about 20-mL differences in their intraspinal CSF volumes (68.36 versus 88.11 mL) at the initial stage (Figs 2 and 3). It was difficult to determine whether their intraspinal CSF volumes were reduced by only using the absolute volumes. The male patient had higher ECSF than the female patient (103.32 versus 79.11 mL). With ECSF as a reference, both patients had significantly reduced CSF volumes with the intraspinal CSF percentage of about 85% causing orthostatic headache and other image abnormalities. Their intradural CSF volumes during recovery were 80.04 and 109.15 mL, respectively. Therefore, ECSF volumes might serve as an important reference for the diagnosis and evaluation of disease severity.

SIH-associated brain changes can be explained by the Monro-Kellie doctrine,[18] wherein decreases in intracranial CSF volumes are accompanied by increased volumes of brain tissue (eg, pituitary hyperemia) or vascular structures (DPE or venous engorgement). In our study, intraspinal CSF volumes and volume percentage in patients with SIH with DPE ($n = 15$) were similar to the values obtained for patients without DPE ($n = 8$). However, the potential effect of venous engorgement on these parameters was less clear. Although there was no significant difference of intraspi-

nal CSF volumes between patients with SIH with ($n = 13$) and without ($n = 10$) venous engorgement, there was a strong trend toward a difference in intraspinal CSF volume percentage between these 2 groups (borderline P value = .058). This trend may become a robustly significant difference with a larger sample size. Venous engorgement was present in patients with more severe CSF depletion and might not be present in those with mild CSF volume loss. In a previous study, we also demonstrated that DPE or venous engorgement reflected a more severe disease status and may not be seen in patients with mild disease.[6] Therefore, we believe that intraspinal CSF volumes and, especially, intraspinal CSF volume percentage may be sensitive markers of SIH progression. Spine MR imaging has also been reported useful for diagnosing SIH, especially at early stages.[19]

Pituitary hyperemia has also been thought to be a sensitive imaging marker of SIH. All the patients in this study had an enlarged pituitary gland, and the pituitary volumes decreased in relation to symptomatic improvement. Pituitary volumes were significantly greater in patients with venous engorgement than in those without it. Although pituitary volumes may reflect disease severity, pituitary volumes vary greatly across individuals, with larger volumes often being seen in young women.[20] The maximum height was seen in the women between 20 and 40 years of age and declined with age.[21] Twelve female patients achieved complete recovery in our study. Their pituitary volumes did not differ from those of male patients. Six of them are between 20 and 40 years of age, and the other 6 are older than 40 years of age. The height and pituitary volume were not significantly different between these 2 groups. Two patients younger than 40 years of age and 1 patient older than 40 years of age had convex-shape pituitary glands. Even though SIH usually occurred in young women, the pituitary size was still variable among subjects. Therefore, using absolute pituitary volumes as a diagnostic criterion of SIH is inappropriate. However, relative change in pituitary volumes is a good parameter for evaluation of treatment effects.

In this study, we found that intradural spinal CSF volumes correlated positively with BH. No correlations were observed with BMI, BW, age, and sex. In previous reports, no correlation was found between intradural CSF and BH,[14] and inverse correlations of lumbosacral intradural CSF with BMI have been reported.[13,22] The number of vertebrae has been used as an indicator of intradural CSF volume.[1] Therefore, we thought that lower limb length might explain the variance in the relationship between BH and intradural CSF volumes across individuals. Additional large-scale studies may better uncover the relationships among clinical findings, brain imaging findings, and intracranial and intraspinal CSF volumes.

Our study has some limitations. First, because of the difficulty of the autosegmentation method in separating extradural CSF from intradural CSF in current status, the intraspinal CSF measurements included both extra- and intradural spaces in SIH-initial and SIH-intermediate measurements. Hence, the CSF that leaked through dural defects was also included in our calculations using our segmentation method. Even though the intraspinal CSF volumes in SIH-initial and SIH-intermediate measurements were still significantly lower than those of healthy controls and SIH-recovery measurements, most of our patients had a significant amount CSF leakage at the spinal nerve roots with epidural fluid accumulation. Therefore, if we took account of only the intradural CSF, we believe that the CSF volumes would be much lower than those in healthy controls in the patients with SIH. Further study with methods that can differentiate intradural CSF from extradural CSF might elucidate the dynamic changes in patients with SIH.

Second, our sample size was small, and intracranial CSF volumes were not measured. Studies with larger sample sizes with measurements of both intracranial and intraspinal CSF volumes may provide more information. Third, although hypovolemia is fundamentally related to SIH, individual variations of intradural CSF volumes do exist. The intraspinal CSF volumes could help monitor treatment effects as well. On the other hand, the method by which intradural CSF volumes are estimated for subjects will be important in making clinical application and accurate diagnoses feasible. ECSF volumes determined on the basis of BH as in our study appear to reflect clinical status well and could be used to help determine whether further treatment is needed. However, the correlation between intradural CSF volumes and BH was not high enough. It still needs to be integrated with clinical symptoms and other imaging findings. How to estimate intradural CSF volumes better still needs to be investigated by using other parameters and larger sample sizes.

CONCLUSIONS

With a threshold-based segmentation method, we demonstrated that spinal CSF hypovolemia was fundamentally related to SIH and may serve as an early detection method before abnormalities are detectable by conventional brain MR imaging. Intraspinal CSF volumes can be used as a sensitive parameter in treatment-response monitoring and in SIH follow-up evaluations.

REFERENCES

1. Miyazawa K, Shiga Y, Hasegawa T, et al. **CSF hypovolemia vs intracranial hypotension in "spontaneous intracranial hypotension syndrome."** *Neurology* 2003;60:941–47 Medline
2. Mokri B, Hunter SF, Atkinson JL, et al. **Orthostatic headaches caused by CSF leak but with normal CSF pressures.** *Neurology* 1998; 51:786–90 CrossRef Medline
3. Spero M, Lazibat I, Stojic M, et al. **Normal pressure form of the spontaneous intracranial hypotension: a case report with pituitary enlargement and asymptomatic pituitary haemorrhage.** *Neurol Sci* 2011;32:933–35 CrossRef Medline
4. Mokri B. **Spontaneous CSF leaks: low CSF volume syndromes.** *Neurol Clin* 2014;32:397–42 CrossRef Medline
5. Yoo HM, Kim SJ, Choi CG, et al. **Detection of CSF leaks in spinal CSF leak syndrome using MR myelography: correlation with radioisotope cisternography.** *AJNR Am J Neuroradiol* 2008;29:649–54 CrossRef Medline
6. Tung H, Liao YC, Wu CC, et al. **Usefulness of phase-contrast magnetic resonance imaging for diagnosis and treatment evaluation in patients with SIH.** *Cephalalgia* 2014;34:584–93 CrossRef Medline
7. Schievink WI, Maya MM, Louy C, et al. **Diagnostic criteria for spontaneous spinal CSF leaks and intracranial hypotension.** *AJNR Am J Neuroradiol* 2008;29:853–56 CrossRef Medline
8. Headache Classification Committee of the International Headache Society (IHS). **The International Classification of Headache Disorders, 3rd edition (beta version).** *Cephalalgia* 2013;33:629–808 CrossRef Medline

9. Chang CI, Chen K, Wang J, et al. **A relative entropy-based approach to image thresholding.** *Pattern Recognition* 1994;27:1275–89 CrossRef
10. Zhang H, Fritts JE, Goldman SA. **Image segmentation evaluation: a survey of unsupervised methods.** *Computer Vision and Image Understanding* 2008;110:260–80 CrossRef
11. Chen X, Wang R, Cao Y, et al. **A novel evaluation method based on entropy for image segmentation.** *Procedia Engineering* 2012;29: 3959–65 CrossRef
12. Liang YC, Cuevas, JR. **An automatic multilevel image thresholding using relative entropy and meta-heuristic algorithms.** *Entropy* 2013; 15:2181–209 CrossRef
13. Hogan QH, Prost R, Kulier A, et al. **Magnetic resonance imaging of cerebrospinal fluid volume and the influence of body habitus and abdominal pressure.** *Anesthesiology* 1996;84:1341–49 Medline
14. Edsbagge M, Starck G, Zetterberg H, et al. **Spinal cerebrospinal fluid volume in healthy elderly individuals.** *Clin Anat* 2011;24:733–40 CrossRef Medline
15. Hodel J, Lebret A, Petit E, et al. **Imaging of the entire cerebrospinal fluid volume with a multistation 3D SPACE MR sequence: feasibility study in patients with hydrocephalus.** *Euro Radiol* 2013;23: 1450–58 CrossRef Medline
16. Kojima S, Suzuki K, Hirata M, et al. **Depicting the semicircular canals with inner-ear MRI: a comparison of the SPACE and TrueFISP sequences.** *J Magn Reson Imaging.* 2013;37:652–59 CrossRef Medline
17. Ucar M, Tokgoz N, Damar, C., et al. **Diagnostic performance of heavily T2-weighted techniques in obstructive hydrocephalus: comparison study of two different 3D heavily T2-weighted and conventional T2-weighted sequences.** *Jpn J Radiol* 2015;33:94 CrossRef Medline
18. Mokri B. **The Monro-Kellie hypothesis: applications in CSF volume depletion.** *Neurology* 2001;56:1746–48 CrossRef Medline
19. Watanabe A, Horikoshi T, Uchida M, et al. **Diagnostic value of spinal MR imaging in spontaneous intracranial hypotension syndrome.** *AJNR Am J Neuroradiol* 2009;30:147–51 Medline
20. MacMaster FP, Keshavan M, Mirza, Y et al. **Development and sexual dimorphism of the pituitary gland.** *Life Sci* 2007;80:940–44 CrossRef Medline
21. Doraiswamy PM, Potts JM, Axelson DA, et al. **MR assessment of pituitary gland morphology in healthy volunteers: age- and gender-related differences.** *AJNR Am J Neuroradiol* 1992;13:1295–99 Medline
22. Sullivan JT, Grouper S, Walker MT, et al. **Lumbosacral cerebrospinal fluid volume in humans using three-dimensional magnetic resonance imaging.** *Anesth Analg* 2006;103:1306–10 CrossRef Medline

Celebrating 35 Years of the AJNR

May 1982 edition

CT Recognition of Lateral Lumbar Disk Herniation

Alan L. Williams[1]
Victor M. Haughton
David L. Daniels
Robert S. Thornton

Although computed tomography (CT) has been shown to be useful in diagnosing posterolateral and central lumbar disk herniations, its effectiveness in demonstrating lateral herniated disks has not been emphasized. The myelographic recognition of those herniations may be difficult because root sheaths or dural sacs may not be deformed. A total of 274 CT scans interpreted as showing lumbar disk herniation was reviewed. Fourteen (5%) showed a lateral disk herniation. The CT features of a lateral herniated disk included: (1) focal protrusion of the disk margin within or lateral to the intervertebral foramen; (2) displacement of epidural fat within the intervertebral foramen; (3) absence of dural sac deformity; and (4) soft-tissue mass within or lateral to the intervertebral foramen. Because it can image the disk margin and free disk fragments irrespective of dural sac or root sheath deformity, CT may be more effective than myelography for demonstrating the presence and extent of lateral disk herniation.

The recognition of a herniated lumbar intervertebral disk by myelography, even with water-soluble contrast agents, may be difficult where the anterior epidural space is large, such as at L5–S1, or when the herniation is lateral [1–5]. Computed tomography (CT) has been shown to be effective in the diagnosis of herniated disks [6–10], particularly the central and posterolateral ones. We illustrate the usefulness of CT in the diagnosis of lateral lumbar disk herniations.

Materials and Methods

During a 3 year period, 1,523 patients with low back and/or sciatic pain were studied with CT at the Milwaukee County Medical Complex. Our CT scanning techniques have been described [6, 8, 10]. In 274 patients (18%), evidence of a herniated lumbar disk was seen by CT. We reviewed the CT scans in these 274 patients to determine the frequency and CT appearance of lateral lumbar disk herniation. We defined a lateral disk herniation as one within or lateral to the intervertebral foramen. These criteria were satisfied in 14 patients. Six of them were confirmed surgically and eight were managed conservatively.

This article appears in the May/June 1982 issue of AJNR and the August 1982 issue of AJR.

Received September 22, 1981; accepted after revision December 28, 1981.

Presented at the annual meeting of the American Society of Neuroradiology, Chicago, April 1981.

[1]All authors: Department of Radiology, Medical College of Wisconsin, and Milwaukee County Medical Complex, 8700 W. Wisconsin Ave., Milwaukee, WI 53226. Address reprint requests to A. L. Williams.

AJNR 3:211–213, May/June 1982
0195–6108/82/0303–0211 $00.00

Results

In the 14 cases, displacement of fat within the interverte
identified in each one, whereas a dural sac deformity was
Focal protrusion of the disk margin resulting in narrowing of
foramen was seen in 12 patients, and a soft-tissue mass late
was identified in three.

Representative Case Reports

Case 1

A 40-year-old woman had 6 weeks of severe left sciatic pain. Ne
revealed left L5 and S1 radiculopathy. CT demonstrated displacemen
L5–S1 intervertebral foramen and a large soft-tissue mass lateral to

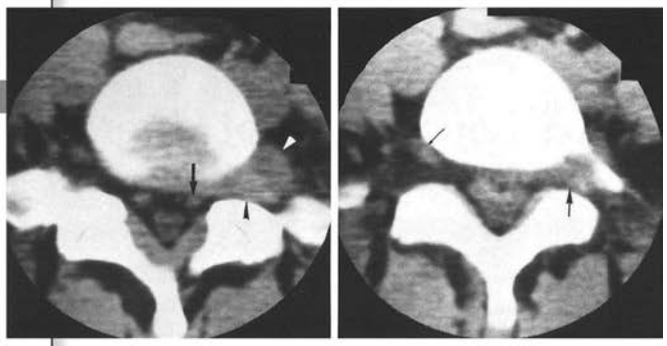

Atrial Diverticula in Severe Hydrocephalus

Thomas P. Naidich[1]
David G. McLone[2]
Yoon S. Hahn[2]
Joseph Hanaway[3]

Massive ventricular dilatation causes stretching and dehiscence of the fornix with formation of unilateral or bilateral pial pulsion diverticula of the inferior medial wall of the atrium. Enlargement of the pial pouch creates a dramatic subarachnoid cyst that may herniate downward through the incisura into the lateral mesencephalic, precentral cerebellar, and superior vermian cisterns where it displaces the brain stem, vermis, and fourth ventricle. Lateral ventricular diverticula may be identified and distinguished from the dilated fourth ventricle and dilated supraipineal recess, with which they are so commonly confused, when all of the following signs are apparent on computed tomography (CT): (1) marked unilateral or bilateral atrial dilatation; (2) focal dehiscence of the medial atrial wall; (3) ipsilateral shortening of the tentorial band in axial section; (4) focal defect in the tentorial band in coronal section; (5) draping of the medial atrial wall over the free margin of tentorium, with continuity of cerebrospinal fluid density around the edge of tentorium in axial and/or coronal sections; (6) bowing of the crus (or crura) of fornix; (7) separation of fornix from splenium, with visualization of the hernia ostium; (8) asymmetrical position of the choroid plexi, which attach to and define the lateral borders of the fornices; (9) contralateral displacement of the internal cerebral veins; and (10) septa separating diverticulum from third ventricle.

Proper surgical management of the patient with massive hydrocephalus and a midline, incisural, cerebrospinal fluid (CSF)-density "cyst" requires accurate preoperative identification of the nature of the "cyst" and its relation to the ventricular system. Primary arachnoid and ependymal cysts, which *cause* hydrocephalus, may be treated by extirpation or direct shunting of the cyst with consequent relief of hydrocephalus. Focal ventricular dilatations that *result* from hydrocephalus are treated most effectively by simple shunting of the lateral ventricles. Initial difficulty in differentiating among primary arachnoid cysts, enlargement of the suprapineal recess of the third ventricle, pulsion diverticulum of the medial atrial wall, and upward bulging of the dilated fourth ventricle led to review of the relevant anatomy and pathology and elaboration of criteria for accurate computed tomographic (CT) diagnosis of the pulsion diverticulum of the medial wall of the atrium.

Materials and Methods

Serial CT scans of 300 pediatric and adult patients with ventricular dilatation were reviewed to select 60 patients satisfying the Meese et al. [1] criteria for extreme hydrocephalus. Patients believed to have atrophy on the basis of clinical or CT criteria were rigorously excluded. In 10 cases, where patient benefit justified the risk, CT diagnoses of atrial diverticula, arachnoid cyst, etc. were confirmed by metrizamide CT ventriculography (MCTV), metrizamide CT cisternography (MCTC), or surgical exploration [2–6].

Anatomic and Pathologic Basis for CT Signs

The medial wall of atrium is formed by the splenium above and behind, the symmetric

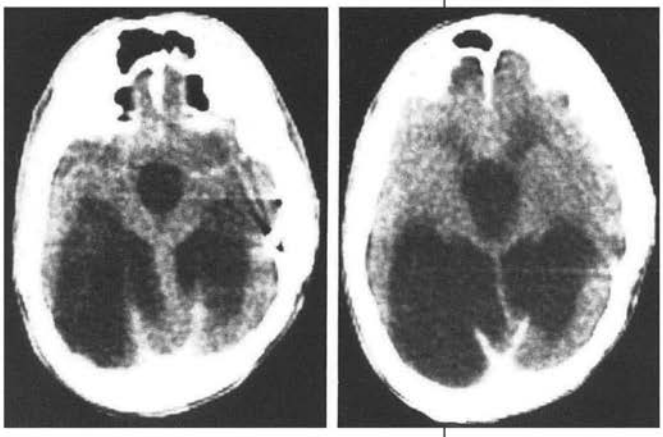

Regarding "MR Imaging of the Cervical Spine in Nonaccidental Trauma: A Tertiary Institution Experience"

We would like to thank Jacob et al for raising an important, relevant issue in their article entitled "MR Imaging of the Cervical Spine in Nonaccidental Trauma: A Tertiary Institution Experience."[1] They reported a relatively high incidence (69%) of cervical spine injury (CSI) in nonaccidental trauma compared with the literature and concluded that positive findings on MR imaging may affect management and, therefore, recommending routine use of MRI in suspected nonaccidental trauma.

However, it is not clear how the authors reached that conclusion. They have not specified how the MR imaging findings impacted management in their study population. Are the authors advocating the use of MR imaging for the diagnosis of nonaccidental trauma, distinguishing accidental from nonaccidental trauma, or management of patients with nonaccidental trauma? Although ligamentous signal on MR imaging was seen in 67% of patients, this was mostly confined to the interspinous and nuchal ligaments. From the description of findings in the study population, would the authors agree that none of the patients had unstable injury? Although this was a retrospective study, would prospective knowledge of these findings change management and in what circumstances?

Previous studies have shown that MR imaging signs of cervical spine injury did not show a statistical relationship with outcome or help discriminate accidental and abusive head trauma.[2] Although cervical spine injury was seen on MR imaging in 36% of patients, none required surgical intervention in the study by Kadom et al.[2]

Despite the higher soft-tissue contrast resolution, MR imaging has not been shown to detect unstable CSIs in patients with CT with negative findings, either in the pediatric or adult population.[3] Choudhary et al[4] found a higher incidence of ligamentous injury in nonaccidental trauma compared with accidental injuries, but the pattern of injuries was similar.[4] Jacob et al[1] used that study as evidence that MR imaging findings actually reflect pathology because the cohort of patients without trauma did not show similar MR imaging abnormalities. However, there was no blinding for the healthy cohort in the study by Choudhary et al. The few studies that have correlated MR imaging findings of ligamentous signal abnormalities with intraoperative or postmortem findings have found a poor correlation.[5] In a comparison of 4 modalities to assess cervical spine instability in pediatric trauma, Brockmeyer et al[6] found MR imaging to be sensitive but not specific (74%). Because of the low specificity, the authors recommended that MR imaging be performed only in patients with neurologic deficits or to follow up a screening study with positive findings.

Performance of MR imaging is not without challenges, risks, and costs in this study population. As per the authors, only 43% of patients in this study had superior quality imaging. The recommendation by the authors of routinely including cervical spine MR imaging as part of the armamentarium of tests while working up a child with nonaccidental trauma probably needs answers to our questions and more evidence.

REFERENCES

1. Jacob R, Cox M, Koral K, et al. **MR imaging of the cervical spine in nonaccidental trauma: a tertiary institution experience.** *AJNR Am J Neuroradiol* 2016 May 26. [Epub ahead of print] CrossRef Medline
2. Kadom N, Khademian Z, Vezina G, et al. **Usefulness of MRI detection of cervical spine and brain injuries in the evaluation of abusive head trauma.** *Pediatr Radiol* 2014;44:839–48 CrossRef Medline
3. Malhotra A, Wu X, Kalra VB, et al. **Utility of MRI for cervical spine clearance after blunt traumatic injury: a meta-analysis.** *Eur Radiol* 2016 Jun 22. [Epub ahead of print] Medline
4. Choudhary AK, Ishak R, Zacharia TT, et al. **Imaging of spinal injury in abusive head trauma: a retrospective study.** *Pediatr Radiol* 2014;44:1130–40 CrossRef Medline
5. Goradia D, Linnau KF, Cohen WA, et al. **Correlation of MR imaging findings with intraoperative findings after cervical spine trauma.** *AJNR Am J Neuroradiol* 2007;28:209–15 Medline
6. Brockmeyer DL, Ragel BT, Kestle JR. **The pediatric cervical spine instability study: a pilot study assessing the prognostic value of four imaging modalities in clearing the cervical spine for children with severe traumatic injuries.** *Childs Nerv Syst* 2012;28:699–705 CrossRef Medline

X. Wu
D. Durand
B. Rao
A. Malhotra
Department of Radiology and Biomedical Imaging
Yale School of Medicine
New Haven, Connecticut

http://dx.doi.org/10.3174/ajnr.A5098

REPLY:

We would like to thank the authors of a letter in reference to our recently published study, "MR Imaging of the Cervical Spine in Nonaccidental Trauma: A Tertiary Institution Experience." The word "clearance" was not in the title of the study as suggested by the preceding letter, and our article did not address whether the MR imaging findings could determine cervical spine stability or instability. However, MR imaging with negative findings has been shown to be useful in clearing the cervical spine,[1] which would have been the case in 31% of our patients. We agree that positive findings relating to instability are less well-defined and posterior ligamentous injury is likely a stable injury. The additional findings of capsular injury with distension (13%) and tectorial ligament injury (4%) are more worrisome, and we believe these would alter management, but again this was not the purpose of our study.

These children do not necessarily have a history of a traumatic incident, and positive findings on MR imaging may be helpful to define the injury as traumatic. We do not advocate the use of MR imaging for defining a ligamentous injury as accidental or nonaccidental because these injuries have similar findings, but the positive findings are significantly more common in the nonaccidental cohort as reported by Choudhary et al.[2] Most interesting, the presence of spinal subdural hemorrhage, likely from redistribution, may be indicative of a nonaccidental mechanism because it was rarely seen in the accidental cohort.[3] Spinal subdural hemorrhage was seen in 18% of our patients.

In our study, the cervical spine injuries were statistically associated with parenchymal brain injury; therefore, poor outcome may not be due to the cervical spine injury but related to the associated brain injury. We realize that the prior study by Kadom et al[4] did not find an association between outcome and cervical spine injury as diagnosed on MR imaging and further study is needed. Additionally, a positive finding on cervical MR imaging would strengthen the case for trauma as an etiology for the brain injury.

The letter indicates that only 43% of the MR imaging studies in our study were of superior quality, but studies of all patients were categorized as superior or diagnostic. It is more important to realize the inherent insensitivity of cervical radiographs in the evaluation of cervical spine injury, especially in young children.[5] Also, most of our injuries were at the cervical-occipital junction, and CT criteria for evaluating this injury have recently been re-evaluated and found to be suboptimal.[6]

In this vulnerable population, MR imaging of the cervical spine may provide additional answers. Many of these examinations can be performed in conjunction with brain MR imaging without additional sedation/anesthesia. A small number of children in our study had normal brain imaging findings and evidence of cervical spine injury. This information would be extremely helpful in the evaluation of a child with suspected nonaccidental trauma. We believe our study supports the use of cervical MR imaging in this cohort of patients.

http://dx.doi.org/10.3174/ajnr.A5111

REFERENCES

1. Frank JB, Lim CK, Flynn JM, et al. **The efficacy of magnetic resonance imaging in pediatric cervical spine clearance.** *Spine* 2002;27:1176–79 CrossRef Medline
2. Choudhary AK, Ishak R, Zacharia TT, et al. **Imaging of spinal injury in abusive head trauma: a retrospective study.** *Pediatr Radiol* 2014;44:1130–40 CrossRef Medline
3. Choudhary AK, Bradford RK, Dias MS, et al. **Spinal subdural hemorrhage in abusive head trauma: a retrospective study.** *Radiology* 2012;262:216–23 CrossRef Medline
4. Kadom N, Khademian Z, Vezina G, et al. **Usefulness of MRI detection of cervical spine and brain injuries in the evaluation of abusive head trauma.** *Pediatr Radiol* 2014;44:839–48 CrossRef Medline
5. Moore JM, Hall J, Ditchfield M, et al. **Utility of plain radiographs and MRI in cervical spine clearance in symptomatic non-obtunded pediatric patients without high-impact trauma.** *Childs Nerv Syst* 2016 Dec 6. [Epub ahead of print] CrossRef Medline
6. Corcoran B, Linscott LL, Leach JL, et al. **Application of normative occipital condyle-C1 interval measurements to detect atlanto-occipital injury in children.** *AJNR Am J Neuroradiol* 2016;37:958–62 CrossRef Medline

T.N. Booth
Children's Health Dallas
University of Texas Southwestern Medical Center
Dallas, Texas
R. Jacob
University Medical Center Health System
Texas Tech University
Lubbock, Texas
C. Greenwell
K. Reeder
K. Koral
Children's Health Dallas
University of Texas Southwestern Medical Center
Dallas, Texas

Intracranial Arteriovenous Shunting Detection with Arterial Spin-Labeling and Susceptibility-Weighted Imaging: Potential Pitfall of a Venous Predominant Parenchymal Arteriovenous Malformation

I read with great interest the study of Hodel et al,[1] which demonstrated that the combined use of arterial spin-labeling (ASL) and susceptibility-weighted imaging was significantly more sensitive and equally specific compared with conventional angiographic MR imaging for the detection of arteriovenous shunting. In Fig 2 of this article, a lesion with increased signal intensity on ASL images was subsequently confirmed as a developmental venous anomaly (DVA) based on the presence of a classic umbrella-shaped appearance on the venous phase cerebral angiogram.[1]

Most DVAs are not associated with perfusion changes on ASL imaging. In a large study of 652 DVAs, only a minority of DVAs (8%) demonstrated signal abnormalities on ASL maps,[2] and intrinsically increased ASL signal or increased signal in a draining vein associated with a DVA are potentially imaging biomarkers of arteriovenous shunting.[2,3] It may be argued that the presence of a typical venous phase cerebral angiogram with a caput medusa appearance will confirm the DVA. However, direct arteriovenous shunting into dilated medullary veins characteristic of a DVA without a typical nidus has been repeatedly reported in the literature. These arterialized DVAs have been described with various terminology, but Im et al[4] proposed the name of "venous-predominant parenchymal AVMs" on the basis of clinical, angiographic, surgical, and histologic findings in a series of 15 cases. Of note, the cerebral angiograms of these lesions demonstrated an abnormal blush in the early arterial phase, followed by diffuse vascular and capillary parenchymal staining in the mid-arterial phase and immediate drainage into a network of radially arranged dilated medullary veins.[4] These lesions consistently showed a caput medusa appearance very similar to the appearance of DVAs, with the absence of enlarged arterial feeders and lack of a typical AVM nidus.

In summary, a lesion with increased signal intensity on an ASL map is suspicious for arteriovenous shunting, and a caput medusa appearance on the venous phase of a cerebral angiogram is not sufficient to make the diagnosis of DVA. Careful attention to the arterial phase of the angiogram would be prudent to exclude a venous-predominant parenchymal arteriovenous malformation.

REFERENCES

1. Hodel J, Leclerc X, Kalsoum E, et al. **Intracranial arteriovenous shunting: detection with arterial spin-labeling and susceptibility-weighted imaging combined.** *AJNR Am J Neuroradiol* 2017;38:71–76 CrossRef Medline
2. Iv M, Fischbein NJ, Zaharchuk G. **Association of developmental venous anomalies with perfusion abnormalities on arterial spin labeling and bolus perfusion-weighted imaging.** *J Neuroimaging* 2015;25:243–50 CrossRef Medline
3. Nabavizadeh SA, Mamourian AC, Vossough A, et al. **The many faces of cerebral developmental venous anomaly and its mimicks: spectrum of imaging findings.** *J Neuroimaging* 2016;26:463–72 CrossRef Medline
4. Im SH, Han MH, Kwon BJ, et al. **Venous-predominant parenchymal arteriovenous malformation: a rare subtype with venous drainage pattern mimicking developmental venous anomaly.** *J Neurosurg* 2008;108:1142–47 CrossRef Medline

S.A. Nabavizadeh
Department of Radiology
Hospital of University of Pennsylvania
Perelman School of Medicine at the University of Pennsylvania
Philadelphia, Pennsylvania

http://dx.doi.org/10.3174/ajnr.A5108

REPLY:

We thank Dr Nabavizadeh for his interest in our article, "Intracranial Arteriovenous Shunting: Detection with Arterial Spin-Labeling and Susceptibility-Weighted Imaging Combined."[1]

We agree that arterial spin-labeling (ASL) hypersignal in developmental venous anomalies (DVAs) may suggest transitional or mixed malformations with arteriovenous shunting. DVA may also coexist with a true arteriovenous malformation, as reported by Erdem et al,[2] with selective arterial embolization of the AVM while preserving the DVA. As highlighted by Dr Nabavizadeh, the presence of dilated deep medullary veins in a "spoke wheel" or caput medusae at the venous phase of angiograms is not sufficient for the diagnosis of DVA. Careful attention must be paid to the arterial phase to rule out arteriovenous shunting resulting in early opacification of the draining vein at the arterial phase of the angiogram. In all 8 patients with DVAs included in our study, the main draining vein was never opacified in the early and mid-arterial phases of the angiograms. Only a capillary stain was observed in 2 patients, forming a blush at the arterial phase, without any arteriovenous communication. These findings are in agreement with those reported by Roccatagliata et al,[3] suggesting that a large spectrum of lesions exists from typical DVAs to clearly distinct AVMs. These cases probably correspond to DVAs surrounded by dilated arteriolar-capillary channels that may exceptionally lead to ischemic or hemorrhagic complications. This pattern may be due to the lack of adaptability to variations in intracranial venous equilibrium, as suggested by the authors.[3]

However, the natural history, prognosis, and therapeutic management of such lesions remain unclear and are widely debated in the literature. For a systematic review of digital subtraction angiography images in our study, we chose to classify the vascular malformations as DVAs when angiograms demonstrated a caput medusae appearance without opacification of the main draining vein at the arterial phase of the angiograms. If we had decided to classify these atypical DVAs on DSA as arteriovenous shunting, the specificity of ASL would have been even higher than that reported.

Signal abnormalities on ASL images may be located either in the brain parenchyma surrounding the DVA or within the draining vein of the DVA. We agree that it may be speculated that a hypersignal of a part of the DVA on ASL images may potentially reflect the presence of an arteriovenous shunting, but little data exist in the literature comparing ASL signal with DSA in patients with DVA. In addition, erroneous interpretation of CBF may be made in patients with prolonged arterial arrival times. Thus, further studies are required to understand the real significance of these findings.

http://dx.doi.org/10.3174/ajnr.A5131

REFERENCES

1. Hodel J, Leclerc X, Kalsoum E, et al. **Intracranial arteriovenous shunting: detection with arterial spin-labeling and susceptibility-weighted imaging combined.** *AJNR Am J Neuroradiol* 2017;38:71–76 CrossRef Medline
2. Erdem E, Amole AO, Akdol MS, et al. **Developmental venous anomaly coexisting with a true arteriovenous malformation: a rare clinical entity.** *J Neurointerv Surg* 2012;4:e19 CrossRef Medline
3. Roccatagliata L, van den Berg R, Soderman M, et al. **Developmental venous anomalies with capillary stain: a subgroup of symptomatic DVAs?** *Neuroradiology* 2012;54:475–80 CrossRef Medline

J. Hodel
Department of Radiology
Hôpital Saint Joseph
Paris, France
Department of Neuroradiology
AP-HP
Hôpitaux Universitaires Henri Mondor
Créteil, France
Faculty of Medicine
Université Paris Est Créteil
Créteil, France
R. Blanc
Department of Interventional Neuroradiology
Fondation Rothschild
Paris, France
E. Kalsoum
Department of Neuroradiology
AP-HP
Hôpitaux Universitaires Henri Mondor
Créteil, France
M. Zins
Department of Radiology
Hôpital Saint Joseph
Paris, France
X. Leclerc
Department of Neuroradiology
Hôpital Roger Salengro
Lille, France

3D Ultrasound for Imaging and Quantifying Carotid Ulcers

In their recent article, Yuan et al[1] stated that they "highlight the merits and limitations of various imaging techniques for identifying carotid plaque ulceration." It is curious, therefore, that they made no mention of 3D sonography (3DUS). Although ulceration seen on angiography predicted risk in the North American Symptomatic Carotid Endarterectomy Trial,[2] it was clear that imaging of the lumen by angiography was not a reliable way to assess ulceration.[3]

Schminke et al[4] reported that 3DUS was a better way to image ulceration than 2D sonography. In 2011, we reported that the number of carotid ulcers (Fig 1) was as strong a predictor of risk among patients with asymptomatic carotid stenosis; patients with ≥3 ulcers in either carotid artery had a risk equivalent to that of patients with microemboli on transcranial Doppler sonography.[5]

In 2104, we reported that ulcer volume predicted cardiovascular risk among patients attending cardiovascular prevention clinics (Fig 2).[6] It is likely that the best way to image and quantify carotid ulceration is with 3DUS.

Disclosures: J. David Spence—*UNRELATED*: *Other*: Dr Spence is an officer of Vascularis Inc.

http://dx.doi.org/10.3174/ajnr.A5130

REFERENCES

1. Yuan J, Usman A, Das T, et al. **Imaging carotid atherosclerosis plaque ulceration: comparison of advanced imaging modalities and recent developments.** *AJNR Am J Neuroradiol* 2016 Dec 22. [Epub ahead of print] CrossRef Medline
2. Eliasziw M, Streifler JY, Fox AJ, et al. **Significance of plaque ulceration in symptomatic patients with high-grade carotid stenosis: North American Symptomatic Carotid Endarterectomy Trial.** *Stroke* 1994; 25:304–08 CrossRef Medline
3. Streifler JY, Eliasziw M, Fox AJ, et al. **Angiographic detection of carotid plaque ulceration: comparison with surgical observations in a multicenter study—North American Symptomatic Carotid Endarterectomy Trial.** *Stroke* 1994;25:1130–32 CrossRef Medline
4. Schminke U, Motsch L, Hilker L, et al. **Three-dimensional ultrasound observation of carotid artery plaque ulceration.** *Stroke* 2000;31:1651–55 CrossRef Medline
5. Madani A, Beletsky V, Tamayo A, et al. **High-risk asymptomatic carotid stenosis: ulceration on 3D ultrasound vs TCD microemboli.** *Neurology* 2011;77:744–50 CrossRef Medline
6. Kuk M, Wannarong T, Beletsky V, et al. **Volume of carotid artery ulceration as a predictor of cardiovascular events.** *Stroke* 2014;45: 1437–41 CrossRef Medline

J.D. Spence
Stroke Prevention and Atherosclerosis Research Centre
Robarts Research Institute
Western University
London, Ontario, Canada

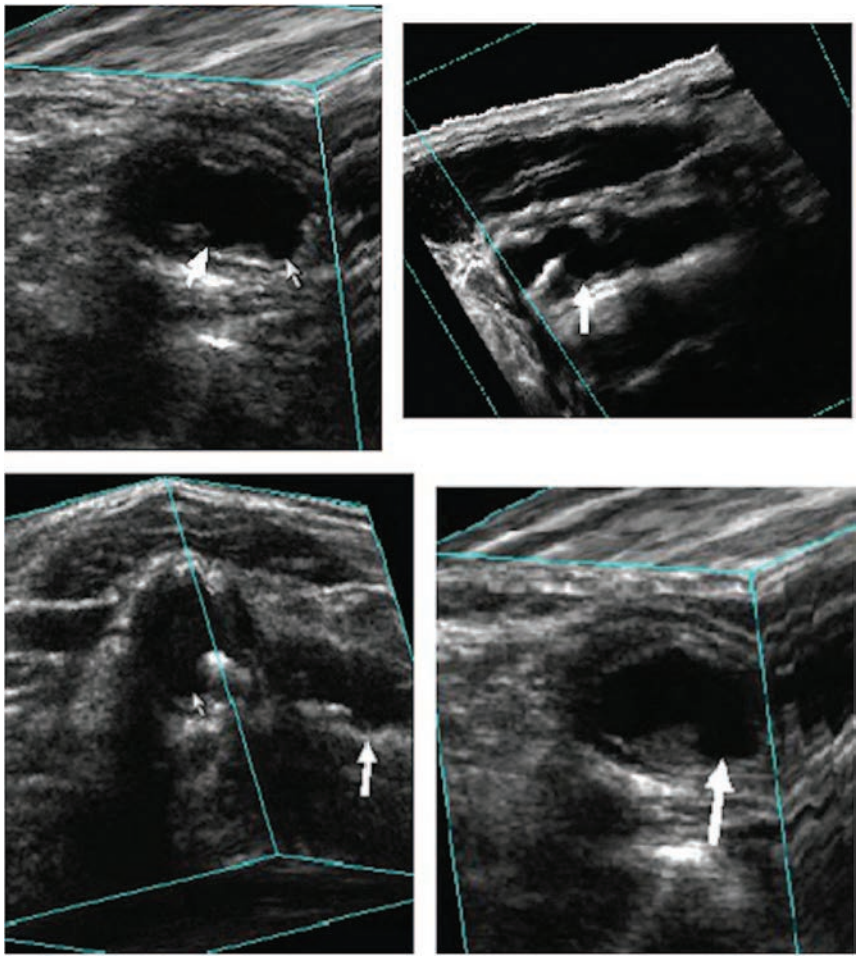

FIG 1. Number of carotid ulcers. The carotid artery can be examined in any axis for detection of ulcers in atherosclerotic plaques. *White arrows* show ulcers. Reproduced with permission of Wolters Kluwer from Madani et al.[5]

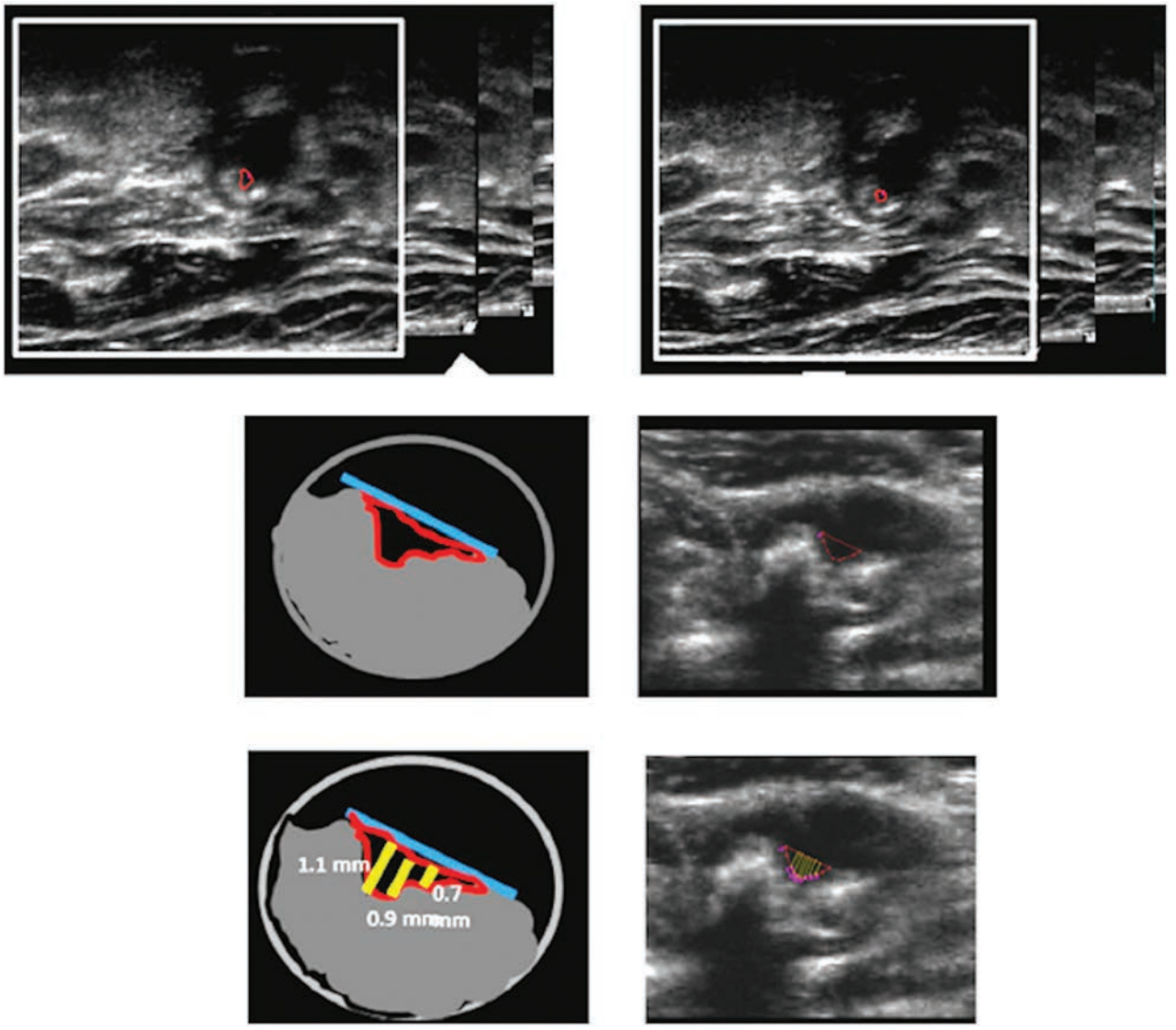

FIG 2. Measurement of ulcer volume and ulcer depth. Contours of ulcers were traced, and the depth of ulcers was measured in cross-sectional views. Each section had a thickness of 1 mm; ulcer volume was computed from the sum of the volumes of all sections in which ulceration was traced. Reproduced with permission of Wolters Kluwer from Kuk et al.[6]

REPLY:

We thank Dr J. David Spence for his interest in our Review Article, "Imaging Carotid Atherosclerosis Plaque Ulceration: Comparison of Advanced Imaging Modalities and Recent Developments."[1] We also thank the Editor of the *American Journal of Neuroradiology* for giving us the opportunity to respond to his comments.

The principles, usage, advantage, and related studies of 3D sonography (US) are discussed in the last paragraph of the "Sonography" section.[1] The application of 3D US in measuring plaque stenosis and volume is mentioned in the same paragraph. An example of comparing 3D and 2D US in depicting carotid ulceration is shown in Fig 4. In the On-line Table, we cite the study by Heliopoulos et al[2] (reference 36 in the article), which demonstrates that the 3D US shows the ulceration more frequently than 2D US and has slightly superior interobserver reproducibility.[2]

The purpose of this Review Article was to compare imaging modalities in the evaluation of carotid ulceration. We primarily reviewed studies that compared multiple methods, as summarized in the On-line Table. We thank Dr Spence for bringing to our attention his valuable work with 3D US in imaging ulcerations.[3,4]

http://dx.doi.org/10.3174/ajnr.A5146

REFERENCES

1. Yuan J, Usman A, Das T, et al. **Imaging carotid atherosclerosis plaque ulceration: comparison of advanced imaging modalities and recent developments.** *AJNR Am J Neuroradiol* 2016 Dec 22. [Epub ahead of print] CrossRef Medline
2. Heliopoulos J, Vadikolias K, Piperidou C, et al. **Detection of carotid artery plaque ulceration using 3-dimensional ultrasound.** *J Neuroimaging* 2011;21:126–31 CrossRef Medline
3. Madani A, Beletsky V, Tamayo A, et al. **High-risk asymptomatic carotid stenosis ulceration on 3D ultrasound vs TCD microemboli.** *Neurology* 2011;77:744–50 CrossRef Medline
4. Kuk M, Wannarong T, Beletsky V, et al. **Volume of carotid artery ulceration as a predictor of cardiovascular events.** *Stroke* 2014;45:1437–41 CrossRef Medline

J. Yuan
M. Graves
Department of Radiology
University of Cambridge
Addenbrooke's Hospital
Cambridge, UK